Systematic Studies on 3d-3d and 3d-4f Multimetallic Complexes with Interesting Magnetic and/or Luminescent Properties

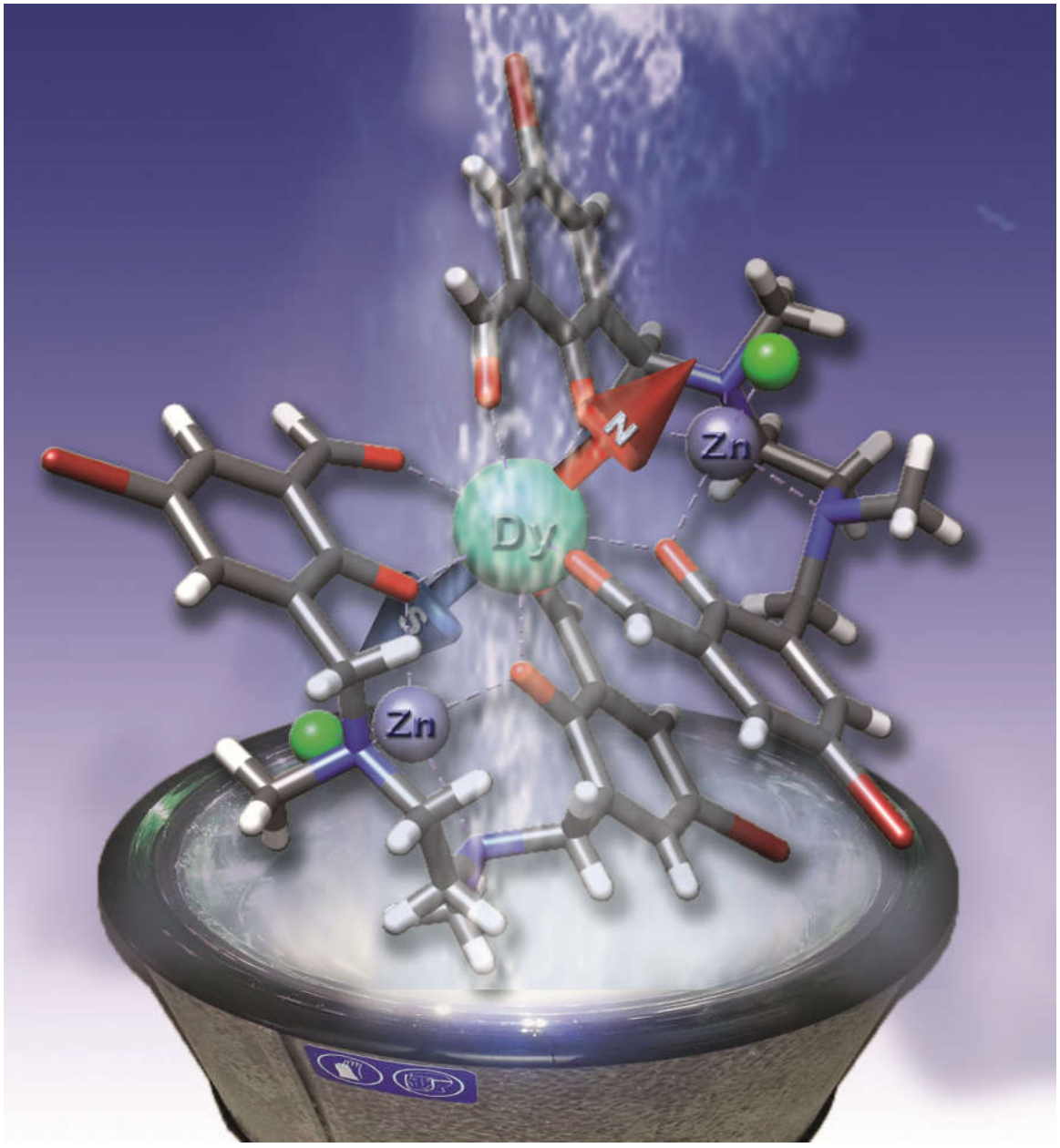

eman ta zabal zazu

Universidad del País Vasco

Euskal Herriko Unibertsitatea

Itziar Oyarzabal Epelde

Diciembre 2015

eman ta zabal zazu

Universidad del País Vasco
Euskal Herriko Unibertsitatea

Departamento de Química Aplicada/Kimika Aplikatua Saila

Systematic Studies on 3d-3d and 3d-4f Multimetallic Complexes with Interesting Magnetic and/or Luminescent Properties

Memoria presentada por

Itziar Oyarzabal Epelde

Para optar al grado de

Doctora por la Universidad del País Vasco/Euskal Herriko Unibertsitatea

Donostia-San Sebastián, diciembre 2015

Eskerrak

En primer lugar, debo agradecer de manera especial y sincera a mis directores José Manuel Seco y Enrique Colacio. Al primero por la confianza depositada en mí, por invitarme a su grupo cuando todavía era una estudiante de licenciatura y por todo el apoyo recibido durante estos cuatro años. Al segundo, por todo su apoyo, conocimiento, paciencia y dedicación. Porque entre los dos habéis hecho de todo esto una realidad.

A la Dra. María Ángeles Garralda, y por extensión, a todo el grupo de Química Inorgánica de la Facultad de Química. Bereziki Eider San Sebastián eta Claudio Mendicute doktoreei, lau urte hauetan emandako babesagatik eta Andoni Zabala lankideari, tesiaren azken txanpa honetan bere laguntza ezinbestekoa izan delako.

A Luis Botana por toda la colaboración prestada, pero sobre todo, por los buenos momentos que me ha dado y a Betty, por transmitirnos tanta alegría y positivismo.

A los colaboradores de la Universidad de Granada y en especial a los tres "Antonios" (Rodríguez, Calahorro y Mota), por haberme ayudado en todo lo que ha estado en su mano.

Al Dr. Juan Manuel Gutiérrez, por haberme acogido en su grupo de investigación y a Beñat, Amaia, Aroa, Jagoba, Saioa y Santi, por haberme hecho sentir que formaba parte del grupo. Beñat Artetxe eta Amaia Iturrospe doktoreei batez ere, luminiszentzia neurketengatik lehenengoari eta kotxe bidaietan izandako elkarrizketa eta emandako babesagatik bigarrenari. Era berean Javier Cepeda eta Sonia Perez doktoreei, eskainitako "posta" zerbitzuagatik.

Thanks to Dr. Euan Brechin and his group, Ross, Sergio, Anders, Joselillo, Helen and Priyanka, for making me feel like at home and helping me in everything. Thanks also to Carlos, for all the funny moments and to Julia, for the good moments and for taking care of me.

A los Doctores Eliseo Ruiz y Daniel Aravena por los cálculos teóricos y a los Doctores Marco Evangelisti y Agustín Camón por las medidas magnéticas en dc a bajas temperaturas.

Eusko Jaurlaritzako Hezkuntza, Hizkuntza Politika eta Kultura Sailari doktoretza aurreko bekagatik eta Euskal Herriko Unibertsitateari.

A los servicios generales (SGIKER) de la Universidad del País Vasco y, en especial, a los doctores Leire San Felices, Mihail Ipatov, Iñaki Orue y Javier Sangüesa, ya que su buen hacer ha sido fundamental para el desarrollo de este trabajo.

2006ko irail hartan kimikako fakultatean gure bizitzak lehenengo aldiz gurutzatu zirenetik ondoan izan ditudan Aintzane, Eneko, Irati, June, eta Nereari, eta laguna izateaz gain familia ere baden Aitziberri. Eta nola ez, betidanik alboan izan ditudan koadrilako kideei.

Azkenik, nire bihotzean leku garrantzitsuena okupatzen duen familiari, bereziki, ama, aita eta ahizpari, beraiek gabe sekula ez nintzatekeelako naizena izango.

Eskerrik asko denoi bihotz-bihotzez

A Pepe, la persona que más hubiese disfrutado leyendo este trabajo

TABLE OF CONTENTS

ABBREVIATIONS and ACRONYMS

Abbrev. / Acronyms	Meaning
H_2L	N,N'-dimethyl-N,N'-bis(2-hydroxy-3-formyl-5-bromobenzyl)-ethylenediamine
H_2L^1	N,N',N"-trimethyl-N,N"-bis(2-hydroxy-3-methoxy-5-methylbenzyl)-diethylenetriamine
POM	Polyoxometalate
MOF	Metal-Organic-Framework
MeOH	Methanol
EA	Elemental Analysis
TGA	Thermogravimetric Analysis
XRPD	X-Ray Powder Diffraction
CshM	Continuous Shape Measurements
SC-XRD	Single Crystal X-ray Diffraction
DR-UV-vis	Diffuse Reflectance UV-vis Spectroscopy
PL	Photoluminescence Spectroscopy
DFT	Density Functional Theory
CASSCF	Complete Active Space Self-Consistent Field
RASSI	Restricted Active Space State Interaction
H	Applied Magnetic Field
χ_M	Molar Magnetic Susceptibility
M	Magnetization
F	Ferromagnetic
AF	Antiferromagnetic
J	Coupling Constant
zJ'	Intermolecular Interactions
g	Zeeman Factor
ZFS	Zero Field Splitting
D	Zero Field Splitting Parameter
S	Spin
L	Angular Orbital Momentum
λ	Spin-orbit Coupling Parameter
κ	Orbital Reduction Factor

Abbrev. / Acronyms	Meaning
MMMF	Functional Magnetic Molecular Material (FMMM in English)
MMMMF	Multifunctional Magnetic Molecular Material (MFMMM in English)
SIM	Single Ion Magnet
SMM	Single Molecule Magnet
SCM	Single Chain Magnet
EMC	Magneto-Caloric Effect (MCE in English)
RMI	Magnetic Resonance Imaging (MRI in English)
SCO	Spin Crossover
MMFCC	Functional Magnetic Molecular Coordination Compounds (FMMCC in English)
χ_M'	In-phase Magnetic Molar Susceptibility
χ_M''	Out-of-Phase Magnetic Molar Susceptibility
U	Energy Barrier
U_{eff}	Effective Energy Barrier
T_B	Blocking Temperature
τ_0	Flipping Rate
τ	Relaxation Time
QTM	Quantum Tunneling of the Magnetization
τ_{QTM}	Flipping Rate due to QTM
B	Raman Relaxation Parameter
n	Raman Relaxation Exponential Parameter
KD	Kramer's Doublet

SUMMARY

The work presented in this Ph.D. dissertation falls within the research areas of *Molecular Magnetism* and *Photochemistry*. The aim of this work is not only the preparation of coordination complexes with interesting magnetic (such as *Single Molecule Magnet* (SMM) behaviour) and luminescent properties, but also the establishment of synthetic strategies for obtaining molecule-base materials with desired properties.

The **Introduction** deals with the basic topics of the research area on which this Ph.D. thesis has been focused and with the motivation of the work in the current context. Specifically, the main characteristics of SMMs, lanthanide based luminescent compounds and molecular refrigerants are described. The chapter concludes with the main objectives of this Ph.D. thesis.

Chapter 1 collects the synthesis and characterization of six novel Ni(II) complexes, ranging from mononuclear to tetranuclear, which were prepared from the versatile polytopic Mannich base ligand N,N'-dimethyl-N,N'-bis(2-hidroxy-3-formyl-5-bromo-benzyl)ethylenediamine (H_2L). The anionic coligands (nitrate, acetylacetonate, thiocyanate, acetate and azide) and reaction conditions play crucial roles in determining the final structure of these compounds and consequently, their magnetic properties. DFT calculations on the X-ray structures were performed to support the magneto-structural data.

In **Chapter 2**, four new dinuclear complexes were prepared from the compartmental ligand N,N',N"-trimethyl-N,N"-bis(2-hidroxy-3-methoxy-5-methylbenzyl)-diethylenetriamine (H_2L^1) and different carboxylate ligands, which were magnetically and structurally characterized. The ferromagnetic coupling observed in these complexes was justified by the phenomenon of the countercomplementarity between diphenoxo and carboxylate bridging ligands, which was supported by DFT calculations on the X-ray structures and model compounds.

Chapter 3 focuses on the magnetic and luminescent properties of a series of dinuclear Zn(II)Ln(III) complexes prepared from the ligand H_2L, $Zn(OAc)_2{\cdot}2H_2O$ and $Ln(NO_3)_3{\cdot}nH_2O$, Ln standing for all the lanthanide ions from Pr to Yb with the exception of Pm (all its isotopes are radioactive). The Nd(III), Dy(III), Er(III) and Yb(III) derivatives show field-induced slow relaxation of the magnetization, with U_{eff} (thermal energy barrier for the reversal of magnetization) values ranging from 14.12 to 41.55 K when considering only the Orbach relaxation process. The chromophoric L^{2-} ligand is able to act as an "antenna" group, sensitizing the near-infrared (NIR) Nd(III) and Yb(III)-based

luminescence and therefore, both compounds can be considered as dual magneto-luminescent materials. In addition, the Sm(III), Eu(III) and Tb(III) derivatives exhibit characteristic emissions in the visible region.

Chapter 4 describes the changes on SMM properties caused by the substitution of diamagnetic Zn(II) ions for paramagnetic metals (M(II) = Cu, Ni, Co) in the ZnLn dinuclear species reported in Chapter 3. The magnetic exchange interactions between the 3d metal and lanthanide {Ln(III) = Nd, Gd, Tb, Dy, Er} ions are studied and supported by DFT calculations carried out on Gd based analogues. Despite the SIM (Single Ion Magnet) properties shown by ZnDy and ZnEr compounds, the NiDy, NiEr and CoDy analogues show a weak relaxation of the magnetization, whereas no frequency dependence of the *ac* (*alternating current*) signal is observed for CuDy, CuEr, NiNd and CoEr compounds. This behaviour can be due either to the small separation of the low lying split sublevels generated by the weak magnetic exchange interactions between the 3d and 4f metal ions or to the random transversal field for the Ln(III) ions created by the paramagnetic metal ion, which favours the fast QTM (Quantum Tunneling of the Magnetization) process. However, as seen in bibliography, isotropic paramagnetic 3d ions such as Cr(III) induce stronger exchange interactions between the 3d and 4f metal ions, which reduces the QTM and therefore, leads to an enhancement of the effective energy barrier. Moreover, the CoY analogue shows field-induced slow relaxation of the magnetization with a U_{eff} value of 15.68 K when considering only the Orbach relaxation process. This value is much lower than the expected value, which indicates that the relaxation takes place *via* Raman mechanism.

Chapter 5 collects the synthesis and characterization of nine dinuclear and tetranuclear MnGd and MnDy species prepared from both H_2L and H_2L^1 ligands. Antiferromagnetic and very weak ferromagnetic interactions are found in the MnGd compounds, which are supported by DFT calculations on X-ray structures. Experimental magneto-structural correlations are carried out from these and other complexes found in bibliography. The importance of MnGd systems comes from their enhanced magneto-caloric effect (MCE), which makes them useful for cooling applications *via* adiabatic demagnetisation.

Chapter 6 shows how the simple model based on the prolate-oblate electron-density distribution of the Ln(III) ions can be used to rationally design mononuclear lanthanide-based complexes with SIM behaviour and high energy barriers. Specifically, the compartmental ligand H_2L is used to form several Zn-Dy-Zn species, in which the Dy(III) ions exhibit a DyO_8 coordination sphere with square antiprism geometry and

strong easy-axis anisotropy of the ground state. *Ab initio* calculations performed on the complex [ZnCl(μ-L)Ln(μ-L)ClZn][$ZnCl_3(CH_3OH)$]·$3CH_3OH$ support the easy-axis anisotropy of the ground Kramer's doublet (KD), the direction of the anisotropy axis deducted from the oblate electron-density distribution and the thermally activated mechanism for the slow relaxation of the magnetization. In fact, this compound shows a thermal energy barrier for the reversal of the magnetization of 140 K in zero field, whereas the isostructural Zn-Er-Zn complex does not present significant SIM behaviour, as expected for the prolate electron-density distribution of the Er(III) ion. By substituting the halogen atoms and counteranions six additional complexes can be obtained, which exhibit U_{eff} values ranging from 144 to 170 K in zero *dc* field.

On the other hand, the replacement of the counteranion for PF_6^- leads to a more symmetrical structure where there exists a C_2 axis on the Dy(III) ion. The presence of the C_2 axis imposes collinearity of the anisotropic axes of the two lowest KDs, so that the thermal activated relaxation is suppressed *via* the first excited KD and takes place *via* the second excited state, giving rise to a dramatic increase in the effective energy barrier (U_{eff} = 268 K in zero field). *Ab initio* calculations support that the relaxation of the magnetization is symmetry driven and that it occurs *via* the second excited state.

The grafting of Single Ion Magnets into polyoxometalates (POMs) is studied in **Chapter 7** with the aim of taking advantage of the rigidity and insulating ability of POMs, which could help to minimize the intermolecular interactions responsible for QTM. For this purpose, the Keggin-type tungstosilicate α-$K_8[SiW_{11}O_{39}]$·$13H_2O$ is chosen, which allows the grafting of lanthanide complexes with highly symmetric axial coordination environments in its vacant position. However, the obtained compound only shows a modest relaxation of the magnetization. This behaviour could be due to the potassium and water bridges that connect different entities, which prevent the formation of well isolated molecules in the crystal lattice, thus disfavouring the SIM behaviour. The distortion of the DyO_8 coordination polyhedron from the ideal geometry and the fact that there are not clear shortest Dy-O distances in the DyO_8 coordination polyhedron as to create an axial ligand field for the oblate electron-density of the Dy(III) would also help to such worsening of the SIM behaviour.

To end up, the **Chapter 8** deals with new experiments that are planned for the near future to complete or even improve this work, which includes studying the SMM properties of several Co(II) compounds, changing the acetate bridging groups of ZnLn dinuclear complexes for other bridges in order to improve the luminescent properties

and grafting SIMs into surfaces. Additional works that have been carried out during this Ph.D. thesis but are not included in this work are also mentioned in this section.

INTRODUCCIÓN

I. QUÍMICA DE LA COORDINACIÓN Y MAGNETISMO MOLECULAR

Una de las áreas más activas y de mayor interés en Ciencia de Materiales es la que se dedica al desarrollo, caracterización y explotación tecnológica de *Materiales Magnéticos Moleculares Funcionales* (MMMF).[1] Entre los MMMF ocupan un lugar destacado los que se encuentran basados en compuestos de coordinación, ya que utilizando la versatilidad de la Química de Coordinación y eligiendo adecuadamente los bloques precursores que se van a ensamblar, es posible construir moléculas magnéticas que, debido a su reducido tamaño, presenten propiedades físicas novedosas como, por ejemplo, efectos cuánticos, efectos de memoria, etc. Las *Moléculas Imán* (SMM, "single molecule magnet"),[2] las *Cadenas Imán* (SCM, "single chain magnet"),[3] los *Materiales Magnéticos Moleculares Multifuncionales* (MMMMF) que presentan asociación de varias propiedades físicas (magnetoópticas, magnetoconductoras, magnéticas y nanoporosidad, etc),[4] los *nanorrefrigerantes*,[2a,2c,5] los *agentes de contraste en resonancia magnética de imagen* (RMI)[6] y los materiales magnéticos inteligentes, que responden a estímulos externos (luz, presión, temperatura…), tales como los compuestos *transición de espín* (spin crossover, SCOs)[7] son solo algunos ejemplos de *Materiales Magnéticos Funcionales basados en Compuestos de Coordinación* (MMFCC).

Estos materiales presentan aplicaciones potenciales en campos tan diversos como el almacenamiento de información, computación cuántica, imágenes por resonancia magnética nuclear, spintrónica molecular, refrigeración magnética, sensores químicos, etc.[8] Con el estudio de estos MMFCC se pretenden establecer las bases metodológicas que permitan entender las propiedades de los materiales ya obtenidos, para posteriormente diseñar y obtener de manera controlada, nuevos materiales con mejores propiedades para aplicaciones tecnológicas.

En este trabajo se abordará, fundamentalmente, el diseño, preparación, caracterización físico-química y estudio teórico de nuevos compuestos de coordinación homo y polinucleares de tipo 3d, 4f, 3d-4f y 3d-4f-3d que puedan ayudar a establecer correlaciones magneto-estructurales y que se puedan comportar como *moléculas imán* (SMMs) y, en algunos casos, como materiales duales SMMs/luminiscentes.

II. CORRELACIONES MAGNETO-ESTRUCTURALES

El primer paso en el diseño de *moléculas imán* consiste en entender cuáles son los principales factores estructurales que gobiernan las interacciones magnéticas. Los requisitos fundamentales para observar comportamiento de SMM son dos: un estado fundamental de espín alto y, esencialmente, una alta anisotropía magnética.[9] En los complejos homo y heteronucleares el espín del estado fundamental depende, sobre todo, de la naturaleza de los iones metálicos, de las interacciones de canje magnético entre estos y de su topología. Por ello, entender las características estructurales que rigen las interacciones de canje magnético a través de los ligandos puente constituye un primer paso necesario para el diseño de materiales magnéticos basados en compuestos de coordinación. En este sentido, hay que indicar que las correlaciones magneto-estructurales resultan ser herramientas muy útiles, ya que permiten evaluar cualitativamente el acoplamiento magnético en compuestos de coordinación y obtener, posteriormente, compuestos con las propiedades magnéticas deseadas.

En vista de lo anteriormente expuesto, la elección adecuada del ligando, coligandos e iones metálicos juega un papel crucial en la arquitectura final que adopta un determinado compuesto de coordinación y en consecuencia, en sus propiedades magnéticas.

Por lo que respecta al ligando, se puede destacar que los ligandos compartimentales de tipo bases de Schiff han sido ampliamente utilizados en Química de Coordinación y Magnetismo Molecular. Cuando este tipo de ligandos presentan sitios de coordinación internos bis(iminofenol) N_2O_4, la coordinación en este sitio a átomos metálicos de diferentes radios iónicos se puede encontrar limitada por la rigidez de la estructura inducida por los dobles enlaces imino C=N.[10]. Por el contrario, las bases de Mannich, que no contienen dobles enlaces C=N, muestran mayor flexibilidad y, por tanto, mayor facilidad para coordinarse a metales con diferentes radios iónicos en el sitio interno del ligando compartimental. Por ello, y por no contener átomos de hidrógeno unidos a los grupos amino, que pudieran eventualmente formar enlaces de hidrógeno intermoleculares y enmascarar las propiedades magnéticas provenientes de las moléculas de compuestos de coordinación aisladas, se eligieron este tipo de ligandos.

En cuanto a los coligandos, durante los últimos años los aniones formados por tres átomos, tipo aziduro o tiocianato, han sido extensamente utilizados debido a las siguientes ventajas que presentan.[11] En primer lugar, favorecen las interacciones

magnéticas entre centros metálicos, ya que no son demasiado largos (sólo tres átomos). En segundo lugar, pueden presentar diferentes modos de coordinación de tipo puente entre centros metálicos, lo que posibilita la construcción de diversas e interesantes estructuras con interacciones magnéticas eficientes entre centros metálicos. Dentro de este tipo de ligandos triatómicos, uno de los más versátiles y utilizados es el ligando aziduro.[11,12] Este ligando presenta diferentes modos de coordinación (Figura 1.a) y se puede decir que cuando actúa de puente entre dos iones metálicos a través de un solo átomo de nitrógeno (modo de coordinación *end-on*), la interacción es ferromagnética, mientras que si se coordina por los dos átomos de nitrógeno de los extremos (*end-to-end*) la interacción es de naturaleza antiferromagnética. El ligando tiocianato, en cambio, no muestra tantos modos de coordinación como el aziduro (Figura 1.b) y no es tan efectivo para la transmisión del acoplamiento magnético.[11] Aunque, en este caso, la coordinación tipo *end-on* esté favorecida energéticamente, existen numerosos complejos en los que el ligando tiocianato actúa de puente y la interacción transmitida a través de este ligando puede ser tanto ferromagnética como antiferromagnética.[11]

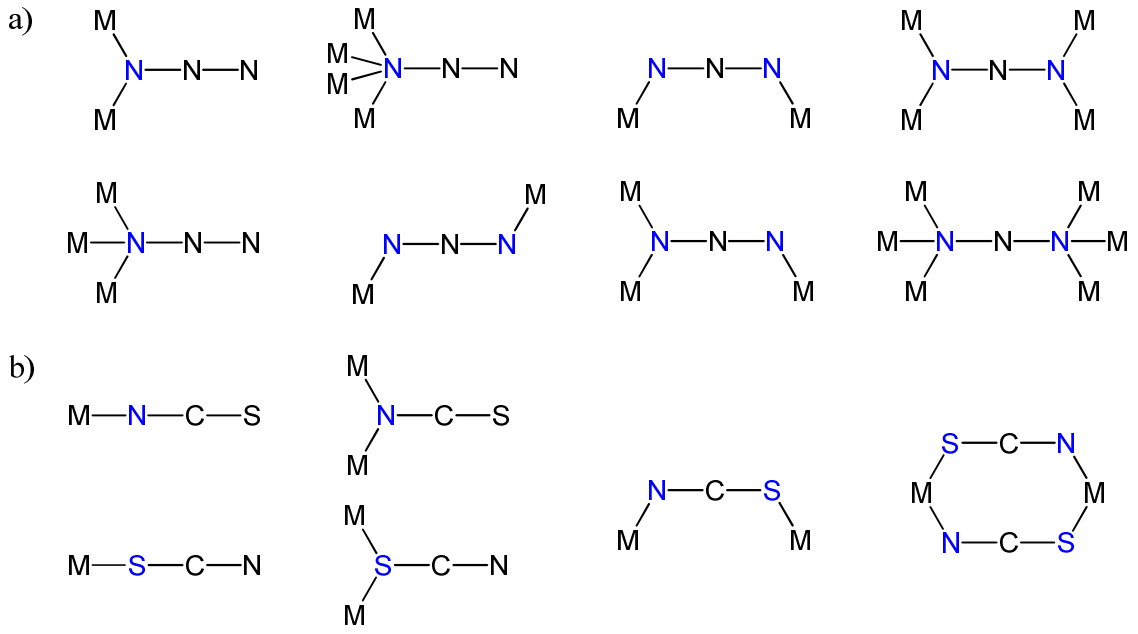

Figura 1.- Representación de los modos del coordinación de los ligandos aziduro (a) y tiocianato (b).

Por otra parte, los coligandos carboxilato de tipo *syn-syn* son conocidos por transmitir acoplamiento antiferromagnético entre los iones metálicos. Sin embargo, si

otros puentes están presentes, puede ser que sus efectos se sumen (complementaridad orbital) o que se contrabalanceen (contracomplementaridad orbital).[13] De este modo, algunos complejos que contienen puentes mixtos *syn-syn* carboxilato junto a puentes alcoxo,[14] hidroxo[15] o aqua,[16] exhiben interacciones ferromagnéticas o antiferromagnéticas muy débiles debido al fenómeno de la contracomplementaridad.

Finalmente, por lo que respecta a la elección de átomos metálicos, cabe indicar que se han realizado numerosas correlaciones magneto-estructurales en compuestos que poseen átomos de Cu(II), los cuales, debido a su bajo espín y, sobre todo, a su carácter isotrópico, no son buenos candidatos para obtener imanes moleculares. Sin embargo, el ión Ni(II) tiene una considerable anisotropía magnética generada por el acoplamiento espín-órbita de segundo orden y un mayor espín, por lo que, es un candidato prometedor para la preparación de SMMs. A pesar de ello, sólo se han obtenido hasta el momento unos pocos ejemplos de imanes moleculares de Ni(II).[17]

Una parte de este trabajo de Tesis se dedica a la caracterización magneto-estructural de complejos polinucleares de Ni(II) con ligandos compartimentales de tipo bis(fenoxoamino) y otros ligandos auxiliares (puente o terminales de tipo aziduro, carboxilato, tiocianato, acetilacetonato, metóxido, etc) con objeto de conocer los factores estructurales (tanto de los ligandos como del ión metálico) que conducen a interaciones ferromagnéticas y a estados fundamentales de espín alto, los cuales podrían favorecer el comportamiento de molécula imán.

III. MOLÉCULAS IMÁN (SMMs)

El campo del Magnetismo Molecular basado en compuestos de coordinación ha experimentado un fuerte impulso en los últimos años con el descubrimiento de que algunos compuestos de coordinación polinucleares de tipo clúster y tamaño nanoscópico mostraban relajación lenta de la magnetización e histéresis magnética por debajo de una determinada temperatura denominada temperatura de bloqueo (T_B). En estos nanoimanes moleculares, denominados *moléculas imán* (SMMs),[2] la histéresis proviene de la combinación de dos factores: por una parte, una interacción de canje magnético fuerte, que conduce a un estado fundamental de alto espín bien separado de los niveles excitados y, por otra parte, de una anisotropía uniaxial grande

(*D*). Estos dos factores generan una barrera térmica que impide la inversión del sentido de la magnetización (*U*).

Así, cuando se enfría el sistema en ausencia de campo magnético externo ($H_z = 0$), los estados fundamentales de espín $M_s = \pm S$ tienden a poblarse (Figura 2.a). Si se enfría aplicando un campo externo suficientemente intenso ($H_z \neq 0$), el espín de las moléculas se orienta en la dirección del campo aplicado, poblando uno de los estados fundamentales de espín debido a que, por efecto Zeeman (que provoca la ruptura de la degeneración de los niveles), energéticamente se hace más favorable y la magnetización (*M*) alcanza la saturación (Figura 2.b). Al anular el campo externo, la magnetización tiende a relajarse para volver a su estado de equilibrio ($M = 0$), pero para ello necesita superar la barrera de energía (Figura 2.c). Si la temperatura está por debajo de T_B, la magnetización queda bloqueada en una de sus orientaciones y, por tanto, tiende muy lentamente hacia el equilibrio. Es decir, el material presenta entonces histéresis magnética (histéresis o tendencia a conservar una propiedad en ausencia del estímulo que la ha generado), pues una vez se ha anulado el campo aplicado, la magnetización es diferente a cero.

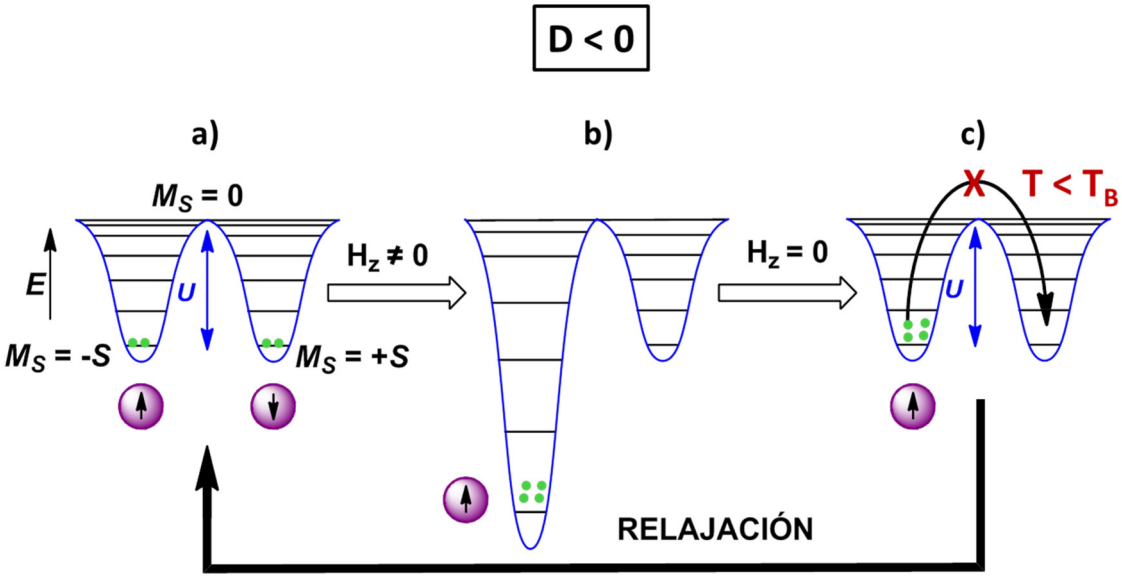

Figura 2.- Representación esquemática de la orientación de la magnetización al enfriar (a), aplicar un campo (b) y el proceso de relajación al eliminar el campo (c) para sistemas con $D < 0$ y *S* entero.

La altura de dicha barrera térmica, que impide la reorientación, depende del valor de espín y del parámetro de desdoblamiento a campo cero (anisotropía) según las ecuaciones:

$$U = S^2|D| \{S = \text{entero}\} \qquad \textit{(Ecuación 1)}$$

$$U = (S^2 - ¼)|D| \{S = \text{semientero}\} \qquad \textit{(Ecuación 2)}$$

Cabe destacar que para una molécula imán con espín entero *D* debe ser negativo, puesto que si *D* fuese positivo los estados M_s se colocarían, energéticamente hablando, de manera inversa; es decir, el estado fundamental sería $M_s = 0$ y por ello el sistema no sería activo magnéticamente. En cambio, los sistemas con *S* semientero no generan estados $M_s = 0$ (multiplicidad de espín = $2S + 1$), por lo que en principio el valor de *D* puede ser tanto positivo como negativo.

Aunque la mayor parte de los SMMs muestran un valor de *D* negativo, recientemente han sido publicados algunos complejos de Fe(I), Co(II) e Yb(III) que, teniendo valores de *S* semienteros y valores de *D* positivos, exhiben comportamiento de molécula imán.[18]

¿Pero cuál es el mecanismo por el que transcurre la relajación? Podemos decir que, en general, la relajación del espín de los sistemas paramagnéticos se puede producir por tres mecanismos diferentes de acoplamiento espín-fonón (Figura 3):[19]

1.- Proceso directo: El espín relaja absorbiendo o emitiendo un fonón con la misma energía que la diferencia de energía entre los dos estados de espín, $\hbar\omega$.

2.- Proceso Raman: El espín absorbe un fonón con una determinada frecuencia, ω_1, pasando a un estado virtual desde el cual relaja rápidamente emitiendo un nuevo fonón de frecuencia ω_2. Así, la energía transferida a la red es la diferencia entre la absorbida y la emitida por los dos fonones.

3.- Proceso Orbach: Es un proceso en dos etapas, en el cual se absorbe por proceso directo un fonón con una determinada frecuencia (ω_1) que excita el espín a un estado excitado, desde el cual relaja emitiendo un nuevo fonón de frecuencia ω_2. Por lo tanto, el espín es transferido indirectamente desde un nivel al otro del doblete fundamental pasando por un estado excitado.

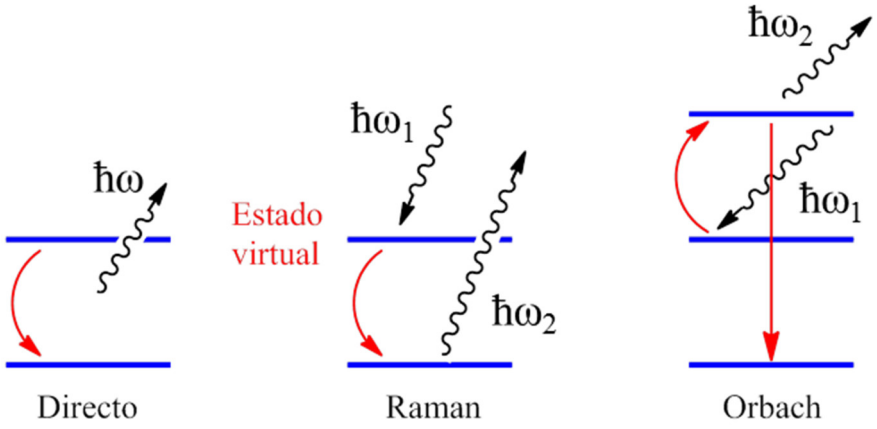

Figura 3.- Representación esquemática de los tres procesos de relajación.

El proceso Raman no tiene ninguna restricción en lo que respecta a la energía del fonón incidente, de forma que todo el espectro de fonones puede dar lugar a este proceso y, por tanto, se puede producir en todo el intervalo de temperaturas, desde temperatura ambiente a muy baja temperatura. La velocidad de relajación ($1/\tau$) dependerá de la siguiente ecuación:

$$\tau^{-1} = bT^n \qquad \textit{(Ecuación 3)}$$

donde b es un parámetro constante, T es la temperatura y los valores típicos del parámetro exponencial n son:

n = 9 (dobletes no-Kramer's (espín semientero))

n = 7 (dobletes Kramer's (espín entero))

n = 5 (multipletes con pequeño desdoblamiento)

Aún así, dependiendo de la estructura de los niveles, valores de n de entre 1 y 6 pueden ser considerados como razonables.[20]

Sin embargo, el proceso directo y el de Orbach utilizan energías que se encuentran localizadas en bandas muy estrechas. Como el proceso directo se da con fonones de baja energía se produce a bajas temperaturas, mientras que el proceso Orbach requiere fonones que sean capaces de excitar los espines a un estado excitado, de modo que este proceso prevalece a las temperaturas que corresponden a la diferencia de energía producida por el campo ligando. En este último caso, la velocidad de

relajación ($1/\tau$) depende del valor de la altura de la barrera (U) y de la temperatura (T), de acuerdo con la ecuación de Arrhenius:

$$\tau^{-1} = \tau_0^{-1} \exp(-U / k_B T) \qquad \textit{(Ecuación 4)}$$

donde τ_0 es la velocidad de cambio de la magnetización si no hubiese barrera de activación y K_B es la constante de Boltzmann.

Por otra parte, la naturaleza cuántica de estas moléculas posibilita la inversión del momento magnético por efecto túnel (QTM), es decir, sin tener que superar la barrera energética. Para sistemas con $D < 0$ y S = número entero, la anisotropía transversal permite la mezcla de estados degenerados M_s a ambos lados de la barrera favoreciendo, de esta forma, el túnel cuántico (Figura 4.a). Sin embargo, si S es un número semientero (sistema Kramer's), la mezcla de los estados M_s debido a la anisotropía transversal está prohibida a campo cero, ya que el teorema de Kramer's predice que el mínimo número posible de estados degenerados es dos. No obstante, el efecto túnel puede ser inducido tanto por interacciones dipolares, entre los momentos magnéticos de diferentes moléculas, como por interacciones hiperfinas, entre el espín electrónico y el espín nuclear, que crean un campo magnético transversal que permite la mezcla de los estados y el túnel cuántico.

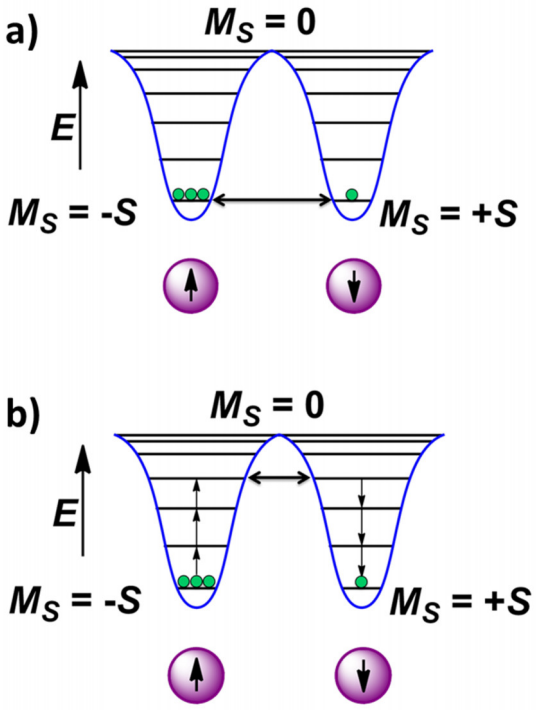

Figura 4.- Inversión de la magnetización por efecto túnel entre los estados de más baja energía (a) y por efecto túnel cuántico térmicamente activado (b).

A su vez, el efecto túnel puede tener lugar entre pares de estados excitados degenerados (Figura 4.b). Este es el fenómeno conocido como túnel cuántico térmicamente activado. Cuando ocurre este proceso, existe una barrera de activación térmica efectiva, U_{eff}, que es menor que la barrera de activación térmica esperada según la Ecuación 1.

Una estrategia para suprimir el túnel cuántico consiste en diluir los compuestos, es decir, formar complejos isoestructurales de metales diamagnéticos que cocristalizan con el compuesto a estudiar. De este modo, se eliminan las interacciones dipolares causantes del túnel cuántico. Otra estrategia consiste en aplicar un pequeño campo magnético *dc* (corriente continua), ya que dicho campo estabiliza los niveles M_s negativos respecto a los positivos y, por tanto, elimina la degeneración de estos estados a ambos lados de la barrera (Figura 5). El sistema queda entonces fuera de resonancia, por lo que se favorece el proceso de relajación térmicamente activado. De esta forma se determinaría, en los casos en los que hay túnel cuántico, un valor más cercano al esperado para la barrera de activación térmica.

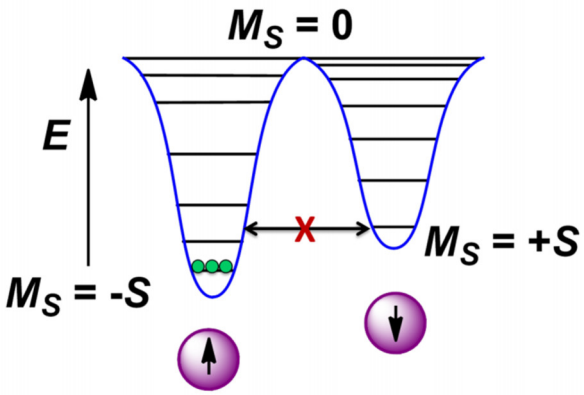

Figura 5.- Estrategia para suprimir el túnel cuántico.

Sin embargo, si se sigue aumentando el campo llegará un momento en el que un par de niveles + M_s y – M_{s+n} (n = 1, 2, 3…) tendrán la misma energía y se producirá el túnel cuántico otra vez. Esta es la razón por la que aparecen escalones en las curvas de histéresis de estos sistemas. La Figura 6 representa, como ejemplo, las curvas de histéresis magnética del compuesto $[Mn_{12}O_{12}(O_2CCH_2Br)_{16}(H_2O)_4]\cdot 4CH_2Cl_2$ a diferentes temperaturas.[21] Las zonas verticales, donde la magnetización varía rápidamente, son las correspondientes al túnel cuántico, mientras que en las horizontales no hay túnel cuántico.

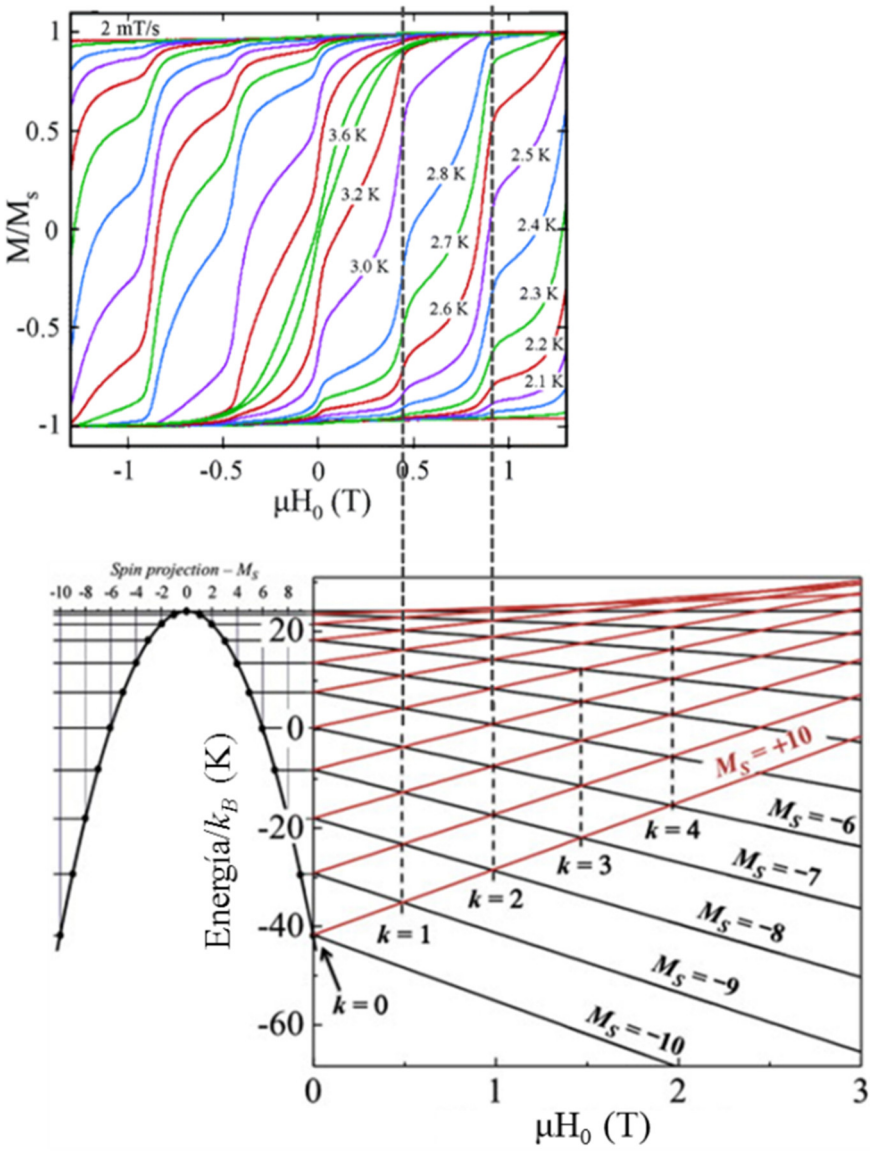

Figura 6.- Arriba: curvas de histéresis magnética a diferentes temperaturas. Abajo: variación de la energía de los diferentes estados magnéticos en función del campo magnético aplicado para el sistema Mn_{12}.[21]

II.1. Detección del comportamiento SMM

El estudio del comportamiento SMM se puede llevar a cabo mediante dos tipos de medidas magnéticas. El primer método consiste en medir la dependencia de la magnetización con el campo y comprobar si hay histéresis, controlando los cambios que hay en la magnetización del compuesto al variar el campo cíclicamente de + *H* a – *H* y de nuevo a + *H* a temperaturas muy bajas (Figura 6, arriba). La aparición de

histéresis en la gráfica resultante demuestra que la magnetización se mantiene a pesar de anular el campo ($M \neq 0$ a $H = 0$) y que, por lo tanto, el complejo muestra una barrera de energía para la reorientación de la magnetización a la temperatura a la que se ha llevado a cabo la medida. La temperatura de bloqueo (T_B), será aquella en la que se abre el ciclo de histéresis en las medidas de magnetización con respecto al campo y depende de la velocidad de barrido (barrido más rápido = ciclo más ancho).

El segundo método, generalmente el más utilizado, consiste en medir la susceptibilidad magnética en campo alterno (*ac*). Cuando se aplica un campo magnético oscilante, la magnetización de las moléculas que presentan relajación lenta de la magnetización no puede seguir los cambios de dirección del campo magnético si su frecuencia es muy rápida, por lo que aparece una dependencia de χ' (parte real) y χ'' (parte imaginaria) con la frecuencia del campo (Figura 7). En los complejos sin barrera energética para la relajación, en cambio, la magnetización cambia de sentido tan rápido como lo hace la fase del campo, exhibiendo, por tanto, únicamente el componente en fase (χ_M') de la susceptibilidad *ac* ($\chi_M'' = 0$). Hay que mencionar que la señal χ_M'' depende de la temperatura y de la frecuencia del campo *ac*, desplazándose el máximo a temperaturas más altas cuando se incrementa la frecuencia.

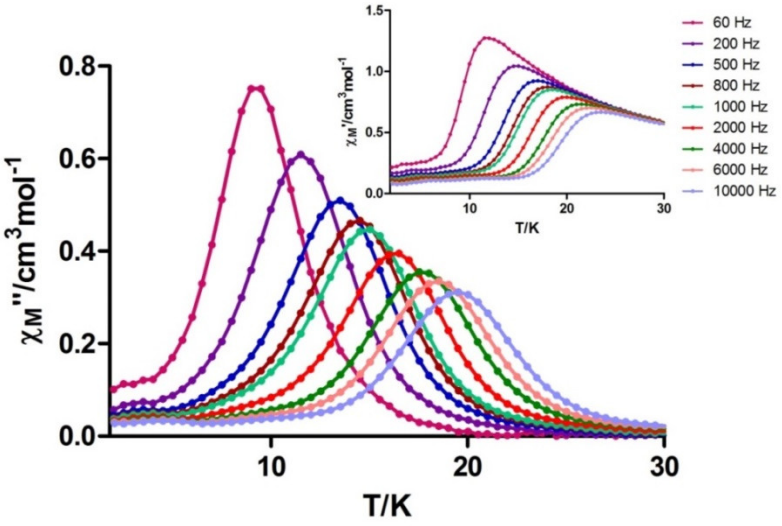

Figura 7.- Ejemplo de medidas de susceptibilidad *ac* en fase y fuera de fase (recuadro interior) en función de la temperatura a diferentes frecuencias.

Los datos *ac* también se pueden utilizar para cuantificar la relajación de la magnetización. Del ajuste de las curvas obtenidas en las gráficas χ_M'' vs. frecuencia

(Figura 8) a la ecuación de Casimir-Du Prè[22] (Apéndice, Sección V), se pueden obtener los tiempos de relajación (τ) para cada temperatura.

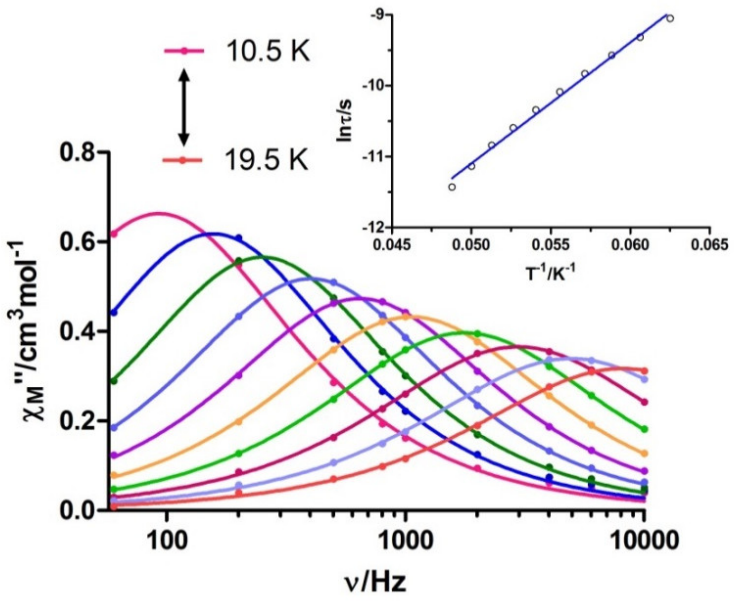

Figura 8.- Ejemplo de gráficas χ_M" vs. frecuencia. Las líneas sólidas representan el ajuste a la ecuación de Casimir-Du Prè para la obtención de los tiempos de relajación para cada temperatura. Recuadro interior: Ajuste de Arrhenius para los tiempos de relajación.

Cuando la relajación espín-red se da por el proceso Orbach, los tiempos de relajación siguen la ley de Arrhenius (Ecuación 4), siendo posible obtener de dicho ajuste los valores de la barrera de energía para la reorientación de la magnetización (*U*) y la velocidad de cambio de la magnetización si no hubiese barrera de activación (τ_0). La desviación de la linealidad de los tiempos de relajación, a bajas temperaturas, indica la existencia de diversos procesos de relajación. Así, cuando el proceso Orbach compite con procesos de relajación Raman o QTM, los datos se pueden ajustar a las siguientes ecuaciones, las cuales tienen en cuenta la contribución de ambos procesos:

$$\tau^{-1} = \tau_{QTM}^{-1} + \tau_0^{-1} \exp(-U_{eff}/k_B T) \qquad \textit{(Ecuación 5)}$$

$$\tau^{-1} = BT^n + \tau_0^{-1} \exp(-U_{eff}/k_B T) \qquad \textit{(Ecuación 6)}$$

En ambas ecuaciones el segundo término corresponde al proceso de relajación Orbach. En la Ecuación 5, el término τ_{QTM}^{-1} corresponde a la frecuencia de relajación

del proceso QTM, mientras que el primer término de la Ecuación 6 cuantifica el proceso Raman.

Otro factor importante en el análisis del comportamiento SMM es el parámetro α. Este parámetro proporciona información sobre el número de procesos térmicos y/o cuánticos que rigen la relajación de la magnetización y se obtiene a partir de las gráficas χ_M' vs. χ_M'' (conocidas como gráficas Cole-Cole). Las gráficas Cole-Cole se construyen a partir de los datos de susceptibilidad *ac* a diferentes temperaturas, obteniendo curvas semicirculares para cada temperatura (Figura 9). Ajustando dichas curvas al modelo de Debye[23] (Apéndice, Sección V), se obtiene el parámetro α para cada temperatura, el cual tiene un valor comprendido entre 0 y 1. Si α = 0, sólo habrá un proceso de relajación térmica, mientras que valores más altos de α indicarán la presencia de múltiples procesos de relajación. De estos ajustes y del valor del máximo de cada curva semicircular (donde $\omega\tau = 1$), se pueden extraer también los tiempos de relajación.

Por último, cabe destacar que a pesar de que las medidas de susceptibilidad *ac* son buenos indicadores del comportamiento SMM, para tener la certeza de que un compuesto tiene tal comportamiento es necesario medir las curvas de histéresis. Sin embargo, los ciclos de histéresis a menudo no son evidentes hasta que la medida se realiza a temperaturas por debajo de la capacidad de la mayoría de los magnetómetros (< 1.8 K), lo que dificulta esta comprobación del comportamiento SMM.

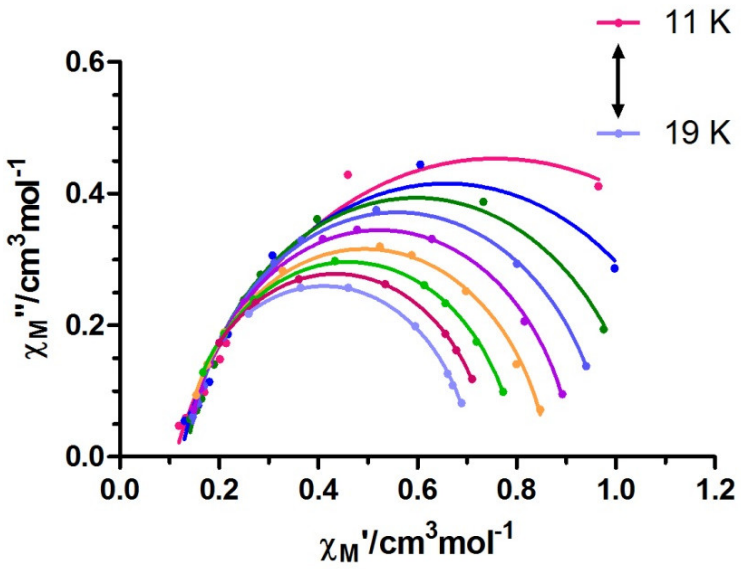

Figura 9.- Ejemplo de gráfica Cole-Cole en el intervalo de temperatura 11 - 19 K.

II.2. Antecedentes y resultados previos

El primer cluster sobre el que se observó este comportamiento de SMM fue el compuesto $[Mn_{12}O_{12}(acetato)_{16}](H_2O)_4$, conocido dentro de la comunidad del Magnetismo Molecular como Mn12-ac (Figura 10).[24] Esta molécula se caracteriza por poseer un estado fundamental de espín S = 10, que proviene de las interacciones antiferromagnéticas no compensadas entre los espines S = 3/2 de los iones Mn(IV) y los espines S = 2 de los iones Mn(III).

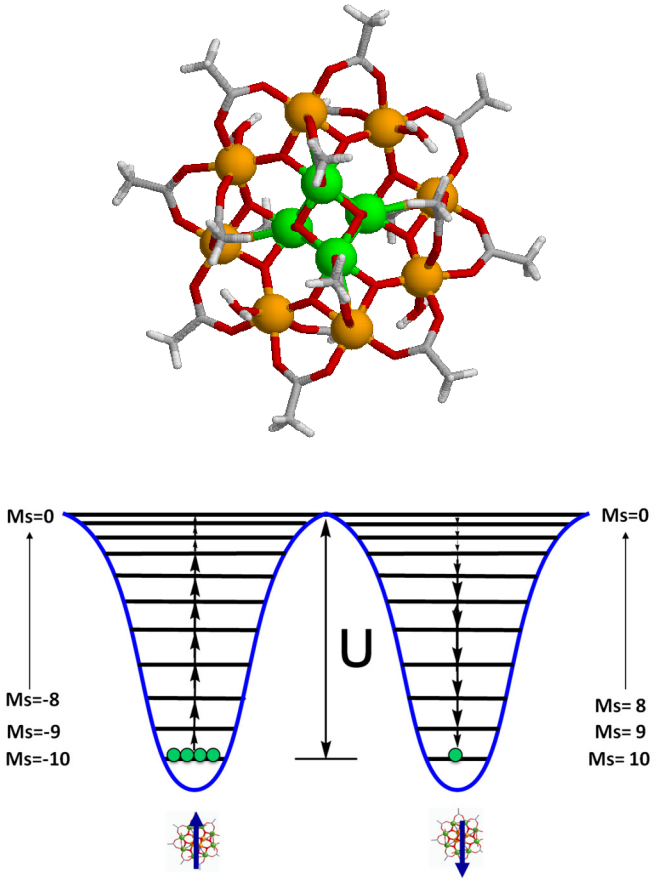

Figura 10.- Estructura cristalina (arriba, código de colores: O = rojo, C = gris, H = blanco, Mn(IV) = verde, Mn(III) = naranja) y niveles de energía (abajo) en el Mn12-ac.

Debido a una anisotropía magnética axial importante (D < 0), producida, principalmente, por la distorsión Jahn-Teller provocada por los iones Mn(III), el estado S = 10 se desdobla en 21 niveles. Cada nivel, caracterizado por un número cuántico de espín ($- S \leq M_s \leq + S$), tendrá una energía $E(M_S) = M_s^2 D$, siendo D = -0.70 K para el Mn12-ac. Debido al signo negativo de D, se necesitará cierta energía (barrera de

energía) para reorientar el espín desde el estado M_s = -10 al estado M_s = 10 pasando por el estado perpendicular M_s = 0, lo que se conoce como anisotropía de eje fácil. Si dicha barrera es importante, el espín del compuesto se podrá magnetizar en una dirección. De este modo, el Mn12-ac con una barrera de energía de $E(M_s = 0) - E(M_s = \pm 10) = 100D \approx 70$ K se puede magnetizar a 2 K aplicando y después quitando un campo magnético, siendo la relajación de la magnetización tan lenta, que al cabo de dos meses a 2 K, la magnetización es aproximadamente del 40 % del valor de saturación.

Desde dicho descubrimiento, en 1993, se ha logrado preparar y estudiar una gran variedad de complejos con metales de transición, de tipo cluster, que presentan comportamiento SMMs, lo cual ha permitido profundizar en el origen de sus propiedades. De gran relevancia fue el estudio realizado por el grupo del Dr. E. K. Brechin en 2007,[25] en el que se estudiaron las propiedades magnéticas de una familia de SMMs basados en el complejo hexanuclear $[Mn(III)_6O_2(sao)_6(O_2CH)_2(MeOH)_4]$ (sao = 2-hidroxibenzaldehil oxima). Los cambios en el ángulo de torsión Mn-N-O-Mn debido a la incorporación de grupos carboxilato u oximas derivadas (Et-saoH_2, Me-saoH_2), hicieron posible controlar el espín del estado fundamental, que variaba de S = 4 a S = 12 (puediendo tener S valores intermedios de 5, 6, 7, 9 y 11). Como cabía esperar, los compuestos con mayor valor de S presentaron las barreras más altas para la reorientación de la magnetización, llegando a conseguir una barrera de 86.41 K para un complejo con S = 12.

Sin embargo, la barrera energética observada para sistemas basados en metales de transición sigue siendo relativamente pequeña y, como consecuencia de ello, los SMMs sólo se comportan como imán a temperaturas muy bajas. Hoy en día, el record de barrera energética más alta mostrada por un complejo 3d lo tiene un compuesto de Fe(I),[26] que presenta una barrera de 325 K (226 cm^{-1}) y una temperatura de bloqueo T_B = 4.5 K.

En un intento para aumentar la magnitud de la barrera de activación térmica se han introducido, en los clúster magnéticos, iones de tierras raras, en particular iones lantánidos, ya que presentan una elevada anisotropía magnética intrínseca y un elevado momento magnético en el estado fundamental. Las diferencias entre el comportamiento de los iones 3d y 4f se pueden atribuir a los siguientes tres factores:[27]

1.- La mayoría de los electrones 4f se colocan en los orbitales de las capas interiores y están protegidos por los electrones 5s y 5p, lo que los vuelve más inertes,

en comparación con los electrones 3d, al efecto producido por los electrones de los ligandos. Debido a que el campo ligando que experimentan los electrones 4f es pequeño (del orden de 10^2 cm^{-1}), el momento orbital de los iones Ln(III) no se atenúa por los efectos de dicho campo.

2.- Como consecuencia de dicho momento orbital, el acoplamiento espín-órbita es mucho más fuerte en los lantánidos (del orden de 10^3 cm^{-1}) que en los iones del bloque 3d.

3.- El acoplamiento magnético entre los iones lantánidos es mucho más débil debido a que se produce entre orbitales 4f muy internos y, por lo tanto, protegidos.

Teniendo en cuenta lo expuesto anteriormente, podemos decir que las repulsiones interelectrónicas, el acoplamiento espín-órbita y los efectos del campo de los ligandos son diferentes para los iones 3d y los iones 4f. En la Figura 11 se muestran los niveles de energía que se forman en los iones lantánidos a causa de los 3 efectos anteriores, conocidos como subniveles Stark.

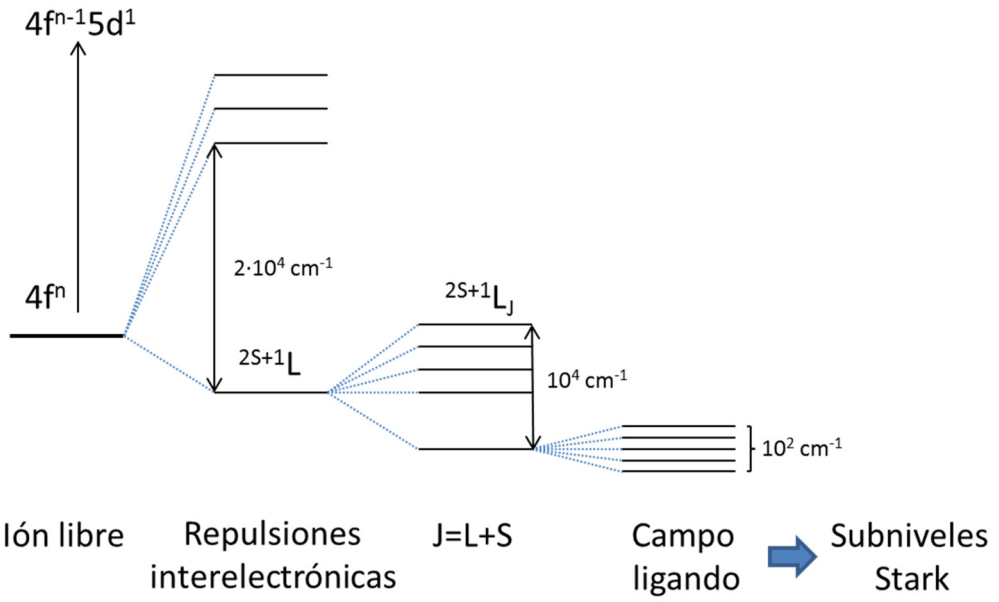

Figura 11.- Representación esquemática de la formación de los subniveles Stark para los iones Ln(III).

Siguiendo esta estrategia, en los últimos años ha surgido una nueva generación de SMMs basados en compuestos de coordinación mixtos (3d-4f) o complejos mononucleares y polinucleares de Dy(III), Tb(III), Ho(III) y Er(III), que aportan nuevas

ventajas (anisotropía, diferente número de electrones desapareados, etc).[2b] Como cabía esperar, el record de barrera efectiva para la inversión de la orientación de la magnetización y de temperatura de bloqueo han sido logrados por compuestos basados en iones de lantánidos,[28] concretamente por el complejo tipo sándwich de ftalocianina Tb(Pc)(Pc') (Figura 12, arriba) con U_{eff} = 652 cm^{-1} (938 K) y por el complejo dinuclear de Tb(III) con puentes radicales de N_2^{3-} (Figura 12, abajo) con T_B = 14 K (velocidad de barrido: 0.9 mT/s). Por otra parte, en la Tabla 1 se recogen algunos ejemplos de los valores de U_{eff} y de T_B más altos logrados hasta ahora en complejos mono y polinucleares de Ln(III).

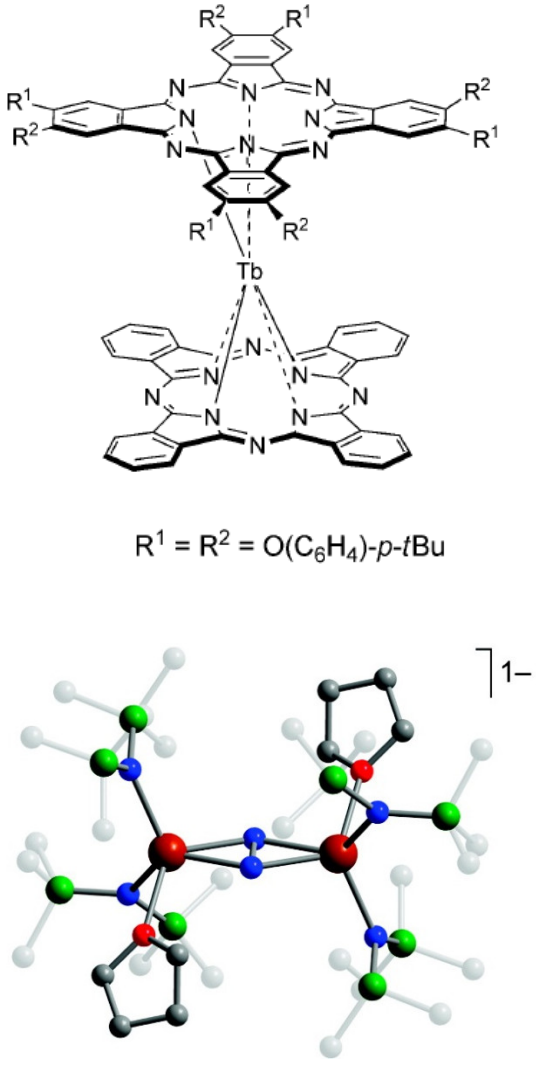

Figura 12.- Arriba: representación esquemática de la estructura del complejo Tb(Pc)(Pc'). Abajo: estructura cristalina de la unidad aniónica del complejo [K(18-crown-6)$(THF)_2$][{$[(Me_3Si)_2N]_2(THF)Tb$}$_2$(μ-η^2:η^2-N_2)]. Código de colores: Tb = marrón, Si = verde, O = rojo, N = azul, C = gris. Por claridad los átomos de hidrógeno han sido omitidos y los grupos metilo atenuados.

Tabla 1.- Valores de U_{eff} y T_B exhibidos por complejos mono y polinucleares de Ln(III).

Complejo[a]	U_{eff} **(cm^{-1})**	T_B **(K)**	**Ref.**
$[Tb_{0.2}Y_{0.8}Pc_2]TBA$	230 (330 K)	-	29
$[TbPc_2]$TBA diluido con matrices diamagnéticos TBA-Br en diferentes proporciones	584-641 (840-922 K)	-	30
$[TbPc'_2]$ (Pc' = Pc sustituidos)	556 (800 K)	7	31
[TbPcPc'] (Pc' = Pc sustituidos)	394-642 (567-924 K)	-	28a
[Er(Cp*)(COT)]	137 y 225 (197 y 323 K)	5	32
$[Zn_2DyL^2_2]NO_3\cdot H_2O$	305 (439 K)	11	33
$[DyZn(L^3)(sal)(MeO)(NO_3)Br]$	234 (337 K)	-	34
$[K(18\text{-crown-}6)(THF)_2][\{[(Me_3Si)_2N]_2(THF)Tb\}_2(\mu\text{-}\eta^2\text{:}\eta^2\text{-}N_2)]$	123 (177 K)	8.3	28c
$[Dy_4K_2O(O^tBu)_{12}]$	481 (692 K)	-	28b
$[DyY_3K_2O(O^tBu)_{12}]$	641 (922 K)	-	28b
$[Dy_5O(O^iPr)_{13}]$	368 (530 K)	-	35
$[\{Cp'_2Dy(\mu\text{-}SSiPh_3)\}_2]$	133 (192 K)	-	36

[a]TBA = $[N(Bu)_4]^+$; Cp* = pentametilciclopentadieno, COT = ciclooctatetraeno, H_3L^2 = 2,2',2"-(((nitrilotris(etano-2,1-diil))tris(azanodiil))tris(metilen))tris(4-bromofenol), H_2L^3: condensación de o-vanilina y 2,2'-dimetilpropanodiamina, Hsal =salicilaldehido, Cp': metilciclopentadieno.

II.3. Aplicaciones de los SMMs

Los SMMs han demostrado ser moléculas muy interesantes con propiedades magnéticas especiales, pero su descubrimiento también trajo consigo la posibilidad de

su utilización en aplicaciones tecnológicas sustituyendo los materiales ferromagnéticos convencionales. Con el uso de SMMs en el procesamiento y almacenamiento de información, probablemente su aplicación más perseguida, no sólo se pretende utilizar un nuevo material para la misma tarea, sino que abre la posibilidad de tener dispositivos de almacenamiento de información de densidad ultra-alta o dispositivos de procesamiento de información ultra-rápidos.

Una de las mayores necesidades que tiene hoy en día la tecnología es la de encontrar formas más eficientes de almacenar y procesar la información digital, tarea que se puede llevar a cabo desde dos enfoques distintos. El primer enfoque consiste en utilizar nanopartículas magnéticas más pequeñas que las que se utilizan hoy en día, lo que permitiría almacenar más información en dispositivos más pequeños.[8a] El uso de SMMs permitiría que la unidad de almacenamiento de información fuera, teóricamente, tan pequeña como una molécula, la cual sería capaz de almacenar un bit de información binaria. Así, las orientaciones de la magnetización hacia arriba y hacia abajo representarían, por ejemplo, el 0 y el 1, respectivamente. En principio, una molécula con un diámetro de 1-2 nm, presentaría una densidad de almacenamiento de información en superficie de ~ 30 Tbits/cm^2, la cual es cuatro órdenes de magnitud mayor que la densidad de almacenamiento que se puede conseguir con la tecnología basada en películas de aleaciones magnéticas (Figura 13).

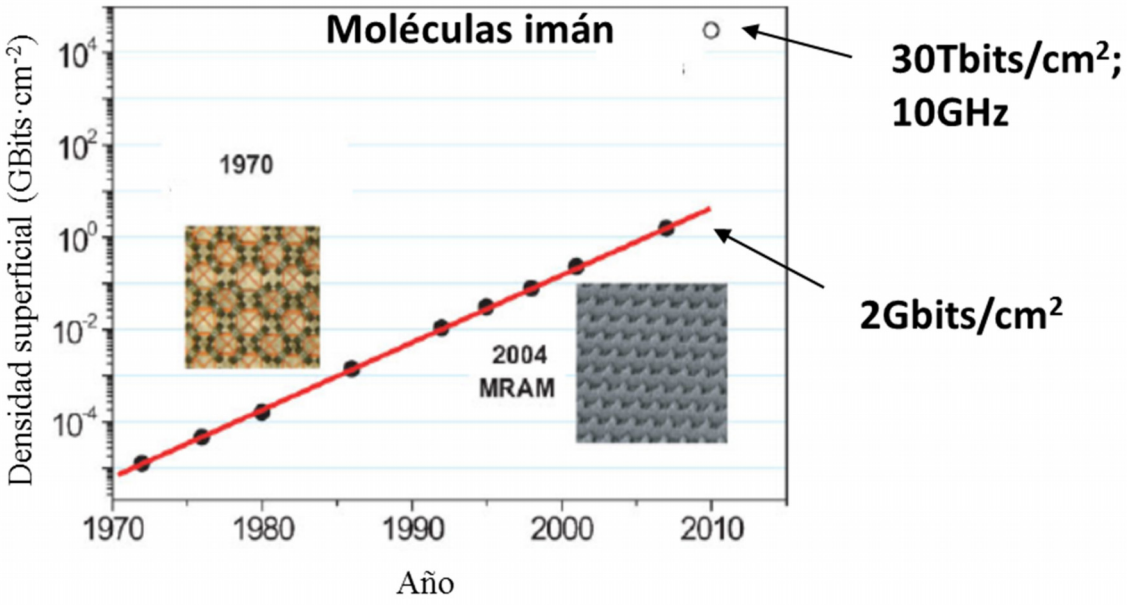

Figura 13.- Evolución de la densidad de información en el tiempo.

El segundo enfoque, consiste en desarrollar diferentes formas de procesar la información, como por ejemplo la computación cuántica. El bit tradicional sólo puede entregar resultados binarios (0 y 1), mientras que el qubit (del inglés, *quantum bit*), aprovechando las propiedades de la mecánica cuántica, puede tener ambos valores al mismo tiempo (0 y 1), lo que habilita una velocidad de procesamiento mucho mayor. Además, cada uno de los procesos del qubit es independiente, lo que permite resolver más de una operación al mismo tiempo. Dado que los SMMs se encuentran en la interfase de la naturaleza cuántica y clásica, también podrían encajar perfectamente en este segundo enfoque.[8a,37]

Los SMMs también se pueden utilizar en el campo de la *Espintrónica Molecular*, que consiste en la manipulación de las moléculas con el fin de intentar modificar su espín o momento de giro de los electrones integrantes.[5a] De este modo, se pueden conseguir algunas funciones específicas, como por ejemplo la conmutabilidad, ya sea con la luz, campo eléctrico, etc. Un ejemplo reciente de los avances en este campo incluye el dispositivo electrónico híbrido de tres electrodos basado en nanotubos de carbono y las moléculas imán Tb(Pc)(Pc'),[38] descritas en la sección anterior. Los SMMs, acoplados a cada nanotubo mediante interacciones π-π (Figura 14), actúan como polarizadores de espín, controlando la conductividad electrónica.

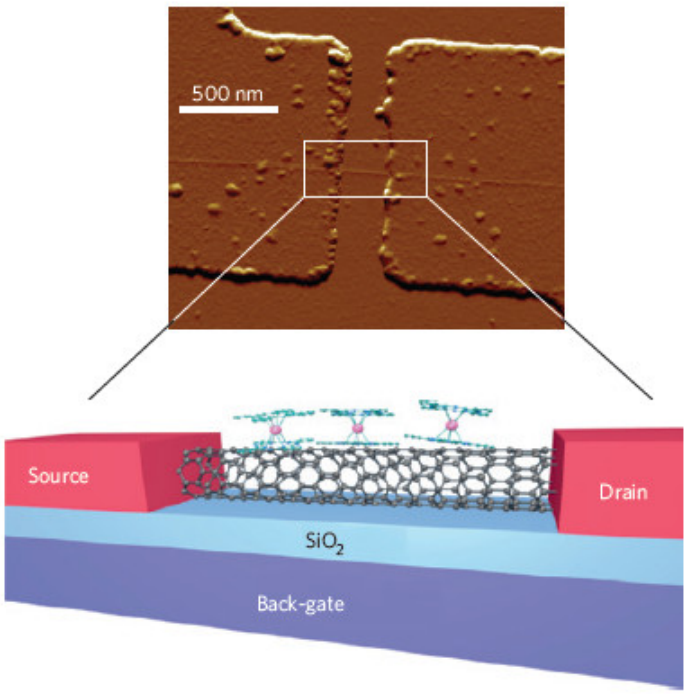

Figura 14.- Esquema de la válvula de espín compuesta por SMMs Tb(Pc)(Pc') y nanotubos de carbono, junto a la micrografía de fuerza atómica.[38]

Al aplicar un campo magnético externo, el dispositivo se comporta como una válvula de espín, es decir, si el campo aplicado es capaz de alinear los espines de las moléculas depositadas sólo uno de los canales de espín es efectivo en la conducción, mientras que si el campo es menor sólo algunas moléculas están alineadas con él y la conductividad es mínima a través de los dos canales de espín. Esta válvula presenta una magnetorresistencia (capacidad de variar la resistencia eléctrica por la aplicación de un campo magnético) de un 300 % a temperaturas inferiores a 1 K. La magnetorresistencia, que hoy en día puede ser de hasta 600 %, es la propiedad que utilizan los discos duros de los ordenadores para su funcionamiento. Cuando un bit, que es como un pequeño imán, pasa por la cabeza de lectura eléctrica de un disco duro, hay una variación de la resistencia, la cual se puede detectar y utilizar para leer la información guardada en el dispositivo fácilmente.

Sin embargo, existen dos problemas principales que deben ser resueltos antes de que las aplicaciones tecnológicas propuestas se puedan llevar a cabo. En primer lugar, como ya se ha comentado, hay que aumentar la temperatura a la que los SMMs son funcionales, ya que hoy en día la inmensa mayoría de los SMMs publicados funcionan a la temperatura del helio líquido (~4 K), hecho que los aleja de cualquier aplicación práctica en almacenamiento y procesamiento de información. En segundo lugar, para poder fabricar dispositivos a partir de SMMs es necesario desarrollar nuevas tecnologías, ya que hasta el momento existen pocos ejemplos de SMMs que hayan sido depositados y organizados en superficies con la perspectiva de incorporarlos en dispositivos nanoscópicos.

IV. LUMINISCENCIA EN COMPLEJOS CON IONES LANTÁNIDOS

Una de las áreas de investigación de mayor dinamismo, junto al magnetismo, dentro del campo de los compuestos de coordinación basados en iones lantánidos, es el estudio de las propiedades fotofísicas, especialmente de sus propiedades luminiscentes.[39] Esto es debido a que el pequeño efecto provocado por el *campo ligando*, que hace que las transiciones electrónicas (que cubren las regiones del visible (VIS) y del infrarrojo cercano (NIR)) sean de tipo f-f, es el responsable de que las bandas de absorción y emisión sean muy estrechas, dando lugar a colores de emisión extremadamente puros.

Debido a que las transiciones f-f están prohibidas por la regla de Laporte, los espectros electrónicos de los lantánidos presenta una intensidad muy pequeña. Sin embargo, los tiempos de vida media de los estados excitados son largos (del orden, incluso, de milisegundos), lo cual es de gran interés para su uso en distintas aplicaciones tecnológicas. Como la excitación directa de los iones lantánidos resulta ineficaz, debido a que presentan coeficientes de absorción (ε) muy bajos, para utilizar complejos de lantánidos como materiales emisores es necesario solucionar este contratiempo. Para ello, tradicionalmente, se ha recurrido al conocido "efecto antena", que consiste en coordinar los iones Ln(III) con ligandos orgánicos que presenten bandas de absorción muy intensas. La excitación de estos ligandos ("antenas") va seguida de un proceso de transferencia de energía desde el ligando a niveles excitados del centro metálico y la posterior emisión característica del ión lantánido considerado (Figura 15).[40]

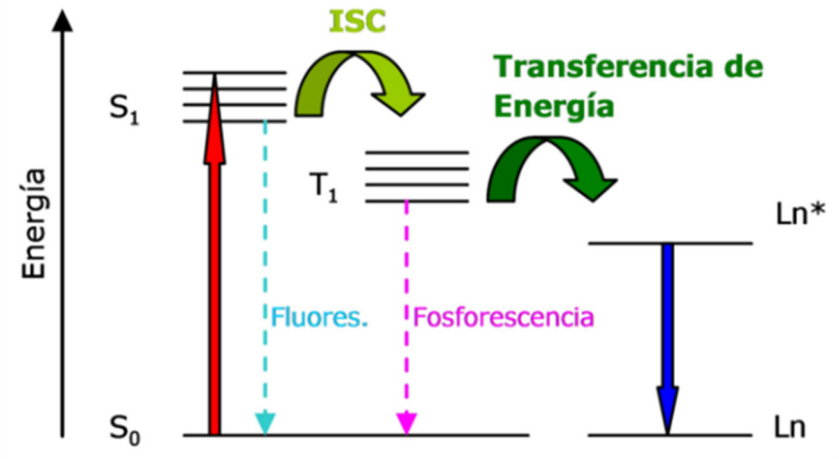

Figura 15.- Diagrama de Jablonsky simplificado.

Si bien la mayoría de los iones Ln(III) son luminiscentes, no todos emiten con la misma intensidad, ya que esta propiedad depende de la facilidad con la que puedan ser poblados los estados excitados, así como de la minimización de los procesos de desactivación por vía no radiativa. El rendimiento cuántico de la emisión depende, esencialmente, de la separación entre el nivel de energía excitado más bajo y el subnivel más alto del multiplete del estado fundamental. Cuánto más pequeña sea esta separación, más fácil será la desactivación por procesos no radiativos.[41] En las Figuras 16 y 17, se presentan a modo de ejemplo, respectivamente, los niveles de energía más significativos de los iones lantánidos y los espectros de emisión de los

complejos tris-β-dicetonatos de lantánidos.[42] Como el efecto del campo ligando sobre los niveles de acoplamiento espín-orbita en los iones lantánidos es relativamente pequeño, las bandas de emisión de cada ión lantánido aparecen, prácticamente, a la misma energía en todos sus complejos.

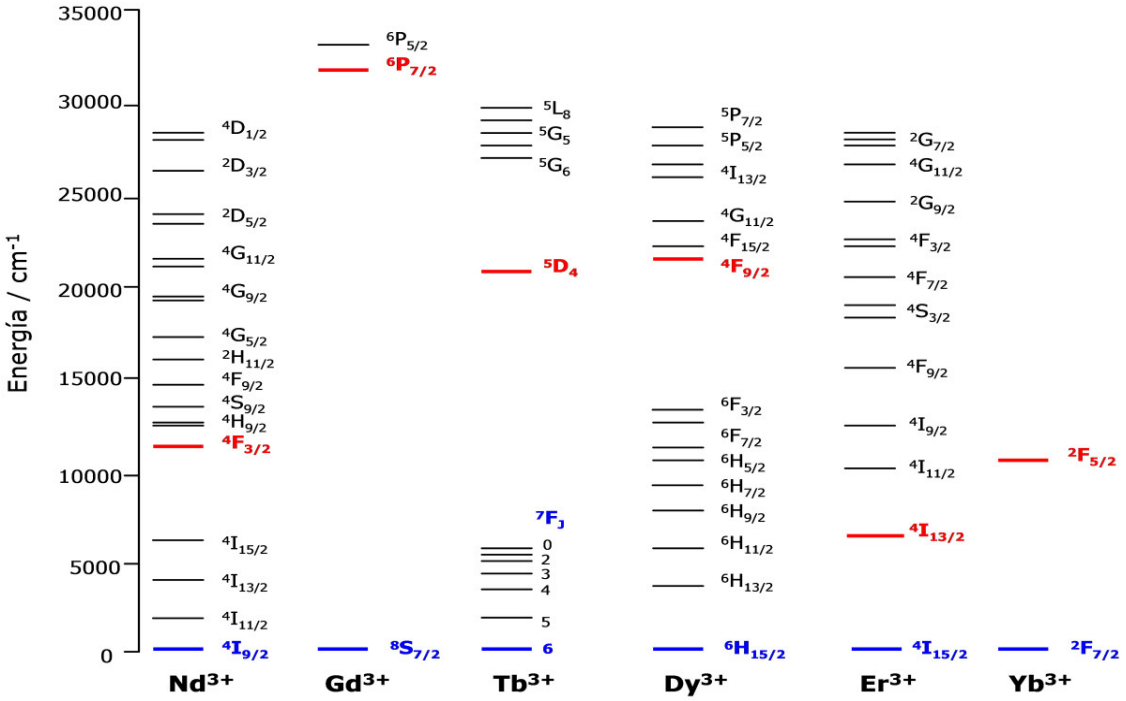

Figura 16.- Representación de los niveles de energía más significativos de los iones lantánidos.

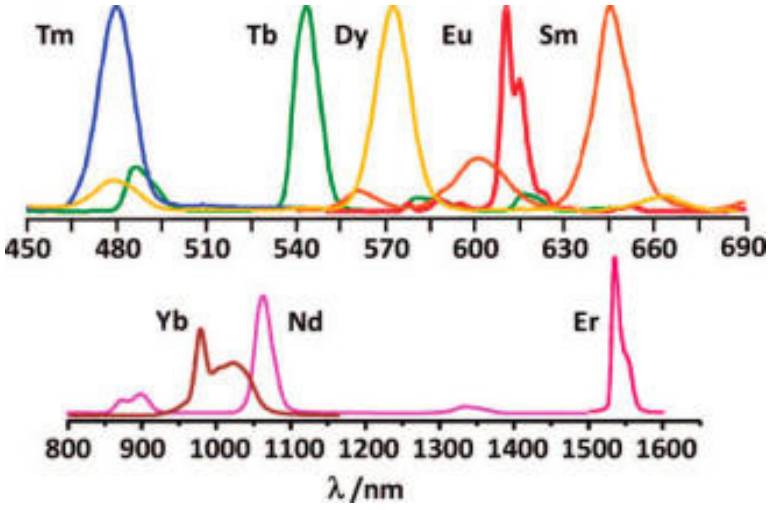

Figura 17.- Espectros de emisión de complejos tris-β-dicetonatos de lantánidos.

Los complejos de los iones lantánidos que emiten en la región del visible, particularmente Eu(III) y Tb(III), con tiempos de vida muy grandes (entre 1 y 10 ms), son los más ampliamente utilizados, entre otras aplicaciones, en análisis biomédico e imagen de células y tejidos.[43] No obstante, en la última década, se ha generado un creciente interés por el estudio de las propiedades luminiscentes de complejos metálicos de iones lantánidos cuya radiación luminiscente aparezca en la región espectroscópica del infrarrojo cercano [Pr(III), Nd(III), Er(III) e Yb(III)], pues presentan aplicaciones en dispositivos ópticos y electrónicos, especialmente para comunicaciones ópticas, aplicaciones biológicas y como sensores.[44]

Esta radiación luminiscente en la región del IR cercano (850 - 1600 nm) es importante por dos razones muy diferentes:

1.- Desde un punto de vista biomédico, porque el tejido humano es transparente a la radiación entre 800 - 1000 nm, por lo que iones tales como Nd(III) o Yb(III), que emiten a 880 y 980 nm respectivamente, son candidatos ideales para formar parte de biomarcadores luminiscentes *in vivo*, pues su emisión puede detectarse a través de una capa de piel considerablemente gruesa.[44b,45]

2.- Las redes ópticas de telecomunicaciones basadas en fibra de vidrio hacen uso de la radiación en el infrarrojo cercano (1000 - 1600 nm) para el envío de información, ya que la sílice no absorbe en dicho intervalo. Así, iones como Pr(III) (λ_{em} = 1300nm, $^1G_4 \rightarrow {}^3H_5$) y Er(III) ($\lambda_{em}$ = 1500nm, $^4I_{13/2} \rightarrow {}^4H_{15/2}$) se utilizan como amplificadores en estas redes ópticas, ya que su emisión coincide con la "ventana de transparencia" de la sílice.[46]

En vista de las interesantes propiedades luminiscentes que presentan los complejos de los iones lantánidos, es necesaria más investigación fundamental en este área.

V. NANORREFRIGERANTES

La refrigeración magnética, que se basa en el *efecto magnetocalórico* (EMC), es una tecnología muy eficiente desde el punto de vista energético y cuidadosa con el medio ambiente.[2a,2c,5] Como se puede apreciar en la Figura 18, el EMC describe el cambio de anisotropía magnética (ΔS_m) y de la temperatura adiabática (ΔT_{ad}) de una sustancia cuando se varía el campo magnético aplicado.[5a,47] De este modo, al

magnetizar una sustancia aplicando un campo, la entropía magnética se ve afectada, ya que el campo cambia el orden magnético del material. La sustancia, inicialmente en un estado A (Figura 18), está a una temperatura T_i y a un campo H_i. Bajo condiciones adiabáticas, es decir, cuando la entropía total del sistema se mantiene constante, el cambio en entropía magnética se compensa con un cambio de entropía de la red, resultando en un cambio en la temperatura del material. Es decir, el cambio adiabático del campo $H_i \rightarrow H_f$ lleva al sistema a un estado C (T_f, H_f), con el resultante cambio de temperatura ΔT_{ad} (flecha horizontal en la Figura 18). Por otra parte, si en un estado B (T_f, H_i) el campo magnético se cambia isotérmicamente a H_f, el sistema pasa a un estado C (T_f, H_f), dando como resultado un cambio de entropía magnética ΔS_m (flecha vertical en la Figura 18). Ambos factores, ΔS_m y ΔT_{ad}, son parámetros característicos del EMC. Si el cambio magnético ΔH reduce la entropía ($\Delta S_m < 0$), ΔT_{ad} es positivo, mientras que si ΔS_m es positivo, $\Delta T_{ad} < 0$. El valor máximo de entropía magnética para un sistema con espín S viene dada por la siguiente ecuación:

$$S_m = R\ln(2S + 1) \qquad \text{(Ecuación 7)}$$

donde R es la constante de los gases ideales.

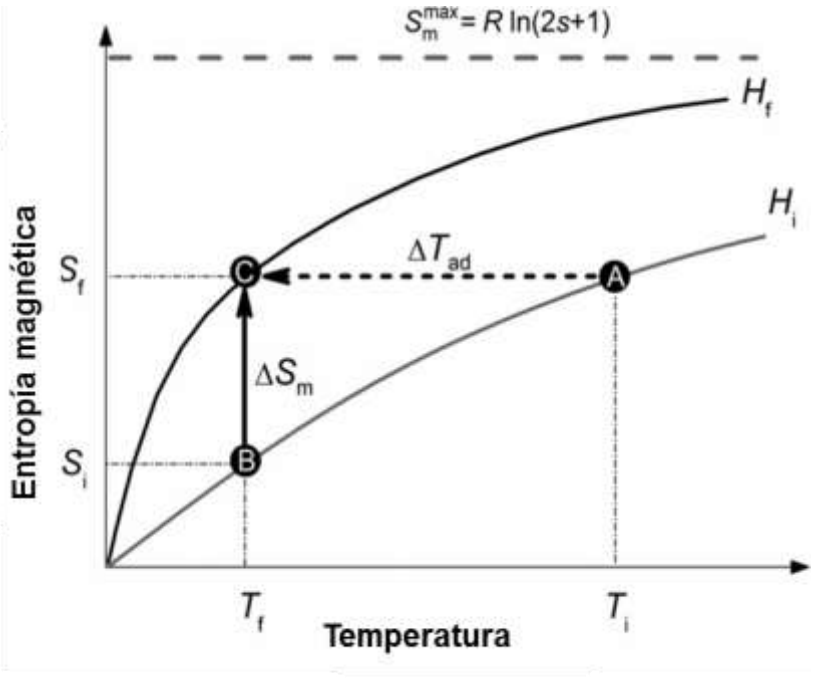

Figura 18.- Dependencia de la entropía molar magnética con la temperatura en un sistema paramagnético.[47]

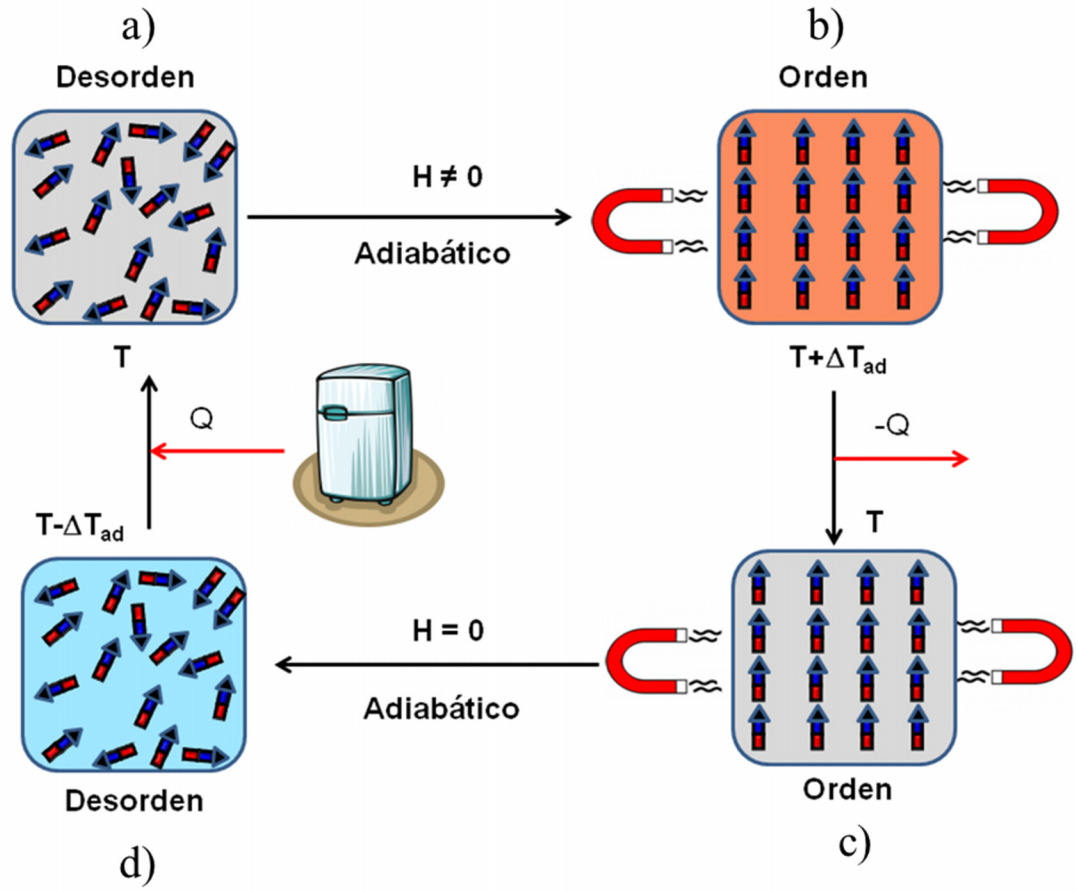

Figura 19.- Ciclo de refrigeración.

El ciclo de refrigeración (Figura 19) consta de los siguientes pasos:

1.- Magnetización adiabática: una sustancia magnetocalórica se coloca en un entorno aislado (Figura 19.a). El campo magnético externo (+ *H*) cada vez mayor provoca el alineamiento de los dipolos magnéticos de los átomos, disminuyendo así la entropía magnética (Figura 19.b). Dado que la energía total no se pierde (todavía) y, por lo tanto, la entropía total no se reduce (de acuerdo con leyes de la termodinámica), el resultado neto es que la sustancia se calienta ($T + \Delta T_{ad}$).

2.- Transferencia entálpica isomagnética: el calor añadido se puede eliminar (- *Q*) mediante un fluido o gas, como por ejemplo el helio líquido o gaseoso. El campo magnético se mantiene constante para evitar que los dipolos reabsorban el calor (Figura 19.c) y una vez que se ha enfriado suficiente, la sustancia magnetocalórica y el refrigerante se separan.

3.- Desmagnetización adiabática: el campo magnético se reduce, la energía térmica hace que los momentos magnéticos superen el campo ($\Delta S_m > 0$), y por lo tanto, la muestra se enfría, es decir, hay un cambio de temperatura adiabática ($T - \Delta T_{ad}$) (Figura 19.d). La energía (y entropía) se transfiere de entropía térmica a entropía magnética (desorden de los dipolos magnéticos).

4.- Transferencia entrópica isomagnética: el campo magnético se mantiene constante para evitar que el material se recaliente. El material se coloca en contacto con el medio a refrigerar y el calor migra al material (+ Q).

Una vez que el refrigerante y el medio a refrigerar están en equilibrio térmico, el ciclo se puede reiniciar.

Aunque el EMC es una propiedad intrínseca de cualquier material magnético, sólo en unos pocos casos los cambios son suficientemente grandes como para poder utilizarlos en aplicaciones prácticas. El reciente descubrimiento de que el EMC puede ser mayor en los compuestos de coordinación polinucleares que en las aleaciones intermetálicas y de lantánidos,[5d] estudiadas y utilizadas convencionalmente para aplicaciones de enfriamiento a baja temperatura, ha supuesto un fuerte estímulo para la investigación en este campo. Esto representa, sin duda, una perspectiva muy interesante que mantiene a los *materiales moleculares magnéticos* en primera línea de investigación en el contexto de la *nanociencia* y *nanotecnología*.

Para que se observe un gran efecto magneto-calórico en un compuesto de coordinación es necesario que[5d]:

- Al igual que los SMMs, el estado fundamental tenga un espín muy alto, ya que la entropía magnética está relacionada con el espín de acuerdo a la Ecuación 7.

- Al contrario que los SMMs, no presente anisotropía magnética.

- Presente alta degeneración de espín, controlada por la interacción de canje magnético entre los iones metálicos, la cual es necesario que sea pequeña para que haya muchos niveles cercanos en energía.

- La relación metal/ligando sea grande, pues de esta forma hay menos cantidad de elementos diamagnéticos pasivos. Este último requisito es más fácil de conseguir en los clusters de coordinación pequeños que en los grandes.

Por tanto, que se obtengan *SMMs* o *refrigerantes magnéticos* va a depender de la simple elección de un determinado tipo de metal con un determinado estado de oxidación (por ejemplo, Gd(III) que es isotrópico frente a Mn(III) que es anisotrópico) y una adecuada elección del ligando que favorezca la interacción ferromagnética entre los iones metálicos generando un estado de espín muy alto.

Teniendo en cuenta estas consideraciones, se han obtenido clusters moleculares de alto espín, tales como $\{Fe_{14}\}$, $\{Mn_{10}\}$, $\{Mn_{14}\}$, $\{Mn_{32}\}$, $\{Mn_{17}\}$, and $\{Mn_{19}\}$ que muestran un importante efecto magnetocalórico,[5b,5c] consecuencia del alto espín del estado fundamental y/o de la alta degeneración de espín a bajas temperaturas, lo cual hace que estos sistemas sean buenos candidatos para refrigeración a baja temperatura.[48] Hay que señalar que la *nanorrefrigeración* es de gran interés por su uso, entre otras aplicaciones, en instrumentos analíticos que operen en el espacio exterior, pues representan una alternativa válida a la refrigeración por dilución ^{3}He - ^{4}He, cuyo uso es muy complicado por la ausencia de gravedad y en la licuefacción de hidrógeno y gas natural a ultra bajas temperaturas.

Por lo descrito anteriormente, el ión Gd(III) es el ideal para el efecto MCE, ya que tiene un espín isotrópico muy alto (S = 7/2). Además, como los electrones 4f son muy internos, la interacción de canje es muy pequeña. Además de sistemas clusters de Gd(III) tales como $\{Gd_2\}$ and $\{Gd_7\}$,[5b,5c] también se emplean sistemas 3d-4f, en los que la interacción entre el Gd(III) y el ión 3d suele ser ferromagnética, favoreciendo, de esta forma, la adopción de un estado fundamental de espín muy alto. Así, se han preparado recientemente complejos 3d-4f tales como $\{Mn_4Gd_4\}$, $\{Cu_5Gd_4\}$, $\{Ni_6Gd_6\}$, $\{Ni_{12}Gd_{36}\}$ con grandes efectos magnetocalóricos.[5b,5c] Quizás la combinación 3d-4f más apropiada sea la Mn(II)/Gd(III), pues ambos iones son isotrópicos y tiene un alto espin, 5/2 y 7/2, respectivamente.[49]

VI. OBJETIVOS

Basicamente, los objetivos que se persiguen en este trabajo son:

1.- Establecer correlaciones magneto-estructurales que ayuden a entender cuáles son los principales factores estructurales que rigen las interacciones de canje magnético en compuestos polinucleares de Ni(II), bien solo a través de ligandos puente de tipo di- y triaminobis(fenoxo) (ver Figuras 1.1 y 1.2 de los Capítulos 1 y 2,

respectivamente), o bien a través de estos y otros ligandos puente (puentes mixtos). Posteriormente se podrían diseñar materiales con propiedades deseadas, fundamentalmente con interacciones ferromagnéticas y un estado fundamental de espín alto con iones anisotrópicos, que pudieran eventualmente presentar propiedades de molécula imán.

2.- Preparar compuestos con puentes mixtos di-μ-fenoxo/*syn-syn* carboxilato, en los que cada tipo de puente transmite una interacción antiferromagnética, para ver si se produce el efecto de la contracomplementariedad, y lograr una interacción global ferromagnética.

3.- Preparar compuestos de coordinación con iones lantánidos que presenten propiedades de SMM con altas barreras de activación térmica, intentando encontrar una estrategia que ayude a diseñar racionalmente complejos de lantánidos con gran anisotropía magnética de eje fácil (axial).

4.- Conocer si algunos de los complejos que se comportan como molécula imán tienen también propiedades luminiscentes, preferentemente en el IR cercano, y que, por tanto, puedan considerarse como materiales bifuncionales magnético luminiscentes.

5.- Aprovechando la experiencia adquirida, preparar complejos polinucleares M(n)Gd(III) {M(n) = Fe(III), Mn(II), Cu(II)} que presenten grandes efectos magnetocalóricos con aplicaciones potenciales como nanorrefrigerantes.

6.- Anclar o depositar las moléculas que presenten propiedades interesantes sobre soportes sólidos.

VII. BIBLIOGRAFIA

[1] **a)** *Magnetism: Molecules to Materials*, Vol. I-V, (eds. Miller, J. S.; Drillon, M.), Wiley-VCH, Weinheim, **2001-2005**; **b)** D. Gatteschi, L. Bogani, A. Cornia, M. Manini, L. Sorace, R. Sessoli, *Solid. State Sci.*, **2008**, *10*, 1701.

[2] **a)** R. A. Layfield, M. Murugesu (eds), *Lanthanides and Actinides in Molecular Magnetism*, Wiley-VCH, Weinheim, Germany, **2015**; **b)** H. L. C. Feltham, S. Brooker, *Coord. Chem. Rev.,* **2014**, *276*, 1; **c)** B. W. Wang, S. Gao, *The Rare Earth Elements*

Fundamental and Applications, D. A. Atwood, John Wiley and sons, **2012**; **d)** R. E. P. Winpenny, *Molecular Cluster Magnets*, World Scientific Books, Singapore, **2011**; **e)** E. K. Brechin, *Molecular Magnets*, volumen especial, *Dalton Trans.*, **2010**, *39*, 4671.

[3] W.-X. Zhang, R. Ishikawa, B. Breedlove, M. Yamashita, *RSC Adv*., **2013**, *3*, 3772.

[4] L. Ouahab, *Multifunctional Molecular Materials*, CRC Press, Taylor & Francis Group, USA, **2012**.

[5] **a)** J. Bartolomé, F. Luis, J. F. Fernández (eds.), *Molecular Magnets, Physics and Applications*, Springer-Verlag, Berlin-Heidelberg, **2014**; **b)** Y.-Z. Zheng, G.-J. Zhou, Z. Zheng, R. E. P. Winpenny, *Chem. Soc. Rev*., **2014**, *43*, 1462; **c)** J.-L. Liu, Y.-C. Chen, F.-S. Guo, M.-L. Tong, *Coord. Chem. Rev*., **2014**, *281*, 26; **d)** M. Evangelisti, E. K. Brechin, *Dalton Trans*., **2010**, *39*, 4672.

[6] **a)** D. V. Hingorani, A. S. Bernstein, M. D. Pagel, *Contrast Media Mol. Imaging*, **2015**, *10*, 245; **b)** P. Caravan, R. B. Lauffer, *Clinical Magnetic Resonance Imaging, capítulo 13: Contrast agents: Basic Principles,* 3ª Ed. R. R. Edelman, J. Hesselinck, M. Zlatkin, Eds. Saunders, **2005**.

[7] **a)** S. Brooker, *Chem. Soc. Rev*., **2015**, *44*, 2880; **b)** M. A. Halcrow, *Spin-Crossover Materials: Properties and Applications*, Wiley-VCH, Weinheim, Germany, **2013**; **c)** A. Bousseksou, G. Molnár, L. Salmon, W. Nicolazzi, *Chem. Soc. Rev*., **2011**, *40*, 3313.

[8] **a)** M. Affronte, *J. Mater. Chem*., **2009**, *19,* 1731; **b)** P. C. E. Stamp, A. Gaita-Ariço, *J. Mater. Chem*., **2009**, *19*, 1718; **c)** L. Bogani, W. Wernsdorfer, *Nat. Mater*., **2008**, *7*, 179; **d)** A. Ardavan,O. Rival, J. J. L. Morton, S. J. Blundell, A. M. Tyryshkin, G. A. Timco, R. E. P. Winpenny, *Phys. Rev. Lett.*, **2007**, *98*, 057201/1; **e)** A. R. Rocha, V. M. García-Suárez, S. W. Bailey, C. J. Lambert, J. Ferrerand, S. Sanvito, *Nat. Mater.,* **2005**, *4,* 335; **f)** M. N. Leuenberger, D. Loss, *Nature,* **2001**, *410*, 789.

[9] D. Gatteschi, R. Sessoli, J. Villain, *Molecular Nanomagnets*, Oxford University Press, Oxford, UK, **2006**.

[10] Some examples: **a)** J. P. Costes, L. Vendier, *Eur. J. Inorg. Chem*., **2010**, *2010*, 2768; **b)** M. Andruh, J. P. Costes, C. Diaz, S. Gao, *Inorg. Chem*., **2009**, *48*, 3342; **c)** T. Kajiwara, K. Takahashi, T. Hiraizumi, S. Takaisi, M. Yamashita, *CrystEngComm*., **2009**, *11*, 2110; **d)** J. P. Costes, J. Garcia-Tojal, J. P. Tuchagues, L. Vendier, *Eur. J. Inorg. Chem.*, **2009**, *2009*, 3801; e) T. Kajiwara, M. Nakano, S. Takaishi, M. Yamashita, *Inorg. Chem*., **2008**, *47*, 8604.

[11] X.-Y. Wang, Z.-M. Wang, S. Gao, *Chem. Commun*., **2008**, 281.

[12] A. Escuer, J. Esteban, S. P. Perlepes, T. C. Stamatatos, *Coord. Chem. Rev*., **2014**, 275, 87.

[13] **a)** Y. Nishida, S. Kida, *J. Chem. Soc., Dalton Trans*., **1986**, 2633; b) V. McKee, M. Zvagulis, C. A. Reed, *Inorg. Chem*., **1985**, *24*, 2914; **c)** V. McKee, M. Zvagulis, J. V. Dagdigian, M. G. Patch, C. A. Reed, *J. Am. Chem. Soc*., **1984**, *106*, 4765; **d)** L. L. Wang, Y. M. Sun, Z. N. Qi, C. B. Liu, *J. Chem. Phys. A*, **2008**, *112*, 8418 and references.

[14] S. Mandal, V. Balamurugan, F. Lloret, R. Mukherjee, *Inorg. Chem*., **2009**, *48*, 7544.

[15] **a)** L. Gutierrez, G. Alzuet, J. A. Real, J. Cano, J. Borrás, A. Castiñeiras, *Inorg. Chem*., **2000**, *39*, 3608; **b)** L. Gutierrez, G. Alzuet, J. A. Real, J. Cano, J. Borras, A. Castiñeiras, *Eur. J. Inorg. Chem*., **2002**, *8*, 2094.

[16] **a)** L. Cañadillas-Delgado, O. Fabelo, J. Pasán, F. S. Delgado, F. Lloret, M. Julve, C. Ruiz-Pérez, *Inorg. Chem*., **2007**, *46*, 7458; **b)** R. Biswas, P. Kar, Y. Song, A. Ghosh, *Dalton Trans*., **2011**, *40*, 5324; **c)** R. Biswas, S. Giri, S. K. Saha, A. Ghosh, *Eur. J. Inorg. Chem*., *2012*, 2916; **d)** X. M. Zhang, X. H. Jing, E. Q. Gao, *Inorg. Chim. Acta*, **2011**, *365*, 240.

[17] **a)** R. Biswas, Y. Ida, M. L. Baker, S. Biswas, P. Kar, H. Nojiri, T. Ishida, A. Ghosh, *Chem. Eur. J*., **2013**, *19*, 3943; **b)** S. Petit, P. Neugebauer, G. Pilet, G. Chastanet, A. L. Barra, A. B. Antunes, W. Wernsdorfer, D. Luneau, *Inorg. Chem*., **2012**, *51*, 6645 and references therein; **c)** D. I. Alexandropoulos, C. Papatriantafyllopoulou, G. Aromi, O. Roubeau, S. J. Teat, S. P. Perlepes, G. Christou, T. C. Stamatatos, *Inorg. Chem*., **2010**, *49*, 3962; **d)** R. T. W. Scott, L. F. Jones, I. Tidmarsh; S. B. Breeze, R. H. Laye, J. Wolowska, D. J. Stone, A. Collins, S. Parsons, W. Wernsdorfer, G. Aromi, E. J. L. McInnes, E. K. Brechin, *Chem. Eur. J*., **2009**, *15*, 12389; **e)** A. K. Boudalis, M. Pissas, C. P. Raptopoulou, V. Psycharis, B. Abarca, R. Ballesteros, *Inorg. Chem.*, **2008**, *47*, 10674; **f)** A. Ferguson, J. Lawrence, A. Parkin, J. Sanchez-Benitez, K. V. Kamenev, E. K. Brechin, W. Wernsdorfer, S. Hill and M. Murrie, *Dalton Trans*., **2008**, 6409; **g)** A. Bell, G. Aromí, S. J. Teat, W. Wernsdorfer, R. E. P. Winpenny, *Chem. Commun*., **2005**, 2808; **h)** H. Andres, R. Basler, A. J. Blake, C. Cadiou, G. Chaboussant, C. M. Grant, H. U. Güdel, M. Murrie, S. Parsons, C. Paulsen, F. Semadini, V. Villar, W. Wernsdorfer, R. E. P. Winpenny, *Chemistry*, **2002**, *8*, 4867.

[18] **a)** S. Gómez-Coca, D. Aravena, R. Morales, E. Ruiz, *Coord. Chem. Rev*., **2015**, *289-290*, 379; **b)** P. P. Samuel, K. C. Mondal, N. Amin Sk, H. W. Roesky, E. Carl, R. Neufeld, D. Stalke, S. Demeshko, F. Meyer, L. Ungur, L. F. Chibotaru, J. Christian, V. Ramachandran, J. van Tol, N. S. Dalal, *J. Am. Chem. Soc*., **2014**, *136*, 11964; **c)** E. Colacio, J. Ruiz, E. Ruiz, E. Cremades, J. Krzystek, S. Carretta, J. Cano, T. Guidi, W. Wernsdorfer, E. K. Brechin, *Angew. Chem. Int. Ed*., **2013**, *52*, 9130; **d)** J. Vallejo, I. Castro, R. Ruiz-Garcia, J. Cano, M. Julve, F. Lloret, G. De Munno, W. Wernsdorfer, E.

Pardo, *J. Am. Chem. Soc*., **2012**, *134*, 15704; **e)** J.-L. Liu, K. Yuan, J.-D. Leng, L. Ungur, W. Wernsdorfer, F.-S. Guo, L. F. Chibotaru, M.-L. Tong, *Inorg. Chem*., **2012**, *51*, 8538.

[19] A. Abragam, B. Bleaney, *Electron Paramagnetic Resonance of Transition Ions*, Clarendon Press: Oxford, UK, **1970**.

[20] K. N. Shirivastava, *Phys. Status Solidi B,* **1983**, *117*, 437.

[21] N. E. Chakov, S.-C. Lee, A. G. Harter, P. L. Kuhns, A. P. Reyes, S. O. Hill, N. S. Dalal, W. Wernsdorfer, K. A. Abboud, G. Christou, *J. Am. Chem. Soc*., **2006**, *128*, 6975.

[22] H. B. G. Casimir, D. Bijl, F. K. du Pré, *Physica (The Hague)*, **1941**, *8*, 449.

[23] K. S. Cole, H. R. Cole, *J. Chem. Phys*, **1941**, *9*, 341.

[24] **a)** R. Sessoli, H.-L. Tsai, A. R. Schake, S. Wang, J. B. Vincent, K. Folting, D. Gatteschi, G. Christou, D. N. Hendrickson, *J. Am. Chem. Soc*., **1993**, 115, 1804; **b)** R. Sessoli, D. Gatteschi, A. Caneschi, M. A. Novak, *Nature*, **1993**, 365, 141.

[25] C. J. Milios, R. Inglis, A. Vinslava, R. Bagai, W. Wernsdorfer, S. Parsons, S. P. Perlepes, G. Christou, E. K. Brechin, *J. Am. Chem. Soc*., **2007**, *129*, 12505.

[26] J. M. Zadrozny, D. J. Xiao, M. Atanasov, G. J. Long, F. Grandjean, F. Neese, J. R. Long, *Nat. Chem*., **2013**, *5*, 557.

[27] S. Gao (Eds), *Molecular Nanomagnets and Related Phenomena*, Springer-Verlag, Berlin-Heidelberg, **2015**.

[28] **a)** C. R. Ganivet, B. Ballesteros, G. de La Torre, J. M. Clemente-Juan, E. Coronado, T. Torres, *Chem. Eur. J.,* **2013**, *19*, 1457; **b)** R. J. Blagg, L. Ungur, F. Tuna, J. Speak, P. Comar, D. Collison, W. Wernsdorfer, E. J. L. McInnes, L. F. Chibotaru, R. E. P. Winpenny, *Nat. Chem*., **2013**, *5*, 673; **c)** J. D. Rinehart, M. Fang, W. J. Evans, J. R. Long, *Nat. Chem*. **2011**, *3*, 538; **d)** J. D. Rinehart, M. Fang, W. J. Evans, J. R. Long, *J. Am. Chem. Soc*., **2011**, *133*, 14236.

[29] N. Ishikawa, M. Sugita, T. Ishikawa, S.-Y. Koshihara, Y. Kaizu, *J. Am. Chem. Soc*., **2003**, *125*, 8694.

[30] F. Branzoli, P. Carretta, M. Filibian, G. Zoppellaro, M. J. Graf, J. R. Galan-Mascaros, O. Fuhr, S. Brink,M. Ruben, *J. Am. Chem. Soc*., **2009**, *131*, 4387.

[31] M. Gonidec, R. Biagi, V. Corradini, F. Moro, V. de Renzi, U. del Pennino, D. Summa, L. Muccioli, C. Zannoni, D. B. Amabilino, J. Veciana, *J. Am. Chem. Soc*., **2011**, *133*, 6603.

[32] S.-D. Jiang, B.-W. Wang, H.-L. Sun, Z.-M. Wang, S. Gao, *J. Am. Chem. Soc*., **2011**, *133*, 4730.

[33] J.-L. Liu, Y.-C. Chen, Y.-Z. Zheng, W.-Q. Lin, L. Ungur, W. Wernsdorfer, L. F. Chibotaru, M.-L. Tong, *Chem. Sci*., **2013**, *4*, 3310.

[34] A. Watanabe, A. Yamashita, M. Nakano, T. Yamamura, T. Kajiwara, *Chem. Eur. J*., **2011**, *17*, 7428.

[35] R. J. Blagg, C. A. Muryn, E. J. L. McInnes, F. Tuna, R. E. P. Winpenny, *Angew. Chem. Int. Ed.*, **2011**, *50*, 6530.

[36] F. Tuna, C. A. Smith, M. Bodensteiner, L. Ungur, L. F. Chibotaru, E. J. L. McInnes, R. E. P. Winpenny, D. Collison, R. A. Layfield, *Angew. Chem. Int. Ed*., **2012**, *51*, 6976.

[37] J. Tejada, E. M. Chudnovsky, E. del Barco, J. M. Hernandez, T. P. Spiller, *Nanotechnology*, **2001**, *12*, 181.

[38] M. Urdampilleta, S. Klyatskaya, J-P. Cleuziou, M. Ruben, W. Wernsdorfer, Nat. Mat. **2011**, *10*, 502.

[39] **a)** P. Hänninen, H. Härmä (Eds), *Lanthanide Luminescence, Photophysical, Analytical and Biological Aspects*, Springer-Verlag, Berlin-Heidelberg, **2011**; **b)** K. Binnemans, *Chem. Rev*., **2009**, *109*, 4283; **c)** M. D. Ward, *Coord. Chem. Rev*., **2007**, *251*, 1663; **d)** J.-C. G. Bünzli, *Acc. Chem. Res*., **2006**, *39*, 53; **e)** W. C. Chan, D. J. Maxwell, X. Gao, R. E. Bailey, M. Han, S. Nie, *Curr. Opin. Biotechnol*., **2002**, *13*, 40.

[40] **a)** R. C. Evans, P. Douglas, C. J. Winscom, *Coord. Chem. Rev.,* **2006**, *250*, 2093; **b)** J. Silver, en: M. D. Ward (Ed.), *Comprehensive Coordination Chemistry,* vol. 9, 2nd Ed., Elsevier, Oxford, **2004**, p. 689.

[41] S. V. Eliseeva, D. N. Pleshkov, K. A. Lyssenko, L. S. Lepnev, J.-C. G. Bünzli, N. P. Kuzmina, *Inorg. Chem*., **2010**, *49*, 9300.

[42] S. V. Eliseeva, M. Ryazanov, F. Gumy, S. I. Troyanov, L. S. Lepnev, J.-C. G. Bünzli, N. P. Kuzmina, *Eur. J. Inorg. Chem*., **2006**, 4809.

[43] J.-C. G. Bünzli, *Chem. Rev*., **2010**, *110*, 2729.

[44] **a)** A. Dossing, *Eur. J. Inorg. Chem*., **2005**, 1425; **b)** J. C. Bünzli, C. Piguet, *Chem. Soc. Rev.*, **2005**, *34*, 1048; **c)** V. Vicinelli, P.Ceroni, M. Maestri, V. Balzani, M. Gorka, F. Vögtle, *J. Am. Chem. Soc.*, **2002**, *124*, 6461; **d)** S. I. Klink, G. A. Hebbink, L.Grave, F. G. A. Peters, F. C. J. M. van Veggel, D. N. Reinhoudtand, J. W. Hofstraat, *Eur. J. Org. Chem*., **2000**, 1923; **e)** W. D. Horrocks Jr, J. P. Bolender, W. D. Smith, R. M.Supkowski, *J. Am. Chem. Soc.,* **1997**, *119*, 5972.

[45] S. Faulkner, J. L. Matthews, *Fluorescent and luminescent complexes for Biomedical Applications,* in Volume 9 of *Comprehensive Coordination Chemistry*, 2nd Edition, ed. M. D. Ward, Elsevier, Oxford, **2003,** pp 913-944.

[46] **a)** E. Desurvire en *Erbium-doped amplifiers. Principles and Applications,* **1994**, John Wiley & Sons, New York; **b)** Y. Oshishi, T. Kanamori, Y. Kitagawa, S. Takashashi, E. Snitzer, G. H. Sigel Jr, *Opt. Lett.,* **1991**, *16*, 1747.

[47] R. Sessoli, *Angew. Chem. Int. Ed.*, **2012**, *51*, 43.

[48] C. Zimm, A. Jastrab, A. Sternberg, V. K. Pecharsky, K. A. Gschneidner Jr., M. Osborne, I. Anderson, *Adv. Cryog. Eng.,* **1998**, 43, 1759.

[49] **a)** E. Colacio, J. Ruiz, G. Lorusso, E. K. Brechin, M. Evangelisti, *Chem. Commum.*, **2013**, *49*, 3845; **b)** Y.-Z. Zheng, E. M. Pineda, M. Helliwell, R. E. P. Winpenny. *Chem. Eur. J., **2012**, 18,* 4161.

CHAPTER 1

AN EXPERIMENTAL AND THEORETICAL MAGNETO-STRUCTURAL STUDY OF POLYNUCLEAR NI(II) COMPLEXES

1.1. INTRODUCTION

In order to design systems with high spin ground states, it is very helpful to understand which are the main structural factors governing the magnetic exchange interactions through the bridging ligands. In this regard, the experimental and theoretical magneto-structural correlations are very useful tools for qualitatively assessing the magnetic coupling in coordination clusters and then for obtaining molecule based materials with predicted magnetic properties. Therefore, the suitable choice of ligand (with specific donor sites and bridging modes), metal ions (with specific spin and preferred stereochemistry) and anionic coligands (either with an ancillary or bridging function) plays a crucial role in determining the final architecture of the polynuclear complex and consequently its ground state and magnetic properties.

The best strategy for achieving the objectives of this work consists on using polydentate ligands containing nitrogen donor atoms and alkoxo- and/or phenoxo-groups that can act as bridges between two or more metal atoms. The ligand N,N'-dimethyl-N,N'-bis(2-hidroxy-3-formyl-5-bromobenzyl)ethylenediamine, hereafter H_2L, shown in Figure 1.1, fulfills these requirements and presents different coordination modes, being those the reasons why it is chosen for carrying out this work.

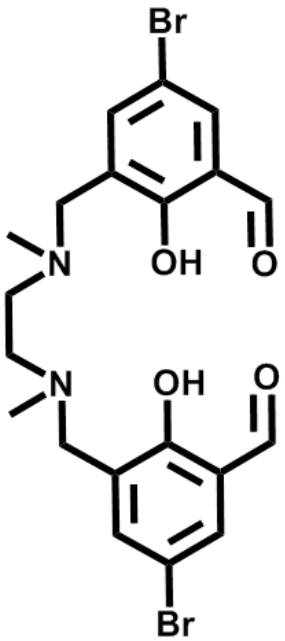

H_2L

Figure 1.1.- Structure of the ligand H_2L.

The ligand H_2L was first synthesized in 1996 by the Mannich reaction of N,N'-dimethyletylenediamine, 5-bromosalicylaldehyde and formaldehyde, in ethanol at the refluxing temperature.[1] Although this ligand has given rise to the formation of many complexes, in most of them the ligand acts as a precursor of other macrocycles, such as those shown in Figure 1.2.

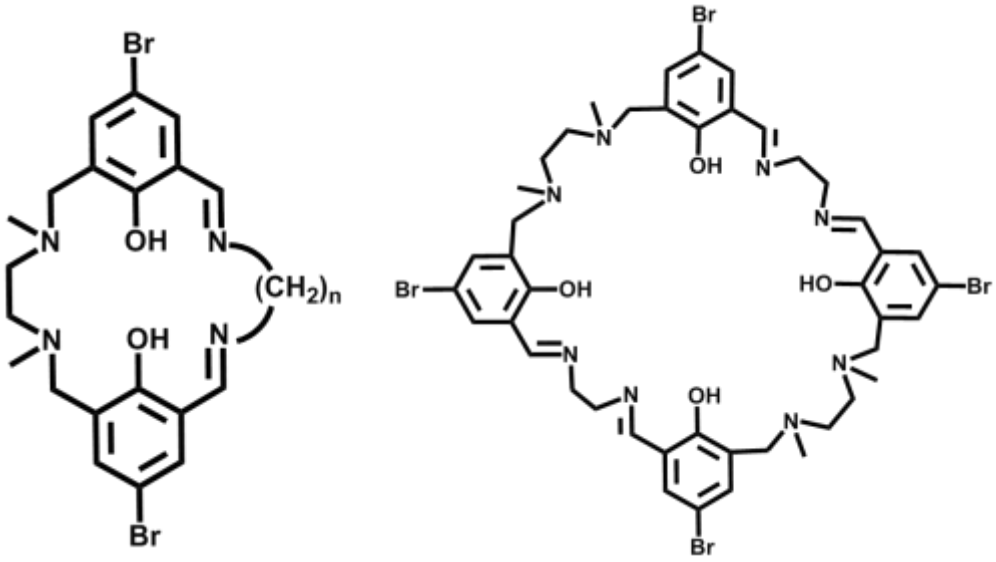

Figure 1.2.- Examples of the macrocycles prepared from the ligand H_2L.

In addition, the ligand H_2L displays a wide variety of coordination modes (Figure 1.3) and we believe that with the help of appropriate coligands, numerous mononuclear or polynuclear complexes could be obtained.

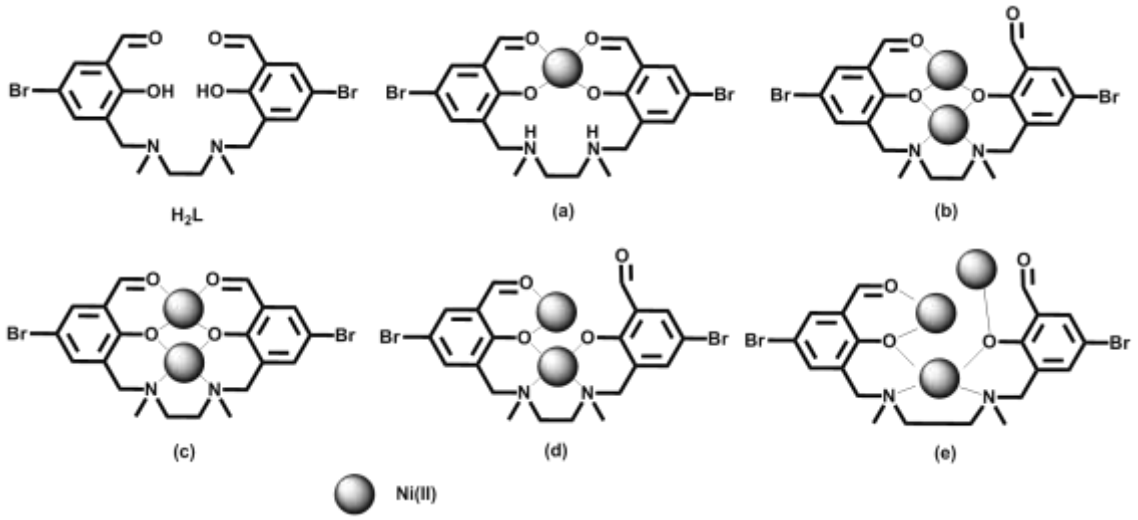

Figure 1.3.- Structure of H_2L and its coordination modes.

This chapter collects the synthesis, structural characterization, magnetic properties and DFT theoretical calculations of six new polynuclear Ni(II) complexes with different anionic coligands (acetate, azide, thiocyanate, methoxo and acetylacetonate) where the H_2L ligand acts in an open form with different coordination modes. The Ni(II) ion has been chosen because it has considerable magnetic anisotropy generated from the second order spin–orbit coupling and therefore it is a promising candidate for preparing SMMs (despite this, only a few examples of Ni(II) single-molecule magnets have been reported so far).[2] It should be noted that the combination of a di-μ-phenoxo bridged Ni(II) fragment with other bridging ligands may lead to uncommon mixed-bridged fragments able to mediate ferromagnetic interactions between the metal ions, thus favouring a high spin ground state of the complex.

1.2. PREPARATION OF COMPLEXES

1.2.1. $[Ni(H_2L)(NO_3)(H_2O)]NO_3 \cdot H_2O$ (1)

A solution of $Ni(NO_3)_2 \cdot 6H_2O$ (36.4 mg, 0.125 mmol) and H_2L (64.3 mg, 0.125 mmol) in MeOH (5 mL) was stirred for 5 minutes and left undisturbed at room temperature. X-ray-quality green crystals were formed from the solution after several days, which were collected by filtration, washed with MeOH and dried in vacuum. Yield: 52 %. Anal. Calc. for $C_{20}H_{26}N_4O_{12}Br_2Ni$. C, 32.77; H, 3,58; N, 7,64. Found: C, 32,88; H, 3,60; N, 7,58.

1.2.2. $[Ni_2(\mu\text{-}L)(acac)_2(H_2O)] \cdot CH_3CN$ (2)

To a suspension of $Ni(acac)_2$ (64.2 mg, 0.25 mmol) in CH_3CN (5 mL), 64.3 mg of H_2L (0.125 mmol) and drops of water were added. The mixture was stirred for 15 minutes and then kept undisturbed until the thin solid was decanted. The resulting solution was separated and kept at room temperature for several days, affording few X-ray-quality crystals. Yield: 8 %. Anal. calc. for $C_{32}H_{39}N_3O_9Br_2Ni_2$: C, 43.34; H, 4.43; N, 4.74. Found: C, 43.78; H, 4.55; N, 4.88.

1.2.3. $[Ni_2(\mu\text{-}L)(\mu\text{-}OAc)(NCS)]$ (3)

To a solution of $Ni(OAc)_2 \cdot 4H_2O$ (62.2 mg, 0.25 mmol) in MeOH (10 mL), were added with continuous stirring 64.3 mg of H_2L (0.125 mmol) and 122 mg of KSCN (1.25 mmol). The mixture was stirred for 30 minutes, filtered and the filtrate was kept

undisturbed at room temperature. After two days, green crystals of **3** were obtained, which were filtered off, washed with MeOH and dried in vacuum Yield: 49 %. Anal. calc. for $C_{23}H_{23}N_3O_6SBr_2Ni_2$: C, 37.00; H, 3.11; N, 5.63. Found: C, 37.07; H, 3.15; N, 5.55.

1.2.4. $[Ni_3(\mu\text{-}L)_2(\mu\text{-}OH_2)_2(H_2O)(CH_3CN)](NO_3)_2\cdot 4CH_3CN$ (4)

H_2L (64.3 mg, 0.125 mmol), drops of water and Et_3N (25.3 mg, 0.25 mmol) were successively added to a solution of $Ni(NO_3)_2\cdot 6H_2O$ (54.7 mg, 0.188 mmol) in CH_3CN (10 mL). The mixture was stirred during 30 minutes and then was filtered to eliminate any amount of insoluble material. The filtrate was allowed to stand at room temperature for a day, whereupon green X-ray quality crystals of **4** were formed. Yield: 71 %. Anal. calc. for $C_{50}H_{61}N_{11}O_{17}Br_4Ni_3$: C, 37.92; H, 3.88; N, 9.73. Found: C, 37.72; H, 3.94; N, 9.59.

1.2.5. $[Ni_4(\mu\text{-}L)_2(\mu\text{-}OAc)_2(\mu\text{-}OCH_3)_2]\cdot 6H_2O\cdot 2CH_3OH$ (5)

To a solution of $Ni(OAc)_2\cdot 4H_2O$ (62.2 mg, 0.25 mmol) in MeOH (5 mL) the ligand H_2L (64.3 mg, 0.125 mmol) was added and the mixture was stirred for 30 minutes, filtered, and the filtrate left undisturbed at room temperature. After several days, X-ray quality green crystals were formed, which were collected by filtration, washed with MeOH and dried in vacuum. Yield: 62 %. Anal. calc. for $C_{48}H_{72}N_4O_{22}Br_4Ni_4$: C, 35.78; H, 4.50; N, 3.48. Found: C, 35.86; H, 4.60; N, 3.56.

1.2.6. $[Ni_4(\mu\text{-}L)_2(\mu\text{-}OAc)_2(\mu\text{-}N_3)_2]\cdot 2H_2O\cdot CH_3OH$ (6)

This compound was prepared following the procedure described for **3**, except that NaN_3 (8.13 mg, 0.125 mmol) was added instead of KSCN. Yield: 54 %. Anal. calc. for $C_{45}H_{54}N_{10}O_{15}Br_4Ni_4$: C, 35.34; H, 3.56; N, 9.16. Found: C, 35.42; H, 3.63; N, 9.05.

1.3. EXPERIMENTAL RESULTS

The reaction of the H_2L ligand with $Ni(NO_3)_2\cdot 6H_2O$ in a 1:1 molar ratio and using methanol as solvent afforded the mononuclear cationic complex **1** (Scheme 1.1), in which the active protons of the ligand migrate from the phenolic oxygen atoms to the nitrogen atoms and, as a result, the ligand shows the zwitterionic coordination mode depicted in Figure 1.3.a.

The reaction of $Ni(acac)_2$ with H_2L in a mixture acetonitrile-water, using a H_2L/Ni(II) 1:2 molar ratio led to the dinuclear complex **2** (Scheme 1.1), where the deprotonated ligand exhibits the coordination mode b shown in Figure 1.3. The basic character of the acetylacetonate anion allows for the deprotonation of the ligand. The addition of triethylamine and drops of water to a solution of the ligand and $Ni(NO_3)_2{\cdot}6H_2O$ (H_2L/Ni(II) 1:1.5 molar ratio) in acetonitrile allowed the preparation of green crystals of the bent trinuclear complex **4**, in which the fully deprotonated ligand exhibits the coordination mode d depicted in Figure 1.3.

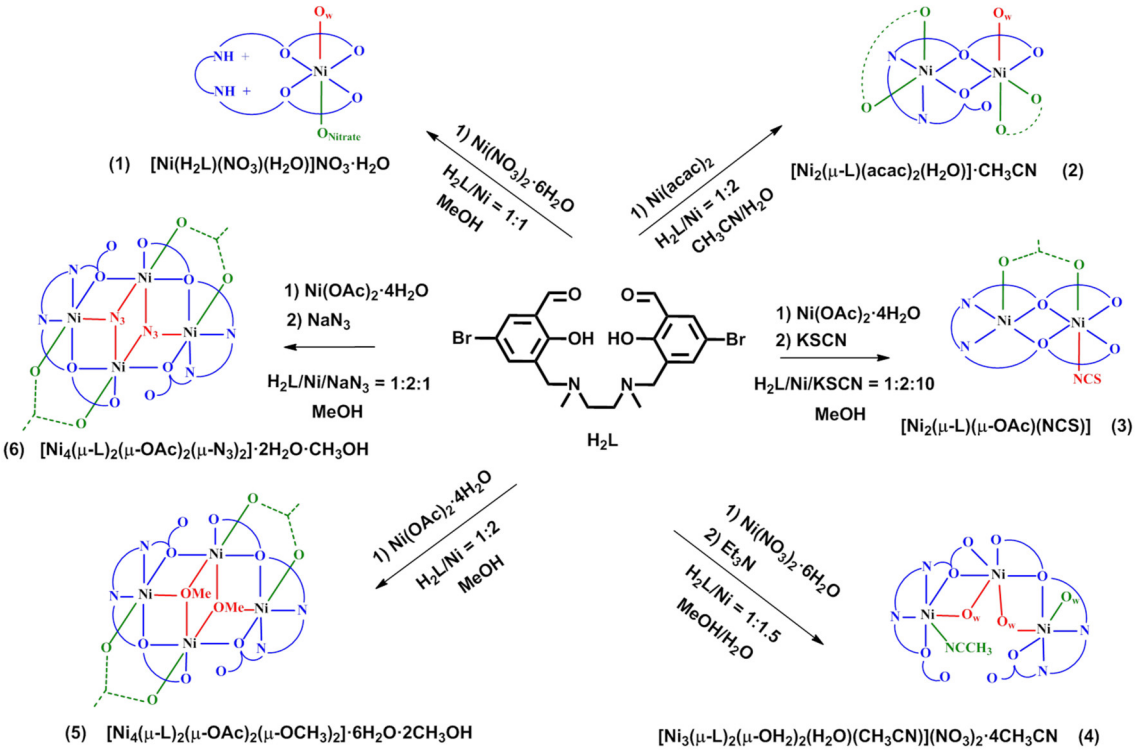

Scheme 1.1.- Ni(II) complexes prepared from the H_2L ligand.

The reaction between $Ni(OAc)_2{\cdot}4H_2O$ and H_2L in methanol and using a H_2L/Ni(II) 1:2 ratio leads to the formation of the tetranuclear face-sharing defective dicubane complex **5**. In the formation process, two open dinuclear $[Ni_2L_2(\mu\text{-OAc})]^+$ building units are assembled by methoxo anions that occupy two vertices of the common face of the final defective dicubane structure. The ligand exhibits the coordination mode e (Figure 1.3) and its deprotonation is provoked by the basic acetate anion. Although methanol is a weaker acid than acetic acid and therefore the formation of methoxo anion from a solution of acetate in methanol is not favoured, the very small amount of methoxo anion in the equilibrium may be enough to connect the $[Ni_2L_2(\mu\text{-OAc})]^+$ units, shifting

the reaction to the formation of complex **5**. The same reaction as for **5**, but using NaN_3 in a 1:2:1 H_2L/Ni(II)/NaN_3 molar ratio afforded the tetranuclear face-sharing defective dicubane complex **6**, in which the azide anions occupy the same positions as the methoxo anions in the isostructural complex **5**. Using the same reaction conditions as for the formation of **5** and an excess of KSCN (1:5 Ni(II)/KSCN ratio), the dinuclear compound **3** was obtained, in which the ligand is fully deprotonated and exhibits the coordination mode c of the Figure 1.3.

All these results clearly show the important role of the anionic coligand (X), solvent and ratio of reactants in determining the final structure of the L/Ni(II)/X system.

1.3.1. Crystal structures of complexes 1-6

The crystal structure of **1** is shown in Figure 1.4 and consists of mononuclear $[Ni(H_2L)(NO_3)(H_2O)]^+$ cationic units, nitrate anions and one crystallization water molecule, all involved in hydrogen bond interactions. Selected bond lengths for **1** are given in Appendices, Table A.2.

Within the mononuclear $[Ni(H_2L)(NO_3)(H_2O)]^+$ unit, the ligand is coordinated to the Ni(II) ion in a O4 neutral zwitterionic form through the two deprotonated phenolic oxygen atoms and the two aldehyde oxygen atoms, therefore acting in a 1κ-O_{1A}, 1κ-O_{2A}, 1κ-O_{3A}, 1κ-O_{4A}-tetradentate coordination mode (O_{2A} and O_{3A} represent the phenolic oxygen atoms). The zwitterion is formed by proton migration from the phenolic oxygen atoms to the nitrogen atoms. Analogous processes have been observed for other complexes containing bis(phenol)diamine Mannich and Schiff base ligands.[3] The Ni(II) ion exhibits a NiO_6 distorted octahedral coordination environment, in which the O4 donor atoms of the ligand H_2L are located at the equatorial positions, whereas the coordinated water molecule (O1W) and the coordinated nitrate group (O1C) occupy the axial positions.

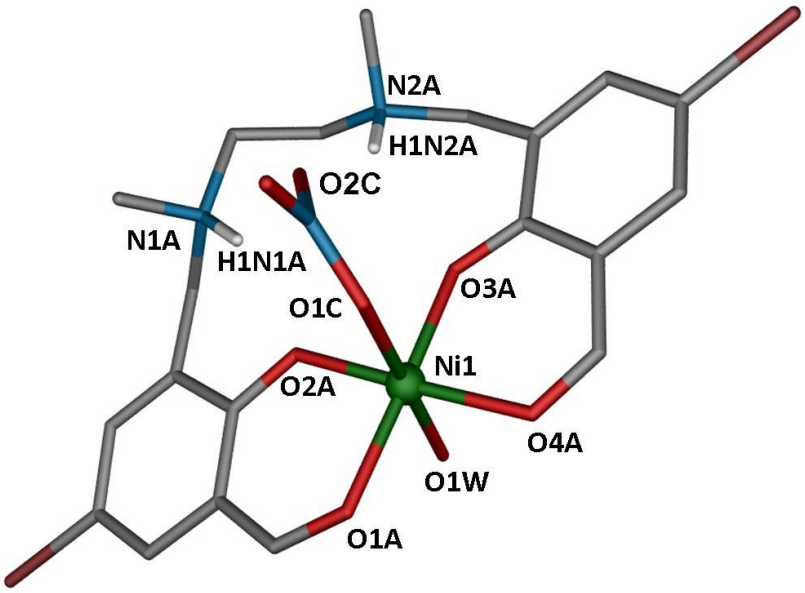

Figure 1.4.- Perspective view of the cationic unit in **1**. Nickel, oxygen, nitrogen, carbon and bromine atoms are coloured green, red, blue, grey and brown, respectively. Nitrate counteranion, hydrogen atoms (except H1N1A and H1N2A, in white) and solvent molecules are omitted for the sake of clarity.

The Ni-O distances are found in the 1.965(2)-2.123(2) Å ranges, those involving the phenoxo groups being significantly shorter than those involving the aldehyde oxygen atoms, as expected. The variation in angles between *trans* donor atoms at the metal centre is very small (1°), whereas the variation in cisoid angles spans a wide range 87.17(9)-92.84(9)°. The aromatic rings of the ligand are practically planar (dihedral angle 3.83°).

The protonated nitrogen atoms N1A and N2A of the zwitterion are involved in moderate intramolecular hydrogen bond interactions with the oxygen atom O2C of the coordinated nitrate group and the nearest phenolic oxygen atoms (O2A and O3A) of the ligand, with O···N distances in the 2.648(4)-2.895(4) Å range (Figure 1.5). In addition, the coordinated and noncoordinated water molecules and the nitrate counteranion are involved in an intricate hydrogen bond network with O···O distances in the range of 2.710(4)-2.764(4) Å.

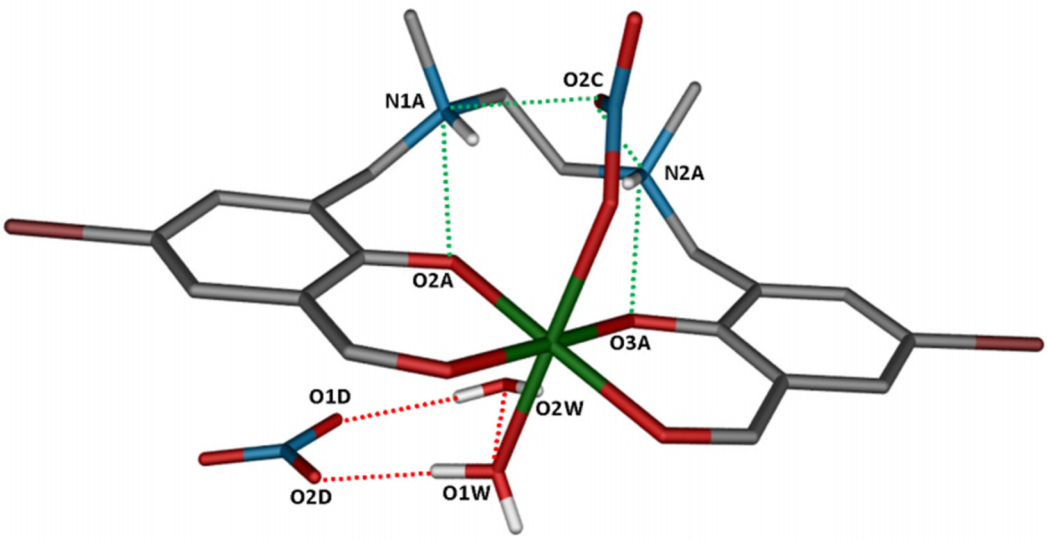

Figure 1.5.- A perspective view of the structure of **1** together with intramolecular (green dotted lines) and intermolecular (red dotted lines) hydrogen bonds.

Complex **2** is formed by a neutral dinuclear [Ni(acac)(μ-L)Ni(acac)(H_2O)] (acac = acetylacetonate) unit and one crystallization acetonitrile molecule. A perspective view of the structure is given in Figure 1.6, whereas selected bond lengths and angles are given in Appendices, Table A.2. In the dinuclear unit, the ligand acts in a 2κ-O_{1A}, 1κ-O_{2A}:2κ-O_{2A}, 1κ^2-N,N′, 1κ-O_{3A}:2κ-O_{3A} pentadentate bridging mode (O_{2A} and O_{3A} represent the phenolic oxygen atoms), which is represented as coordination mode b in Figure 1.3.

Within the [Ni(acac)(μ-L)Ni(acac)(H_2O)] dinuclear unit two cristallographically independent nickel atoms can be identified, labelled Ni1 and Ni2, which are bridged by two μ_2-phenoxo oxygen atoms (O2A and O3A). Both Ni(II) ions exhibit distorted octahedral coordination environments. The Ni1 atom displays a NiN_2O_4 coordination sphere which is composed by two nitrogen atoms and two phenoxo-bridging oxygen atoms of the deprotonated ligand (L^{2-}) and two oxygen atoms of the coordinated acac chelate coligand. In the case of Ni2, the NiO_6 coordination sphere is formed by the oxygen atoms that belong to the two phenoxo bridges and one aldehyde group (O1A) of the ligand, the second acac chelate coligand and a coordinated molecule of water. The Ni-O distances are in the ranges 2.011(3)-2.125(2) Å and 1.980(2)-2.091(2) Å for Ni1 and Ni2, respectively, whereas the Ni···Ni distance of 3.203(1) Å is comparable to those found in other similar dinuclear nickel(II) complexes having a diphenoxo bridge.[4]

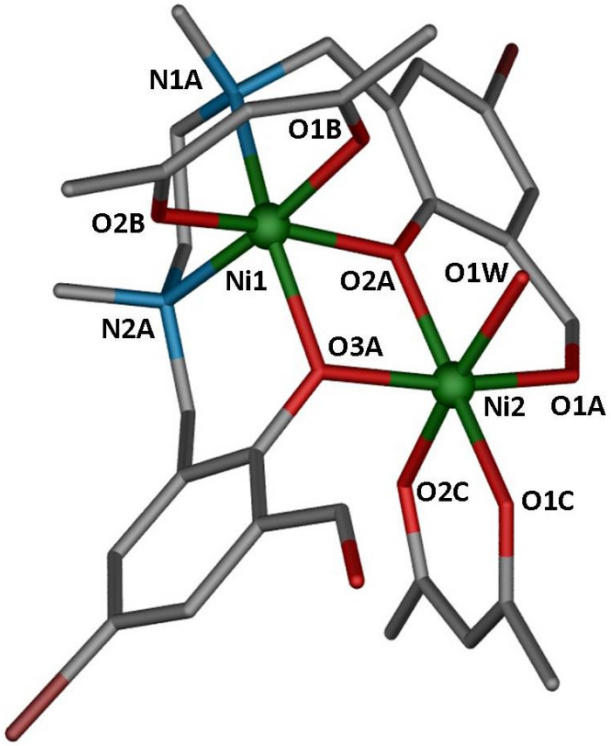

Figure 1.6.- Perspective view of the molecular structure of **2**. Nickel, oxygen, nitrogen, carbon and bromine atoms are coloured green, red, blue, grey and brown, respectively. Hydrogen atoms and solvent molecules are omitted for the sake of clarity.

Due to a non planar configuration of the ligand, the dihedral angle between aromatic rings is 79.94°. Each bridging phenoxo oxygen atom is asymmetrically bounded, with one Ni-O bond slightly longer [Ni1-O2A 2.125(2) Å; Ni(1)-O3A 2.060(2) Å] than the other [Ni2-O2A 2.032(2) Å, Ni2-O3A 2.058(2) Å]. The two phenoxo bridging angles (θ), Ni1-O2A-Ni2 and Ni1-O3A-Ni2 are 100.79(7)° and 102.16(8)°, respectively, and the Ni_2O_2 group is almost planar with a dihedral angle between the two O-Ni-O planes (hinge angle, β) of 8.86° (Figure 1.7). Finally, the mean value of the out-of-plane displacements of the O-C bond belonging to the phenoxo bridging group from the NiONi plane (τ) are 40.35° and 1.45° for O2A-C3A and O3A-C15A bonds, respectively.

The dinuclear Ni_2 units are held together in pairs by a couple of symmetrically related hydrogen bonds involving the non-coordinated carbonyl oxygen atom (O4A) of one molecule and the oxygen atom of the coordinated water (O1W) of the adjacent molecule, with a O···O distance of 2.778(3) Å.

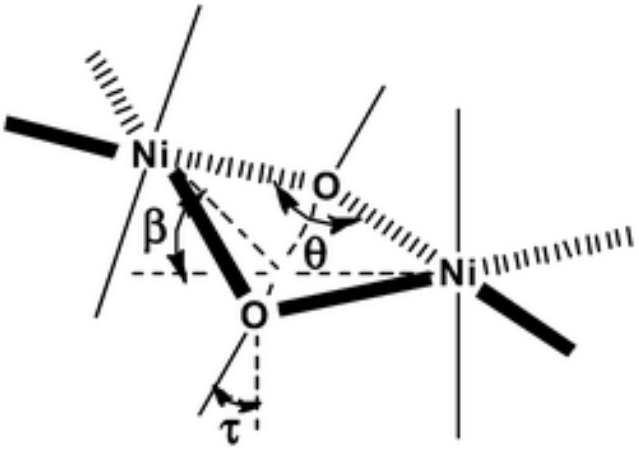

Figure 1.7.- The θ, τ and β angles in the Ni-(μ-O)$_2$-Ni bridging fragment.

The structure of **3** (Figure 1.8) is made of neutral dinuclear [Ni(μ-L)(μ-OAc)Ni(NCS)] units, in which the Ni(II) ions are bridged by two phenoxo groups of the deprotonated (L^{2-}) ligand (adopting the compartmental coordination mode c in Figure 1.3) and one *syn–syn* acetate anion. The inner site of the ligand is occupied by a Ni(II) ion that exhibits a NiN_2O_3 square pyramidal coordination sphere. In this description, the two nitrogen atoms and the two phenoxo-bridging oxygen atoms of the ligand are located at the basal positions, whereas the apical position is occupied by an oxygen atom of the acetate bridge. The outer Ni(II) ion exhibits a slightly distorted NiO_5N octahedral coordination sphere, which is made by the two phenoxo bridging oxygen atoms, the two aldehyde oxygen atoms, one oxygen atom of the acetate bridging group and the nitrogen atom that belongs to the SCN^- group. The acetate oxygen atom and the nitrogen atom are located in *trans* positions and, consequently, the oxygen atoms of the ligand are located in the equatorial plane of the slightly distorted octahedron. The Ni···O and the Ni···N distances are around 2 Å, whereas the Ni···Ni distance is 2.954(1) Å (Appendices, Table A.2).

The bridging acetate group forces the structure to be folded with a hinge angle (β) for the Ni-(μ-O)$_2$-Ni bridging fragment of 33.60°. As a consequence of the structure folding, the Ni-O-Ni bridging angles (θ) and the intradinuclear Ni···Ni distance decrease with respect to those observed in **2** to reach values of 94.1(1)°, 95.4(1)° and 2.954(1) Å, respectively. The values of the out-of-plane displacements of the O-C bonds belonging to the phenoxo bridging groups from the Ni1(O2A)Ni2 and Ni1- (O3A)Ni2 planes are 42.75° and 31.35°, respectively.

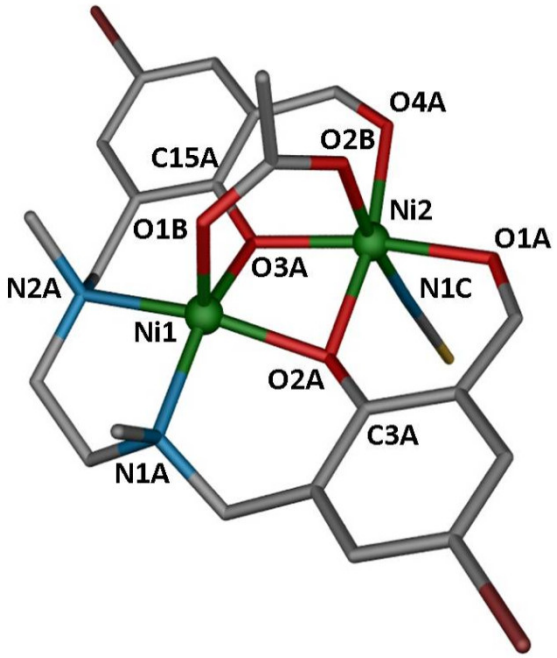

Figure 1.8.- Perspective view of the molecular structure of **3**. Nickel, oxygen, nitrogen, carbon and bromine atoms are coloured green, red, blue, grey and brown, respectively. Hydrogen atoms are omitted for the sake of clarity.

Complex **4** is made of bent trinuclear asymmetric cationic entities of formula $[Ni_3(\mu\text{-}L)_2(\mu\text{-}OH_2)_2(H_2O)(CH_3CN)]^{2+}$, two nitrate anions and four crystallization acetonitrile molecules (Figure 1.9). All the Ni(II) ions of the trinuclear unit are crystallographically independent. The central Ni2 ion is connected to the outer Ni1 and Ni3 ions through two double phenoxo/water bridging groups. The μ-phenoxo groups belong to two different fully deprotonated L^{2-} ligands (labelled A and B), which adopt a 2κ-O_1, 2κ-O_2:*n*κ-O_2, nκ^2-N,N′, *n*κ-O_3 (*n* is 1 or 3) pentadentate coordination mode, with bridging and monocoordinated phenoxo groups and uncoordinated and monocoordinated aldehyde groups (coordination mode d in Figure 1.3).

The central Ni2 atom exhibits a distorted octahedral NiO_6 coordination sphere, which is formed by the two water bridging molecules in *cis* positions, the two phenoxo bridging oxygen atoms in *trans* positions and two aldehyde oxygen atoms (O1A and O1B) belonging to two different L^{2-} ligands in a *cis* arrangement. The outer Ni1 ion presents a distorted octahedral NiN_3O_3 coordination environment, which is made by the two amine nitrogen atoms, one monocoordinated phenoxo oxygen atom (O3A), the phenoxo bridging oxygen atom (O2A) of the same deprotonated L^{2-} ligand, the nitrogen

atom of the coordinated acetonitrile molecule (N1P) and the oxygen atom of the water bridging group (O1P). The three oxygen atoms and, consequently, the three nitrogen atoms are in *fac* dispositions. In the case of outer Ni3, the NiN_2O_4 coordination environment is similar to that of Ni1 but the acetonitrile molecule is replaced by a water molecule.

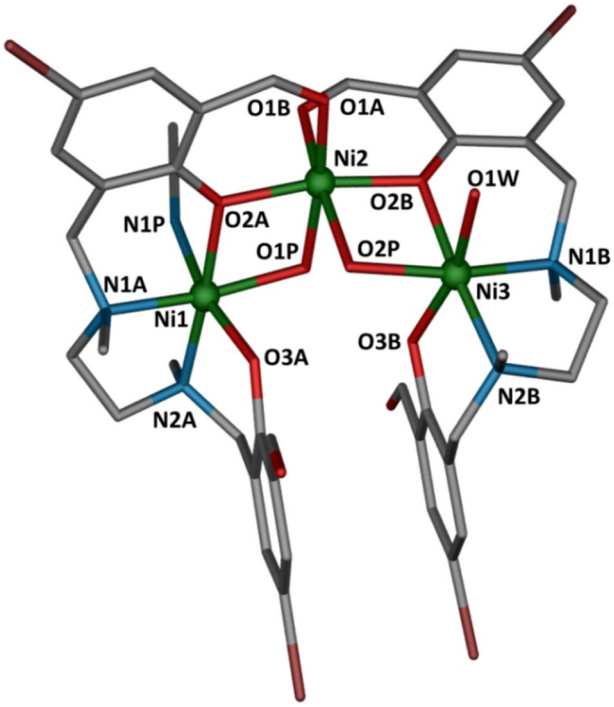

Figure 1.9.- Perspective view of the molecular structure of **4**. Nickel, oxygen, nitrogen, carbon and bromine atoms are coloured green, red, blue, grey and brown, respectively. Hydrogen atoms, nitrate counteranions and solvent molecules are omitted for the sake of clarity.

The Ni-O distances are in the 1.983(3)-2.137(3) Å range (selected bond length and angles are given in Appendices, Table A.2). The values of the out-of-plane displacements of the O-C bonds belonging to the phenoxo bridging groups from the Ni1(O2A)Ni2 and Ni3(O2B)Ni2 planes are 5.3° and 10.05°, respectively.

It should be noted that each water bridge molecule forms a bifurcated hydrogen bond (Figure 1.10, top) involving the monocoordinated phenoxo groups with a O···O donor acceptor mean distance of 2.582 Å and one of the nitrate counteranions with a O···O donor acceptor mean distance of 2.666 Å. The former hydrogen bonds are the main responsible for the bent conformation of the Ni_3 molecules. One of the nitrate

anions is involved in an additional hydrogen bond with the water molecule coordinated to Ni_3 belonging to a neighbouring trinuclear unit (O···O donor acceptor distance of 2.723 Å), giving rise to a chain running along the *b* axis (Figure 1.10, bottom). Neighbouring Ni···Ni intramolecular distances are 3.136(1) Å and 3.118(1) Å, whereas the shortest Ni···Ni intertrinuclear distance is 8.143(1) Å.

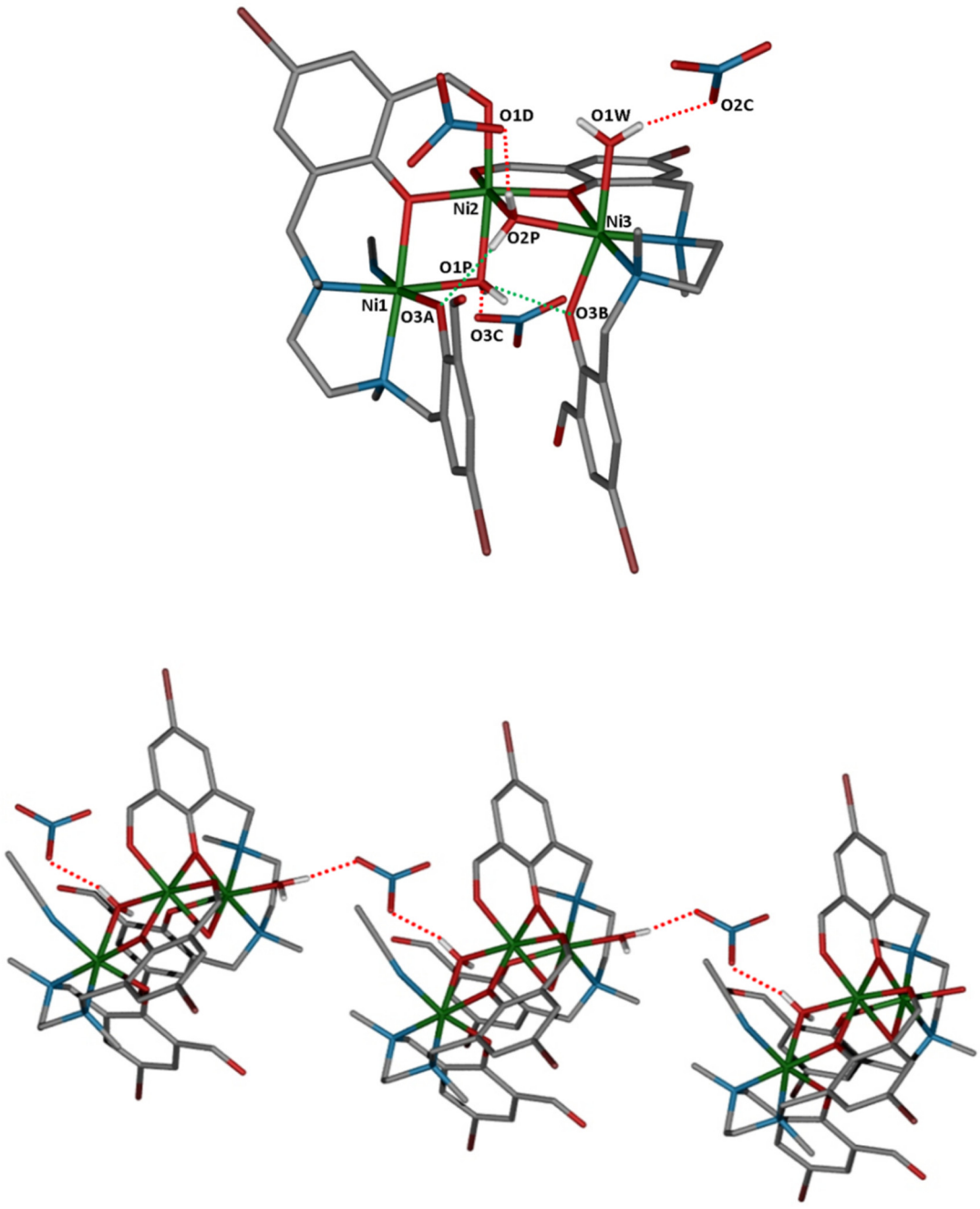

Figure 1.10.- A perspective view of the structure of **4** together with intramolecular (green dotted lines) and intermolecular (red dotted lines) hydrogen bonds (top) forming a chain expanding along the *b* axis (bottom).

The crystal structures of the tetranuclear complexes **5** and **6** are shown in Figure 1.11.

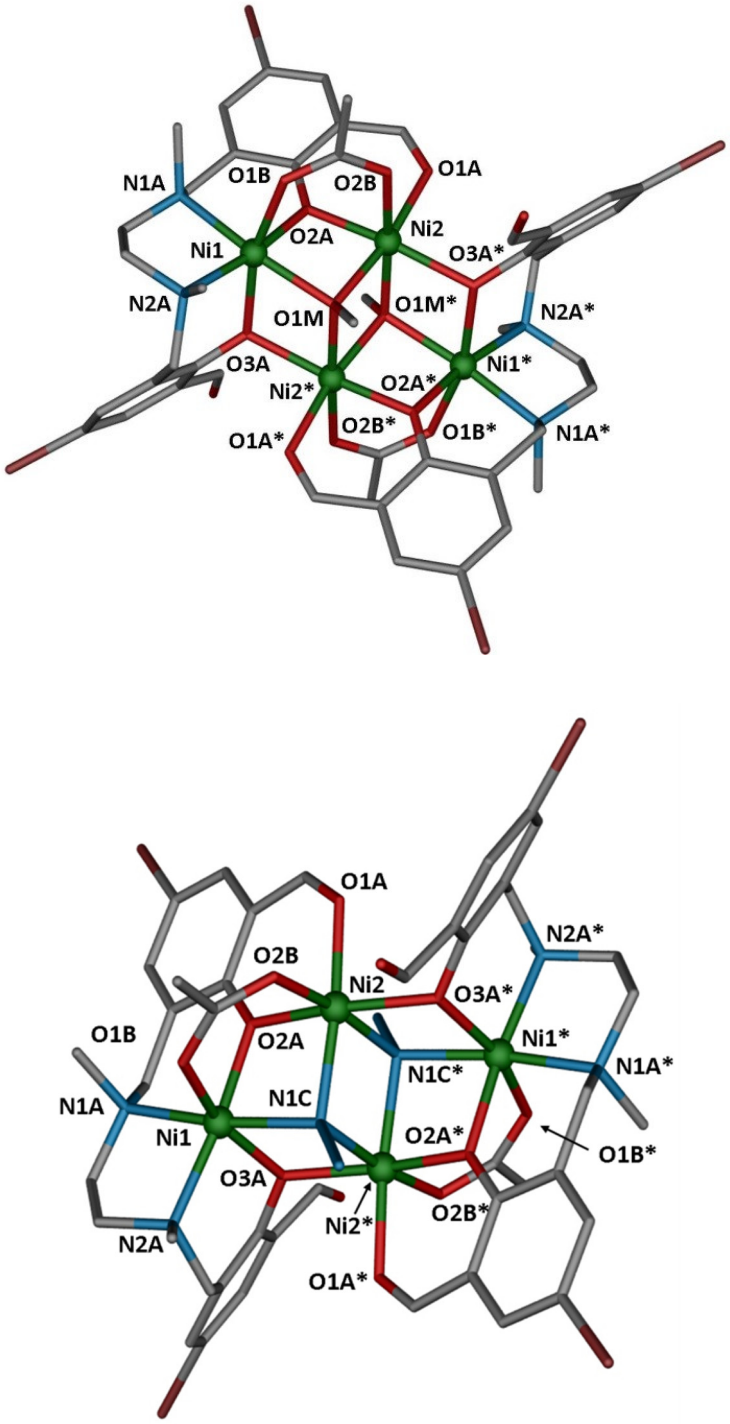

Figure 1.11.- Perspective view of the molecular structures of **5** (top) and **6** (bottom). Nickel, oxygen, nitrogen, carbon and bromine atoms are coloured green, red, blue, grey and brown, respectively. Hydrogen atoms and solvent molecules are omitted for the sake of clarity.

The structure analysis reveals that both complexes are made of centrosymmetric tetranuclear Ni(II) units, containing two deprotonated (L^{2-}) ligands, two *syn–syn* acetate bridging groups and two triple $\mu_{1,1,1}$-bridging groups (either methoxo or azido), and crystallization solvent molecules (six water and two methanol molecules for **5** and two water and one methanol molecules for **6**). In complex **6** two identical crystallographically independent Ni_4 units are present (**6A** and **6B**), which slightly differ in bond lengths and angles.

Both compounds exhibit very similar face-sharing defective dicubane-like cores with two missing vertices. The common face of the defective dicubane unit in **5** and **6** is formed by two crystallographically related Ni2 and Ni2* atoms and either the oxygen atom of the $\mu_{1,1,1}$-methoxo bridging groups in the former or the N1 and N1′ nitrogen atoms of the $\mu_{1,1,1}$-end-on azido bridging groups in the latter.

In both complexes, the dideprotonated ligand L^{2-} is coordinated to the Ni(II) ions by the two amine nitrogen atoms, the two phenoxo oxygen atoms, which bridge Ni1 and Ni2 atoms and occupy vertices of the dicubane core, and one of the aldehyde oxygen atoms, thus exhibiting a 2κ-O_{1A}, 2κ-O_{2A}:1κ-O_{2A}, 1κ^2-N,N′, 1κ-O_{3A}:2κ-O_{3A}, pentadentate coordination mode (mode e in Figure 1.3). In addition to the phenoxo bridge, the metal centers Ni1 and Ni2 are also bridged by a *syn–syn* acetate group, whereas either $\mu_{1,1,1}$-methoxo or $\mu_{1,1,1}$-azido bridging groups connect two crystallographically equivalent Ni2 atoms between them and with each Ni1 atom.

The two couples of centrosymmetrically related nickel atoms exhibit an octahedral coordination geometry. In **5**, the Ni1 atoms show NiN_2O_4 coordination environments formed by two nitrogen and two phenoxo bridging oxygen atoms belonging to the same ligand (L^{2-}), one oxygen atom, O(1B), from the acetate bridging group and one oxygen atom, O(1M), from the $\mu_{1,1,1}$-methoxo group. The Ni2 atoms exhibit NiO_6 coordination spheres, which are formed by the coordination of two phenoxo bridging oxygen atoms belonging to two different ligands O(2A), O(3A), one oxygen atom from the acetate bridging group (O2B), one aldehyde oxygen atom O(1A) and the two $\mu_{1,1,1}$-methoxo oxygen atoms. The coordination environments around Ni1 and Ni2 atoms in **6** are similar to those observed in **5**, but changing the oxygen atoms of the $\mu_{1,1,1}$-methoxo bridging groups by the nitrogen atoms of the $\mu_{1,1,1}$-azido bridging groups, and therefore exhibit NiN_3O_3 and NiN_2O_4 octahedral coordination polyhedra, respectively.

The Ni(II) atoms in **5** and **6** have a similar environment and follow a similar trend in their bond distances; the largest Ni-O distances corresponding to the phenoxo oxygen

atoms O(3A). The Ni-X-Ni (X = O/N) bridging angles span a wide range of values varying between 93.8(1)–103.8(1)° for **5** and 91.1(2)–102.9(2)° for **6**. The Ni2-(μ-O_2)-Ni2* and Ni2-(μ-N_2)-Ni2* bridging fragments are coplanar, whereas the mean hinge angle for the double μ-phenoxo/$\mu_{1,1,1}$-methoxo or μ-phenoxo/$\mu_{1,1,1}$-azido bridged Ni_2 fragments is of 6.03° for **5** and 6.90° for **6**. As expected, the additional *syn-syn* acetate bridge in the third bridging fragment increases the mean hinge angle to 19.15° and 19.92° in **5** and **6**, respectively. The Ni1···Ni2 and Ni2···Ni2* mean distances are 3.110 Å and 3.067 Å, respectively, for **5** and 3.149 and 3.172 Å, respectively, for **6**. Bond lengths and angles in the coordination environment of the Ni(II) atoms in **5** and **6** are listed in Appendices, Table A.2.

Crystallographic data for complexes **1**-**6** can be found in Appendices, Table A.1. The degree of distortion of the Ni(II) coordination polyhedra in **1**-**6** have been calculated by using the continuous shape measure theory with the SHAPE software,[5] concluding that the NiX_6 coordination spheres are found in the OC-6 ↔ TPR-6 deformation pathway and are close to the octahedral geometry somewhat distorted to trigonal prismatic (Appendices, Table A.20 and A.21).

1.3.2. Magnetic properties of complexes 2-6

The temperature dependence of the $\chi_M T$ product for complexes **2**-**6** (χ_M being the molar paramagnetic susceptibility of the compound) under a constant magnetic field of 0.1 T in the 2-300 K range are displayed in Figures 1.12, 1.14 and 1.15.

At room temperature the $\chi_M T$ value for complex **2** is 2.1 $cm^3 \cdot K \cdot mol^{-1}$, which is in good agreement with the expected value for two non-interacting Ni(II) ions (S = 1) with g = 2.0 (2.0 $cm^3 \cdot K \cdot mol^{-1}$). When the temperature is lowered, the $\chi_M T$ product remains almost constant until 100 K, and then drops abruptly to reach a value very close to zero at 2 K. This magnetic behaviour points out the presence of antiferromagnetic exchange interactions within the Ni(II) dinuclear unit. In keeping with this, the thermal variation of the χ_M shows a maximum at 20 K.

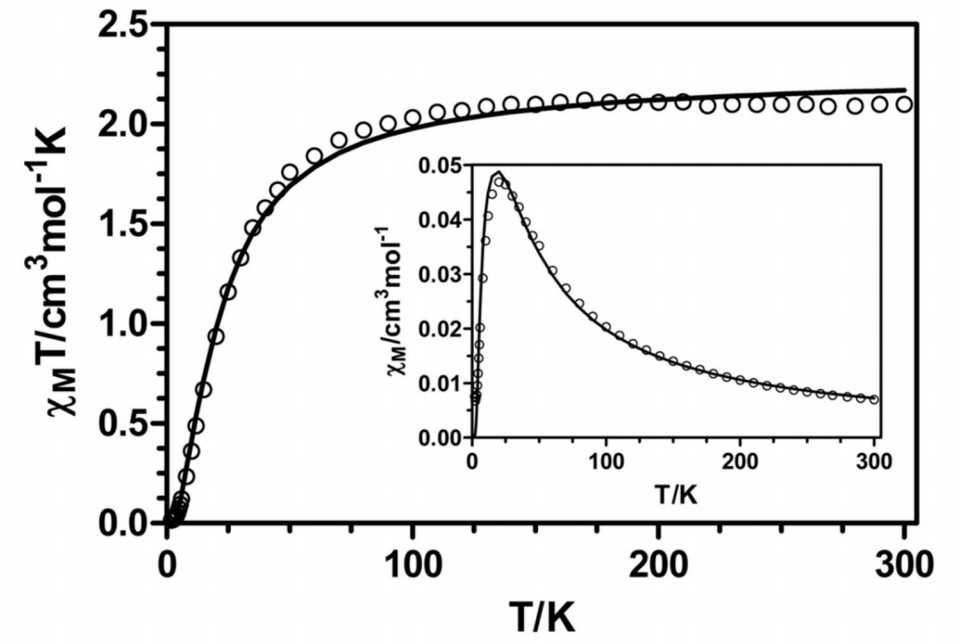

Figure 1.12.- Temperature dependence of the $\chi_M T$ product for **2** in the 2–300 K range. Inset: temperature dependence of the χ_M for **2**. The solid lines are generated from the best fit to the magnetic parameters.

The magnetic behaviour of complex **2** has been modelled using the following Hamiltonian:

$$\mathcal{H} = -JS_{Ni1}S_{Ni2} + \sum_{i=1}^{2} D_{Ni}S_{Niz}^2 - zJ'\langle S_z \rangle S_z \quad (\textit{Equation 1.1})$$

where J is the magnetic exchange pathway through the di-μ-phenoxo double bridge and D_{Ni} is the axial single ion zero field splitting parameter, which is assumed to be the same for both Ni(II) ions, and $-zJ' < S_z > S_z$ accounts for the intermolecular interactions by means of the molecular field approximation. Since zJ' and D_{Ni} are strongly correlated and provoke the same result at low temperature, and in view of the fact that the influence of D is very weak compared to the intramolecular antiferromagnetic interaction, very difficult to evidence from the magnetic susceptibility data,[6] the magnetic data were analysed by using the isotropic spin Heisenberg Hamiltonian, in which the local anisotropy of the Ni(II) ions and the intermolecular interactions were not taken into account. The fit of the experimental susceptibility data using the full-matrix diagonalization PHI program[7] afforded the following set of parameters: J = -12.6 cm^{-1}

and g = 2.13 with R = 6.5 × 10^{-4} ($R = \Sigma[(\chi_M T)_{exp.} - (\chi_M T)_{calcd.}]^2/\Sigma((\chi_M T)_{exp})^2$). The antiferromagnetic exchange observed in complex **2** leads to a diamagnetic ground state (S_T = 0) as confirmed by the isothermal magnetization measurements at 2 K, which show values lower than 0.05 $N\mu_B$ at high fields (Figure 1.13).

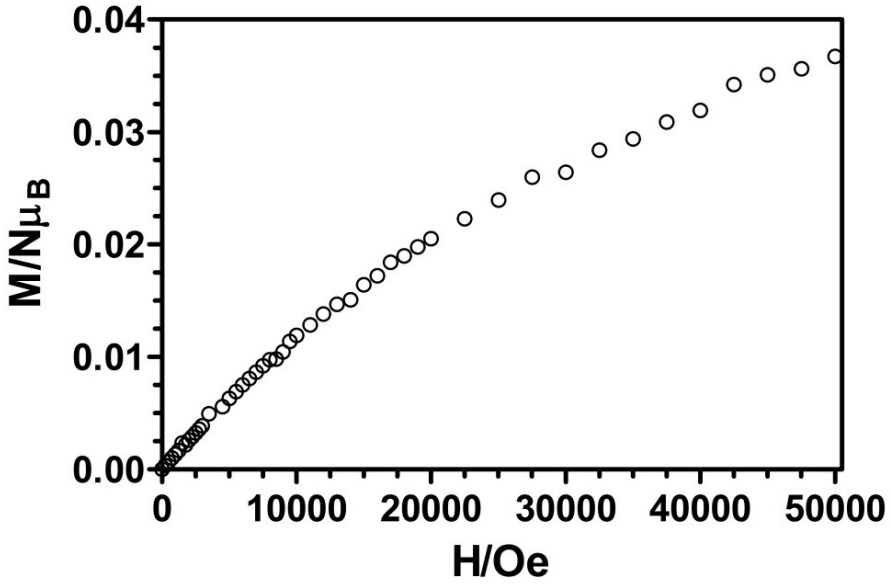

Figure 1.13.- Field dependence of the magnetization for **2**.

On the other hand, complexes **3** and **4** show slightly higher $\chi_M T$ values at room temperature (2.58 $cm^3 \cdot K \cdot mol^{-1}$ and 3.83 $cm^3 \cdot K \cdot mol^{-1}$, respectively) than those expected for two and three uncoupled Ni(II) (S = 1) ions, respectively, with g = 2.0 (2.0 $cm^3 \cdot K \cdot mol^{-1}$ for **3** and 3.0 $cm^3 \cdot K \cdot mol^{-1}$ for **4**). On lowering temperature, the $\chi_M T$ products for **3** and **4** remain almost constant until 20 K and then drop abruptly reaching values of 1.38 $cm^3 \cdot K \cdot mol^{-1}$ and 2.44 $cm^3 \cdot K \cdot mol^{-1}$ at 2 K, respectively. This behaviour suggests the existence of very weak intramolecular magnetic interactions between the Ni(II) ions in these complexes (either F or AF) together with intermolecular antiferromagnetic interactions and/or zero field splitting effects promoted by the local anisotropy of the Ni(II) ions, which are the main responsible for the decrease on $\chi_M T$ values at very low temperatures.

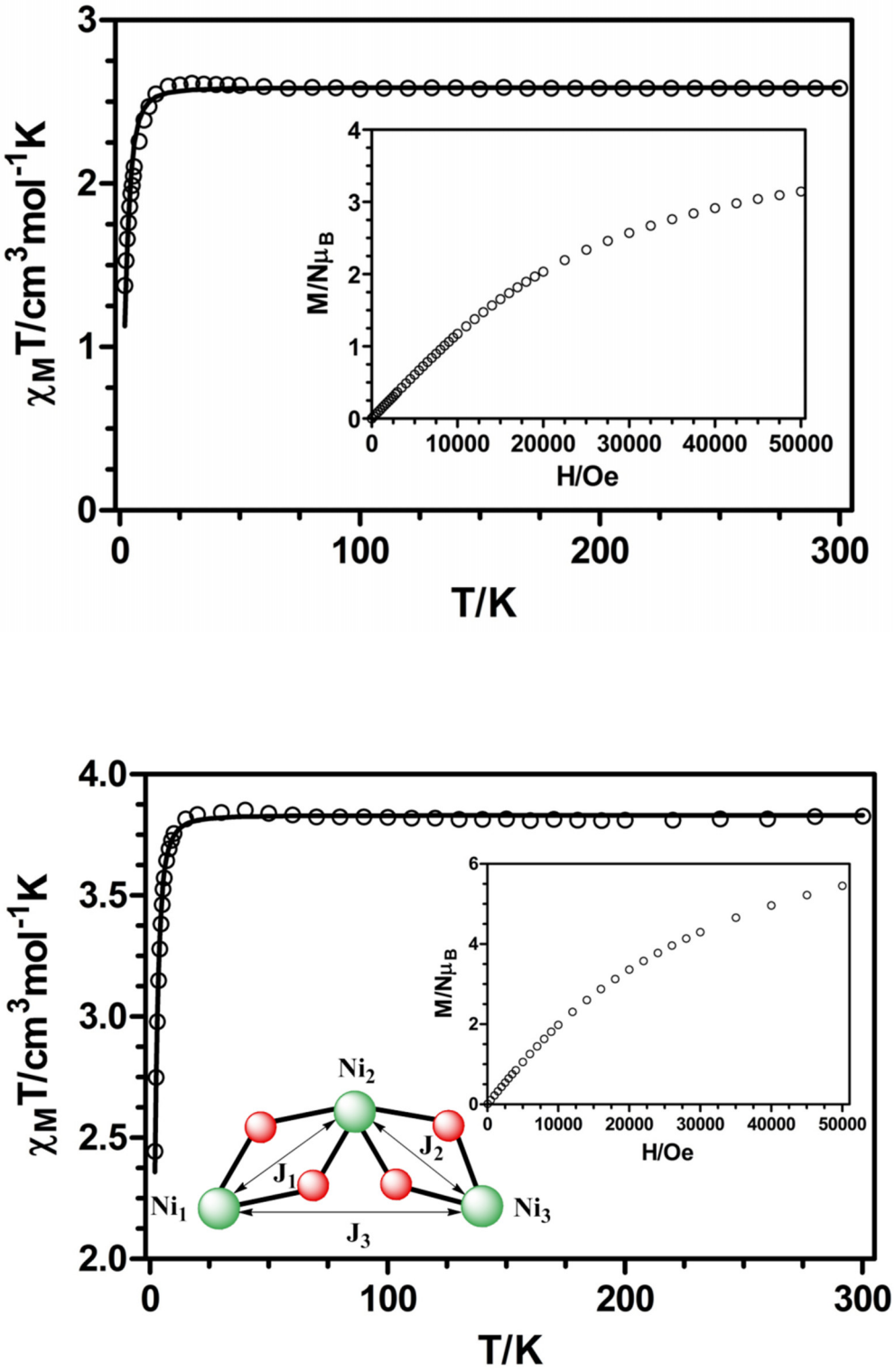

Figure 1.14.- Temperature dependence of the $\chi_M T$ products for **3** (top) and **4** (bottom) in the 2-300 K range. The solid lines are generated from the best fit to the magnetic parameters. Insets: field dependence of the magnetization for **3** and **4** and the magnetic exchange pathways in compound **4**.

The experimental susceptibility values for **3** and **4** were analysed with the respective Hamiltonians that take into account the isotropic interaction between the Ni(II) centres and their axial single ion zero field splitting parameters. However, different set of parameters with very small positive and negative *J* values and similar *R* values were obtained from the corresponding fitting procedures. In view of this, we decided to model the experimental susceptibility data for complexes **3** and **4** taking into account only the single ion zero field splitting parameter. The best fit of the experimental data led to the following set of parameters: g = 2.27 and D = 6.26 cm^{-1} with R = 6.96 × 10^{-4} for **3** and g = 2.26 and D = 4.21 cm^{-1} with R = 3.8 × 10^{-5} for **4**. Negative values of *D* led to worse fits of the susceptibility data. The extracted *D* parameters include the effects of intra- and intermolecular magnetic exchange interactions.

The field dependence of the molar magnetization at 2 K for complexes **3** and **4** shows a gradual increase with the applied external field without reaching a complete saturation at 5 T. This behaviour is due to the presence of significant anisotropy and/or low-lying excited states that are partially (thermally and field-induced) populated, which are in agreement with the weak magnetic interactions observed for these complexes.

To end up, the $\chi_M T$ values at room temperature for the tetranuclear compounds (5.03 $cm^3 \cdot K \cdot mol^{-1}$ for **5** and 5.31 $cm^3 \cdot K \cdot mol^{-1}$ for **6**) are significantly higher than the expected value for four uncoupled Ni(II) ions with g = 2.0 (4.0 $cm^3 \cdot K \cdot mol^{-1}$), which is mainly due to the orbital contribution of the Ni(II) ions. Upon cooling, the $\chi_M T$ product steadily increases to reach a maximum at 36 K (5.31 $cm^3 \cdot K \cdot mol^{-1}$) and 8.0 K (10.6 $cm^3 \cdot K \cdot mol^{-1}$) for **5** and **6**, respectively. Below these temperatures, $\chi_M T$ decreases quite fast reaching values of 3.46 $cm^3 \cdot K \cdot mol^{-1}$ for **5** at 5 K and 9.81 $cm^3 \cdot K \cdot mol^{-1}$ for **6** at 2 K. This magnetic behaviour indicates the presence of ferromagnetic exchange interactions between the Ni(II) ions together with antiferromagnetic intermolecular interactions and/or zero field splitting of the resulting ground state, which is responsible for the decrease of $\chi_M T$ at low temperatures.

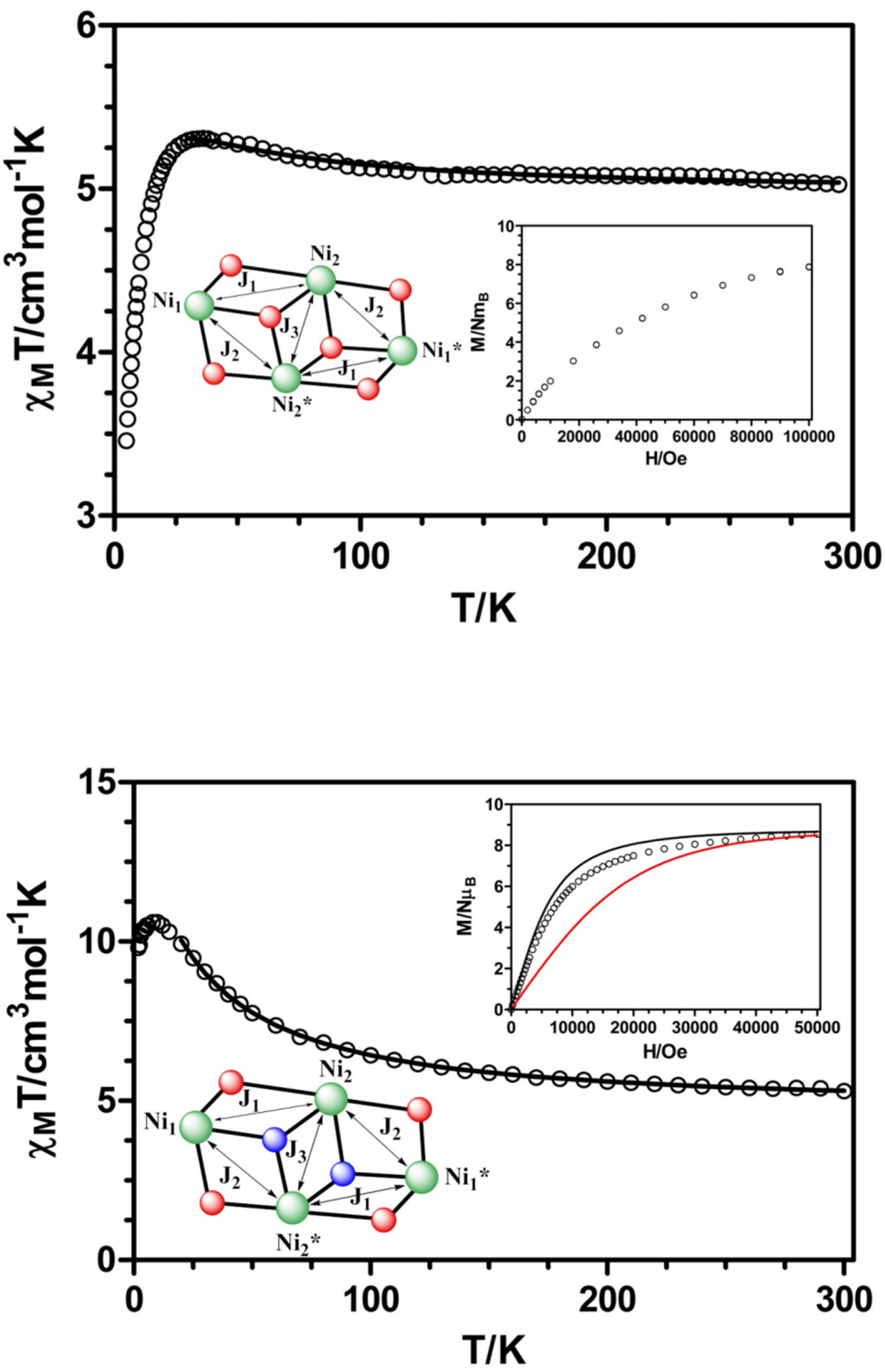

Figure 1.15.- Temperature dependence of the $\chi_M T$ products for **5** (top) and **6** (bottom). The solid lines are generated from the best fit to the magnetic parameters. Insets left: magnetic exchange pathways in compounds **5** and **6**. Insets right: field dependences of the magnetization for **5** and **6**. The black and red solid lines represent the Brillouin function for an *S* = 4 ground state and for the sum of four Ni(II) ions with *S* = 1, respectively.

Taking into account the centrosymmetric face-sharing defective dicubane-like structure of complex **5**, the magnetic data have been analysed with the following three-*J* Hamiltonian:

$$\mathcal{H} = -J_1(S_{Ni1}S_{Ni2} + S_{Ni1*}S_{Ni2*}) - J_2(S_{Ni1}S_{Ni2*} + S_{Ni1*}S_{Ni2}) - J_3(S_{Ni2}S_{Ni2*}) \quad (\textit{Equation 1.2})$$

where J_1, J_2 and J_3 describe the exchange pathway through the μ-phenoxo/$\mu_{1,1,1}$-methoxo/*syn-syn* acetate, μ-phenoxo/$\mu_{1,1,1}$-methoxo and di-$\mu_{1,1,1}$-methoxo bridges, respectively (see inset of Figure 1.15). The external Ni1 atoms are too far (5.417 Å) to have significant magnetic interactions and therefore, the magnetic exchange between them has not been taking into account. In order to avoid overparametrization we have fitted the data above 30 K to eliminate the effect of the anisotropy and possible intermolecular interactions. The best fit parameters were: J_1 = + 4.2 cm^{-1}, J_2 = - 4.8 cm^{-1}, J_3 = + 11.5 cm^{-1} and g = 2.23 with $R = 1.3 \times 10^{-5}$. These parameters indicate the presence of moderate ferromagnetic exchange interactions between Ni1-Ni2, Ni1*-Ni2* and Ni2-Ni2* ions and antiferromagnetic interactions between Ni1-Ni2* and Ni1*-Ni2 ions, which are competing interactions.

The magnetization (M) measured at 2 K for complex **5** exhibits a gradual increase with the increasing field but does not reach saturation even at 10 T. The fact that the magnetization continues increasing at higher fields could be due to the presence of significant anisotropy in the ground state and/or accessible low-lying excited states that are partially populated at 2 K.

Due to the similarity of the structures of complexes **5** and **6**, we have used the same Hamiltonian as for **5**, where J_1, J_2 and J_3 account for μ-phenoxo/$\mu_{1,1,1}$-azido/*syn-syn* acetate, μ-phenoxo/$\mu_{1,1,1}$-azido and di-$\mu_{1,1,1}$-azido exchange pathways, respectively (see inset Figure 1.15). The fit of the experimental susceptibility data above 20 K, which are not affected by the effects of D and intermolecular interactions, lead to the following best fit parameters: J_1 = + 5.6 cm^{-1}, J_2 = + 9.8 cm^{-1}, J_3 = + 43.8 cm^{-1} and g = 2.18 with $R = 2.3 \times 10^{-5}$.

The field dependence of the molar magnetization at 2 K for complex **6** (Figure 1.15, inset) is slightly below the Brillouin function for a S = 4 and g = 2.18, which corroborates the existence of ferromagnetic interactions between the Ni(II) ions. The deviation from the Brillouin function is more likely due to the zero-field splitting effects of the S = 4 ground state and possible intermolecular interactions.

In order to know the nature and magnitude of the magnetic coupling interactions in complexes **3** and **4**, and to support the experimental *J* values found for complexes **2**, **5** and **6** we carried out DFT calculations on the X-ray structures using the broken-symmetry approach. Table 1.1 presents the summary of the calculated *J* values of all the compounds and technical details of the calculations are described in Appendices, Section VI.

Table 1.1.- Magnetic pathways and magnetic coupling constants for complexes **2**-**6**.

Complex	**Magnetic pathways**	J_{exp} **(cm^{-1})**	J_{calc} **(cm^{-1})**
2	Di-μ-phenoxo	-12.6	-16.0
3	Di-μ-phenoxo/*syn-syn* acetate	-	+2.90
4	μ-phenoxo/μ-water (Ni1-Ni2)	-	-3.5 (J_1)
	μ-phenoxo/μ-water (Ni2-Ni3)	-	-5.0 (J_2)
	External Ni(II) ions (Ni1-Ni3)	-	-0.85 (J_3)
5	μ-phenoxo/$\mu_{1,1,1}$-methoxo/*syn-syn* acetate	+4.2 (J_1)	+10.0 (J_1)
	μ-phenoxo/$\mu_{1,1,1}$-methoxo	-4.8 (J_2)	-7.4 (J_2)
	di-$\mu_{1,1,1}$-methoxo	+11.5 (J_3)	+11.2 (J_3)
	External Ni(II) ions (Ni1-Ni1*)	-	+0.06 (J_4)
6	μ-phenoxo/$\mu_{1,1,1}$-azido/*syn-syn* acetate	+5.6 (J_1)	+13.35 (J_1)[a]
	μ-phenoxo/$\mu_{1,1,1}$-azido	+9.8 (J_2)	+15.05 (J_2)[a]
	di-$\mu_{1,1,1}$-azido	+43.8 (J_3)	+34.65 (J_3)[a]
	External Ni(II) ions (Ni1-Ni1*/Ni3-Ni3*)	-	-0.11 (J_4)[a]

[a]These values are the media calculated for both independent Ni_4 units. Unit 1 (composed by Ni1 and Ni2): J_1 = + 14.8 cm^{-1}, J_2 = + 15.6 cm^{-1}, J_3 = + 38.6 cm^{-1}, J_4 = - 0.152 cm^{-1}; unit 2: (composed by Ni3 and Ni4): J_1 = + 11.9 cm^{-1}, J_2 = + 14.5 cm^{-1}, J_3 = + 30.7 cm^{-1}, J_4 = - 0.077 cm^{-1}.

The calculated magnetic exchange coupling constants for **3** and **4** are weak, in agreement with the experimental results. Thus, for complex **3**, the calculated magnetic exchange coupling through the di-μ-phenoxo/*syn–syn* acetate triple bridge is ferromagnetic in nature with J = + 2.90 cm^{-1}. For **4** the magnetic exchange couplings through the double μ-phenoxo/μ-water bridges are antiferromagnetic with J_1 = − 3.5 cm^{-1} and J_2 = - 5.0 cm^{-1} for Ni1-Ni2 and Ni2-Ni3 ions, respectively, whereas the magnetic coupling between the external Ni(II) ions is, as expected, much weaker with J_3 = - 0.85 cm^{-1} (see inset Figure 1.14).

For complexes **2**, **5** and **6** the calculated values are in rather good agreement in sign and magnitude with those of the experimental results. The difference between the experimental and calculated values could be due to limitations inherent to the method, and, as usual, the former are smaller than the latter ones.

The calculated spin density distributions for the ground state in complexes **2**-**6** (Figure 1.16) show the predominance of the delocalization mechanism through a σ type exchange pathways involving the dx^2-y^2 and dz^2 magnetic orbitals of the Ni(II) atoms and the p orbitals of the ligand bridging donor groups (Table 1.2). As expected, the spin density is mainly found at the Ni(II) ions, with values in the range 1.65-1.74 e^-.

Table 1.2.-. Spin densities of complexes **2-6**.

Atoms	2	3	4	5	6A	6B
Ni1	+1.6907	+1.6554	+1.6610	−1.6873	+1.6683	+1.6711
Ni2	−1.7206	+1.7375	−1.7230	−1.7203	+1.6797	+1.6804
Ni3	–	–	+1.6718	+1.6872	+1.6683	+1.6711
Ni4	–	–	–	+1.7203	+1.6797	+1.6804
$O_{phenoxo}$	+0.0083 −0.0059	+0.0900[a]	+0.0624[a] −0.0166[a]	−0.0000[a,d] +0.0001[a,d]	+0.0758[a]	+0.0722[a]
$O_{aldehyde}$	−0.0380	+0.0455[a]	−0.0598	−0.0344 +0.0344	+0.0414[a]	+0.0449[a]
$O_{acetate}$	–	+0.0595[a]	–	−0.0410[a] +0.0410[a]	+0.0474[a]	+0.0472[a]
O_{acac}	+0.0476[a] −0.0592[a]	–	–	–	–	–
$O_{methoxo}$	–	–	–	−0.0554 +0.0554	–	–
O_{water}	−0.0292	–	−0.0592[a,c] +0.0161	–	–	–
N_{en}[b]	+0.0640[a]	+0.0677[a]	+0.0916[a]	−0.0625[a] +0.0626[a]	+0.0703[a]	+0.0707[a]
N_{SCN}	–	+0.0690	–	–	–	–
$N_{acetonitrile}$	–	–	+0.0454	–	–	–
N_{azido}					+0.1944[e]	+0.1889[e]

[a] Mean values. [b] From the ethylenediamine moiety of the ligand. [c] Bridged molecules. [d] Due to the symmetry of the system. [e] Sum of the three *N* atoms of the azide ligand.

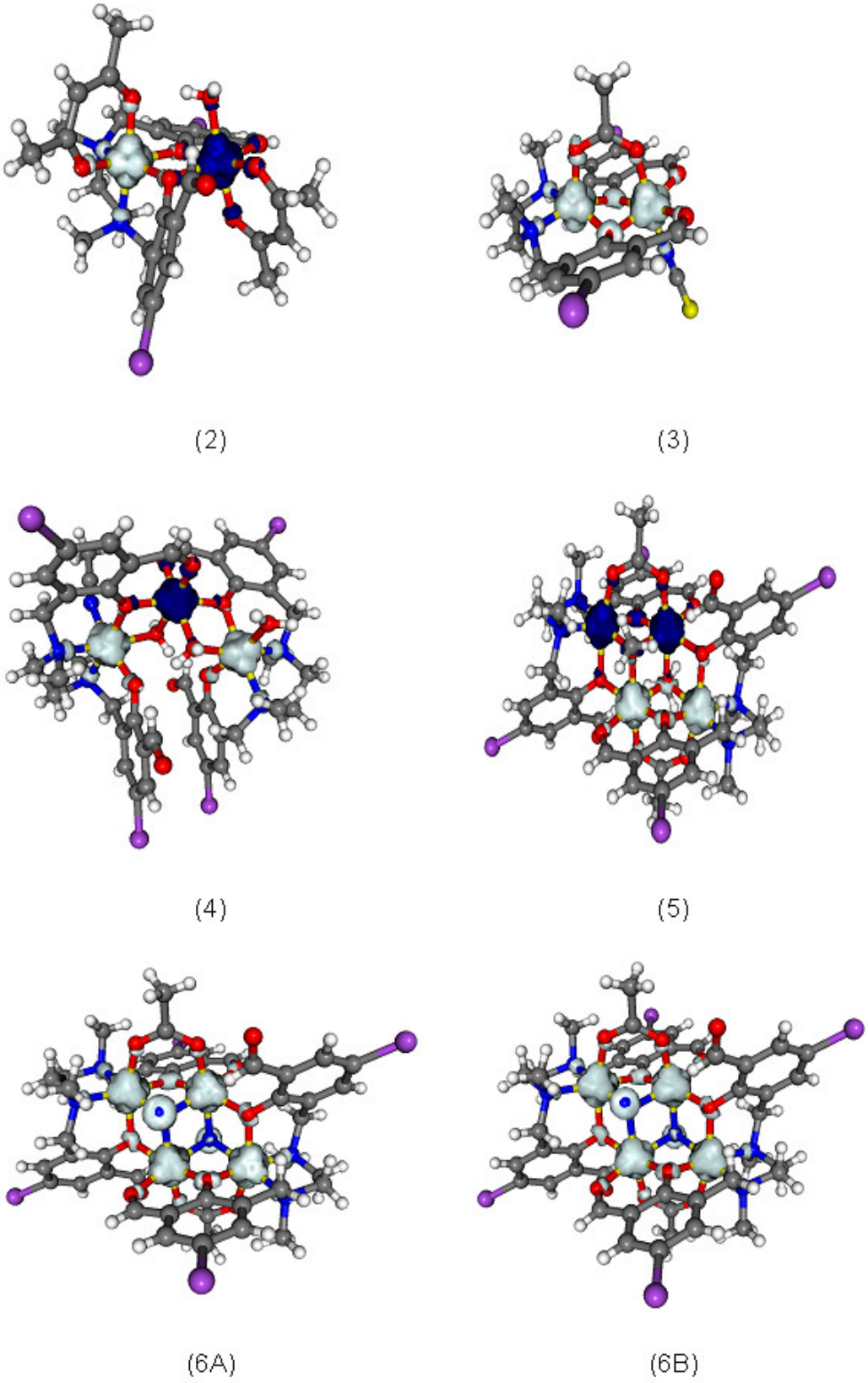

Figure 1.16.- Calculated spin densities for structures **2**-**6**. The isodensity surfaces represented correspond to a cut-off value of 0.012 e bohr^{-3}. Grey and blue colours represent positive and negative spin density values, respectively.

Finally, it is worth mentioning that dynamic *alternating current* (*ac*) magnetic susceptibility measurements as a function of temperature at different frequencies were performed on complex **6**, which exhibits a relatively large ground spin state *S* = 4. The compound does not show frequency dependency of the in-phase (χ_M') and out-of-phase signals (χ_M'') even in the presence of an external direct current (*dc*) field of 1000 G and, therefore, does not exhibit SMM behaviour above 2 K.

1.3.3. Magneto-structural correlations for 2-6

Let us start with complex **2**. Experimental and theoretical magneto-structural correlations[8] have clearly shown that the major factor controlling the exchange coupling in planar hydroxo-, alkoxo- and phenoxo- Ni-(μ-O)$_2$-Ni complexes is the bridging Ni-O-Ni angle (θ). According to these magneto-structural correlations, ferromagnetic coupling is expected below the critical Ni-O-Ni angle of ~96 - 98° and the exchange coupling becomes antiferromagnetic above it. Moreover, it has also been seen from theoretical studies[8a] that the out-of-plane displacement of the phenyl carbon atom from the Ni$_2$O plane (τ) and the hinge angle between the O-Ni-O planes in the bridging fragment (β) also play a significant role in determining the magnitude of the magnetic coupling. Thus, the AF interaction increases when τ and/or β decrease so it is reasonable to think that small θ angles (close to 90-95°) combined with larger τ (>30-40°) and β (>20°) angles should lead to weak AF or even F interactions in this kind of compounds. Taking these magneto-structural correlations into account, the antiferromagnetic interaction between the Ni(II) ions observed for **2** is not unexpected, as the mean θ, τ and β angles are of 101.5°, 20.9° and 8.86°, respectively.

In the case of complex **3**, the mean θ, τ and β angles are 94.74°, 37.05° and 33.60°, respectively, and therefore a weak F interaction between the Ni(II) ions is expected, which is in good agreement with the calculated value and experimental results. Moreover, the presence of an additional *syn-syn* acetate bridge between the two Ni(II) centres favours the ferromagnetic interaction due to the counter-complementarity effects between the di-μ-phenoxo and carboxylate bridging ligands.[9] In fact, DFT calculations on di-μ-phenoxo/*syn-syn* acetate compounds where the *syn-syn* acetate bridge has been substituted by two water molecules clearly show that this bridging group provides ferromagnetic contribution to the exchange through orbital countercomplementarity.[8a]

The trinuclear Ni_3 complex **4** has two non-equivalent double μ-phenoxo/μ-water magnetic exchange pathways between the central and external Ni(II) ions, which are described by J_1 and J_2. It should be noted that, to the best of our knowledge, **4** is only the second example of a structurally and magnetically characterized Ni(II) polynuclear complex where the mixed double μ-phenoxo/μ-water bridge is present.[10] The first example is the tetranuclear complex $[Ni_4L^4(\mu_3\text{-}OH)(\mu_2\text{-}H_2O)_2(ClO_4)](ClO_4)_2\cdot 2CH_3COCH_3\cdot H_2O$ (H_4L^4 = 36-membered octaaminotetraphenol macrocyclic ligand),[10] which exhibits an antiferromagnetic exchange coupling through this mixed double bridge with J = -8.1 cm^{-1}. However, this value is not comparable to that of **4** because, in order to avoid overparametrization, the four exchange pathways with Ni-O-Ni angles ranging from 78.8° to 132.3° were considered to be equivalent. For the Ni-O_{water}-Ni angles of 94.13° and 94.92° ferromagnetic couplings are expected whereas the Ni-$O_{phenoxo}$-Ni angles of 100.96° and 101.27° should promote antiferromagnetic interactions. The calculated magnetic exchange coupling constants (J_1 = - 3.5 cm^{-1} and J_2 = - 5.0 cm^{-1}) indicate that antiferromagnetic interactions prevail over the ferromagnetic ones in **4**. On the other hand, the weak antiferromagnetic coupling between the external Ni(II) ions (J_3 = - 0.85 cm^{-1}) is in good agreement with that expected for two unbridged Ni(II) ions with a Ni···Ni distance of 5.047 Å.

To the best of our knowledge, complex **5** is the first example reported to date with this type of structure. The defective dicubane core of **5** exhibits three different types of exchange pathways between the Ni(II) ions: (i) triple μ-phenoxo/$\mu_{1,1,1}$-methoxo/*syn–syn* acetate bridges (described by J_1), (ii) double μ-phenoxo/$\mu_{1,1,1}$-methoxo bridges (described by J_2) and (iii) double di-$\mu_{1,1,1}$-methoxo bridge (described by J_3). Let us start with the first exchange pathway. As in complex **3**, the weak ferromagnetic interaction between the Ni(II) ions found for the magnetic exchange pathway (i) is not unexpected in view of the values for the angles in the phenoxo/$\mu_{1,1,1}$-methoxo Ni-$(\mu\text{-}O)_2$-Ni bridging fragment (θ = 94.2°, τ = 34.25° and β = 19.11°) and the counter-complementarity effects of *syn–syn* acetate bridges. As far as we know, the magnetic exchange pathway through the double μ-phenoxo/$\mu_{1,1,1}$-methoxo mixed bridge (ii), has been observed for the first time in Ni(II) containing complexes. The antiferromagnetic nature of the experimental magnetic coupling constant through this pathway is not unexpected taking into account the mean values of the θ, τ and β angles with values of 101.7°, 41.8° and 6.12°, respectively. Regarding the magnetic exchange pathway through the di-$\mu_{1,1,1}$-methoxo bridge (iii), the values of the θ and τ angles in the Ni-$(\mu\text{-}O)_2$-Ni symmetric planar bridging fragment (97.1° and 52.7°, respectively) predict weak F

interactions, which again matches well with the experimental and theoretical results. The magnitude of the ferromagnetic interaction through pathways (i) and (iii) are in accordance with the exchange interactions found in the four structurally similar complexes with the general formula $[Ni_4(L^5)_2(\mu\text{-}N_3)_2(\mu\text{-}OAc)_2(\mu\text{-}OMe)_2]\cdot xCH_3OH\cdot yH_2O$ (HL^5 = 2,6-bis[(2-hydroxy-ethylimino)-methyl]-4-methylphenol and derivatives), which range from + 4.32 to + 11.6 cm^{-1}.[11]

Finally, to the best of our knowledge, complex **6** is also the first example reported to date with this type of structure. This complex exhibits the same structure as **5**, but in which the $\mu_{1,1,1}$-methoxo bridges are replaced by $\mu_{1,1,1}$-azido bridges. Therefore, **6** exhibits three different types of exchange pathways between the Ni(II) ions: (i) triple μ-phenoxo/$\mu_{1,1,1}$-azido/*syn-syn* acetate bridges (described by J_1), (ii) double μ-phenoxo/$\mu_{1,1,1}$-azido bridges (described by J_2) and (iii) double di-$\mu_{1,1,1}$-azido bridge (described by J_3). It is well known that azido bridges generally promote ferromagnetic interactions between the Ni(II) ions and, therefore, the exchange of methoxo by azido bridges is expected to lead to stronger ferromagnetic interactions, which is in accordance with the experimental and theoretical results.

It should be noted that **6** is only the third nickel complex containing a mixed triple μ-phenoxo/μ-azido/*syn–syn* acetate bridge (i).[12] The first example is the trinuclear bent complex $[Ni_3L^6{}_2(OAc)_2(\mu_{1,1}\text{-}N_3)_2(H_2O)_2]$ (L^6 = 2-[(3-dimethylaminopropylimino)-methyl]-phenol)[12b] that exhibits a ferromagnetic exchange coupling through this mixed triple bridge with J = + 16.51 cm^{-1}. The second example is the zig-zag hexanuclear complex $[Na_2Ni_4(\mu\text{-}L^7)_2(\mu\text{-}OAc)_2(\mu\text{-}N_3)_4(CH_3OH)_4]\cdot 2CH_3OH$ (H_2L^7 is N,N′-dimethyl-N,N′-bis(2-hydroxy-3-methoxy-5-methylbenzyl)ethylenediamine) with J_1 = + 28.8 cm^{-1}.[12a] The observed ferromagnetic interactions in these complexes through the exchange pathway (i) are not only due to the presence of $\mu_{1,1,1}$-azido bridges and relatively small Ni-$O_{phenoxo}$-Ni angles but also to countercomplementarity effect of the *syn–syn* acetate bridge. Therefore, the ferromagnetic exchange coupling observed for **6** via the exchange pathway (i) with Ni-$O_{phenoxo}$-Ni and Ni-O_{azido}–Ni mean angles of 96.2° and 90.73° is not unexpected.

Regarding the exchange pathway (ii), as far as we know, only another example of a complex containing a double phenoxo/$\mu_{1,1,1}$-azido mixed bridge between Ni(II) ions has been reported so far.[12a] In this complex, $[Ni_4(\mu\text{-}L^7)_2(\mu\text{-}N_3)_4(CH_3OH)_2]\cdot 2CH_3OH$, the exchange pathway (ii) transmits a ferromagnetic interaction with J = + 2.0 cm^{-1}. It should be noted that recent DFT theoretical studies[13] on Ni(II) model complexes

containing double μ-phenoxo/$\mu_{1,1}$-azido bridges have predicted that the ferromagnetic interaction increases with increasing the Ni-N_{azido}-N/Ni-N_{azido} ratio and the asymmetry of the two Ni–N_{azido} distances, and decreases with increasing the Ni-$O_{phenoxo}$-Ni/Ni-$O_{phenoxo}$ ratio, so that phenoxo and $\mu_{1,1}$-azido bridges have countercomplementary effects on the magnetic exchange coupling. Assuming that these magneto-structural correlations are also valid for Ni(II) complexes with double μ-phenoxo/$\mu_{1,1,1}$-azido bridges, for complex **6**, with a similar Ni-N_{azido}-N/Ni-N_{azido} ratio to that observed in $[Ni_4(\mu\text{-}L^7)_2(\mu\text{-}N_3)_4(CH_3OH)_2]\cdot 2CH_3OH$ but with a smaller Ni-$O_{phenoxo}$-Ni/Ni-$O_{phenoxo}$ ratio, a larger ferromagnetic interaction is expected through this exchange pathway, which agrees well with the experimental and theoretical results.

Finally, as for the exchange pathway (iii) with a double ($\mu_{1,1,1}$-N_3)-bridging unit, the ferromagnetic nature of the experimental magnetic coupling constant is not unexpected as it is well known that $\mu_{1,1,1}$-N_3 bridges transmit ferromagnetic interactions, which increase with the increase of the Ni-N_{azido}-Ni angle and decrease with the deviation of the $\mu_{1,1,1}$-azido bridging ligand from the Ni-$(N_{azido})_2$-Ni plane.[12a] Taking into account these magneto-structural correlations, the low value found for this exchange pathway in **6** (J_3 = + 43.8 cm^{-1}) compared to those observed for planar ($\mu_{1,1}$-N_3)-bridged dinuclear Ni(II) complexes (typically between + 60 and + 80 cm^{-1}),[12a,14] could be due to the low Ni-N_{azido}-Ni angle of 97.35° and the large deviation of the $\mu_{1,1,1}$-azido bridging ligand from the Ni-(N_{azido})-Ni plane of 52.9°.

1.4. CONCLUSIONS

Using the flexible polytopic ligand N,N′-dimethyl-N,N′-bis(2-hidroxy-3-formyl-5 bromobenzyl)ethylenediamine (H_2L) and different anionic coligands and reaction conditions (metal to ligand molar ratio and solvent) we were able to prepare six Ni(II) complexes, ranging from mononuclear to tetranuclear compounds, with structural and magnetic diversity, in which the ligand adopts a variety of bridging coordination modes. Thus, the dinuclear complexes exhibit either double di-μ-phenoxo or triple di-μ-phenoxo/*syn-syn* acetate bridges, which promote moderate AF and very weak F interactions, respectively. The Ni_3 complex presents a bent structure with rare double μ-phenoxo-μ-water bridges between central and external Ni(II) ions, which promote very weak AF interactions. The weak magnetic exchange interactions for the Ni_3 complex and the Ni_2 complex with triple di-μ-phenoxo/*syn-syn* acetate bridges were

determined by DFT calculations on their respective X-ray crystal structures. Their sign and magnitude are related to the values of the Ni-O-Ni bridging angles and, in the case of the latter, to the additional countercomplementarity effect exerted by the *syn-syn* acetate bridging group. Two Ni_4 complexes were obtained, which present similar defective dicubane like topologies with three distinct types of bridges between the Ni(II) ions. The main structural difference between both Ni_4 complexes is the presence in one of them of $\mu_{1,1,1}$-methoxo bridges and in the other one of $\mu_{1,1,1}$-azido bridges. In the Ni_4 compound containing methoxo group, the triple mixed μ-phenoxo/$\mu_{1,1,1}$-methoxo/*syn–syn* acetate bridge and the double di-$\mu_{1,1,1}$-methoxo bridge propagate weak F interactions between the Ni(II) ions, whereas the unusual μ-phenoxo/$\mu_{1,1,1}$-methoxo bridge mediates weak AF interactions. It should be noted that the substitution of $\mu_{1,1,1}$-methoxo bridges by $\mu_{1,1,1}$-azido bridges provokes that all the magnetic pathways promote ferromagnetic interactions, which are stronger than those found for the compound containing $\mu_{1,1,1}$-methoxo bridges. The sign and nature of the experimental *J* values found for these Ni_4 species were supported by DFT calculations.

1.5. BIBLIOGRAPHY

[1] M. Yonemura, Y. Matsumura, M. Ohba, H. Okawa, D. E. Fenton, *Chem. Lett*., **1996**, 601.

[2] **a)** A. K. Boudalis, M. Pissas, C. P. Raptopoulou, V. Psycharis, B. Abarca, R. Ballesteros, *Inorg. Chem*., **2008**, *47*, 10674; **b)** A. Ferguson, J. Lawrence, A. Parkin, J. Sanchez-Benitez, K. V. Kamenev, E. K. Brechin, W. Wernsdorfer, S. Hill, M. Murrie, *Dalton Trans*., **2008**, 6409; **c)** A. Bell, G. Aromí, S. J. Teat, W. Wernsdorfer, R. E. P. Winpenny, *Chem. Commun*., **2005**, 2808 ; **d)** D. I. Alexandropoulos, C. Papatriantafyllopoulou, G. Aromi, O. Roubeau, S. J. Teat, S. P. Perlepes, G. Christou, T. C. Stamatatos, *Inorg. Chem*., **2010**, *49*, 3962; **e)** S. Petit, P. Neugebauer, G. Pilet, G. Chastanet, A. L. Barra, A. B. Antunes, W. Wernsdorfer, D. Luneau, *Inorg. Chem*., **2012**, *51*, 6645 and references therein; **f)** R. Biswas, Y. Ida, M. L. Baker, S. Biswas, P. Kar, H. Nojiri, T. Ishida, A. Ghosh, *Chem. Eur. J*., **2013**, *19*, 3943; **g)** H. Andres, R. Basler, A. J. Blake, C. Cadiou, G. Chaboussant, C. M. Grant, H. U. Güdel, M. Murrie, S. Parsons, C. Paulsen, F. Semadini, V. Villar, W. Wernsdorfer, R. E. P. Winpenny, *Chemistry*, **2002**, *8*, 4867; **h)** R. T. W. Scott, L. F. Jones, I. Tidmarsh, S. B. Breeze, R. H. Laye, J. Wolowska, D. J. Stone, A. Collins, S. Parsons, W. Wernsdorfer, G. Aromi,

E. J. L. McInnes, E. K. Brechin, *Chem. Eur. J*., **2009**, *15*, 12389; **i)** S. Hameury, L. Kayser, R. Pattacini, G. Rogez, W. Wernsdorfer and P. Braunstein, Dalton Trans., **2013**, *42*, 5013.

[3] **a)** J. Ruiz, A. J. Mota, A. Rodríguez-Diéguez, S. Titos, J. M. Herrera, E. Ruiz, E. Cremades, J. P. Costes, E. Colacio, *Chem. Commun*., **2012**, *48*, 7916; **b)** J. P. Costes, F. Dahan, F. Nicodème, *Inorg. Chem*., **2003**, *42*, 6556.

[4] R. Biswas, P. Kar, Y. Song, A. Ghosh, *Dalton Trans*., **2011**, *40*, 5324.

[5] M. Llunell, D. Casanova, J. Cirera, J. M. Bofill, P. Alemany, S. Alvarez, M. Pinsky, D. Avnir, *SHAPE*, v1.1b; Barcelona, Spain, **2005**.

[6] **a)** P. Mukherjee, M. G. B. Drew, C. J. Gómez-García, A. Gosh, *Inorg. Chem*., **2009**, *48*, 5848; **b)** A. J. Mota, A. Rodríguez-Diéguez, M. A. Palacios, J. M. Herrera, D. Luneau, E. Colacio, *Inorg. Chem*., **2010**, *49*, 8986.

[7] N. F. Chilton, R. P. Anderson, L. D. Turner, A. Soncini, K. S. Murray, *J. Comput. Chem*., **2013**, *34*, 1164.

[8] **a)** M. P. Palacios, A. J. Mota, J. E. Perea-Buceta, F. J. White, E. K. Brechin, E. Colacio, *Inorg. Chem*., **2010**, *49*, 10156; **b)** R. Biswas, S. Giri, S. K. Saha, A. Ghosh, *Eur. J. Inorg. Chem*., **2012**, 2916; **c)** K. K. Nanda, L. K. Thompson, J. N. Bridson, K. Nag, *J. Chem. Soc., Chem. Commun*., **1994**, 1337; **d)** M. A. Halcrow, J. S. Sun, J. C. Huffman, G. Christou, *Inorg. Chem*., **1995**, *34*, 4167; **e)** J. M. Clemente-Juan, B. Chansou, B. Donnadieu, J. P. Tuchages, *Inorg. Chem*., **2000**, *39*, 5515; **f)** X. H. Bu, M. Du, L. Zhang, D. Z. Liao, J. K. Tang, R. H. Zhang, M. Shionoya, *J. Chem. Soc., Dalton Trans*., **2001**, 593.

[9] **a)** P. Mukherjee, M. G. B. Drew, V. Tangoulis, M. Estrader, C. Diaz, A. Ghosh, *Inorg. Chem. Commun*., **2009**, *12*, 929; **b)** J. Ruiz, A. J. Mota, A. Rodríguez-Diéguez, I. Oyarzabal, J. M. Seco, E. Colacio, *Dalton Trans*., **2012**, *41*, 14265.

[10] **a)** S. Mohanta, K. K. Nanda, R. Werner, W. Haase, A. K. Mukherjee, S. K. Dutta, K. Nag, *Inorg. Chem*., **1997**, *36*, 4656; **b)** K. K. Nanda, K. Venkatsubramanian, D. Majumdar, K. Nag, *Inorg. Chem*., **1994**, *33*, 1581.

[11] **a)** S. S. Tandon, S. D. Bunge, R. Rakosi, Z. Xu, L. K. Thompson, *Dalton Trans*., **2009**, 6536; **b)** S.-Y. Lin, G.-F. Xu, L. Zhao, Y.-N. Guo, J. Tang, Q.-L. Wang, *Inorg. Chim. Acta*, **2011**, 173.

[12] **a)** L. Botana, J. Ruiz, A. J. Mota, A. Rodríguez-Diéguez, J. M. Seco, I. Oyarzabal, E. Colacio, *Dalton Trans*., **2014**, *43*, 13509; **b)** R. Biswas, S. Mukherjee, P. Kar, A. Gosh, *Inorg. Chem*., **2012**, *51*, 8150.

[13] S. Sasmal, S. Hazra, P. Kundu, S. Dutta, G. Rajaraman, E. C. Sañudo, S. Mohanta, *Inorg. Chem*., **2011**, *50*, 7257.

[14] **a)** A. Escuer, J. Esteban, S. P. Perlepes, T. C. Stamatatos, *Coord. Chem. Rev.*, **2014**, *275*, 87; **b)** A. Solanki, M. Monfort, S. B. Baran Kumar, *J. Mol. Struct.*, **2013**, *1050*, 197.

CHAPTER 2

RATIONAL DESIGN OF FERROMAGNETIC COUPLED DINUCLEAR NICKEL (II) COMPLEXES

2.1. INTRODUCTION

It is well known that the *syn–syn* carboxylate bridging coordination mode transmits antiferromagnetic coupling between metal ions. However, if other types of bridge are also present, they could add (orbital complementarity) or counterbalance (orbital countercomplementarity) their effects.[1] Thus, some mixed-bridged complexes containing *syn–syn* carboxylate and either alkoxo,[2] hydroxo[3] or water[4] bridging ligands, exhibit countercomplementarity leading to either ferromagnetic or very weak AF interactions.

To further study the dynamics of countercomplementarity effects four new di-μ-phenoxo/carboxylate bridged Ni(II) dinuclear complexes with the compartmental ligand N,N′,N″-trimethyl-N,N″-bis(2-hydroxy-3-methoxy-5-methylbenzyl)diethylenetri-amine (H_2L^1) have been prepared. The ligand H_2L^1 (Figure 2.1.) was prepared for the first time in 2011, in our research group, by the Mannich reaction of N,N',N"-trimethyldiethylenetriamine, 2-methoxy-4-methylphenol and paraformal-dehyde, in methanol at the refluxing temperature.[5] This ligand has allowed the preparation of many compounds and some of them show SMM behaviour, luminescent properties and magneto caloric effects.[6] Although initially this ligand shows different coordination modes as ligand H_2L, in the complexes reported so far only two modes have been observed (Figure 2.1.a and 2.1.b)

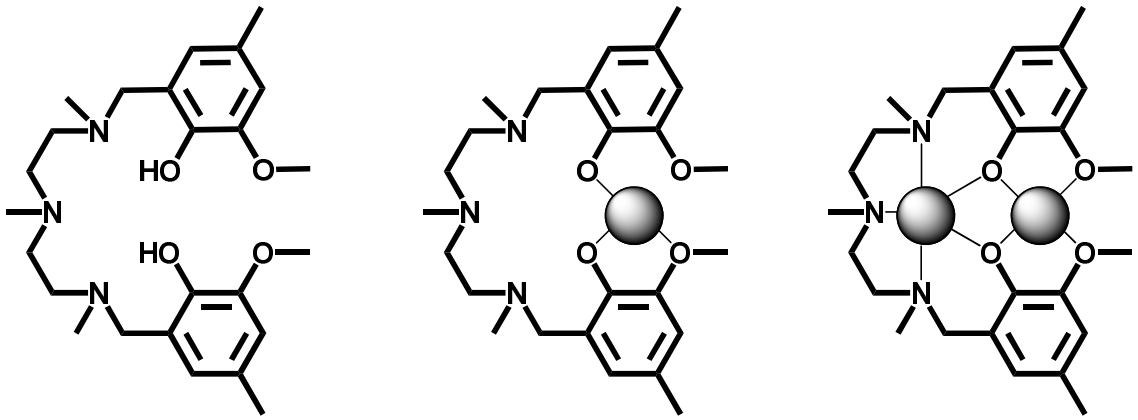

H_2L^1 (a) (b)

Figure 2.1.- Schematic representation of the ligand H_2L^1 and its coordination modes presented in the obtained compounds.

This study aims to: (i) confirm that the magnetic exchange interaction in these complexes is ferromagnetic in nature, (ii) investigate how the structural parameters of the bridging fragment, and consequently the ferromagnetic coupling, vary when the carboxylate bridging ligand is modified, (iii) know how the replacement of a water molecule on the coordination sphere of the outer Ni(II) ion by other ancillary ligands affects the magnetic properties, and (iv) perform DFT theoretical calculations on these complexes and the corresponding model complexes originated by substitution of the carboxylate bridging group by two water molecules to know whether or not the countercomplementarity mechanism is active in these complexes.

2.2. PREPARATION OF COMPLEXES

2.2.1. $[Ni_2(\mu\text{-}L^1)(\mu\text{-}OAc)(H_2O)_2]NO_3$ (7)

To a solution of H_2L^1 (55.7 mg, 0.125 mmol) in 5 mL of MeOH were added with continuous stirring 31.1 mg (0.125 mmol) of $Ni(OAc)_2{\cdot}4H_2O$ and 36.4 mg (0.125 mmol) of $Ni(NO_3)_2{\cdot}6H_2O$. The resulting green solution was filtered and allowed to stand at room temperature. After several days, well-formed prismatic green crystals of **7** were obtained with a yield of 45 %. Anal. calc. for $C_{27}H_{44}N_4O_{11}Ni_2$: C, 45.16; H, 6.18; N, 7.80. Found: C, 44.99; H, 6.31; N, 7.58.

2.2.2. $[Ni_2(\mu\text{-}L^1)(\mu\text{-}OBz)(H_2O)(MeOH)]NO_3{\cdot}3MeOH$ (8)

$Ni(NO_3)_2{\cdot}6H_2O$ (72.8 mg, 0.25 mmol) and sodium benzoate (NaOBz) (18.0 mg, 0.125 mmol) were subsequently added with continuous stirring to a solution of H_2L^1 (55.7 mg, 0.125 mmol) in 5 mL of MeOH. After two days the filtered solution afforded green crystals of **8** with a 50 % yield. Anal. calc. for $C_{36}H_{60}N_4O_{14}Ni_2$: C, 48.57; H, 6.79; N, 6.29. Found: C, 48.32; H, 6.89; N, 6.32.

2.2.3. $[Ni_2(\mu\text{-}L^1)(\mu\text{-}9\text{-}An)(H_2O)(MeOH)]NO_3$ (9)

The synthesis of this compound is similar to that of **8** but adding a solution containing 27.8 mg of 9-anthracenecarboxylic acid (H_2-9-An) (0.125 mmol) and 0.125 mmol of triethylamine (Et_3N) instead of NaOBz. The resulting solution was filtered, eliminating any amount of insoluble material, and allowed to stand at room temperature for several days, whereupon green crystals of **9** were formed with a yield of 45 %. Anal. calc. for $C_{41}H_{52}N_4O_{11}Ni_2$: C, 55.07; H, 5.86; N, 6.27. Found: C, 55.29; H, 5.41; N, 6.18.

2.2.4. $[Ni_2(\mu\text{-}L^1)(\mu\text{-}OAc)(H_2O)(N_3)]\cdot CH_3OH$ (10)

To a solution of H_2L^1 (55.7 mg, 0.125 mmol) in 5 mL of MeOH were subsequently added with continuous stirring 31.1 mg (0.125 mmol) of $Ni(OAc)_2\cdot 4H_2O$, 36.4 mg (0.125 mmol) of $Ni(NO_3)_2\cdot 6H_2O$ and 24.4 mg (0.375 mmol) of NaN_3. The resulting green solution was filtered and allowed to stand at room temperature. After several days, well-formed prismatic green crystals of **10** were obtained with a yield of 45 %. Anal. calc. for $C_{28}H_{46}N_6O_8Ni_2$: C, 47.23; H, 6.51; N, 11.80. Found: C, 47.29; H, 6.31; N, 11.68.

2.3. EXPERIMENTAL RESULTS

The reaction between the H_2L^1 ligand, $Ni(OAc)_2\cdot 4H_2O$ and $Ni(NO_3)_2\cdot 6H_2O$ in 1:1:1 molar ratio led to the di-μ-phenoxo/*syn-syn* acetate bridged dinuclear complex $[Ni(\mu\text{-}L^1)(\mu\text{-}OAc)Ni(H_2O)_2]NO_3$ (**7**). Similar complexes bearing carboxylate bridging groups other than acetate, were prepared by reacting a methanolic solution containing H_2L^1 and $Ni(NO_3)_3\cdot 6H_2O$ in 1:2 molar ratio with either NaOBz or a 9-anthracene-carboxylic acid/Et_3N mixture in 1:1 molar ratio, giving rise to the complexes $[Ni(\mu\text{-}L^1)(\mu\text{-}OBz)Ni(H_2O)(MeOH)]NO_3\cdot 3MeOH$ (**8**) and $[Ni(\mu\text{-}L)(\mu\text{-}9\text{-}An)Ni(H_2O)(MeOH)]NO_3$ (**9**). Finally, the reaction of H_2L^1 with $Ni(OAc)_2\cdot 4H_2O$, $Ni(NO_3)_2\cdot 6H_2O$ and, subsequently, with NaN_3 in 1:1:1:3 molar ratio afforded the di-μ-phenoxo/*syn-syn* acetate bridged complex $[Ni(\mu\text{-}L^1)(\mu\text{-}OAc)Ni(H_2O)(N_3)]\cdot CH_3OH$ (**10**), where a monodentate azide ligand is coordinated to the outer Ni(II) ion.

2.3.1. Crystal structures of complexes 7-10

The structure of **7** (Figure 2.2) consists of cationic dinuclear $[Ni(\mu\text{-}L^1)(\mu\text{-}OAc)Ni(H_2O)_2]^+$ units and NO_3^- anions involved in hydrogen bond interactions. Selected bond lengths and angles for **7** are given in Appendices, Table A.4.

Within the dinuclear unit, Ni(II) ions are bridged by two phenoxo groups of the $(L^1)^{2-}$ ligand and one *syn–syn* acetate anion. The $(L^1)^{2-}$ ligand wraps around the inner Ni(II) ions in such a way that the three nitrogen atoms, and consequently the three oxygen atoms, occupy *fac* positions on the slightly distorted NiN_3O_3 coordination polyhedron. The outer Ni(II) ion also exhibits a slightly distorted NiO_6 coordination sphere which is

composed of the two phenoxo bridging oxygen atoms, one of the methoxo oxygen atoms, one oxygen atom from the acetate bridging group and two oxygen atoms belonging to two water molecules. The water molecules are located in *cis* positions and together with the coordinated methoxo group adopt a *fac* configuration on the Ni(II) coordination sphere.

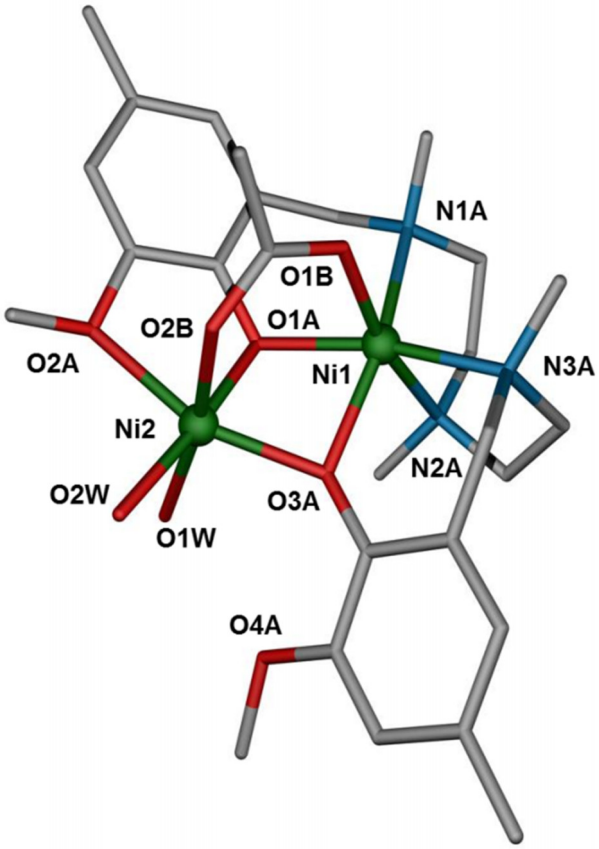

Figure 2.2.- A perspective view of the structure of compound **7**. Colour code: N = blue, O = red, C = gray, Ni = green. H atoms and the counteranion have been omitted for the sake of clarity.

The calculation of the degree of distortion of the Ni(II) coordination polyhedra with respect to ideal six-vertex polyhedra, by using the continuous shape measure theory with the SHAPE software,[7] indicates that both NiN_3O_3 and NiO_6 coordination spheres are found in the OC-6 ↔ TPR-6 deformation pathway and are close to the octahedral geometry somewhat distorted to trigonal prismatic (Appendices, Table A.22). It is of interest that the bridging acetate group forces the structure to be folded giving rise to a hinge angle (β) for the Ni-(μ-O)$_2$-Ni bridging fragment of 35.45°. As a consequence of the structure folding, the Ni-O-Ni bridging angles (θ) and the intra-dinuclear Ni···Ni distance diminish to 94.15(6)° and 95.96(6)°, and 3.013(1) Å, respectively. Finally, the

mean values of the shift of the phenyl groups directly linked to the phenoxo oxygen atoms with respect the Ni-Ni-O plane in the bridging region (τ angle) are 58° and 21°.

Dinuclear cationic entities are held together in pairs by a couple of centrosymmetrical and complementary hydrogen bonds involving one of the oxygen atoms of the carboxylate bridging group and the water molecule *trans* to the phenoxo group, with a donor–acceptor distance of 2.734 Å (Figure 2.3). Moreover, two oxygen atoms of the nitrate anion are involved in two hydrogen bonds with the oxygen atoms of the water molecules with donor acceptor distances of 2.736 and 2.763 Å. The noncoordinated methoxo group forms an intramolecular hydrogen bond with the water molecule *trans* to the oxygen atom of the acetate bridging group, the donor-acceptor distance being 2.726 Å.

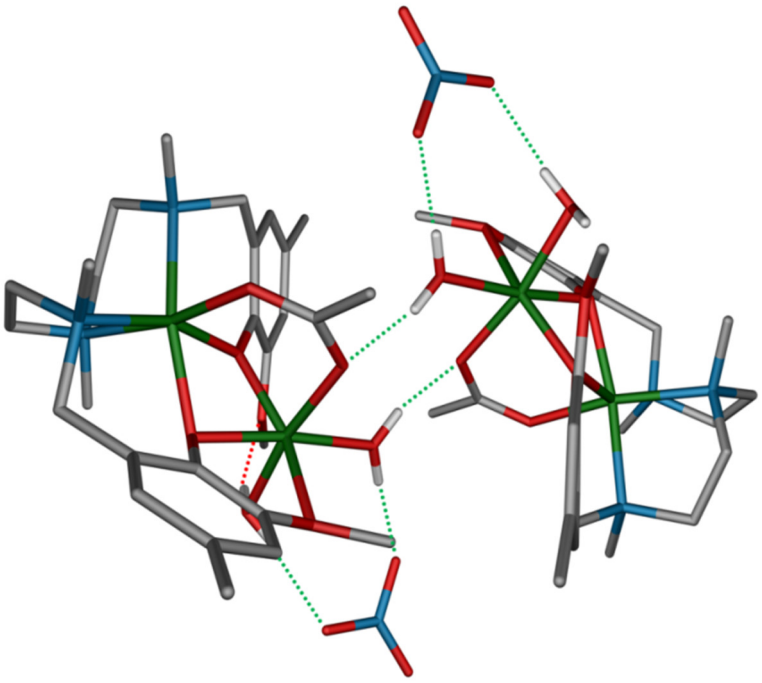

Figure 2.3.- A perspective view of the structure of **7** together with intramolecular (red dotted lines) and intermolecular (green dotted lines) hydrogen bonds.

The structures of complexes **8** and **9** (Figure 2.4) are very similar to that of complex **7**, exhibiting the same di-μ-phenoxo/carboxylate bridging fragment with only minor changes affecting distances and angles (see Appendices, Table A.4). Complex **9** presents two crystallographically independent molecules in the asymmetric unit, which slightly differ in bond lengths and angles.

The most important structural differences concern the coordination sphere of the outer Ni(II) ions, in which the water molecule has been substituted by a molecule of methanol. In **8**, the dihedral angle between the mean plane of the benzene ring and the carboxylate plane, both belonging to the OBz^- bridging ligand, is 7.4°, whereas in **9**, the analogous dihedral angles for the 9-An^- bridging ligands are 72.8 and 74.6°, respectively.

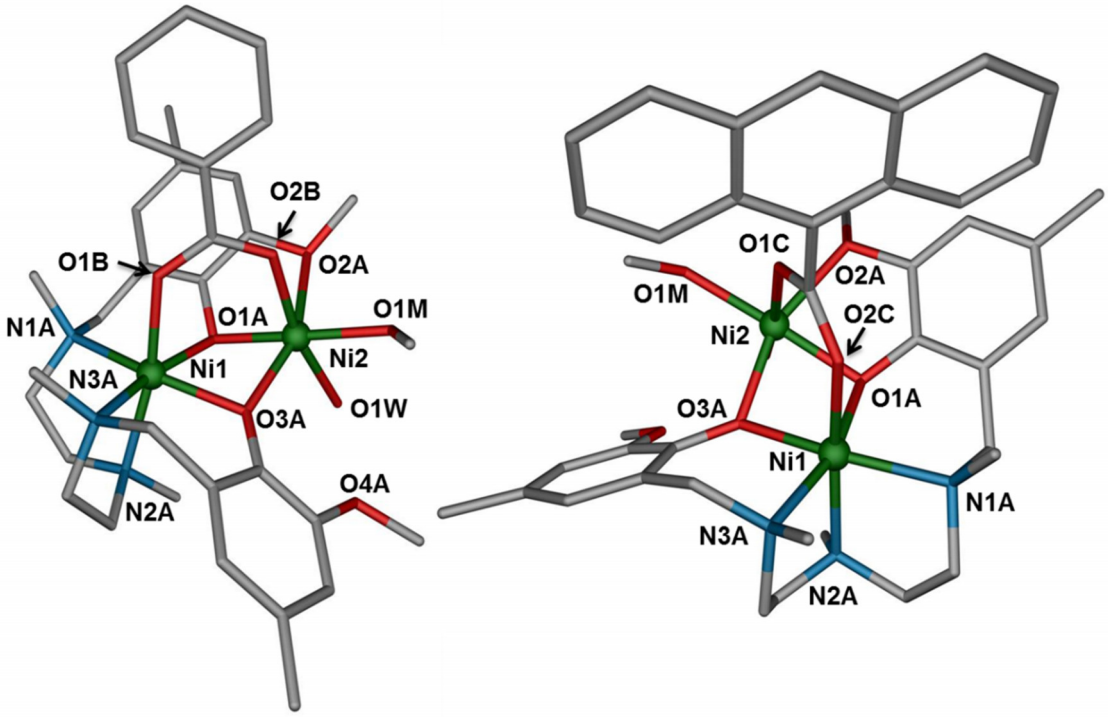

Figure 2.4.- A perspective view of the structure of **8** (left) and **9** (right). Colour code: N = blue, O = red, C = gray, Ni = green. H atoms, solvent crystallization molecules and the counteranions have been omitted for the sake of clarity.

For **8**, dinuclear cationic entities are also held together in pairs by a couple of symmetrical and complementary hydrogen bonds involving the water molecule and the oxygen atom of the phenoxo group *trans* to the methanol molecule with an O···O distance of 2.823 Å. An additional hydrogen bond connects the methanol molecule to one of the oxygen atoms of the nitrate anion with a O···O distance of 2.689 Å (Figure 2.5).

For **9** the dinuclear cationic entities are held together in pairs simply by means of a hydrogen bond involving centrosymmetrically related water molecules with an O···O distance of 2.824 Å (Figure 2.5). One of the nitrate anions is linked to one of the

cationic entities by two hydrogen bonds involving the water and methanol molecules with donor–acceptor distances of 2.696 and 2.759 Å, respectively, whereas the other nitrate anion forms a hydrogen bond with the molecule of methanol of the other dinuclear cationic entity with an O···O distance of 2.746 Å. As in **7**, compounds **8** and **9** exhibit an intramolecular hydrogen bond involving the methoxo group and the water molecule with donor-acceptor distances of 2.687, and 2.710 and 2.731 Å, respectively.

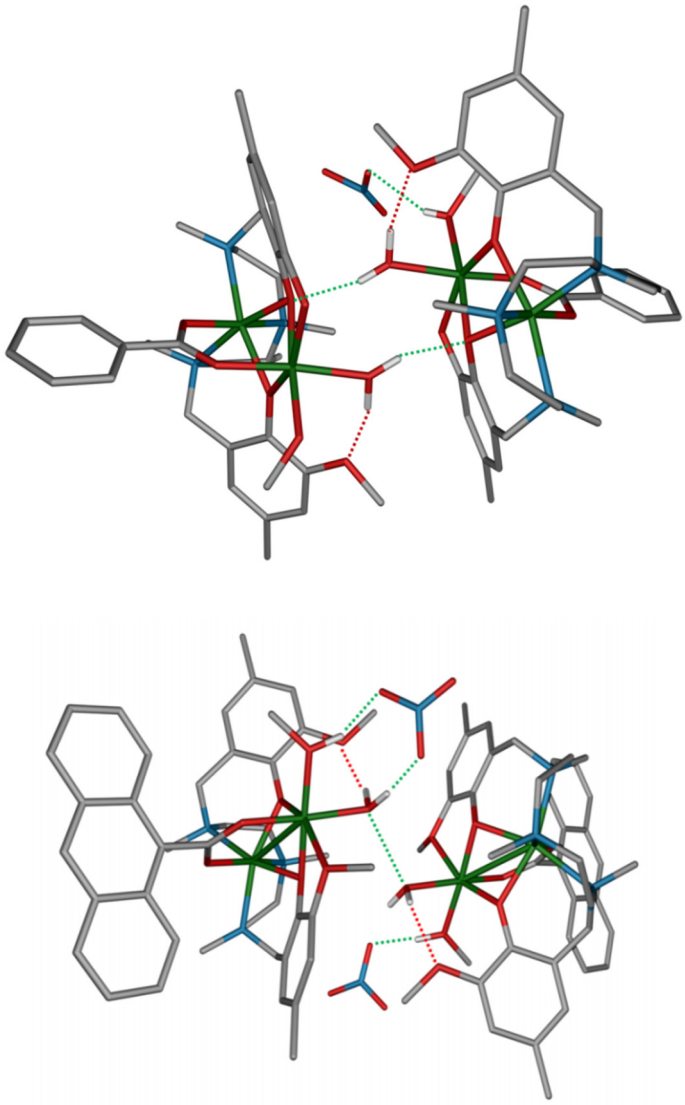

Figure 2.5.- A perspective view of the structures of **8** (top) and **9** (bottom) together with intramolecular (red dotted lines) and intermolecular (green dotted lines) hydrogen bonds.

Finally, in the structure of **10** (Figure 2.6), which is also related to that of **7**, the water molecule coordinated to the outer Ni(II) ion located in a *trans* position to one of

the phenoxo-bridging groups has been substituted by an azide anion, resulting in neutral molecules.

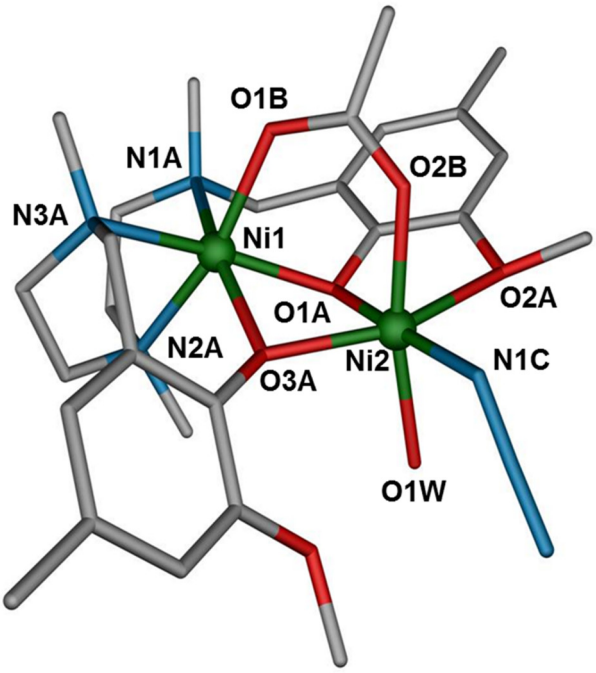

Figure 2.6.- A perspective view of the structure of **10**. Colour code: N = blue, O = red, C = gray, Ni = green. H atoms have been omitted for the sake of clarity.

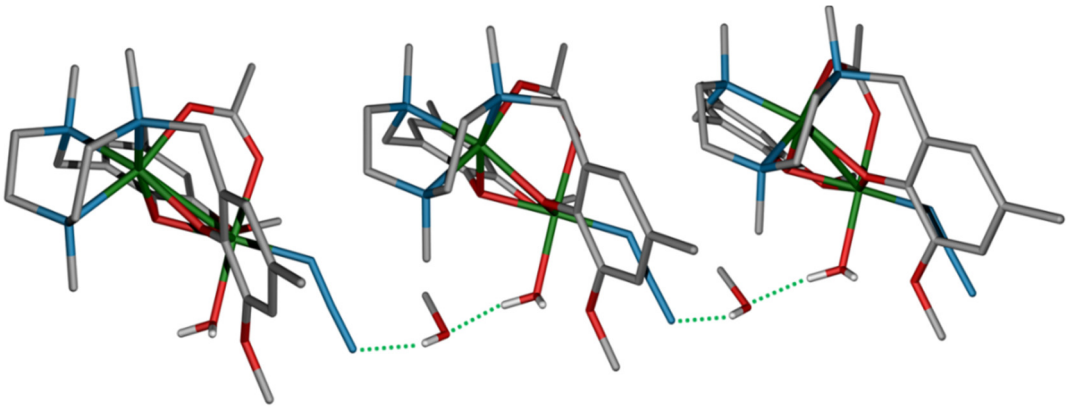

Figure 2.7.- The structure of **10** together with intermolecular (green dotted lines) hydrogen bonds forming a chain running along the *a* axis.

The rest of the molecule is very similar to that of **7**, and any further description will therefore be omitted. Molecules are connected by hydrogen bonds involving the methanol molecule, on the one side, and the water molecule and the terminal nitrogen

atom of the azide ligand belonging to neighbouring molecules, on the other side, with O···O and O···N distances of 2.741 and 2.822 Å, respectively. These hydrogen bonds generate chains that expand along the *a* crystallographic axis. The intramolecular hydrogen bond involving the coordinated water molecule and the neighbouring methoxo group presents an O···O distance of 2.692 Å.

2.3.2. Magnetic properties of complexes 7-10

The temperature dependence of the $\chi_M T$ product for compounds **7**-**10** ($\chi_M T$ being the molar magnetic susceptibility per two Ni(II) ions) are displayed in Figure 2.8.

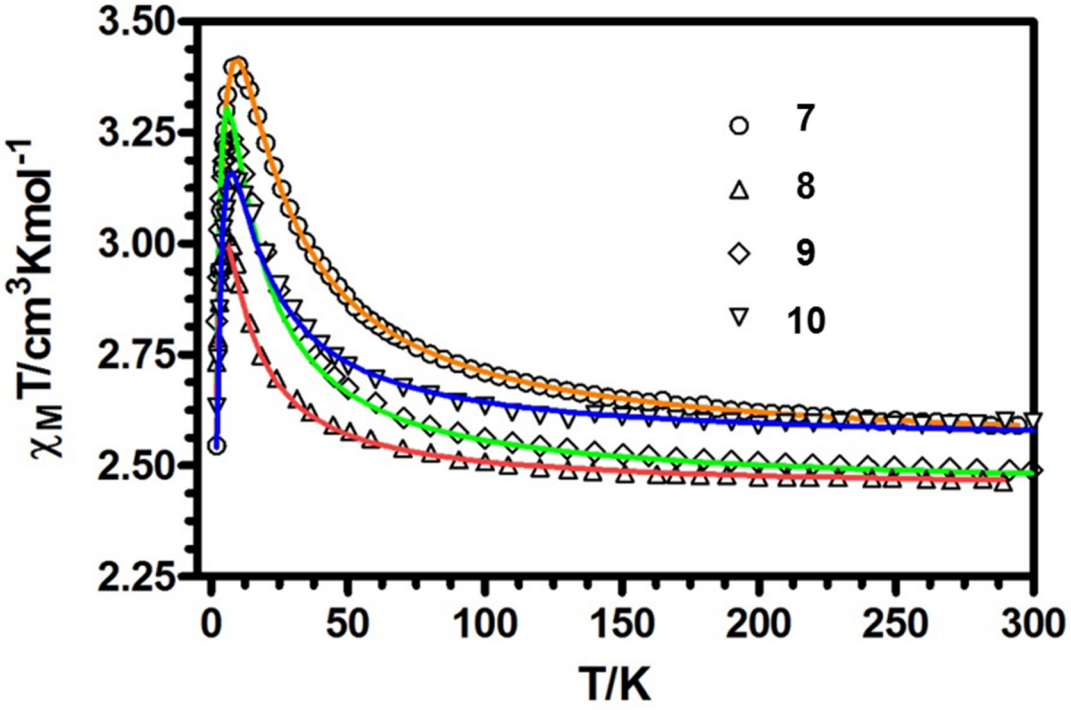

Figure 2.8.- Thermal dependence of the $\chi_M T$ product for complexes **7**-**10**. Solid lines are generated from the best fit magnetic parameters.

The compounds show room temperature $\chi_M T$ values in the range 2.4-2.6 $cm^3 \cdot K \cdot mol^{-1}$, which are typical for two non-interacting Ni(II) ions (S = 1) with g > 2, as expected. When the temperature is lowered, all the compounds (**7**-**10**) show a steady increase in the $\chi_M T$ product reaching a maximum of 3.4 (at 10 K), 3.02 (at 6 K), 3.34 (at 8 K) and 3.14 (at 8 K) $cm^3 \cdot K \cdot mol^{-1}$, respectively. Below the temperature of the maximum, $\chi_M T$ decreases quite fast to reach values of 2.54, 2.73, 2.82 and 2.63

$cm^3 \cdot K \cdot mol^{-1}$ at 2 K for **7** to **10**, respectively. This magnetic behaviour points out the presence of ferromagnetic exchange interactions within the Ni(II) dinuclear complexes together with antiferromagnetic interdimer interactions and/or zero field splitting of the resulting S = 2 spin ground state, which are responsible for the decrease in $\chi_M T$ at low temperatures.

The magnetic properties of these compounds have been modelled by using the following Hamiltonian:

$$\mathcal{H} = -JS_{Ni1}S_{Ni2} + \sum_{i=1}^{2} D_{Ni}S_{Niz}^2 \quad (\textit{Equation 2.1})$$

where J accounts for the magnetic exchange coupling between the Ni(II) ions and D_{Ni} accounts for the axial single ion zero-field splitting parameter of the Ni(II) ions (D_{Ni} is assumed to be the same for both Ni(II) ions). The fit of the experimental susceptibility data with the above Hamiltonian using the full-matrix diagonalization MAGPACK program[8] afforded the following set of parameters: J = + 7.7 cm^{-1}, g = 2.25, D = 6.5 cm^{-1} for **7**, J = + 2.2 cm^{-1}, g = 2.22, D = 3.9 cm^{-1} for **8**, J = + 4.9 cm^{-1}, g = 2.21, D = 4.8 cm^{-1} for **9**, and J = + 4.2 cm^{-1}, g = 2.26, D = 2.0 cm^{-1} for **10**. The D_{Ni} values are in agreement with the expected single-ion values reported in the literature.[9] When D_{Ni} was fixed to zero and a term accounting for the intermolecular interactions by means of the molecular field approximation, $-zJ' < S_z > S_z$, was introduced in the Hamiltonian, the fit was significantly improved (solid lines in Figure 2.8) leading to the following magnetic parameters: J = + 8.8 cm^{-1}, g = 2.25, zJ' = − 0.29 cm^{-1} for **7**, J = + 3.3 cm^{-1}, g = 2.21, zJ' = − 0.26 cm^{-1} for **8**, J = + 6.1 cm^{-1}, g = 2.21, zJ' = − 0.21 cm^{-1} for **9** and J = + 4.8 cm^{-1}, g = 2.26, zJ' = − 0.03 cm^{-1} for **10**. The D_{Ni} values obtained with zJ' = 0 and the zJ' values obtained with D_{Ni} = 0 can be considered as the limit values for these parameters, as zJ' and D_{Ni} are strongly correlated. Data simulations with the above Hamiltonian including intermolecular interactions have demonstrated that small changes in zJ' have the same effect as significant changes in D_{Ni}. Therefore, these parameters cannot be accurately determined by the fit of the magnetic data. So, we will keep the data extracted with D_{Ni} set to zero for further discussions. In order to support the experimental J values found for compounds **7**-**10**, DFT calculations using the broken-symmetry approach were carried out on the X-ray structures as found in solid state (further details can be found in Appendices, Section VI). As can be observed in Table 2.1, the calculated values are in good agreement in sign and magnitude with those of the experimental results.

Table 2.1.- Magneto-structural data for complexes **7**-**10**.

Complex	$J_{exp.}$/cm^{-1}	$J_{calc.}$[b]/cm^{-1}	θ[a] (°)	τ[a] (°)	β
7	+8.8	+8.2 (-1.5)	95.06	34.4	35.5
8	+3.3	+4.0 (-7.8)	96.55	32.1	32.6
9	+6.1	+2.9/+6.1 (-8.3/-4.1)	95.82/96.0	42.1	35.6[a]
10	+4.8	+2.4 (-4.5)	95.80	37.1	35.0

[a] Average value. [b] The values in brackets correspond to the model complexes where the carboxylate group has been replaced by two water molecules.

The field dependence of the molar magnetization at 2 K for these compounds (Figure 2.9), are close to the Brillouin function for *S* = 2, thus corroborating the existence of ferromagnetic interaction between the Ni(II) ions. In general, for **7**-**10** the Brillouin function is above the experimental magnetization data at high fields, which is more likely due to the combined effects of interdimer antiferromagnetic interactions and/or zero-field splitting of the *S* = 2 ground state.

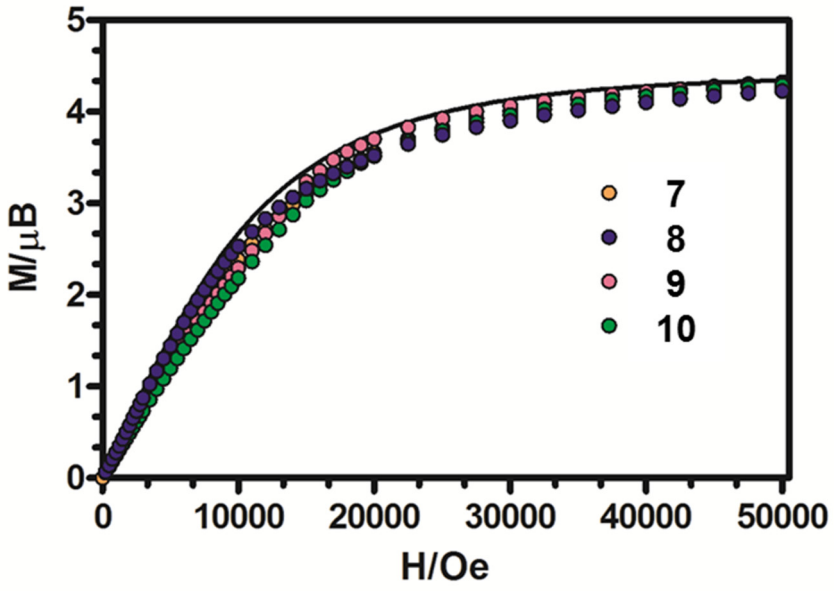

Figure 2.9.- Field dependence of the molar magnetization at 2 K for **7**-**10**. The solid line represents the Brillouin function for an *S* = 2 ground state.

2.3.3. Magneto-structural correlations for 7-10

As seen in Chapter 1, experimental and theoretical magneto-structural correlations[10] have clearly shown that the Ni-O-Ni bridging angle (θ) is the main factor affecting the nature of the magnetic exchange interaction in planar hydroxo-, alkoxo- and phenoxo- Ni-(μ-O)$_2$-Ni complexes. Thus, for Ni-O-Ni angles close to 90°, a ferromagnetic coupling is expected. As the Ni-O-Ni angle deviates from 90°, the ferromagnetic coupling decreases and becomes antiferromagnetic at values of ~96–98° (the AF coupling is favoured when θ increases). Moreover, it has been shown from theoretical studies[10a] that, on the one side, the AF interaction increases when τ decreases and, on the other side, the AF increases when β decreases (hinge angle between the O–Ni–O planes in the bridging region). In view of this, it is reasonable to assume that small θ angles (in the vicinity of 90–95°) combined with larger τ (>30–40°) and β values (>20°) should lead to weak AF or even F interactions in di-μ-phenoxo bridged nickel(II) complexes.

A first approximation would be that where the magnetic coupling through the axial *syn–syn* carboxylate bridging group is not operative. If so, complexes **7**–**10**, with θ, τ and β angles in the 95.1-96.6°, 32.1-42.1° and 32.6-35.6° ranges, respectively, should exhibit weak AF or F interactions between the Ni(II) ions of the folded Ni-(μ-O)$_2$-Ni units, which is in good agreement with the observed values. Compounds **7** and **8**, exhibiting the largest and smallest θ angles of the series (β and τ angles have similar values in both compounds), respectively, present the strongest and weakest ferromagnetic interactions, respectively, as expected. Complexes **9** and **10** have almost coincident θ values and therefore should exhibit similar values for the ferromagnetic coupling constant. However, the magnitude of the ferromagnetic interaction for the former is significantly stronger than for the latter, which could be justified by the larger β and τ values observed for **9**.

A second approximation could be adopted to explain the ferromagnetic coupling observed in **7**-**10**, which is compatible with the above discussion and takes into account the magnetic exchange pathway through the carboxylate bridging group. It is well known that the *syn–syn* bridging coordination mode exhibited by carboxylate groups in **7**-**10** causes a moderate to strong AF coupling.[11] However, if other bridges are also present, they could add or counterbalance their effects, giving rise to the phenomena called by Nishida et al.[1a] and McKee et al.[1b,c] as orbital complementarity and countercomplementarity, respectively. Such opposite behaviours are due to the

different interaction between the HOMOs of each of the bridging ligands with the symmetric and antisymmetric combinations of the magnetic orbitals. Thus, if this interaction increases the energy gap $\Delta = |\varepsilon_a - \varepsilon_s|$ (ε_a and ε_s are the energy of the singly occupied molecular orbitals), the antiferromagnetic contribution (J_{AF}) to the magnetic coupling also increases (Δ is the dominant factor in determining the magnitude of J_{AF}, so that the larger Δ is, the stronger the J_{AF}),[11] ultimately leading to a strong dominant AF coupling through orbital complementarity ($J = J_F + J_{AF}$ with J_F positive and J_{AF} negative and $|J_{AF}| \ggg |J_F|$). Conversely, if the interaction decreases Δ (orbital countercomplementarity), the J_{AF} will decrease leading to either weak AF or F interactions depending on the relative magnitude of J_{AF} and J_F. In connection with this, it has been shown that Ni(II) and Cu(II) dinuclear metal complexes bearing *syn–syn* carboxylate bridges and either alkoxo,[2] hydroxo-,[3] or water[4] bridging ligands exhibit countercomplementarity effects leading to either F or very weak AF interactions.

Therefore, the existence of the axial magnetic exchange pathway through the *syn–syn* carboxylate bridge in **7**-**10** may also contribute (in addition to the smaller θ and larger τ and β angles) to the observed F interaction in these compounds through orbital countercomplementarity. In order to support this hypothesis, we have performed DFT calculations on model compounds, which were built by replacing the *syn–syn* carboxylate group in **7**-**10** by two non-bridging water molecules, while keeping the rest of the X-ray structure unmodified (complexes **7′**-**10′**, hereafter). The calculated *J* values (see Table 2.1), clearly show that the magnetic coupling between the Ni(II) ions is AF in nature. As expected, there exists a good relationship between the calculated *J* values and θ (Figure 2.10) because β and τ angles have relatively close values and therefore can be considered as constant factors. The crossing point between AF and F interactions occurs at 94.7°.

Therefore, the AF magnetic coupling observed for the model compounds where the *syn-syn* carboxylate has been substituted by two water molecules is a good supporting evidence of the countercomplementarity effect caused by the *syn-syn* carboxylate bridging ligand in these compounds. From the calculated *J* values for the X-ray structures and model compounds, the magnitude of the countercomplementarity effect is estimated to be in the range 7-11 cm^{-1}. We have also performed DFT calculations on compound **7** in order to know how the variation of the $C_{carboxylate}$-O distance affects the magnetic coupling in di-μ-phenoxo/carboxylate bridged complexes. When both Ni-$O_{carboxylate}$ distances are simultaneously varied between 2.0 and 2.2 Å, the *J* parameter slightly decreases from + 8.8 cm^{-1} to + 7.3 cm^{-1} (Table 2.2).

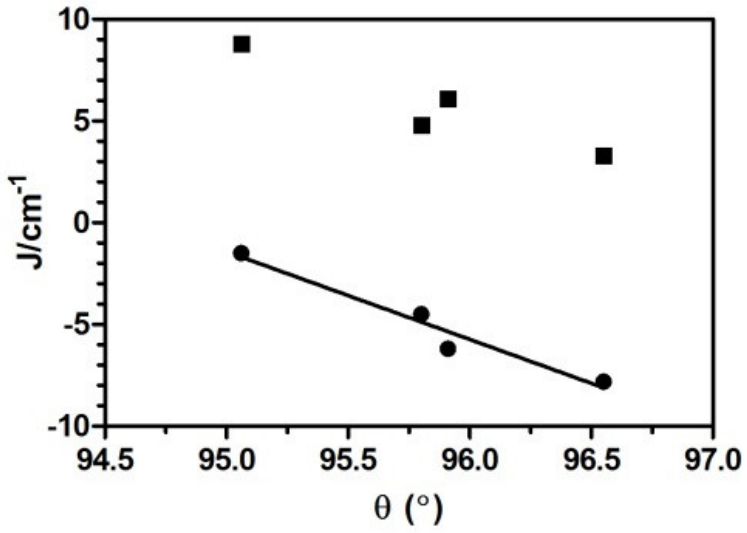

Figure 2.10.- Scatter plot of experimental (squares) and calculated (circles) *J* values vs. the mean Ni-O-Ni angle θ respectively for **7**-**10** and **7′**-**10′**. The solid line represents the linear fitting of model compounds **7′**-**10′**.

Table 2.2.- Variation of the calculated *J* with the Ni-$O_{carboxylate}$ distance

J	**dNi-$O_{carboxylate}$**
+8.6	2.0
+8.2	2.05
+7.9	2.1
+7.6	2.15
+7.3	2.2

The low value of *J* calculated for complex **10** seems to point out that the change in the coordination sphere of the outer Ni(II) ion of a coordinated oxygen atom belonging to a water molecule by the less electronegative nitrogen atom of the azide group, favours the antiferromagnetic interaction through the diphenoxo bridging fragment, thus decreasing the overall ferromagnetic interaction. A similar behaviour has been previously observed for oxalate-bridged complexes, in which the change of O-coordinated by N-coordinated peripheral ligands increases the AF coupling between the Ni(II) ions.[12]

Finally, the spin density distributions for the triplet ground state in **7**-**10** and the single ground state in **7′**-**10′** (the spin density of **7** and **7′** is given as a example in Figure 2.11) show the predominance of the delocalization mechanism through a σ type exchange pathway involving the $dx^2 - y^2$ and dz^2 magnetic orbitals of the Ni(II) atoms and the p orbitals of the diphenoxo and carboxylate bridging groups.

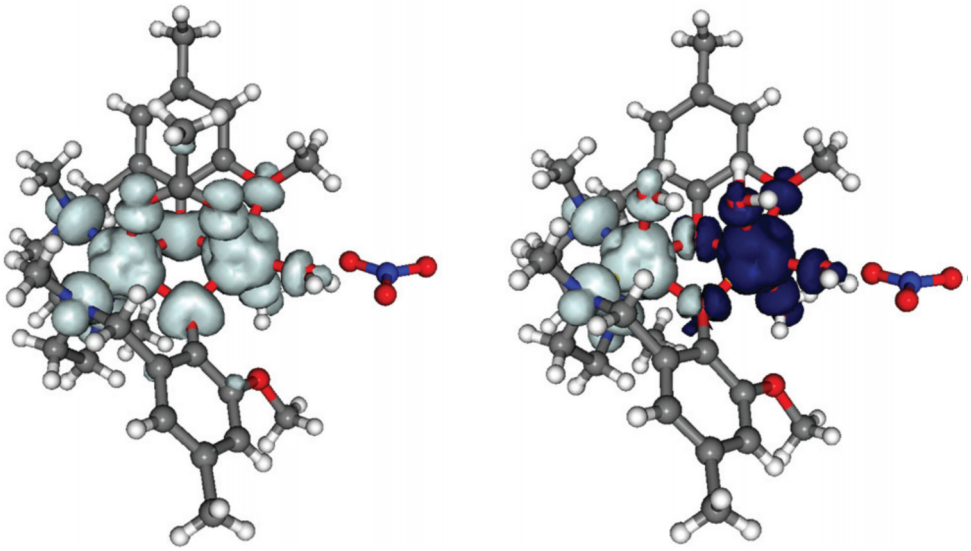

Figure 2.11.- Calculated spin densities for the triplet state of **7** (left) and broken-symmetry singlet of the model compound **7′** (right). The isodensity surfaces represented correspond to a cut-off value of 0.0015 e $bohr^{-3}$. Grey and blue colours represent positive and negative spin density values, respectively.

It should be noted that the spin densities (Table 2.3) delocalized over oxygen atoms of the diphenoxo bridging groups in **7** (average value 0.099 e $bohr^{-3}$) are higher than those over the oxygen atoms of the acetate bridging group (average value 0.046 e $bohr^{-3}$). As expected, the spin density is mainly found at the Ni(II) ions (average value for **7** of 1.670 e $bohr^{-3}$).

Table 2.3.- Spin density values (in e^-) on selected atoms for complex **7**.

Atoms[a]	Acetate bridge	Replaced bridge by water
Ni1/Ni2	+1.6701/+1.7381	+1.6593/-1.7240
$N1_{amine}$[b]	+0.0597	+0.0703
$O1,2_{phen\text{-}bridge}$[b]	+0.0991	-0.0187
$O1,2_{acet\text{-}bridge}$[b]	+0.0459	-[c]
$O2_{methoxo}$	+0.0245	-0.0251
$O2_{water}$[b]	+0.0319	-0.0391
$O1_{add\text{-}water}/O2_{add\text{-}water}$	-[c]	+0.0318/-0.0230

[a] Indexes 1 and 2 refers to the Ni1 (left) and Ni2 (right) moieties, respectively. [b] Mean value. [c] No applicable.

2.4. CONCLUSIONS

It has been exploited the great tendency of the Ni(II) ion coordinated at the N_3O_2 inner site of the compartmental ligand $(L^1)^{2-}$ to adopt an octahedral coordination, for preparing, in a deliberate manner, a series of di-μ-phenoxo/carboxylate bridged dinuclear Ni(II) complexes. The sixth position of the inner Ni(II) coordination sphere is saturated by the oxygen atom of a syn-syn carboxylate group connecting both inner and outer Ni(II) ions. The coordination of the *syn-syn* carboxylate group promotes the following changes in the Ni-$(\mu\text{-}O)_2$-Ni bridging fragment: (i) the structure is folded with large hinge angles in the range 32-35°, (ii) the Ni-O-Ni bridging angle (θ) is considerably reduced, and (iii) the τ angle increases to reach values in the 34-42° range. All these changes favour the decrease of the AF contribution to such an extent that weak AF or F couplings should be expected if, as a first approximation, the magnetic pathway through the *syn–syn* carboxylate group is not taken into account. In good agreement with this hypothesis, complexes **7**-**10** exhibit ferromagnetic coupling between the Ni(II) ions. A comparative analysis of the magneto-structural data for **7**-**10** and other di-μ-phenoxo/carboxylate bridged dinuclear nickel(II) complexes allows one to conclude that, in addition to θ, the β and τ angles play an important role in determining the magnetic coupling in this kind of compounds. When the magnetic exchange pathway through the *syn-syn* carboxylate group is also considered for the

magnetic coupling of complexes **7**-**10**, the phenomenon of the countercomplementarity between diphenoxo and carboxylate bridging ligands immediately emerges. DFT calculations unequivocally support the existence of countercomplementarity effects in **7**-**10**, which are essential for the ferromagnetic coupling observed in **7**-**10**.

From the magneto-structural data for di-μ-phenoxo/carboxylate triply bridged dinuclear Ni(II) complexes reported so far, including **7**-**10**, the following magneto-structural correlation can be established: for $\theta > \sim 97°$ and $\tau < 20°$ the countercomplementary effect of the axial *syn-syn* carboxylate group is not able to counterbalance the strong antiferromagnetic coupling transmitted through the diphenoxo bridging fragment and an overall medium AF coupling is observed, whereas for $\theta < \sim 97°$ and $\tau > 30°$ the axial *syn–syn* carboxylate group is able to counterbalance the AF interaction, leading to a global very weak AF or F coupling.

2.5. BIBLIOGRAPHY

[1] **a)** Y. Nishida, S. Kida, *J. Chem. Soc., Dalton Trans*., **1986**, 2633; b) V. McKee, M. Zvagulis, C. A. Reed, *Inorg. Chem*., **1985**, *24*, 2914; **c)** V. McKee, M. Zvagulis, J. V. Dagdigian, M. G. Patch, C. A. Reed, *J. Am. Chem. Soc*., **1984**, *106*, 4765; **d)** L. L. Wang, Y. M. Sun, Z. N. Qi, C. B. Liu, *J. Chem. Phys. A*, **2008**, *112*, 8418 and references.

[2] S. Mandal, V. Balamurugan, F. Lloret, R. Mukherjee, *Inorg. Chem*., **2009**, *48*, 7544.

[3] **a)** L. Gutierrez, G. Alzuet, J. A. Real, J. Cano, J. Borrás, A. Castiñeiras, *Inorg. Chem*., **2000**, *39*, 3608; **b)** L. Gutierrez, G. Alzuet, J. A. Real, J. Cano, J. Borras, A. Castiñeiras, *Eur. J. Inorg. Chem*., **2002**, *8*, 2094.

[4] **a)** L. Cañadillas-Delgado, O. Fabelo, J. Pasán, F. S. Delgado, F. Lloret, M. Julve, C. Ruiz-Pérez, *Inorg. Chem*., **2007**, *46*, 7458; **b)** R. Biswas, P. Kar, Y. Song, A. Ghosh, *Dalton Trans*., **2011**, *40*, 5324; **c)** R. Biswas, S. Giri, S. K. Saha, A. Ghosh, *Eur. J. Inorg. Chem.*, **2012**, 2916; **d)** X. M. Zhang, X. H. Jing, E. Q. Gao, *Inorg. Chim. Acta,* **2011**, *365*, 240.

[5] E. Colacio, J. Ruiz-Sanchez, F. J. White, E. K. Brechin, *Inorg. Chem*., **2011**, *50*, 7268.

[6] **a)** E. Colacio, J. Ruiz, A. J. Mota, M. A. Palacios, E. Cremades, E. Ruiz, F. J. White, E. K. Brechin, *Inorg. Chem*., **2012**, *51*, 5857; **b)** E. Colacio, J. Ruiz, A. J. Mota, M. A. Palacios, E. Ruiz, E. Cremades, M. M. Hänninen, R. Sillanpää, E. K. Brechin, *C. R. Chimie*, **2012**, *15*, 878; **c)** J. Ruiz, A. J. Mota, A. Rodríguez-Diéguez, S. Titos, J. M.

Herrera, E. Ruiz, E. Cremades, J. P. Costes, E. Colacio, *Chem. Commun.,* **2012**, *48*, 7916; **d)** E. Colacio, J. Ruiz, E. Ruiz, E. Cremades, J. Krzystek, S. Carretta, J. Cano, T. Guidi, W. Wernsdorfer, E. K. Brechin, *Angew. Chem. Int. Ed*., **2013**, *52*, 9130; **e)** E. Colacio, J. Ruiz, G. Lorusso, E. K. Brechin, M. Evangelisti, *Chem. Comm*., **2013**, *49*, 3845; **f)** S. Titos-Padilla, J. Ruiz, J. M. Herrera, E. K. Brechin, W. Wersndorfer, F. Lloret, E. Colacio, *Inorg. Chem*., **2013**, *52*, 9620; **g)** M. A. Palacios, S. Titos-Padilla, J. Ruiz, J. M. Herrera, S. J. A. Pope, E. K. Brechin, E. Colacio, *Inorg. Chem*., **2014**, *53*, 1465; **h)** J. Ruiz, G. Lorusso, M. Evangelisti, E. K. Brechin, S. J. A. Pope, E. Colacio, *Inorg. Chem*., **2014**, *53*, 3586.

[7] M. Llunell, D. Casanova, J. Cirera, J. M. Bofill, P. Alemany, S. Alvarez, M. Pinsky, D. Avnir, *SHAPE*, v1.1b; Barcelona, Spain, **2005**.

[8] **a)** J. J. Borrás-Almenar, J. Clemente, E. Coronado, B. S. Tsukerblat, *Inorg. Chem*., **1999**, *38*, 6081; **b)** J. J. Borrás-Almenar, J. Clemente, E. Coronado, B. S. Tsukerblat, *J. Comput. Chem*., **2001**, *22*, 985.

[9] **a)** S. K. Dey, M. S. El Fallah, J. Ribas, T. Matsushita, V. Gramlich, S. Mitra, *Inorg. Chim. Acta*, **2004**, *357*, 1517; **b)** Q. R. Cheng, J. Z. Chen, Z. Zhou, Z. Q. Pan, *J. Coord. Chem*., **2011**, *64*, 1139; **c)** K. K. Nanda, R. Das, L. K. Thompson, K. Venkatsubramanian, K. Nag, *Inorg. Chem*., **1994**, *33*, 5934; **d)** R. Das, K. K. Nanda, K. Venkatsubramanian, P. Paul, K. Nag, *J. Chem. Soc., Dalton. Trans*., **1992**, 1253; **e)** P. Mukherjee, M. G. B. Drew, C. J. Gómez- García, A. Ghosh, *Inorg. Chem*., **2009**, *48*, 5848; **f)** Z. Q. Pan, K. Ding, H. Zhou, Q. R. Cheng, Y. I. Cheng, Q. M. Huang, *Polyhedron*, **2011**, *30*, 2268.

[10] M. A. Palacios, A. J. Mota, J. E. Perea-Buceta, F. J. White, E. K. Brechin, E. Colacio, *Inorg. Chem*., **2010**, *49*, 10156; **b)** R. Biswas, S. Giri, S. K. Saha, A. Ghosh, *Eur. J. Inorg. Chem*., **2012**, 2916; **c)** K. K. Nanda, L. K. Thompson, J. N. Bridson, K. Nag, *J. Chem. Soc., Chem. Commun.*, **1994**, 1337; **d)** M. A. Halcrow, J. S. Sun, J. C. Huffman, G. Christou, *Inorg. Chem*., **1995**, *34*, 4167; **e)** J. M. Clemente-Juan, B. Chansou, B. Donnadieu, J. P. Tuchages, *Inorg. Chem*., **2000**, *39*, 5515; **f)** X. H. Bu, M. Du, L. Zhang, D. Z. Liao, J. K. Tang, R. H. Zhang, M. Shionoya, *J. Chem. Soc., Dalton Trans*., **2001**, 593.

[11] O. Kahn, *Molecular Magnetism*, VCH, Weinheim, Germany, 1993.

[12] P. Román, C. Guzmán-Miralles, A. Luque, J. I. Beitia, J. Cano, F. Lloret, M. Julve, S. Alvarez, *Inorg. Chem*., **1996**, *35*, 3741.

CHAPTER 3

A FAMILY OF DIPHENOXO/ACETATE TRIPLY BRIDGED DINUCLEAR Zn(II)Ln(III) COMPLEXES

3.1. INTRODUCTION

Although the requirements to behave as SMMs are not easily fulfilled by transition metal complexes, the use of heavy lanthanide ions is a good strategy for obtaining single molecule magnets, because lanthanides have large inherent angular momentum in the ground multiplet state and large magnetic anisotropy.[1] Of particular interest are the Dy(III) containing coordination compounds as the ligand field splits the ground $^6H_{15/2}$ multiplet in such a way that usually the M_J = -15/2 is the ground Kramer's doublet, which ensures large magnetic moment, bistability (parallel/antiparallel orientation along the polarizing magnetic field) and easy-axis anisotropy when only the ground state is significantly populated.[2]

As for the photophysical properties, lanthanides exhibit intense, narrow-line, and long-lived (nanosecond, microsecond, or millisecond) emissions, which cover a spectral range from the near UV to the NIR region. Because f-f transitions are parity forbidden, the absorption coefficients are normally very low. However, organic ligands with strongly absorbing chromophores that transfer energy to the lanthanide can be used to circumvent that drawback (antenna effect).[3]

In addition to the coordination modes shown by H_2L in Chapter 1, this ligand could also allow the preparation of dinuclear 3d-4f complexes presenting the coordination mode shown in Figure 3.1. These complexes could be prepared in two steps, first reacting the compartmental ligand H_2L with the 3d metal salt and then, with the lanthanide salt or compound. The more oxophilic lanthanide ions would occupy the external O_4 coordination site and both ions would saturate their coordination spheres with donor atoms, which could come from a bridging ligand connecting the Ln(III) and transition metal ions. In fact, the ligand H_2L has already been used to prepare 3d-4f systems, obtaining the tetranuclear compounds with the general formula ($\{[MLn(L')(CH_3COO)(H_2O)]ClO_4 \cdot nCH_3OH \cdot nH_2O\}_2$), where M can be Ni(II), Cu(II) or Zn(II) and Ln(III) can be Gd(III) or Lu(III) (Scheme 3.1). In these complexes, one of the formyl groups of the H_2L ligand is transformed into a hemiacetal group, leading to the ligand H_2L'.

$$H_2L + MX_2 \cdot nH_2O \xrightarrow{S} ML \xrightarrow{LnZ_3} [M(\mu - L)(\mu - X)Ln(?)]?$$

M = transition metal *Ln = lanthanide* *? S = solvent; X, Z = counterions*

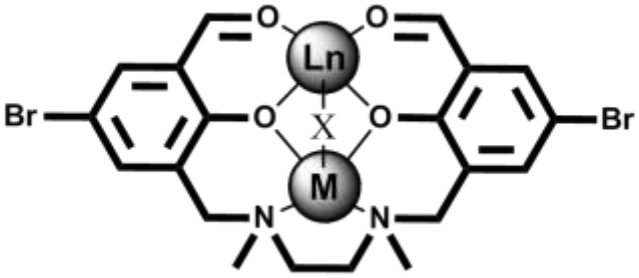

Figure 3.1.- Strategy for the preparation of 3d-4f dinuclear systems.

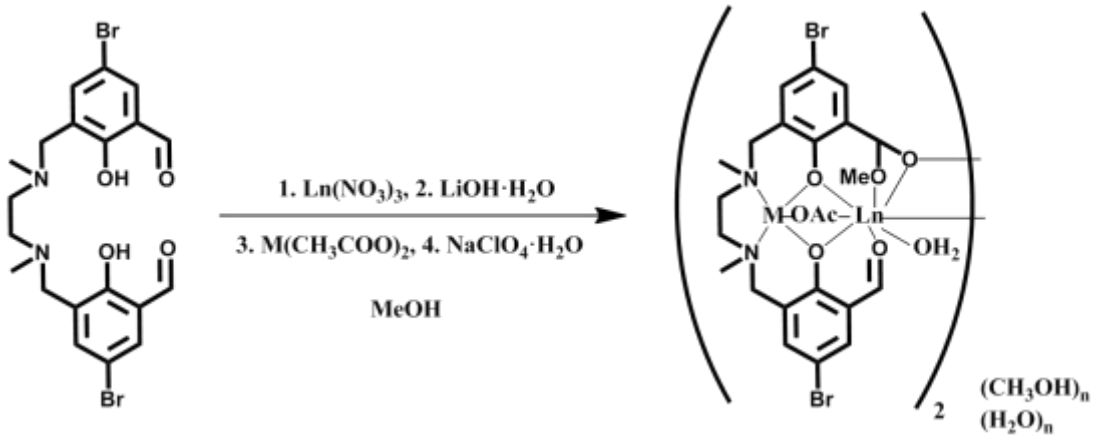

Scheme 3.1.- Synthesis of the tetranuclear compounds with the schematic representation of the dinuclear unit.

It should be noted that for 3d/4f systems, U_{eff} values as high as 82 cm^{-1} (118 K) and observable hysteresis loops up to 3.7 K have been reported.[4] On the other hand, as it was indicated in the introduction, mononuclear and low-nuclearity 4f metal complexes generally possess energy barriers of an order of magnitude higher than the observed in 3d/4f polymetallic clusters, with U_{eff} and T_B (temperature at which the hysteresis opens) values as high as 652 cm^{-1} (938 K) and 14 K, respectively. In the former systems the

SMM behaviour is commonly due to the individual Ln(III) ions rather than to the whole molecule, whereas in the latter the height of the magnetization relaxation barrier is directly related to the 3d-4f magnetic exchange interactions. Thus when the 3d-4f magnetic exchange coupling is strong, the exchange coupled levels are well separated and the QTM is suppressed, so that large energy barriers (up to 82 cm^{-1}) and hysteresis loops are observed. However, as the 3d-4f magnetic exchange couplings are generally weak, the separations between the low-lying split sublevels are small and consequently modest energy barriers for magnetization reversal are observed. In this regard, an effective and relatively easy approach to improve the SMM properties of the 3d/4f aggregates would be that of removing the very weak M(II)–Ln(III) interactions that split the ground sublevels of the Ln(III) ion by substituting the paramagnetic M(II) ions by diamagnetic ions. In fact, experimental results and theoretical calculations carried out by our group and others[5] have shown that the incorporation of diamagnetic metal ions, such as Co(III) and Zn(II), generally leads to higher U_{eff} than the MDy (M = Co and Ni) and homononuclear Dy counterparts. This phenomenon could be due to two factors: (i) the diminution of the intermolecular magnetic interactions provoked by the presence of diamagnetic ions (some kind of magnetic dilution), which could reduce the faster QTM process that usually masks the slow relaxation process and the opening of the hysteresis loops at zero field in lanthanide containing complexes (although U_{eff} values of Ln-based species are very large infrequently show an open hysteresis loop at zero field) and (ii) the possible increase of electron density on the bridging oxygen donor atoms connecting the diamagnetic and Dy(III) ions provoked by the coordination to the diamagnetic ion, which in turn induces a large electrostatic interaction with the lanthanide ion, giving rise to large separations of its crystal field levels and consequently to an increase of U_{eff}. This hypothesis was recently supported by theoretical calculations in Zn-Dy complexes.[6] In this regard, it should be noted that the electron density and spatial arrangement of the oxygen donor atoms coordinated to the Dy(III) play a decisive role in determining the SMM behaviour of Dy(III) containing complexes. Our group and others have shown that the ligand substitution on the Dy coordination sphere and even more, subtle changes as the replacement of counteranion, have a great influence on the dynamic properties of 3d-Dy SMMs.[7]

Following the cited strategy, this chapter collects the synthesis, structural characterization and magnetic and luminescent properties of a family of Zn(II)Ln(III) dinuclear complexes {Ln(III) = Pr, Nd, Sm, Eu, Gd, Tb, Dy, Ho, Er, Tm, Yb} with the ligand H_2L.

3.2. PREPARATION OF COMPLEXES

3.2.1. $[Zn(\mu\text{-}L)(\mu\text{-}OAc)Ln(NO_3)_2]\cdot CH_3CN$, Ln(III) = Pr (11), Nd (12), Sm (13), Eu (14), Gd (15), Tb (16), Dy (17), Ho (18), Er (19), Tm (20) and Yb (21)

A general procedure was used for the preparation of these complexes: To a solution of 27.4 mg (0.125 mmol) of $Zn(OAc)_2\cdot 2H_2O$ in 5 mL of acetonitrile/methanol (80:20) mixture were added with continuous stirring 64.3 mg (0.125 mmol) of H_2L, leading to the formation of a yellow precipitate that corresponds to the Zn(II) complex. The successive addition of 0.125 mmol of $Ln(NO_3)_3\cdot nH_2O$ afforded a yellow solution, from which a yellow powder precipitated after several minutes of stirring. The yellow powder was collected by filtration and dried in vacuum (yield: 60-70 %, see Table 3.1), whereas the resulting solution was allowed to stand at room temperature for a week affording prismatic crystals of compounds **11**-**21**.

The powdered and crystalline samples were proved to be the same by X-ray diffraction (Appendices, Section III) and, in addition, the purity of the powdered compounds was checked by elemental analysis (Table 3.1).

Table 3.1.- Elemental analyses and yields for complexes **11**-**21**.

Complex	Yield (%)	Formula	% C calc./found	% H calc./found	% N calc./found
11	69	$C_{24}H_{26}N_5O_{12}Br_2ZnPr$	30.58/30.64	2.78/2.81	7.43/7.47
12	71	$C_{24}H_{26}N_5O_{12}Br_2ZnNd$	30.47/30.52	2.77/2.79	7.40/7.42
13	65	$C_{24}H_{26}N_5O_{12}Br_2ZnSm$	30.28/30.35	2.75/2.76	7.36/7.39
14	60	$C_{24}H_{26}N_5O_{12}Br_2ZnEu$	30.23/30.25	2.75/2.78	7.34/7.38
15	63	$C_{24}H_{26}N_5O_{12}Br_2ZnGd$	30.06/30.13	2.73/2.75	7.30/7.35
16	62	$C_{24}H_{26}N_5O_{12}Br_2ZnTb$	30.01/30.09	2.73/2.75	7.29/7.34
17	68	$C_{24}H_{26}N_5O_{12}Br_2ZnDy$	29.90/29.94	2.72/2.76	7.26/7.30
18	61	$C_{24}H_{26}N_5O_{12}Br_2ZnHo$	29.82/29.88	2.71/2.73	7.24/7.28
19	70	$C_{24}H_{26}N_5O_{12}Br_2ZnEr$	29.75/29.83	2.71/2.75	7.23/7.30
20	58	$C_{24}H_{26}N_5O_{12}Br_2ZnTm$	29.70/29.72	2.70/2.71	7.22/7.25
21	63	$C_{24}H_{26}N_5O_{12}Br_2ZnYb$	29.57/29.61	2.69/2.70	7.18/7.21

3.3. EXPERIMENTAL RESULTS

The reaction of H_2L with $Zn(OAc)_2 \cdot 2H_2O$ and $Ln(NO_3)_3 \cdot nH_2O$ in CH_3CN/MeOH and at a 1:1:1 molar ratio led to the formation of powdered yellow compounds with the general formula $[Zn(\mu\text{-}L)(\mu\text{-}OAc)Ln(NO_3)_2] \cdot CH_3CN$ (Ln(III) = Pr (**11**), Nd (**12**), Sm (**13**), Eu (**14**), Gd (**15**), Tb (**16**), Dy (**17**), Ho (**18**), Er (**19**), Tm (**20**), Yb (**21**)). The solution obtained after the filtration of the powdered compound afforded few X-ray quality crystals, which allowed the characterization of the compounds. Elemental analyses and powder X-ray diffractograms, together with their comparison to the simulated patterns from single-crystal X-ray diffractions, show that both powdered and crystalline samples are the same compound (Appendices, Figures A.3 and A.4). As the powdered compounds are obtained with yields in the 58-71 % range whereas only few crystals precipitate, the study of the magnetic and luminescent properties has been realized on powdered samples.

3.3.1. Crystal structures of complexes 11-21

Complexes **11**-**21** are isostructural between them and crystallize in the monoclinic $P2_1/n$ space group. The structure of **11-21** is given in Figure 3.2, whereas crystallographic data and selected bond lengths and angles for these complexes are given in Appendices, Tables A.5 and A.6, respectively.

The structures of compounds **11**-**21** consist of dinuclear Zn(II)-Ln(III) molecules, in which the Ln(III) and Zn(II) ions are bridged by two phenoxo groups of the L^{2-} ligand and one *syn-syn* acetate bridge. In all these compounds, the fully deprotonated L^{2-} ligand adopts a $2\kappa\text{-}O_{1A}$, $1\kappa\text{-}O_{2A}$:$2\kappa\text{-}O_{2A}$, $1\kappa^2\text{-}N,N'$, $1\kappa\text{-}O_{3A}$:$2\kappa\text{-}O_{3A}$, $2\kappa\text{-}O_{4A}$ hexadentate coordination mode, being O_{2A} and O_{3A} the phenolic oxygen atoms. The Zn(II) ions lie in the inner coordination site of the ligand, presenting a ZnN_2O_3 coordination sphere, which is made of two phenoxo bridging oxygen atoms and two nitrogen atoms of the ligand and one oxygen atom of the *syn-syn* acetate bridge. The calculation of the degree of distortion of the Zn(II) coordination polyhedron with respect to ideal five-vertex polyhedral, by using the continuous shape measure theory and SHAPE software[8] (Appendices, Table A.23), indicates that the ZnN_2O_3 coordination sphere can be considered as square pyramid but close to vacant octahedron and trigonal bipyramid. The Zn-O and Zn-N distances are found in the 1.951(4)-2.149(3) and

2.090(5)-2.133(3) Å ranges, respectively, being the shortest distances those corresponding to the Zn-$O_{acetate}$ bonds.

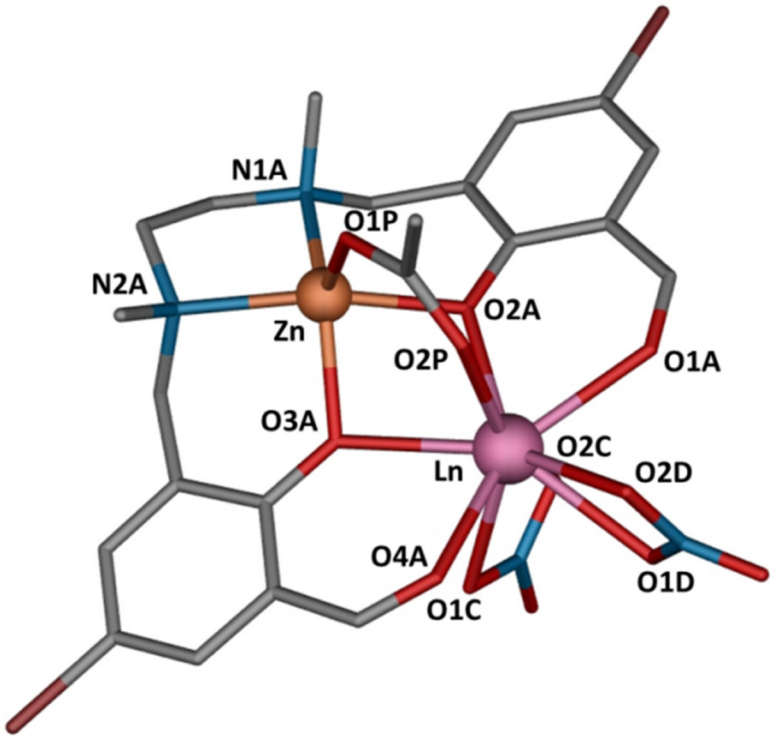

Figure 3.2.- A perspective view of the structure of **11-21**. Colour code: N = blue, O = red, C = gray, Br = brown, Zn = light brown, Ln = pink. H atoms and crystallization acetonitrile molecules have been omitted for the sake of clarity.

The Ln(III) ions exhibit LnO_9 coordination spheres, which are made by the two phenoxo bridging oxygen atoms, the two aldehyde oxygen atoms, one oxygen atom from the acetate bridging group and four oxygen atoms belonging to two bidentate nitrate anions. These coordination spheres are rather asymmetric, with relatively short Ln-O distances in the 2.241(2)-2.393(3) Å range that correspond to the Ln-$O_{acetate}$ bonds, intermediate Ln-O_{ligand} bond distances in the 2.303(2)-2.471(3) Å range and large Ln-$O_{nitrate}$ distances in the 2.406(2)-2.573(3) Å range. In fact, the use of the continuous shape measure theory and SHAPE software indicates that the LnO_9 coordination spheres can be considered as intermediate between several nine-vertex polyhedral (Appendices, Table A.24). The intradinuclear Zn···Ln distances are in the range 3.360(1)-3.437(1) Å and as expected, these distances and the distances corresponding to the Ln-O_{ligand} and Ln-$O_{acetate}$ bonds decrease from Pr(III) to Yb(III) following the lanthanide contraction. Figure 3.3 shows the linear dependence of Zn···Ln

distances and Ln-$O_{acetate}$ and Ln-$O_{phenoxo}$ (average) bond distances with the Ln(III) ionic radii, with correlation coefficients of $r^2 > 0.97$. The shortest Ln···Ln distance between neighboring dimers is in the 8.170(1)-8.233(1) Å range.

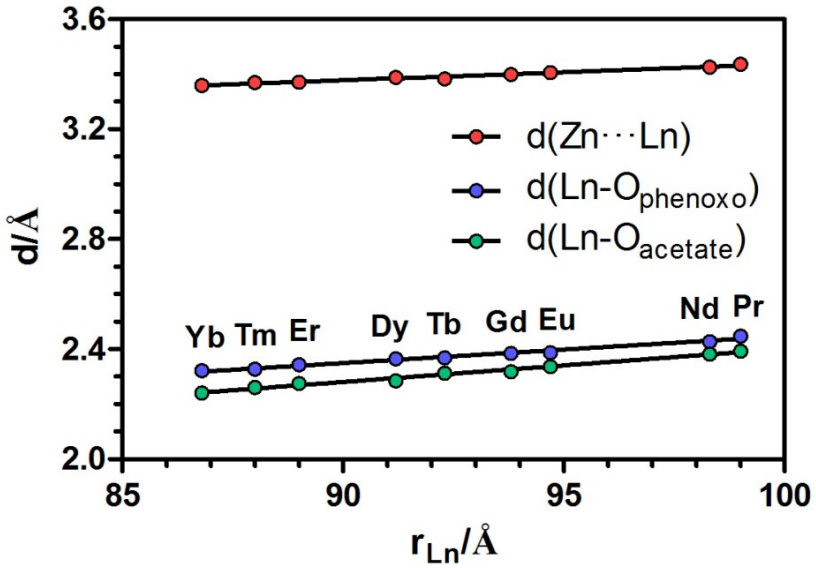

Figure 3.3.- Plots of the Zn···Ln, Ln-$O_{phenoxo}$ and Ln-$O_{acetate}$ distances versus the Ln(III) ionic radius.

The average Ln-O-Zn angles vary between 97.26(11)-99.33(7)° in complexes **11**-**21** and the bridging acetate group forces the structure to be folded with average hinge angles of the Zn-(μ-O)$_2$-Ln bridging fragment that range from 32.59 to 33.40° (the hinge angle, β, is the dihedral angle between the O-Zn-O and O-Ln-O planes in the bridging fragment). In these complexes, the L^{2-} ligand wraps around the Zn(II) and Ln(III) ions in such a way that the both aromatic rings of the ligand almost fall in the same plane, forming dihedral angles ranging from 11.46 to14.64°.

3.3.2. Magnetic properties of complexes 11-21

The temperature dependences of the magnetic susceptibilities for the dinuclear Zn(II)Ln(III) complexes were measured on powdered samples in the 4.5-300 K temperature range under an applied field of 0.1 T. The data for complexes **11**, **12** and **15**-**21** are shown in Figure 3.4 as $\chi_M T$ versus T plots, where χ_M is the molar magnetic susceptibility per dinuclear Zn(II)Ln(III) molecule and T is the absolute temperature.

Let us start with the simplest case concerning the magnetic properties of rare earth compounds, the Zn(II)Gd(III) complex **15**. The ground state arising from the $4f^7$ configuration of the Gd(III) ion is $^8S_{7/2}$ and since L = 0, there is no spin-orbit coupling. As the molecules are well isolated in the crystal, the intermolecular antiferromagnetic interactions are negligible and therefore, the magnetic properties only arise from the 7 unpaired electrons of the Gd(III) ion. According to the free-ion approximation, the $\chi_M T$ value at room temperature should be of 7.88 $cm^3 \cdot K \cdot mol^{-1}$ for a Gd(III) ion (S = 7/2 with g_J = 2) and in the absence of any type of interaction this value should remain constant upon cooling, which matches well with the experimental behaviour.

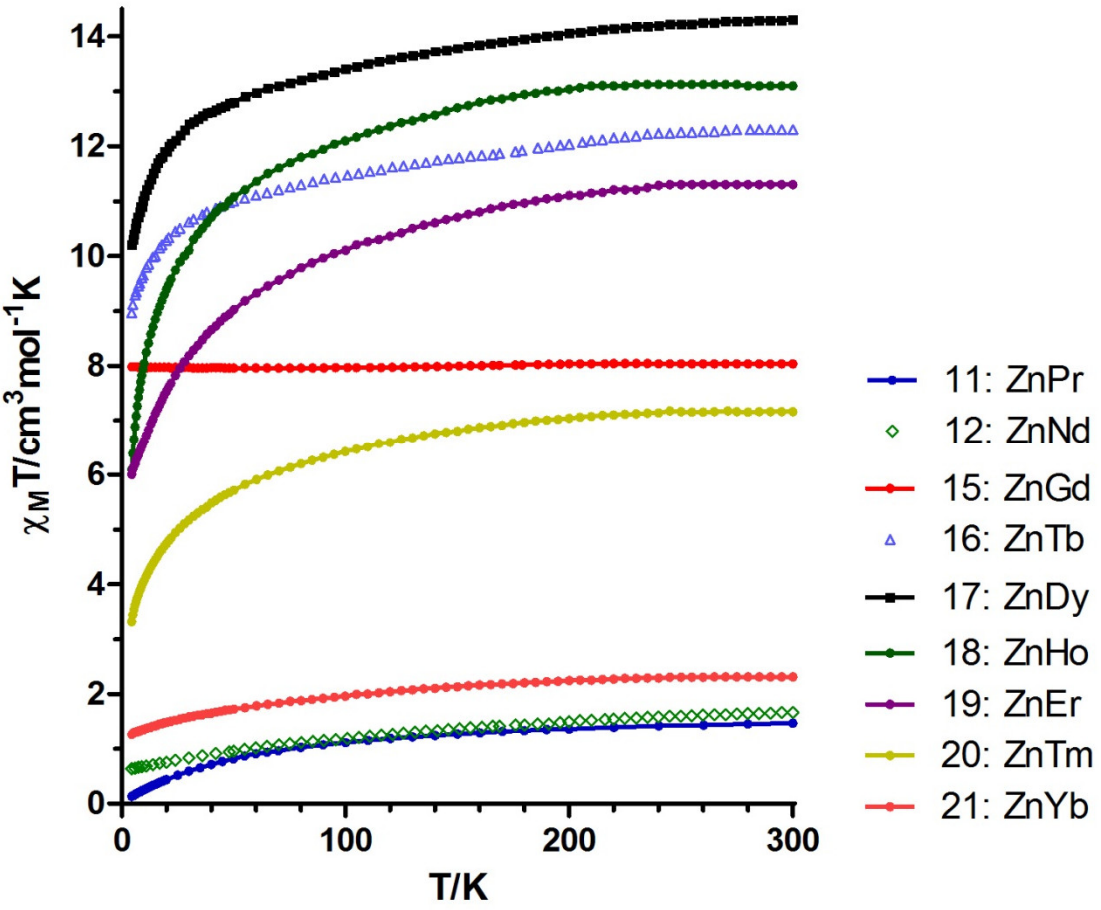

Figure 3.4.- Temperature dependence of the $\chi_M T$ product at 1000 Oe for complexes **11**, **12** and **15**-**21**.

In the case of complexes **11**-**12** and **16**-**21**, the $\chi_M T$ products at room temperature are close to the calculated values for independent Ln(III) ions in the free-ion approximation (Table 3.2). When lowering the temperature, the $\chi_M T$ values steadily

decrease in the whole temperature range, reaching values that are listed in Table 3.2 at 4.5 K. This behaviour is due to the depopulation of the Stark sublevels of the Ln(III) ion, which arise from the splitting of the ground term by the ligand field. At room temperature, all the Stark sublevels of the ground term are statistically populated and the free-ion approximation is fulfilled. However, when the temperature is lowered, the depopulation of the Stark sublevels results in non-Curie behaviour and in anisotropy.

Table 3.2.- *Direct current* magnetic data for complexes **11**-**21**.

Complex	Ln(III) ion	Ground state of Ln(III) ion[a]	χ_MT theor.[b] at 300K/exp. at 300 K/exp. at 4.5 K ($cm^3 \cdot K \cdot mol^{-1}$)	M theor.[c]/M exp. at 2 K ($N\mu_B$)
11	Pr	$^3H_4$, g_J = 4/5	1.60/1.46/0.13	3.2/0.23
12	Nd	$^4I_{9/2}$, g_J = 8/11	1.64/1.66/0.63	3.27/1.35
13	Sm	$^6H_{5/2}$, g_J = 2/7	0.09/0.406/0.078	0.71/0.13
14	Eu	$^7F_0$, g_0 = 5	0/1.56/0.03	0/0.04
15	Gd	$^8S_{7/2}$, g_J = 2	7.88/8.03/7.98	7/6.85
16	Tb	$^7F_6$, g_J = 3/2	11.82/12.3/8.96	9/4.91
17	Dy	$^6H_{15/2}$, g_J = 4/3	14.17/14.3/10.2	10/5.94
18	Ho	$^5I_8$, g_J =5/4	14.07/13.1/6.09	10/5.33
19	Er	$^4I_{15/2}$, g_J = 6/5	11.48/11.3/6.00	9/4.28
20	Tm	$^3H_6$, g_J = 7/6	7.15/7.16/3.32	7/2.54
21	Yb	$^2F_{7/2}$, g_J =8/7	2.57/2.31/1.26	4/1.72

[a] $J = L - S\ (Pr - Eu);\ J = L + S\ (Tb - Yb);\ g_j = \frac{3}{2} + \frac{S(S+1)-L(L+1)}{2J(J+1)};\ g_0(Eu(III)) = 2 + S$

[b] $\chi_M T = \frac{N\beta^2}{3k}\{g_j^2 J(J+1)\}$

[c] $M_s = g_J J N \mu_B$

On the other hand, the magnetic behaviour of complexes **13** (Zn(II)Sm(III)) and **14** (Zn(II)Eu(III)) (Figure 3.5) is quite different to that of the previous compounds, which is due to the presence of thermally populated excited states. For Sm(III) and Eu(III) ions the energy gap between the ground state and the first excited state is lower than in other ions, which leads to the population of the first excited state. As a consequence, the values reached by χ_MT in the high temperature domain are far above the values calculated by the free-ion approximation (Table 3.2). For the Sm(III) based complex, the temperature dependence of χ_MT decreases linearly as the temperature is lowered

to reach the low temperature limit of 0.089 $cm^3 \cdot K \cdot mol^{-1}$ predicted by the free-ion approximation theory. The $\chi_M T$ product of the Eu(III) derivative also decreases as the temperature is lowered, tending to a value very close to zero as T approaches 0 K. The magnetic behaviour for both compounds can be modelled to evaluate their respective spin-orbit coupling parameters.

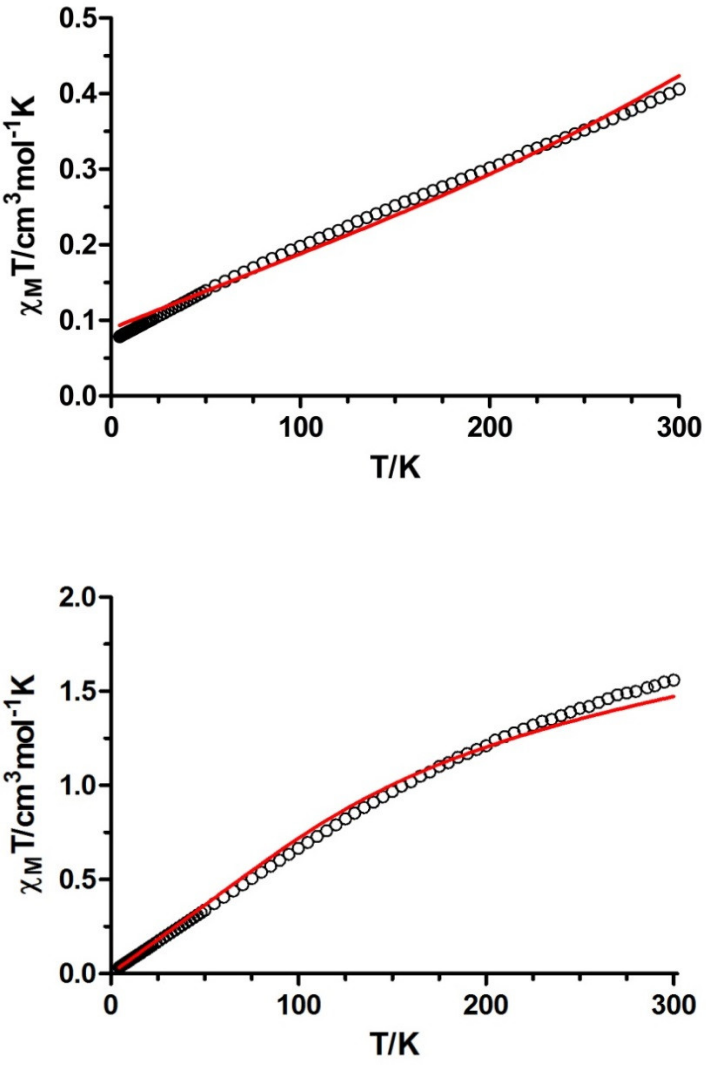

Figure 3.5.- Temperature dependence of the $\chi_M T$ product at 1000 Oe for complexes **13** (top) and **14** (bottom). The red solid line represents the best fit to Equations 3.4 and 3.5 respectively for compounds **13** and **14**.

As the ^6H ground term for Sm(III) is split by spin-orbit coupling into six levels, whose energies increase from $^6H_{5/2}$ to $^6H_{15/2}$, the Van Vleck formula for the magnetic susceptibility can be expressed as:[9]

$$\chi = \frac{\sum_{J=5/2}^{J=15/2}(2J+1)\chi(J)e^{[-E(J)/kT]}}{\sum_{J=5/2}^{J=15/2}(2J+1)e^{[-E(J)/kT]}} \quad (\textit{Equation 3.1})$$

where:

$$\chi(J) = \frac{Ng_J^2\beta^2J(J+1)}{3kT} + \frac{2N\beta^2(g_J-1)(g_J-2)}{3\lambda} \quad (\textit{Equation 3.2})$$

and:

$$E(J) = \frac{\lambda\left[J(J+1)-\frac{35}{4}\right]}{2} \quad (\textit{Equation 3.3})$$

χ may be expanded as:

$$\chi_M = \left(\frac{N\beta^2}{3kTx}\right)\left[a_1x + b_1 + (a_2x + b_2)e^{-\frac{7x}{2}} + (a_3x + b_3)e^{-8x} + (a_4x + b_4)e^{-\frac{27x}{2}} + (a_5x + b_5)e^{-20x} + (a_6x + b_6)e^{-55x/2}\right]/\left[3 + 4e^{-7x/2} + 5e^{-8x} + 6e^{-27x/2} + 7e^{-20x} + 8e^{-55x/2}\right] \quad (\textit{Equation 3.4})$$

where *N* is the Avogadro number, *β* the electronic Bohr magneton, *k* the Boltzmann constant, *T* the temperature and x is defined as x = λ/kT, λ being the spin-orbit coupling parameter. *a* and *b* are constant parameters with the following values: a_1 = 2.143, b_1 = 7.347, a_2 = 42.92, b_2 = 1.641, a_3 = 283.7, b_3 = -0.6571, a_4 = 620.6, b_4 = -1.9400, a_5 = 1122, b_5 = -2.835, a_6 = 1813 and b_6 = -3.556. The best fit of this expression to the experimental behaviour was obtained for λ = 215 cm^{-1}, which is close to the expected value of 200 cm^{-1} expected for Sm(III) compounds.[9]

Likewise, the ground term of Eu(III) (^{7}F) is splitted by the spin-orbit coupling into seven ^7F_J states, with energies that increase from $^7F_0$ to $^7F_6$. For Eu(III) compounds χ may be expanded as:

$$\chi_M = \left(\frac{N\beta^2}{3kTx}\right)\left[24 + \left(\frac{27x}{2} - \frac{3}{2}\right)e^{-x} + \left(\frac{135x}{2} - \frac{5}{2}\right)e^{-3x} + \left(\frac{189x}{2} - \frac{7}{2}\right)e^{-6x} + \left(\frac{405x}{2} - \frac{9}{2}\right)e^{-10x} + \left(\frac{1485x}{2} - \frac{11}{2}\right)e^{-15x} + \left(\frac{2457x}{2} - \frac{13}{2}\right)e^{-21x}\right]/\left[1 + 3e^{-x} + 5e^{-3x} + 7e^{-6x} + 9e^{-10x} + 11e^{-15x} + 13e^{-21x}\right] \quad (\textit{Equation 3.5})$$

The best fit of this expression to the experimental behaviour of **14** was obtained for λ = 286.6 cm^{-1}, which is close to the value of 300 cm^{-1} expected for Eu(III) compounds.[9]

The field dependence of the magnetization at 2 K for all complexes is shown in Figure 3.6. The isothermal magnetization plot of Gd(III) based complex **15** shows a

relatively rapid increase of the magnetization up to 2 T and then a linear increase to reach a value of 6.85 μβ at 5 T. This curve is well reproduced by the Brillouin function for a magnetically isolated Gd(III) ion with *g* = 2.0, which together with the susceptibility data confirms the absence of antiferromagnetic intermolecular interactions. Sm(III) and Eu(III) containing compounds show values very close to zero at 5 T, as expected. The rest of the compounds show a relatively rapid increase in the magnetization at low field and then a very slow linear increase, except the Ho(III) based compound, which continues increasing relatively fast. The values reached at the maximum applied field of 5 T are rather lower than the expected saturation values (Table 3.2). The observed behaviour is likely due to a significant magnetic anisotropy due to crystal fields effects and/or more likely due to the presence of low-lying excited states that are partially (thermally and field-induced) populated.

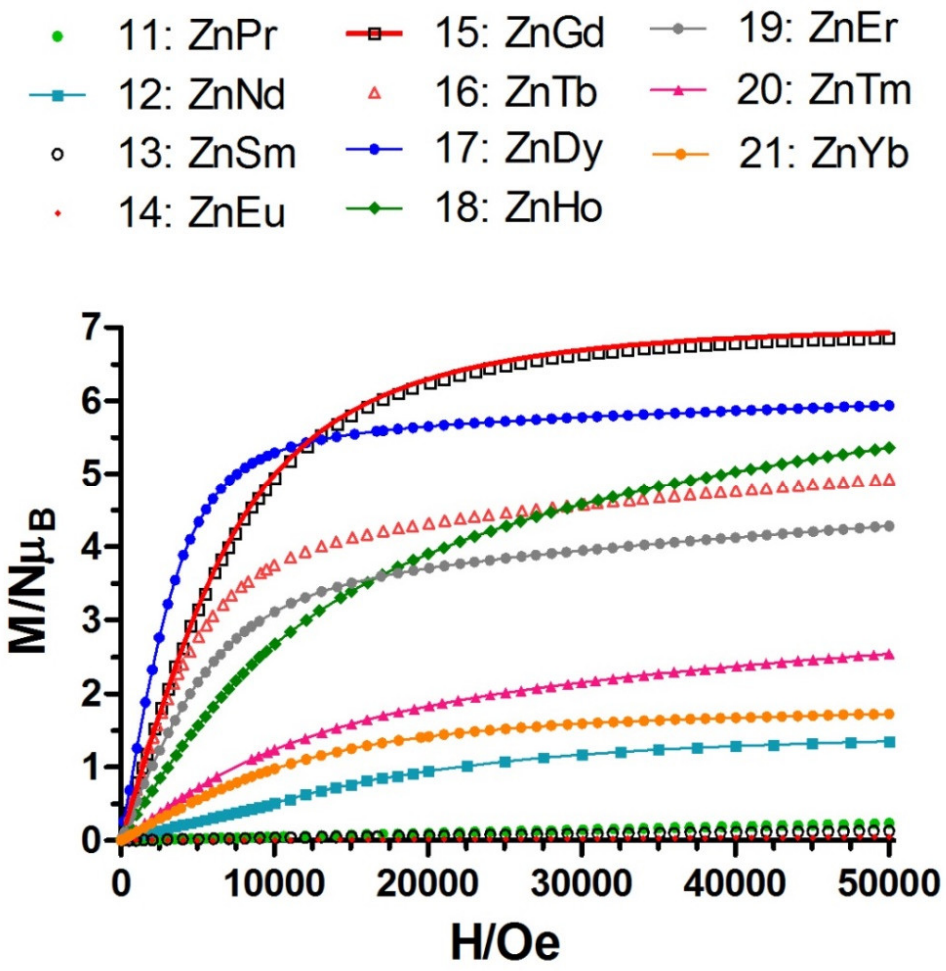

Figure 3.6.- *M* vs. *H* plots for complexes **11**-**21**. The red solid line represents the Brillouin function for an S = 7/2 ground state. The rest of the lines are a guide to the eye.

Dynamic *alternating current* (*ac*) magnetic susceptibility measurements as a function of the temperature at different frequencies were performed, but only the Dy(III) derivative showed weak frequency dependence at zero applied magnetic field (Figure 3.7). This behaviour indicates that either these compounds do not behave as SMMs or that a quantum tunnelling of the magnetization (QTM) is occurring, which leads to a flipping rate that is too fast to observe the maximum in the χ_M" vs. T plot above 2 K. When the *ac* measurements were performed in the presence of a small external field of 1000 Oe to partly or fully suppress the quantum tunnelling of the magnetization, the Nd (**12**), Dy (**17**), Er (**19**) and Yb (**21**) compounds showed typical SMM behaviour (Figures 3.8-3.12).

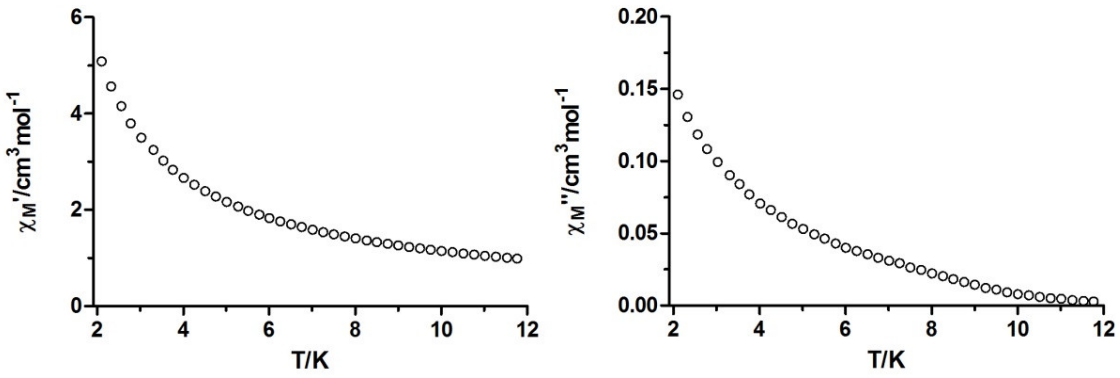

Figure 3.7.- Temperature dependence of in-phase χ_M' (left) and out-of-phase χ_M" (right) components of the *ac* susceptibility for complex **17** measured under zero applied *dc* field.

It should be noted that, to the best of our knowledge, slow relaxation of magnetization has been infrequently observed in Nd(III) based compounds. Apart from some 3d-Nd complexes,[10] where the magnetic properties are the result of both 3d and 4f ions, only four examples of homonuclear Nd(III) compounds have shown this behaviour. The first reported complex showing single-ion magnet (SIM) behaviour was $NdTp_3$ (Tp^- = trispyrazolylborate), which exhibited an energy barrier for the reorientation of magnetization of 2.8 cm^{-1}.[11] These results incited other groups to study the magnetic properties of Nd(III) compounds, leading to the discovery of another SIM, one MOF (Metal-organic-framework) and a layered compound of Nd(III) that show this behaviour.[12]

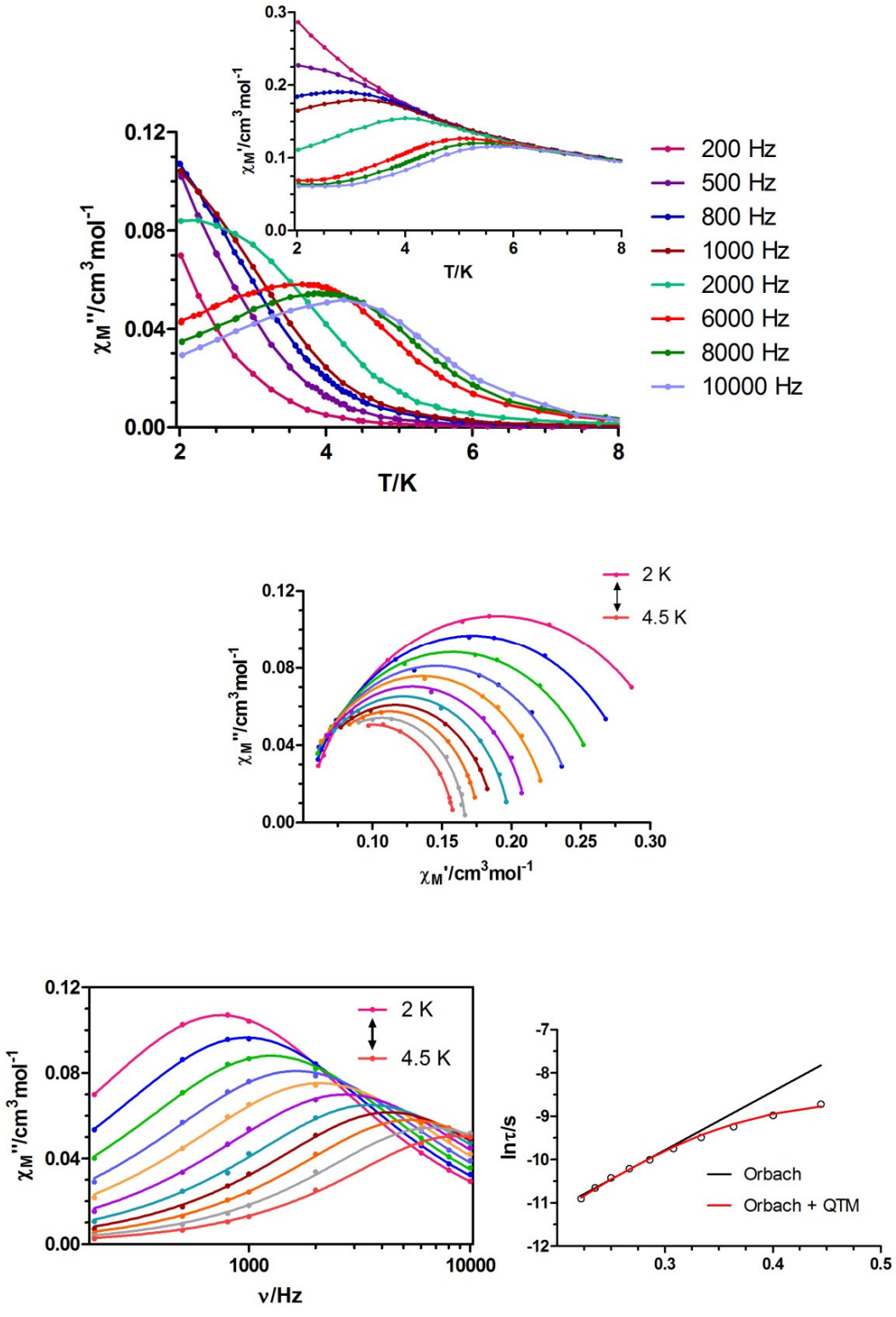

Figure 3.8.- Top: temperature dependence of in-phase χ_M' (inset) and out-of phase χ_M'' components of the *alternating current* (*ac*) susceptibility for complex **12** under an applied field of 1000 Oe. Medium: Cole-Cole plot. Bottom left: variable-temperature frequency dependence of the χ_M'' signal. Bottom right: Arrhenius plots for the relaxation of **12** (black line). The red line corresponds to the fit for Orbach + QTM.

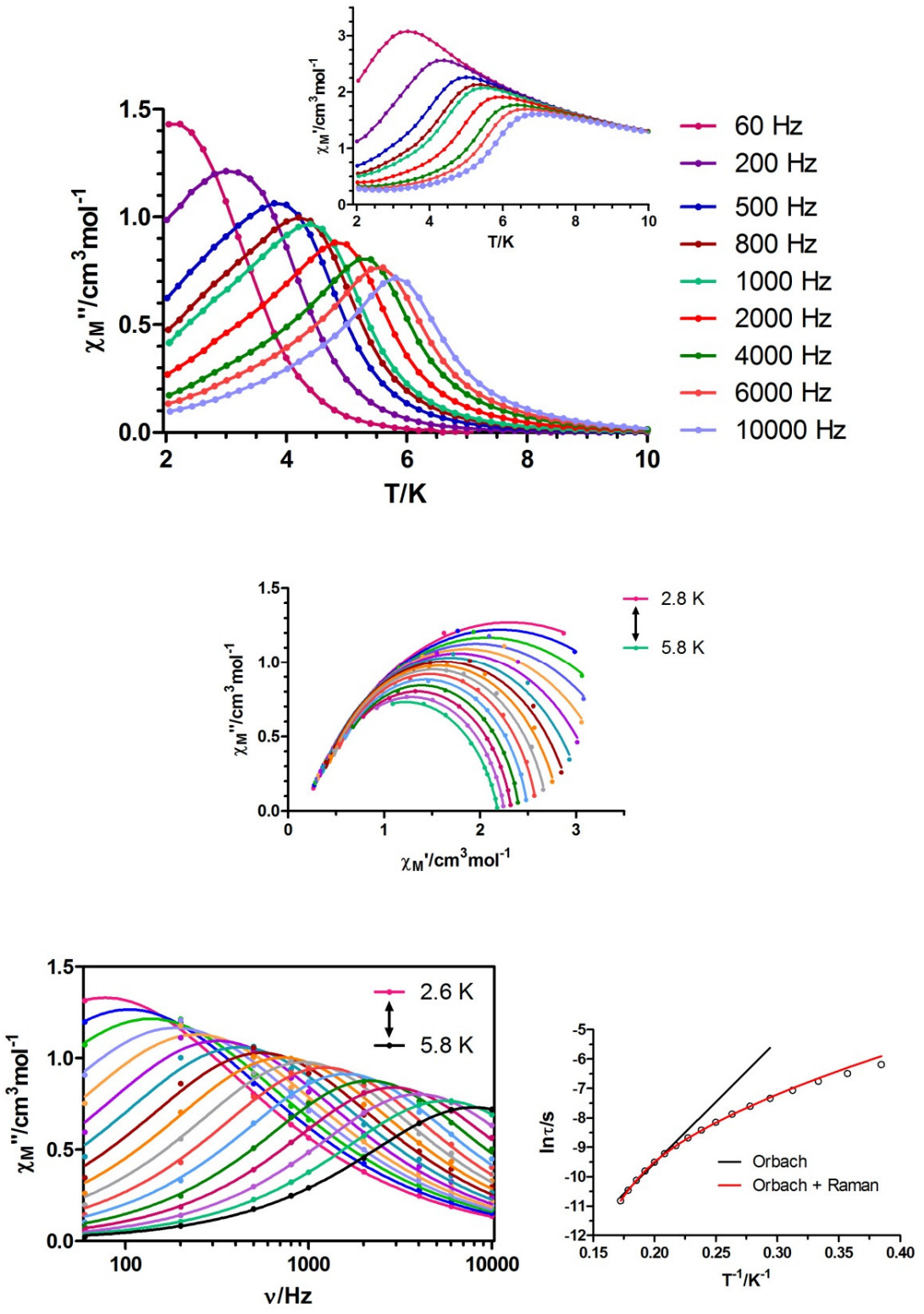

Figure 3.9.- Top: temperature dependence of in-phase χ_M' (inset) and out-of phase χ_M'' components of the *alternating current* (*ac*) susceptibility for complex **17** under an applied field of 1000 Oe. Medium: Cole-Cole plot. Bottom left: variable-temperature frequency dependence of the χ_M'' signal. Bottom right: Arrhenius plots for the relaxation of **17** (black line). The red line corresponds to the fit for Orbach + Raman.

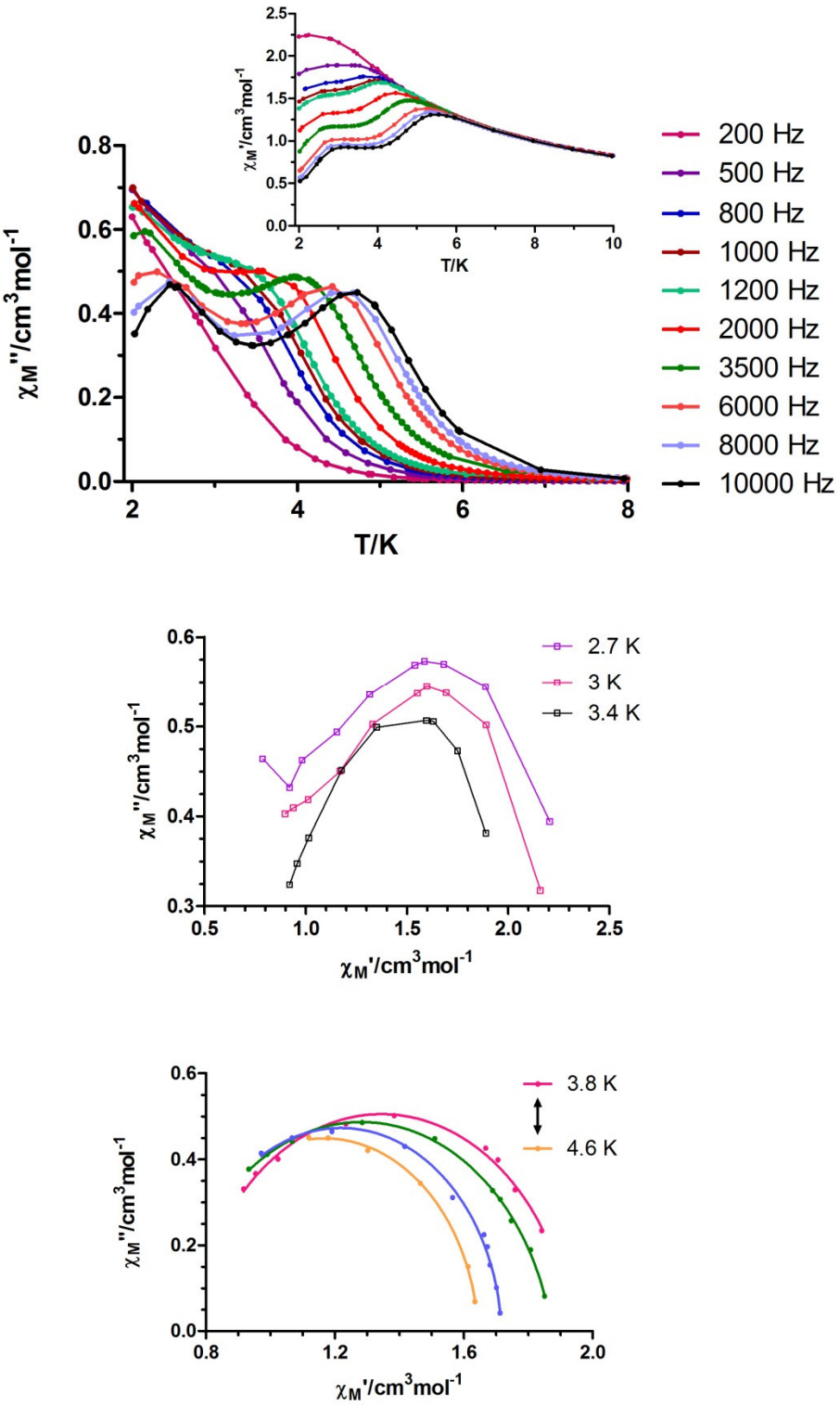

Figure 3.10.- Top: temperature dependence of in-phase χ_M' (inset) and out-of phase χ_M'' components of the *alternating current* (*ac*) susceptibility for complex **19** under an applied field of 1000 Oe. Medium: Cole-Cole plot in the 2.7-3.4 K temperature range. Solid lines are a guide for the eye. Bottom: Cole-Cole plot in the 3.8-4.6 K temperature range. Solid lines represent the best fit of the data to a generalized Debye model.

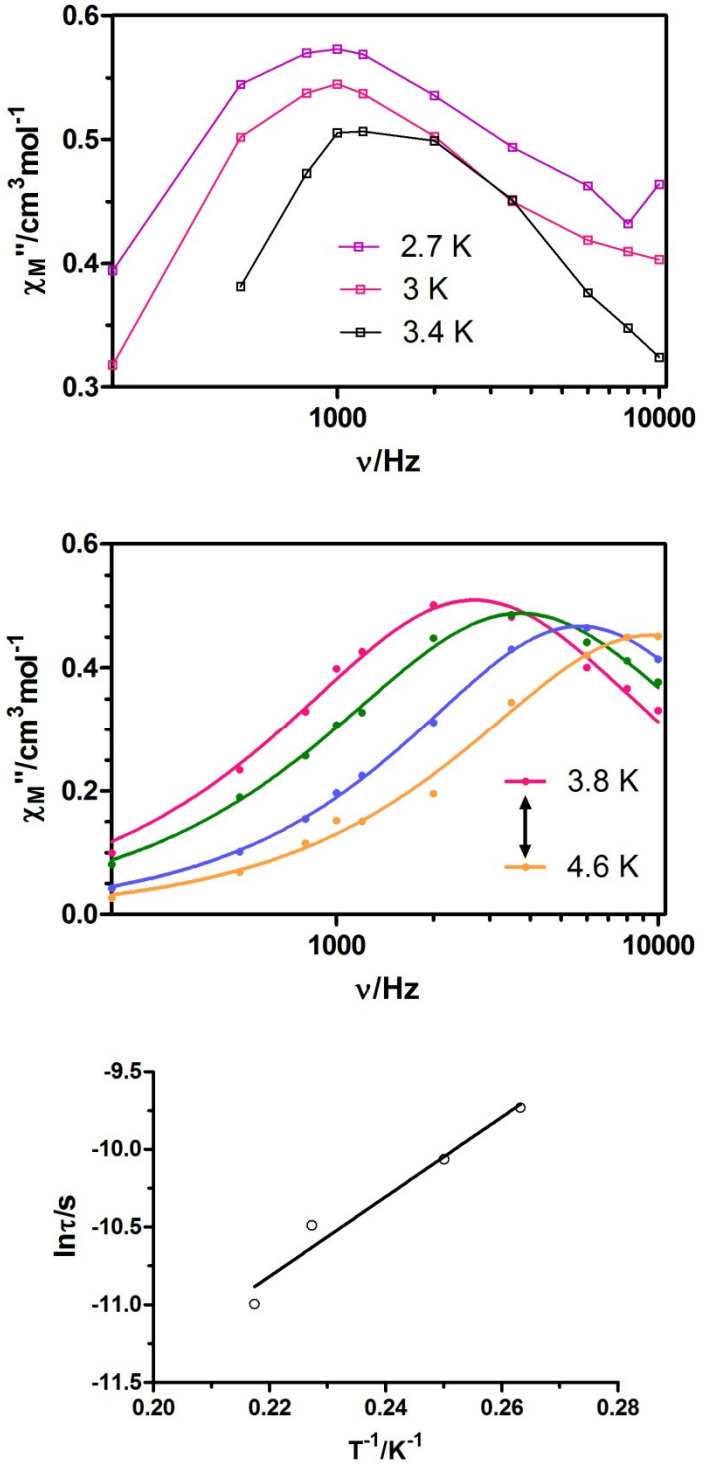

Figure 3.11.- Top: variable-temperature frequency dependence of the χ_M'' signal in the 2.7-3.4 K temperature range. Solid lines are a guide for the eye. Medium: variable-temperature frequency dependence of the χ_M'' signal in the 3.8-4.6 K temperature range. Solid lines represent the best fit of the data to a generalized Debye model. Bottom right: Arrhenius plots for the relaxation times.

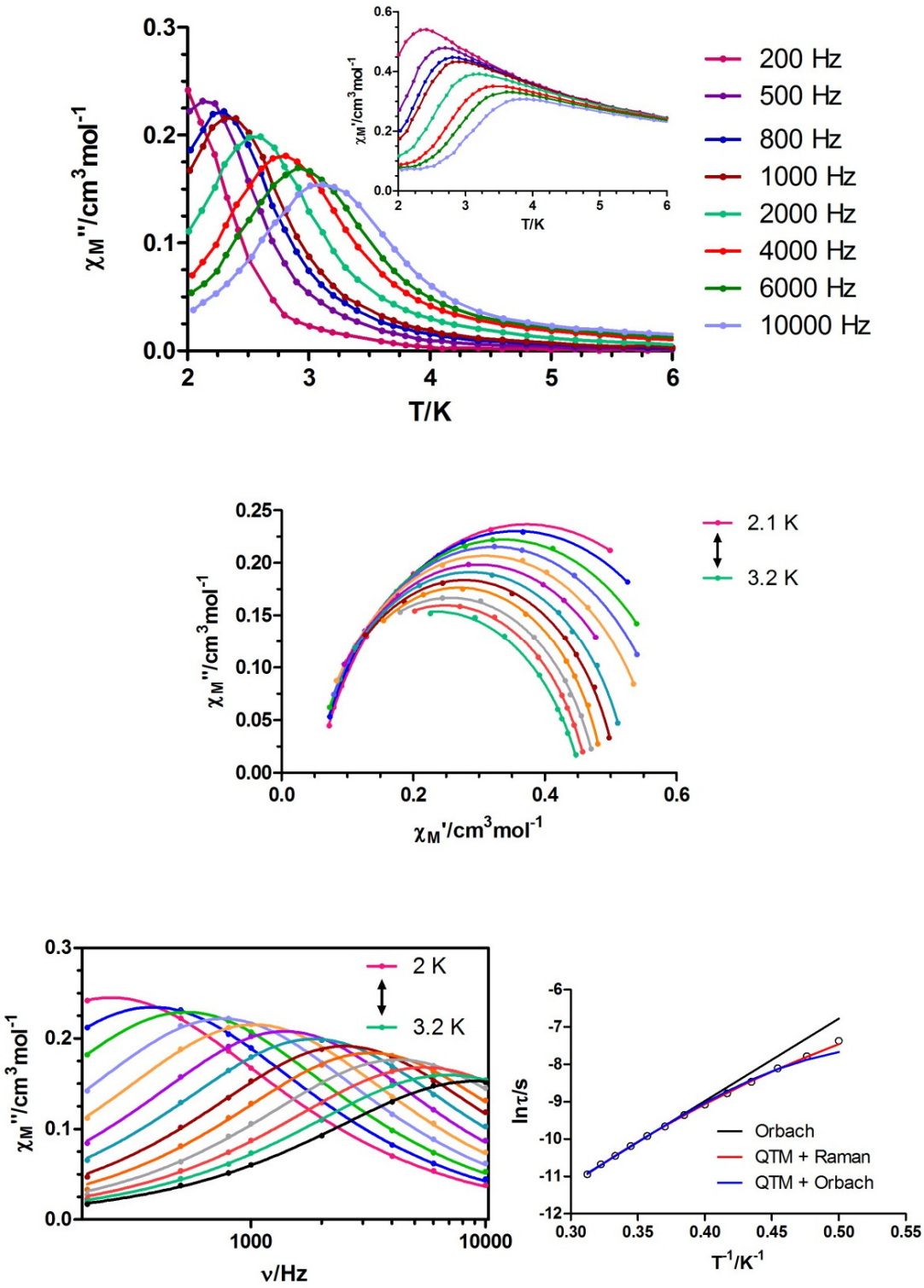

Figure 3.12.- Top: temperature dependence of in-phase χ_M' (inset) and out-of phase χ_M'' components of the *alternating current* (*ac*) susceptibility for complex **21** under an applied field of 1000 Oe. Medium: Cole-Cole plot. Bottom left: variable-temperature frequency dependence of the χ_M'' signal. Bottom right: Arrhenius plots for the relaxation of **21** (black line). The red and blue solid lines correspond to the fit for QTM + Raman and QTM + Orbach processes, respectively.

Complex **12** presents slow relaxation of the magnetization with the maxima of the out-of-phase signals (χ_M") in the 2 K (1000 Hz) - 4.25 K (10000 Hz) range, being the maxima of lower frequencies out of the window of measurements (Figure 3.8). The Er complex **19** displays two distinct relaxation processes, as shown by two distinct frequency-dependent peaks with maxima at 2.5 K and 4.7 K when measured at 10000 Hz (Figure 3.9). However, the first relaxation process is hardly appreciable at lower frequencies and in Cole-Cole and χ_M" vs. frequency plots (Figures 3.10 and 3.11) and therefore, only the second process has been characterized. The existence of several relaxation mechanisms has been usually attributed to different environments of the lanthanide ions,[13] but recently Ramos Silva et al. showed that the Er(III) complex [Er(tpm)$_3$(bipy)], with only one type of Er(III) environment and one relaxation process under zero *dc* field, also exhibited two thermally activated relaxation processes when applying a *dc* field of 1000 Oe.[14] Regarding the Dy(III) and Yb(III) complexes, both complexes show typical SMM behaviour with maxima in the 2.25 K (60 Hz) - 5.8 K (10000 Hz) and 2.1 K (500 Hz) - 3.2 (10000 Hz) ranges, respectively.

The relaxation times (τ) for complexes **12**, **17**, **19** and **21** were extracted from the fitting of the frequency dependence of χ_M" at each temperature to the generalized Debye model (Figures 3.8-3.12). The fit of the high temperature data to the Arrhenius equation afforded effective energy barriers for the reversal of the magnetization and τ_0 (flipping rate) values that are indicated in Table 3.3. The Arrhenius plots, constructed from the temperatures and frequencies of the maxima observed for the χ_M" signals lead virtually to the same Δ and τ_0 parameters, as expected. The relatively high values of τ_0 suggest that the applied field of 1000 Oe is unable to fully suppress the quantum pathway of the relaxation in these compounds, especially for complex **12**. The observed behaviour for this compound could be due to the existence of significant intermolecular interactions, which cannot be fully eliminated by application of a small magnetic *dc* field, as seen in previously reported Nd(III) single-ion magnets (SIMs).[11]

In view of this, the relaxation times for **12** were also fitted to an equation that considers the simultaneous presence of both the thermal and QTM process (Equation 5, Introduction), leading to a small increase of U_{eff} and a decrease in τ_0 (Table 3.3). The obtained energy barrier value for **12** is consistent with the two recently reported Nd(III) SIMs (U_{eff} = 3.9 K and 21 K).

The relaxation times for **21** were also fitted to the above equation, obtaining the values listed in Table 3.3. However, it should be noted that for most part of the Yb(III)

complexes, Raman relaxation processes have been proposed.[15] Therefore, the relaxation times were fitted to an equation that considers the simultaneous presence of both the Raman and QTM processes (Equation 3.6, Figure 3.12), affording the parameters B = 7.6, n = 7.7 and τ_{QTM} = 0.0048 s.

$$\tau^{-1} = \tau_{QTM}^{-1} + BT^{n} \quad (\textit{Equation 3.6})$$

In general, n = 9 for Kramer's ions,[16] but depending on the structure of the levels, n values between 1 and 6 can be considered as reasonable.[17]

To end up, the deviation of experimental relaxation times from linearity for compound **17** suggests the presence of competing Raman and Orbach processes. The experimental data were fitted to Equation 6 (Introduction), obtaining the following set of parameters: B = 2.46, n = 5.24, $\tau_0 = 7.28 \cdot 10^{-12}$ s and U = 89.9 K. These results seem to indicate that the Raman relaxation process significantly affects the Orbach relaxation process, as the obtained energy barrier U_{eff} when considering both effects is more than the double obtained only when considering the Orbach process.

Table 3.3.- U_{eff}, τ_0 and τ_{QTM} values for complexes **12**, **17**, **19** and **21**.

Compound	χ_M'' signal at H = 0 Oe	U_{eff} (K) at H = 1000 Oe[a]	τ_0 (s)[a]	τ_{QTM} (s)
12	no	17.10 (14.12)	$4.71 \cdot 10^{-7}$ ($8.57 \cdot 10^{-7}$)	$1.89 \cdot 10^{-4}$
17	yes	41.55	$1.79 \cdot 10^{-8}$	
19	no	21.0	$2.28 \cdot 10^{-7}$	
21	no	23.65 (18.9)	$1.14 \cdot 10^{-8}$ ($5.48 \cdot 10^{-8}$)	$6.63 \cdot 10^{-4}$

[a] The values in brackets correspond to the fit to the Arrhenius law using high temperature data.

The Cole-Cole plots (Figures 3.8-3.12) with α values in the 0.17(2 K)−0.07(4.5 K), 0.29(3.2 K)-0.11(5.8 K), 0.10(3.8 K)−0.04(4.6 K) and 0.18(2.2 K)−0.14(3.2 K) ranges respectively for **12**, **17**, **19** and **21**, indicate the presence of multiple relaxation processes in the low temperature region.

3.3.2. Photophysical properties of complexes 11-21

The direct excitation of lanthanide ions results inefficient due to the forbidden Laporte rule for f-f transitions, presenting weak absorption bands. However, a good strategy to increase the luminescence excitation is that of coordinating lanthanide ions to organic ligands that act as “antenna groups”, transferring energy to lanthanides through an intramolecular energy transfer process. Regarding the “antenna group”, Salen-type Schiff ligands have proved to be effective sensitizers for lanthanide emission and considering the similarity between them and the ligand H_2L, rich photophysical properties are expected for samples **11**-**21**.

As can be seen in the reflectance spectrum (Figure 3.13), the ligand H_2L absorbes in the UV region from 220 nm to 380 nm, with picks corresponding to π-π^* electronic transitions of the aromatic group and n-π^* transitions of the aldehyde group respectively at 280 nm and 360 nm. As expected, the bands that correspond to the ligand H_2L are also present in the reflectance spectrums of **11**-**21** (Figure 3.14), where additional weak bands that belong to forbidden f-f transitions of Ln(III) ions can be observed.

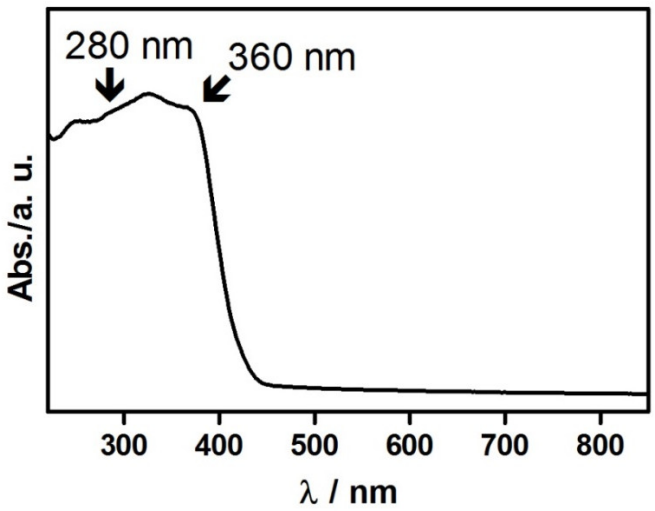

Figure 3.13.- Reflectance spectrum of the ligand.

In view of the absorption spectra, the potential emitters in the visible region were irradiated at 280 nm and 375 nm to study the emissive properties of these compounds. The solid state photoluminescence spectra were recorded at 10 K, 77 K, 150 K and at room temperature and the characteristic emission bands recorded upon irradiation at

280 nm and a temperature of 10 K are shown in Figures 3.15-3.17, as well as the thermal evolution of the most intense bands recorded at 280 and 375 nm.

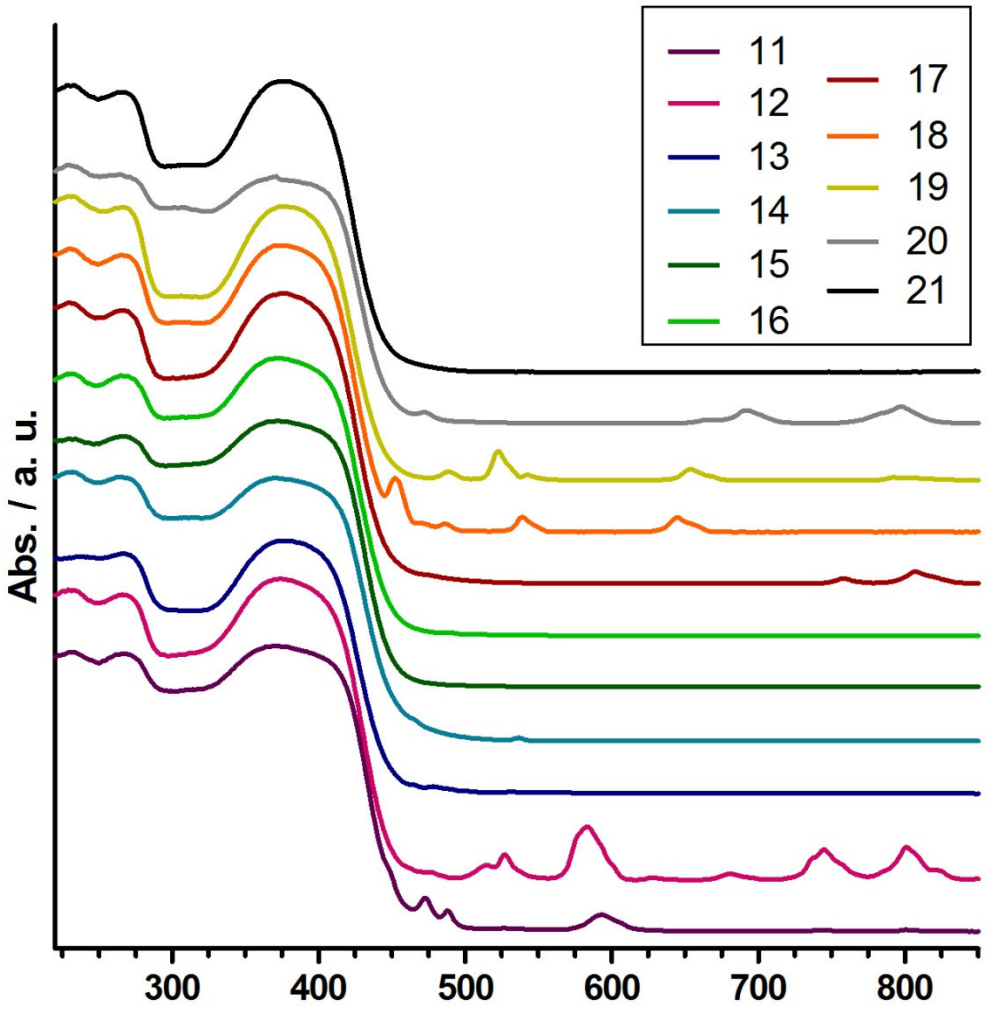

Figure 3.14.- Reflectance spectra of compounds **11**-**21**.

The Pr(III), Dy(III) and Tm(III) based compounds do not show significant emissive properties even at 10 K. This behaviour could be due to the fact that the energy gap between the triplet state of the ligand, from which the energy is transferred to the lanthanides, and the $^3P_0$, $^4F_{9/2}$ and $^1G_4$ energy levels, respectively, of Pr(III), Dy(III) and Tm(III) is too small, which allows back energy transfer processes.[18]

In the case of Samarium compound (**13**), excitation into the UV π-π* and n-π* absorption bands of the ligand L^{2-} at 280 and 375 nm resulted in the appearance of the characteristics Sm(III) emission bands centred at 560, 600, 645, 710 and 790 nm (Figure 3.15), which are assigned to the transitions of $^4G_{5/2}$ to ^6H_J (J = 5/2, 7/2, 9/2,

11/2 and 13/2, which are splitted by the ligand crystal field). The increase of the temperature leads to broader bands due to the increase in the kinetic (thermal) energy of the bonding electrons and to a decrease of the intensity of the signals.

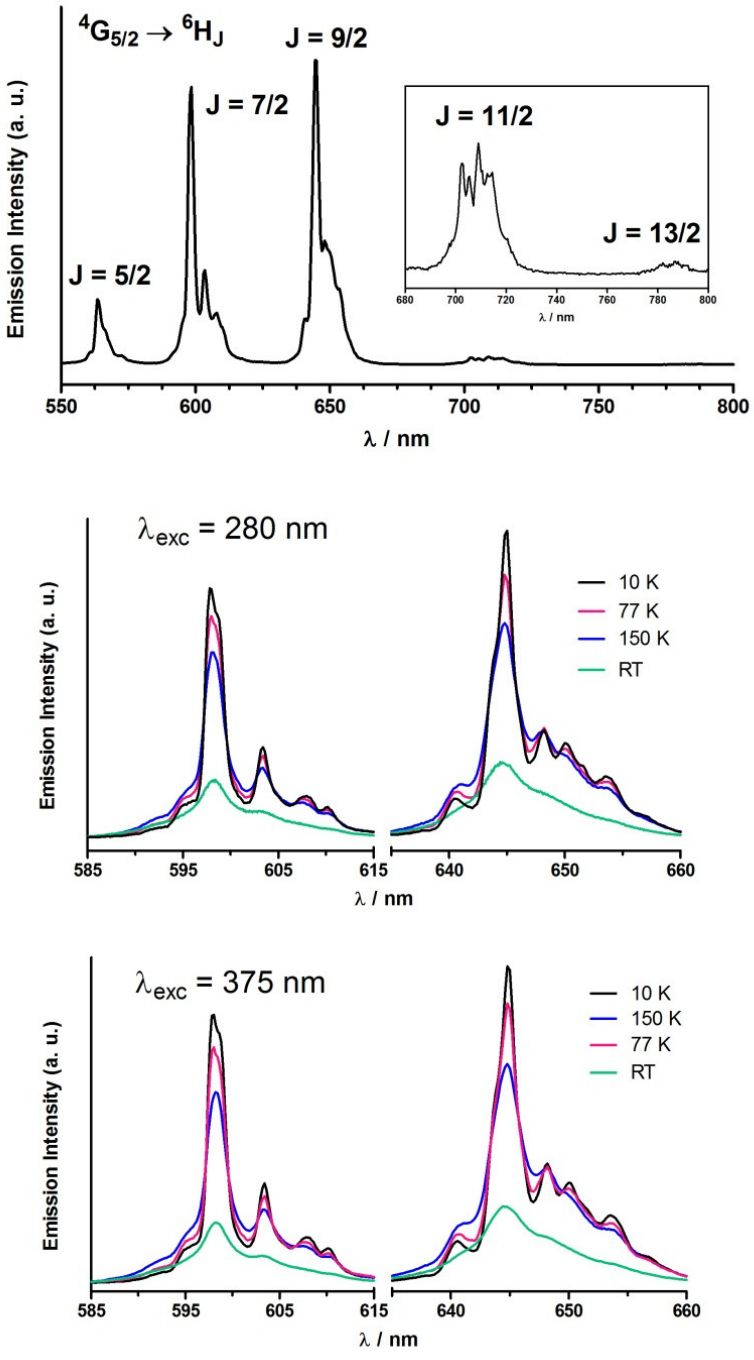

Figure 3.15.- Solid state photoluminescence spectra for Sm(III) compound **13** recorded at 10 K upon excitation at 280 nm (top). The inset shows a detailed view of the less intense transition bands. Thermal evolution of the most intense transition bands after excitation at 280 nm (middle) and 375 nm (bottom).

Regarding the europium compound (**14**), upon excitation at 280 and 375 nm it displays five sets of bands occurring at around 580, 590-595, 614-621, 650-655 and 690-710 nm (Figure 3.16) that can be assigned to $^5D_0 \rightarrow {}^7F_J$ transitions (J = 0, 1, 2, 3 and 4, respectively). The most intensive set of bands is originated from the induced electric dipole transition $^5D_0 \rightarrow {}^7F_2$, while the magnetic dipole-allowed transition $^5D_0 \rightarrow {}^7F_1$ is of moderate intensity. The presence of the weak symmetry-forbidden $^5D_0 \rightarrow {}^7F_0$ transition indicates the absence of an inversion centre (it is forbidden because there is no increment of J), which is in agreement with the crystal structure obtained by X-ray diffraction.

Due to the low symmetry of Eu(III) ions (computed shape measures indicate that the EuO_9 coordination sphere is intermediate between D_{3h}, C_{4V} and C_s symmetries), the emission bands of the $^5D_0 \rightarrow {}^7F_J$ (J = 1, 2, 3 and 4) transitions should split into 3, 5, 7 and 9 peaks, respectively.[19] At 10 K, most of these bands are observed. However, when increasing the temperature the bands are broadened due to the increase in the kinetic (thermal) energy, leading to not well-shaped bands.

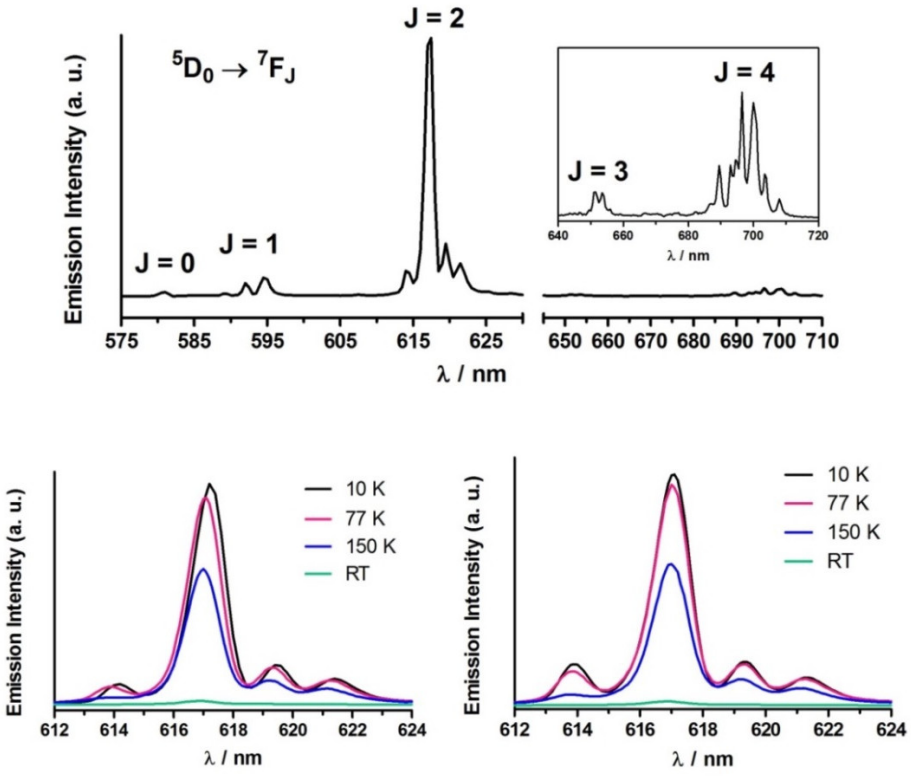

Figure 3.16.- Top: solid state photoluminescence spectra for Eu(III) compound **14** recorded at 10 K upon excitation at 280 nm. The inset shows a detailed view of the less intense transition bands. Bottom: Thermal evolution of the most intense transition bands after excitation at 280 nm (left) and 375 nm (right).

The Tb compound (**16**) shows seven groups of signals which correspond to the $^5D_4 \rightarrow {}^7F_J$ (J = 6, 5, 4, 3, 2, 1, 0) transitions (Figure 3.17). As expected, the $^5D_4 \rightarrow {}^7F_5$ is the strongest one according to its largest probability for both electric-dipole and magnetic-dipole induced transitions.

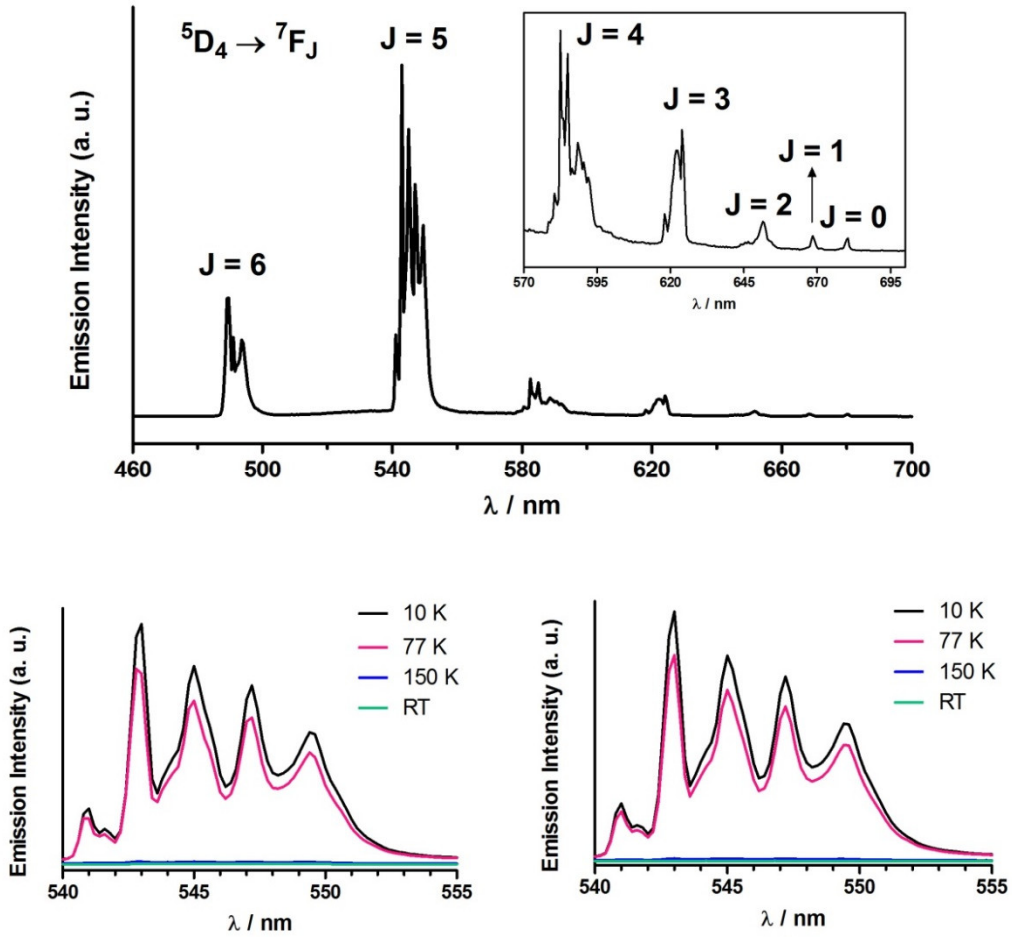

Figure 3.17.- Top: solid state photoluminescence spectra for Tb(III) compound **16** recorded at 10 K upon excitation at 280 nm. The inset shows a detailed view of the less intense transition bands. Bottom: Thermal evolution of the most intense transition bands after excitation at 280 nm (left) and 375 nm (right).

Regarding the expected sensitized emission characteristic of potential emitters in the infrared region, only the emission characteristics of Nd (**12**) and Yb (**21**) ions were observed when the compounds were excited at 325 nm (Figures 3.18 and 3.19). The Ho(III) and Er(III) complexes do not show any emission characteristics, which is probably due to the poor spectroscopic overlap existing between the ligand emission

and the f-f excited states of Ln(III) ions that could act as energy acceptors. The Nd(III) compound **12** displays three emission bands between 865-920 nm ($^4F_{3/2} \rightarrow {}^4I_{9/2}$), 1040-1090 nm ($^4F_{3/2} \rightarrow {}^4I_{11/2}$) and 1310-1365 ($^4F_{3/2} \rightarrow {}^4I_{13/2}$) in the NIR region, being the band which is potentially applicable to laser emission, fluoroimmunoassays and in vivo detection ($^4F_{3/2} \rightarrow {}^4I_{11/2}$) dominant.[20]

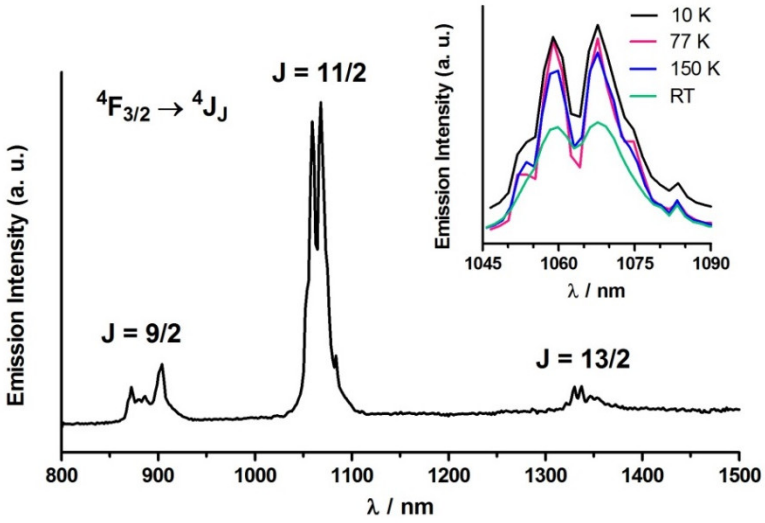

Figure 3.18.- Solid state photoluminescence spectra for Nd(III) compound **12** recorded at 10 K upon excitation at 325 nm. The inset shows the thermal evolution of the most intense bands.

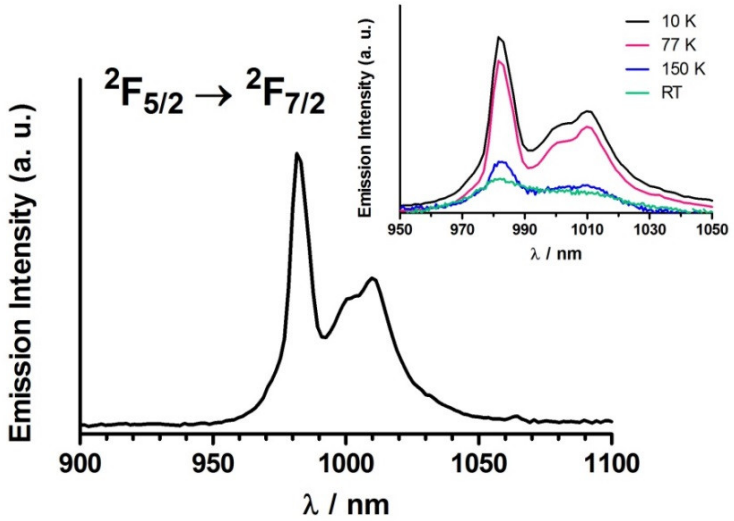

Figure 3.19.- Solid state photoluminescence spectra for Yb(III) compound **21** recorded at 10 K upon excitation at 325 nm. The inset shows the thermal evolution of the transition bands.

To end up with the Yb(III) compound, upon excitation at 325 nm it shows its characteristic emission set of bands $^2F_{5/2} \rightarrow {}^2F_{7/2}$ at around 970-1030 nm. If we consider the shoulder at 971 nm as a band, four bands located at 971, 981, 1049 and 1058 nm can be observed, which arise from the ligand field splitting of the $^2F_{7/2}$ multiplet. The energy gap between the ground and first excited states calculated from the position of the first two bands is approximately of 144 K, which is much higher than the obtained effective energy barrier from the magnetic *ac* susceptibility data (18.9 K when considering only the Orbach process). These results clearly suggest the presence of additional relaxation mechanisms (such as Raman and QTM) that reduce the effective energy barrier dramatically, as already discussed in the magnetic properties section.

The measurement of the experimental emission decay curves from the $^4G_{5/2}$ (Sm(III)), $^5D_0$ (Eu(III)) and $^5D_4$ (Tb(III)) excited states after excitation at 280 and 375 nm allowed us to effectively estimate the lifetimes at the most intense line of the main transitions (645 nm for Sm(III), 617 nm for Eu(III) and 545 nm for Tb(III)) at different temperatures (Table 3.4, Figures 3.20-3.25).

The decay curves of Sm(III) were fitted to the single-exponential function $I_t = A_0 + A_1\exp(-t/\tau)$, whereas the Tb(III) compound **16** revealed the occurrence of two decay components and was fitted to the double exponential function $I_t = A_0 + A_1\exp(-t/\tau) + A_2\exp(-t/\tau)$, where τ accounts for the luminescence lifetimes and A_0 and A_n are the background and the weighting parameter, respectively. The Eu(III) compound **14** also showed two decay components, but one of the components involved less than 5 % of the whole process and as a consequence, the decay curves of **14** were fitted to the single-exponential function. However, the weight of the second component involved around 20 % of the process when measured at 10 K after excitation at 375 nm and therefore, this decay curve has been fitted to the double exponential function. The measurements performed at different temperatures showed that the lifetimes of Sm and Eu compounds remained constant or with slight changes when increasing the temperature, whereas the Tb compound showed an abrupt decrease. It should be noted that the lifetime of ~1 μs obtained at RT for the Tb derivative might come from the lamp, being the emissive properties of this compound very weak at room temperature. The obtained luminescent times for Eu(III) and Sm(III) at room temperature are in agreement with reported values in literature.[21]

Table 3.4.- Luminescence lifetimes of samples **13**, **14** and **16** at different temperatures after excitation at 280 and 375 nm.

	τ_{exp} (μs)					
	Sm (13)		**Eu (14)**		**Tb (16)**	
Temp.	**280**	**375**	**280**	**375**	**280**	**375**
10	35.79	35.91	805.51	758.19/1005.45	355.78/864.91	357.76/841.29
77	35.52	35.80	805.83	813.54	351.89/883.62	359.21/843.33
150	36.73	36.66	801.73	796.29	5.90/27.57	4.81/21.42
RT	36.74	37.24	692.08	512.23	1.32 /11.28	1.38/13.20

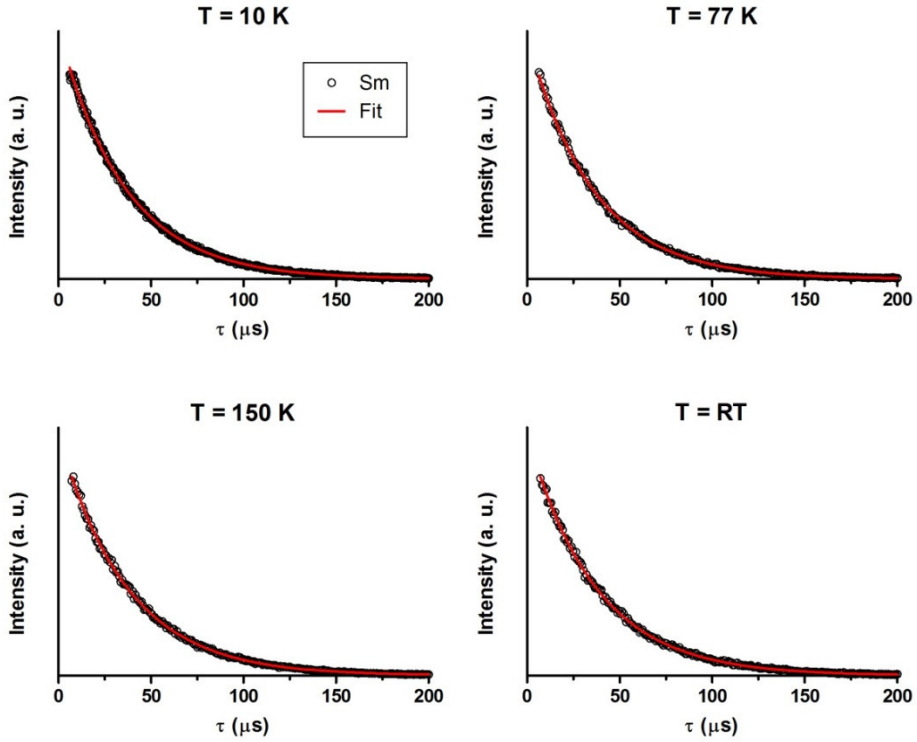

Figure 3.20.- Luminescence decay curves at different temperatures after excitation at 280 nm for Sm compound **13** monitored at 645 nm.

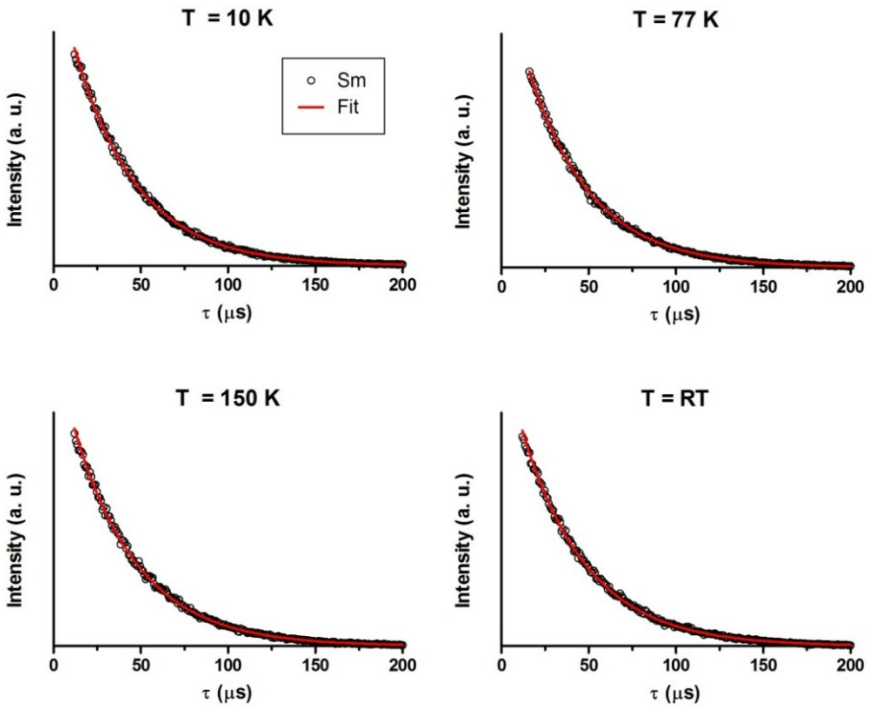

Figure 3.21.- Luminescence decay curves at different temperatures after excitation at 375 nm for Sm compound **13** monitored at 645 nm.

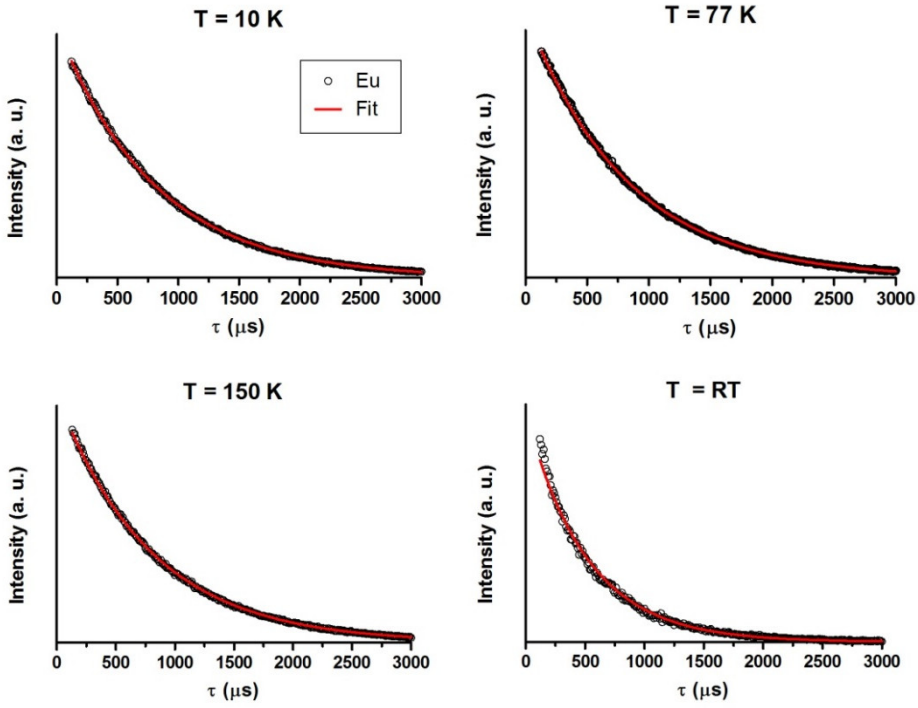

Figure 3.22.- Luminescence decay curves at different temperatures after excitation at 280 nm for Eu compound **14** monitored at 617 nm.

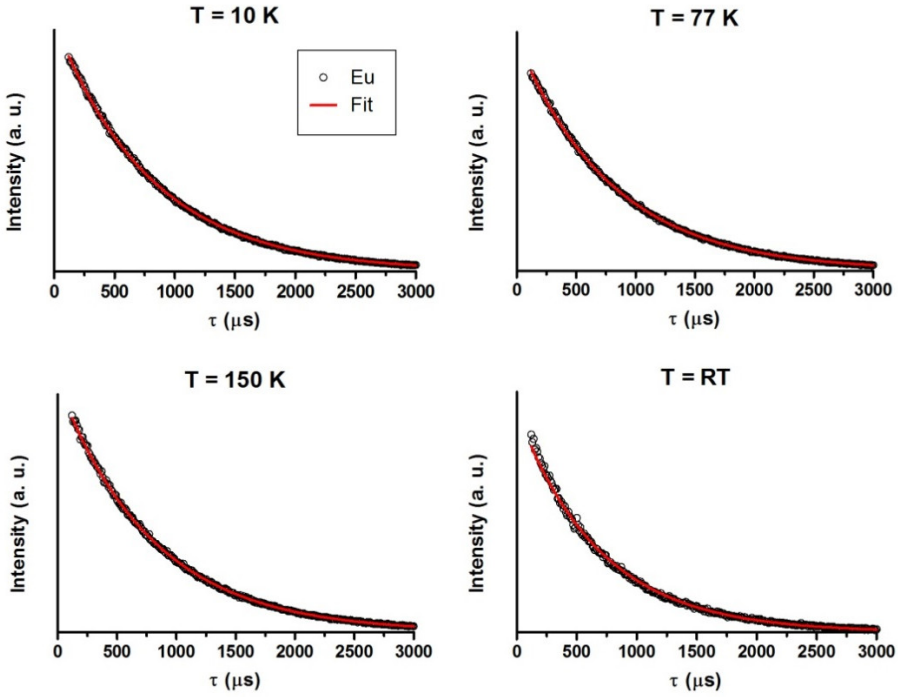

Figure 3.23.- Luminescence decay curves at different temperatures after excitation at 375 nm for Eu compound **14** monitored at 617 nm.

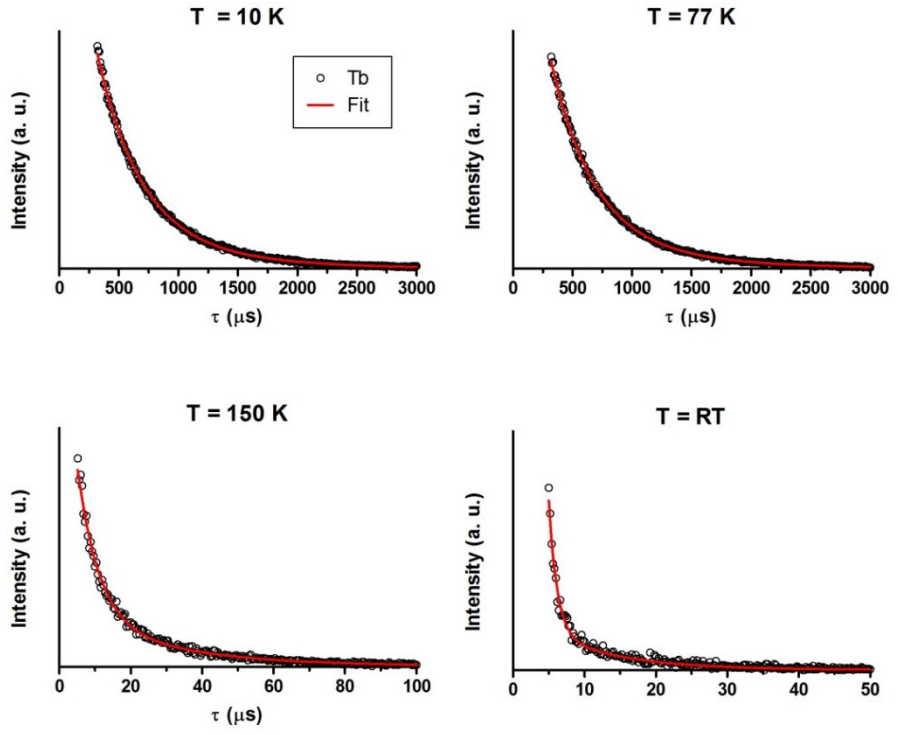

Figure 3.24.- Luminescence decay curves at different temperatures after excitation at 280 nm for Tb compound **16** monitored at 545 nm.

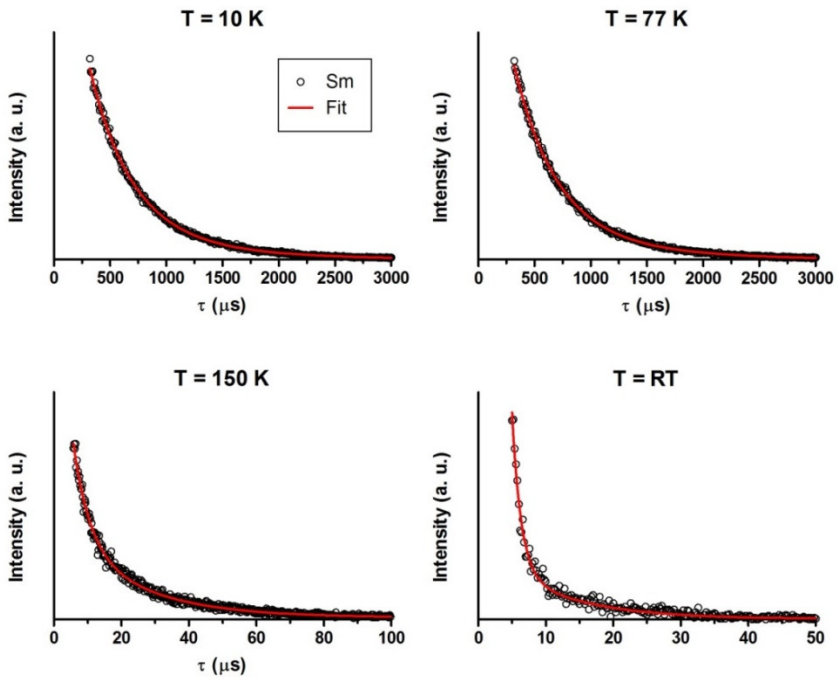

Figure 3.25.- Luminescence decay curves at different temperatures after excitation at 375 nm for Tb compound **16** monitored at 545 nm.

Finally, it should be mentioned that excitation at 280 nm causes brilliant “orange”, red and green emissions of compounds **13**, **14** and **16**, respectively (Figures 3.26 and 3.27).

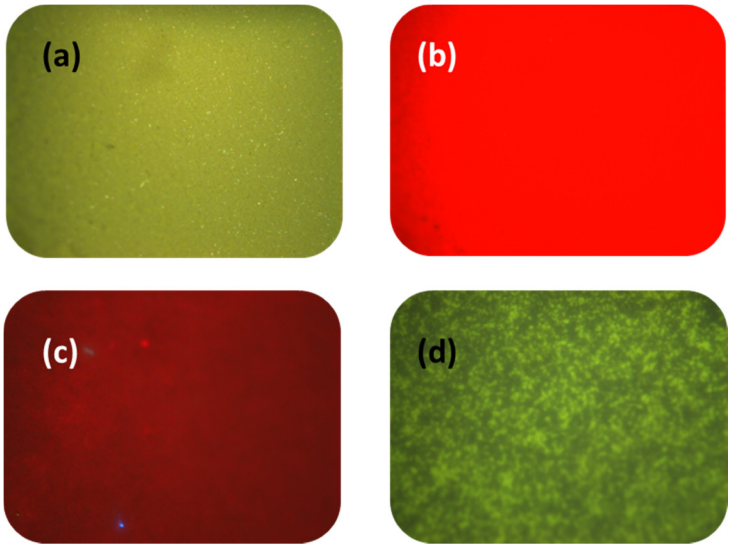

Figure 3.26.- Micro-photoluminescence images taken on powdered samples after irradiation with white light (reference) (a) and after excitation at 280 nm for Sm(III) (b), Eu(III) (c) and Tb(III) (d) derivatives at room temperature.

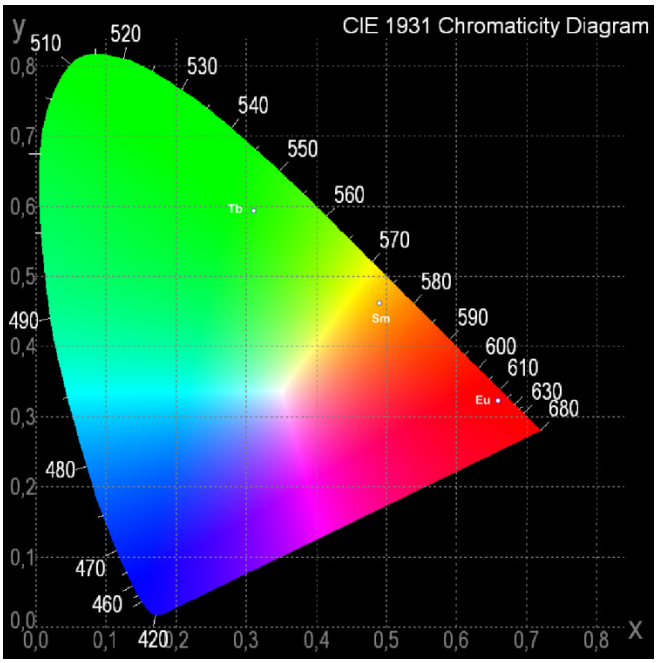

Figure 3.27.- Colour space chromatic diagram, Commission Internationale de l'Éclairage (CIE) 1931 *x,y* chromaticity coordinates as a function of the excitation wavelength.

3.4.- CONCLUSIONS

In summary, the compartmental ligand H_2L (H_2L = N,N'-dimethyl-N,N'-bis(2-hydroxy-3-formyl-5-bromobenzyl)ethylenediamine) allows the preparation of dinuclear Zn(II)Ln(III) complexes, in which the Zn(II) ion occupies the internal N_2O_2 site and the oxophilic Ln(III) ion occupies the external O_4 site. The fifth position of the Zn(II) coordination sphere is occupied by a bridging acetate ion, leading to di-μ-phenoxo-acetate triple bridged species. The ZnNd, ZnDy, ZnEr and ZnYb complexes exhibit field-induced single-ion magnet (SIM) behaviour, with effective thermal energy barriers in the 14.12-41.55 K range when considering only the Orbach relaxation process.

The photophysical properties of these complexes have also been studied, showing the ability of the ligand L^{2-} to sensitize Sm(III), Eu(III) and Tb(III)-based luminescence in the visible region. Moreover, the ZnNd and ZnYb derivatives exhibit characteristic luminescence in the NIR region and therefore, both compounds can be considered as dual magneto-luminescent materials combining NIR emission and field-induced SIM behaviour.

3.5.- BIBLIOGRAPHY

[1] A recent review: L. C. Humphrey, S. B. Feltham, *Coord. Chem. Rev*., **2014**, *276*, 1.

[2] J. D. Rinehart, J. R. Long, *Chem. Sci*., **2011**, *2*, 2078.

[3] **a)** J. C. G. Bünzli, C. Piguet, *Chem. Soc. Rev*. **2005**, *34*, 1048; **b)** D. Parker, *Chem. Soc. Rev*., **2004**, *33*, 156; **c)** Y. Hasegawa, Y. Wada, S. J. Yanayida, *Photochem. Photobiol*. *C*, **2004**, *5*, 183.

[4] K. C. Mondal, A. Sundt, Y. Lan, G. E. Kostakis, O. Waldmann, L. Ungur, L. F. Chibotaru, C. E. Anson, A. K. Powell, *Angew. Chem. Int. Ed*., **2012**, *51*, 7550.

[5] **a)** M. A. Palacios, S. Titos-Padilla, J. Ruiz, J. M. Herrera, S. J. Pope, E. K. Brechin, E. Colacio, *Inorg. Chem*., **2014**, *53*, 1465; **b)** A. Upadhyay, S. K. Singh, C. Das, R. Mondol, S. K. Langley, K. S. Murray, G. Rajaraman, M. Shanmugam, *Chem. Commun*., **2014**, *50*, 8838; **c)** J.-L. Liu, Y.-C. Chen, Y.-Z. Zheng, W.-Q. Lin, L. Ungur, W. Wernsdorfer, L. F. Chibotaru, M.-L. Tong, *Chem. Sci*., **2013**, *4*, 3310; **d)** S. Titos-Padilla, J. Ruiz, J. M. Herrera, E. K. Brechin, W. Wersndorfer, F. Lloret, E. Colacio, *Inorg. Chem*., **2013**, *52*, 9620; **e)** M. Maeda, S. Hino, K. Yamashita, Y. Kataoka, M. Nakano, T. Yamamura, T. Kajiwara, *Dalton Trans*., **2012**, *41*, 13640; **f)** A. Watanabe, A. Yamashita, M. Nakano, T. Yamamura, T. Kajiwara, *Chem. Eur. J*., **2011**, *17*, 7428; **g)** T. Kajiwara, M. Nakano, K. Takahashi, S. Takaishi, M. Yamashita, *Chem. Eur. J*., **2011**, *17*, 196.

[6] A. Upadhyay, S. K. Singh, C. Das, R. Mondol, S. K. Langley, K. S. Murray, G. Rajaraman, M. Shanmugam, *Chem. Commun.,* **2014,** *50*, 8838.

[7] J. P. Costes, S. Titos-Padilla, I. Oyarzabal, T. Gupta, C. Duhayon, G. Rajaraman, E. Colacio, *Chem. Eur. J*., **2015**, 21, 15785.

[8] M. Llunell, D. Casanova, J. Cirera, J. M. Bofill, P. Alemany, S. Alvarez, M. Pinsky, D. Avnir, *SHAPE*, v1.1b, Barcelona, Spain, **2005**.

[9] Kahn, O. *Molecular Magnetism*, VCH, New York, **1991**.

[10] **a)** M.-X. Yao, Q. Zheng, K. Qian, Y. Song, S. Gao, J.-L. Zuo, *Chem. Eur. J*., **2013**, *19*, 294; **b)** H. Ke, L. Zhao, Y. Guo, J. Tang, *Dalton Trans*., **2012**, *41*, 2314; **c)** V. Mereacre, D. Prodius, A. M. Ako, N. Kaur, J. Lipkowski, C. Simmons, N. Dalal, I. Geru, C. E. Anson, A. K. Powell, C. Turta, *Polyhedron,* **2008**, *27,* 2459; **d)** A. Mishra, W. Wernsdorfer, K. A. Abboud, G. Christou, *J. Am. Chem. Soc*., **2004**, *126*, 15648.

[11] J. D. Rinehart, J. R. Long, *Dalton Trans*., **2012**, *41*, 13572.

[12] **a)** P. Vrábel, M. Orendáč, A. Orendáčová, E. Čižmár, R. Tarasenko, S. Zvyagin, J. Wosnitza, J. Prokleska, V. Sechovský, V. Pavlík, S. Gao, *J. Phys.: Condens. Matter* **2013**, *25*, 186003; **b)** A. Arauzo, A. Lazarescu, S. Shova, E. Bartolomé, R. Cases, J.

Luzón, J. Bartolomé, C. Turta, *Dalton Trans*., **2014**, *4*3, 12342; **c)** J. J. Le Roy, S. I. Gorelsky, I. Korobkov, M. Murugesu, *Organometallics,* **2015**, *34*, 1415.

[13] **a)** A. Venugopal, F. Tuna, T. P. Spaniol, L. Ungur, L. F. Chibotaru, J. Okuba, R. A. Layfield, *Chem. Commun.* **2013**, *49*, 901; **b)** S.-D. Jiang, B.-W. Wang, H.-L. Sun, Z.-M. Wang, S. Gao, *J. Am. Chem. Soc*., **2011**, *133*, 4730; **c)** P.-H. Lin, W.-B. Sun, M.-F. Yu, G.-M. Li, P.-F. Yan, M. Murugesu, *Chem. Commun*., **2011**, *47*, 10993.

[14] P. Martín-Ramos, M. Ramos Silva, J. T. Coutinho, L. C. J. Pereira, P. Chamorro-Posada, J. Martín-Gil, *Eur. J. Inorg. Chem.,* **2014**, 511.

[15] J. Ruiz, G. Lorusso, M. Evangelisti, E. K. Brechin, S. J. Pope, E. Colacio, *Inorg. Chem*., **2014**, *53*, 3586.

[16] A. Abragam, B. Bleaney, *Electron Paramagnetic Resonance of Transition Ions*, Clarendon Press. Oxford, **1970**.

[17] K. N. Shirivastava, *Phys. Status Solidi B,* **1983**, *117*, 437.

[18] S. V. Eliseeva, D. N. Pleshkov, K. A. Lyssenko, L. S. Lepnev, J.-C. G. Bünzli, N. P. Kuzmina, *Inorg. Chem*., **2010**, *49*, 9300.

[19] P. A. Tanner, *Chem. Soc. Rev.,* **2013**, *42*, 5090.

[20] **a)** C. Janiak, *Dalton Trans.,* **2003**, 2781; **b)** J. C. G. Bünzli, S. V. Eliseeva, *J. Rare Earths,* **2010**, *28*, 824.

[21] **a)** J. Cepeda, S. Pérez-Yáñez, G. Beobide, O. Castillo, J. A. Garcia, M. Lanchas, A. Luque, *Dalton Trans*., **2015**, *44*, 6972; **b)** A.-L. Wang, D. Zho, X.-Y. Wei, Z.-X. Wang, Y.-R. Qu, H.-X. Zhang, Y.-N. Chen, J.-J. Li, H.-B. Chu, Y.-L. Zhao, *J. Lumin*., **2015**, *160*, 238.

CHAPTER 4

STUDY OF THE SMM PROPERTIES OF DINUCLEAR M(II)Ln(III) SPECIES WITH PARAMAGNETIC 3d IONS

4.1. INTRODUCTION

The magnetic coupling of heavy lanthanide ions with 3d metal ions sometimes gives a more suitable design for SMMs, since the ferromagnetic 3d-4f magnetic interactions can lead to ground states with even larger magnetic moments and the magnetic anisotropy can be derived from both d- and f- elements.[1] However, it has been experimentally shown[2] that the mixing of highly anisotropic lanthanide ions with paramagnetic 3d metal ions often has a counteractive effect, leading to small effective energy barriers for the magnetization reversal. Due to the very efficient shielding of the 4f orbitals of the Ln(III) ions by the fully occupied 5s and 5p orbitals, the 3d-4f magnetic exchange interactions are usually very weak and this generates multiple low-lying excited states, decreasing the effective energy barrier of the system. The observed behaviour can also be due to the random transversal field for the Ln(III) ions created by the paramagnetic metal ions, which favours the faster QTM process.[3] In spite of the above considerations, the recently reported Cr(III)Dy(III) based complex $[Cr(III)_2Dy(III)_2(OMe)_2(O_2CPh)4(mdea)_2(NO_3)_2]$ (H_2mdea = N-methyldi-ethanolamine)[4] is an example of how the incorporation of isotropic paramagnetic ions can improve the SMM properties when compared to the diamagnetic Co(III) based analogue, which is due to the fact that the exchange interaction between the Dy(III) and Cr(III) ions is unusually strong, leading to a multilevel exchange type barrier[5] and to the suppression of the QTM. However, in the Co(III) based compound the barrier originates only from one excited state on the individual Dy(III) ions.

This chapter collects the synthesis, structural characterization and magnetic properties of a series of triply bridged M(II)Ln(III) dinuclear complexes (M = Cu, Ni and Co; Ln = Nd, Gd, Tb, Dy, Er, Y) with the ligand H_2L. This study aims to (i) examine the magnetic exchange interaction between M(II) and Ln(III) ions and the SMM properties of the complexes and (ii) compare the obtained results with those of the Zn(II)Ln(III) analogues presented in the previous chapter, focusing special attention to changes on SMM properties caused by the replacement of the diamagnetic Zn(II) ions by paramagnetic 3d ions.

4.2. PREPARATION OF COMPLEXES

4.2.1. [Cu(μ-L)(μ-OAc)Ln(NO_3)$_2$]·CH_3CN·H_2O, Ln(III) = Gd (22), Tb (23), Dy (24), Er (25)

A general procedure was used for the preparation of these complexes: To a solution of 25.0 mg (0.125 mmol) of Cu(OAc)$_2$·H_2O in 5 mL of acetonitrile/methanol (80:20) mixture were added with continuous stirring 64.3 mg (0.125 mmol) of H_2L and 0.125 mmol of the corresponding Ln(NO_3)$_3$·nH_2O. The resulting solution was filtered and allowed to stand at room temperature. After several days, well-formed prismatic dark green crystals of compounds **22**-**25** were obtained with yields in the range 35 - 41 % (Table 4.1), which were filtered, washed with acetonitrile and air-dried.

4.2.2. [Ni(CH_3CN)(μ-L)(μ-OAc)Ln(NO_3)$_2$]·CH_3CN, Ln(III) = Nd (26), Gd (27), Tb (28), Dy (29), Er (30), Y(31)

These compounds were prepared with yields in the range 45 - 57 % (Table 4.1) following the procedure for **22**-**25**, but using Ni(OAc)$_2$·4H_2O (31.1 mg, 0.125 mmol) instead of Cu(OAc)$_2$·H_2O.

4.2.3. [Co(CH_3CN)(μ-L)(μ-OAc)Ln(NO_3)$_2$]·CH_3CN, (Ln(III) = Gd (32), Tb (33), Dy (34), Er (35), Y(36)

These compounds were prepared as orange crystals following the same procedure than for **22**-**25**, except that Co(OAc)$_2$·4H_2O was used as source of metal. Yields: 39 - 55 % (Table 4.1).

The purity of the complexes was checked by elemental analysis (Table 4.1).

Table 4.1.- Elemental analyses and yields for complexes **22**-**36**.

Complex	Yield (%)	Formula	% C calc./found	% H calc./found	% N calc./found
22	39	$C_{24}H_{28}N_5O_{13}Br_2CuGd$	29.56/29.62	2.89/2.93	7.18/7.26
23	36	$C_{24}H_{28}N_5O_{13}Br_2CuTb$	29.51/29.44	2.89/2.91	7.17/7.23
24	41	$C_{24}H_{28}N_5O_{13}Br_2CuDy$	29.40/29.46	2.88/2.91	7.14/7.22
25	35	$C_{24}H_{28}N_5O_{13}Br_2CuEr$	29.26/29.20	2.86/2.89	7.11/7.20

Table 4.1.- Continuation.

Complex	Yield (%)	Formula	% C calc./found	% H calc./found	% N calc./found
26	48	$C_{26}H_{29}N_6O_{12}Br_2NiNd$	31.86/31.81	2.98/3.01	8.57/8.46
27	45	$C_{26}H_{29}N_6O_{12}Br_2NiGd$	31.44/31.50	2.94/2.95	8.46/8.53
28	52	$C_{26}H_{29}N_6O_{12}Br_2NiTb$	31.39/31.46	2.94/2.96	8.45/8.53
29	57	$C_{26}H_{29}N_6O_{12}Br_2NiDy$	31.27/31.34	2.93/2.96	8.42/8.50
30	51	$C_{26}H_{29}N_6O_{12}Br_2NiEr$	31.13/31.19	2.91/2.93	8.38/8.30
31	47	$C_{26}H_{29}N_6O_{12}Br_2NiY$	33.76/33.84	3.16/3.18	9.09/9.16
32	42	$C_{26}H_{29}N_6O_{12}Br_2CoGd$	31.43/31.51	2.94/2.95	8.46/8.47
33	50	$C_{26}H_{29}N_6O_{12}Br_2CoTb$	31.38/31.42	2.94/2.96	8.44/8.50
34	55	$C_{26}H_{29}N_6O_{12}Br_2CoDy$	31.27/31.30	2.93/2.93	8.41/8.45
35	39	$C_{26}H_{29}N_6O_{12}Br_2CoEr$	31.12/31.17	2.91/2.93	8.37/8.41
36	49	$C_{26}H_{29}N_6O_{12}Br_2CoY$	33.75/33.82	3.16/3.20	9.08/9.11

4.3. EXPERIMENTAL RESULTS

The reaction of H_2L with $Cu(OAc)_2{\cdot}H_2O$ and $Ln(NO_3)_3{\cdot}nH_2O$ in a CH_3CN/MeOH mixture and in 1:1:1 molar ratio led to dark green crystals of the compounds $[Cu(\mu\text{-}L)(\mu\text{-}OAc)Ln(NO_3)_2]{\cdot}CH_3CN{\cdot}H_2O$ {Ln(III) = Gd (**22**), Tb (**23**), Dy (**24**), Er (**25**)}, which are very similar to the Zn(II)Ln(III) dimers reported in the previous chapter. The same reaction but using $Ni(OAc)_2{\cdot}4H_2O$ instead of $Cu(OAc)_2{\cdot}H_2O$, led to green crystals of the similar dinuclear complexes $[Ni(CH_3CN)(\mu\text{-}L)(\mu\text{-}OAc)Ln(NO_3)_2]{\cdot}CH_3CN$ {Ln(III) = Nd (**26**), Gd (**27**), Tb (**28**), Dy (**29**), Er (**30**), Y (**31**)}, where the most significant differences between the Cu(II) and Ni(II) based dimers are the coordination environment of the 3d metal ions and the disposition of the ligands around them. The use of $Co(OAc)_2{\cdot}4H_2O$ as source of metal led to the formation of dinuclear complexes with the general formula $[Co(CH_3CN)(\mu\text{-}L)(\mu\text{-}OAc)Ln(NO_3)_2]{\cdot}CH_3CN$ {Ln(III) = Gd (**32**), Tb (**33**), Dy (**34**), Er (**35**), Y (**36**)}, which are isostructural to the Ni(II) analogues.

4.3.1. Crystal Structures of Complexes 22-36

Complexes **22-25** crystallize in the monoclinic $P2_1/n$ space group and consist on dinuclear Cu(II)Ln(III) molecules, in which the Ln(III) and Cu(II) ions are bridged by two phenoxo groups of the L^{2-} ligand and one *syn-syn* acetate. The structure of **22-25** is given in Figure 4.1, whereas crystallographic data and selected bond lengths and angles are given in Appendices, Tables A.7 and A.10, respectively.

In all these complexes, the Cu(II) ions exhibit CuN_2O_3 coordination spheres consisting of two phenoxo bridging oxygen atoms, one oxygen atom from the acetate bridging group and two nitrogen atoms from the amine group. The calculation of the degree of distortion of the Cu(II) coordination polyhedron led to similar CshM values (Continues Shape Measurement values) to those obtained for complexes **11**-**21** and therefore, the CuN_2O_3 coordination sphere can be considered as square pyramid but close to vacant octahedron and trigonal bipyramid as the ZnN_2O_3 coordination spheres (Appendices, Table A.25).[6] The Cu-O and Cu-N distances are found respectively in the 1.999(2)-2.146(2) and 2.017(2)-2.024(3) Å ranges. In contrast to the Zn(II) based analogues, where the Zn-$O_{acetate}$ constituted the shortest Zn-O/N bonding distance, in complexes **22**-**25** the largest bonding distances involving the Cu(II) ions correspond to the Cu-$O_{acetate}$ bonds.

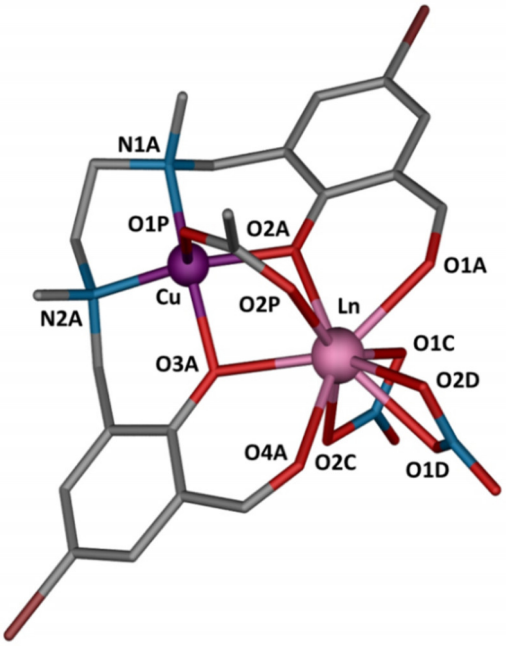

Figure 4.1.- Perspective view of the molecular structure of **22**-**25**. Crystallization solvent molecules are omitted for clarity. Colour code: N = blue, O = red, C = grey, Br = brown, Cu = purple, Ln = pink.

The Ln(III) ions exhibit LnO_9 coordination spheres, which are made by the two phenoxo bridging oxygen atoms, the two aldehyde oxygen atoms, one oxygen atom from the acetate bridging group and four oxygen atoms belonging to two bidentate nitrate anions. The average Ln-O distances are in the 2.254(2)-2.534(2) Å range and follow the same trend as in the Zn(II) based analogues, thus indicating a high degree of asymmetry in the LnO_9 coordination sphere. In fact, the computed shape measures indicate that the LnO_9 coordination spheres can be considered as intermediate between several nine-vertex polyhedral (Appendices, Table A.26). The intradinuclear Cu···Ln distances, in the 3.353(1)-3.383(1) Å range, and the distances corresponding to the Ln-O_{ligand} and Ln-$O_{acetate}$ bonds decrease from Gd(III) to Er(III) following the lanthanide contraction.

The average Ln-O-Cu angles fall in the 99.51(6)-100.29(7)° range in complexes **22**-**25** and due to the bridging acetate group, the average hinge angles of the Cu-(μ-O)$_2$-Ln bridging fragment are relatively high (between 24.29 and 25.07°). Both aromatic rings of the ligand almost fall in the same plane, forming dihedral angles ranging from 15.73 to 16.04°.

Finally, it should be mentioned that complexes **22**-**25** exhibit hydrogen bond interactions between the disordered crystallization water molecules and one of the oxygen atoms of the bidentate nitrate group, one of the oxygen atoms of the acetate bridging group and the nitrogen atom of the crystallization acetonitrile molecule (Figure 4.2).

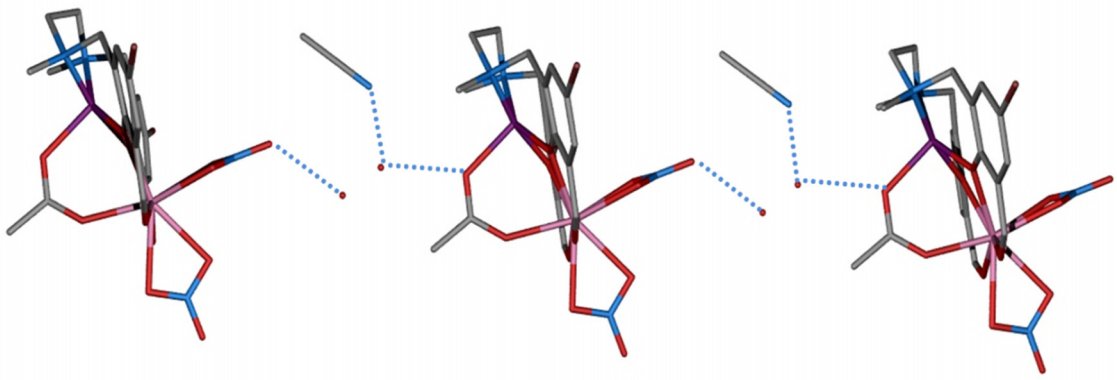

Figure 4.2.- A perspective view of the structure of **22**-**25** together with intermolecular (blue dotted lines) hydrogen bonds.

Complexes **26**-**31** (Figure 4.3) possess very similar molecular structures to that of **11**-**21** and **22**-**25**, but consist of Ni(II)Ln(III) dinuclear units and the coordination environment of Ni(II) ions is different to that of the Zn(II) and Cu(II) ions. Crystallographic data and selected bond lengths and angles are given in Appendices, Tables A.8 and A.11, respectively.

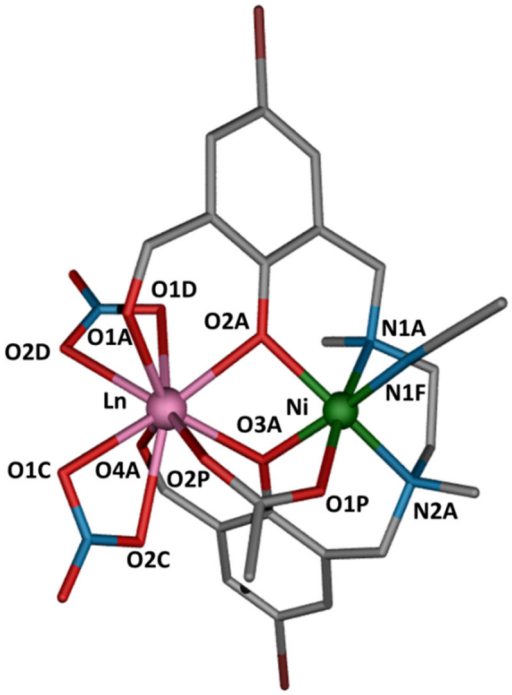

Figure 4.3.- Perspective view of the molecular structure of **26**-**31**. Crystallization solvent molecules are omitted for clarity. Colour code: N = blue, O = red, C = grey, Br = brown, Ni = green, Ln = pink.

In these complexes, the Ni(II) ions are coordinated to an additional nitrogen atom that belongs to an acetonitrile molecule and therefore, exhibit NiN_3O_3 coordination spheres. The three oxygen atoms and consequently, the three nitrogen atoms occupy *fac* positions in these slightly distorted coordination polyhedras. In fact, computed shape measures indicate that NiN_3O_3 coordination spheres are found in the OC-6 ↔ TPR-6 deformation pathway and are close to the octahedral geometry (75.8-77.1 %) somewhat distorted to trigonal prism (Appendices, Table A.27). The Ni-O and Ni-N bond distances are similar to each other and are in the 2.051(6)-2.136(4) Å and 2.060(5)-2.108(4) Å ranges, respectively. The lanthanide ions show similar coordination environments than in previous complexes, exhibiting rather asymmetric coordination spheres where the average Ln-O distances are in the 2.275(2)-2.537(7) Å

range. As a matter of fact, the computed shape measures relative to the ideal nine-vertex polyhedra for the LnO_9 coordination sphere were very close to those obtained for Zn(II) and Cu(II) based dimers (Appendices, Table A.28). The average Ni(II)-Ln(III) distances are in the 3.385(1)-3.437(2) Å range and as expected, the average Ln-O_{ligand} bond distances decrease steadily from Nd(III) to Er(III) following the lanthanide contraction, with a concomitant decrease of the average Ni-Ln and Ln-$O_{acetate}$ bond distances.

The M-O-Ln angles of complexes **26**-**31** are similar to those found in complexes **22**-**25** and are in the 97.6(2)-101.99(7)° range. Compared to the zinc and copper based analogues, the ligand shows more twisted dispositions around the metal ions, in which the dihedral angles between the two aromatic rings are in the 69.92 - 71.39° range. The torsion of the ligand leads to an increase in the hinge angle compared to complexes **22**-**25**, being in the 27.88 - 28.39° range.

To end up, complexes **32**-**36** are isostructural to complexes **26**-**31** but containing Co(II) ions and crystallize in the triclinic *P-1* space group. A perspective view of the structure of **32**-**36** is given in Figure 4.4, whereas crystallographic data and selected bond lengths and angles are given in Appendices, Table A.9 and A.12, respectively.

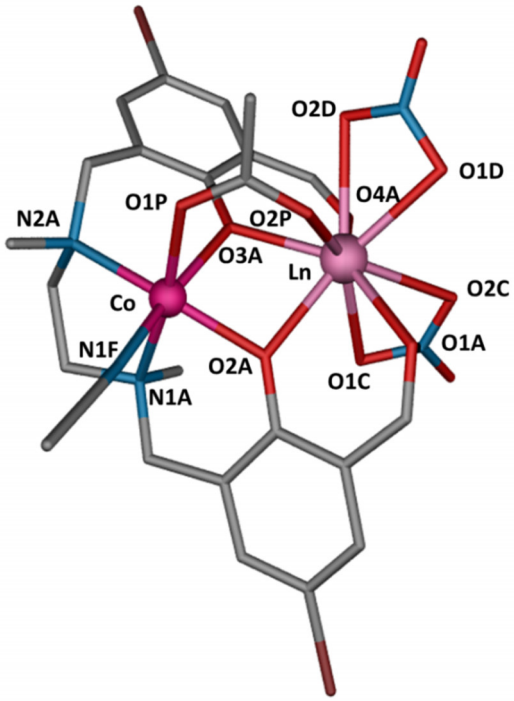

Figure 4.4.- Perspective view of the molecular structure of complexes **32**-**36**. Crystallization solvent molecules are omitted for clarity. Colour code: N = blue, O = red, C = grey, Br = brown, Co = fuchsia, Ln = pink.

The CoN_3O_3 and LnO_9 coordination spheres show similar coordination environments to that found in complexes **26**-**31**, with 71.9-72.7 % octahedral geometry for Co(II) ions (Appendices, Table A.29 and A.30). Bond distances and angles are also close to those found for complexes **26**-**31** and further discussion on the structure of these complexes will be omitted.

4.3.2. Magnetic properties of complexes 22-25

The temperature dependence of the magnetic susceptibility for the dinuclear Cu(II)Ln(III) complexes were measured on polycrystalline samples in the 5-300 K (**22**) and 2-300 K (**23**-**25**) temperature ranges under an applied field of 0.1 T (Figure 4.5).

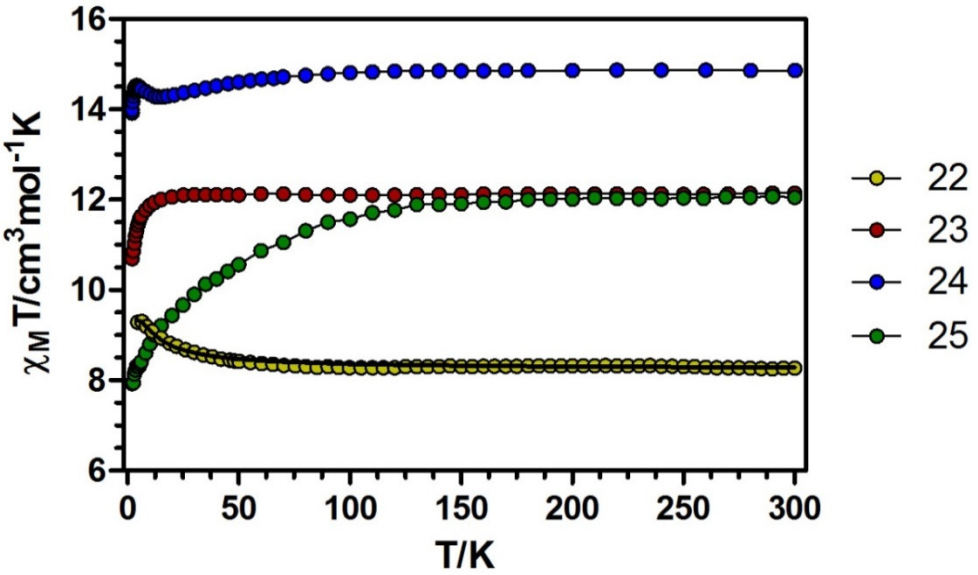

Figure 4.5.- Temperature dependence of the $\chi_M T$ product at 1000 Oe for complexes **22**-**25**. The black solid line show the best fits for complex **22**. The rest of the lines are a guide to the eye.

At room temperature, the $\chi_M T$ value for **22** of 8.27 $cm^3 \cdot K \cdot mol^{-1}$ matches very well with the expected value for non-interacting Cu(II) (S =1/2) and Gd(III) (S = 7/2) ions (8.25 $cm^3 \cdot K \cdot mol^{-1}$ with g = 2). On cooling, the $\chi_M T$ product remains constant until 70 K and then increases at lower temperatures, reaching a maximum value of 9.31 $cm^3 \cdot K \cdot mol^{-1}$ at 5 K, which points out the presence of ferromagnetic exchange interactions within the CuGd dinuclear unit. The field dependence of the molar

magnetization at 2 K for compound **22** (Figure 4.6) shows a relatively rapid increase in the magnetization at low field, in agreement with a high-spin state, and a rapid saturation of the magnetization that is almost complete above 3 T, reaching a value of 7.91 $N\mu_B$ at 5 T. The obtained value is in good agreement with the theoretical value for a $S_T = 4$ spin ground state (8 $N\mu_B$ for $g = 2$).

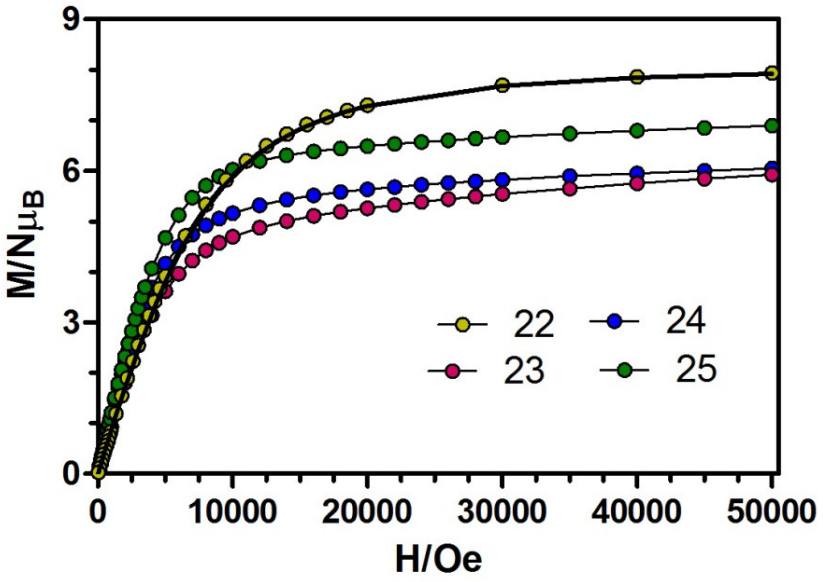

Figure 4.6.- *M* versus *H* plots for complexes **22**-**25** at 2 K. The black solid line shows the best fit for complex **22**. The rest of the lines are a guide to the eye.

The magnetic susceptibility and magnetization data for complex **22** have been simultaneously modelled using the following Hamiltonian:

$$\mathcal{H} = -JS_{Cu}S_{Gd} - zJ'\langle S_z\rangle S_z + g_e\mu_B SH \quad (Equation\ 4.1)$$

where J is the magnetic exchange pathway through the di-μ-phenoxo/*syn-syn* acetate triple bridge, $-zJ' < S_z > S_z$ accounts for the intermolecular interactions by means of the molecular field approximation, g_e is the average g factor, μ_B is the Bohr magneton and H is the magnetic field. The fit of the experimental susceptibility data using the full-matrix diagonalization Phi program[7] afforded the following set of parameters when fixing g to 2.0 for both ions: J = + 2.30 cm^{-1} and zJ' = -0.006 cm^{-1} with $R = 2.08\cdot10^{-5}$.

To support the experimental values of J_{CuGd}, DFT calculations were carried out on the X-ray structures as found in the solid state. The calculated J_{CuGd} parameter of + 2.01 cm^{-1} matches very well in sign and magnitude with the experimental parameters.

Previous theoretical studies carried out on dinuclear Cu-(μ-O)$_2$-Gd complexes indicate that ferromagnetic interactions between Cu(II) and Gd(III) ions increase with the planarity of the Cu-(μ-O)$_2$-Gd bridging fragment and with the increase of the Cu-O-Gd angle.[8] Therefore, the weak ferromagnetic interactions found in this complex are not unexpected if we consider the mean Cu-O-Gd angle of 99.60° and the dihedral β angle of 25.07°. The acetate bridge, which is known to transmit AF interactions as seen in Chapters 1 and 2, will also help to weaken the ferromagnetic interactions.

The χ_MT values of 12.14, 14.87 and 12.06 cm^3·K·mol^{-1} respectively for complexes **23**-**25** at 300 K are compatible with the expected values for pairs of magnetically isolated Cu(II) and Ln(III) ions (Table 4.2). On lowering the temperature, the χ_MT product of the CuDy dimer (**24**) decreases gradually to reach a minimum value of 14.28 cm^3·K·mol^{-1} at 14 K and then increases until 14.53 cm^3·K·mol^{-1} at 4.0 K. Below this temperature, there is a small decrease to reach a value of 13.99 cm^3·K·mol^{-1} at 2.0 K. The magnetic behaviour at low temperatures of this complex is the result of two competing interactions: (1) ferromagnetic exchange interactions between the Cu(II) and Dy(III) ions, which lead to an increase in χ_MT and (2) crystal field splitting of the Dy(III) ions, responsible for the decrease in χ_MT. The fact that χ_MT increases at low temperatures suggests that ferromagnetic interactions prevail over the effect of the crystal field splitting in this complex. On the other hand, the χ_MT products of complexes **23** and **25** remain constant on cooling until 25 and 130 K, respectively, and then drop abruptly to reach respectively values of 10.70 and 7.93 cm^3·K·mol^{-1} at 2 K. The decrease of χ_MT in the low temperature regime for **23** and **25** seems to indicate that in these compounds the effect of ferromagnetic exchange interactions is not as pronounced as in **24**.

Table 4.2.- *Direct current* magnetic data for compounds **23**-**25**.

Complex	Ground state of Ln(III) ion	χ_MT theor.[a] at 300K/exp. at 300 K/exp. at 2 K (cm^3·K·mol^{-1})	M theor.[b]/M exp. at 2 K (Nμ_B)
23	$^7F_6$, g_J = 3/2	12.19/12.14/10.70	10/5.92
24	$^6H_{15/2}$, g_J = 4/3	14.54/14.87/13.99	11/6.04
25	$^4I_{15/2}$, g_J = 6/5	11.85/12.06/7.93	10/6.89

[a] $\chi_M T = \frac{N\beta^2}{3k}\{g_j^2 J(J+1) + g_{Cu}^2 S(S+1)\}$

[b] $J = L + S_T;\ S_T = S_{Ln} + S_{Cu};\ g_j = \frac{3}{2} + \frac{S_T(S_T+1)-L(L+1)}{2J(J+1)};\ M_s = g_J J N\mu_B$

The nature of the exchange interaction between Cu(II) and lanthanide ions displaying spin-orbit coupling can be known by the empirical approach developed by Costes et al.,[9] which consists on representing the temperature dependence of the difference $\Delta\chi_M T = \chi_M T_{(CuLn)} - \chi_M T_{(Zn\text{-}Ln)} = \chi_M T_{(Cu)} + J_{(CuGd)}$, where the contribution of the crystal-field effects of the Ln(III) ions is removed from the $\chi_M T_{(CuLn)}$ data. The results obtained by this procedure are displayed in Figures 4.7a - 4.7c, where the $\Delta\chi_M T$ differences show an increase at low temperatures, thus revealing the occurrence of ferromagnetic interaction between Cu(II) and Ln(III) ions in complexes **23**-**25**.

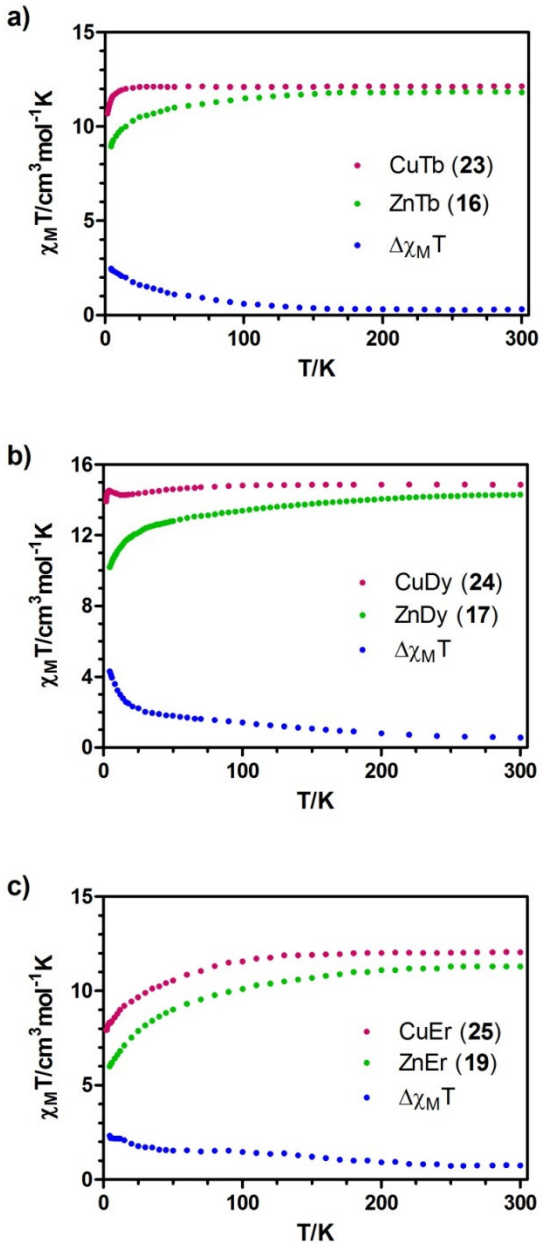

Figure 4.7.- Temperature dependence of the $\chi_M T$ product and the difference $\Delta\chi_M T = \chi_M T_{(CuLn)} - \chi_M T_{(Zn\text{-}Ln)}$ for complexes **23** (a), **24** (b) and **25** (c).

Upon increasing the applied external magnetic field, the magnetization of complexes **23**-**25** show a relatively rapid increase at low magnetic fields and a rapid saturation that is almost complete above 4T, reaching values of 5.92, 6.04 and 6.89 $N\mu_B$ at 5 T respectively. These values are quite far from the expected saturation values (10 $N\mu_B$ for complexes **23** and **25** and 11 $N\mu_B$ for complex **24**), which suggests the presence of a significant magnetic anisotropy due to the crystal field effects and/or more likely the presence of low-lying excited states that are partially (thermally and field-induced) populated.

Finally, it is worth mentioning that dynamic *alternating current* magnetic susceptibility measurements were performed in **23**-**25**, but none of them showed frequency dependency of the in-phase and out-of-phase signals even in the presence of an external *dc* field of 1000 Oe.

4.3.3. Magnetic properties of complexes 26-31

The temperature dependence of $\chi_M T$ for complexes **26**-**31** (χ_M is the molar magnetic susceptibility per NiLn unit) were measured in an applied field of 0.1 T and are displayed in Figure 4.8.

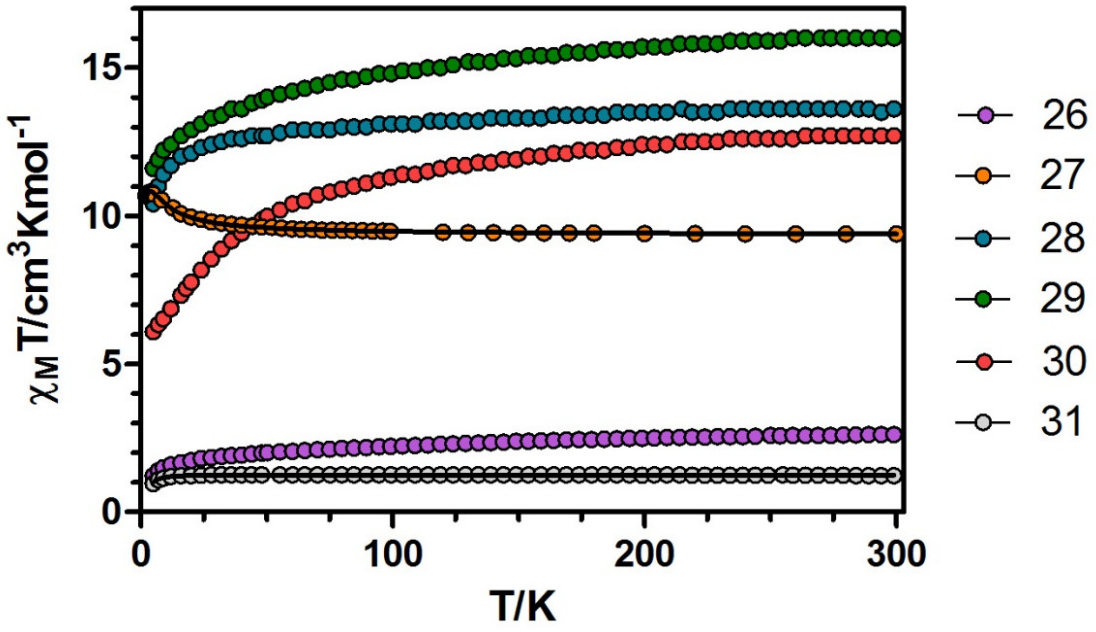

Figure 4.8.- Temperature dependence of the $\chi_M T$ product at 1000 Oe for complexes **26**-**31**. Black solid lines show the best fits for complexes **27** and **31**.

Let us start with the simplest cases, the Ni-Gd (**27**) and Ni-Y (**31**) dimers. At room temperature the $\chi_M T$ value of complex **27** is 9.38 $cm^3 \cdot K \cdot mol^{-1}$, which is slightly high but still in good agreement with the expected value for a couple of non-interacting Ni(II) (S = 1) and Gd(III) (S = 7/2) ions (8.875 $cm^3 \cdot K \cdot mol^{-1}$). The $\chi_M T$ value increases very slowly with decreasing temperature until 70 K and then in a more abrupt way to reach a maximum value of 10.82 $cm^3 \cdot K \cdot mol^{-1}$ at 3.3 K. Below the temperature of the maximum, there is a small decrease to reach a value of 10.67 $cm^3 \cdot K \cdot mol^{-1}$ at 2.0 K (Figure 4.9). The increase in $\chi_M T$ indicates the existence of intramolecular ferromagnetic interactions between Ni(II) and Gd(III) ions, whereas the decrease at low temperatures is more likely due to the zero field splitting effects (ZFS) of the ground state and/or intermolecular antiferromagnetic interactions.

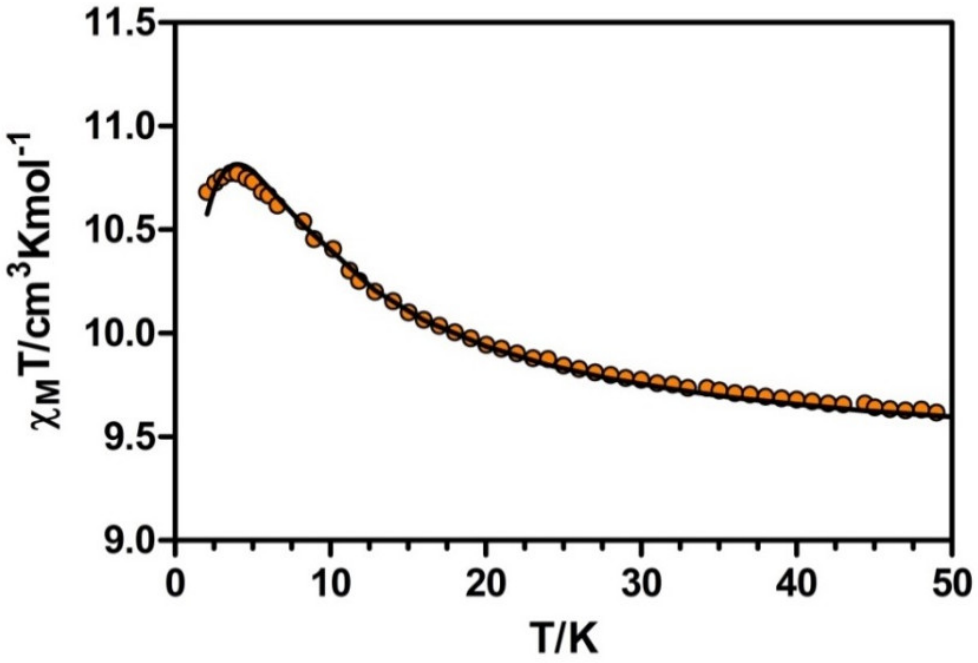

Figure 4.9.- Temperature dependence of $\chi_M T$ product at 1000 Oe for **27** in the low temperature region. The black solid line shows the best fit.

The field dependence of the magnetization at 2 K for **27** (Figure 4.10) reveals a relatively rapid increase at low fields to reach a clear saturation that is almost complete at 3 T, reaching a value of 9.01 $N\mu_B$ at 5 T. This value is in good agreement with the expected value for the fundamental state S_T = 9/2 with g = 2 (9 $N\mu_B$).

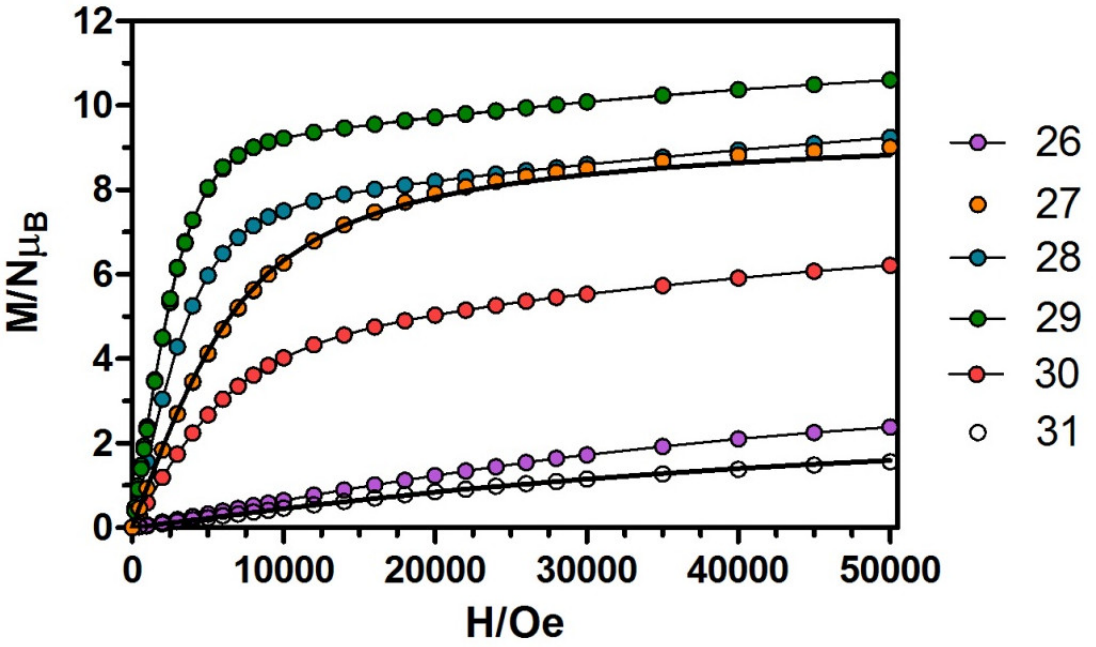

Figure 4.10.- *M* versus *H* plots for complexes **26**-**31** at 2 K. The black solid lines show the best fits for complexes **27** and **31**. The rest of the lines are a guide to the eye.

On the other hand, the $\chi_M T$ value of the NiY complex (**31**) at room temperature is 1.23 $cm^3 \cdot K \cdot mol^{-1}$, which is compatible with the calculated value of 1 $cm^3 \cdot K \cdot mol^{-1}$ for independent Ni(II) ions. On cooling, the $\chi_M T$ value remains almost constant until 18 K and then drops abruptly to reach a value of 0.957 $cm^3 \cdot K \cdot mol^{-1}$ at 5 K, which is due to the zero field splitting (ZFS) of Ni(II) ion. The magnetization of complex **31** shows a gradual increase with the applied external field reaching a value of 1.57 $N\mu_B$ at 5 T, which is lower than the expected from the Brillouin function for an S = 1 ground state (2 $N\mu_B$). This behaviour is due to the strong zero field splitting of the Ni(II) ion, which leads to the split of the S = 1 ground state into two M_s = 0, ±1 components, preventing the magnetization from reaching the expected value.

The magnetic behaviour of complex **27** has been modelled using the following Hamiltonian:

$$\mathcal{H} = -JS_{Ni}S_{Gd} + D_{Ni}S_{Ni}^2 + g_e\mu_B SH \quad (Equation\ 4.2)$$

where J is the coupling constant between the Ni(II) and Gd(III) ions, D_{Ni} is the ZFS parameter for Ni(II) ion, g_e is the average g factor, μ_B is the Bohr magneton and H is the magnetic field. The best-fit parameters to the experimental susceptibility and

magnetization data using the Phi program[7] afforded the following set of parameters: J = + 0.71 cm^{-1}, g = 2.06 and D = 6.73 cm^{-1} with $R = 9.76 \cdot 10^{-6}$. The value of the D_{Ni} parameter for the NiY complex extracted simultaneously from the susceptibility and magnetization data (D_{Ni} = 6.61 cm^{-1}, g = 2.23 and $R = 1.24 \cdot 10^{-4}$, see Figures 4.8 and 4.10) supports the magnitude of the D_{Ni} obtained for the Gd(III) based analogue. Regarding J, it should be noted that when D_{Ni} was fixed to zero and a term accounting for the intermolecular interactions was introduced in the Hamiltonian by means of the molecular field approximation, $-zJ' < S_z > S_z$, the fitting parameters did not significantly change: J = + 0.81 cm^{-1}, g = 2.06 and zJ' = -0.008 cm^{-1} with $R = 3.82 \cdot 10^{-5}$.

In order to support the experimental J value found for complex **27**, DFT calculations were carried out on the X-ray structure using the broken-symmetry approach. The calculated J_{NiGd} parameter of + 0.93 cm^{-1} agrees very well in sign and magnitude with the experimental parameters. The obtained experimental value is at the lower end of the experimental range ~0.3-5 cm^{-1} found for alkoxo and phenoxo bridged Ni_xGd (x = 1, 2, 3) complexes with ferromagnetic interactions,[2b] which is due to the relatively small Ni-O-Gd angle (100.05°) and large Ni-(μ-O)$_2$-Gd dihedral angle (28.29°) found in this complex. In fact, it has been seen from experimental results and DFT calculations[2b] that in diphenoxo bridged dinuclear NiGd complexes the ferromagnetic coupling increases when increasing the planarity of the Ni-(μ-O)$_2$-Gd bridging fragment and the Ni-O-Gd bridging angle. In addition, the effect of a third non-phenoxo bridge in the magnetic exchange coupling was also studied in the structurally similar complex [Ni(μ-L^1)(μ-OAc)Gd(NO_3)$_2$] (H_2L^1 = N,N',N"-trimethyl-N,N"-bis(2-hydroxy-3-methoxy-5-methylbenzyl)diethylenetriamine), which was done by substituting the *syn-syn* acetate bridging group by two non-bridging water molecules. The results of the calculations showed an increase of 0.45 cm^{-1} in J_{NiGd}, indicating that the third bridge has a significant role in decreasing the magnetic exchange coupling in this type of compounds. Therefore, in view of the above considerations the weak ferromagnetic interaction between the Ni(II) and Gd(III) ions is not unexpected.

With respect to complexes **26** and **28**-**30**, at room temperature the $\chi_M T$ values are in general close but slightly higher than the expected values for pairs of magnetically isolated Ni(II) and Ln(III) ions (Table 4.3). On lowering the temperature, the $\chi_M T$ values decrease gradually until ~50 K and then drop abruptly to reach a minimum value of 1.23 cm^3 K mol^{-1} for complex **26** and values that at 5 K are in the 6.04 - 11.6 cm^3 K mol^{-1} range for complexes **28**-**30**. As in the case of complexes **23**-**25**, this behaviour is due to the depopulation of Stark sublevels of the Ln(III) ions. The empirical approach

developed by Costes et al. to know the nature of the interactions between the Ni(II) and Ln(III) ions can not be used for these complexes, as they are not isostructural to the Zn(II)Ln(III) complexes reported in the previous chapter.

Table 4.3.- *Direct current* magnetic data for compounds **26** and **28**-**30**.

Complex	Ground state of Ln(III) ion	$\chi_M T$ theor.[a] at 300K/exp. at 300 K/exp. at 5 K (cm^3 K mol^{-1})	M theor. /M exp. at 2 K ($N\mu_B$)
26	$^4I_{9/2}$, g_J = 8/11	2.64/2.62/1.23	5.27/2.4
28	$^7F_6$, g_J = 3/2	12.82/13.6/10.40	11[b]/9.2
29	$^6H_{15/2}$, g_J = 4/3	15.17/16.0/11.60	12[b]/10.61
30	$^4I_{15/2}$, g_J = 6/5	12.48/12.70/6.09	11[b]/6.2

[a] $\chi_M T = \frac{N\beta^2}{3k}\{g_j^2 J(J+1) + g_{Ni}^2 S(S+1)\}$

[b] $J = L + S_T;\ S_T = S_{Ln} + S_{Ni};\ g_j = \frac{3}{2} + \frac{S_T(S_T+1)-L(L+1)}{2J(J+1)};\ M_s = g_J J N\mu_B$

The magnetization of complexes **28**-**30** (Figure 4.10) show relatively rapid increase at low fields, in accordance with the ferromagnetic interaction between Ni(II) and Ln(III) ions and a lineal increase from 1 T on without reaching a clear saturation at 5T. The magnetization values at 5 T for complexes **28** and **29** (Table 4.3) are close to the expected saturation magnetization values for Ln(III) ions with strong easy-axis anisotropy that behave as Ising types and that are ferromagnetically coupled to Ni(II) ions. The *M* value for **30** at 5T, however, is considerably lower than the expected saturation value, which indicates that the latter compound shows weaker anisotropy than complexes **28** and **29**. Moreover, the magnetization of complex **26** shows a gradual increase with the applied magnetic field, reaching a value of 2.4 $N\mu_B$ at 5 T.

To end up, dynamic *alternating current* magnetic susceptibility measurements were also performed in **26** and **28**-**30**, but only compounds **29** (NiDy) and **30** (NiEr) showed a slight frequency dependency of the out-of-phase signal after applying an external field of 1000 Oe, but without any maxima in the temperature window technically available (Figure 4.11).

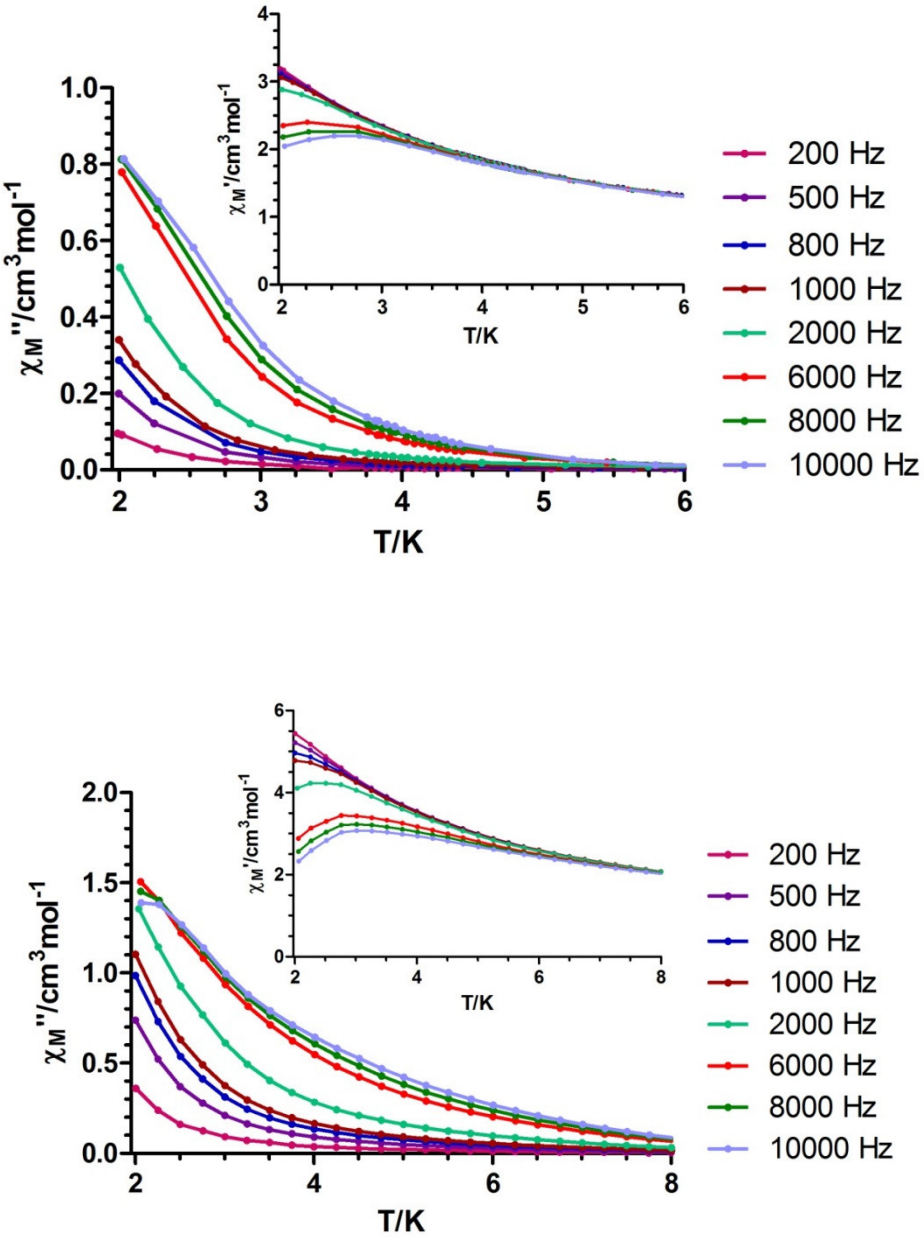

Figure 4.11.- Temperature dependence of in-phase χ_M' (insets) and out-of phase χ_M'' components of the *alternating current* susceptibility for complexes **29** (top) and **30** (bottom) under an applied field of 1000 Oe.

4.3.3. Magnetic properties of complexes 32-36

The temperature dependence of $\chi_M T$ for complexes **32**-**36** (χ_M is the molar susceptibility per Co(II)Ln(III) unit) were measured in an applied field of 0.1 T and are displayed in Figure 4.12.

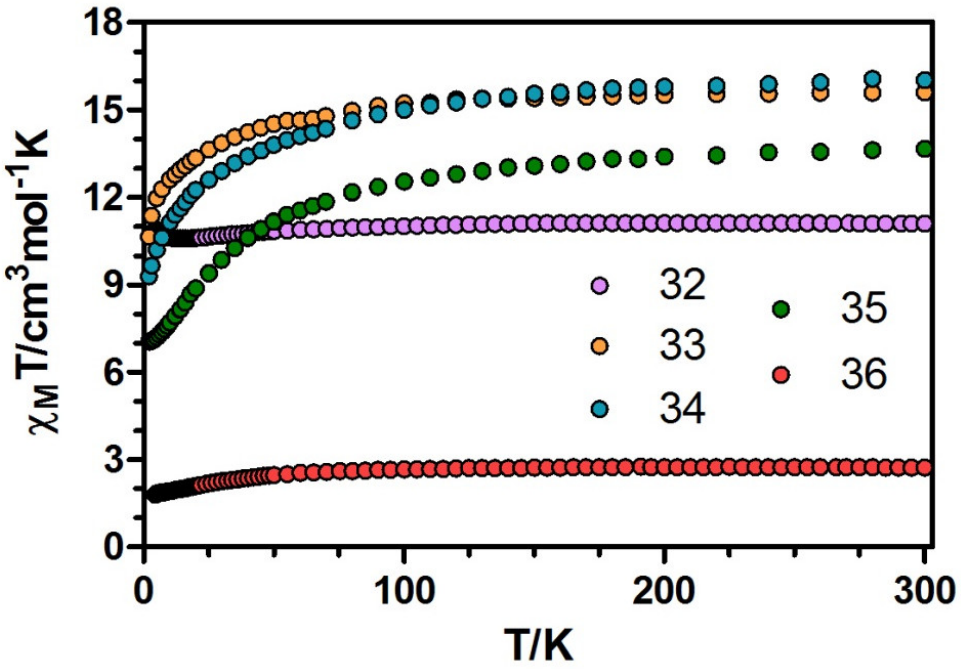

Figure 4.12.- Temperature dependence of the $\chi_M T$ product at 1000 Oe for complexes **32**-**36**.

The magnetic behaviour of Co(II) ions is rather different to that of Cu(II) and Ni(II) due to the strong orbital contribution to the magnetic moment, which leads to a strong magnetic anisotropy. In ideal octahedral Co(II) ions, the ^4F ground term is split into two orbital triplets ($^4T_{1g}$ and $^4T_{2g}$) and one singlet ($^4A_{2g}$) (Figure 4.13). The excited $^4T_{2g}$ and $^4A_{2g}$ states are over 8000 cm^{-1} above the ground $^4T_{1g}$ state and therefore, they are not thermally populated. The ground state presents first-order orbital moment together with spin angular momentum, due to its triplet nature. The first-order spin-orbit coupling splits this ground state into a sextet G' + E'_2 (J = 5/2), a quadruplet G' (J = 3/2) and a doublet E' (J = ½), this last one being the lowest. In addition, the $^4T_1$ levels arising from the ^4F and ^4P terms interact with each other because they have the same symmetry, causing a small admixture between the $^4T_1$(P) level and the ground $^4T_1$ (F) one. As a consequence, there is an orbital reduction if compared to the pure $^4T_1$ (F) triplet and the magnetic data of Co(II) ions is therefore analysed by the following Hamiltonian:

$$\mathcal{H} = -\alpha\lambda LS \quad (Equation\ 4.3)$$

where α is the orbital reduction factor and λ is the spin-orbit coupling parameter.

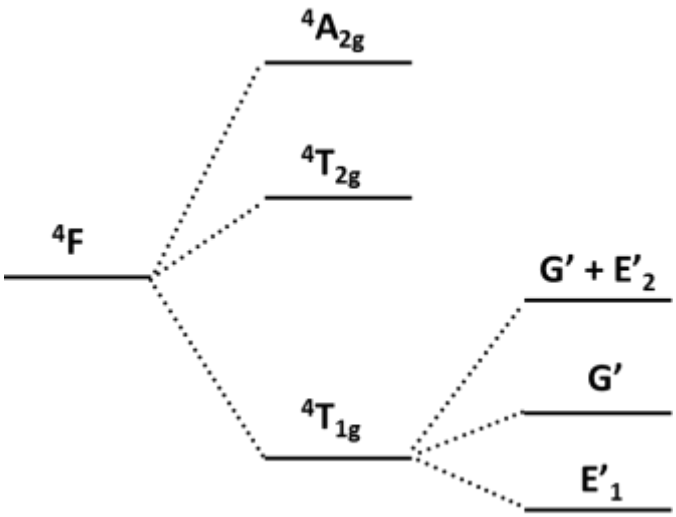

Figure 4.13.- Octahedral ligand field splitting of the ^4F term together with the spin-orbit coupling splitting of the $^4T_{1g}$ state.

The above discussion is only valid for purely octahedral Co(II) ions, as the distortion from the ideal octahedron breaks the degeneracy of the triplet orbital state $^4T_{1g}$. The CoN_3O_3 coordination polyhedron of complexes **26**-**31** show 71.9-72.7 % of octahedral geometry, being in the OC6 ↔ TPR-6 deformation pathway (deviating by less than 5 % from this pathway). This deformation pathway is known as Bailar twist (Figure 4.14) and as the square root sum of the SHAPE measurement values for octahedral and trigonal prism geometries is lower than 4.6 (around 4.3), there is no other significant distortion than the Bailar twist in these complexes.[10]

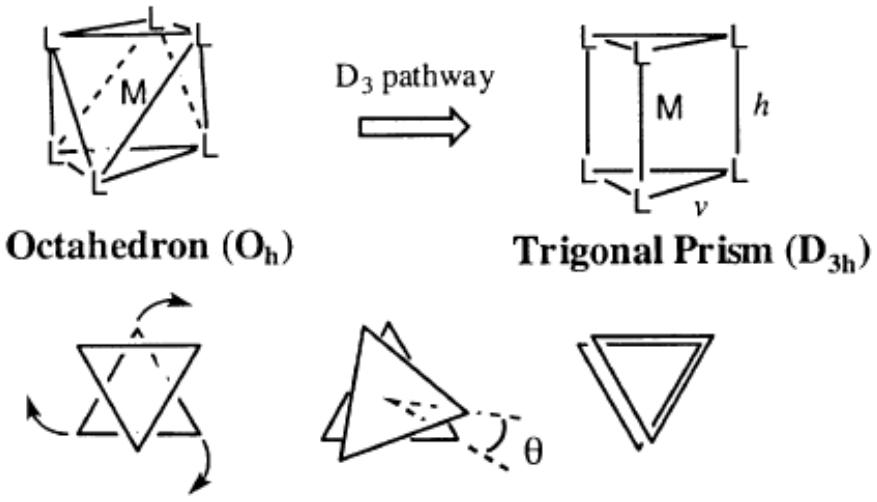

Figure 4.14.- Schematic description of the Bailar trigonal twist.

Due to this deformation, the magnetic properties of the obtained Co(II) compounds can no longer be analysed with the above equation, as the distortion from ideal octahedral geometry must be taken into account. If for the sake of simplicity, we assume C_{3v} local symmetry for these coordination polyhedrons, the triplet $^4T_{1g}$ ground state of Oh symmetry splits into an orbital singlet $^4A_2$ and an orbital doublet ^4E, the energy gap between them being the axial splitting parameter, Δ (Figure 4.15). A further rhombic distortion would lead to the splitting of the excited ^4E term, the energy gap being in this case δ. The terms arising from the rhombic distortion split in turn by spin-orbit coupling giving rise to two and four Kramer's doublets. The magnetic properties of such Co(II) ions can be then analysed by the following Hamiltonian:

$$\mathcal{H} = -\alpha\lambda LS + \Delta\,[L_z^2 - L(L+1)/3] + \delta\left(L_x^2 - L_y^2\right) + \beta H(-\alpha L + g_e S) \quad \textit{(Equation 4.4)}$$

where λ is the spin-orbit coupling parameter, α is the orbital reduction factor and Δ and δ are respectively the axial and rhombic orbital splitting parameters of the T_1 term.

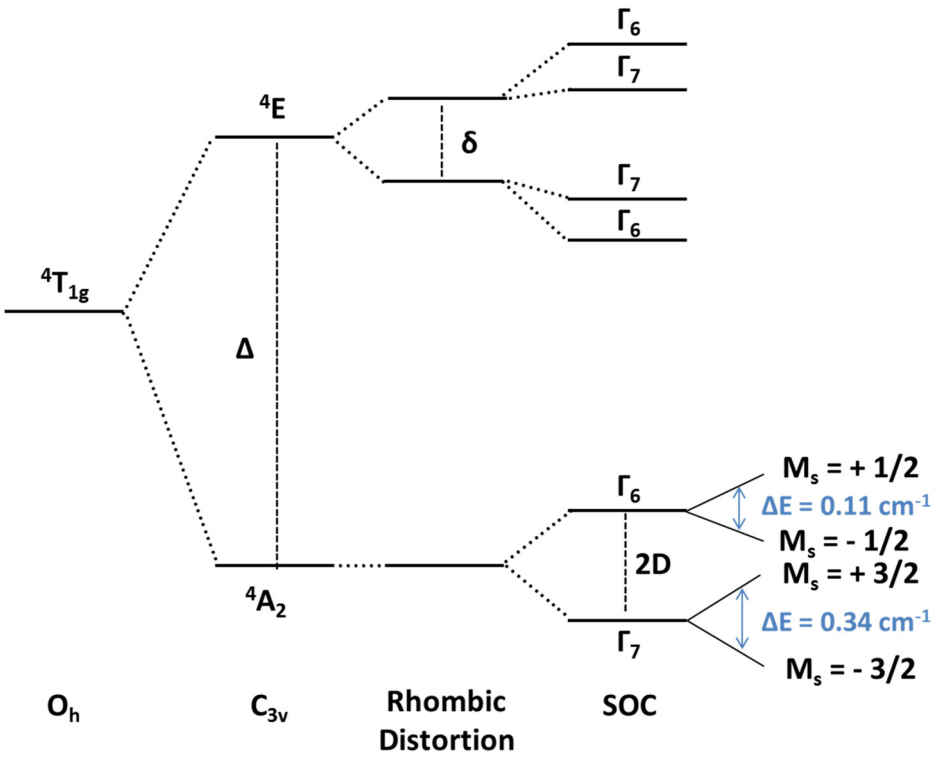

Figure 4.15.- Qualitative splitting of the $^4T_{1g}$ state by axial and rhombic distortions and spin orbit coupling. In blue ΔE values calculated for **36**, obtained from the expression $\Delta E = g\beta H \Delta Ms$ (g = 2.43 as obtained from the fitting to the experimental data, page 160).

When Δ is large enough, only the two lowest Kramer's doublets arising from the $^4A_{2g}$ state (M_s = ± 1/2 and ± 3/2) are thermally populated and then, the energy gap between them (2D) may be considered as a zero field splitting (ZFS) within the quartet state.

The $\chi_M T$ value for the CoY complex **36** at room temperature (2.72 $cm^3 \cdot K \cdot mol^{-1}$) is significantly larger than the spin-only value for a high-spin Co(II) ion (S = 3/2, 1.875 $cm^3 \cdot K \cdot mol^{-1}$ with g = 2), which is indicative of the unquenched orbital contribution of the Co(II) ion in distorted octahedral geometry (Figure 4.16). Upon cooling, $\chi_M T$ remains practically constant in the high temperature range and it decreases sharply below 120 K, reaching a value of 1.82 $cm^3 \cdot K \cdot mol^{-1}$ at 4.5 K. As the molecules are well isolated in the crystal field, this decrease is most likely due to spin-orbit coupling (SOC) effects rather than intermolecular AF interactions. The susceptibility data was fitted to Equation 4.4 with the PHI program,[7] obtaining the following set of parameters: λ = -104.0 cm^{-1}, α = 1.216, Δ = I355.3I cm^{-1} and δ = I89.35I cm^{-1} with R = $3.51 \cdot 10^{-6}$. The fit of the experimental data to the theoretical equation shows that the sign of Δ cannot be unambiguously determined from the susceptibility data, as the agreement factor (R) for positive and negative values are, in general, close. The fitting parameters are in good accordance with previously reported values for distorted octahedral Co(II) complexes.[11]

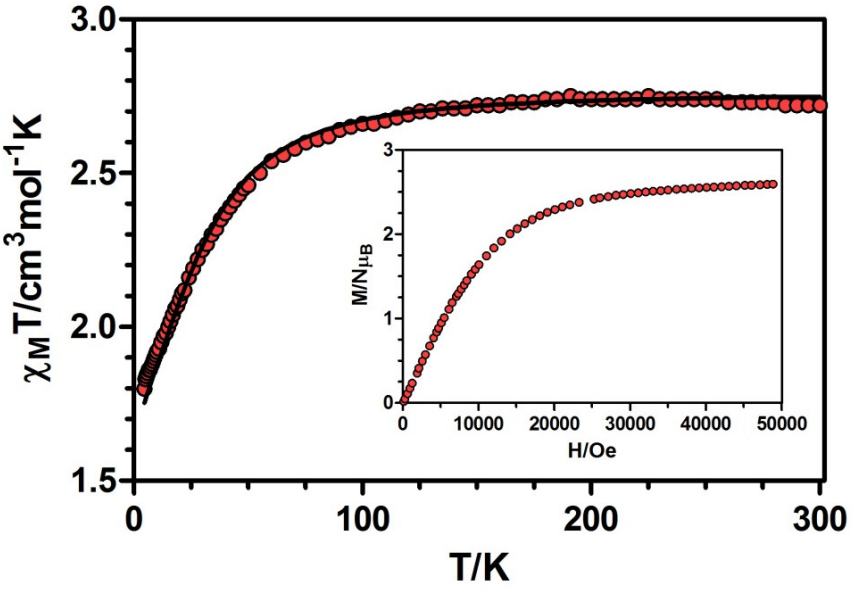

Figure 4.16.- Temperature dependence of the $\chi_M T$ product at 1000 Oe for complex **36**. The black solid line represents the best fit. Inset: M versus H plot for **36** at 2 K.

Regarding the magnetization plot of complex **36**, at applied field of 5 T the magnetization is not fully saturated, reaching a value of 2.6 $N\mu_B$ (Figure 4.16, inset). This value is lower than the expected value of 3 μ_B, which is due to anisotropy. The *M* vs. *H/T* plots obtained between 2 and 7 K at applied magnetic fields ranging from 0.1 to 9 T (Figure 4.17) are not superimposed on a single master curve, indicating that complex **36** shows a significant magnetic anisotropy. In order to quantify this anisotropy, the magnetic susceptibility data was fitted to Equation 4.5 using the PHI program,[7] obtaining the following set of parameters: D = I35.5I cm^{-1} and g = 2.43 with $R = 1.2 \cdot 10^{-4}$.

$$\mathcal{H} = D[S_z^2 - S(S+1)/3] + g_e \mu_B SH) \quad \textit{(Equation 4.5)}$$

where *S* is the spin ground state, *D* is the axial magnetic anisotropy, g_e is the average *g* factor, μ_B is the Bohr magneton and *H* is the magnetic field. The sign of *D* cannot be unambiguously determined from the susceptibility data either in this case.

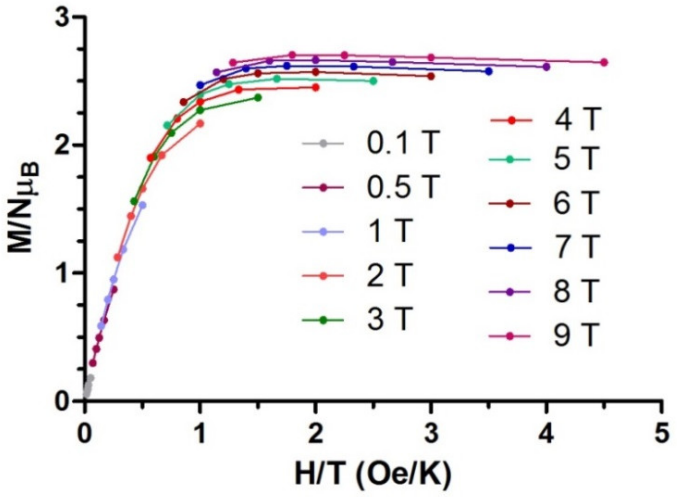

Figure 4.17.- *M* vs. *H/T* plot for **36**. Solid lines are guides for the eye.

Continuing with the CoGd complex **32**, at room temperature the $\chi_M T$ value of 11.09 $cm^3 \cdot K \cdot mol^{-1}$ is slightly larger than the expected value for two non-interacting Co(II) (S = 3/2) and Gd(III) (S = 7/2) ions (9.750 $cm^3 \cdot K \cdot mol^{-1}$ with g = 2.0), which may be due to the orbital contribution of Co(II) ions. On cooling, the $\chi_M T$ product stays constant until 140 K, then starts decreasing to reach a minimum value of 10.58 $cm^3 \cdot K \cdot mol^{-1}$ at 15 K and ends up increasing until 10.90 $cm^3 \cdot K \cdot mol^{-1}$ at 4.5 K (Figure 4.18). The observed decrease of $\chi_M T$ is due to the thermal depopulation of the spin-orbit coupling levels

arising from the $^4T_{1g}$ ground term of Co(II) ions, whereas the increase at low temperature indicates a ferromagnetic interaction between Co(II) and Gd(III) ions.

The magnetic behaviour of complex **32** was analysed by considering both effects, as included in the following Hamiltonian:

$$\mathcal{H} = \alpha\lambda LS - JS_{Co}S_{Gd} \qquad (\textit{Equation 4.6})$$

The fit of the experimental susceptibility data using the above equation led to the following parameters: λ = -111.2 cm^{-1}, α = 0.88, J = + 0.26 cm^{-1} and g = 2.06 (considered to be the same for both ions) with $R = 2.52 \cdot 10^{-5}$. The observed coupling constant is lower than that found for the similar di-μ-phenoxo/*syn-syn* acetate triply bridged compound [Co(μ-L^1)(μ-OAc)Gd(NO$_3$)$_2$] (J = + 0.7 cm^{-1}),[12] and to those found for planar di-μ-phenoxo-bridged Co(II)-Gd(III) complexes containing a compartmental ligand (J ~ 1 cm^{-1}).[13] Following the considerations made for CuGd and NiGd complexes, the observed low value of J is not unexpected if we take into account that **32** has the highest hinge angle.

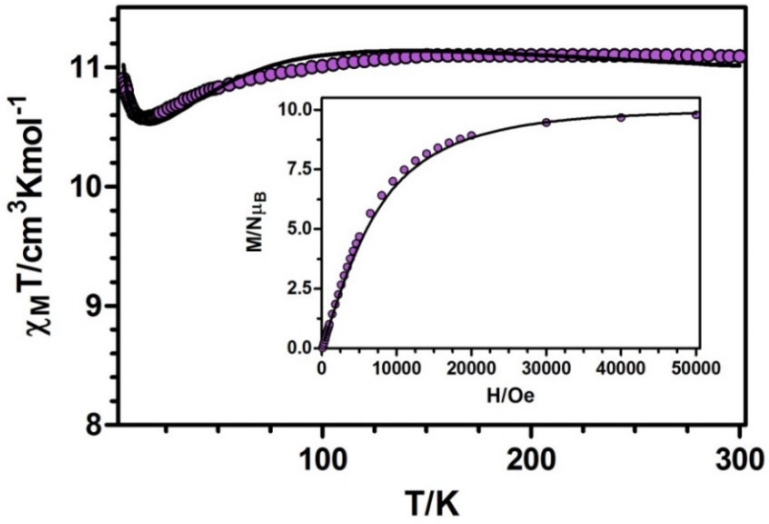

Figure 4.18.- Temperature dependence of $\chi_M T$ product at 1000 Oe for **32**. The black solid line shows the best fit. Inset: *M* versus *H* plot for **32** at 2 K. The black solid line represents the Brillouin function for a pair of non-interacting Co(II) (S = 3/2 and g = 2.06) and Gd(III) ions (S = 7/2 and g = 2.06).

The magnetization isotherm of **32** at 2 K (Figure 4.18, inset) shows a relatively rapid increase at low field, in agreement with a high spin ground state and a rapid

saturation of the magnetization at higher fields to reach a value of 9.79 $N\mu_B$ at 5 T, which is close to the expected saturation value for a couple of Co(II) and Gd(III) ions with *g* = 2.0 (10 $N\mu_B$). The experimental magnetization data falls slightly above the Brillouin curve for a pair of non-interacting Co(II) (*S* = 3/2) and Gd(III) (*S* = 7/2) ions with *g* = 2.06, thus confirming the existence of very moderate ferromagnetic interaction between the metal ions.

We now discuss the magnetic properties of **33**-**35**. At room temperature, the $\chi_M T$ values are higher than those calculated for independent Co(II) (*S* = 3/2, *g* = 2) and Ln(III) ions in the free-ion approximation (Figure 4.12, Table 4.4), which is mainly due to the orbital contribution of the Co(II) ion. The $\chi_M T$ products remain constant with decreasing temperature until 100 K and then decrease abruptly reaching the values listed in Table 4.4 at 2 K. This behaviour is due to both thermal depopulation of the levels that arise from spin-orbit coupling in the Co(II) ion and the thermal depopulation of the Stark sublevels of the Ln(III) ion.

Table 4.4.- *Direct current* magnetic data for compounds **33**-**35**.

Complex	Ground state of Ln(III) ion	$\chi_M T$ theor.[a] at 300K/exp. at 300 K/exp. at 2 K (cm^3 K mol^{-1})	M theor.[b]/M exp. at 2 K ($N\mu_B$)
33	$^7F_6$, g_J = 3/2	13.69/15.59/10.64	12/7.87
34	$^6H_{15/2}$, g_J = 4/3	16.04/16.01/9.27	13/8.49
35	$^4I_{15/2}$, g_J = 6/5	13.35/13.66/7.05	12/8.05

[a] $\chi_M T = \frac{N\beta^2}{3k}\{g_j^2 J(J+1) + g_{Co}^2 S(S+1)\}$

[b] $J = L + S_T;\ S_T = S_{Ln} + S_{Co};\ g_j = \frac{3}{2} + \frac{S_T(S_T+1)-L(L+1)}{2J(J+1)};\ M_s = g_J J N\mu_B$

As shown in Figure 4.19, upon increasing the applied external magnetic field, the magnetization of complexes **33**-**35** are increased to 7.87, 8.49 and 8.05 $N\mu_B$ at 5 T, respectively, but do not reach the expected saturation values (Table 4.4) for a couple of Co(II) and Ln(III) ions. The observed behaviour is due to the anisotropy of the Co(II) and Ln(III) ions.

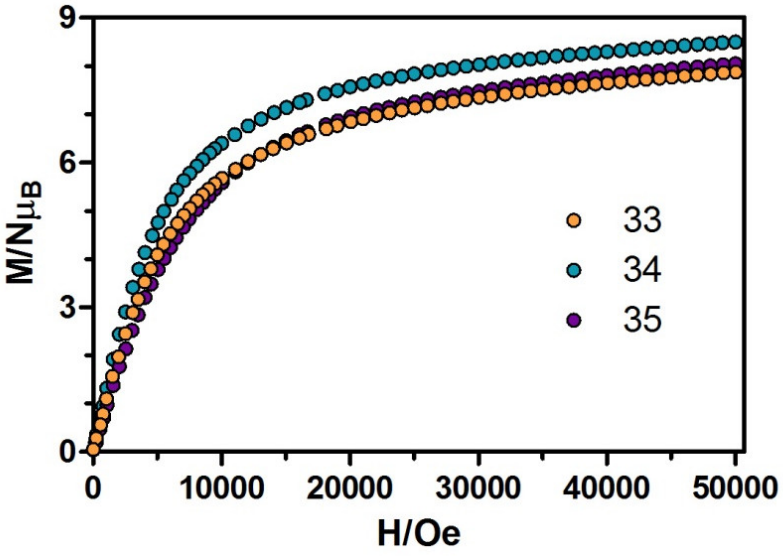

Figure 4.19.- M versus H plots for complexes **33**-**35** at 2 K.

To end up, dynamic *ac* magnetic susceptibility measurements as a function of the temperature at different frequencies were performed on complexes **33**-**36**. Under zero-external field none of them showed frequency dependency of the in-phase (χ_M') and out-of-phase signals (χ_M''), which could be due to fast resonant zero-field quantum of the magnetization (QTM) through degenerate energy levels. However, when the *ac* measurements were performed in the presence of a small external *dc* field of 1000 Oe, complex **34** (CoDy) showed a weak frequency dependency, whereas complex **36** (CoY) shows typical SIM behaviour below 6 K (Figures 4.20 - 4.22). The applied field of 1000 Oe was chosen because it induces the slowest relaxation rate for **36**, which does not significantly vary until fields as high as 3500 Oe (Figure 4.21).

The Cole-Cole diagrams in the temperature range 2-6.4 K for **36** exhibit semicircular shapes, with α values in the 0.27-0.05 range, suggesting multiple relaxation processes.

The temperature dependence of the magnetic relaxation times were used to construct an Arrhenius plot, which led to an effective energy barrier for the reversal of the magnetization of 15.68 K with $\tau_0 = 1.73 \cdot 10^{-6}$ s. The high value of τ_0, together with the low-temperature curvature of the relaxation times (Figure 4.22), strongly suggests that the quantum pathway of relaxation at very low temperatures is not fully suppressed by the effects of the applied field (1000 Oe). In view of this, the experimental relaxation data were fitted to Equation 5 of the Introduction, which takes into account the

simultaneous presence of both the thermal and QTM process, leading to the following set of parameters: τ_{QTM} = 2.14·10^{-4} s, τ_0 = 1.18·10^{-6} s and U_{eff} = 18.56 K. The obtained energy barrier values are still much lower than the expected values from the energy gap between the M_s = ± 1/2 and M_s = ± 3/2 levels (energy gap = 2D = 71 cm^{-1} = 102 K), which indicates that the relaxation takes place through a Raman mechanism. Therefore, the relaxation times where fitted to Equation 3 of the Introduction, obtaining the following parameters: b = 371.9 and n = 2.602 (Figure 4.23).

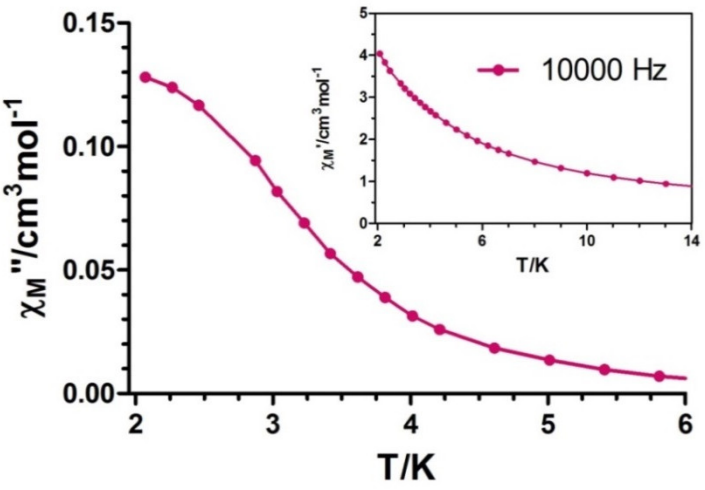

Figure 4.20.- Temperature dependence of in-phase χ_M' (inset) and out-of phase χ_M" components of the *alternating current* (*ac*) susceptibility for complex **34** under an applied field of 1000 Oe and a frequency of 10000 Hz.

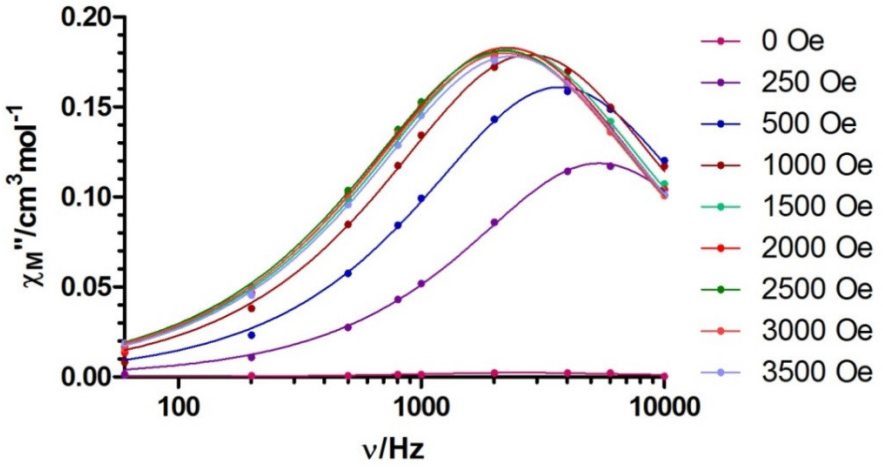

Figure 4.21.- Field dependence of the out-of-phase signal vs. frequency at 4 K for **36**.

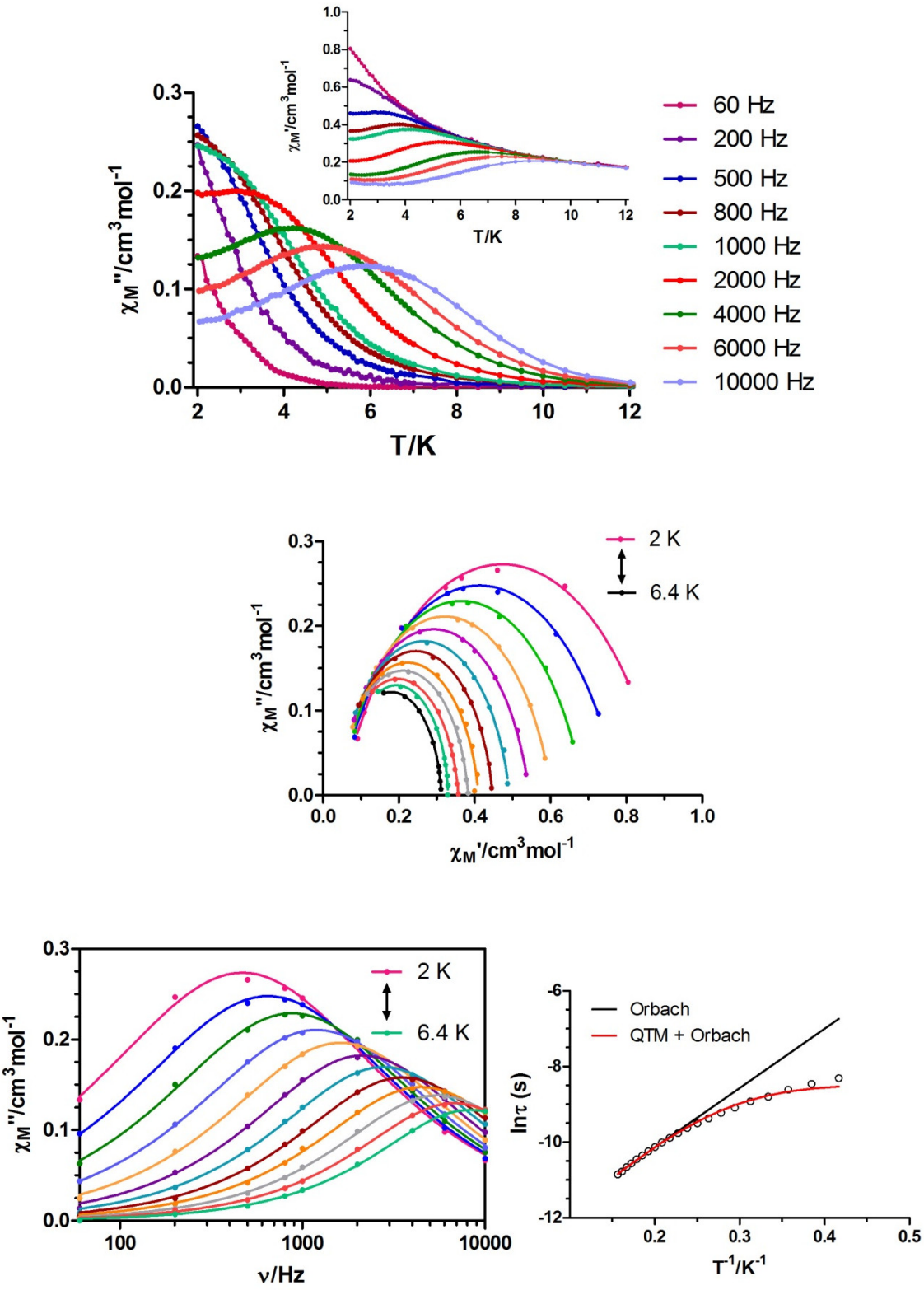

Figure 4.22.- Top: temperature dependence of in-phase χ_M' (inset) and out-of phase χ_M'' components of the *alternating current* susceptibility for complex **36** under an applied field of 1000 Oe. Medium: Cole-Cole plot. Bottom left: variable-temperature frequency dependency of the χ_M'' signal. Bottom right: Arrhenius plots for the relaxation times of **36** (black line). The red line corresponds to the fit for Orbach + QTM.

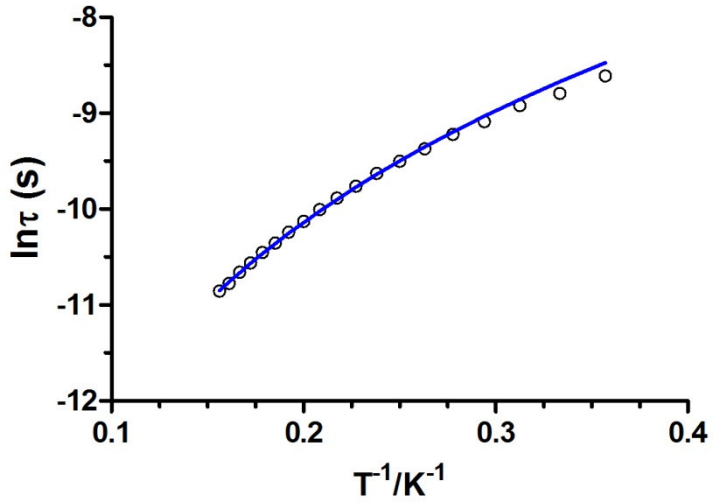

Figure 4.22.- Raman fit for the relaxation times.

In summary, out of the 15 complexes collected in this chapter after replacing the diamagnetic Zn(II) ion by the paramagnetic Cu(II), Ni(II) and Co(II) ions, three show a slight frequency dependency of the out-of-phase signal and only one shows typical SIM behaviour. In fact, this last one can not be compared to the Zn(II) based analogues, as the SIM behaviour comes only from the Co(II) ion. In conclusion, in order to obtain SMMs with high energy barriers, the weak magnetic exchange coupling between anisotropic 3d and 4f ions should be eliminated, as it leads to a small energy separation between the ground and first excited state or it creates a transversal field for the Ln(III) ion, which favours the QTM. On the other hand, the presence of Zn(II) ions or isotropic paramagnetic 3d metals favours the observation of slow relaxation of the magnetization.

4.4. CONCLUSIONS

The Zn(II) ions of complexes **11**-**21** have been substituted for Cu(II), Ni(II) and Co(II) ions, leading to a family of di-μ-phenoxo/*syn-syn* acetate triply bridged dinuclear M(II)Ln(III) complexes. The magnetic interactions between the metallic centres have been studied, obtaining weak positive coupling constants for the Gd(III) based derivatives. The weak coupling constants have been attributed to the fact that all the

complexes present folded structures with high hinge angles and to the presence of acetate bridges.

Ac magnetic measurements have also been performed, but only the NiDy (**29**), NiEr (**30**), CoDy (**34**) and CoY (**36**) dimers have shown frequency dependency of the out-of-phase signals, without any clear maxima in the temperature range technically available in most cases. Only complex **36** has shown SIM behaviour, with a low effective energy barrier of 15.68 K (obtained when considering only the Orbach relaxation process). These results, together with the results obtained in Chapter 3, show that the replacement of diamagnetic ions by paramagnetic anisotropic ions usually decreases the U_{eff} in 3d/4f systems.

4.5. BIBLIOGRAPHY

[1] M. Andruh, J. P. Costes, C. Diaz, S. Gao, *Inorg. Chem*., **2009**, *48*, 3342.

[2] **a)** E. Colacio, J. Ruiz-Sanchez, F. J. White, E. K. Brechin, *Inorg Chem*., **2011**, *50*, 7268; **b)** E. Colacio, J. Ruiz, A. J. Mota, M. A. Palacios, E. Cremades, E. Ruiz, F. J. White, E. K. Brechin, *Inorg. Chem*., **2012**, *51*, 5857; **c)** E. Colacio, J. Ruiz, A. J. Mota, M. A. Palacios, E. Ruiz, E. Cremades, M. M. Hänninen, R. Sillanpää, E. K. Brechin, *C. R. Chim*., **2012**, *15*, 878; **d)** E. Colacio, J. Ruiz, E. Ruiz, E. Cremades, J. Krzystek, S. Carretta, J. Cano, T. Guidi, W. Wernsdorfer, E. K. Brechin, *Angew. Chem., Int. Ed*. **2013**, *52*, 9130; **e)** S. Titos-Padilla, J. Ruiz, J. M. Herrera, E. K. Brechin, W. Wersndorfer, F. Lloret, E. Colacio, *Inorg. Chem.,* **2013**, *52*, 9620; **f)** M. A. Palacios, S. Titos-Padilla, J. Ruiz, J. M. Herrera, S. J. A. Pope, E. K. Brechin, E. Colacio, *Inorg. Chem*., **2014**, *53*, 1465.

[3] A. Bhunia, M. T. Gamer, L. Ungur, L. F. Chibotaru, A. K. Powell, Y. Lan, P. W. Roesky, F. Menges, C. Riehn, G. Niedner-Schatteburg, *Inorg. Chem*., **2012**, *51*, 9589.

[4] S. K. Langley, D. P. Wielechowski, V. Vieru, N. F. Chilton, B. Moubaraki, B. F. Abrahams, L. F. Chibotaru, K. S. Murray, *Angew. Chem. Int. Ed*., **2013**, *52*, 12014.

[5] L. Ungur, M. Thewissen, J.-P. Costes, W. Wernsdorfer, L. F. Chibotaru, *Inorg. Chem*. **2013**, *52*, 6328.

[6] M. Llunell, D. Casanova, J. Cirera, J. M. Bofill, P. Alemany, S. Alvarez, M. Pinsky, D. Avnir, *SHAPE*, v1.1b, Barcelona, Spain, **2005**.

[7] N. F. Chilton, R. P. Anderson, L. D. Turner, A. Soncini, K. S. Murray, *J. Comput. Chem*., **2013**, *34*, 1164.

[8] **a)** T. Rajeshkumar, H. V. Annadata, M. Evangelisti, S. K. Langley, N.F. Chilton, K. S. Murray, G. Rajaraman, *Inorg. Chem.*, **2015**, *54*, 1661; **b)** G. Rajaraman, F. Totti, A. Bencini, A. Caneschi, R. Sessoli, D. Gatteschi, *Dalton Trans.*, **2009**, 3153.

[9] J.P. Costes, F. Dahan, A. Dupuis, J.-P. Laurent, *Chem. Eur. J.*, **1998**, *4*, 1616.

[10] S. Alvarez, D. Avnir, M. Llunell, M. Pinsky, *New J. Chem.*, **2002**, *26*, 996.

[11] V. Chandrasekhar, A. Dey, A. J. Mota, E. Colacio, *Inorg. Chem.*, **2013**, *52*, 4554.

[12] E. Colacio, J. Ruiz, A. J. Mota, M. A. Palacios, E. Ruiz, E. Cremades, M. M. Hänninen, R. Sillanpää, E. K. Brechin, *C. R. Chimie*, **2012**, *15*, 878.

[13] **a)** J. P. Costes, F. Dahan, A. Dupuis, J. P. Laurent, *C. R. Acad. Sci. Paris IIc*, **1998**, 417; **b)** J. P. Costes, F. Dahan, J. Garcia Tojal, *Chem. Eur. J.*, **2002**, *8*, 5430.

CHAPTER 5

DINUCLEAR Mn(II)Ln(III) COMPLEXES, SETTING BASES FOR OBTAINING COMPLEXES WITH LARGE MAGNETO-CALORIC EFFECT

5.1. INTRODUCTION

Heteropolynuclear 3d-Gd(III) complexes are attracting much attention because, amongst other things, they have potential applications as low temperature magnetic coolers. These systems show an enhanced magneto-caloric effect (MCE), which is based on the change of magnetic entropy upon application of a magnetic field, that can be exploited for cooling applications via adiabatic demagnetisation.[1]

In contrast to SMMs, the MCE is greatly enhanced in molecules containing isotropic magnetic ions that exhibit weak ferromagnetic interactions between the metal ions, as this generates multiple low-lying excited and field-accessible states that can contribute to the magnetic entropy of the system. Taking this into account, 3d/Gd(III) complexes containing isotropic transition metals such as Mn(II), Fe(III), Cr(III) and Cu(II) are very good candidates for molecular refrigeration.[2]

This chapter collects the synthesis, structural characterization and magnetic properties of a series of Mn(II)Ln(III) dinuclear and tetranuclear complexes (Ln = Gd and Dy) with the ligands H_2L and H_2L^1. Magneto structural correlations that can help to obtain ferromagnetically coupled Mn(II)Gd(III) complexes have been established from these and other complexes found in bibliography. The large anisotropy of the Dy(III) ions, together with the coupling to paramagnetic isotropic Mn(II) ions, could lead to the presence of SMM behaviour in the Dy(III) derivatives.

5.2. PREPARATION OF COMPLEXES

5.2.1. $[Mn(\mu\text{-}L)(\mu\text{-}OAc)Ln(NO_3)_2]\cdot CH_3CN\cdot H_2O$, Ln (III) = Gd (37), Dy (38)

To a solution of 30.6 mg (0.125 mmol) of $Mn(OAc)_2\cdot 4H_2O$ in 5 mL of acetonitrile/methanol mixture (80:20) were added with continuous stirring 64.3 mg (0.125 mmol) of H_2L and 0.125 mmol of the corresponding $Ln(NO_3)_3\cdot nH_2O$. The resulting yellow solution was filtered and allowed to stand at room temperature. After one day, well-formed prismatic yellow crystals of **37** and **38** were obtained with yields of 32 and 26 %, respectively. Anal. Calcd. for $C_{24}H_{28}N_5O_{13}Br_2MnGd$: C, 29.83; H, 2.92; N, 7.25. Found: C, 29.91; H, 2.93; N, 7.29. Anal. Calcd. for $C_{24}H_{28}N_5O_{13}Br_2MnDy$: C, 29.66; H, 2.90; N, 7.21. Found: C, 29.71; H, 2.91; N, 7.23.

5.2.2. [Mn(CH$_3$OH)(μ-L^1)Dy(NO$_3$)$_3$] (39)

To a solution of H_2L^1 (55.7 mg, 0.125 mmol) in 5 mL of MeOH were subsequently added with continuous stirring 31.4 mg (0.125 mmol) of $Mn(NO_3)_2{\cdot}4H_2O$ and 54.8 mg (0.125 mmol) of $Dy(NO_3)_3{\cdot}5H_2O$. The resulting pistachio green solution was filtered and allowed to stand at room temperature. After several days, well-formed prismatic colourless crystals of [Mn(CH$_3$OH)(μ-L^1)Dy(NO$_3$)$_3$] (**39**) were obtained with a yield of 15 %. Anal. Calcd. for $C_{26}H_{41}N_6O_{14}MnDy$: C, 35.52; H, 4.70; N, 9.56. Found: C, 35.61; H, 4.68; N, 9.59.

5.2.3. [Mn(μ-L^1)(μ-OAc)Ln(NO$_3$)$_2$], Ln(III) = Gd (40), Dy (41)

30.6 mg (0.125 mmol) of $Mn(OAc)_2{\cdot}4H_2O$ and 0.125 mmol of the corresponding $Ln(NO_3)_3{\cdot}nH_2O$ were successively added to a solution of H_2L^1 (55.7 mg, 0.125 mmol) in 5 mL of MeOH. The resulting solution was stirred during 30 minutes and then was filtered to eliminate any amount of insoluble material. The filtrate was allowed to stand at room temperature for several days, whereupon colourless X-ray quality crystals were formed. Yields: 15 and 17 % respectively for **40** and **41**. Anal. Calcd. for $C_{27}H_{40}N_5O_{12}MnGd$: C, 38.66; H, 4.81; N, 8.35. Found: C, 38.71; H, 4.78; N, 8.39. Anal. Calcd. for $C_{27}H_{40}N_5O_{12}MnDy$: C, 38.42; H, 4.78; N, 8.30. Found: C, 38.51; H, 4.79; N, 8.39.

5.2.4. [Mn(μ-L^1)(μ-9-An)Ln(NO$_3$)$_2$]·2CH$_3$CN, Ln (III) = Gd (42), Dy (43)

To a solution of H_2L^1 (55.7 mg, 0.125 mmol) in 5 mL of MeOH were subsequently added 31.4 mg (0.125 mmol) of $Mn(NO_3)_2{\cdot}4H_2O$ and 0.125 mmol of the corresponding $Ln(NO_3)_3{\cdot}nH_2O$ with continuous stirring. To this solution was added dropwise another solution containing 27.8 mg of 9-anthracenecarboxylic acid (0.125 mmol) and 12.6 mg of triethylamine (0.125 mmol), immediately affording a precipitate, which was filtered off and recrystallized from acetonitrile. Yields: 15 and 21 % respectively for **42** and **43**. Anal. Calcd. for $C_{44}H_{52}N_7O_{12}MnGd$: C, 48.79; H, 4.84; N, 9.05. Found: C, 48.81; H, 4.88; N, 9.09. Anal. Calcd. for $C_{44}H_{52}N_7O_{12}MnDy$: C, 48.56; H, 4.82; N, 9.01. Found: C, 48.61; H, 4.79; N, 9.03.

5.2.5. {(μ$_3$-CO$_3$)$_2$[Mn(μ-L^1)Gd(NO$_3$)]$_2$}·2CH$_3$CN (44) and {(μ$_3$-CO$_3$)$_2$[Mn(μ-L^1)Dy(NO$_3$)]$_2$}·2CH$_3$OH (45)

To a solution of H_2L^1 (55.7 mg, 0.125 mmol) in 5 mL of MeOH were subsequently added with continuous stirring 31.4 mg (0.125 mmol) of $Mn(NO_3)_2{\cdot}4H_2O$, 0.125 mmol of

the corresponding $Ln(NO_3)_3 \cdot nH_2O$ and 12.6 mg of triethylamine (0.125 mmol). The resulting solution was filtered and allowed to stand at room temperature, affording colourless crystals of **45**. Compound **44** was recrystallized from acetonitrile in order to obtain X-ray quality crystals. Yields: 16 and 22 % respectively for **44** and **45**. Anal. Calcd. for $C_{60}H_{86}N_{12}O_{20}Mn_2Gd_2$: C, 41.90; H, 5.04; N, 9.77. Found: C, 41.95; H, 5.08; N, 9.79. Anal. Calcd. for $C_{56}H_{90}N_8O_{24}Mn_2Dy_2$: C, 39.70; H, 5.35; N, 6.61. Found: C, 39.81; H, 5.41; N, 6.63.

5.3. EXPERIMENTAL RESULTS

Similarly to what seen in Chapters 3 and 4, the reaction of H_2L with $Mn(OAc)_2 \cdot 4H_2O$ and $Ln(NO_3)_3 \cdot nH_2O$ in acetonitrile/methanol mixture and in 1:1:1 molar ratio allows the formation of di-μ-phenoxo/*syn-syn* acetate triply bridged dinuclear species $[Mn(\mu\text{-}L)(\mu\text{-}OAc)Gd(NO_3)_2] \cdot CH_3CN \cdot H_2O$ (**37**) and $[Mn(\mu\text{-}L)(\mu\text{-}OAc)Dy(NO_3)_2] \cdot CH_3CN \cdot H_2O$ (**38**) (Figure 5.1). The reaction of H_2L^1 with $Mn(NO_3)_2 \cdot 4H_2O$ and $Dy(NO_3)_3 \cdot 5H_2O$ in MeOH and in 1:1:1 ratio led to crystals of complex $[Mn(CH_3OH)(\mu\text{-}L^1)Dy(NO_3)_3]$ (**39**). The same reaction but using $Mn(OAc)_2 \cdot 4H_2O$ instead of $Mn(NO_3)_2 \cdot 4H_2O$ and the appropriated lanthanide led to the two dinuclear complexes $[Mn(\mu\text{-}L^1)(\mu\text{-}OAc)Gd(NO_3)_2]$ (**40**) and $[Mn(\mu\text{-}L^1)(\mu\text{-}OAc)Dy(NO_3)_2]$ (**41**), where the Mn(II) and Ln(III) ions are bridged by the two phenoxo groups of the ligand and an acetate bridge. The acetate bridge could be replaced by 9-anthracenecarboxylate in complexes $[Mn(\mu\text{-}L^1)(\mu\text{-}9\text{-}An)Gd(NO_3)_2] \cdot 2CH_3CN$ (**42**) and $[Mn(\mu\text{-}L^1)(\mu\text{-}9\text{-}An)Dy(NO_3)_2] \cdot 2CH_3CN$ (**43**) by reacting a methanolic solution containing H_2L^1, $Mn(NO_3)_2 \cdot 4H_2O$ and the corresponding $Ln(NO_3)_3 \cdot nH_2O$ (1:1:1 molar ratio) with another methanolic solution containing 9-anthracene carboxylic acid and Et_3N (1:1 molar ratio) and recrystallizing the obtained precipitate from acetonitrile. To end up, the tetrameric complexes $\{(\mu_3\text{-}CO_3)_2[Mn(\mu\text{-}L^1)Gd(NO_3)]_2\} \cdot 2CH_3CN$ (**44**) and $\{(\mu_3\text{-}CO_3)_2[Mn(\mu\text{-}L^1)Dy(NO_3)]_2\} \cdot 2CH_3OH$ (**45**) were obtained using the same reaction conditions as for **39** with the corresponding lanthanide but adding Et_3N, recrystallizating complex **44** from acetonitrile in order to obtain X-ray quality crystals.

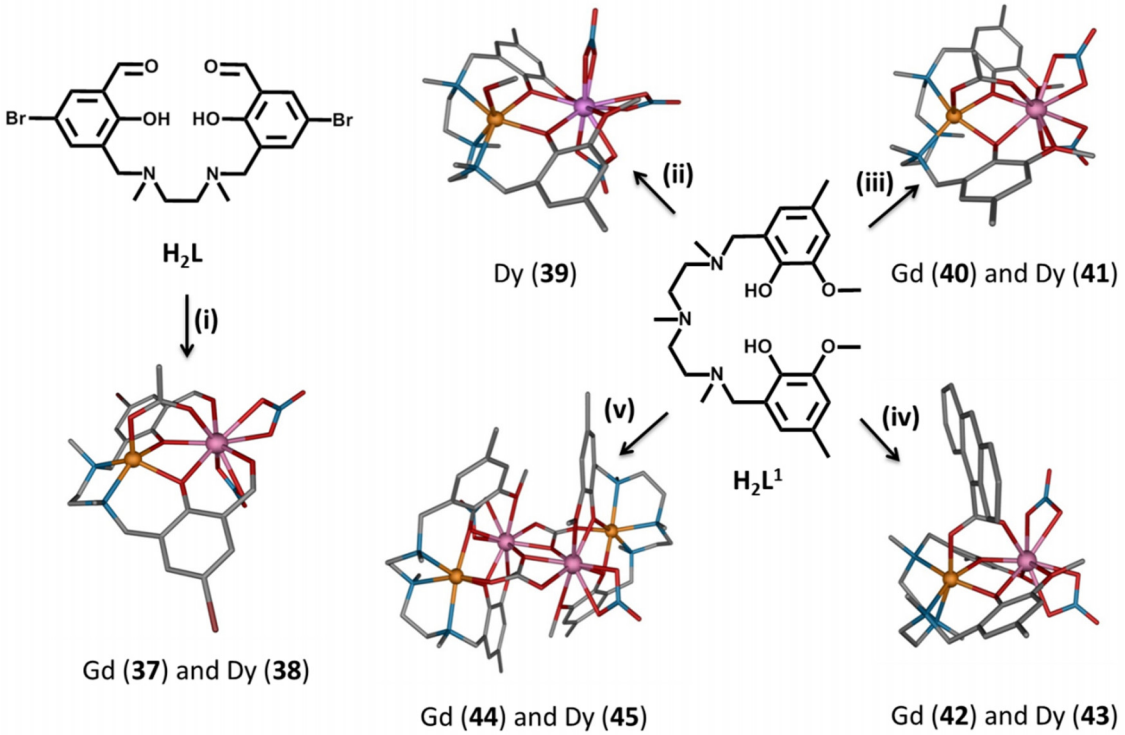

Figure 5.1.- (i) H_2L/$Mn(OAc)_2{\cdot}4H_2O$/ $Ln(NO_3)_3{\cdot}nH_2O$, 1:1:1 in CH_3CN/MeOH (Ln = Gd (**37**), Dy (**38**)). (ii) H_2L^1/$Mn(NO_3)_2{\cdot}4H_2O$/$Dy(NO_3)_3{\cdot}5H_2O$, 1:1:1 in MeOH (**39**). (iii) H_2L^1/$Mn(OAc)_2{\cdot}4H_2O$/ $Ln(NO_3)_3{\cdot}nH_2O$, 1:1:1 in MeOH (Ln = Gd (**40**), Dy (**41**)). (iv) H_2L^1/$Mn(NO_3)_2{\cdot}4H_2O$/$Ln(NO_3)_3{\cdot}nH_2O$/H_2-9-An/Et_3N, 1:1:1:1:1 in MeOH, recrystallization from CH_3CN (Ln = Gd (**42**), Dy (**43**)). (v) H_2L^1/$Mn(NO_3)_2{\cdot}4H_2O$/$Ln(NO_3)_3{\cdot}nH_2O$/Et_3N, 1:1:1:1 in MeOH (Ln = Dy (**45**)) and recrystallization from CH_3CN (Ln = Gd (**44**)).

5.3.1. Crystal Structures of Complexes 37-45

Complexes **37** and **38** crystallize in the *P2₁/n* space group and are very similar to the Zn(II) and Cu(II) based dinuclear complexes presented in Chapters 3 and 4 (Figure 5.1). Bond lengths and angles are found in Appendices (Table A.14), as well as SHAPE measurement results (Table A.31 and A.33). The average Mn-O-Ln angles are of 97.53 and 97.72° respectively for **37** and **38** and the average hinge angles of the Mn-(μ-O)$_2$-Ln bridging fragment are higher than in the Zn(II) and Cu(II) based analogues (34.85° in both of them). The aromatic rings form dihedral angles of 15.08 and 15.38°, respectively for **37** and **38**. Due to the similarity with previously reported complexes, any further discussion on the structures of **37** and **38** will be omitted.

Complex **39** also crystallizes in the *P2₁/n* space group and is isostructural to the Mn(II)Gd(III) complex reported by Colacio, Brechin, Evangelisti et al. in 2013.[3] Its

molecular structure consists of dinuclear molecules in which the Mn(II) and Dy(III) ions are bridged by two phenoxo groups of the $(L^1)^{2-}$ ligand (Figure 5.2).

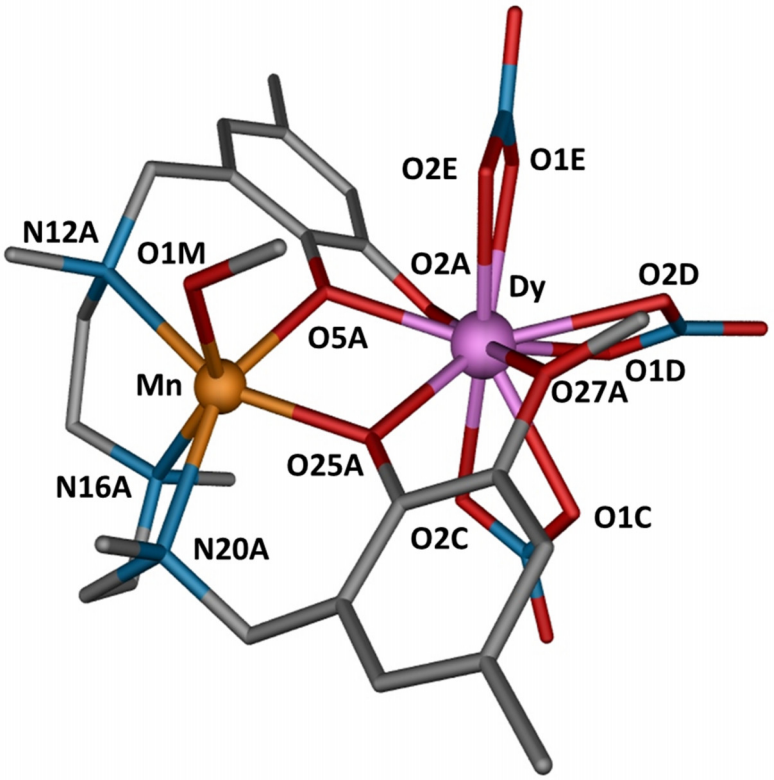

Figure 5.2.- Perspective view of the molecular structure of complex **39**. Hydrogen atoms are omitted for the sake of clarity. Colour code: N = blue, O = red, C = grey, Mn = orange, Ln = pink.

Besides the two phenoxo bridging oxygen atoms, the MnN_3O_3 coordination polyhedron is formed by three nitrogen atoms from the amine group and one oxygen atom belonging to a methanol molecule. The three oxygen atoms and, consequently, the three nitrogen atoms occupy *fac* positions in the trigonally distorted coordination polyhedron, which shows CshM values of 5.542 and 6.578 respectively for trigonal prism and octahedron ideal geometries (Appendices, Table A.32). The Mn-O and Mn-N distances are found in the 2.146(3)-2.217(3) Å and 2.295(4)-2.377(3)Å ranges, respectively.

The DyO_{10} coordination sphere is made of two phenoxo bridging oxygen atoms, two methoxo oxygen atoms and six oxygen atoms belonging to three bidentate nitrate anions. The DyO_{10} coordination sphere is rather asymmetric, exhibiting short Dy-$O_{phenoxo}$ distances of 2.291(3) and 2.312(3) Å, long Dy-$O_{methoxo}$ distances of 2.556(3)

and 2.611(3) Å and intermediate Dy-$O_{nitrate}$ distances (in the 2.464(3)-2.517(3) Å range). The use of the continuous shape measure theory and SHAPE software indicates that the DyO_{10} coordination sphere is close to a sphenocorona but intermediate between several ten-vertex polyhedral (Appendices, Table A.34).

The Mn-(μ-O)$_2$-Dy bridging fragment is almost planar with a hinge angle of 4.49 ° and rather symmetric, with similar pairs of Mn-O bond distances (2.146(3) Å and 2.152(3) Å), Dy-O bond distances (2.291(3) Å and 2.312(3) Å) and Mn-O-Dy bridging angles (110.36(12) and 110.93(12)°). To end up with **39**, it should be stressed out that in this complex, the molecules are held in pairs by a couple of symmetrically related intermolecular hydrogen bonds involving the non-coordinated O atom of one of the bidentate nitrate anions and the methanol molecule, with O···O distances of 2.829 Å (Figure 5.3).

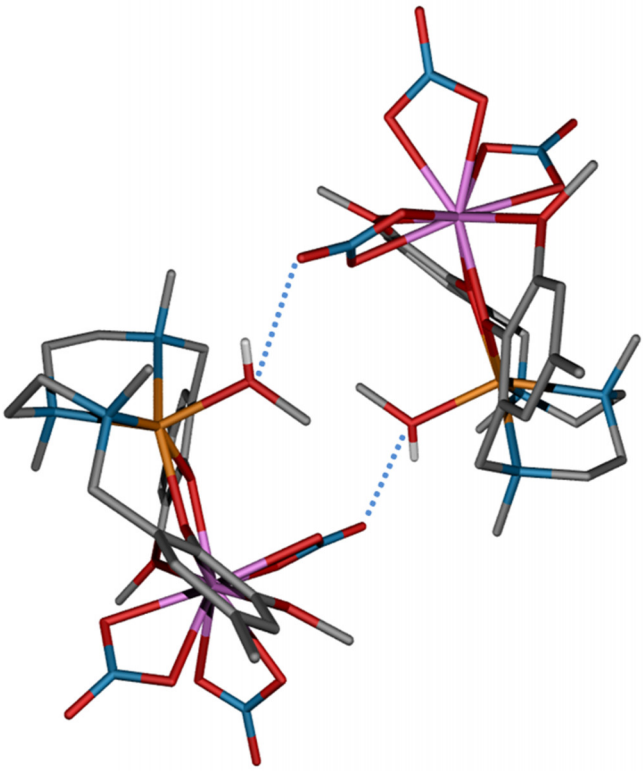

Figure 5.3.- A perspective view of the structure of **39** together with intermolecular (blue dotted lines) hydrogen bonds.

The structures of complexes **40** and **41** are given in Figure 5.4, where the most significant change compared to **39** is the substitution of the coordinated methanol and one of the bidentate nitrate molecules for a bridging acetate group.

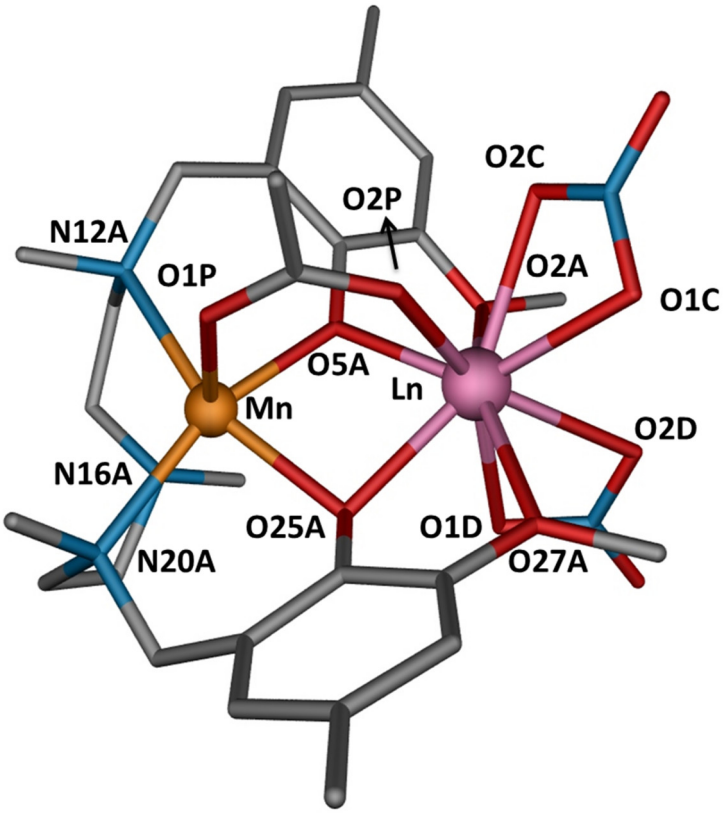

Figure 5.4.- Perspective view of the molecular structure of complexes **40** and **41**. Hydrogen atoms are omitted for the sake of clarity. Colour code: N = blue, O = red, C = grey, Mn = orange, Ln = pink.

As expected, the incorporation of a third bridging fragment forces the structures to be folded with higher hinge angles (23.30° for **40** and 23.51° for **41**), which leads to a decrease in the average Mn-O-Ln angles (101.94° for **40** and 102.06° for **41**). The acetate bridge also affects the MnN_3O_3 coordination spheres, leading to octahedral coordination environments according to SHAPE measurement results (Appendices, Table A.32) and reduces to 9 the number of oxygen atoms coordinated to the lanthanide atoms. These complexes do not show hydrogen bonds.

The structures of complexes **42** and **43** are shown in Figure 5.5 and are very similar to those of complexes **40** and **41** but with a 9-anthracenecarboxylate bridging ligand instead of an acetate ligand connecting the Mn(II) and Ln(III) ions, and with two acetonitrile molecules of crystallization.

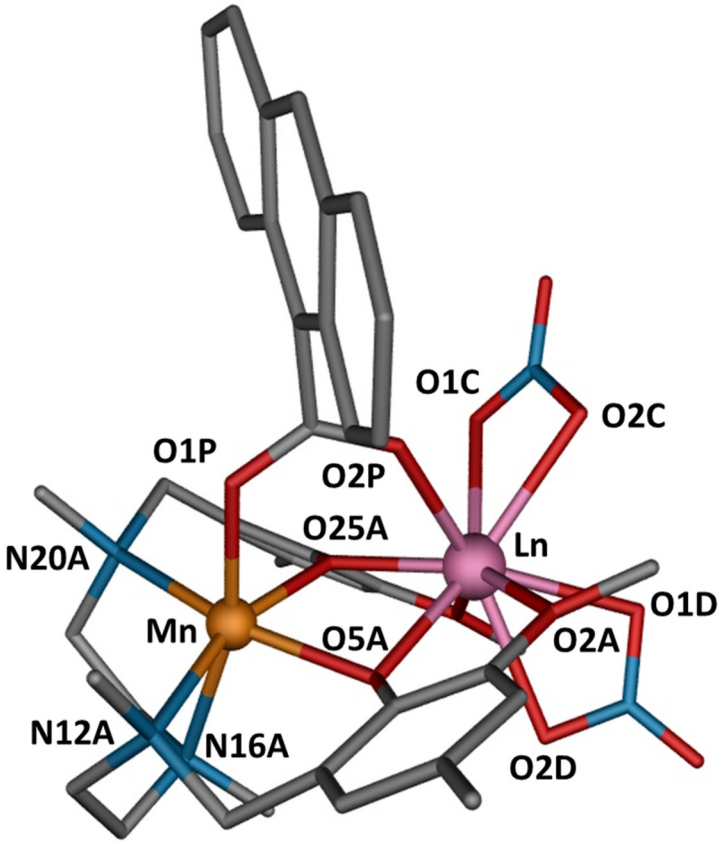

Figure 5.5.- Perspective view of the molecular structure of complexes **42** and **43**. Hydrogen atoms and solvent molecules are omitted for the sake of clarity. Colour code: N = blue, O = red, C = grey, Mn = orange, Ln = pink.

Compared to the acetate bridged analogues, complexes **42** and **43** exhibit similar bond lengths, accompanied with slightly smaller hinge angles (20.73° for **42** and 20.72° for **43**). Bond lengths and angles can be found in Appendices (Table A.15), together with SHAPE measurement results (Tables A.32 and A.33) and further discussion on the structures of these complexes will be omitted.

Finally, complexes **44** and **45** consist in centrosymmetric tetranuclear compounds, which are made by two [Mn(μ-L^1)Ln(NO_3)] dinuclear units connected by two tetradentate carbonate bridging ligands acting in a μ_3-κ^2-O,O':κ-O:κ-O" coordination mode (Figure 5.6). As seen in the isostructural Zn_2Ln_2 (Ln(III) = Gd, Dy and Yb) complexes reported by Colacio et al,[4] the carbonate ligand is generated from the fixation of atmospheric CO_2 in basic medium.

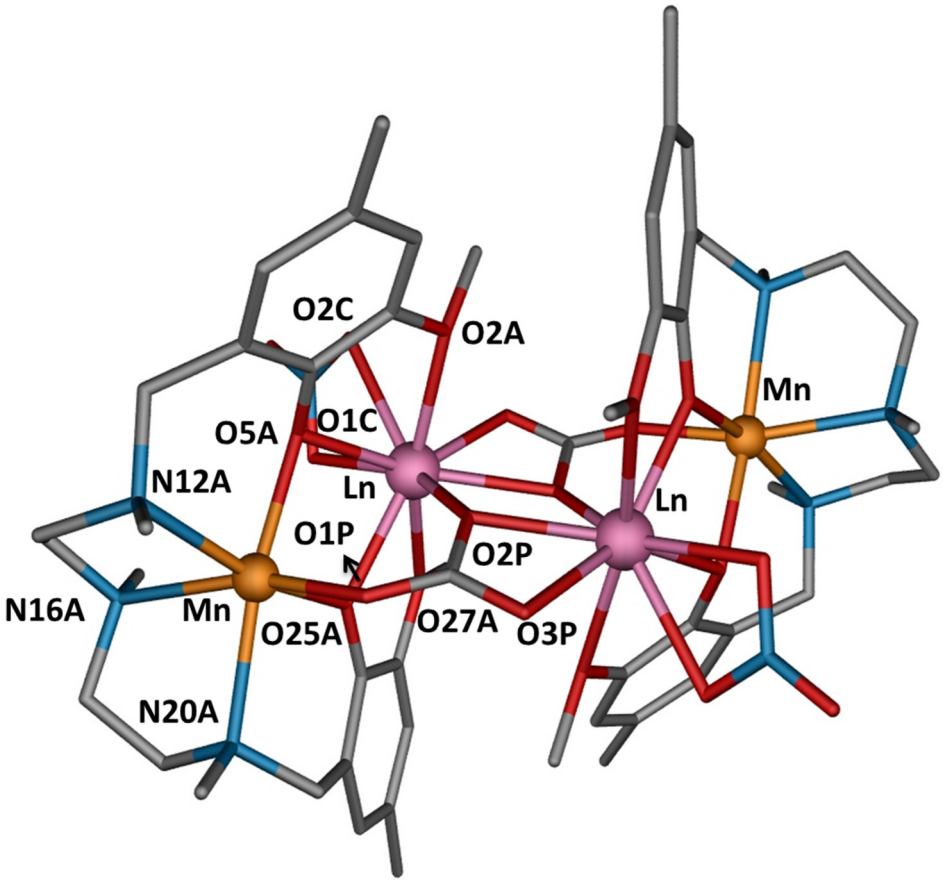

Figure 5.6.- Perspective view of the molecular structure of complexes **44** and **45**. Hydrogen atoms and solvent molecules are omitted for the sake of clarity. Colour code: N = blue, O = red, C = grey, Mn = orange, Ln = pink.

The Mn(II) ions show similar coordination environments to those of complexes **40**-**43**, but they are coordinated to a carbonate bridge instead of to an acetate or anthracetate bridge. The lanthanide ions exhibit rather asymmetric LnO_9 coordination spheres, which are made by the two phenoxo bridging oxygen atoms, the two methoxo oxygen atoms, three oxygen atoms from the carbonate bridging groups and two oxygen atoms belonging to a bidentate nitrate anion. The latter and the chelating part of the carbonate ligand occupy *cis* positions in the Ln(III) coordination spheres. The Ln-O distances are in the 2.316(3)-2.568(3) Å and 2.266(4)-2.567(4) Å ranges respectively for **44** and **45**. In these complexes, the closest ideal geometry according to SHAPE measurements results is the muffin (MFF-9), although the LnO_9 coordination spheres can be considered as intermediate between several reference polyhedron (Appendices, Table A.33).

The Mn-(μ-O)$_2$-Ln bridging fragments show smaller hinge angles than in complexes **40**-**43**, being of 15.88° for **44** and of 13.34° for **45**, whereas the Ln-(μ-O)$_2$-Ln bridging fragments are planar. The intratetranuclear Mn···Ln and Ln···Ln distances are respectively 3.531(2) and 4.025(1) Å for **44** and 3.498(2) and 4.063(1) Å for **45**.

In complex **45** one of the methanol molecules forms bifurcated hydrogen bonds with one of the oxygen atoms of the chelating part of the carbonate ligand and the oxygen atom of a second methanol molecule, with donor−acceptor distances of 2.699 and 2.720 Å, respectively (Figure 5.7).

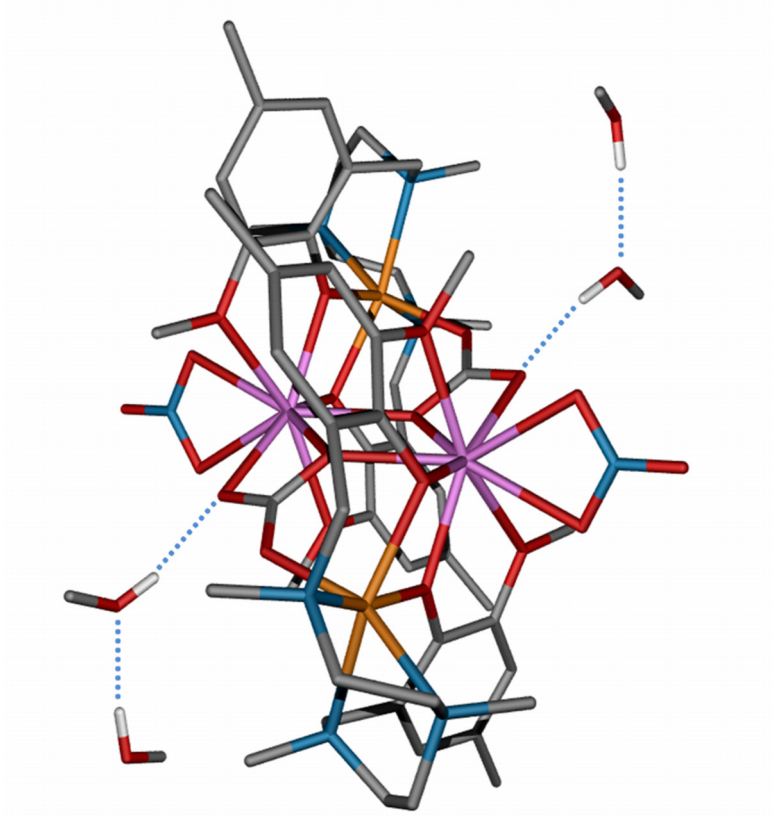

Figure 5.7.- A perspective view of the structure of **45** together with intermolecular (blue dotted lines) hydrogen bonds.

5.3.2. Magnetic Properties of Complexes 37-45

The temperature dependence of the $\chi_M T$ products (χ_M being the molar paramagnetic susceptibility of the compound) of some of the complexes were measured on polycrystalline samples under an applied magnetic field of 0.1 T and are represented in Figures 5.8-5.10.

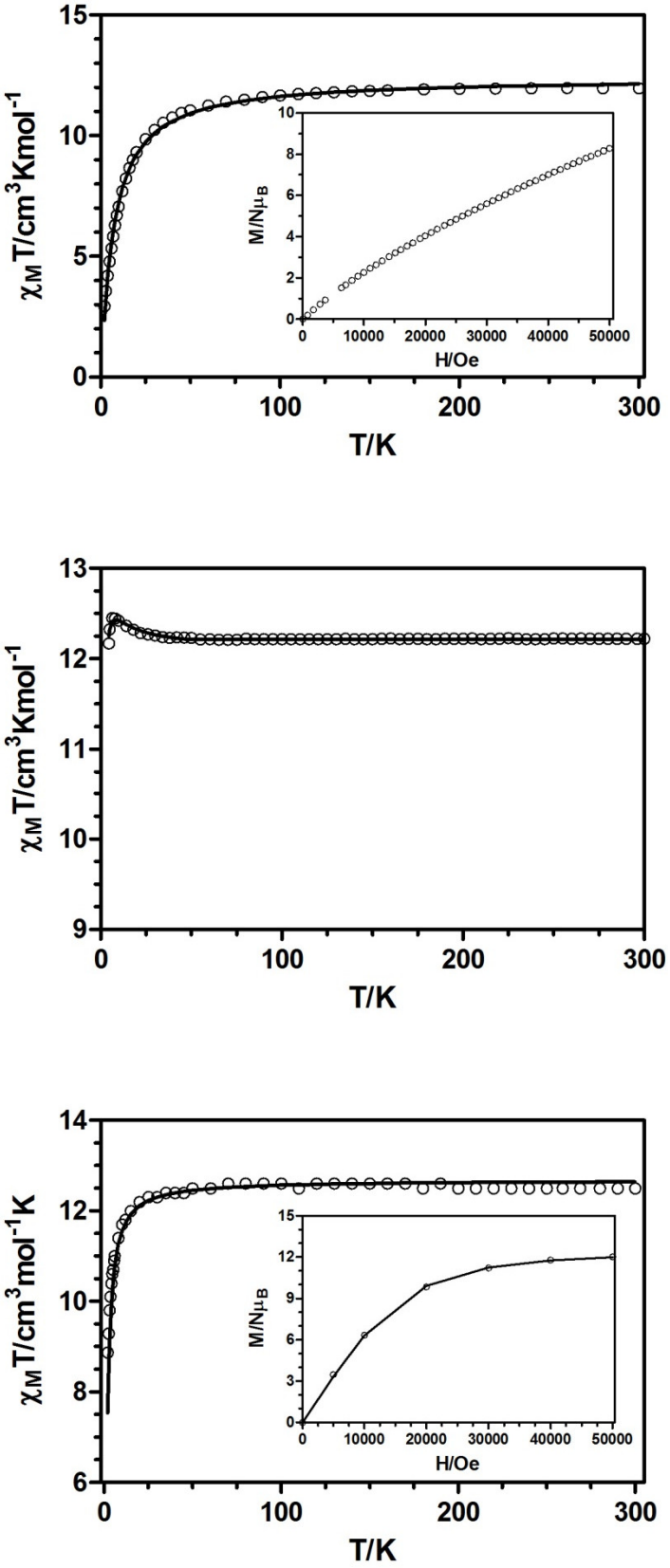

Figure 5.8.- Temperature dependence of the $\chi_M T$ product for **37** (top), **40** (middle) and **42** (bottom). Insets: field dependence of the magnetization for **37** and **42**. The solid lines are generated from the best fit to the magnetic parameters.

Starting with the dinuclear Mn(II)Gd(III) complexes **37** and **42**, the room temperature $\chi_M T$ values of 12.0 and 12.50 $cm^3 \cdot K \cdot mol^{-1}$ are in agreement with the expected value for a pair of non-interacting Mn(II) (S = 5/2) and Gd(III) (S = 7/2) ions (12.25 $cm^3 \cdot K \cdot mol^{-1}$) with g = 2. On lowering the temperature, the $\chi_M T$ product remains constant until 100 and 35 K, respectively for **37** and **42**, and then drops abruptly to reach values of 2.90 and 8.87 $cm^3 \cdot K \cdot mol^{-1}$ at 2 K, respectively. The observed behaviour is due to AF interactions within the dinuclear units, which are stronger in the case of **37**. The field dependence of the magnetization at 2 K for **37** shows a gradual increase when increasing the field, reaching a value of 8.3 $N\mu_B$ at 5 T (Figure 5.8, inset). This value is much lower than the expected value for a S_T = 6 spin ground state (12 $N\mu_B$ for g = 2), which is due to the AF interactions. On the other hand, complex **42** shows a relatively rapid increase in the magnetization at low fields and a rapid saturation that is almost complete above 4 T, reaching a value of 12.02 $N\mu_B$ at 5 T.

The magnetic data for complexes **37** and **42** have been modelled by using the PHI program[5] and the following spin-Hamiltonian:

$$\mathcal{H} = -JS_{Mn}S_{Gd} + g\mu_B S_{Mn}B + g\mu_B S_{Gd}B \qquad (\textit{Equation 5.1})$$

where the first term accounts for the isotropic magnetic exchange coupling between the Mn(II) and Gd(III) ions and the last two are the Zeeman terms, considered to be equal for both atoms. The best fit of the susceptibility data led to the following set of parameters for **37**: J = - 0.82 cm^{-1} and g = 2.0 with $R = 1.8 \cdot 10^{-4}$. On the other hand, the susceptibility and magnetization data were simultaneously fitted for complex **42**, affording the following set of parameters: J = - 0.165 cm^{-1} and g = 2.03 with $R = 5.8 \cdot 10^{-5}$. The obtained experimental exchange coupling constants were supported by DFT calculations on the X-ray structures, which led to values of - 2.22 and - 0.32 cm^{-1}, respectively for **37** and **42**.

The magnetic behaviour of complex **40** is slightly different from that observed for **37** and **42**, as the $\chi_M T$ product shows a weak increase below 35 K to reach a maximum value of 12.45 $cm^3 \cdot K \cdot mol^{-1}$ at 6.5 K and a further decrease dropping until 12.17 $cm^3 \cdot K \cdot mol^{-1}$ at 4.5 K. The observed increase could be due to modest ferromagnetic interactions between Mn(II) and Gd(III) ions, whereas the drop could be provoked by intermolecular interactions. The magnetic susceptibility data were then fitted to the following Hamiltonian, which takes into account both effects:

$$\mathcal{H} = -JS_{Mn}S_{Gd} - zJ'\langle S_z\rangle S_z + g\mu_B S_{Mn}B + g\mu_B S_{Gd}B \qquad (\textit{Equation 5.2})$$

The best fitting parameters were J = + 0.24 cm^{-1}, zJ' = -0.02 cm^{-1} and g = 2.0 for both ions with R = $1.78 \cdot 10^{-6}$. The DFT calculated J_{MnGd} value of + 0.05 cm^{-1} supports the experimentally obtained magnetic coupling constant.

The tetranuclear complex **44** shows a value of 26.1 $cm^3 \cdot K \cdot mol^{-1}$ at 300 K, which agrees well with the expected value for the sum of two Mn(II) and two Gd(III) ions with g = 2.0 (24.5 $cm^3 \cdot K \cdot mol^{-1}$). Upon cooling, this value remains constant until 30 K and then starts decreasing to reach a value of 20.60 $cm^3 \cdot K \cdot mol^{-1}$ at 2 K (Figure 5.9), which suggest the presence of overall AF interactions in the molecule. The magnetization plot for **44**, with a relatively rapid increase in the magnetization at low fields and a rapid saturation that is almost complete above 4 T, shows a saturation value of 25.4 $N\mu_B$ at 5 T, which is in relatively good agreement with the theoretical value for a S_T = 12 spin ground state (24 $N\mu_B$ for g = 2.0, 25.2 $N\mu_B$ for g = 2.1). The magnetic susceptibility and magnetization data of **44** were simultaneously fitted using the following Hamiltonian:

$$\mathcal{H} = -J_1(S_{Mn}S_{Gd} + S_{Mn*}S_{Gd*}) - J_2 S_{Gd}S_{Gd*} - J_3(S_{Mn}S_{Gd*} + S_{Mn*}S_{Gd}) - J_4 S_{Mn}S_{Mn*} + g\mu_B(S_{Mn} + S_{Mn*})B + g\mu_B(S_{Gd} + S_{Gd*})B \quad (\textit{Equation 5.3})$$

where J_1, J_2, J_3 and J_4 account for the exchange pathways described in Figure 5.9. In order to avoid overparametrization, the exchange pathways J_3 and J_4, where the metallic ions are quite far from each other (at distances of 5.525 and 8.353 Å respectively for pathways 3 and 4), were not taken into account. The best fit parameters after fixing g to 2.0 for all the ions were J_1 = - 0.13 cm^{-1} and J_2 = + 0.06 cm^{-1}, with R = $7.12 \cdot 10^{-5}$. The obtained results suggest the presence of very weak AF interactions between the di-μ-phenoxo/carboxylate triply bridged Mn(II) and Gd(III) ions, combined with very weak F interactions between Gd(III) ions. DFT calculations carried out on the X-ray structure support the experimentally obtained values, with J_1 = - 0.065 cm^{-1} and J_2 = + 0.12 cm^{-1} and allow us to know that the exchange coupling through pathways 3 and 4 are ferromagnetic in nature, with J_3 = + 0.10 cm^{-1} and J_4 = + 0.062 cm^{-1}. Being all the coupling constants very weak, it seems that AF interactions prevail over the other exchange pathways, as the overall interactions are AF in nature.

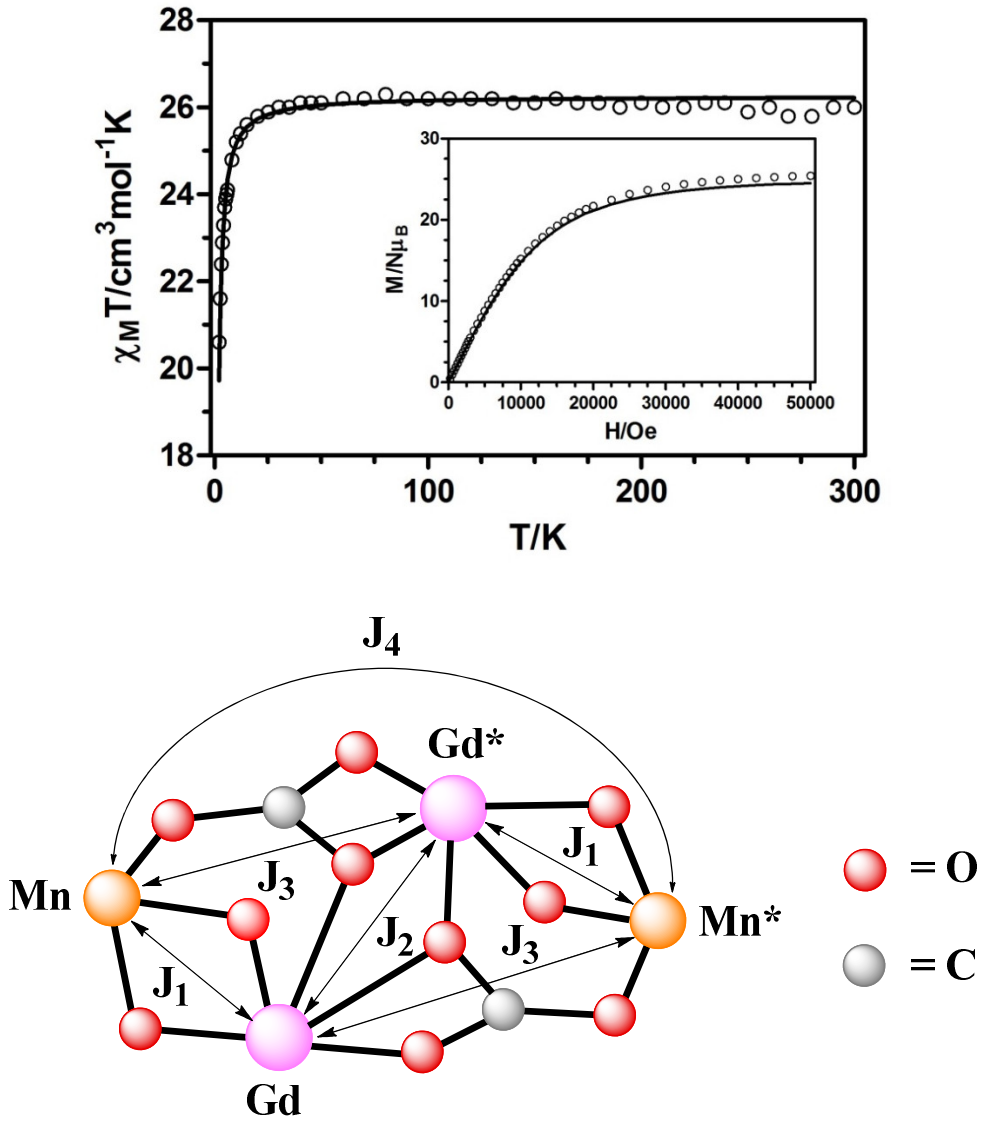

Figure 5.9.- Top: Temperature dependence of the $\chi_M T$ product for **44**. Inset: field dependence of the magnetization for **44**. The solid lines are generated from the best fit to the magnetic parameters. Bottom: magnetic exchange pathways in compound **44**.

Continuing with the Dy(III) based derivatives, the $\chi_M T$ values at 300 K of 18.50, 18.36 and 18.80 $cm^3 \cdot K \cdot mol^{-1}$, respectively for the Mn(II)Dy(III) dinuclear complexes **38**, **41** and **43** (Figure 5.10), are close to the expected value for a pair of non-interacting Mn(II) (S = 5/2, g = 2) and Dy(III) ($4f^9$, J = 15/2, S = 5/2, L = 5, g = 4/3 $^6H_{15/2}$) ions (18.45 $cm^3 \cdot K \cdot mol^{-1}$). On cooling, the $\chi_M T$ product for **38** decreases slowly until 100 K and then in a more abrupt way, reaching a value of 7.82 $cm^3 \cdot K \cdot mol^{-1}$ at 4.5 K. This behaviour is due to the crystal field splitting of the Dy(III) ions and probably due to weak AF interactions between Mn(II) and Dy(III) ions.

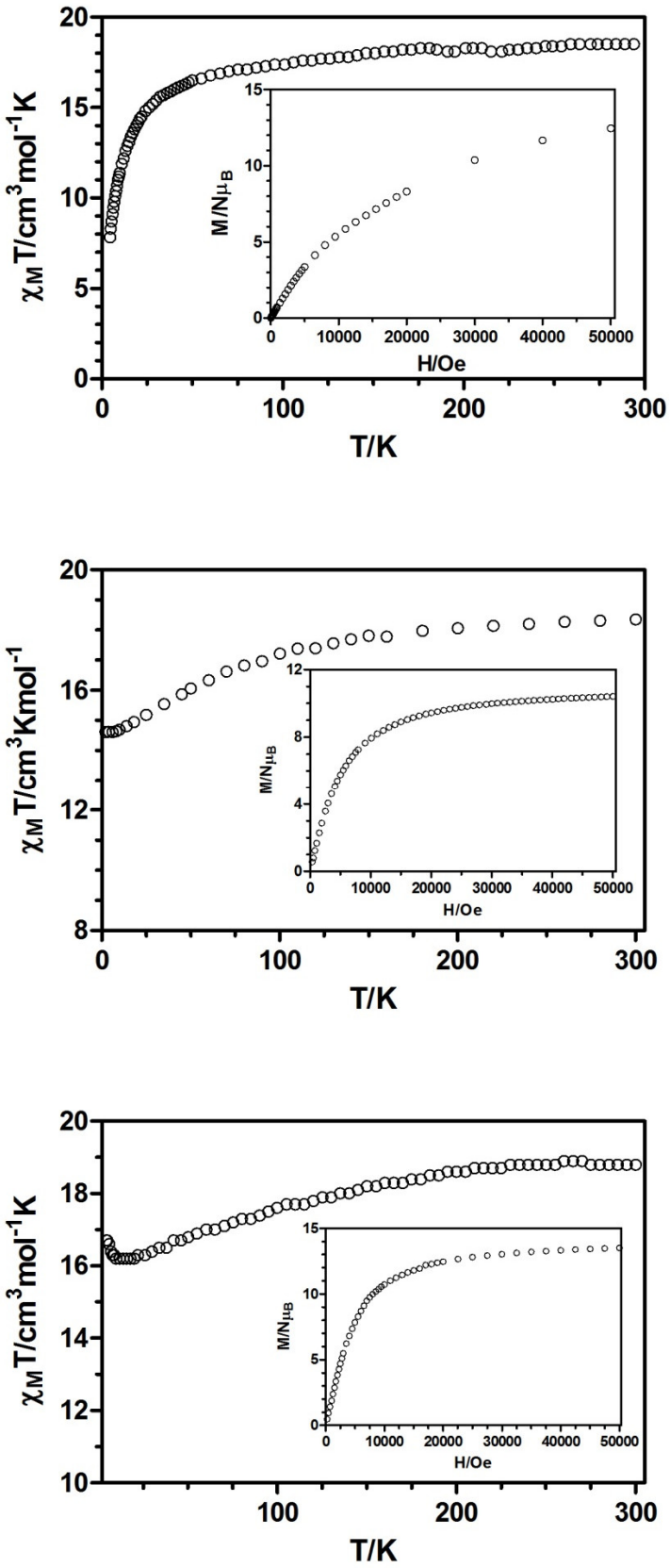

Figure 5.10.- Temperature dependence of the $\chi_M T$ product for **38** (top), **41** (middle) and **43** (bottom). Insets: field dependence of the magnetization for **38** (top), **41** (middle) and **43** (bottom).

On the other hand, the $\chi_M T$ product for **41** stops decreasing in the lowest temperatures region, remaining almost constant below 8 K, which could be due to the presence of very weak F interactions within the metallic ions, as seen in the Gd(III) based isostructural complex **40**. Complex **43** also shows an increase of the $\chi_M T$ in the lowest temperatures (below 16 K), reaching a value of 16.70 $cm^3 \cdot K \cdot mol^{-1}$ at 4.5 K. This behaviour suggest that, in contrast to what observed in the isostructural complex **42**, the Mn(II) and Ln(III) are ferromagnetically coupled at low temperatures.

The magnetization plots of complexes **41** and **43** (Figure 5.10, insets) show a relatively rapid increase in the magnetization at low fields and a rapid saturation of the magnetization, reaching values of 10.41 and 13.50 $N\mu_B$ at 5 T, respectively. On the other hand, complex **38** exhibits a slower increase of the magnetization, which is probably due to the AF interactions that are expected for this complex. The obtained value of 12.46 $N\mu_B$ at 5 T is lower than the expected value of 17 $N\mu_B$ ($M_s = g_J J N \mu_B$), as in the case of complexes **41** and **43**, which is due to the anisotropy of the Dy(III) ions in the case of the three complexes and also due to the probable AF interactions in the case of **38**.

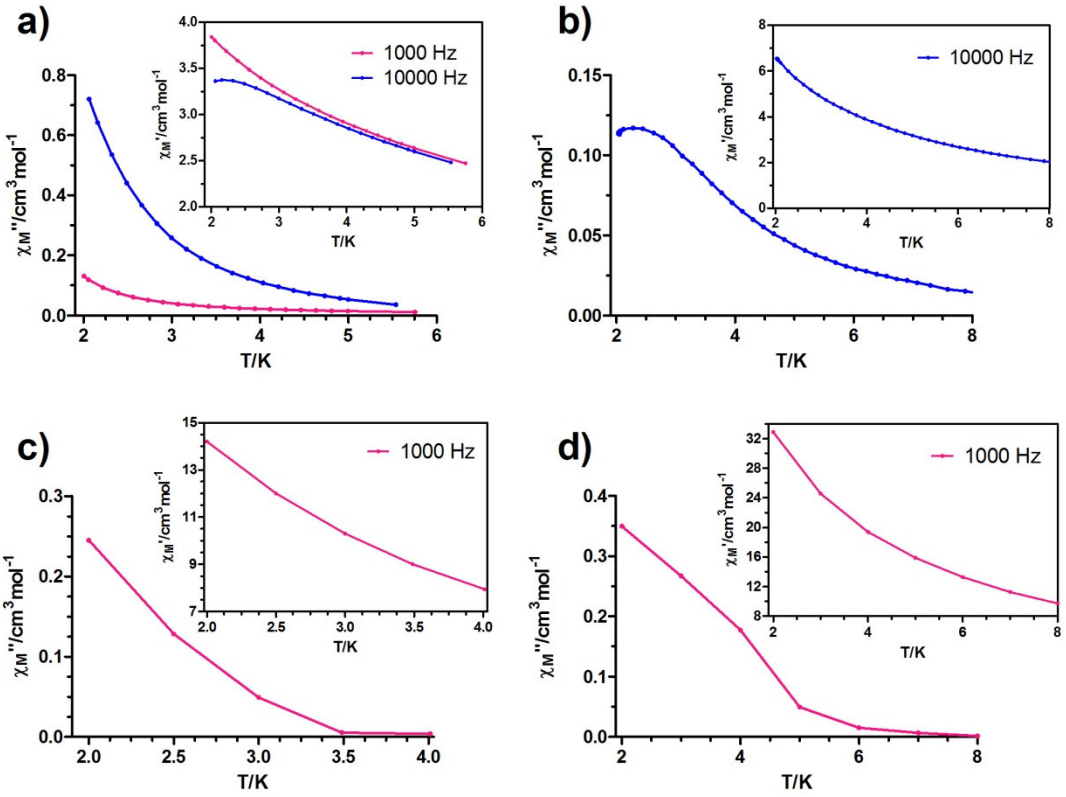

Figure 5.11.- Temperature dependence of in-phase χ_M' (inset) and out-of phase χ_M'' components of the *alternating current* (*ac*) susceptibility for complexes **38** (a), **41** (b), **43** (c) and **45** (d) under an applied field of 1000 Oe.

To end up, it is worth mentioning that complexes **38**, **43** and **45** showed a very modest frequency dependency of the in-phase and out-of-phase susceptibility in the presence of an external *dc* field of 1000 Oe (Figure 5.11). The *dc* magnetic measurements in **39**, **40** (magnetization plot) and **45** and *ac* measurements in **39** are still in progress.

5.3.3. Magneto-caloric Effect

The magneto-thermal properties of **42** have been studied because (i) the Gd(III) and Mn(II) ions show negligible anisotropy due to the absence of orbital contribution; (ii) the Gd(III) and Mn(II) ions exhibit large single-ion spin (S = 7/2 and 5/2, respectively); (iii) the antiferromagnetic interaction between the Gd(III) and Mn(II) ions is very weak, which generates multiple low-lying excited and field-accessible states, each of which can contribute to the magnetic entropy of the system and (iv) the molecule is relatively small with a large metal/ligand mass ratio thus limiting the amount of passive, non-magnetic elements. All the above factors should favour a large MCE.

The magnetic entropy changes ($-\Delta S_m$) that characterize the magneto-caloric properties of **42** can be calculated from the experimental isothermal field dependent magnetization data (Figure 5.12, top) by making use of the Maxwell relation:

$$\Delta S_M = (T, \Delta B) = \int_{B_i}^{B_f} \left[\frac{\partial M(T,B)}{dT} \right]_B dB \quad (\textit{Equation 5.4})$$

where B_i and B_f are the initial and final applied magnetic fields. The values of $-\Delta S_m$ for **42** (Figure 5.12, bottom) under all fields increase as the temperature decreases from 7 to 3 K. The maximum value of $-\Delta S_m$ is 21.51 $J \cdot kg^{-1} \cdot K^{-1}$ at T = 3 K and applied field change ΔB = 5 T. In spite of the antiferromagnetic interactions between the Mn(II) and Gd(III) ions in **42**, there is an important change in $-\Delta S_m$ which is consistent with easy spin polarization at relatively low magnetic field. It should be noted that due to limitations of our instrument, the $-\Delta S_m$ at about 2 K could not be obtained, but it is expected to be even larger as $-\Delta S_m$ increases with decreasing temperature. In connection with this, we have simulated the MCE for **42** using the magnetic parameters extracted from the fitting of the magnetization and susceptibility data and the results show that the $-\Delta S_m$ values are almost coincident with those extracted from the integration of the field dependence of the magnetization at different temperatures and

that the $-\Delta S_m$ value at 5T and 2K (23.7 $J \cdot kg^{-1} \cdot K^{-1}$) is larger than that at 3 K, as expected.

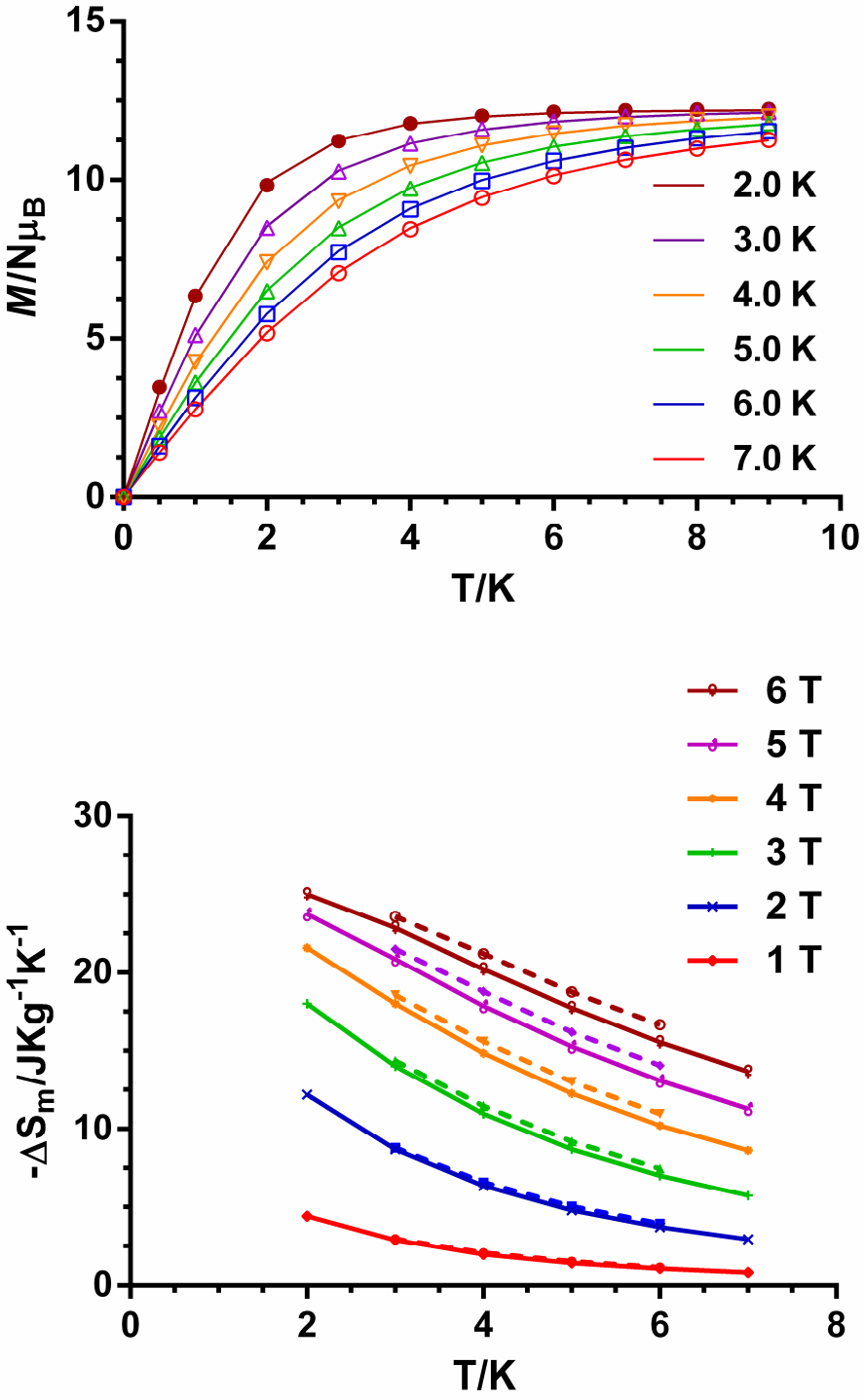

Figure 5.12 .- Isothermal field dependent curves for **42** (top) and the extracted change in the magnetic entropy (bottom). Solid lines represent the simulated values from the magnetic parameters (J = - 0.16 cm^{-1} and g = 2.034), whereas dotted lines represent the values extracted from integration.

The extracted -ΔS_m value at T = 2 K is lower than those calculated for the full magnetic entropy content per mole $R\ln(2S_{Gd} + 1) + R\ln(2S_{Mn} + 1)$ = 3.87 R= 29.7 $J \cdot kg^{-1} \cdot K^{-1}$ for **42**, as expected. It is worth mentioning that, in spite of the smaller metal/ligand mass ratio for compound **42** compared to the previously reported MnGd dinuclear complex $[Mn(CH_3OH)(\mu\text{-}L^1)Gd(NO_3)_3]$,[3] the extracted -$\Delta S_m$ values at 5 T at 3 K for both compounds are virtually identical (~ 21.5 $J \cdot kg^{-1} \cdot K^{-1}$). This fact can be due to the smaller magnetic exchange coupling observed for **42** (- 0.16 cm^{-1} *vs.* + 0.99 cm^{-1}), which lead to multiple low-lying excited and field-accessible states in which the spin polarization at low field is easier. These results show that the MCE is due to the magnitude rather than to the nature of the magnetic coupling and therefore, the same measurements are going to be done in complexes **37**, **40** and **44**. As expected, the extracted -ΔS_m for **42** is lower than those found for other more magnetic dense Mn(II)Gd(III) clusters with larger metal/ligand mass ratio.[6]

5.3.4. Magneto-structural Correlations

As explained previously, DFT calculations[7] and experimental[7b] results have clearly shown that the antiferromagnetic J_{MGd} coupling in di-μ-phenoxo bridged M(II)-Gd(III) complexes (M = Mn, Ni, Cu) decreases when the planarity of the M-(μ-O)$_2$-Gd bridging fragment (β) and the M-O-Gd bridging angle (θ) increase. Both structural factors are correlated, so that the latter increases as the bridging fragment becomes more planar.

Table 5.1 collects the magneto-structual data for dinuclear and trinuclear Mn(II)Gd(III) and Mn(II)Gd(III)Mn(II) complexes reported in bibliography so far. In general, it can be said that the highest ferromagnetic coupling constants are shown by double di-μ-phenoxo bridged complexes, which show the lowest hinge angles accompanied with high θ angles, in agreement with the above considerations. The incorporation of a third bridge to di-μ-phenoxo bridged species leads to more folded structures, which consequently exhibit smaller Mn-O-Gd angles than the planar fragments. If the third bridge is a phenoxo bridge, the magnetic exchange decreases but continues being ferromagnetic as in the case of complexes $[L^8Mn(H_2O)_2]_2[Gd(NO_3)_5(MeOH)]$ and $[L^{10}MnGdMnL^{10}]NO_3$. On the other hand, the incorporation of carboxylate and nitrate bridges leads, in most cases, to very weakly and antiferromagnetically coupled complexes, as seen in the four complexes reported in this chapter and in complex $[(NO_3)Mn_2(L^9)_2(\mu\text{-}NO_3)Gd](NO_3)$. The fact that *syn-syn* acetate and carboxylate bridges transmit AF interactions has already been discussed

in other chapters. In connection with this, DFT calculations were carried out on a model compound of **42**, where the anthracenate bridge was replaced by two non-bridging water molecules, without modifying the remainder of the structure. The calculated coupling constant value increased from - 0.32 to + 0.052 cm^{-1}, underlining that in addition to the hinge angle, the nature of the carboxylate bridge has a significant role in decreasing the magnetic exchange coupling. To end up, the triply alkoxo bridged compound $[MnGd\{pyCO(OEt)pyC(OH)(OEt)py\}_3](ClO_4)_2$ shows the strongest AF coupling, which is consistent with the fact that this complex has the highest β and lowest θ angles.

Table 5.1.- Magneto-structural data for polynuclear $Mn(II)_xGd(III)$ (x = 1, 2) complexes.

Complex	J_{exp}/J_{calc} (cm^{-1})	**N° of bridges**	**θ (°)**[a]	**β (°)**	**Mn···Gd**	**Ref.**
$[MnGd\{pyCO(OEt)pyC(OH)(OEt)py\}_3](ClO_4)_2$	-1.7/-2.7	3	87.61	55.1	3.125	8
$[Mn(CH_3OH)(\mu\text{-}L^1)Gd(NO_3)_3]$	+0.99/+1.27[b]	2	110.48	4.06	3.686	3
$[Mn(\mu\text{-}L)(\mu\text{-}OAc)Gd(NO_3)_2]\cdot CH_3CN\cdot H_2O$	-0.82/-2.22	3	97.53	34.85	3.414	T.w.
$[Mn(\mu\text{-}L^1)(\mu\text{-}OAc)Gd(NO_3)_2]$	+0.24/+0.05	3	101.94	23.30	3.474	T.w.
$[Mn(\mu\text{-}L^1)(\mu\text{-}9\text{-}An)Gd(NO_3)_2]\cdot 2CH_3CN$	-0.16/-0.32	3	103.2	20.73	3.485	T.w.
$\{(\mu_3\text{-}CO_3)_2[Zn(\mu\text{-}L^1)Gd(NO_3)]_2\}\cdot 2CH_3CN$	-0.13/-0.065 +0.10 (calc.)	3 1	102.4 -	15.88 -	3.531 5.525	T.w.
$[L^8Mn(H_2O)_2]_2[Gd(NO_3)_5(MeOH)]$	c	3	93.32	50.71	3.312	9
$[(NO_3)Mn_2(L^9)_2(\mu\text{-}NO_3)Gd](NO_3)$	+0.0/-0.2 +1.6/+1.9	3 2	101.2 102.4	39.8 3.3	3.515 3.709	10
$[L^{10}MnGdMnL^{10}]NO_3$	+0.08 (exp)	3	93.76 93.75	50.33 50.32	3.334 3.335	11

[a] Average values. [b] Calculated after article publication. [c] Overall ferromagnetic exchange coupling observed, exchange constants are not obtained. T.w. = this work.

H_2L^8 = 1,3-bis((methoxysalicylidene)amino)-2,2'-dimethylpropane)

H_2L^9 = N,N′-2,2-dimethylpropylenebis(3-methoxysalicylideneimine)

H_2L^{10} = N,N',N"-tris(2-hydroxy-3-methoxybenzilidene)-2-(aminomethyl)-2-methyl-1,3-propanediamine

However, the complexes reported in Table 5.1 show a rich structural diversity and more specific magneto-structural correlations should be done. With this in mind, DFT calculations were performed on the model compound $[Mn(PMTA)(H_2O)(\mu\text{-}OPh)_2Gd(OCH_3)_2(H_2O)(NO_3)_2)]$ (where PMTA = 1,1,4,7,7-pentamethyldiethylene-

triamine and OPh^- = 4-methylphenolato anion), in which the part of ligand containing the amino nitrogen atoms has been replaced by PMTA, the phenoxo-bridging parts of the ligand by 4-methylphenolato bridging groups and the methoxo groups coordinated to the Gd(III) ion by methanol molecules. In addition, the acetate or anthracenate bridging groups have been replaced by two non-bridging water groups, leading to a di-μ-phenoxo bridged simplified model compound. In the calculations, the hinge angle β was first fixed to zero (planar Mn-(μ-O)$_2$-Gd bridging fragment) and the θ angle was varied in the 100 - 115° range. As can be seen in Figure 5.12, for planar bridging fragments the crossover point (point in which the magnetic interaction changes from antiferromagnetic to ferromagnetic) is located at around 105°, being the exchange coupling ferromagnetic at higher angles. On the other hand, to know how the folding of the structure affects J_{MnGd}, the θ angle was fixed to 105° and β was varied between 0 and 30°. The results show ferromagnetic interactions for all the β angles considered, with an increase in J_{MnGd} when increasing β until around 20° and a decrease in J_{MnGd} from that point on. The variation in J_{MnGd} with β in alkoxo triply bridged Mn(II)Gd(III) compounds was already studied by E. Ruiz et al. in 2012,[7a] using the model compound [MnGd{pyCO(OEt)pyC(OH)(OEt)py}$_3$](ClO$_4$)$_2$ (collected in Table 5.1).[8] They showed that, in the ~35 – 75° β range, the antiferromagnetic contribution increased with the increase of the β angle, which is consistent with our calculations.

The experimental J_{MnGd} value of + 0.99 cm^{-1} obtained for the di-μ-phenoxo doubly bridged complex [Mn(CH$_3$OH)(μ-L^1)Gd(NO$_3$)$_3$], which possesses a hinge angle of 4.06° and a θ of 110.48°, is consistent with the above calculations. In addition, there exists a linear relationship (with r^2 = 0.96) between the θ angles and experimental *J* values obtained for this complex and the four di-μ-phenoxo/carboxylate triply bridged MnGd complexes prepared from ligands H_2L and H_2L^1 reported in this chapter (Figure 5.14), which exhibit similar structures. These results demonstrate, in good agreement with the DFT calculations (Figure 5.13), that the main structural factor governing the nature and sign of the magnetic coupling in di-μ-phenoxo bridged MnGd dinuclear complexes is the Mn-O-Mn bridging angle (θ).The difference between experimental and calculated J_{MnGd} is more likely due to the crude model used in the DFT calculations and to limitations inherent to the method.

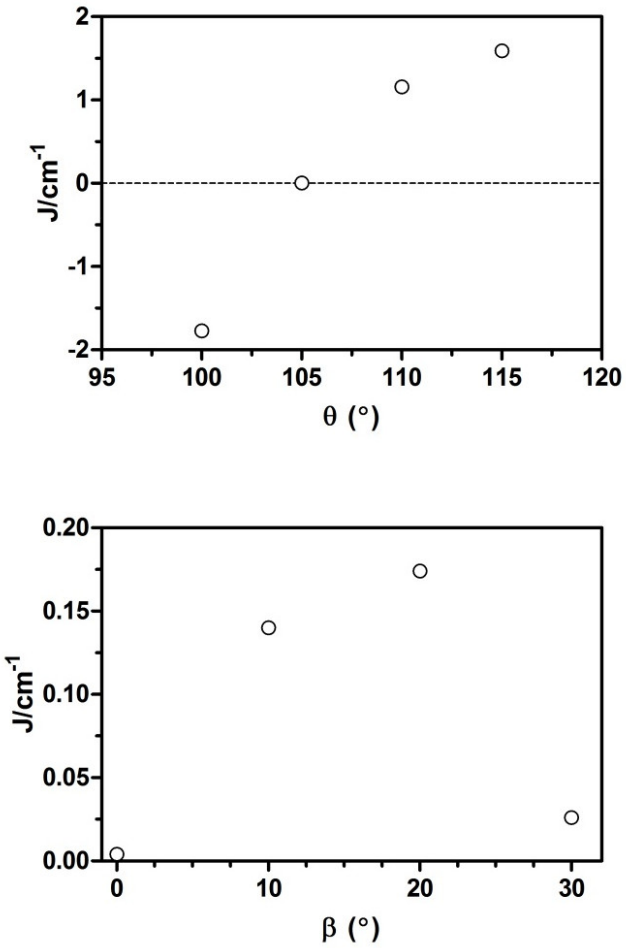

Figure 5.13.- J_{MnGd} versus θ (top) and J_{MnGd} versus β (bottom) plots.

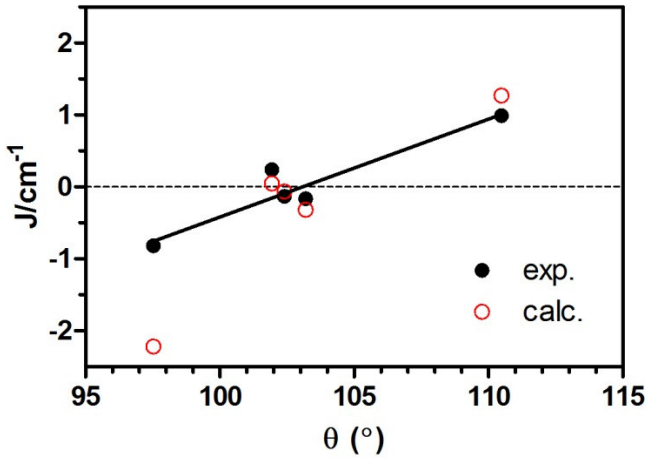

Figure 5.14.- Scatter plot of experimental *J* (black circles) vs. the mean Mn-O-Gd angle (θ) for complexes prepared from ligands H_2L and H_2L^1. The open circles represent the values obtained from DFT calculations. The solid line represents the linear fitting of the experimental values.

5.4. CONCLUSIONS

Nine dinuclear or tetranuclear Mn(II)Ln(III) species (Ln = Gd or Dy) have been prepared using the compartmental ligands H_2L and H_2L^1. *Dc* magnetic measurements have been carried out in seven of them, whereas the measurements in the remaining two compounds are still in progress. According to experimental and DFT calculations results, the magnetic exchange interactions between Mn(II) and Gd(III) ions through di-μ-phenoxo/carboxylate triple bridges are AF or very weak F in nature.

The magneto-thermal properties of **42** have been studied, obtaining a maximum value of $-\Delta S_m$ = 21.51 $J \cdot kg^{-1} \cdot K^{-1}$ at T = 3 K and applied field change of ΔB = 5 T. The results show that the MCE is due to the magnitude rather than to the nature of the magnetic coupling.

To end up, experimental magneto-structural correlations are carried out from these and other complexes found in bibliography. The highest ferromagnetic coupling constants are observed in di-μ-phenoxo bridged complexes, which is due to the planarity of the Mn-(μ-O)$_2$-Gd bridging fragment and to the high Mn-O-Gd angles. The incorporation of a third bridge leads to folded structures, which reduces the magnetic coupling constant.

DFT calculations carried out in a di-μ-phenoxo doubly bridged model compound show that for planar bridging fragments, the crossover point in Mn-O-Gd angle is located at 105°, being the interactions F above this angle and AF below it. The influence of the Mn-(μ-O)$_2$-Gd hinge angle was also studied by fixing the Mn-O-Gd angle to 105° and changing the hinge angle, concluding that J_{MnGd} increases when increasing β until around 20° and decreases from that point on.

5.5. BIBLIOGRAPHY

[1] M. Evangelisti, E. K. Brechin, *Dalton Trans.*, **2010**, *39*, 4672.

[2] M. Andruh, J. P. Costes, C. Diaz, S. Gao, *Inorg. Chem.*, **2009**, *48*, 3342.

[3] E. Colacio, J. Ruiz, G. Lorusso, E. K. Brechin, M. Evangelisti, *Chemm. Com.*, **2013**, *49*, 3845.

[4] **a)** S. Titos-Padilla, J. Ruiz, J. M. Herrera, E. K. Brechin, W. Wersndorfer, F. Lloret, E. Colacio, *Inorg. Chem*., **2013**, *52*, 9620; **b)** J. Ruiz, G. Lorusso, M. Evangelisti, E. K. Brechin, S. J. A. Pope, E. Colacio, *Inorg. Chem*., **2014**, *53*, 3586.

[5] N. F. Chilton, R. P. Anderson, L. D. Turner, A. Soncini, K. S. Murray, *J. Comput. Chem*., **2013**, *34*, 1164.

[6] J.-L. Liu, Y.-C. Chen, F.-S. Guo, M.-L. Tong, *Coord. Chem. Rev*., 2014, 281, 26.

[7] **a)** E. Cremades, S. Gomez-Coca, D. Aravena, S. Alvarez, E. Ruiz, *J. Am. Chem. Soc*., **2012**, *134*, 10532; **b)** E. Colacio, J. Ruiz, A. J. Mota, M. A. Palacios, E. Cremades, E. Ruiz, F. J. White, E. K. Brechin, *Inorg. Chem*., **2012**, *51*, 857.

[8] A. N. Georgopoulou, R. Adam, C. P. Raptopoulou, V. Psycharis, R. Ballesteros, B. Abarca, A. K. Boudalis, *Dalton Trans*., **2010**, *39*, 5020.

[9] V. Chandrasekhar, B. M. Pandian, R. Boomishankar, A. Steiner, R. Clérac, *Dalton Trans*., **2008**, 5143.

[10] J.-P. Costes, J. García -Tojal, J.-P. Tuchagues, L. Vendier, *Eur. J. Inorg. Chem*., **2009**, 3801.

[11] T. Yamaguchi, J. P. Costes, Y. Kishima, M. Kojima, Y. Sunatsuki, N. Brefuel, J. P. Tuchagues, L. Vendier, W. Wernsdorfer, *Inorg. Chem*., **2010**, *49*, 9125.

CHAPTER 6

RATIONAL ELECTROSTATIC DESIGN OF EASY-AXIS MAGNETIC ANISOTROPY IN Zn(II)Dy(III)Zn(II) SINGLE ION MAGNETS WITH HIGH ENERGY BARRIERS

6.1. INTRODUCTION

The free ion electron density of the Dy(III) ion, and more importantly, that of the ground Kramer's doublet with $M_J = \pm 15/2$, have an oblate shape.[1] This electron-density shape is favoured by an axial crystal field, where the donor atoms with the largest electron densities are located above and below the equatorial plane, thus minimizing the repulsive interactions between the ligands and f-electron charge clouds.[1,2] At variance, mononuclear complexes with Ln(III) ions with a prolate electron-density shape, such as Er(III), would require an equatorial crystal field to minimize the repulsive interactions between the ligands and f-electron charge clouds. This simple model based on the electronic shape of the Ln(III) ions has been revealed to be a good strategy to design mononuclear 4f complexes with SIM behaviour.

As the phenoxo oxygen donor atoms have larger negative charges than aldehyde-oxygen donor atoms, a good strategy to achieve strong easy-axis anisotropy would be to place the phenoxo oxygen atoms in opposite positions of the Dy(III) ion; the easy-axis of anisotropy would lie in the direction defined by the phenoxo oxygen atoms. This disposition of the phenoxo oxygen atoms could be achieved in 3d-Dy-3d trinuclear complexes with the compartmental ligand H_2L, where phenoxo bridging groups connect the 3d and 4f metal ions and terminal aldehyde groups are coordinated to the Ln(III) ion. With regard to the 3d metal ion, it would be preferable to use a diamagnetic ion, such as Zn(II) because: 1) as seen in Chapter 4, a paramagnetic anisotropic ion could create a random transversal field for the Dy(III) ions, which would favour a faster tunnelling of the magnetization (QTM) process and mask the slow relaxation process,[3] 2) a diamagnetic ion would mitigate the intermolecular interactions that favour the fast QTM[4] and 3) the weak magnetic exchange coupling interaction between 3d and 4f metal ions, would generally lead to a small energy barrier.

Following this strategy, this chapter collets the synthesis, structural characterization and magnetic properties of a family of trinuclear [ZnX(μ-L)Dy(μ-L)XZn]Y·nS complexes, where X can be Cl, Br, I and azide, Y is the counteranion and S are the solvent molecules. The Er(III) based complex [ZnCl(μ-L)Er(μ-L)ClZn][$ZnCl_3(CH_3OH)$]·$3CH_3OH$ was also prepared for comparative purposes.

6.2. PREPARATION OF COMPLEXES

6.2.1. [ZnCl(μ-L)Ln(μ-L)ClZn][$ZnCl_3(CH_3OH)$]·$3CH_3OH$, Ln (III) = Dy (46), Er (47)

$ZnCl_2$ (17.0 mg, 0.125 mmol) and $Ln(NO_3)_3·5H_2O$ (0.0625 mmol) were added subsequently to a solution of H_2L (64.3 mg, 0.125 mmol) in MeOH (5 mL) with continuous stirring. The resulting yellow solution was filtered and allowed to stand at room temperature. After one week of attending at room temperature, plate yellow crystals of **46** and **47** were obtained with yields respectively of 30 % and 27 % based on Ln. Anal. Calcd. for $C_{44}H_{56}N_4O_{12}Cl_5Br_4Zn_3Dy$: C, 31.30; H, 3.34; N, 3.32. Found: C, 31.39; H, 3.39, N, 3.40. Anal. Calcd. for $C_{44}H_{56}N_4O_{12}Cl_5Br_4Zn_3Er$: C, 31.21; H, 3.33; N, 3.31. Found: C, 31.28; H, 3.42, N, 3.21.

6.2.2. [ZnCl(μ-L)Dy(μ-L)ClZn]$NO_3·CH_3OH$ (48)

To a solution of $ZnCl_2$ (8.52 mg, 0.0625 mmol) in 5 mL of methanol were subsequently added with continuous stirring 64.3 mg (0.125 mmol) of H_2L and 27.6 mg (0.0625 mmol) of $Dy(NO_3)_3·5H_2O$. The resulting yellow solution was filtered to eliminate any amount of insoluble material and allowed to stand at room temperature. After several days, prismatic yellow crystals of **48** were obtained with a yield of 38 %. Anal. Calcd. for $C_{41}H_{44}N_5O_{12}Cl_2Br_4Zn_2Dy$: C, 33.22; H, 2.99; N, 4.72. Found: C, 33.46; H, 3.04; N, 4.81.

6.2.3. [ZnBr(μ-L)Dy(μ-L)BrZn][$ZnBr_3(CH_3OH)$]·$CH_3OH·2H_2O$ (49)

To a solution of $ZnBr_2$ (28.2 mg, 0.125 mmol) in 5 mL of methanol were subsequently added 64.3 mg (0.125 mmol) of H_2L and 27.6 mg (0.0625 mmol) of $Dy(NO_3)_3·5H_2O$ with continuous stirring. The resulting yellow solution was filtered and left undisturbed at room temperature for several days, affording yellow crystals of **49** with a yield of 39 %. Anal. Calcd. for $C_{42}H_{52}N_4O_{12}Br_9Zn_3Dy$: C, 26.80; H, 2.78; N, 2.98. Found: C, 26.88; H, 2.78; N, 3.01.

6.2.4. [ZnBr(μ-L)Dy(μ-L)BrZn]$NO_3·3CH_3OH$ (50)

H_2L (64.3 mg, 0.125 mmol), $Dy(NO_3)_3·5H_2O$ (27.6 mg, 0.0625 mmol) and KBr (14.9 mg, 0.125 mmol) were successively added to a solution of $Zn(NO_3)_2·6H_2O$ (37.2 mg, 0.125 mmol) in methanol (5 mL). The mixture was stirred for 30 minutes, filtered and the filtrate was kept undisturbed at room temperature for several days, whereupon

yellow X-ray quality crystals of **50** were obtained. Yield: 25 %. Anal. Calcd. for $C_{43}H_{52}N_5O_{14}Br_6Zn_2Dy$: C, 31.58; H, 3.20; N, 4.28. Found: C, 31.68; H, 3.24; N, 4.33.

6.2.5. [ZnI(μ-L)Dy(μ-L)IZn]I·CH_3OH·$3H_2O$ (51)

This complex was prepared in a 41 % yield as yellow crystals following the same procedure as for **49**, except that ZnI_2 (39.9 mg, 0.125 mmol) was used instead of $ZnBr_2$. Anal. Calcd. for $C_{41}H_{50}N_4O_{12}I_3Br_4Zn_2Dy$: C, 27.60; H, 2.82; N, 3.14. Found: C, 27.66; H, 2.83; N, 3.15.

6.2.6. [ZnI(μ-L)Dy(μ-L)IZn]NO_3·$3CH_3OH$ (52)

This complex was prepared in a 47 % yield as yellow crystals following the same procedure as for **50**, but using KI (20.8 mg, 0.125 mmol) instead of KBr. Anal. Calcd. for $C_{43}H_{52}N_5O_{14}I_2Br_4Zn_2Dy$: C, 29.86; H, 3.03; N, 4.05. Found: C, 29.91; H, 3.01; N, 4.07.

6.2.7. [ZnN_3(μ-L)Dy(μ-L)N_3Zn]NO_3·CH_3OH·H_2O (53)

Compound **53** was prepared following the same procedure as for **50** and **52**, but adding NaN_3 (8.13 mg, 0.125 mmol) instead of the corresponding halogen salt. Yield: 26 %. Anal. Calcd. for $C_{41}H_{46}N_{11}O_{13}Br_4Zn_2Dy$: C, 32.53; H, 3.06; N, 10.18. Found: C, 32.59; H, 3.09; N, 10.23.

6.2.8. [ZnCl(μ-L)Dy(μ-L)ClZn]PF_6 (54)

To a solution of $ZnCl_2$ (8.52 mg, 0.0625 mmol) in 5 mL of MeOH were subsequently added with continuous stirring 64.3 mg (0.125 mmol) of H_2L, 27.4 mg (0.0625 mmol) of $Dy(NO_3)_3·5H_2O$ and 23.0 mg (0.125 mmol) of KPF_6. The resulting solution was filtered and allowed to stand at room temperature. After several days, well-formed prismatic yellow crystals of **54** were obtained, which were filtered off and dried in vacuum. Yield: 19 %. Anal. Calcd. for $C_{40}H_{40}N_4O_8Br_4Cl_2PF_6DyZn_2$: C, 31.33; H, 2.63; N, 3.65. Found: C, 31.51; H, 2.67; N, 3.72.

6.3. EXPERIMENTAL RESULTS

The reaction of H_2L with $ZnCl_2$ and $Ln(NO_3)_3·nH_2O$ in methanol and in 2:2:1 molar ratio allows the formation of the trinuclear species [ZnCl(μ-L)Dy(μ-

L)ClZn][$ZnCl_3(CH_3OH)$]·3CH_3OH (**46**) and [ZnCl(μ-L)Er(μ-L)ClZn][$ZnCl_3(CH_3OH)$]-·3CH_3OH (**47**). However, if the 2:1:1 molar ratio is used the trinuclear specie [ZnCl(μ-L)Dy(μ-L)ClZn]NO_3·CH_3OH (**48**) is obtained, which contains a different counteranion and less crystallization solvent molecules. The Cl^- anions can be replaced by Br^- anions, obtaining the similar compounds [ZnBr(μ-L)Dy(μ-L)BrZn][$ZnBr_3(CH_3OH)$]·CH_3OH·2H_2O **(49)** and [ZnBr(μ-L)Dy(μ-L)BrZn]NO_3·3CH_3OH **(50)**. The synthesis of **49** is similar to that of **46** but using $ZnBr_2$ instead of $ZnCl_2$, whereas **50** is obtained by the reaction of H_2L with $Zn(NO_3)_2$·6H_2O, $Dy(NO_3)_3$·5H_2O and KBr in methanol and in 2:2:1:2 molar ratio. The same reaction as for **46** and **49** but using ZnI_2 afforded the compound [ZnI(μ-L)Dy(μ-L)IZn]I·CH_3OH·3H_2O **(51)**, where I^- anions act as counteranion as I^- ions are too big for the formation of analog [$ZnI_3(CH_3OH)$] molecules. Complexes [ZnI(μ-L)Dy(μ-L)IZn]NO_3·3CH_3OH (**52)** and [ZnN_3(μ-L)Dy(μ-L)N_3Zn]NO_3·CH_3OH·H_2O **(53)** are prepared following the same reaction than for **50**, but adding KI or NaN_3 in order to substitute the Br^- ions for I^- and N_3^- ions, respectively. Finally, by adding KPF_6 to a methanolic solution containing H_2L, $ZnCl_2$ and $Dy(NO_3)_3$·5H_2O in 2:1:1 molar ratio complex [ZnCl(μ-L)Dy(μ-L)ClZn]PF_6 **(54)** is obtained, where the Dy(III) ions possess C_2 symmetry. All these reactions are summarized in Scheme 6.1.

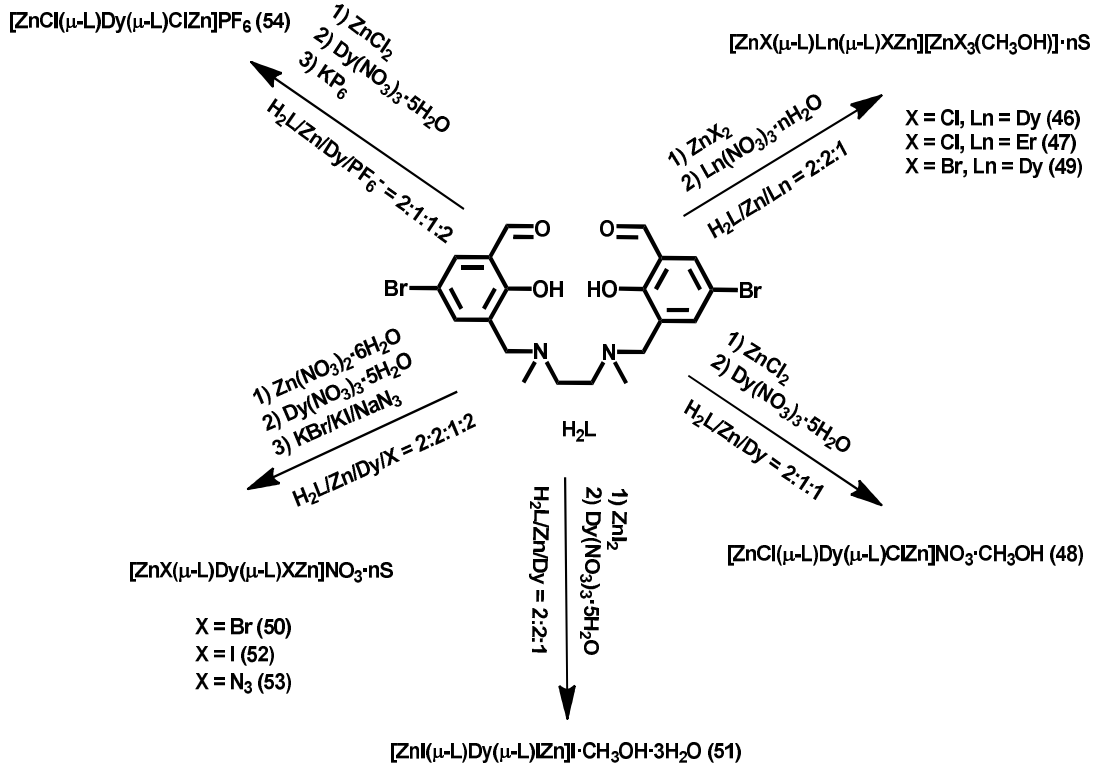

Scheme 6.1.- Summary of the complexes prepared in this chapter.

6.3.1. Crystal structures of 46-54

The structure of **46** is given in Figure 6.1 and consists of non-centrosymmetric trinuclear $[ZnCl(\mu\text{-}L)Dy(\mu\text{-}L)ClZn]^{+}$ cations, $[ZnCl_3(CH_3OH)]^{-}$ anions and three crystallization methanol molecules, all of them involved in hydrogen bond interactions.

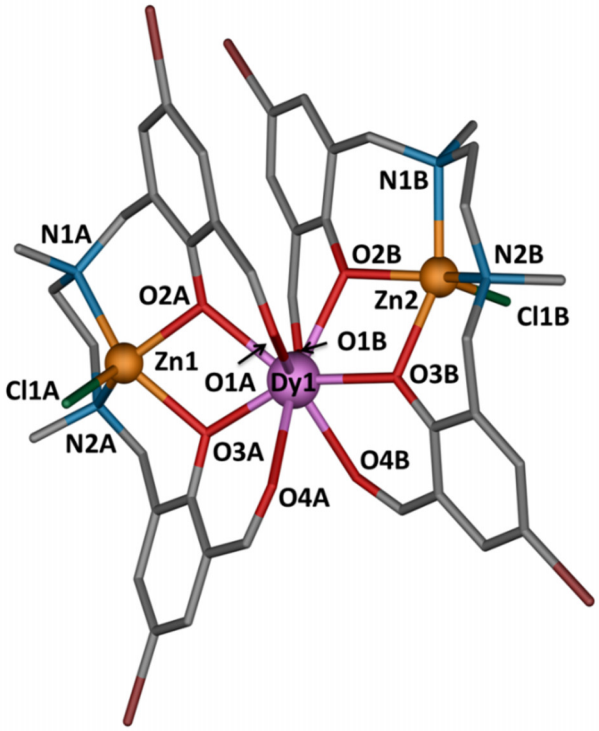

Figure 6.1.- A perspective view of the structure of **46**. Colour code: N = blue, O = red, C = gray, Br = brown, Cl = green, Zn = light brown, Ln = pink. H atoms and crystallization methanol molecules have been omitted for the sake of clarity.

Within the trinuclear Zn-Dy-Zn cation, two $[ZnCl(L)]^{-}$ units are coordinated to the central Dy(III) ion through the phenoxo and aldehyde oxygen atoms that belong to the compartmental ligand H_2L. The Dy(III) ion exhibits a DyO_8 coordination sphere, which is formed by four phenoxo and four aldehyde oxygen atoms, with Dy-O bond distances in the ranges of 2.253(5)-2.349(5) Å and 2.387(4)-2.443(5) Å, respectively. Calculation of the degree of distortion of the DyO_8 coordination polyhedron with respect to an ideal eight vertex polyhedron with continuous shape measure theory and the SHAPE software,[5] led to shape measures relative to the square antiprism (SAPR-8), triangular dodecahedron (TDD-8), and biaugmented triangular prism (BTPR-8) with values of 0.927, 2.173, and 2.862, respectively (Appendices, Table A.36). The shape measures are significantly larger for other reference polyhedra and therefore, the DyO_8

coordination polyhedron can be considered an intermediate between the indicated ideal polyhedra, closest in shape to the SAPR-8 geometry. The distorted square antiprism is compressed as the average distance between the upper and lower planes containing the four oxygen atoms (two phenoxo and two aldehyde) is 2.61 Å, whereas the average distance of the sides of the squares defined by the oxygen atoms in each plane is 2.77 Å (Figure 6.2).

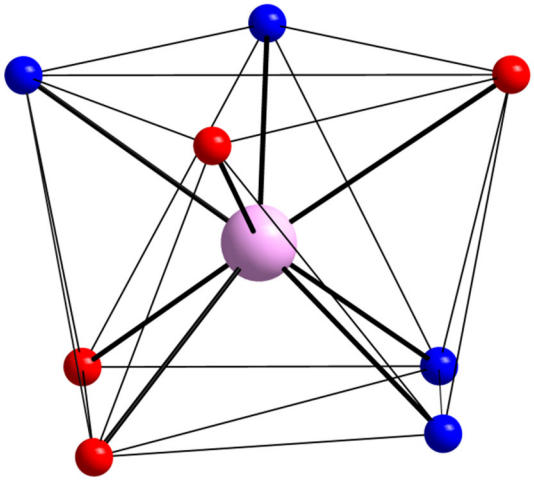

Figure 6.2.- Square antiprism DyO_8 coordination sphere in **46**. Colour code: Dy = pink, $O_{aldehyde}$ = red, $O_{phenoxo}$ = blue.

Zn(II) ions exhibit ZnO_2N_2Cl coordination environment with a geometry intermediate between square-pyramid (SPY-5), trigonal bipyramid (TBPY-5) and vacant octahedron (v-OC5), of which the SPY-5 geometry is the best fit, with shape measures average values of 0.92, 3.77 and 3.99, respectively. In the SPY-5 description, the nitrogen and oxygen atoms occupy the basal positions with Zn-N and Zn-O bonds distances in the ranges 2.099(6)-2.178(6) and 2.041(5)-2.168(6) Å, respectively, whereas the axial position is occupied by the Cl atom at a longer distance (2.216(2) and 2.223(2) Å). The Zn···Dy distances are 3.573(1) and 3.588(1) Å, whereas the Zn–Dy–Zn angle is 141.76°. Within the $[ZnCl_3(CH_3OH)]^-$ unit, the Zn(II) ion displays a geometry intermediate between vacant trigonal bipyramid and tetrahedral, with Zn-Cl bond distances in the range 2.227(3)-2.262(3) Å and a Zn-O bond distance of 2.02(1) Å.

Crystallization methanol molecules and the chloride atoms of the $[ZnCl_3(CH_3OH)]^-$ anion are linked by hydrogen bonds forming chains running along the *c* axis (Figure 6.3). The shortest Dy···Dy distance between neighbouring $[ZnDyZn]^+$ trinuclear cations is 7.349 Å.

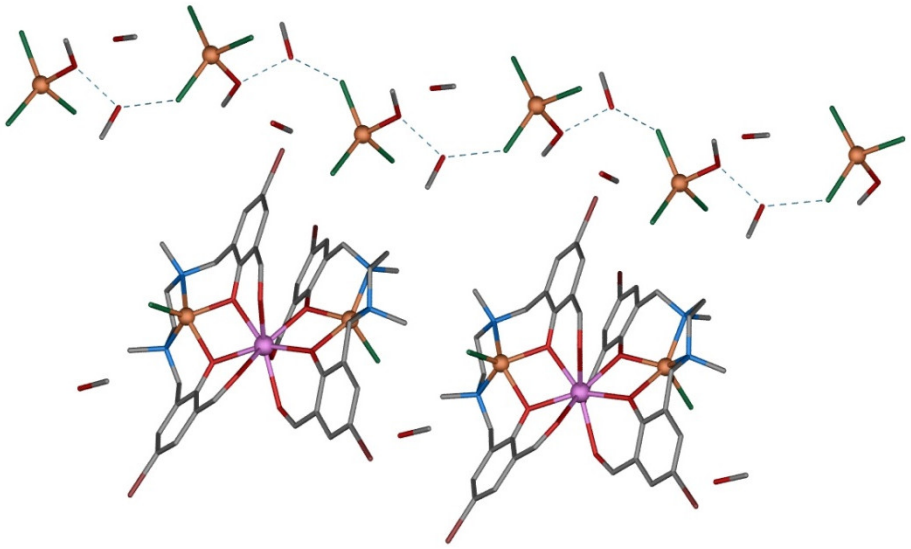

Figure 6.3.- A perspective view of the hydrogen bonds (blue dotted lines) chain formed by the $[ZnCl_3(CH_3OH)]^-$ anions and crystallization methanol molecules.

The Er(III) based complex **47** is isostructural to **46**, with slightly smaller lanthanide bond lengths due to the lanthanide contraction from Dy(III) to Er(III). Complex **48** is similar to **46**, but containing nitrate as counteranion instead of $[ZnCl_3(CH_3OH)]^-$ anion and less crystallization methanol molecules. The change of the counteranion leads to more folded structures, with a Zn-Dy-Zn angle of 105.94°. The distribution of the phenoxo oxygen atoms on the Dy(III) coordination sphere is also affected (Figure 6.4), leading to a more compressed distorted square antiprism, with the average distance between the upper and lower planes of 2.560 Å and similar average distance of the sides of the squares defined by the oxygen atoms (2.78 Å). All these changes lead to a DyO_8 coordination environment that is closer to the square antiprism geometry than that of complex **46**, with a CshM value of 0.504. The shortest Dy···Dy distance between neighbouring $[ZnDyZn]^+$ trinuclear cations is slightly higher than in complex **46** (8.605 Å) and there are hydrogen bond interactions between the crystallization methanol molecules and nitrate counteranions, with donor-acceptor distance of 2.748 Å.

The structures of complexes **49**-**53** are very similar to that of complexes **46** and **48**, but with different coligands connected to Zn(II) ions and different counteranions. All these complexes can be described by the general formula [ZnX(μ-L)Dy(μ-L)XZn]Y·nS, where X is the coligand connected to the Zn(II) ions (X = Br, I and N_3), Y is the

counteranion and S are the crystallization solvent molecules. The change of the coligand and counteranions leads to different disposition of the oxygen atoms in the DyO_8 coordination sphere, which are collected in Figure 6.4. SHAPE measurement results can be found in Appendices, Table A.36 and some of the structural factors of these compounds are summarized in Table 6.1. Due to the similarity between these complexes and complexes **46**-**48**, any further structural description will be omitted.

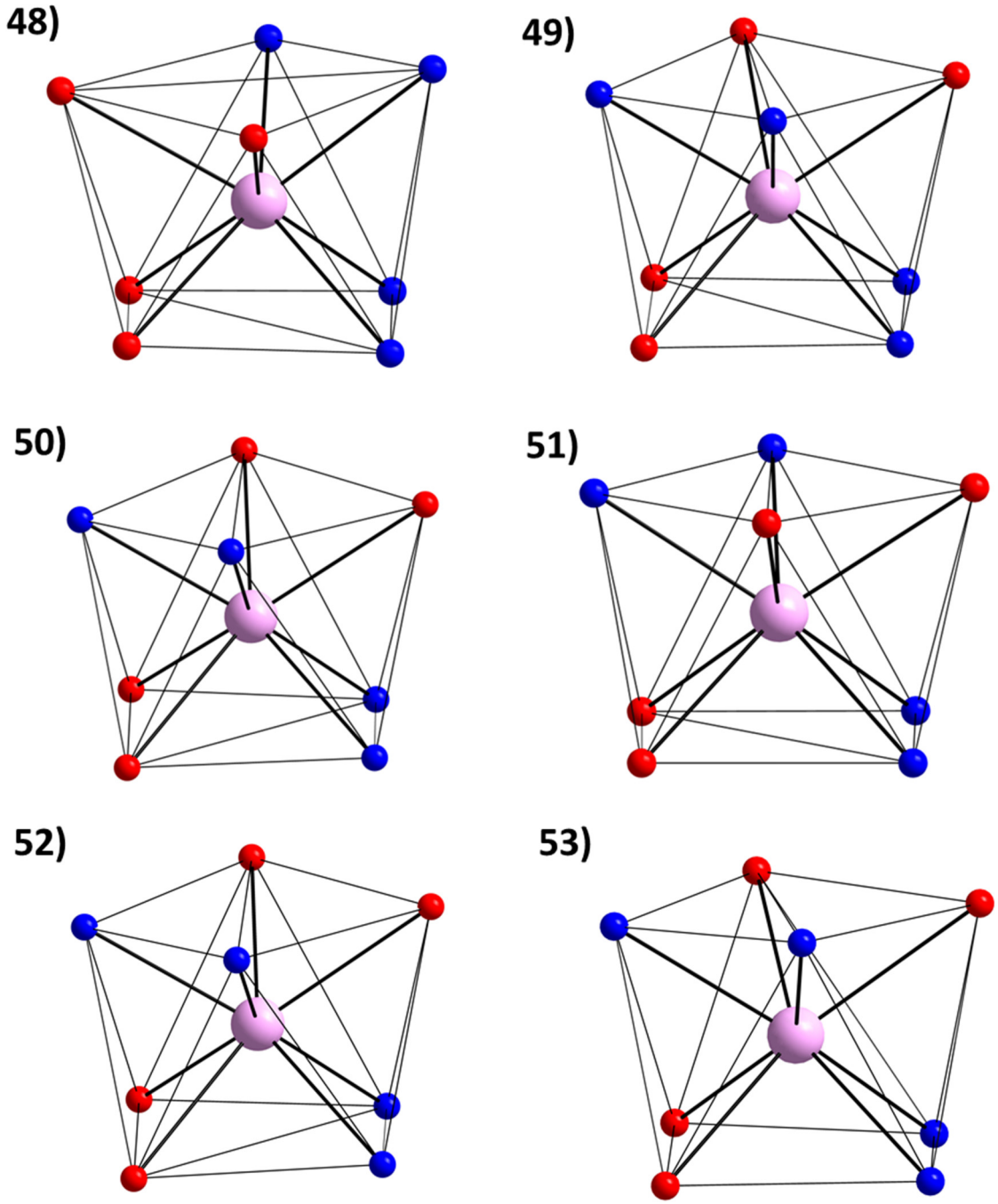

Figure 6.4.- Square antiprism DyO_8 coordination sphere in **48-53**. Colour code: Dy = pink, $O_{aldehyde}$ = red, $O_{phenoxo}$ = blue.

Table 6.1.- Structural features of [ZnX(μ-L)Dy(μ-L)XZn]Y·nS complexes **49**-**53**.

Complex	X	Y	S	Zn-Ln-Zn angle (°)	Dist. upper-lower planes (Å)	Square sides dist. (Å)
49	Br	$[ZnBr_3(CH_3OH)]^-$	MeOH 2 H_2O	143.73	2.599	2.78
50	Br	NO_3^-	3 MeOH	146.77	2.680	2.75
51	I	I^-	MeOH 3H_2O	146.25	2.613	2.74
52	I	NO_3^-	3 MeOH	146.95	2.590	2.77
53	N_3^-	NO_3^-	MeOH H_2O	141.56	2.770	2.61

Finally, complex **54** shows a very similar structure to that of **46** but with a different counteranion, $[PF_6]^-$. The change of the counteranion leads to a more symmetrical structure, the two halves of the trinuclear cation of **54** being symmetrically related by a C_2 axis passing through the Dy and P atoms. The position of the oxygen atoms around the Dy(III) ion is similar to that found in complex **48** (Figure 6.4).

Calculations of the degree of distortion of the DyO_8 coordination polyhedron with respect to an ideal eight-vertex polyhedron using the continuous shape measure theory and the SHAPE software (Appendices, Table A.36) pointed out that the DyO_8 coordination polyhedron can be considered as an intermediate between square antiprism, triangular dodecahedron and biaugmented triangular prism ideal polyhedra, but closer to the former geometry. In the square antiprism description, the average distance between the upper and lower planes containing the four oxygen atoms is 2.565 Å, whereas the average distance of the sides of the squares defined by the oxygen atoms in each plane is 2.782 Å and therefore, the distorted square-antiprism is

compressed. Compared to **46**, **54** shows a DyO_8 coordination sphere that is closer to the square antiprism.

Zn(II) ions exhibit a distorted square pyramid ZnO_2N_2Cl coordination environment, in which the nitrogen and phenoxo oxygen atoms occupy the basal positions with Zn-N bonds distances of 2.106(3) Å and 2.153(3) Å and Zn-O bond distances of 2.066(3) Å and 2.138(3) Å, whereas the axial position is occupied by the Cl atom at a longer distance of 2.217(1) Å. The Zn···Dy distance is 3.550(1) Å, whereas the Zn-Dy-Zn angle is 109.48°. The shortest Dy···Dy distance between neighbouring $[ZnDyZn]^+$ trinuclear cations is 9.199 Å.

6.3.2. Magnetic properties of 46

The *direct-current* magnetic susceptibility of complex **46** was measured on a randomly oriented polycrystalline sample in the 2-300 K temperature range under an applied magnetic field of 0.1 T (Figure 6.5).

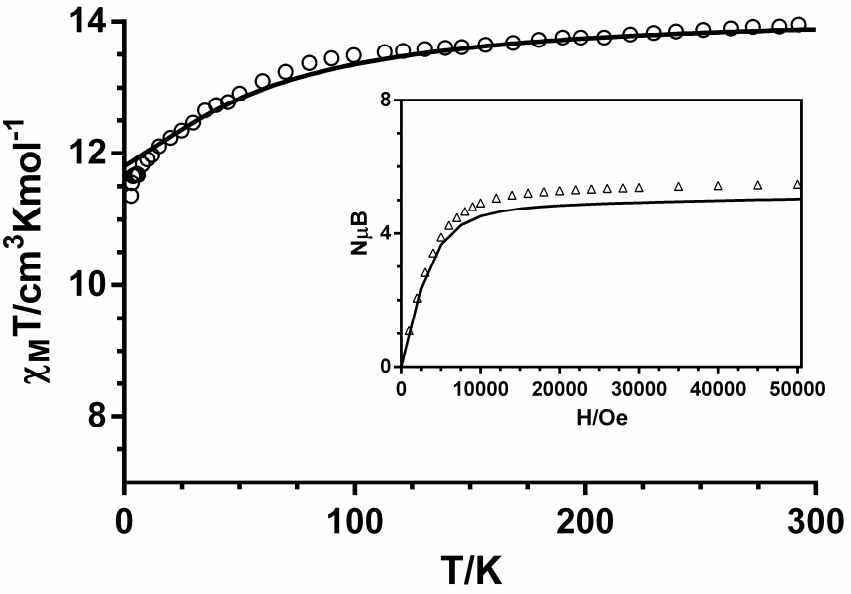

Figure 6.5.- Temperature dependence of $\chi_M T$ for **46**. Inset: Field dependence of the molar magnetization for randomly oriented microcrystals. Solid lines are the *ab initio* calculated curves.

The $\chi_M T$ value of 13.97 $cm^3 \cdot K \cdot mol^{-1}$ at 300 K for **46** is compatible with the calculated value of 14.17 $cm^3 \cdot K \cdot mol^{-1}$ for the ground state of the Dy(III) ion ($4f^9$, J = 15/2, S = 5/2, L = 5, g = 4/3 $^6H_{15/2}$) in the free-ion approximation. On cooling, the $\chi_M T$ product decreases monotonically to a value of 11.65 $cm^3 \cdot K \cdot mol^{-1}$ at 4 K. Below this temperature, there is a change of curvature and $\chi_M T$ decreases more abruptly, reaching a value of 11.36 $cm^3 \cdot K \cdot mol^{-1}$. This behaviour is due to the depopulation of the M_J sublevels of the dysprosium ion, which arise from the splitting of the $^6H_{15/2}$ ground term by the ligand field and/or possible very weak intermolecular interactions between the Dy(III) ions, which could be responsible for the sharp decreases in $\chi_M T$ below 4 K.

The *M* versus *H* plot at 2 K (Figure 6.5, inset) shows a relatively rapid increase in the magnetization, which saturates for magnetic fields larger than 2 T. The saturation value of 5.47 $N\mu_B$ is apparently lower than that expected for a Dy(III) ion ($M_S = gjN\mu_B$ = 10 $N\mu_B$), likely because of crystal field effects leading to a significant magnetic anisotropy.

Dynamic *alternating current* magnetic susceptibility measurements as a function of the temperature and frequency (Figures 6.7 and 6.8) were performed on a microcrystalline powder sample of **46** to determine whether or not it exhibits SIM properties.

As expected from the easy-axis anisotropy of the Dy(III) ion, this complex shows frequency dependence of the out-of-phase magnetic susceptibility (χ_M") under zero external field below 40 K, which can be attributed to the presence of slow relaxation of the magnetization, indicating that **46** functions as a SIM. In the 17 K (200 Hz) - 26 K (10000 Hz) range, there is a peak that overlaps with a tail at low temperature (χ_M" does not go to zero below the maxima, but increases up to 2 K). The appearance of this tail clearly indicates the existence of fast QTM. As Dy(III) is a Kramer's ion, at zero field, dipole-dipole and hyperfine interactions should be responsible for the mixing of the two Kramer's ground states that allows the zero-field quantum tunneling dynamics of the magnetization. The Cole–Cole diagram for **46** in the temperature range 17-30 K (Figure 6.6) exhibits semicircular shapes and can be fitted by using the generalized Debye model. The obtained α values are in the 0.47 (17 K) - 0.09 (30 K) range, thus suggesting the existence of multiple relaxation processes. The relaxation times extracted from the frequency-dependent susceptibility data follow an Arrhenius law with an effective energy barrier for the reversal of the magnetization of U_{eff} = 140 K (97 cm^{-1}) and $\tau_0 = 1.4 \cdot 10^{-7}$ s (Figure 6.7, bottom). The U_{eff} is somewhat lower than the value

predicted from the *ab initio* calculations (energy gap between the ground and first excited Kramer's doublet, Table 6.2 in Section 6.3.3); which is primarily due to the existence of QTM. The relatively large value of τ_0 confirms that QTM remains operative even where the thermal relaxation is prevailing and therefore relaxation of the magnetization in **46** is not a purely thermally activated Orbach process. The Arrhenius plot constructed from the temperatures and frequencies of the maxima observed for the χ_M" signals gives to the same result, as expected.

The QTM can be partly or fully suppressed by application of a small external *dc* field, often resulting in an increase of the U_{eff}. Thus, when the *ac* measurements on **46** were performed in the presence of a small external *dc* field of 1000 Oe (this field was chosen because it induces the slowest relaxation rate, which does not significantly vary until fields as high as 3000 Oe, Figure 6.6), the tails at low temperature almost disappeared and the high temperature peaks remained roughly at the same temperatures as those observed under zero *dc* applied field and exhibited similar intensity (Figure 6.8). The fact that magnetic fields as high as 3000 Oe are not able to fully eliminate the QTM relaxation process suggests that the remaining QTM process is promoted by intermolecular magnetic dipolar interactions. An appropriate manner to try to eliminate the intermolecular interactions and therefore, the QTM process would be to dilute the sample by co-crystallizing **46** with the isostructural diamagnetic complex of Y(III). However, all attempts to obtain crystals of the diluted complex have been unsuccessful thus far.

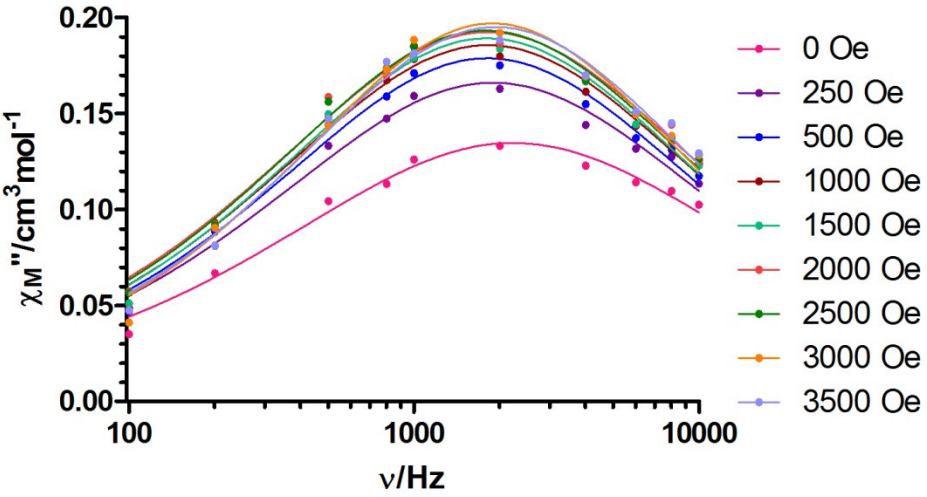

Figure 6.6.- Field dependence of the out-of-phase signal vs. frequency at 20 K for **46**.

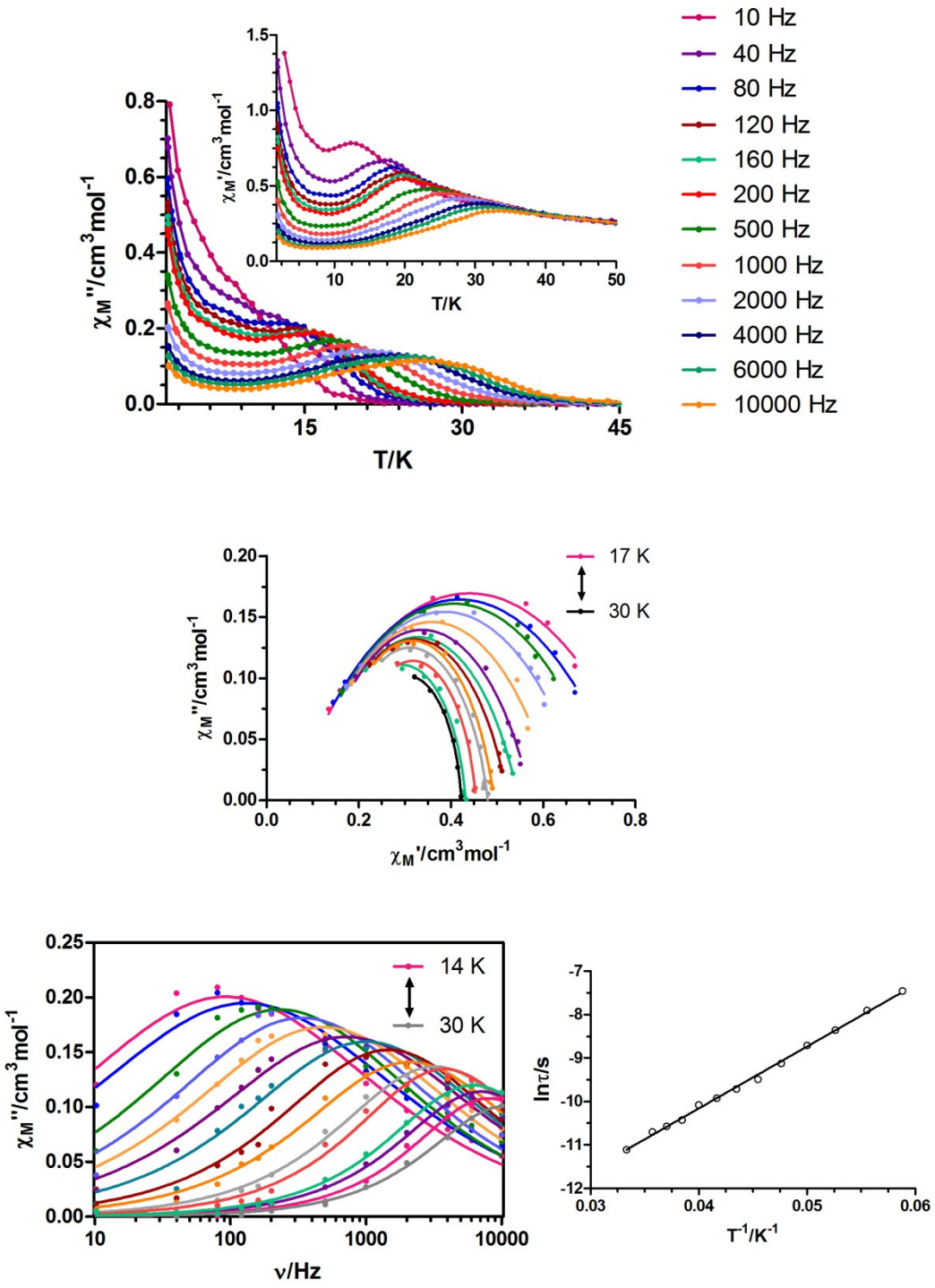

Figure 6.7.- Top: temperature dependence of in-phase χ_M' (inset) and out-of phase χ_M'' components of the *alternating current* (*ac*) susceptibility for complex **46** under zero dc applied field. Medium: Cole-Cole plot. Bottom left: variable-temperature frequency dependence of the χ_M'' signal. Bottom right: Arrhenius plots for the relaxation of **46** (black line).

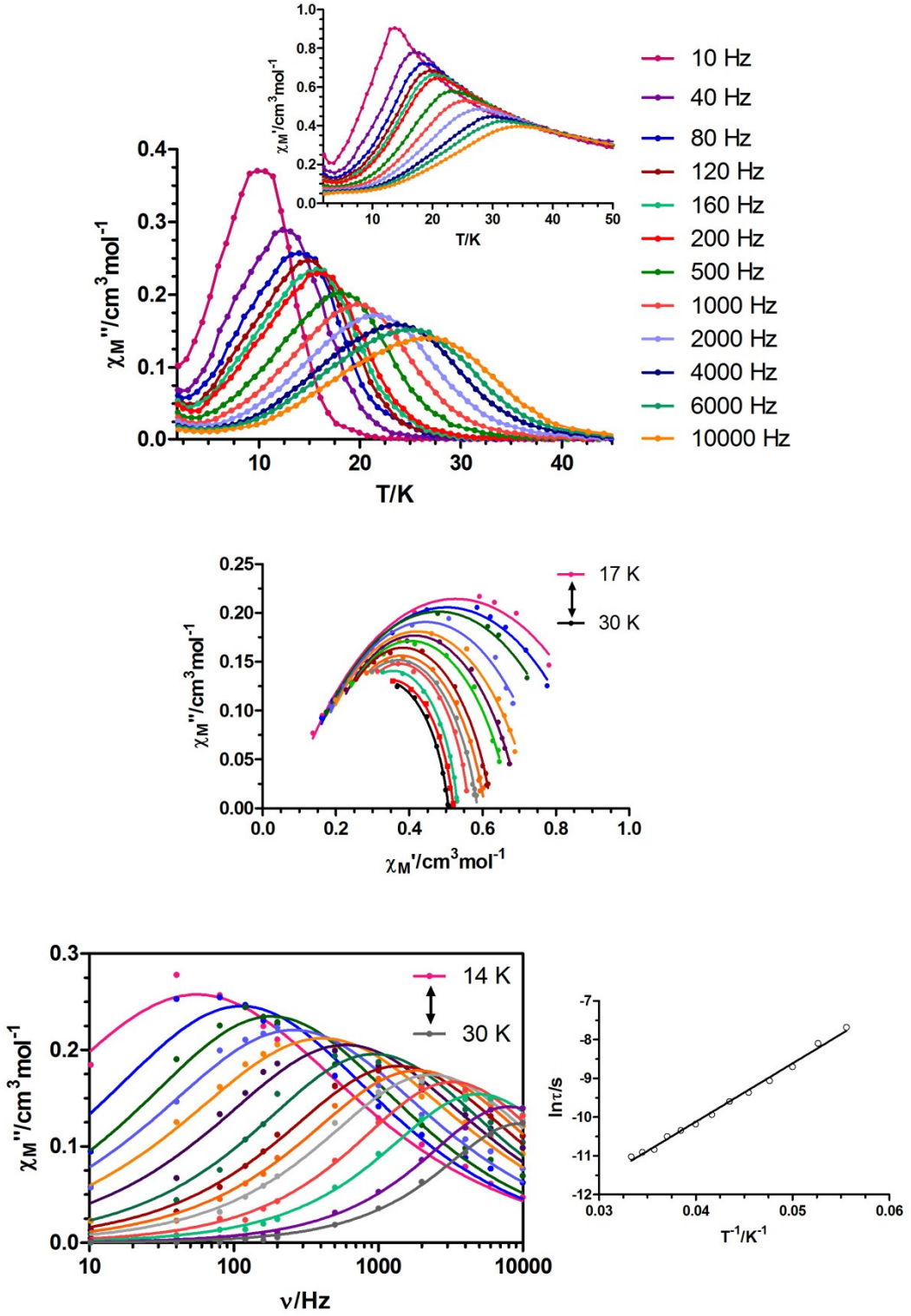

Figure 6.8.- Top: temperature dependence of in-phase χ_M' (inset) and out-of phase χ_M'' components of the *alternating current* (ac) susceptibility for complex **46** under 1000 Oe applied external field. Medium: Cole-Cole plot. Bottom left: variable-temperature frequency dependence of the χ_M'' signal. Bottom right: Arrhenius plots for the relaxation of **46** (black line).

The fit of the relaxation times versus 1/T data in the 17 K-30 K temperature range to the Arrhenius law (Figure 6.8) leads to a small increase of the thermal energy barrier and a decrease of τ_0 (U_{eff} = 148 K (103 cm^{-1}) and τ_0 = $1.07 \cdot 10^{-7}$ s). In the above temperature region, the α values extracted from the Cole-Cole plot are in the 0.44-0.12 range, which points to the existence of a distribution of the relaxation times. The τ_0 value is still larger than that usually observed for pure thermally activated processes, thus supporting the existence of QTM at such relatively high temperatures.

Magnetization hysteresis loop measurements have been performed on a powder sample of **46** at 0.4 and 2 K and different sweeping rates by using a micro Hall-effect magnetometer with the aim of studying the magnetization dynamics and to confirm the SIM properties of **46** (Figure 6.9). This complex exhibits at 2 K butterfly-shaped hysteresis loops with a large step near zero field (Figure 6.9, top), which is consistent with the QTM generally found for 4f-containing complexes and the tail that this compound exhibits at low temperatures in the χ_M" versus T plot. As expected for SIMs, the coercivity increases with increasing field sweep rates. The fact that the coercive field at 0.4 K is lower than at 2 K, when the opposite trend is expected, can be ascribed to a reduction of the tunneling due to thermal activations around the tunnel splitting.[6]

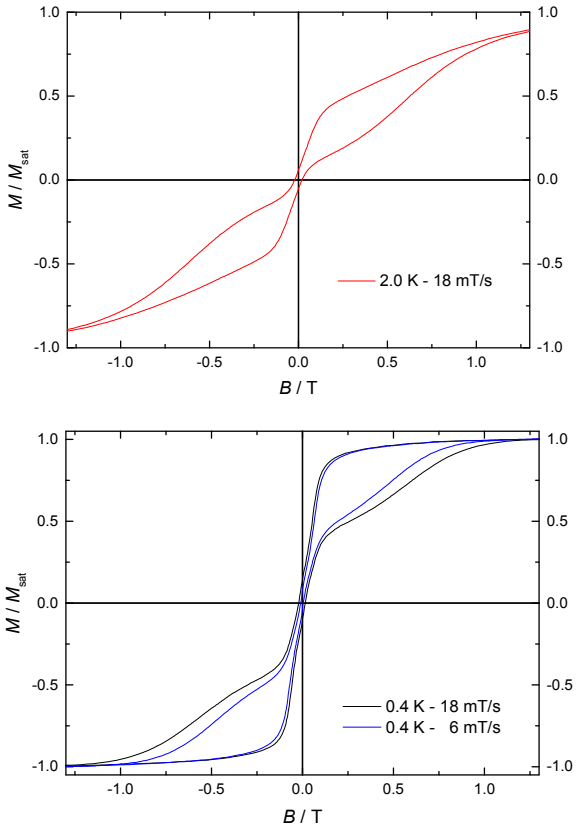

Figure 6.9.- Magnetic hysteresis loops for **46** within -1.5 < *H*/T < 1.5 at the indicated sweep rates and temperatures.

6.3.3. *Ab initio* calculations on 46

To support the presence of axial anisotropy and to deepen the insight of the mechanism of the slow magnetic relaxation properties of **46**, electronic calculations based on the CASSCF + RASSI method were performed.[7] This methodology allows the description of the highly multiconfigurational character (CASSCF step) of the low-lying spectrum of Dy(III) complexes due to the presence of several low-energy excited states, associated with the small ligand field splitting that is observed in lanthanide coordination compounds. Spin-orbit coupling effects are included in a second step (RASSI), considering the previously converged CASSCF wave functions (technical details of the calculations are described in Appendices, Section VI).

Table 6.2 presents the calculated energies and *g* factors for the eight lowest Kramer's doublets. These states span an energy interval of 560 cm^{-1}, this range being normal for Dy(III) complexes[8] and being a consequence of the small orbital splitting associated with ligand field effects.

Table 6.2.- Calculated energies (cm^{-1}) and *g* factors for the eight lowest Kramer's doublets.

Doublet	Energy (cm^{-1})	g_z	g_y	g_x
1	0.0	19.430	0.001	0.000
2	129.0	16.488	0.075	0.071
3	257.0	13.046	0.381	0.274
4	334.4	9.932	3.412	1.896
5	374.4	3.211	6.757	9.294
6	455.4	13.404	1.061	0.381
7	502.3	16.541	1.420	0.456
8	560.6	19.453	0.134	0.102

The excitation energy between the ground and second Kramer's doublets is 129 cm^{-1}, which is also in the typical range for Dy(III) CASSCF + RASSI calculations. The ground doublet state is calculated to be fundamentally pure $M_J = \pm 15/2$ and markedly axial ($g_z = 19.430$), with almost vanishing transversal components of *g* (that is to say an almost ideal Ising state) in accordance with their zero-field SIM properties.[9] The experimental temperature dependence of the $\chi_M T$ product and the field dependence of

the magnetization can both be well reproduced from the energy levels obtained in the *ab initio* calculations (Figure 6.5), thus supporting the calculated low-lying state energies for **46**. Furthermore, the calculated excitation energies in the CASSCF step are also favourable for a strongly anisotropic magnetic moment, with an almost two-fold degenerate ground state (first excitation energy 1.7 cm^{-1}) and a higher second excited state (205.7 cm^{-1}). The plotted beta density of the 4f Dy(III) electrons obtained in the CASSCF step for the first three states are represented in Figure 6.10 (Dy(III) is $4f^9$ and the seven alpha electrons give an isotropic spherical electron density). This energy profile favours the mixing of mostly the first two CASSCF states in the ground RASSI wave function resulting in an oblate beta electron density for this state,[7b] because only the third state, that is high in energy, has a different electron-density shape.

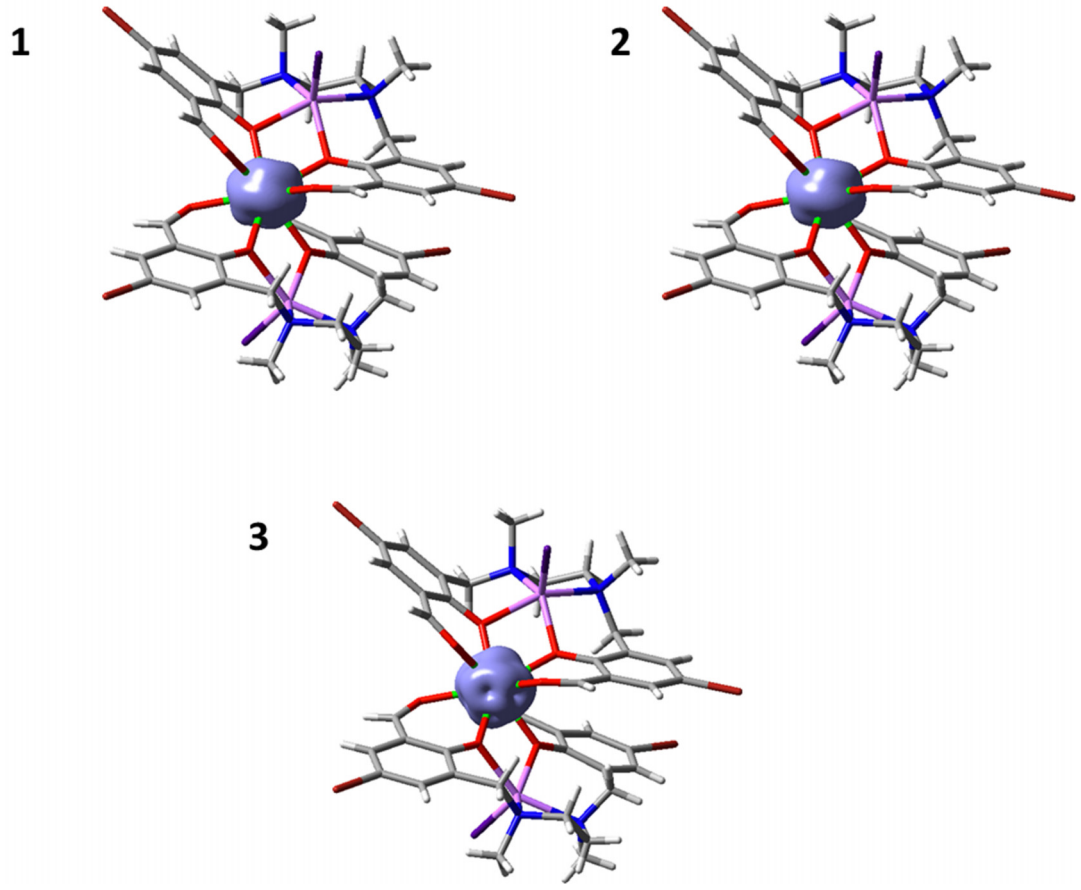

Figure 6.10.- Beta spin density of the Dy(III) f electrons for the first three spin-free CASSCF states.

The calculated magnetic moment of the ground state (Figure 6.11) lies between the planes formed by the two Dy-O-Zn-O moieties, roughly collinear with the two shortest

Dy-O distances (2.252 and 2.258 Å, with 12.78 and 21.88° deviations between the magnetic moment and the Dy-O bond vectors, respectively) and as expected, perpendicular to the oblate shape electron density. This feature highlights the appropriateness of an axially repulsive coordination environment for achieving SIM properties in Dy(III) compounds, as qualitatively predicted by the oblate–prolate model.[1,2]

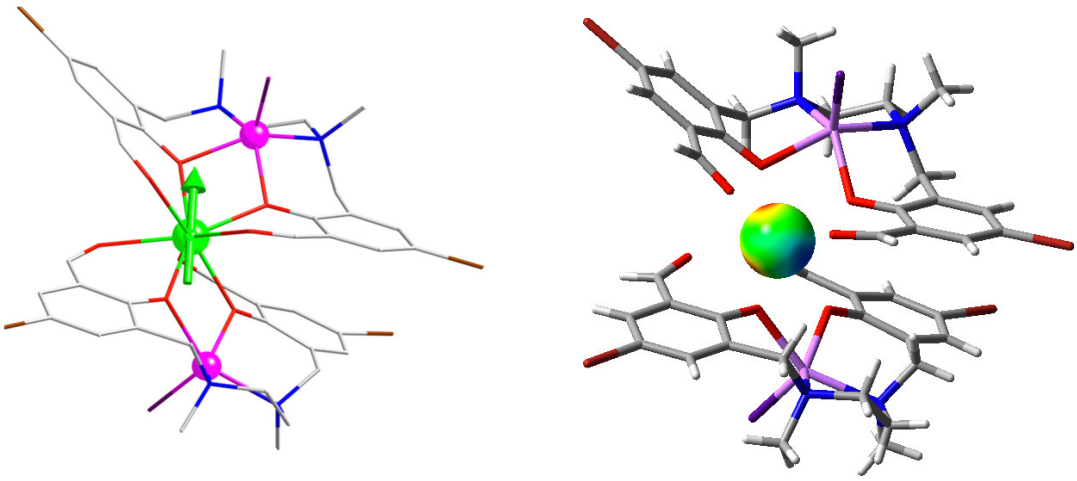

Figure 6.11.- Left: molecular structure of **46**. Colour code: Dy (green); Zn (magenta); Br (brown); Cl (purple); O (red); N (blue); C (gray). Hydrogens are omitted for clarity. The direction of the magnetic moment of the ground state is indicated as a green arrow. Right: DFT calculated (B3LYP/TZV) electrostatic potential of the coordination environment (only ligands) projected in a sphere located at the Dy position (1 Å radius). Blue regions correspond to low potential (less repulsive) while highly repulsive regions are indicated in red.

To verify the influence of the ligand potential in the anisotropy of the 4f density of the Dy(III) cation, electrostatic potential maps caused by the ligands projected in the Dy(III) position were constructed by means of DFT calculations. In short, the electrostatic potential gives information about the more (red in Figure 6.11) and less (blue) repulsive regions from the position of the Dy(III) ion. Hence, the beta electron density of the ground state (mixing of the two first states of Figure 6.10) is accommodated in the region with less repulsion (green and blue in Figure 6.11) to reduce electronic repulsion, while in the perpendicular direction, the magnetic moment is pointing towards the strongest repulsion regions (red in Figure 6.11) corresponding to the shortest Dy-O bonds. According with these electrostatic arguments, the direction of the anisotropy axes of the Dy(III) ions have also been calculated by using the

Chilton's method, which consists of assigning the charge of the ligand by using a minimal valence bond model and then constructing an electrostatic crystal field potential. Minimization of the electrostatic energy yields the orientation of the magnetic moments, as stated previously by different authors.[7a,10] As expected, the orientation of the anisotropy axis for each Dy(III) ion using a simple electrostatic approach (Figure 6.12) compare rather well with that obtained by *ab initio* methods (Figure 6.11, left).

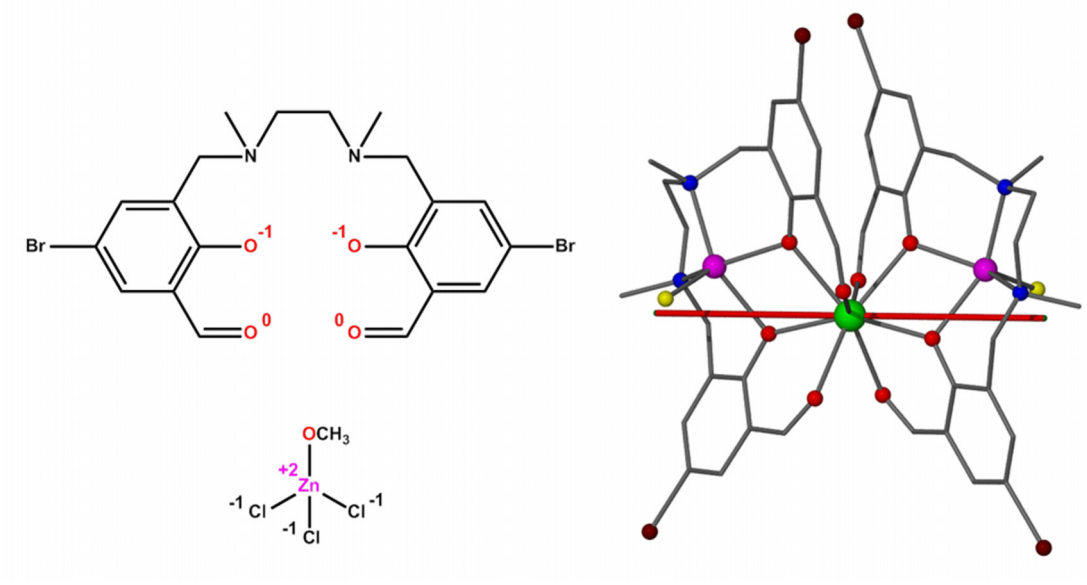

Figure 6.12.- Left: Partial charges assigned to the charged ligands. The rest of the atoms have zero charge. Right: Anisotropy axis for the Dy(III) ion (red line). The local magnetic moment forms an angle with the shorter Dy-O distances plane of 14.43° and 13.99°, which are close to the direction of that extracted using CASSCF *ab initio* calculations.

6.3.4. Magnetic Properties of complex 47

The isostructural [ZnCl(μ-L)Er(μ-L)ClZn][$ZnCl_3(CH_3OH)$]·$3CH_3OH$ complex (**47**), only exhibits a slight frequency dependence of the out-of-phase (χ_M") signals below approximately 6 K under zero field but without reaching a neat maximum above 2 K even at frequencies as high as 4000 Hz (Figure 6.13). The lack of a maximum in χ_M" versus T plot for **47**, points to either the existence of a fast QTM or an energy barrier for the flipping of the magnetization that is not high enough to block the magnetization above 2 K. However, under a 1000 Oe applied *dc* field, the QTM is almost suppressed and several maxima appear at high frequencies in the 2.2 K (2000 Hz)-3.3 K (10000 Hz) range (Figure 6.15).

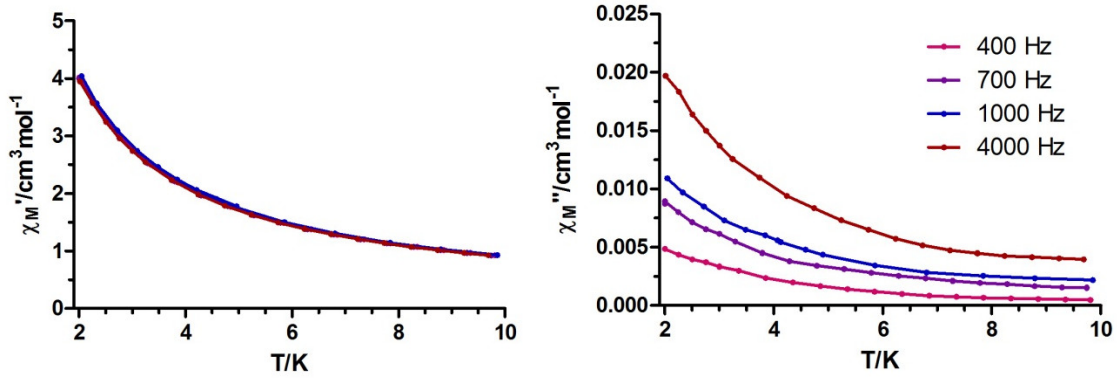

Figure 6.13.- Temperature dependence of the *ac* susceptibility for complex **47** measured under zero applied field.

From the Arrhenius law the effective energy barrier for **47** has been estimated to be 9.3 cm^{-1} with a pre-exponential factor of $\tau_0 = 4.5 \cdot 10^{-7}$ s. The absence of a significant energy barrier for the reorientation of the magnetization even at H_{dc} = 1000 Oe should be due to the lack of easy-axis anisotropy in the ground doublet state; this can be justified by using the simple oblate-prolate model. Er(III) has a prolate electron-density distribution and, to avoid the electrostatic repulsion with the negatively charged phenoxo groups, the magnetic moment (and the f electron cloud) should be located almost perpendicular to the shorter Er-O bonds in the mean plane of the aldehyde groups and without a well-defined orientation (Figure 6.14). This would lead to an easy-plane anisotropy stabilizing a ground state with a low M_J value, which would explain the absence of SIM behaviour in **47**.

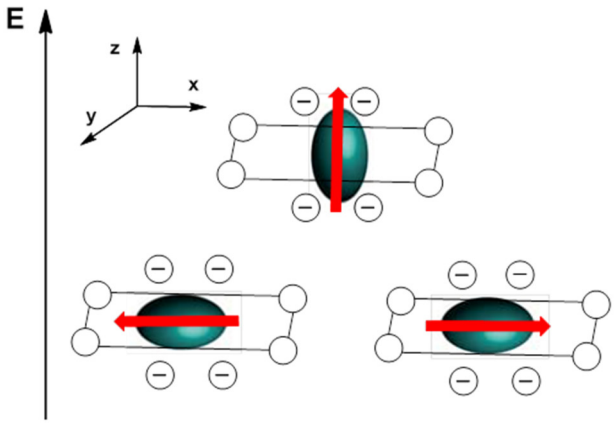

Figure 6.14.- To diminish electrostatic repulsion, the magnetic moment of **47** is located in the xy plane.

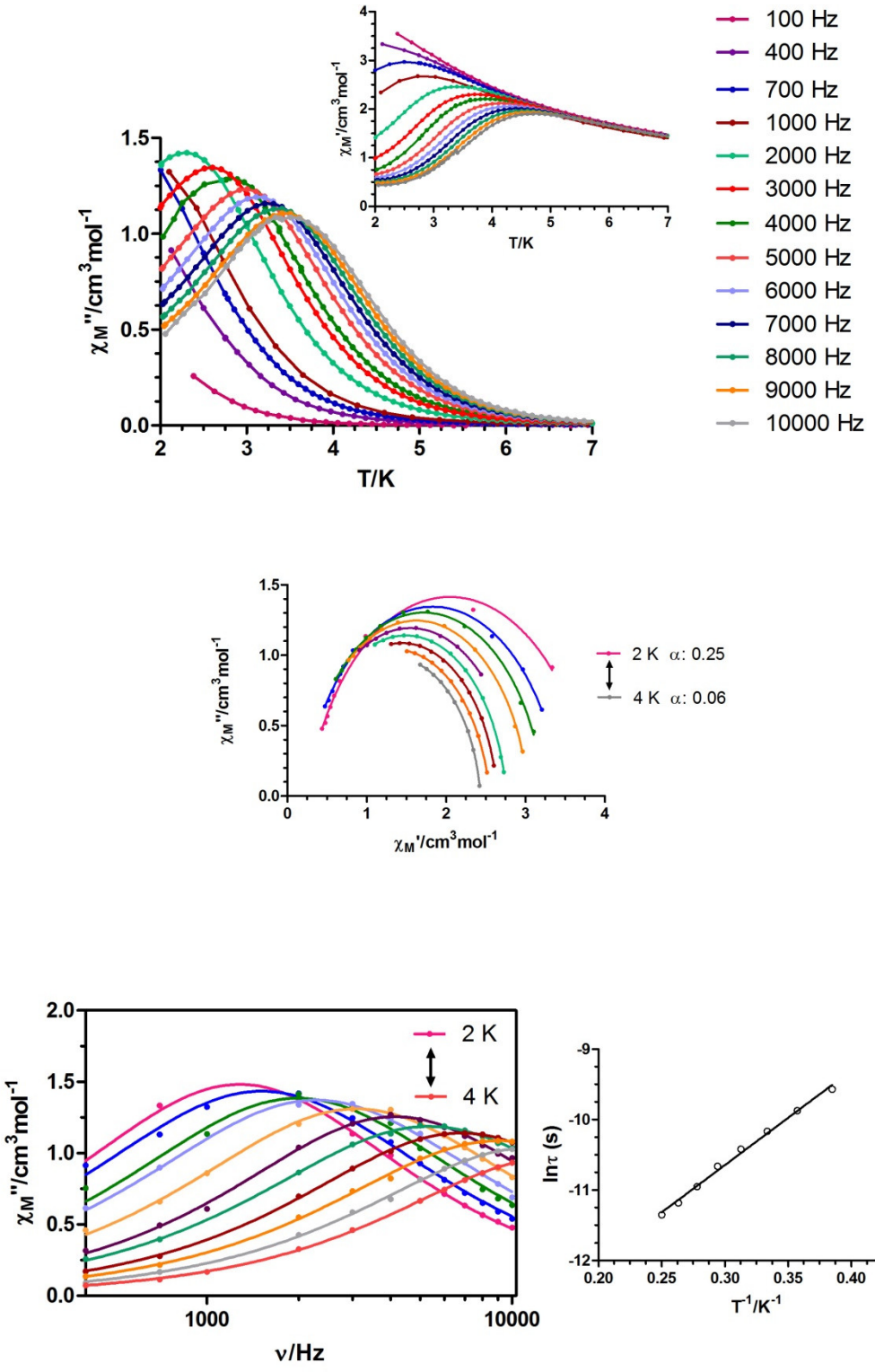

Figure 6.15.- Top: temperature dependence of in-phase χ_M' (inset) and out-of phase χ_M'' components of the *alternating current* susceptibility for complex **47** under 1000 Oe applied external field. Medium: Cole-Cole plot. Bottom left: variable-temperature frequency dependence of the χ_M'' signal. Bottom right: Arrhenius plots for the relaxation of **47** (black line).

6.3.5. Magnetic Properties of Complexes 48-53

In order to know if the similar complexes **48**-**53** also exhibit SIM properties, dynamic *alternating current* magnetic susceptibility measurements as a function of the temperature and frequency were performed (Figures 6.16-6.27). All these complexes show similar magnetic behaviour to that of **46** and the obtained energy barriers are collected in Table 6.3.

Table 6.3.- U_{eff} and τ_0 values for complexes **48**-**53**.

Complex	U_{eff} (K) at H = 0 Oe	τ_0 (s) at H = 0 Oe	U_{eff} (K) at H = 1000 Oe	τ_0 (s) at H = 1000 Oe
48	170	$4.30\cdot10^{-7}$	178	$4.14\cdot10^{-8}$
49	164	$6.09\cdot10^{-8}$	165	$4.80\cdot10^{-8}$
50	150	$6.18\cdot10^{-8}$	154	$4.94\cdot10^{-8}$
51	144	$1.01\cdot10^{-7}$	147	$9.03\cdot10^{-8}$
52	156	$4.30\cdot10^{-8}$	163	$4.40\cdot10^{-8}$
53	159	$3.08\cdot10^{-8}$	167	$2.40\cdot10^{-8}$

The obtained energy barriers under zero external *dc* field are in the 144-170 K range and as in the case of **46**, the application of a small external field of 1000 Oe leads to slightly higher U_{eff} values (in the 147-178 K range) and slightly lower τ_0 values. The variation on the U_{eff} values can be explained if we take into account the disposition of the oxygen atoms in the DyO_8 coordination polyhedron. As can be seen in Figures 6.2 and 6.4 of the crystal structures section, the oxygen atoms are distributed in three general ways in the DyO_8 coordination environments. That is to say, after defining the same oxygen disposition in the lower plane for all the complexes, the two phenoxo oxygen atoms of the upper plane can be located at a) the left and the back, as in **46** and **51**; b) the left and the front as in **49**, **50**, **52** and **53** and c) at the right and the back as in **48**. The U_{eff} seems to be conditioned by the disposition of the oxygen atoms as complexes with the first coordination environment show the lowest U_{eff} values, complexes with the second oxygen disposition show intermediate U_{eff} values and complex **48**, with the third coordination environment, has the highest U_{eff} value. Nevertheless, this conclusion should be taken with caution because other factors, such the Dy-O distances and O-Dy-O angles can also have influence on the magnitude of

the U_{eff}. We are now performing *ab initio* calculations for supporting the above hypotheses.

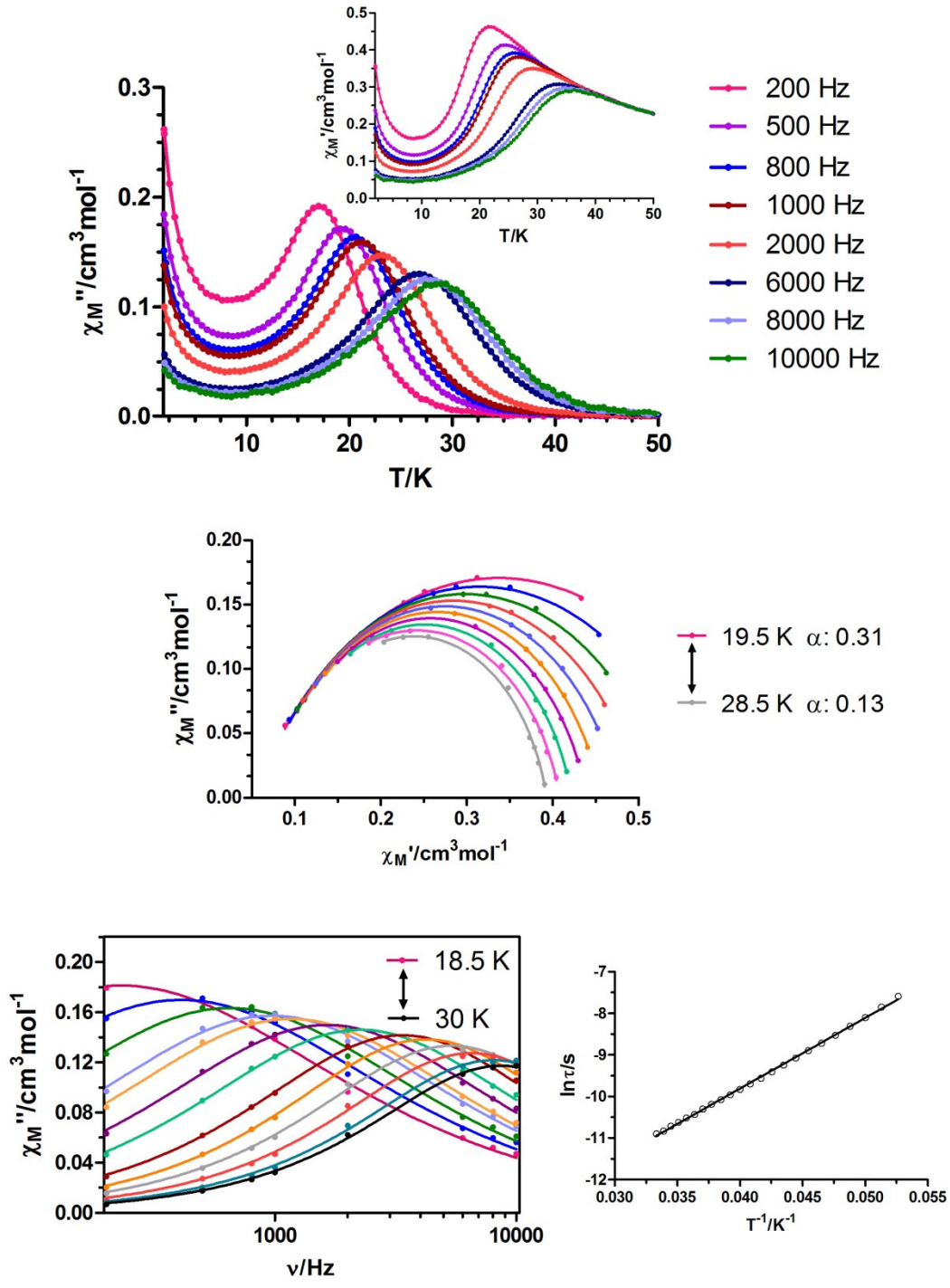

Figure 6.16.- Top: temperature dependence of in-phase χ_M' (inset) and out-of phase χ_M" components of the *alternating current* susceptibility for complex **48** under zero applied external field. Medium: Cole-Cole plot. Bottom left: variable-temperature frequency dependence of the χ_M" signal. Bottom right: Arrhenius plots for the relaxation of **48** (black line).

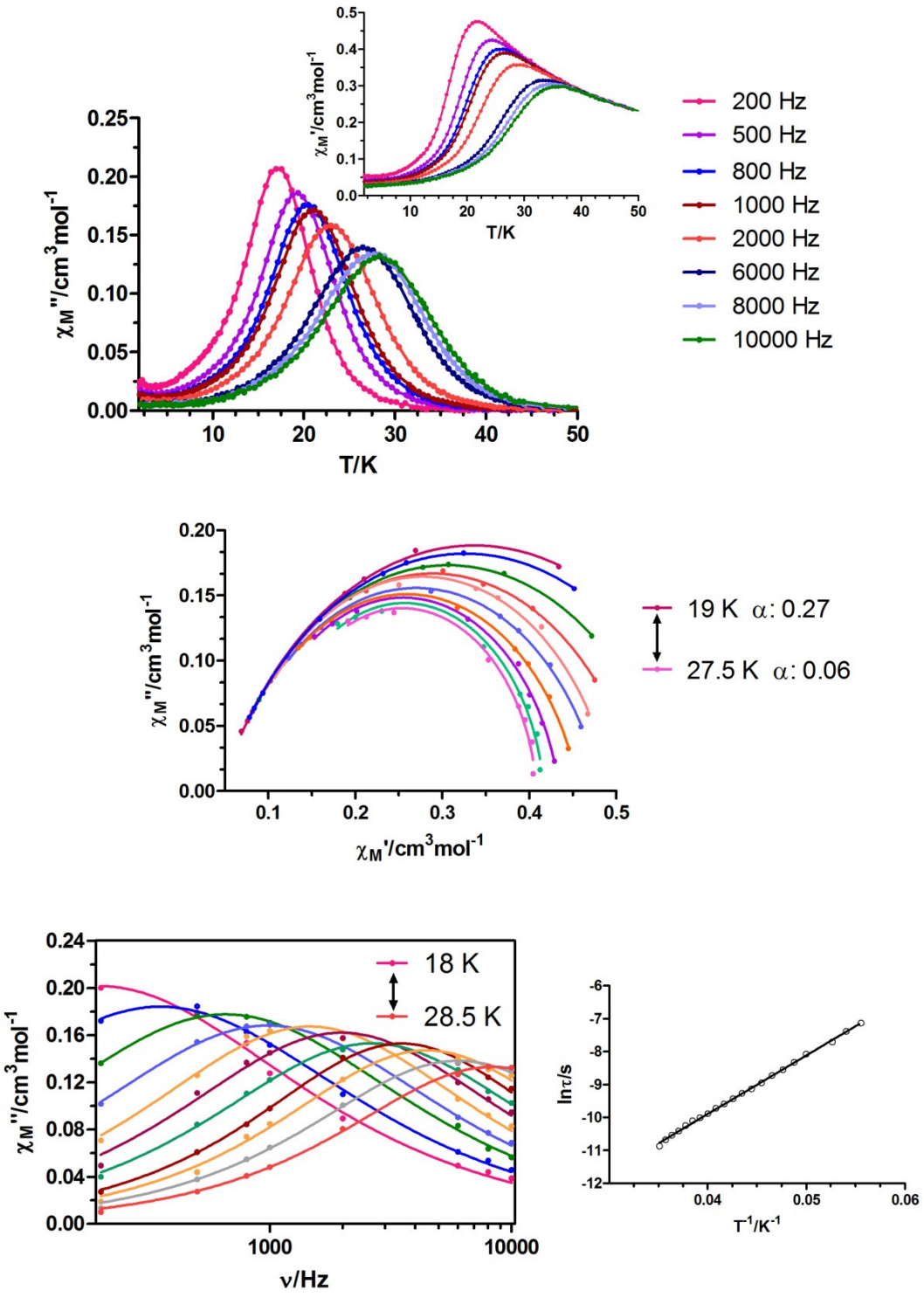

Figure 6.17.- Top: temperature dependence of in-phase χ_M' (inset) and out-of phase χ_M'' components of the *alternating current* susceptibility for complex **48** under 1000 Oe applied external field. Medium: Cole-Cole plot. Bottom left: variable-temperature frequency dependence of the χ_M'' signal. Bottom right: Arrhenius plots for the relaxation of **48** (black line).

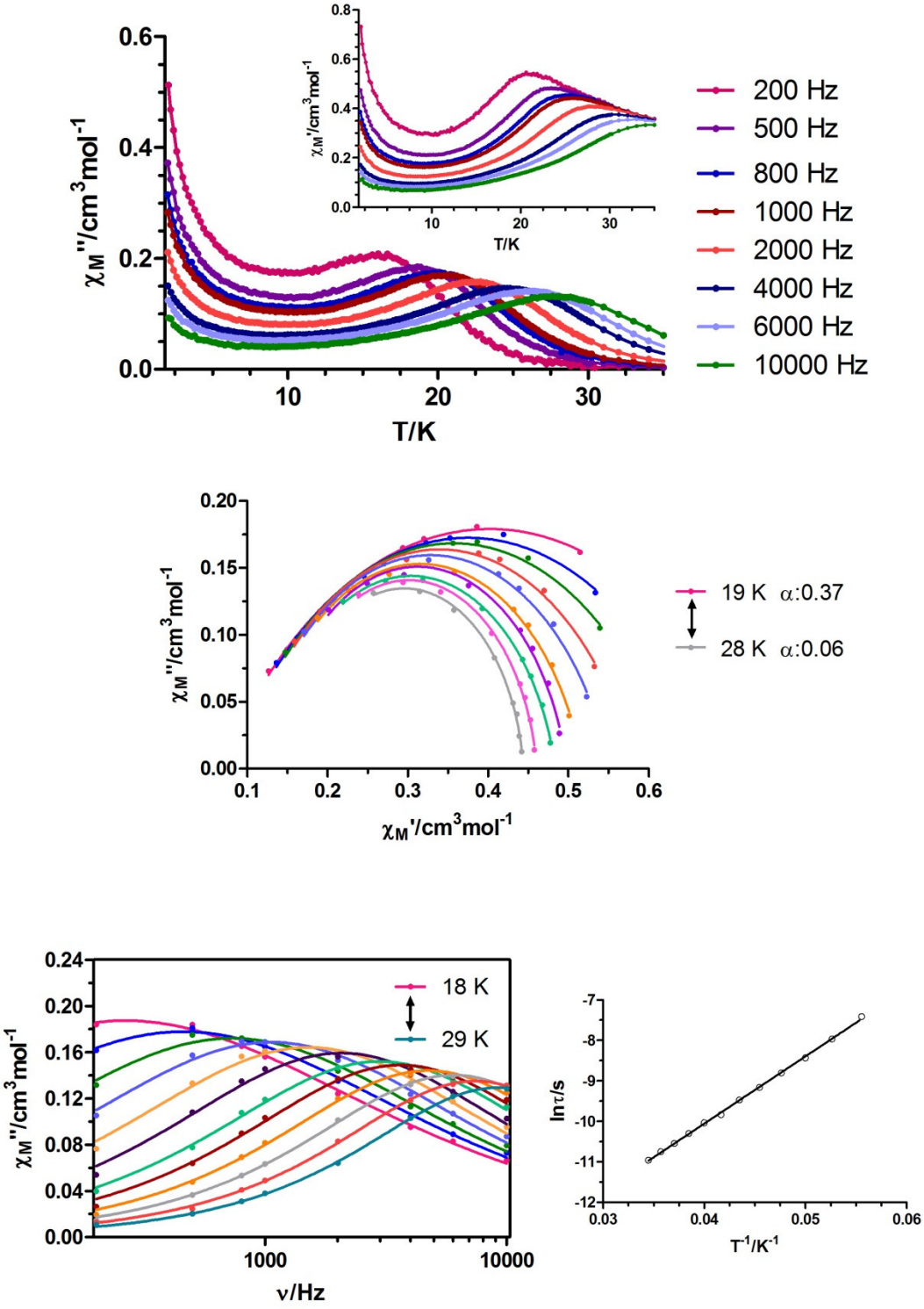

Figure 6.18.- Top: temperature dependence of in-phase χ_M' (inset) and out-of phase χ_M'' components of the *alternating current* susceptibility for complex **49** under zero applied external field. Medium: Cole-Cole plot. Bottom left: variable-temperature frequency dependence of the χ_M'' signal. Bottom right: Arrhenius plots for the relaxation of **49** (black line).

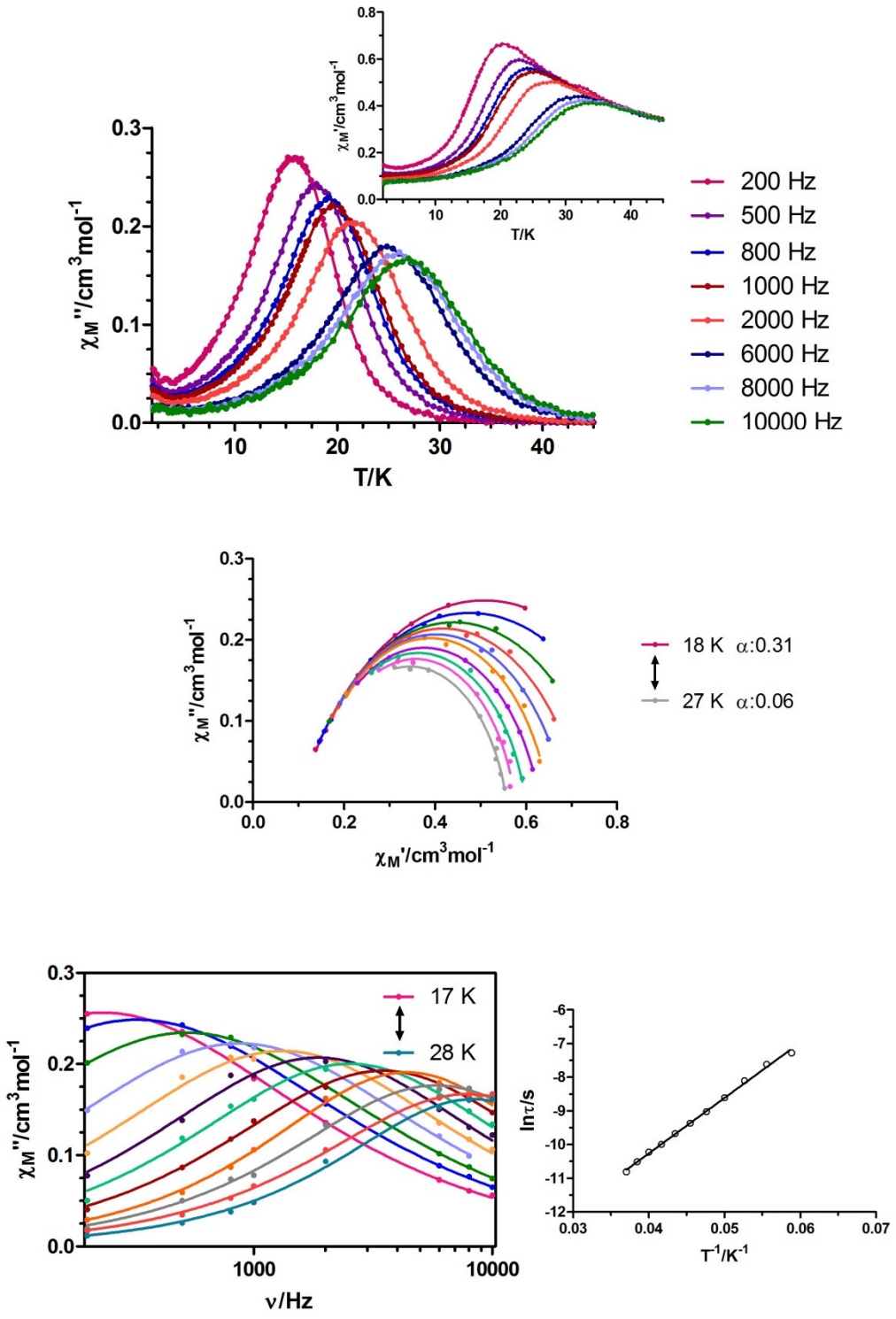

Figure 6.19.- Top: temperature dependence of in-phase χ_M' (inset) and out-of phase χ_M" components of the *alternating current* susceptibility for complex **49** under 1000 Oe applied external field. Medium: Cole-Cole plot. Bottom left: variable-temperature frequency dependence of the χ_M" signal. Bottom right: Arrhenius plots for the relaxation of **49** (black line).

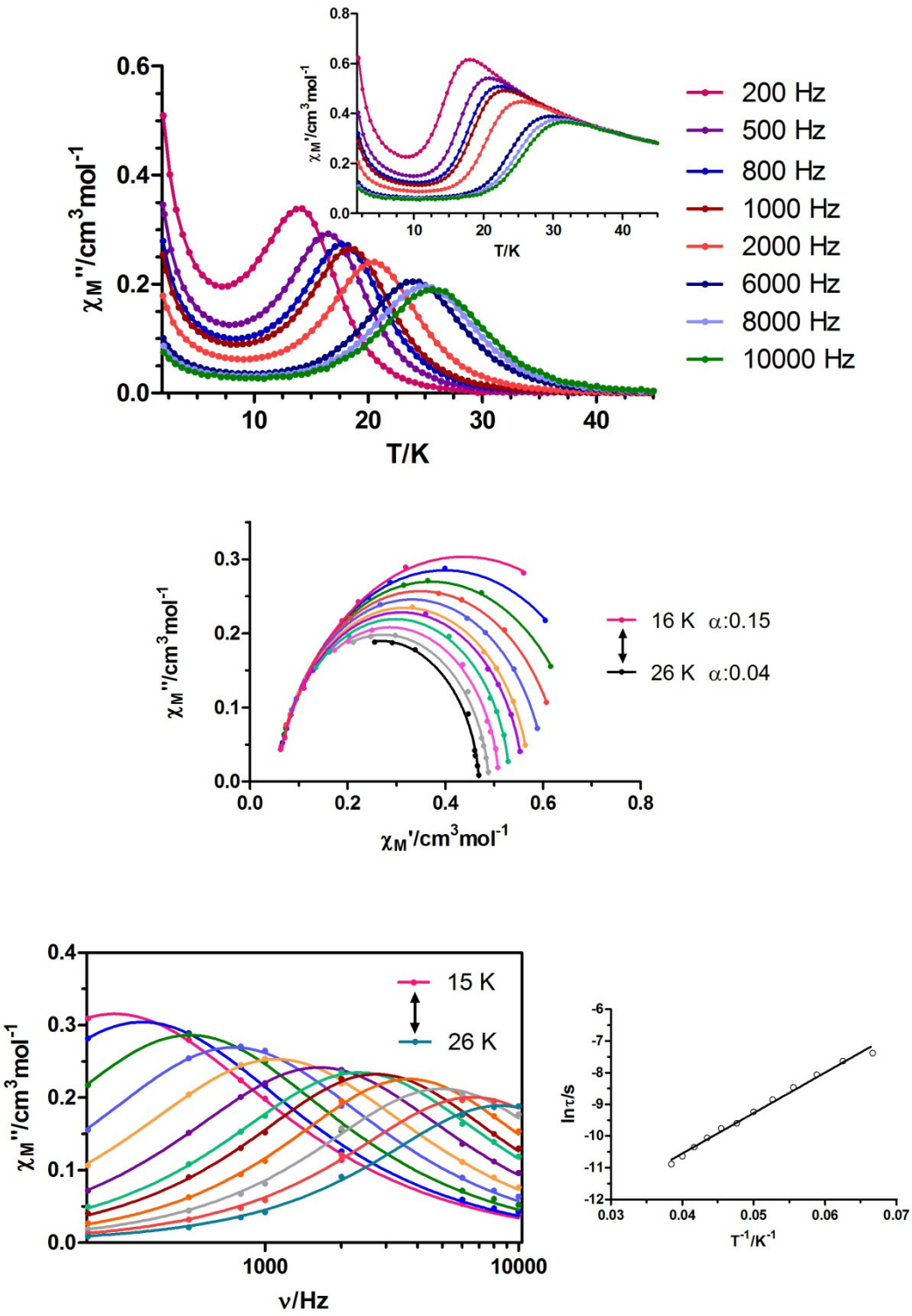

Figure 6.20.- Top: temperature dependence of in-phase χ_M' (inset) and out-of phase χ_M'' components of the *alternating current* susceptibility for complex **50** under zero applied external field. Medium: Cole-Cole plot. Bottom left: variable-temperature frequency dependence of the χ_M'' signal. Bottom right: Arrhenius plots for the relaxation of **50** (black line).

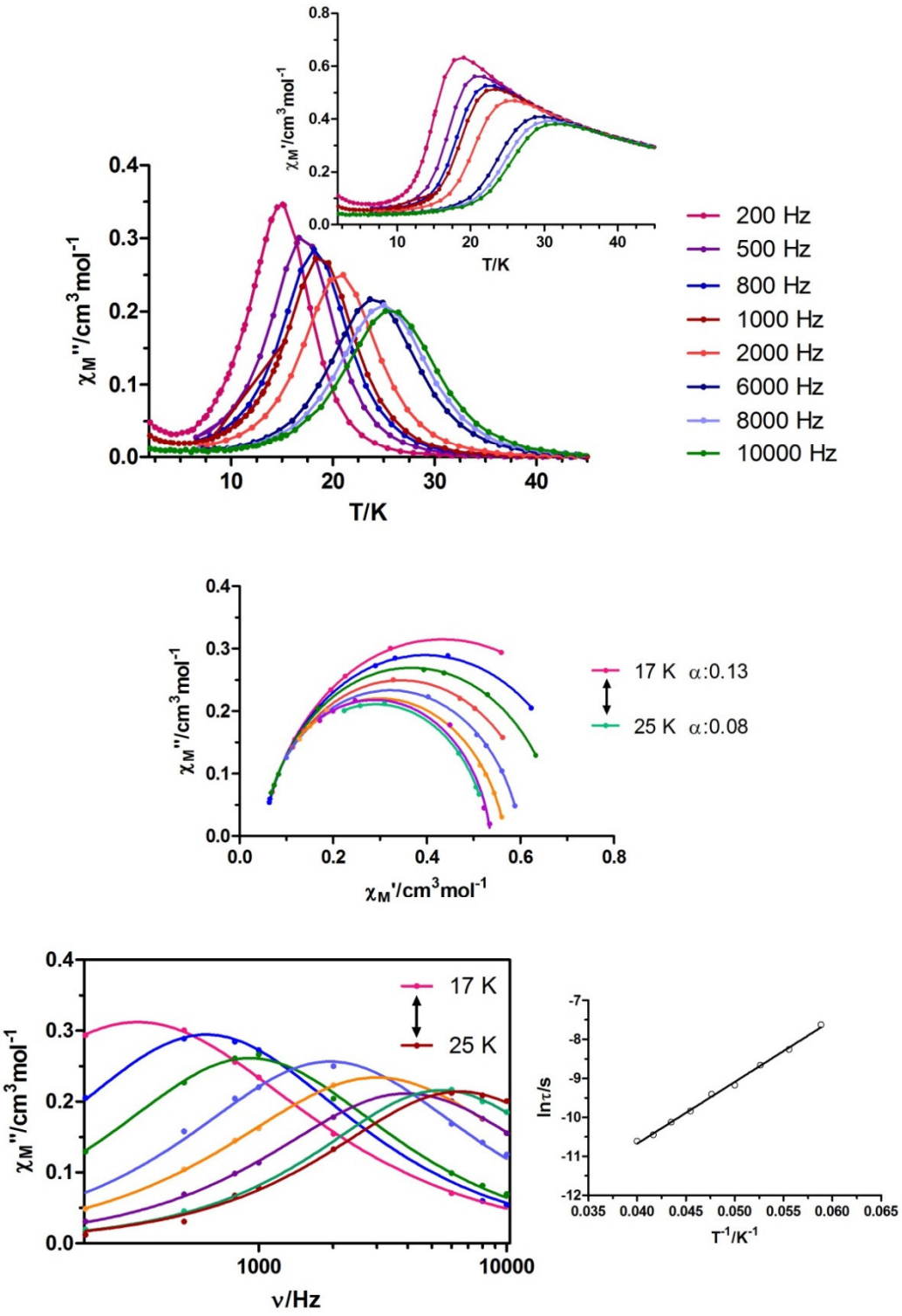

Figure 6.21.- Top: temperature dependence of in-phase χ_M' (inset) and out-of phase χ_M'' components of the *alternating current* susceptibility for complex **50** under 1000 Oe applied external field. Medium: Cole-Cole plot. Bottom left: variable-temperature frequency dependence of the χ_M'' signal. Bottom right: Arrhenius plots for the relaxation of **50** (black line).

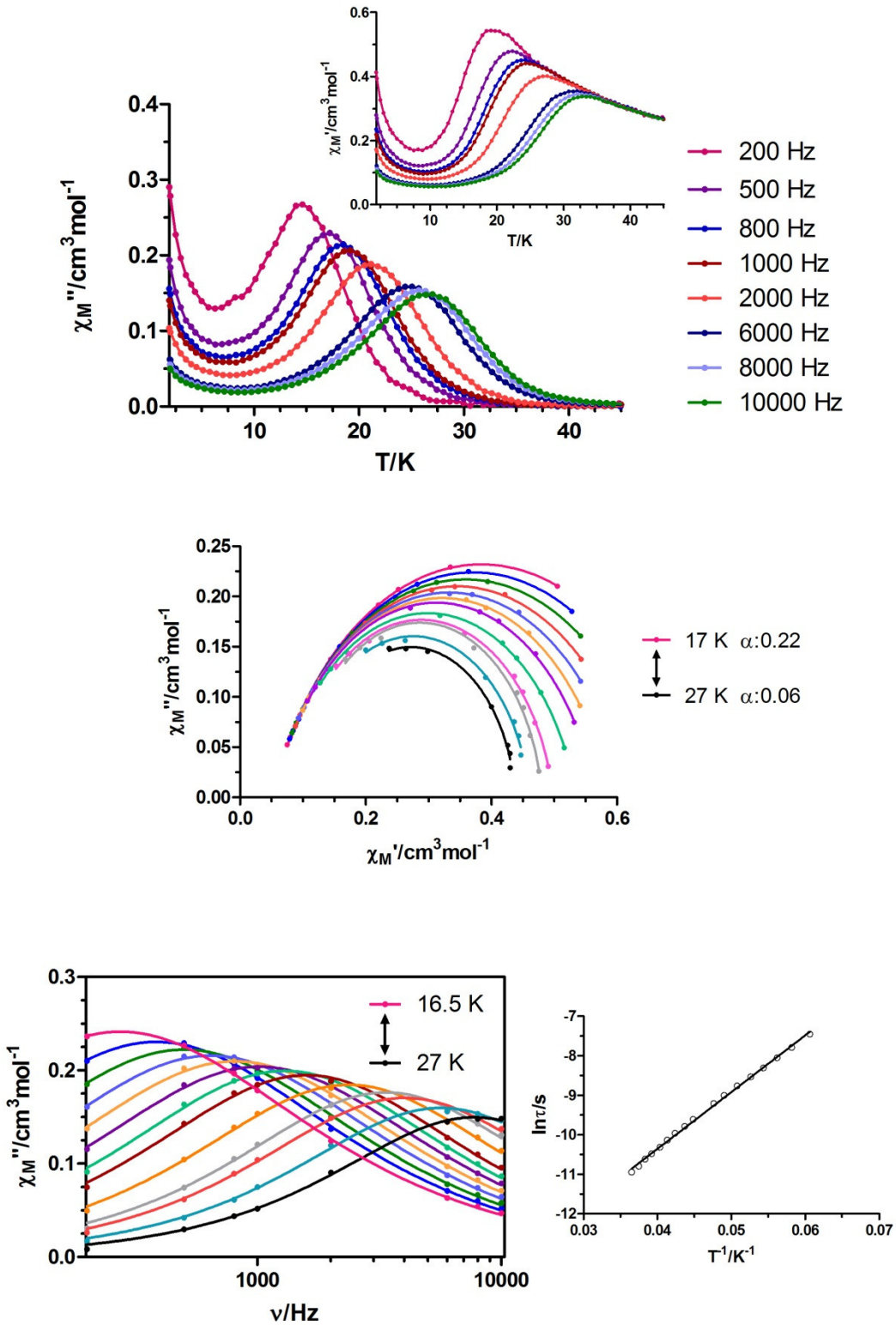

Figure 6.22.- Top: temperature dependence of in-phase χ_M' (inset) and out-of phase χ_M'' components of the *alternating current* susceptibility for complex **51** under zero applied external field. Medium: Cole-Cole plot. Bottom left: variable-temperature frequency dependence of the χ_M'' signal. Bottom right: Arrhenius plots for the relaxation of **51** (black line).

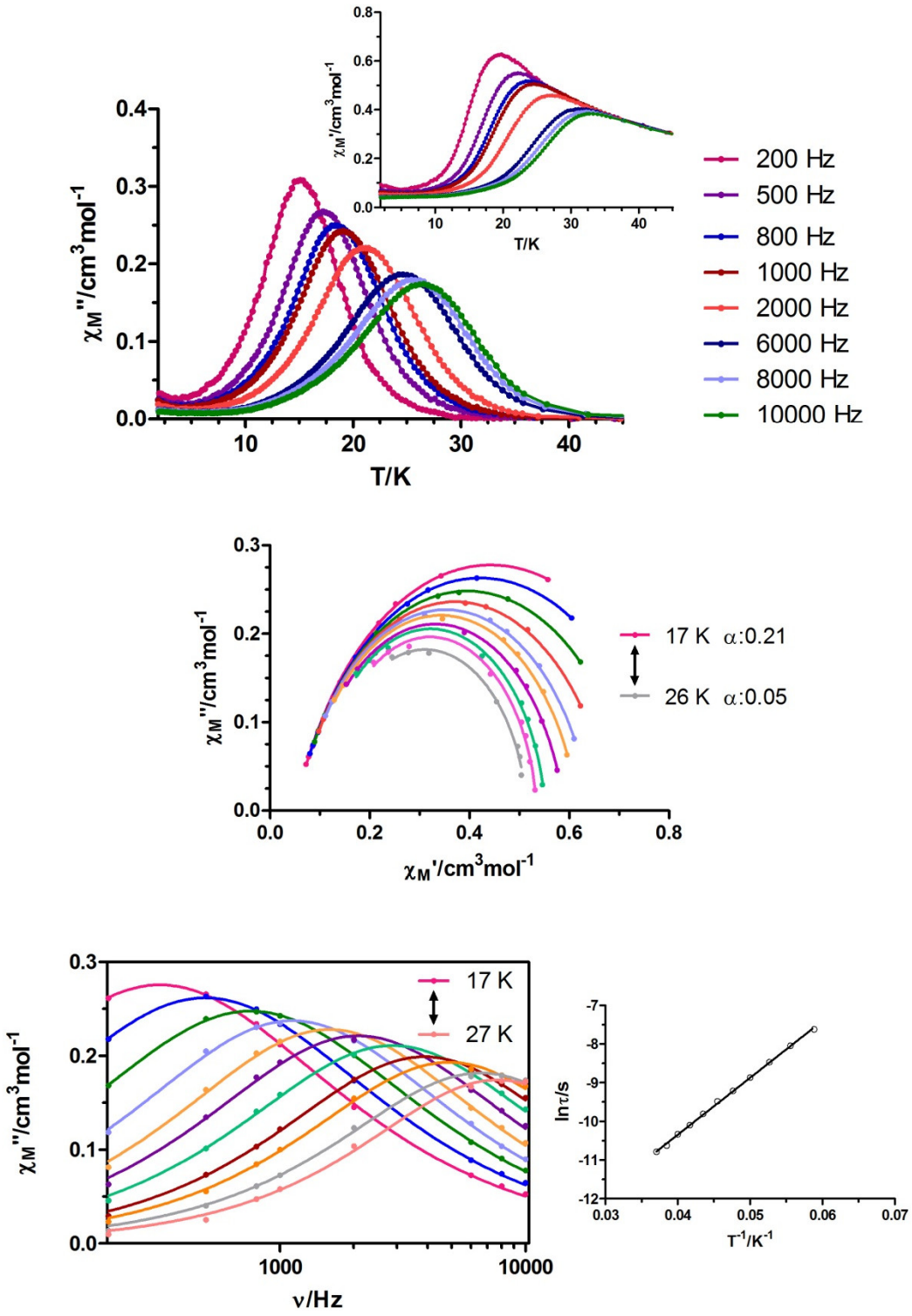

Figure 6.23.- Top: temperature dependence of in-phase χ_M' (inset) and out-of phase χ_M'' components of the *alternating current* susceptibility for complex **51** under 1000 Oe applied external field. Medium: Cole-Cole plot. Bottom left: variable-temperature frequency dependence of the χ_M'' signal. Bottom right: Arrhenius plots for the relaxation of **51** (black line).

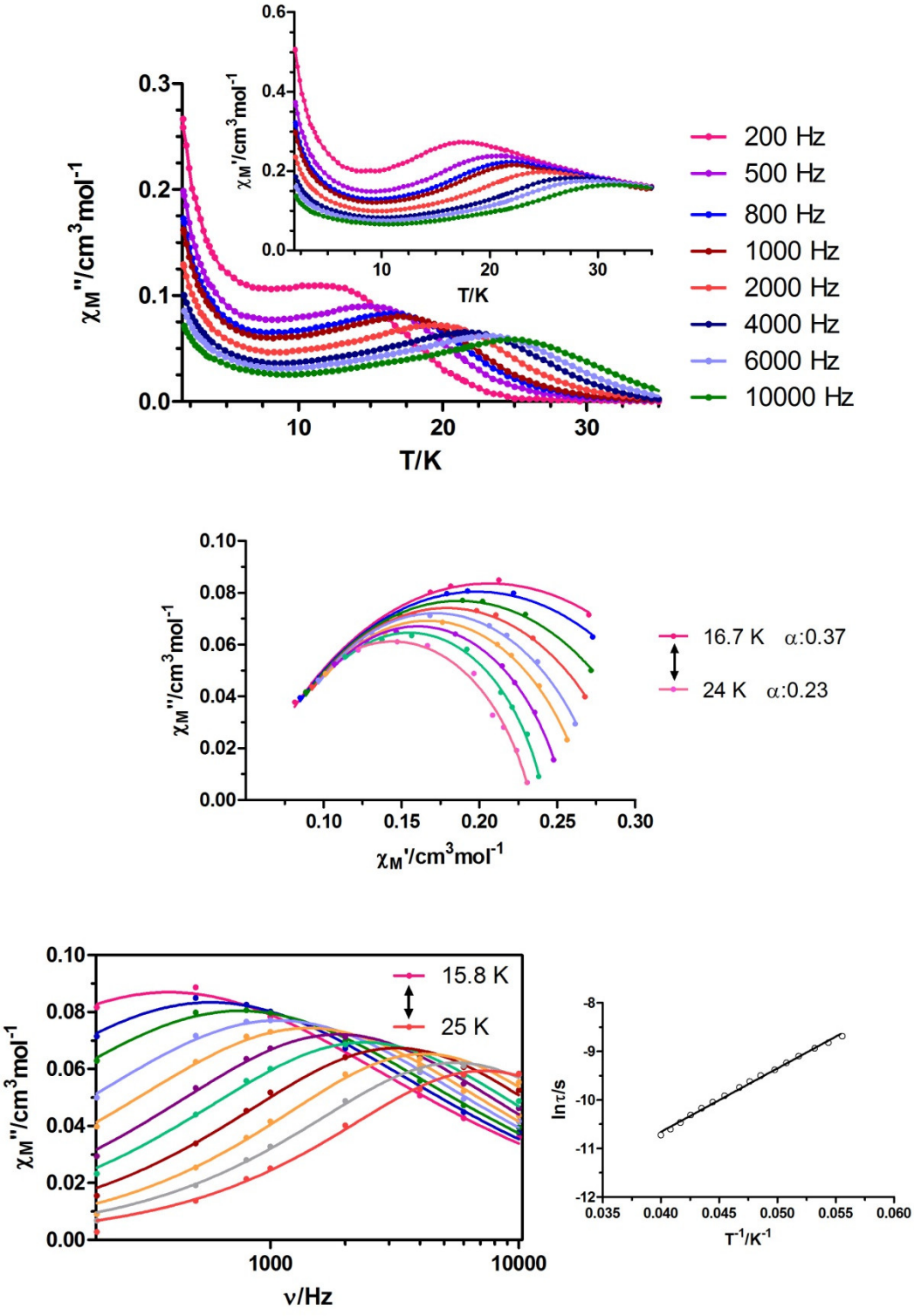

Figure 6.24.- Top: temperature dependence of in-phase χ_M' (inset) and out-of phase χ_M'' components of the *alternating current* susceptibility for complex **52** under zero applied external field. Medium: Cole-Cole plot. Bottom left: variable-temperature frequency dependence of the χ_M'' signal. Bottom right: Arrhenius plots for the relaxation of **52** (black line).

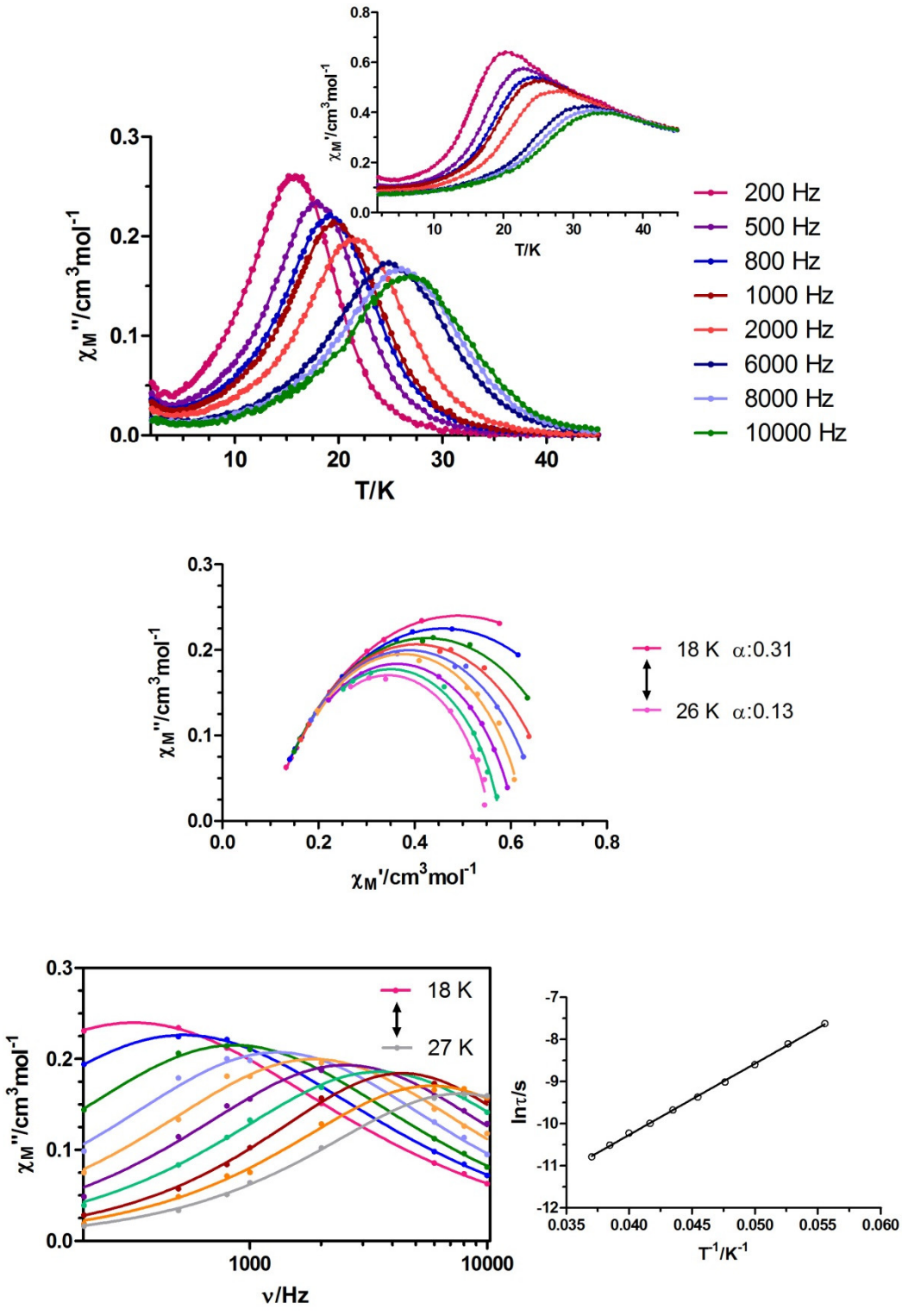

Figure 6.25.- Top: temperature dependence of in-phase χ_M' (inset) and out-of phase χ_M'' components of the *alternating current* susceptibility for complex **52** under 1000 Oe applied external field. Medium: Cole-Cole plot. Bottom left: variable-temperature frequency dependence of the χ_M'' signal. Bottom right: Arrhenius plots for the relaxation of **52** (black line).

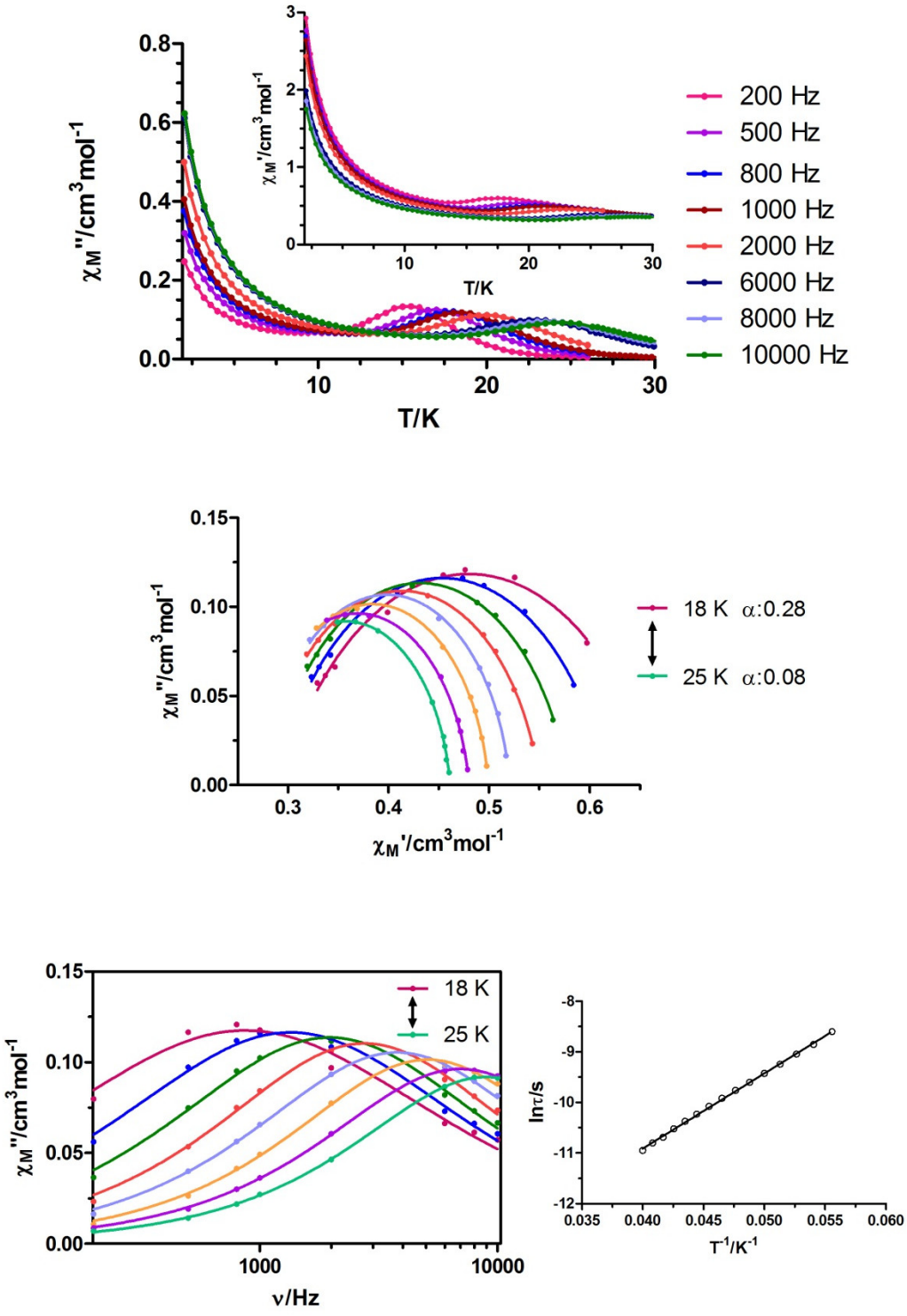

Figure 6.26.- Top: temperature dependence of in-phase χ_M' (inset) and out-of phase χ_M'' components of the *alternating current* susceptibility for complex **53** under zero applied external field. Medium: Cole-Cole plot. Bottom left: variable-temperature frequency dependence of the χ_M'' signal. Bottom right: Arrhenius plots for the relaxation of **53** (black line).

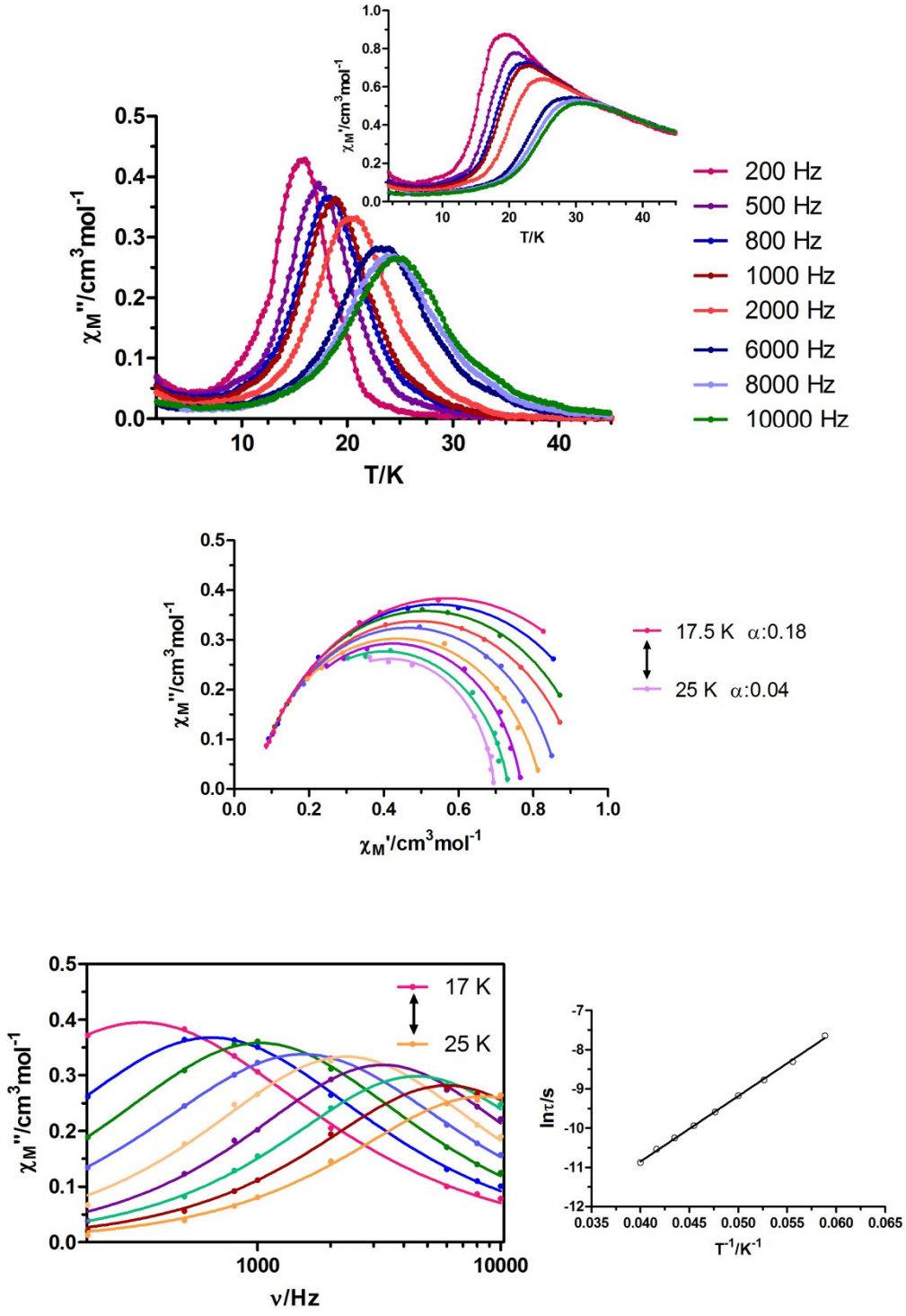

Figure 6.27.- Top: temperature dependence of in-phase χ_M' (inset) and out-of phase χ_M'' components of the *alternating current* susceptibility for complex **53** under 1000 Oe applied external field. Medium: Cole-Cole plot. Bottom left: variable-temperature frequency dependence of the χ_M'' signal. Bottom right: Arrhenius plots for the relaxation of **53** (black line).

6.3.6. Magnetic Properties of Complex 54

Direct-current magnetic susceptibility measurements were carried out on a randomly oriented polycrystalline sample of **54** in the 2-300 K temperature range and under an applied magnetic field of 0.1 T (Figure 6.28). The room temperature $\chi_M T$ value for **54** of 14.45 $cm^3 \cdot K \cdot mol^{-1}$ is compatible with the calculated value of 14.17 $cm^3 \cdot K \cdot mol^{-1}$ for the ground state of the Dy(III) ion in the free ion approximation. Upon cooling, the $\chi_M T$ product decreases steadily to a value of 12.40 $cm^3 \cdot K \cdot mol^{-1}$ at 5 K. Below this temperature, the $\chi_M T$ decreases sharply, reaching a value of 10.15 $cm^3 \cdot K \cdot mol^{-1}$ at 2 K. This behaviour is associated with the magnetic anisotropy of the Dy(III) ion and possible weak intermolecular interactions, which could be responsible for the sharp decrease in $\chi_M T$ below 5 K. The field dependence of the magnetization at 2 K shows a relatively rapid increase at low field, reaching almost saturation for magnetic fields larger than 2 T. The saturation value of 5.10 $N\mu_B$ agrees well with those observed for Dy(III) complexes with strong magnetic anisotropy.[2a,4a,8a,11]

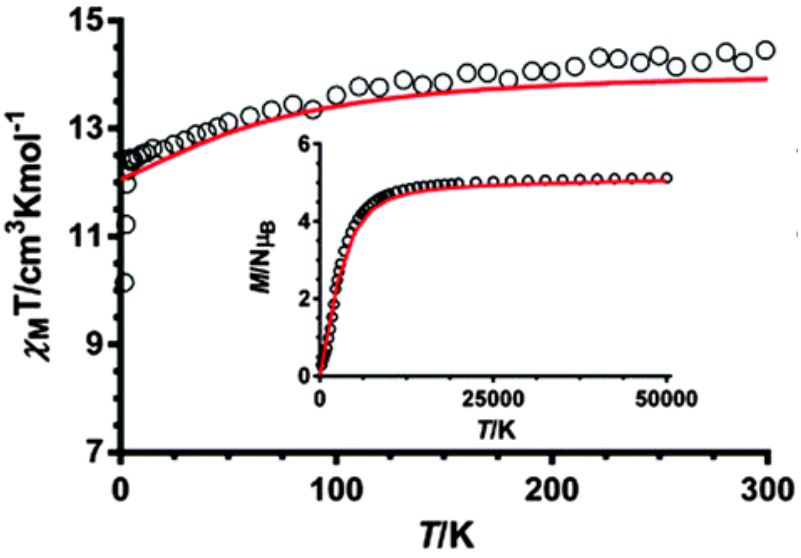

Figure 6.28.- Temperature dependence of $\chi_M T$ for **54**. Inset: Field dependence of the molar magnetization for randomly oriented microcrystals. Solid lines are the *ab initio* calculated curves.

In order to know if **54** exhibits SIM properties, dynamic *alternating current* magnetic measurements were performed as a function of both temperature and frequency on a microcrystalline powder sample (Figures 6.29 and 6.30).

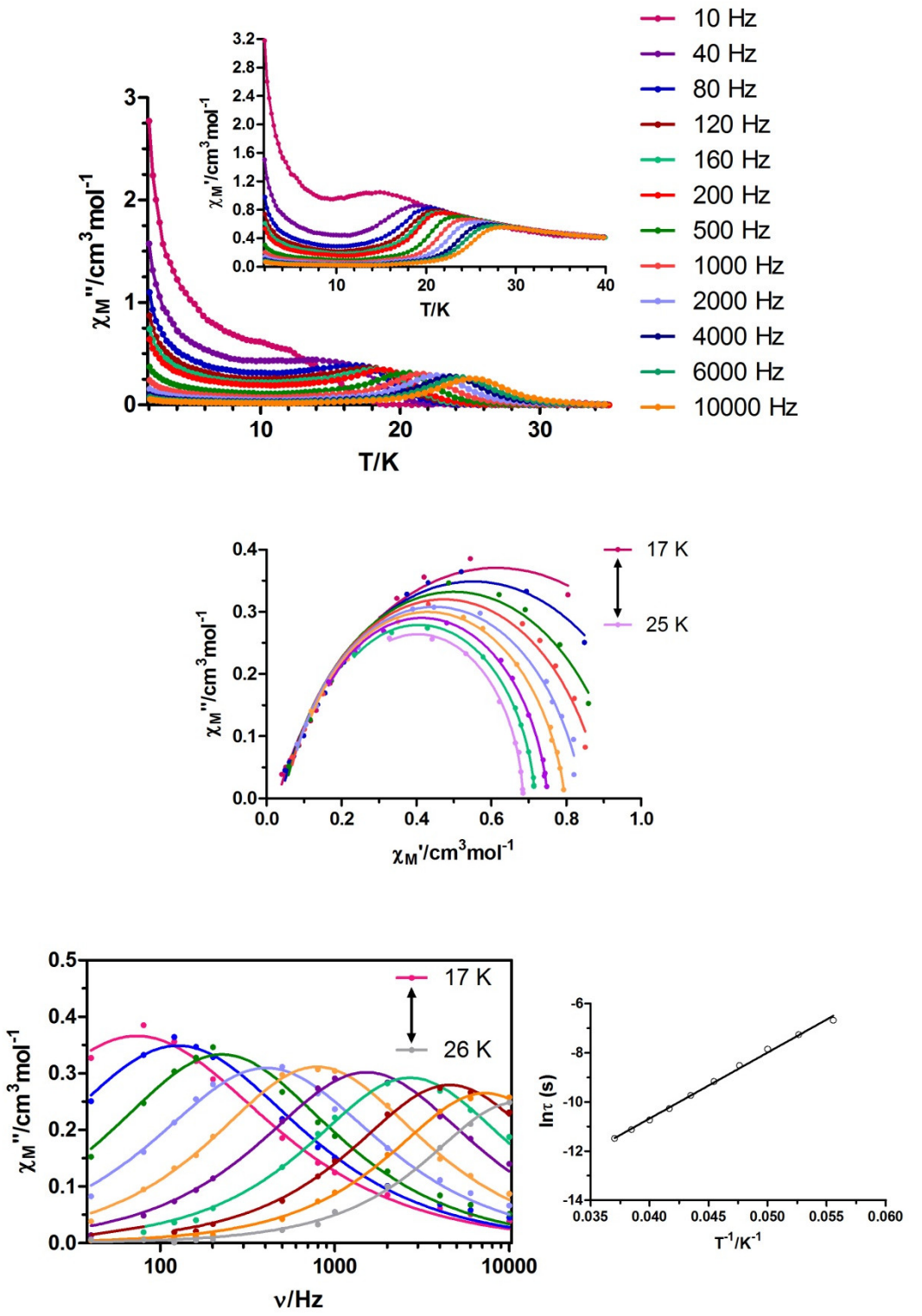

Figure 6.29.- Top: temperature dependence of in-phase χ_M' (inset) and out-of phase χ_M'' components of the *alternating current* susceptibility for complex **54** under zero applied external field. Medium: Cole-Cole plot. Bottom left: variable-temperature frequency dependence of the χ_M'' signal. Bottom right: Arrhenius plots for the relaxation of **54** (black line).

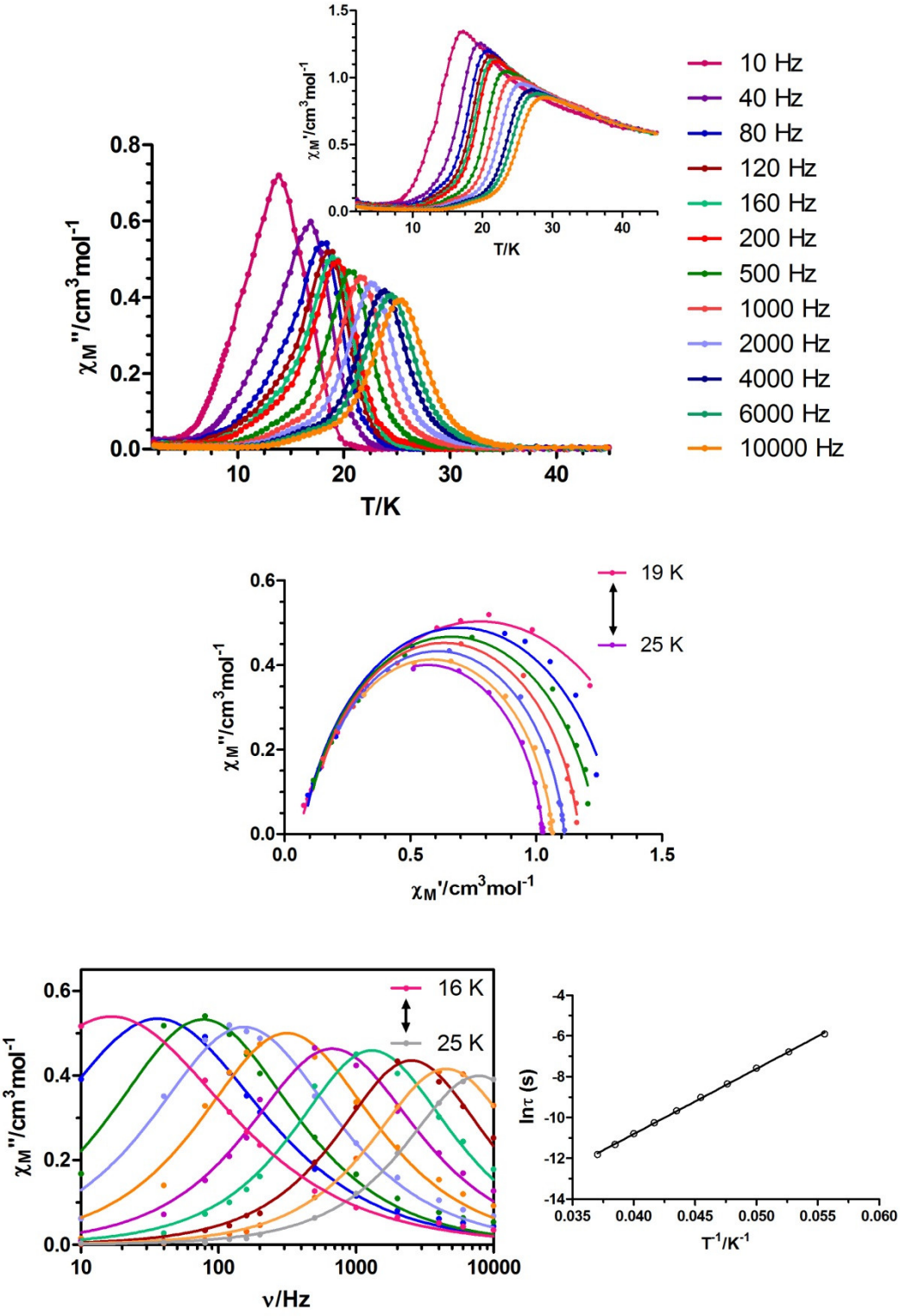

Figure 6.30.- Top: temperature dependence of in-phase χ_M' (inset) and out-of phase χ_M'' components of the *alternating current* susceptibility for complex **54** under zero applied external field. Medium: Cole-Cole plot. Bottom left: variable-temperature frequency dependence of the χ_M'' signal. Bottom right: Arrhenius plots for the relaxation of **54** (black line).

At zero *dc* field, **54** exhibits a strong frequency dependence of the out-of-phase susceptibility (χ_M") signals below 35 K, which clearly indicates the occurrence of slow relaxation of the magnetization and SIM behaviour in this compound. This behaviour is not surprising in view of the easy-axis anisotropy of the Dy(III) ion (see Section 6.3.7 for *ab initio* calculations). The fact that both χ_M' and χ_M" components do not go to zero below the maxima at low temperature, points out to the existence of fast relaxation of the magnetization via a QTM mechanism. The Cole-Cole plot shows semicircular shapes with α values in the 0.28 (17 K) - 0.04 (25 K) range, thus suggesting the existence of multiple relaxation processes.

The relaxation times extracted from the frequency-dependent susceptibility data in the 18-27 K range were fitted to the Arrhenius law, affording an effective energy barrier for the reversal of the magnetization of 268 K (186 cm^{-1}) with $\tau_0 = 4.98 \cdot 10^{-10}$ s (Figure 6.29, bottom right).

When the *ac* measurements on **54** were performed in the presence of a small external *dc* field of 1000 Oe (this field was chosen because under its application the relaxation process was shown to be the slowest) to partly or fully suppress the QTM, the tails at low temperatures almost disappeared and the high temperature peaks remained at similar temperatures and with comparable intensities to those observed under zero *dc* applied field (Figure 6.30). The fit of the relaxation times in the 18-27 K range to the Arrhenius law leads, as expected, to an increase of the thermal energy barrier and a decrease of τ_0 (U_{eff} = 320 K (222 cm^{-1}) with $\tau_0 = 5.66 \cdot 10^{-11}$ s). In the high temperature region, the α values extracted from the Cole–Cole plot are in the 0.22 (19 K)-0.08 (25 K) range, which points to the existence of a distribution of the relaxation times.

Finally, at 2 K and using the sweep rate accessible in a conventional SQUID magnetometer, complex **54** exhibits a butterfly shaped hysteresis loop with almost negligible magnetization at zero field (Figure 6.31), which is consistent with the QTM generally found for 4f containing complexes and with the tail that **54** exhibits at low temperature in the χ_M" vs. T plot at zero applied field.

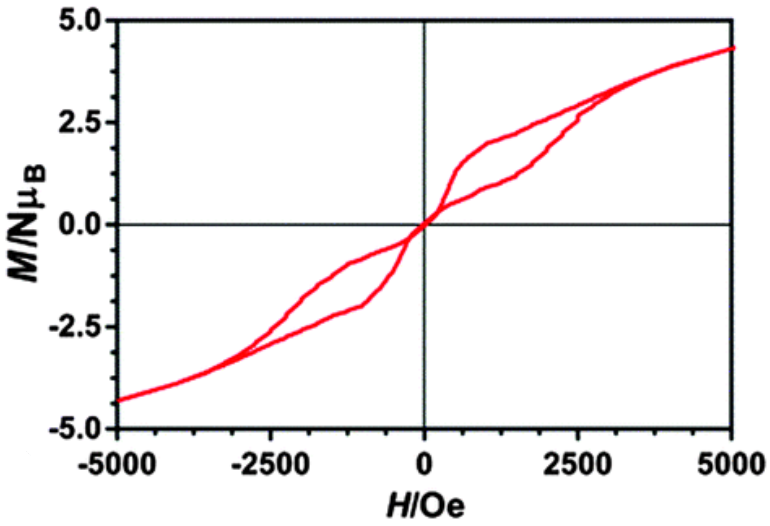

Figure 6.31.- Magnetic hysteresis loops for **54** within -5 < H/kOe < 5 at 2 K.

6.3.7. *Ab initio* calculations on 54

The energy barrier for **54** is approximately twice that of **46**. With the aim of rationalizing this surprising increase of the energy barrier promoted by the change of the counteranion, we have performed *ab initio* electronic calculations based on the CASSCF + RASSI/SINGLE_ANISO[12] method using the MOLCAS 7.8 code[7b,13] (Table 6.4). The energy spectrum of the eight Kramer's doublets (KDs) spans up to 491.8 cm^{-1} and the energy gap between the ground and first excited state is 144.2 cm^{-1}, which are rather normal values for Dy(III) complexes.

Table 6.4.- Calculated energies (cm^{-1}) and *g* factors for the eight lowest Kramer's doublets.

Doublet	Energy (cm^{-1})	g_z	g_y	g_x	Angle wrt. ground doublet (degrees)
1	0.0	19.636	0.000	0.000	-
2	144.2	16.561	0.045	0.041	2.4
3	243.3	11.630	4.457	1.959	47.5
4	264.7	8.895	3.944	2.703	61.9
5	323.3	6.866	2.722	0.859	14.8
6	347.4	2.488	8.210	11.024	22.7
7	369.2	19.499	0.737	0.428	89.9
8	491.8	19.581	0.002	0.001	53.1

The ground Kramer's doublet (KD1) is almost pure (M_J = ±15/2) with effective g_z and $g_{x,y}$ values approaching 20 and zero, respectively. Therefore KD1 is an almost ideal Ising state which favours the slow relaxation of the magnetization and the SIM behaviour, in accordance with the zero field SIM properties observed for **54**. It is worth mentioning that the *ab initio* calculations accurately reproduce the *direct current* magnetic susceptibility and magnetization data for **54** (Figure 6.28), which gives confidence in the calculated low-lying KDs energies. The main magnetic axis of the KD1 lies close to the two Dy-O2A vectors (Figure 6.32), which shows the tendency of this axis to point to the donor atoms with greater electron density and shorter Dy–O distances (O2A phenoxo bridging atoms of the ligands with Dy–O2A = 2.275 Å). This orientation of the magnetic moment forces the oblate electron density of the Dy(III) to be perpendicular to the O2A atoms thus diminishing electrostatic repulsions. The O2A phenoxo atoms are roughly located at axial positions on the DyO_8 coordination sphere, thus emphasizing the suitability of an axially repulsive coordination environment for achieving SIM properties in Dy(III) compounds, as qualitatively anticipates the oblate-prolate model.[1] DFT calculations of the electrostatic potential maps provoked by the ligands projected on the Dy(III) position (Figure 6.32, right) agree with the above qualitative electrostatic predictions.

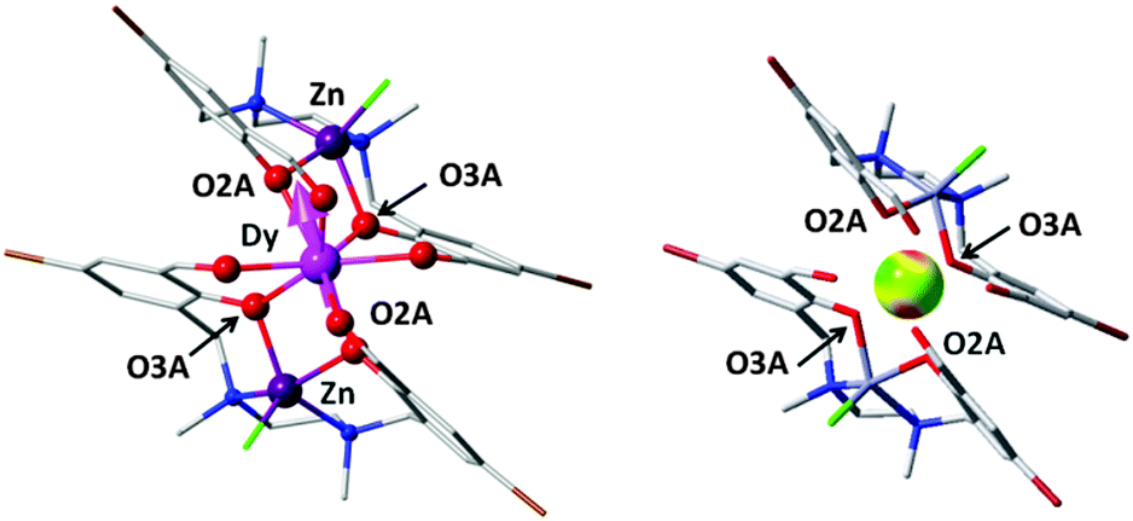

Figure 6.32.- Left: *Ab initio* computed orientation of the magnetic moment of the ground state for **54** (pink arrow). Right: DFT calculated (B3LYP/TZV) electrostatic potential of the coordination environment (only ligands) projected in a sphere located at the Dy position (1 Å radius). Yellow-green regions on the sphere correspond to low potential (less repulsive) while highly repulsive regions are indicated as red spots.

Thus, the oblate beta electron density of the ground state (which is formed by mixing in the ground RASSI wave function the two first, almost degenerate, states in the CASSCF step; Figure 6.33 and Table 6.4) is hosted in the region with less repulsion (yellow-green in Figure 6.32, right) whereas the magnetic moment is pointing towards the strongest repulsion regions (red in Figure 6.32, right).

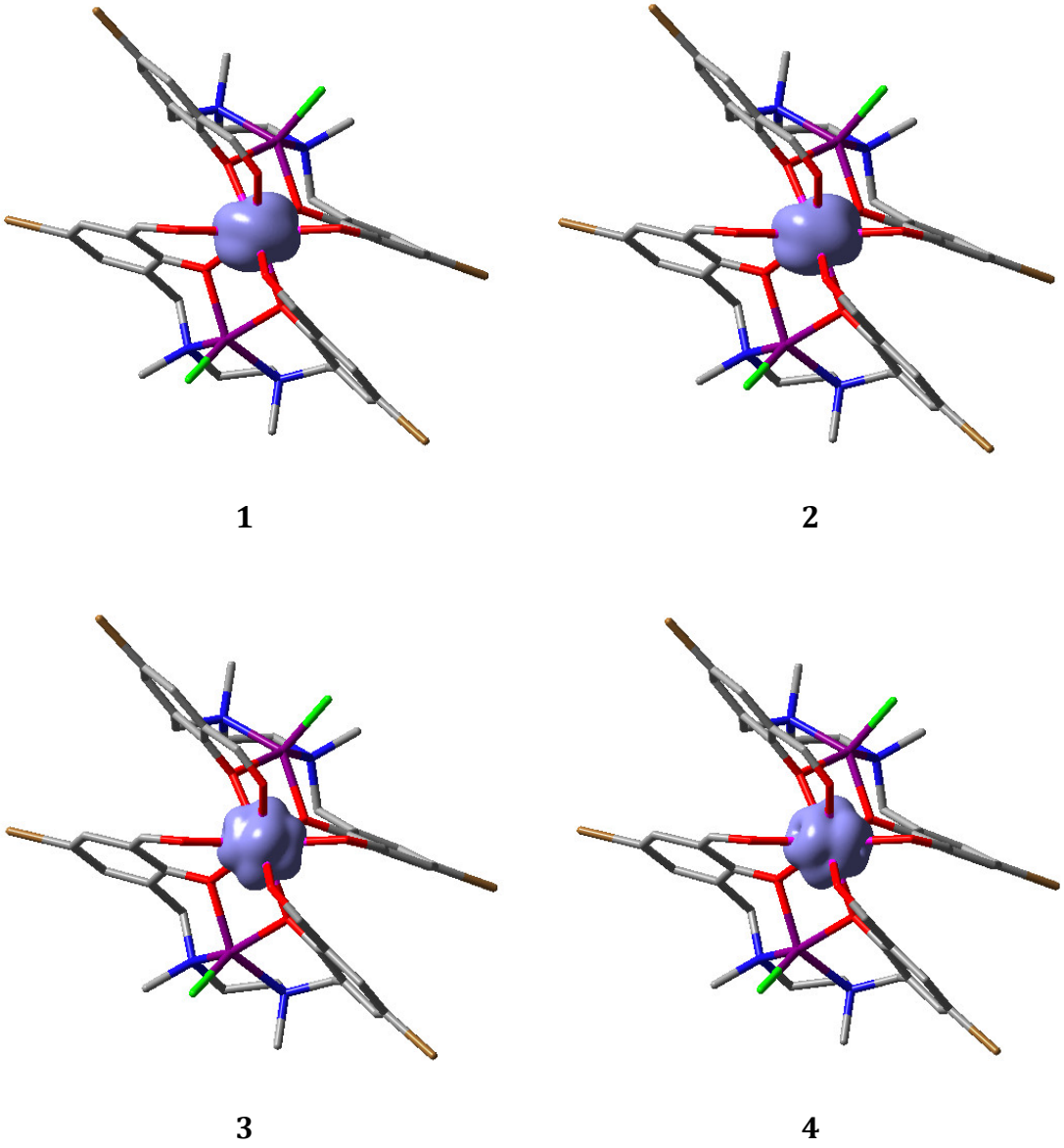

Figure 6.33.- Beta spin density of the Dy(III) f electrons for the first 4 non-relativistic states.

Table 6.5.- First excitation energies (cm^{-1}) from the states stemming form the ground ^6H term at CASSCF level.

State	Energy (cm^{-1})
1	0.0
2	0.6
3	200.6
4	236.2
5	305.5
6	346.1
7	394.5
8	418.3
9	424.7
10	562.1
11	562.2

It should be noted that the extracted effective energy barrier at zero *dc* field is 40 cm^{-1} larger than the energy gap between the ground and first excited KDs and therefore the relaxation of the magnetization cannot take place *via* the first excited state. However, the relaxation could occur through the second excited KD, which would be located 243.3 cm^{-1} above the ground KD. In such a case, the extracted U_{eff} would be lower than that predicted using electronic structure calculations, which could be justified by the existence of fast QTM relaxation. In fact, the value of the energy barrier extracted from the *ac* measurements under an applied *dc* field of 1 kOe (U_{eff} = 222 cm^{-1}), when the QTM relaxation is almost suppressed, is close to the energy of the second excited state. The relaxation *via* the first excited state is suppressed because the main anisotropy axes of the ground and first excited states (the latter is an almost pure Ising state with M_J = ±13/2, g_z ~ 17 and $g_{x,y}$ < 0.05) are not only Ising like, but also almost parallel (the angle is 2.41°). The collinearity of the principal anisotropy axes up to the first excited KD, which is due to the presence of a C_2 axis around the Dy(III) ion, blocks Orbach relaxation.[11b,14]

In order to probe the magnetization relaxation mechanism in **54**, the transition magnetic moment matrix elements between the connecting pairs of opposite magnetization have been computed (Figure 6.34).

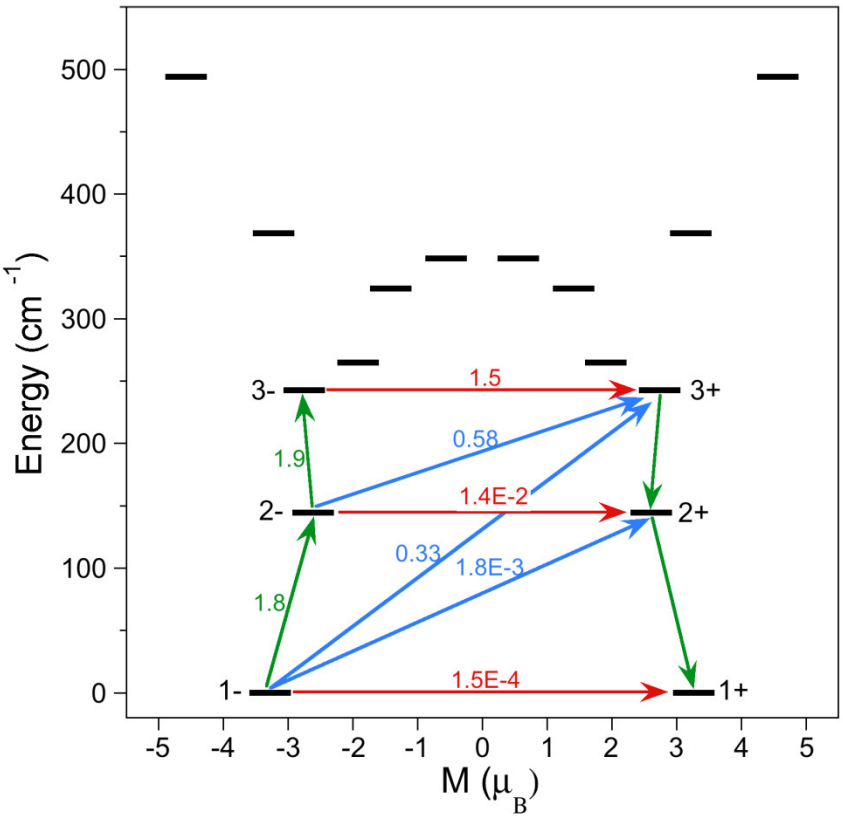

Figure 6.34.- Eight lowest Kramer's doublets (KDs) and *ab initio* computed relaxation mechanism in **54**. The thick black lines imply KDs as a function of their magnetic moment along the main anisotropy axis. The red lines correspond to ground state QTM and TA-QM *via* the first and second excited KDs, blue lines show possible Orbach relaxation processes. The values located close to the arrows indicate the matrix elements of the transition magnetic moments.

Owing to the almost pure Ising nature of the ground state, QTM is expected to be very weak, which is supported by the low magnitude of the transition magnetic moment element between the ground state KDs (~ 10^{-4} μ_B). This must be the reason why **54** exhibits SIM behaviour at zero field. The same argument can be used to justify the absence of thermal-assisted quantum tunnelling of magnetization (TA-QTM) through the first excited state. However, the TA-QTM mechanism *via* the second excited KD (± 3 states) becomes dominant as it exhibits the largest value of the transition magnetic moment element (1.5 μ_B). As expected for the collinearity of the main anisotropy axes of the ground and first excited KDs, the off diagonal term connecting these KDs (related with the Orbach process) is very small (~ 10^{-3} μ_B). Nevertheless, the Orbach process is operative *via* the second excited state as the transversal magnetic moments

are moderate (0.33 and 0.58 μ_B). Therefore, the relaxation of the magnetization occurs through the second excited state *via* Orbach/TA-QTM processes.

Although the Dy-O distances in **54** and the other trinuclear compounds are very similar and the disposition of the oxygen atoms in the DyO_8 coordination sphere is close to that of **48**, the fact that the former exhibits a C_2 symmetry axis around the Dy(III) ion would ultimately be the responsible for the differences in the SIM behaviour of these compounds.

6.4. CONCLUSIONS

The ongoing results represent clear examples of how the simple model based on the prolate-oblate electron density distribution of the Ln(III) ions can be used to rationally design mononuclear lanthanide based complexes with strong easy axis anisotropy and slow relaxation of the magnetization. Specifically, Zn-Dy-Zn species have been prepared using the compartmental ligand H_2L, in which the Dy(III) ion exhibits a DyO_8 coordination environment with slightly distorted axial D_{4d} symmetry. In the DyO_8 coordination sphere, two pairs of large negatively charged phenoxo groups with short Dy-O distances are arranged at opposite sides of the Dy(III) ion, whereas the remaining position are occupied by neutral aldehyde oxygen donor atoms. The phenoxo oxygen donor atoms exert a strong crystal field and force the oblate electron density to be perpendicular to them in order to minimize electrostatic repulsions. This electrostatic charge distributions would stabilize the strongly axial $M_J = \pm 15/2$ ground Kramer's doublet, with the anisotropic axis pointing to the donor atoms with the greatest electron density and shorter Dy-O distances. According to these considerations, experimental magnetic data of these complexes suggest large easy-axis anisotropy, which is responsible of the high thermal energy barriers for the reversal of the magnetization in zero field, which are in the 144 - 170 K range. *Ab initio* calculations in one of them support the easy-axis anisotropy of the ground Kramer's doublet, the direction of the anisotropy axis and the thermally activated mechanism for the slow relaxation of the magnetization.

We have established for the Zn-Dy-Zn complexes a correlation between the disposition of the oxygen atoms (phenoxo and aldehyde) in the DyO_8 coordination sphere and the value of U_{eff}. Nevertheless, this hypothesis should be supported by *ab initio* calculations.

A Zn-Er-Zn complex has also been prepared, which does not present significant SIM behaviour as expected for the prolate electron-density distribution of the Er(III) ion.

To end up, the replacement of the counteranion for PF_6^- has provoked a change towards a more symmetric structure where there exists a C_2 axis on the Dy(III) ion. The presence of the C_2 axis imposes collinearity of the anisotropic axes of the two lowest KDs, so that the thermal activated relaxation is suppressed *via* the first excited KD and takes place *via* the second excited state, giving rise to a dramatic increase in the effective energy barrier. This is one of the few cases where this type of symmetry-driven relaxation mechanism has been observed[11b,14b,c] and the first case where it is due to a structural change promoted by the replacement of the counteranion.

6.5. BIBLIOGRAPHY

[1] J. D. Rinehart, J. R. Long, *Chem. Sci.*, **2011**, *2*, 2078.

[2] **a)** A. Watanabe, A. Yamashita, M. Nakano, T. Yamamura, T. Kajiwara, *Chem. Eur. J.*, **2011**, *17*, 7428; **b)** T. Kajiwara, M. Nakano, K. Takahashi, S. Takaishi, M. Yamashita, *Chem. Eur. J.*, **2011**, *17*, 196.

[3] L. Ungur, M. Thewissen, J.-P. Costes, W. Wernsdorfer, L. F. Chibotaru, *Inorg. Chem*., **2013**, *52*, 6328.

[4] **a)** S. Titos-Padilla, J. Ruiz, J. M. Herrera, E. K. Brechin, W. Wernsdorfer, F. Lloret, E. Colacio, *Inorg. Chem.*, **2013**, *52*, 9620; **b)** K. R. Meihaus, J. D. Rinehart, J. R. Long, *Inorg. Chem*., **2011**, *50*, 8484.

[5] M. Llunell, D. Casanova, J. Cirera, J. M. Bofill, P. Alemany, S. Alvarez, M. Pinsky, D. Avnir, *SHAPE*, v1.1b; Barcelona, Spain, **2005**.

[6] S. Titos-Padilla, J. Ruiz, J. M. Herrera, E. K. Brechin, W. Wernsdorfer, F. Lloret, E. Colacio, *Inorg. Chem*., **2013**, *52*, 9620.

[7] **a)** D. Aravena, E. Ruiz, *Inorg. Chem*., **2013**, *52*, 13770; **b)** F. Aquilante, L. De Vico, N. Ferré, G. Ghigo, P.-Å. Malmqvist, P. Neogrády, T. B. Pedersen, M. Pitoňák, M. Reiher, B. O. Roos, L. Serrano-Andrés, M. Urban, V. Veryazov, R. J. Lindh, *Comput. Chem.,* **2010**, *31*, 224.

[8] **a)** J.-L. Liu, Y.-C. Chen, Y.-Z. Zheng, W.-Q. Lin, L. Ungur, W. Wernsdorfer, L. F. Chibotaru, M.-L. Tong, *Chem. Sci.,* **2013**, *4*, 3310; **b)** J. Ruiz, A. J. Mota, A. Rodríguez-Diéguez, S. Titos, J. M. Herrera, E. Ruiz, E. Cremades, J. P. Costes, E. Colacio, *Chem. Commun*., **2012**, *48*, 7916.

[9] H. L. C. Feltham, Y. Lan, F. Klçwer, L. Ungur, L. F. Chibotaru, A. K. Powell, S. Brooker, *Chem. Eur. J.*, **2011**, *17*, 4362.

[10] N. F. Chilton, D. Collinson, E. J. L. McInnes, R. E. P. Winpenny, A. Soncini, *Nature Commun.*, **2013**, *4*, 2551.

[11] **a)** K. S. Bejoymohandas, A. Dey, S. Biswas, M. L. P. Reddy, R. Morales, E. Ruiz, S. Titos- Padilla, E. Colacio, V. Chandrasekhar, *Chem. Eur. J.*, **2015**, *21*, 6449; **b)** A. Upadhyay, S. Kumar Singh, C. Das, R. Mondol, S. K. Langley, K. S. Murray, G. Rajaraman, M. Shanmugam, *Chem. Commun.*, **2014**, *50*, 8838.

[12] **a)** L. F. Chibotaru, L. J. Ungur, *Chem. Phys.*, **2012**, *137*, 064112; **b)** P. A. Malmqvist, B. O. Roos, B. Schimmelpfennig, Chem. Phys. Lett., **2002**, 357, 230.

[13] **a)** J. A. Duncan, *J. Am. Chem. Soc.*, **2009**, *131*, 2416; **b)** V. Veryazov, P. O. Widmark, L. Serrano-Andres, R. Lindh, B. O. Roos, *Int. J. Quantum Chem.*, **2004**, 100, 626; **c)** G. Karlstrom, R. Lindh, P. A. Malmqvist, B. O. Roos, U. Ryde, V. Veryazov, P. O. Widmark, M. Cossi, B. Schimmelpfennig, P. Neogrady and L. Seijo, *Comput. Mater. Sci.*, **2003**, *28*, 222.

[14] **a)** Y.-N. Guo, L. Ungur, G. E. Granroth, A. K. Powell, C. Wu, S. E. Nagler, J. Tang, L. F. Chibotaru, D. Cui, *Sci. Rep.*, **2014**, *4*, 5471; **b)** S. K. Singh, T. Gupta, M. Shanmugam, G. Rajaraman, *Chem. Commun.*, **2014**, *50*, 15513; **c)** R. J. Blagg, L. Ungur, F. Tuna, J. Speak, P. Comar, D. Collison, W. Wernsdorfer, E. J. L. McInnes, L. F. Chibotaru, R. E. P. Winpenny, *Nat. Chem.*, **2013**, *5*, 673.

CHAPTER 7

Dy(III) SINGLE MOLECULE MAGNET BASED ON POLYOXOMETALATES

7.1. INTRODUCTION

Polyoxometalates (POMs) are anionic clusters composed of metal and oxygen atoms that form a unique class of compounds due to its electronic, topologic and reactive versatility,[1] as well as for their wide range of potential applications in fields like catalysis,[2] magnetism,[3] materials science[4] or biomedicine.[5]

POMs can be described by the general formula $[X_xM_mO_y]^{q-}$, where M implies metallic elements from groups 5 and 6, mostly Mo, W and V in their highest oxidation states, and less frequently, Nb, Ta and Cr.[6] These metals show a suitable combination of charge and ionic radius as well as empty and accessible *d* orbitals available for electronic back-donation in the formation of M-O bonds. On the other hand, around 70 different elements from all the groups of the periodic table, with the exception of noble gases, can act as the X heteroatom.

Depending on their composition, POMs can be classified into two main groups: *isopolyoxometalates*, of general formula $[M_mO_y]^{q-}$, are exclusively constituted by early transition metals and oxygen, and *heteropolyoxometalates*, of general formula $[X_xM_mO_y]^{q-}$, contain not only metal and oxygen, but also additional elements known as heteroatoms (X).

Examples of well-known heteropolytungstates include:

- The $[XW_6O_{24}]^{n-}$ Anderson-Evans anion, which contains an octahedral heteroatom (X = first row transition metals, Al(III), Ga(III), Rh(III), Pt(IV), Sb(V), Te(VI), I(VII)).[7]

- The Keggin anion $[XW_{12}O_{40}]^{n-}$, which contains a tetrahedral heterogroup (usually X = B(III), Si(IV), Ge(IV), P(V), As(V)).[8]

- The Wells-Dawson anion $[X_2W_{18}O_{62}]^{n-}$ derived from the Keggin structure and showing two tetrahedral heteroatoms (X = typically from the group 15).[9]

Despite the wide variety of structures, most POMs exhibit some features in common:[10]

- They usually show high charge, size and symmetry, as well as thermal and solution stability.

- The formation equilibria of POMs are highly dependent on the concentration of the reactants, pH, ionic strength, presence of extra ligands, counterions employed, temperature or pressure (hydrothermal synthesis, microwave assisted reactions). It is highly usual that different POM species coexist in solution at a given pH value.

- Species containing alkaline counterions are usually water soluble, whereas organic counterions confer high solubility in organic solvents on the polyanions.

- POMs can be used as inorganic ligands due to their ability to coordinate cations, anions or neutral molecules with the oxygen atoms located at the surface.

From a magnetic point of view, the combination of the intrinsically large magnetic anisotropy and large ground state spin values displayed by lanthanide ions under certain ligand fields with the rigidity and insulating ability of POMs (which hinder alterations in the ligand field or intermolecular magnetic interactions from taking place) have been proven to result in molecular systems that show slow relaxation of the magnetization. Different 4f-containing POMs have been reported to behave as effective single-ion or single-molecule magnets (SIMs or SMMs) or spin qubits in recent years, even with chemically controlled reversible switching of the SMM behaviour,[11] and this might pave their way to being applied in memory-storage systems, sensor devices, or in quantum computation.

The aim of this chapter is the grafting of 4f metal complexes into POM surfaces by taking advantage of the unique ability of POMs to act as rigid ligands, which offers a powerful tool for designing metal complexes with tailored symmetries. For this purpose, the Keggin-type tungstosilicate α-$K_8[SiW_{11}O_{39}]\cdot 13H_2O$ has been chosen, which allows the grafting of lanthanide complexes with highly symmetric axial coordination environments in its vacant position.

The monovacant α-($SiW_{11}O_{39}$) specie can be obtained by removing one or more octahedral from the parent α-$SiW_{12}O_{40}$ Keggin anion, which is constituted by four $\{W_3O_{13}\}$ trimers formed by three edge-sharing WO_6 octahedra. Thus, Keggin type anions, stable at acid medium, experiment the breaking of M-O bonds when increasing the pH of the medium, which leads to the formation of species such as $[SiW_{11}O_{39}]^{8-}$, $[SiW_{10}O_{36}]^{8-}$ and $[SiW_9O_{34}]^{10-}$ by the disappearance of one, two or three adjacent WO_6 octahedron, respectively. These new species are known as lacunary species and the

chemical equilibria of Keggin-type tungstosilicates in water solution is summarized in Figure 7.1. The β and γ isomers are formed by the 60° rotation of one and two trimers from the parent α-Keggin anion, respectively. All the species represented can be prepared and isolated as alkaline salts from mixtures of silicate and tungstate sources as a function of the pH, by following the procedures reported by Téze & Hervé.[12]

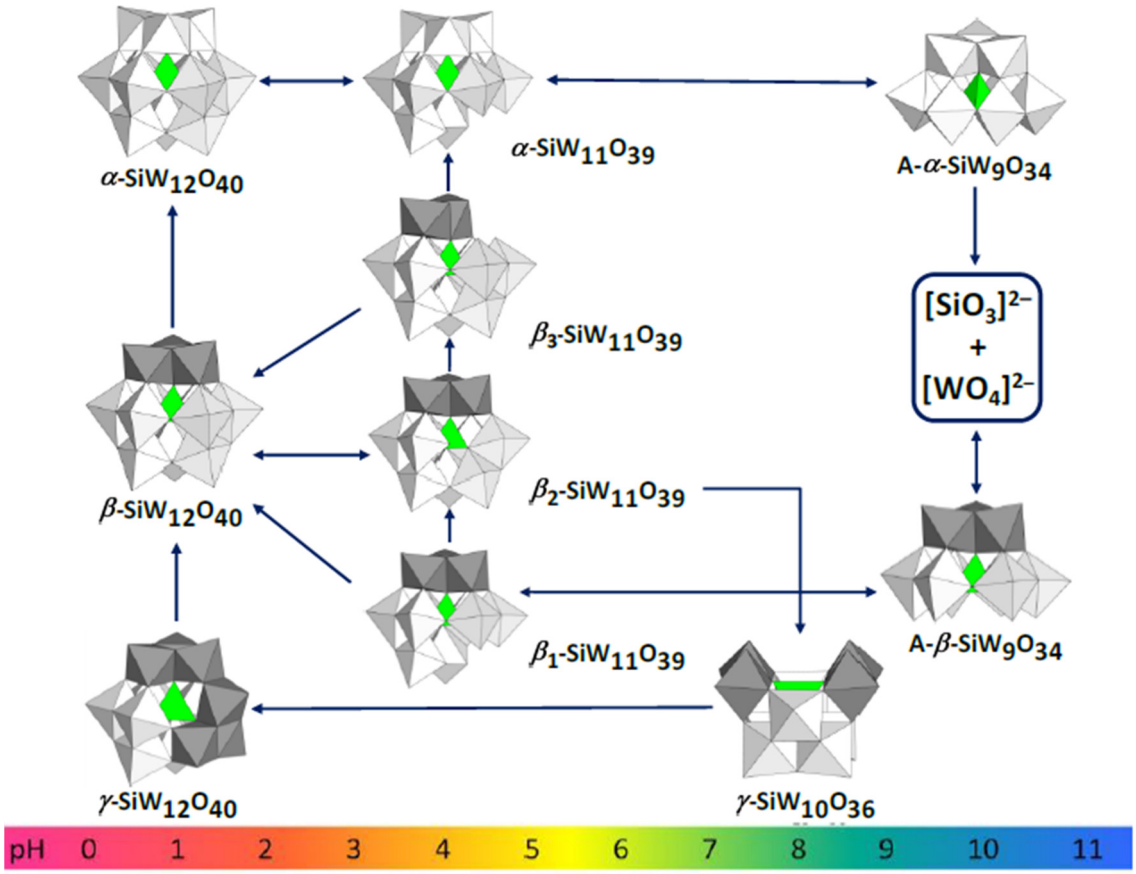

Figure 7.1.- Scheme of the chemical equilibria between different plenary and lacunary Keggin-type tungstosilicates.

7.2. PREPARATION OF COMPLEX 55

7.2.1. α-$K_8[SiW_{11}O_{39}]\cdot 13H_2O$

α-$K_8[SiW_{11}O_{39}]\cdot 13H_2O$ was prepared according to a published method.[12]

7.2.2. $\{K_5[Dy(H_2L)(\alpha\text{-}SiW_{11}O_{39})]\}_6 \cdot 46H_2O$ (55)

A methanolic solution (5 mL) of 37.7 mg (0.1 mmol) of $DyCl_3 \cdot 6H_2O$ and 51.4 mg (0.1 mmol) of H_2L was added dropwise to a hot 1 M KAc/HAc buffer solution (30 mL) containing 322.0 mg (0.1 mmol) of $\alpha\text{-}K_8[SiW_{11}O_{39}] \cdot 13H_2O$. The reaction mixture was stirred for 2 h at 60° and the solid filtered off. The resulting solution was left to evaporate, affording few yellow X-ray quality crystals after one month. Yield of the initial precipitate: 42 %. Yield of the crystals: 1 %.

Due to the difficulties of deducting the number of water molecules from the X-ray structure, TGA curves were performed on compound **55**. The initial mass loss below 204.0°C corresponds to dehydration and implies a weight loss of 3.68 %, which corresponds to 46 water molecules per 6 $[Dy(H_2L)(\alpha\text{-}SiW_{11}O_{39})]^{5-}$ units (Figure 7.2).

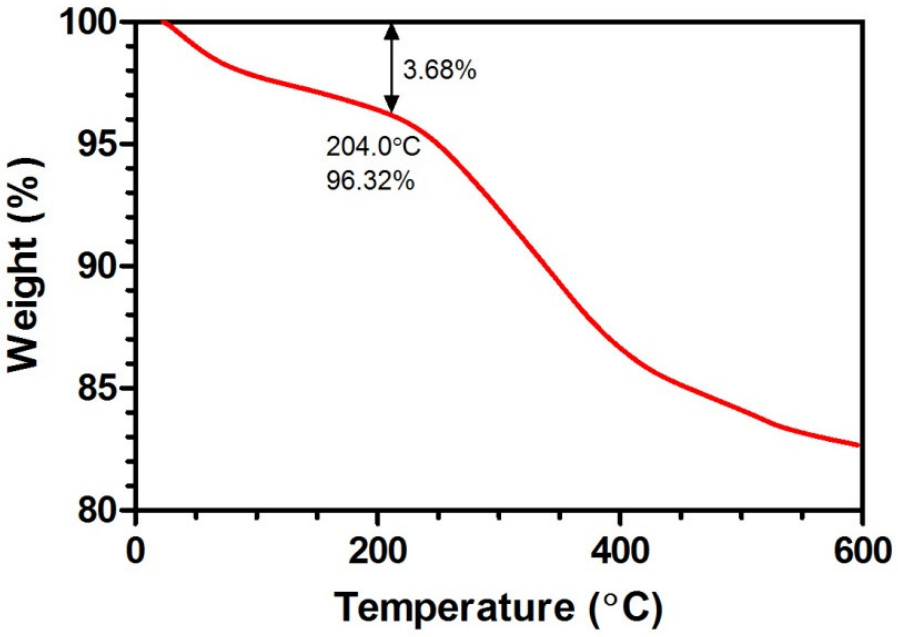

Figure 7.2.- TGA curve for complex **55**.

7.3. EXPERIMENTAL RESULTS

The Dy(III) containing compound $\{K_5[Dy(H_2L)(\alpha\text{-}SiW_{11}O_{39})]\}_6 \cdot 46H_2O$ (**55**) was synthesized by the reaction of the monovacant lacunary silicotungstate $\alpha\text{-}K_8[SiW_{11}O_{39}] \cdot 13H_2O$ with one equivalent of $DyCl_3 \cdot 6H_2O$ and H_2L. The pH of the

reaction media was settled to 4.8 by using a 1 M KAc/HAc buffer solution, in order to avoid the formation of different lacunary species.

7.3.1. Crystal Structure of Complex 55

The crystal structure of complex **55** is shown in Figure 7.3 and consists of Dy(III) cations coordinated to neutral H_2L ligands and $[SiW_{11}O_{39}]^{8-}$ anionic silicotungstates forming three crystallographic independent $[Dy(H_2L)(\alpha\text{-}SiW_{11}O_{39})]^{5-}$ units, which differ slightly in bond lengths and angles. The $[Dy(H_2L)(\alpha\text{-}SiW_{11}O_{39})]^{5-}$ units are held in groups of 6 by coordinated potassium atoms and water molecules, the potassium atoms being the responsible of balancing the charge of the anionic units. Crystallization water molecules are also present in the structure. Crystallographic data and selected bond lengths are given in Appendices, Tables A.18 and A.19, respectively.

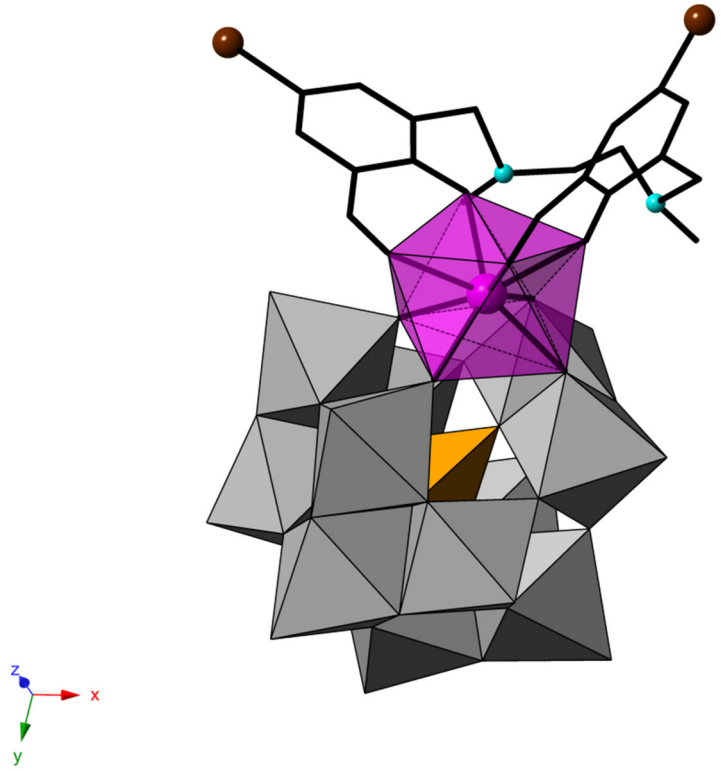

Figure 7.3.- Combined ball & stick/polyhedral representation of $[Dy(H_2L)(\alpha\text{-}SiW_{11}O_{39})]^{5-}$ units. Grey and yellow polyhedrons represent octahedral and tetrahedral coordination environments of W and Si atoms, respectively, where the vertexes of the polyhedrons account for oxygen atoms. The Dy(III) atom is in pink and the nitrogen and bromine atoms of the ligand in blue and brown, respectively.

Within each mononuclear $[Dy(H_2L)(\alpha\text{-}SiW_{11}O_{39})]^{5-}$ unit, the ligand is coordinated to the Dy(III) ion in a O_4 neutral zwitterionic form through the two deprotonated phenolic oxygen atoms and the two aldehyde oxygen atoms, as in the monomeric complex $[Ni(H_2L)(NO_3)(H_2O)]NO_3{\cdot}H_2O$ (**1**) presented in Chapter 1. The Dy(III) ion is further coordinated to the four oxygen atoms of the vacant site of the $[\alpha\text{-}SiW_{11}O_{39}]^{8-}$ unit, giving rise to a DyO_8 coordination environment. Calculation of the degree of distortion of the DyO_8 coordination polyhedron with respect to an ideal eight-vertex polyhedron with continuous shape measure theory and the SHAPE software,[13] led to shape measures relative to biaugmented trigonal prism (BTPR-8), square antiprism (SAPR-8), biaugmented trigonal prism J50 (JBTPR-8) and triangular dodecahedron (TDD-8), with values listed in Appendices, Table A.37. The shape measures are significantly larger for other reference polyhedra and therefore the DyO_8 coordination polyhedron can be considered an intermediate between the above indicated ideal polyhedra, closest in shape to the BTPR-8 geometry.

The Dy-O bond distances are in the 2.279(12)-2.473(13) Å ranges, being the shortest and largest distances the ones corresponding to the phenolic and aldehyde oxygen atoms, respectively. Despite the size of the POM ligands that are encapsulating the Dy(III) ions, the shortest Dy···Dy distance is similar to those found in the trinuclear Zn-Dy-Zn compounds presented in the previous chapter (shortest Dy···Dy distance of 8.012 Å).

About the crystal packing, complex **55** can be best described as alternating sequences of metalorganic and double inorganic regions along the *z* axis, forming therefore rows in *a* direction (Figure 7.4). The double inorganic layer is constructed by $[Dy(H_2L)(\alpha\text{-}SiW_{11}O_{39})]^{5-}$ units connected by potassium and oxygen atoms.

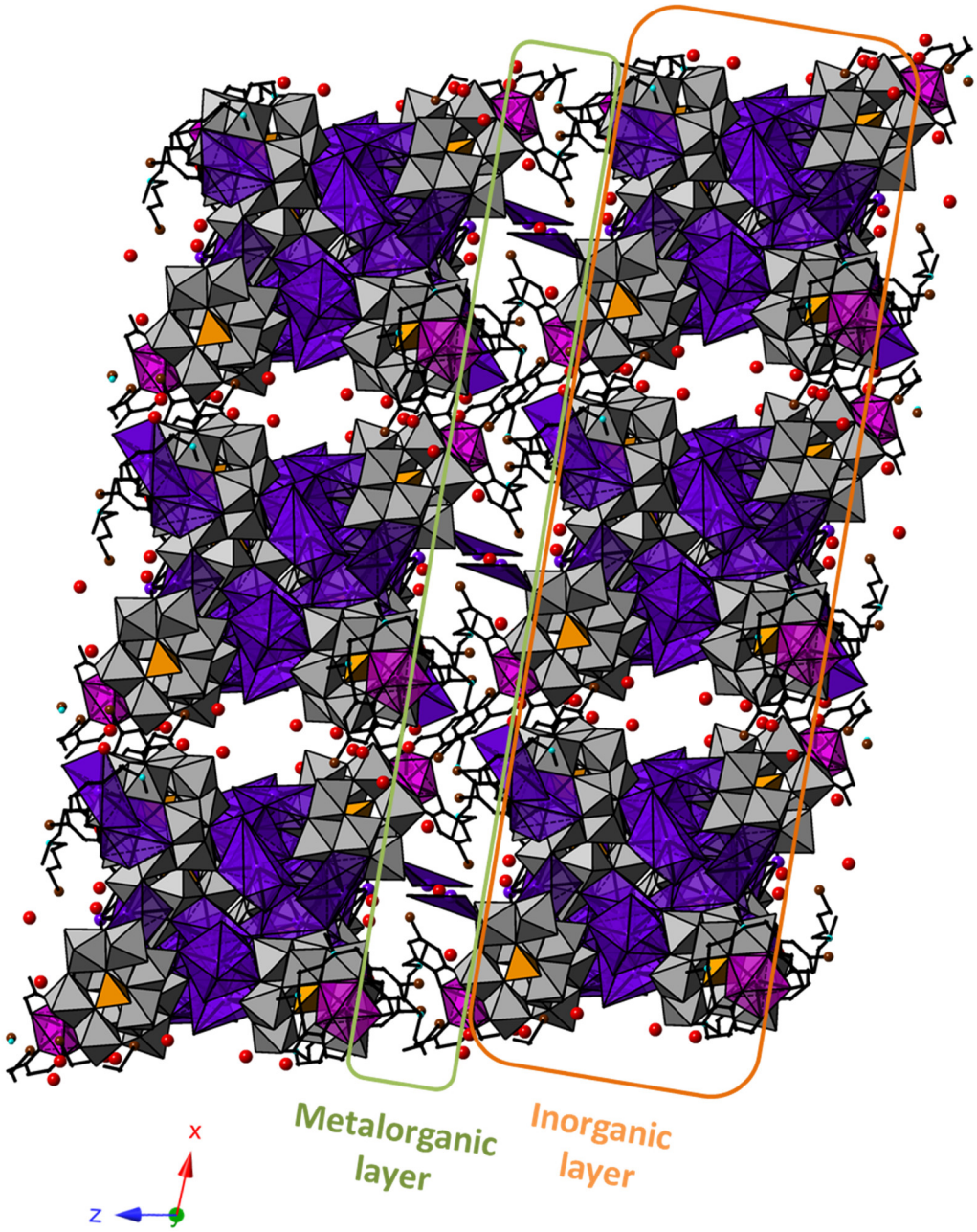

Figure 7.4.- Crystal packing of complex **55** in *xz* plane. In purple the polyhedrons formed by K atoms, the vertexes account for oxygen atoms.

7.3.2. Magnetic Properties of Complex 55

The temperature dependence of the $\chi_M T$ product for **55** (χ_M being the molar paramagnetic susceptibility per Dy(III) ion) under a constant magnetic field of 0.1 T in the 2-300 K range is displayed in Figure 7.5.

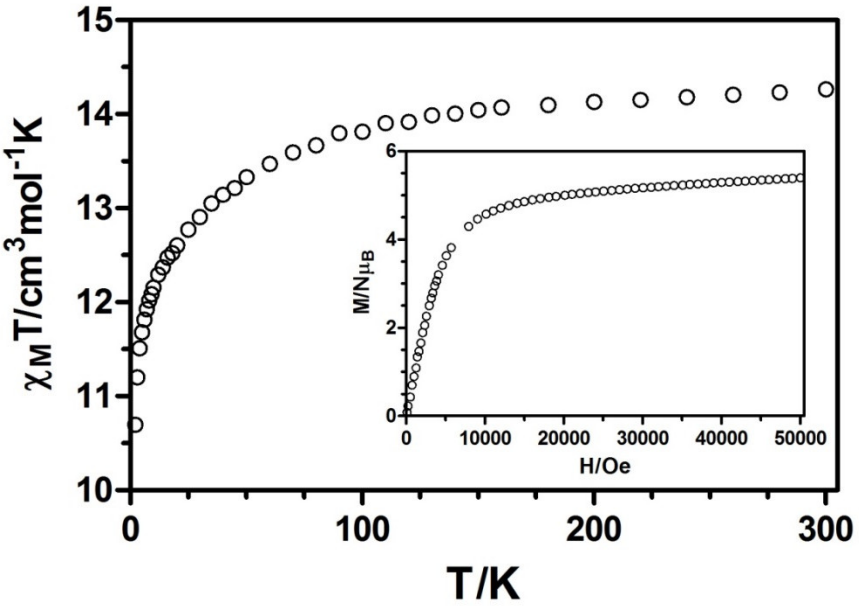

Figure 7.5.- Temperature dependence of the $\chi_M T$ product for **55** in the 2-300 K range. Inset: field dependence of the magnetization for **55**.

The $\chi_M T$ value of 14.26 $cm^3 \cdot K \cdot mol^{-1}$ at 300 K for **55** is compatible with the calculated value of 14.17 $cm^3 \cdot K \cdot mol^{-1}$ for the ground state of the Dy(III) ion in the free-ion approximation. On cooling, the $\chi_M T$ product steadily decreases to reach a value of 10.70 $cm^3 \cdot K \cdot mol^{-1}$ at 2 K. This behaviour is mainly due to the depopulation of the Stark sublevels of the Dy(III) ion, which arise from the splitting of the $^6H_{15/2}$ ground term by the ligand field. The magnetization plot at 2 K (Figure 7.5, inset) shows a relatively rapid increase at low fields and a slow linear increase from 1 T on, reaching a value of 5.40 $N\mu_B$ at the maximum applied field of 5 T. This value is rather lower than the expected saturation value for Dy(III) ions (10 $N\mu_B$), which is due to crystal-field effects that lead to magnetic anisotropy.

In order to know if the strategy of grafting Dy(III) compounds into POM surfaces can lead to SMM behaviour, *alternating current* magnetic measurements were performed on **55**. A slight frequency dependency of the out-of-phase (χ_M'') signal was observed under zero *dc* external field, but without any maxima in the temperature window technically available, which could be due to QTM (Figure 7.6). When the measurements were performed under an applied field of 1000 Oe, no significant improvement was observed, showing only a slight frequency-dependency of the out-of-phase magnetic susceptibility.

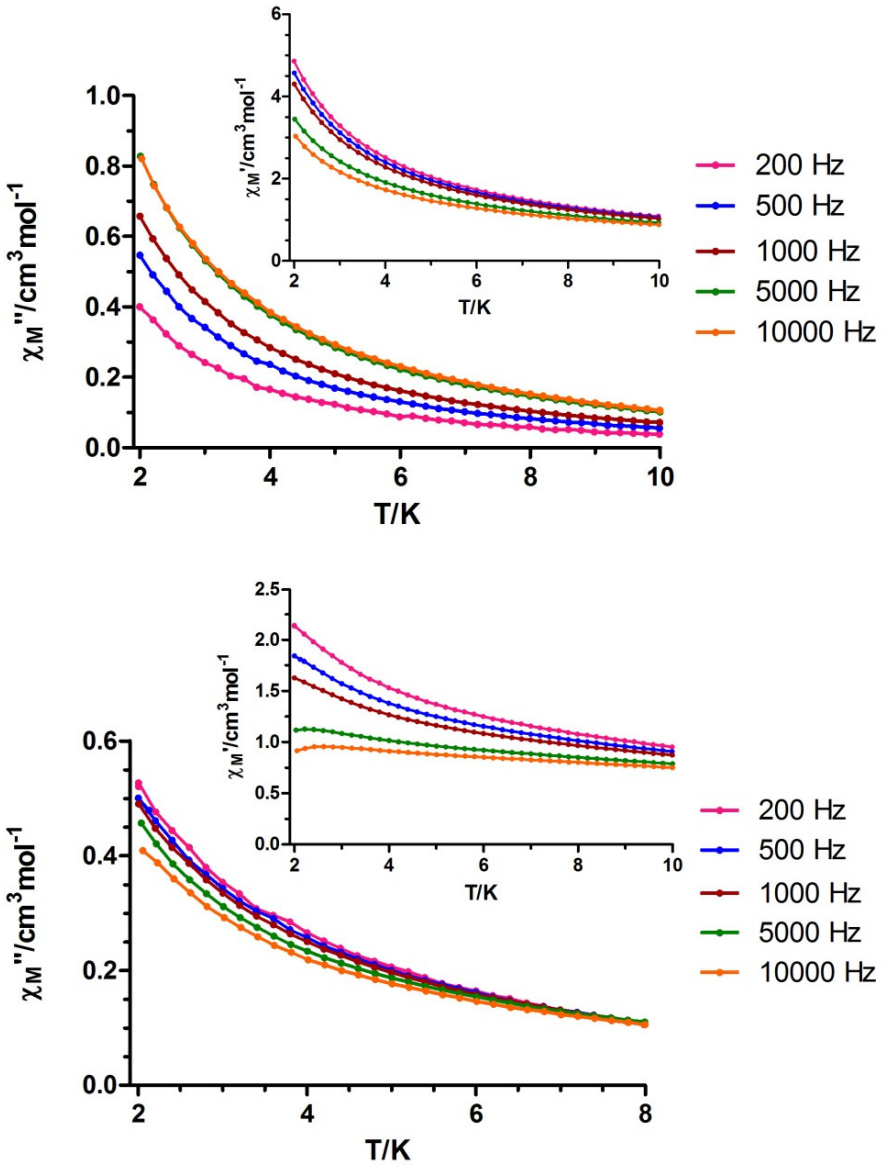

Figure 7.6.- Temperature dependence of in-phase χ_M' (inset) and out-of phase χ_M'' components of the *alternating current* susceptibility for complex **55** under zero external field (top) and an applied field of 1000 Oe (bottom).

The observed behaviour could be due to the potassium and water bridges that connect different $[Dy(H_2L)(\alpha\text{-}SiW_{11}O_{39})]^{5-}$ units, which prevent the formation of well isolated molecules in the crystal lattice, thus disfavouring the SMM behaviour. It should be noted that other Dy(III) compounds with biaugmented trigonal prism (BTPR-8) geometry exhibit SMM behaviour.[14] The fact that compound **55** does not show such a behaviour can also be due to: (i) the distortion of the DyO_8 coordination polyhedron from the ideal geometry, which provokes the mixing of the ground state with excited

states of lower M_j value, thus increasing the QTM and (ii) the fact that there are not clear shortest Dy-O distances in the DyO_8 coordination polyhedron as to create an axial ligand field for the oblate electron density of the Dy(III) ion.

7.4. CONCLUSIONS

This work illustrates the potential of the well-known family of Keggin-type tungstosilicates to prepare lanthanide containing POMs, thanks to their vacant positions. As a result, the Dy(III) containing compound $\{K_5[Dy(H_2L)(\alpha\text{-}SiW_{11}O_{39})]\}_6 \cdot 46H_2O$ (**55**) has been prepared, where the Dy(III) atoms are coordinated to neutral H_2L ligands in their zwitterionic form and $[SiW_{11}O_{39}]^{8-}$ anionic silicotungstates. This compound does not show significant SMM behaviour, as concluded from the slight frequency dependency of the out-of-phase susceptibility signal. The lack of SMM behaviour could be due to (i) the fact that the $[Dy(H_2L)(\alpha\text{-}SiW_{11}O_{39})]^{5-}$ units are held in groups of 6 by coordinated potassium atoms and water molecules, what prevents the units to behave as independent entities magnetically speaking, which favours QTM, (ii) the distortion of the DyO_8 coordination polyhedron from the ideal geometry, which provokes mixing of the ground state with excited states of lower M_j value, thus increasing the QTM and (iii) the fact that there are not clear shortest Dy-O distances in the DyO_8 coordination polyhedron as to create an axial ligand field for the oblate electron density of the Dy(III) ion.

7.5. BIBLIOGRAPHY

[1] M. T. Pope, *Heteropoly and Isopoly Oxometalates*; Springer-Verlag: Berlin, **1983**.

[2] **a)** M. Sun, J. Zhang, P. Putaj, F. Lefebvre, J. Pelletier, J.-M. Basset, *Chem. Rev*., **2014**, *114*, 981; **b)** J. J. Stracke, R. G. Finke, *ACS Catal*., **2014**, *4*, 909; **c)** M. Misono, *Stud. Surf. Sci. Catal*., **2013**, *176*, 97; **d)** M. Carraro, A. Sartorel, M. Ibrahim, N. Nsouli, C. Jahier, S. Nlate, U. Kortz, M. Bonchio in *Innovative Catalysis in Organic Synthesis: Oxidation, Hydrogenation, and C–X Bond Forming Reactions*; P. G. Andersson, Ed.; Wiley-VCH: Weinheim, Germany, **2012**; **e)** Q. Yin, J. M. Tan, C. Besson, Y. V. Geletti, D. G. Musaev, A. E. Kuznetsov, Z. Luo, K. I. Hardcastle, C. L. Hill, *Science*, **2010**, *328*, 342; **f)** K. Kamata, K. Yonehara, Y. Sumida, K. Yamaguchi, S. Hikichi, N. Mizuno, *Science*, **2003**, *300*, 964; **g)** I. Kozhevnikov in *Catalysis by Polyoxometalates*; S. M.

Roberts, Ed.; Catalysts for Fine Chemical Synthesis (Vol. 2); John Wiley & Sons: Chichester, U.K., **2002**; **h)** R. Neumann, M. Dahan, *Nature*, **1997**, *388*, 353.

[3] **a)** J. M. Clemente-Juan, E. Coronado, C. J. Gómez-García, *Chem. Soc. Rev.*, **2012**, *41*, 7464; **b)** U. Kortz, A. Müller, J. Van Slageren, J. Schnack, N. S. Dalal, M. Dressel, *Coord. Chem. Rev.*, **2009**, *253*, 2315; **c)** J. M. Clemente-Juan, E. Coronado, *Coord. Chem. Rev.,* **1999**, *193-195*, 361; **d)** A. Müller, F. Peters, M. T. Pope, D. Gatteschi, *Chem. Rev.,* **1998**, *98*, 239.

[4] **a)** M. Ammam, *J. Mater. Chem. A*, **2013**, 1, 6291; **b)** Y.-F. Song, R. Tsunashima, *Chem. Soc. Rev*., **2012**, *41*, 7384; **c)** H. N. Miras, J. Yan, D.-L. Long, L. Cronin, *Chem. Soc. Rev*., **2012**, *41*, 7403; **d)** D.-L. Long, E. Burkholder, L. Cronin, *Chem. Soc. Rev*., **2007**, *36*, 105; **e)** E. Coronado, C. J. Gómez-García, Chem. Rev., **1998**, *98*, 273.

[5] **a)** K. Stroobants, G. Absillis, E. Moelants, P. Proost, T. N. Parac-Vogt, T. N. *Chem. Eur. J.* **2014**, *20*, 3894*;* **b)** T. Yamase, *Prog. Mol. Subcell. Biol.* **2013**, *54*, 65; **c)** B. Hasenknopf, *Front. Biosci*., **2005**, *10*, 275; **d)** J. T. Rhule, C. L. Hill, D. A. Judd, R. F. Schinazi, *Chem. Rev.,* **1998**, *98*, 327.

[6] **a)** M. Nyman, *Dalton Trans*., **2011**, *40*, 8049; **b)** M. Nyman, F. Bonhomme, T. M. Alam, M. A. Rodriguez, B. R. Cherry, J. L. Krumhansl, T. M. Nenoff, A. M. Sattler, *Science*, **2002**, 297, 996; **c)** M. Filopwitz, R. K. C. Ho, W. G. Klemperer, W. Shum, *Inorg. Chem*., **1979**, *18*, 93; **d)** I. Lindqvist, B. Aronsson, *Ark. Kemi*, **1953**, *7*, 49.

[7] **a)** U. Lee, H. Ichida, A. Kobayashi, Y. Sasaki, *Acta Crystallogr*., **1984**, *C40*, 5; **b)** A. Perloff, *Inorg. Chem*., **1970**, *9*, 2228; **c)** H. T. Evans, *Acta Crystallogr*., **1974**, *B30*, 2095; **d)** H. T. Evans, *J. Am. Chem. Soc*., **1948**, *70*, 1291.

[8] J. F. Keggin, *Nature,* **1933**, *132*, 351.

[9] B. Dawson, *Acta Crystallogr.,* **1953**, *6*, 113.

[10] **a)** M. T. Pope in *Encyclopedia of Inorganic Chemistry*; R. B. King, Ed.; John Wiley & Sons: Chichester, UK, **1994**; pp. 3361-3371; **b)** *Polyoxometalates: from Platonic Solids to Anti Retroviral Activity*; M. T. Pope, A. Müller, Eds.; Kluwer: Dordrecht, The Netherlands, **1994**; **c)** M. T. Pope in *Comprehensive Coordination Chemistry*; G. Wilkinson, R. D. Gillard, J. A. McCleverty, Eds.; Pergamon Press: New York, NY, USA, **1987**, pp. 1023-1058; **b)** *Polyoxometalates: from Platonic Solids to Anti Retroviral Activity*; M. T. Pope, A. Müller, Eds.; Kluwer: Dordrecht, The Netherlands, **1994**.

[11] See, for example: **a)** K. Suzuki, R. Sato, N. Mizuno, *Chem. Sci*., **2013**, *4*, 596; **b)** F. Li, W. Guo, L. Xu, L. Ma, Y. Wang, *Dalton Trans*., **2012**, *41*, 9220; **c)** S. Cardona-Serra, J. M. Clemente-Juan, E. Coronado, A. Gaita-Ariño, A. Camón, M. Evangelisti, F. Luis, M. J. Martínez-Pérez, J. Sesé, *J. Am. Chem. Soc*., **2012**, *134*, 14982; **d)** J. M. Clemente-Juan, E. Coronado, A. Gaita-Ariño, *Chem. Soc. Rev*., **2012**, *41*, 7464.

[12] A. Tézé, G. Hervé, *Inorg. Synth.,* **1990**, *27*, 85.

[13] M. Llunell, D. Casanova, J. Cirera, J. M. Bofill, P. Alemany, S. Alvarez, M. Pinsky, D. Avnir, *SHAPE*, v1.1b; Barcelona, Spain, **2005**.

[14] **a)** D.-P. Li, X.-P. Zhang, T.-W. Wang, B.-B. Ma, C.-H. Li, Y.-Z. Li, X.-Z. You, *Chem. Commun*., **2011**, *47*, 6867; X.-L. Li, C.-L. Chen, Y.-L. Gao, C.-M. Liu, X.-L. Feng, Y.-H. Gui, S.-M. Fang, *Chem. Eur. J.*, **2012**, *18*, 14632; **b)** M. M. Hänninen, A. J. Mota, D. Aravena, E. Ruiz, R. Sillanpää, A. Camon, M. Evangelisti, E. Colacio, *Chem. Eur. Jour*., **2014**, 20, 8410.

CHAPTER 8

FUTURE PERSPECTIVES AND ADDITIONAL WORK

8.1. FUTURE PERSPECTIVES

During the realization of this Ph.D. thesis, more experimental results have been obtained, which are not included in this work due to time constraints. New experiments are also planned for the near future to complete or even improve this work. All these considerations are compiled in this section.

Chapter 1

As seen in Chapter 4, Co(II) ions show higher magnetic anisotropy than Ni(II) ions and therefore, Co(II) complexes are more likely to show SMM behaviour than their Ni(II) analogues. Keeping this in mind, five new polynuclear Co(II) complexes have been prepared from the ligand H_2L, which are summarized in Scheme 8.1 and Figure 8.1. In complexes **57** and **60**, one of the two formyl groups of the ligand is transformed into a hemiacetal group leading to the ligand H_2L', as have been already seen in bibliography (*Synth. React. Inorg. Met.-Org. Chem.*, **2001**, *31*, 1443).

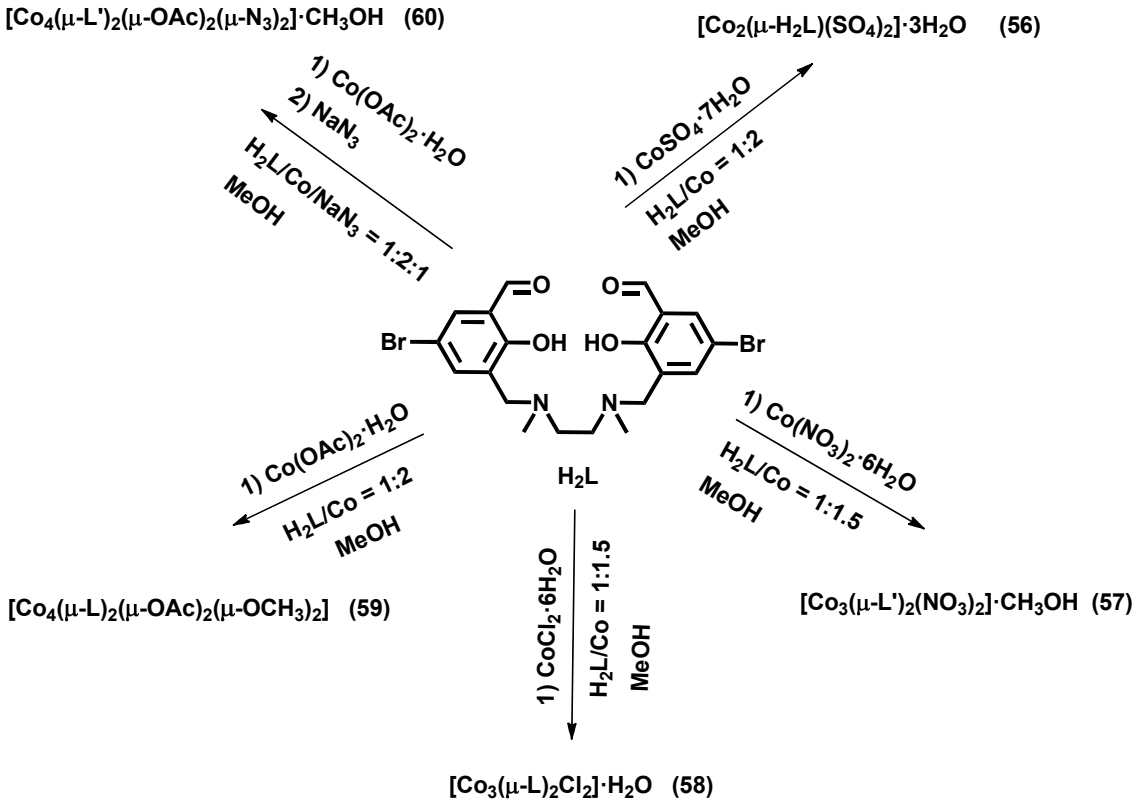

Scheme 8.1.- Co(II) complexes prepared using the ligand H_2L.

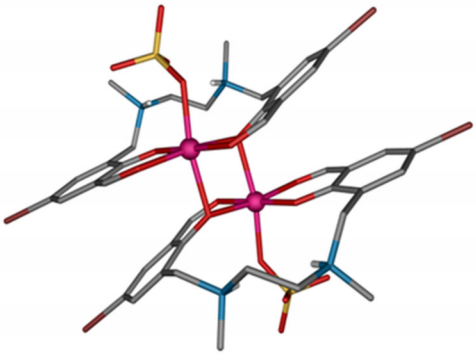

$[Co_2(\mu\text{-}H_2L)(SO_4)_2] \cdot 3H_2O$ **(56)**

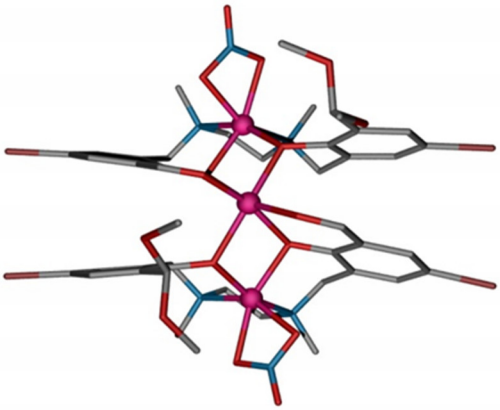

$[Co_3(\mu\text{-}L')_2(NO_3)_2] \cdot CH_3OH$ **(57)**

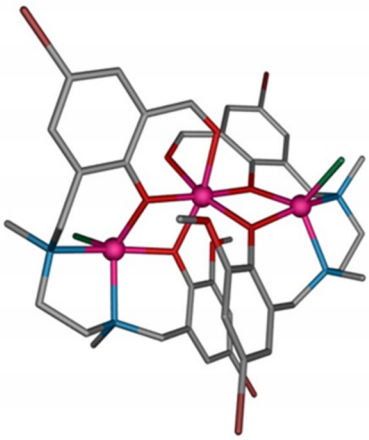

$[Co_3(\mu\text{-}L)_2Cl_2] \cdot H_2O$ **(58)**

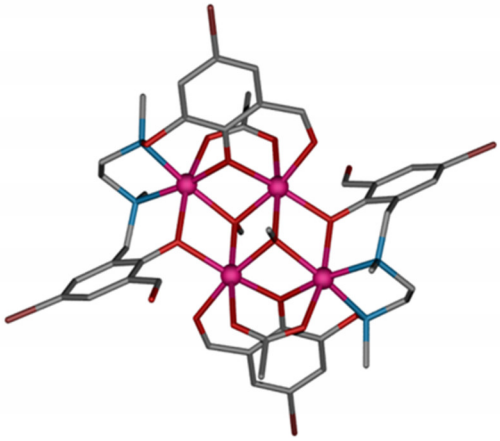

$[Co_4(\mu\text{-}L)_2(\mu\text{-}OAc)_2(\mu\text{-}OCH_3)_2]$ **(59)**

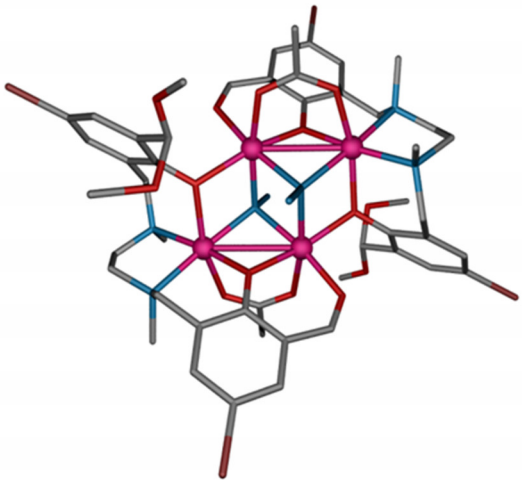

$[Co_4(\mu\text{-}L')_2(\mu\text{-}OAc)_2(\mu\text{-}N_3)_2] \cdot CH_3OH$ **(60)**

Figure 8.1.- A perspective view of the structure of Co(II) complexes. Colour code: N = blue, O = red, C = gray, Br = brown, S = yellow, Co = fuchsia, H = white. H atoms (except H atoms coordinated to amine N atoms in **56**) and crystallization molecules have been omitted for the sake of clarity.

Although this work is still in progress, the *ac* susceptibility measurements have already been carried out. Complex **59** is the only one that does not show any frequency dependency of the out-of phase susceptibility signal, whereas the other complexes show modest frequency dependency, without any clear maxima at frequencies as high as 10000 Hz in most cases.

Chapter 3

1) The incorporation of good antenna groups, such as 9-anthracenecarboxylate (9-An) to complexes reported in Chapter 3 could improve the efficiency of the energy transfer to the excited levels of the lanthanide ions. In this regard, complexes with the general formula $[Zn(\mu\text{-}L)(\mu\text{-}9\text{-}An)Ln(NO_3)_2]\cdot CH_3CN$ have been prepared (Figure 8.2).

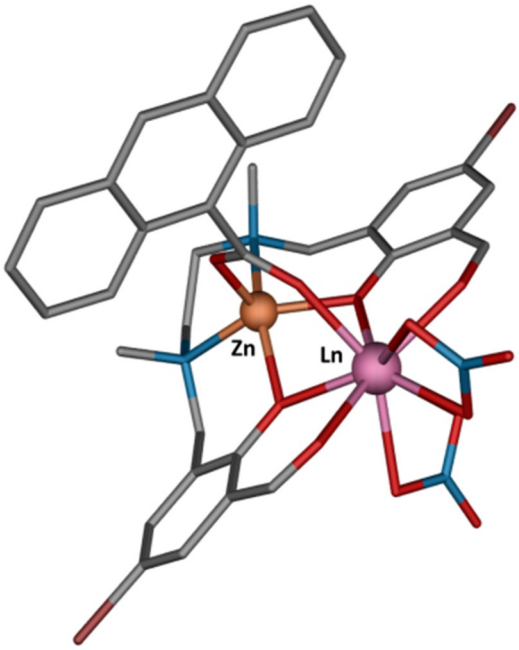

Figure 8.2.- A perspective view of the structure of complexes $[Zn(\mu\text{-}L)(\mu\text{-}9\text{-}An)Ln(NO_3)_2]\cdot CH_3CN$. Colour code: N = blue, O = red, C = gray, Br = brown, Zn = light brown, Ln = pink. H atoms and crystallization acetonitrile molecules have been omitted for the sake of clarity.

The Dy(III) derivative shows field-induced SIM behaviour and further magnetic and luminescent measurements are still in progress.

2) The organization of SMMs on surfaces seems to be the first step towards final applications of these molecules. Although this has turned to be a hard task due to the poor stability against water, temperature or other factors of SMMs, we would like to try to deposit our complexes into surfaces. For this purpose, the dinuclear complexes with the general formula $[Zn(\mu\text{-}L)(\mu\text{-}OAcr)Ln(NO_3)_2]\cdot CH_3CN$ (OAcr = acrylate) have been prepared (Figure 8.3) and the grafting of dinuclear units into polyacrylic surfaces will be tried in the future.

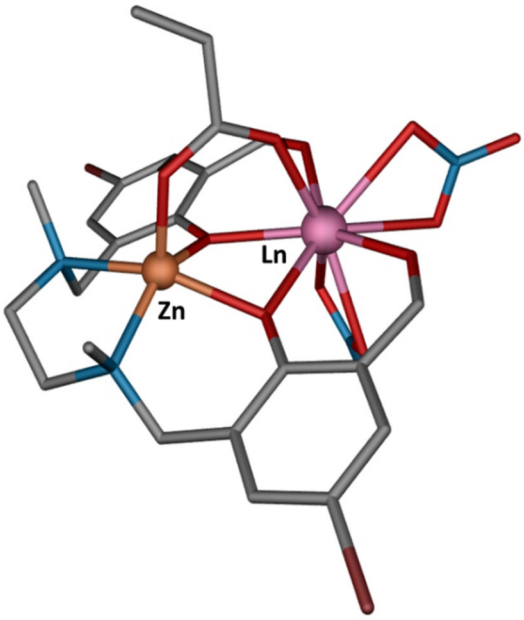

Figure 8.3.- A perspective view of the structure of complexes $[Zn(\mu\text{-}L)(\mu\text{-}Acr)Ln(NO_3)_2]\cdot CH_3CN$. Colour code: N = blue, O = red, C = gray, Br = brown, Zn = light brown, Ln = pink. H atoms and crystallization acetonitrile molecules have been omitted for the sake of clarity.

8.2. ADDITIONAL WORKS

A great part of the work carried out during this Ph.D. thesis is collected in this manuscript as independent chapters or is compiled in the previous section. However, additional work that has conducted to excellent results has also been performed, which is not included due to the extent of the manuscript.

This way, I have collaborated with Dr. J. P. Costes by analysing the magnetic properties of three new Zn(II)Dy(III)Zn(II) trinuclear complexes, which have been

prepared according to a complex-as-ligand strategy (Scheme 8.2). These complexes behave as field-free single-ion magnets (SIMs) with effective energy barriers (U_{eff}) for the reversal of the magnetization of 96.9(6) K, 146.8(5) K and 146.1(10) K. The role of the peripheral ligands coordinated to Zn(II) (H_2O, Br and Cl) has been investigated, concluding that compared with water, the peripheral halide ligands coordinated to the Zn(II) ions increase the barrier height. These complexes also exhibit metal-centered luminescence and these results have been published in *Chemistry - A European Journal* (*Chem. Eur. J.*, **2015**, *21*, 15785).

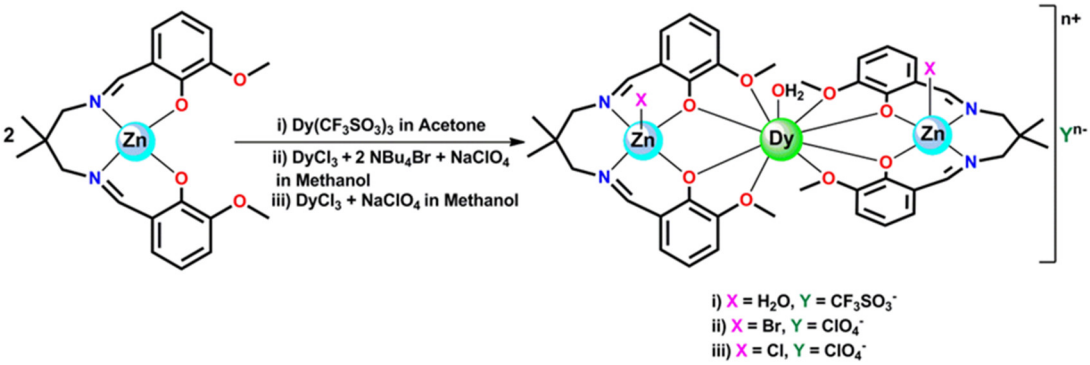

Scheme 8.2.- Synthesis of the complexes.

Additionally, in order to complete the magnetic study of lanthanide ions, a novel family of metal-organic-frameworks (MOFs) with the general formulas $\{[Ln(ant)_{1.5}(DMF)_2]\cdot(DMF)\}_n$ {Ln (III) = Pr, Nd, Gd, Tb, Dy, Er} and $[Yb(ant)(NO_3)(DMF)_2]_n$ have been synthesized, which are based on the 9,10-anthracenecarboxylate linker (ant) (Figure 8.4). These results are not described in detail as they are not based on any of the two ligands prepared for this report.

These materials display intense photoluminescence properties in the solid state at room temperature. What is more interesting, some of them exhibit slow relaxation of magnetization with activation barriers of 22.9, 15.4, 52.7, 13.0 and 16.2 K for Nd(III), Gd(III), Dy(III), Er(III) and Yb(III), respectively. The Nd(III) and Yb(III) materials are the first examples of 3D- and 2D-MOFs, respectively, that show slow relaxation of magnetization. This work has been accepted in *Dalton Transactions*.

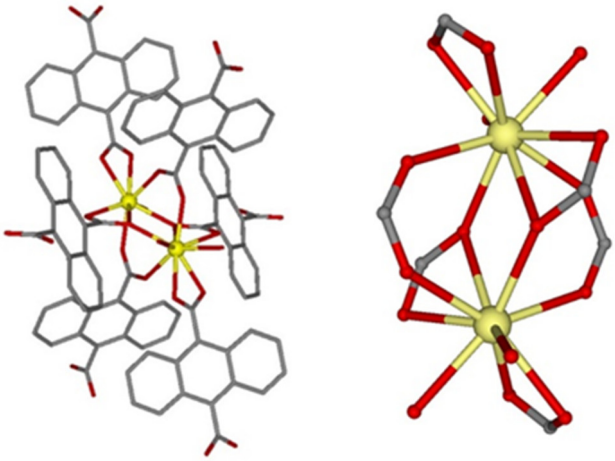

Figure 8.4.- Left: Dinuclear entity formed by two lanthanide atoms and six anthracene dicarboxylic linkers. Right: Lanthanide coordination polyhedral. Hydrogen atoms have been omitted for clarity. Colour code: O = red, C = grey, Lanthanide = yellow.

8.3. SCIENTIFIC PUBLICATIONS AND CONTRIBUTIONS TO MEETINGS

Some of the results obtained during this Ph.D. thesis are already published in the following scientific journals, which are ordered following the chronological order:

- *Rational design of ferromagnetic coupled diphenoxocarboxylate triply bridged dinuclear nickel(II) complexes: orbital countercomplementarity of the bridging ligands.* J. Ruiz, A. J. Mota, A. Rodríguez-Diéguez, I. Oyarzabal, J. M. Seco, E. Colacio, *Dalton Trans.,* **2012***, 41*, 14265.

- *Rational Electrostatic Design of Easy-Axis Magnetic Anisotropy in a Zn^{II}–Dy^{III}–Zn^{II} Single-Molecule Magnet with a High Energy Barrier.* I. Oyarzabal, J. Ruiz, J. M. Seco, M. Evangelisti, A. Camón, E. Ruiz, D. Aravena, E. Colacio, *Chem. Eur. J.*, **2014**, *20*, 14262.

- *An experimental and theoretical magnetostructural study of polynuclear Ni^{II} complexes assembled from a versatile bis(salicylaldehyde)diamine polytopic ligand.* I. Oyarzabal, J. Ruiz, A. J. Mota, A. Rodríguez-Diéguez, J. M. Seco, E. Colacio, *Dalton Trans.,* **2015***, 41*, 14265.

- *Increasing the effective energy barrier promoted by the change of a counteranion in a Zn–Dy–Zn SMM: slow relaxation via the second excited state*. I.

Oyarzabal, J. Ruiz, E. Ruiz, D. Aravena, J. M. Seco, E. Colacio, *Chem. Commun.*, **2015**, *51*, 12353.

In addition, the obtained results have been presented in several meetings:

- Poster presentation at "15ª Reunión Científica Plenaria de Química Inorgánica y 9ª Reunión Científica Plenaria de Química del Estado Sólido (QIES 2012)" (Girona, **2012**). Title: *Estructura y propiedades magnéticas de compuestos dinucleares de Ni (II) con ligandos multitópicos de tipo N_3O_4 y acetato puente.*

- Poster presentation at "IX Simposio de Investigadores Jóvenes RSEQ-Sigma Aldrich" (Zaragoza, **2012**). Title: *Interacción ferromagnética por efectos de contra-complementaridad en compuestos dinucleares de Ni (II) con triples puentes difenoxoacetato.*

- Poster presentation at "X Simposio de Investigadores Jóvenes RSEQ-Sigma Aldrich" (Madrid, **2013**). Title: *Propiedades magnéticas y caracterización estructural de complejos trinucleares Zn(II)-Dy(III)-Zn(II).*

- Oral communication at "16ª Reunión Científica Plenaria de Química Inorgánica y 10ª Reunión Científica Plenaria de Química del Estado Sólido (QIES 2014)" (Almeria, **2014**). Title: *Diseño electrostático de anisotropía uniaxial en la molécula imán Zn(II)-Dy(III)-Zn(II) con alta barrera energética para la relajación de la magnetización*.

- Poster presentation at "XXXV Reunión Bienal de la Real Sociedad Española de Química" (A Coruña, **2015**). Title: *Relajación de la magnetización a partir del segundo doblete excitado en un complejo trinuclear Zn(II)-Dy(III)-Zn(II).*

- Poster presentation at "5th European Conference on Molecular Magnetism" (Zaragoza, **2015**). Title: *Analysis of the role of peripheral ligands coordinated to Zn(II) and counteranion in rising the anisotropy energy barrier of a series of zero-field Zn-Dy-Zn Single Molecule Magnets.*

CONCLUSIONS

The main goal of the research work developed in this PhD was the design, synthesis and characterization of new materials based on coordination complexes showing interesting magnetic (SMM behaviour) and/or luminescent properties. To achieve these objectives, the two compartmental ligands N,N'-dimethyl-N,N'-bis(2-hydroxy-3-formyl-5-bromobenzyl)ethylenediamine (H_2L) and N,N',N"-trimethyl-N,N"-bis(2-hydroxy-3-methoxy-5-methylbenzyl)diethylenetriamine (H_2L^1) were synthesized following reported procedures.

The results and discussions presented in this manuscript allow drawing the following conclusions:

Chapter 1

1) Six new Ni(II) complexes ranging from mononuclear to tetranuclear were prepared using the ligand H_2L, where the ligand shows a rich variety of coordination modes.

2) The mononuclear complex has the general formula $[Ni(H_2L)(NO_3)(H_2O)]NO_3 \cdot H_2O$ (**1**), where the Ni(II) atom shows a NiO_6 coordination environment. The magnetic properties of this complex are not included.

3) The dinuclear complexes $[Ni_2(\mu\text{-}L)(acac)_2(H_2O)] \cdot CH_3CN$ (**2**) and $[Ni_2(\mu\text{-}L)(\mu\text{-}OAc)(NCS)]$ (**3**) exhibit either double di-μ-phenoxo or triple di-μ-phenoxo/*syn-syn* acetate bridges, which promote moderate AF and very weak F interactions, respectively. The magnetic exchange interactions for **2** are quantified experimentally and supported by DFT calculations on its X-ray crystal structure, whereas for **3** were only determined by DFT calculations. Their sign and magnitude are related to the values of the Ni-O-Ni bridging angles and, in the case of the latter, to the additional countercomplementarity effect exerted by the *syn-syn* acetate bridging group.

4) The trinuclear complex $[Ni_3(\mu\text{-}L)_2(\mu\text{-}OH_2)_2(H_2O)(CH_3CN)](NO_3)_2 \cdot 4CH_3CN$ (**4**) presents a bent structure with rare double μ-phenoxo-μ-water bridges between central and external Ni(II) ions, which promote very weak AF interactions. The weak magnetic exchange interactions in this complex were determined by DFT calculations and their sign and magnitude are related to the values of the Ni-O-Ni bridging angles.

5) The tetranuclear complexes $[Ni_4(\mu\text{-}L)_2(\mu\text{-}OAc)_2(\mu\text{-}OCH_3)_2] \cdot 6H_2O \cdot 2CH_3OH$ (**5**) and $[Ni_4(\mu\text{-}L)_2(\mu\text{-}OAc)_2(\mu\text{-}N_3)_2] \cdot 2H_2O \cdot CH_3OH$ (**6**) present similar defective dicubane like

topologies with three distinct types of bridges between the Ni(II) ions. The main structural difference between both Ni_4 complexes is the presence in one of them of $\mu_{1,1,1}$-methoxo bridges and in the other one of $\mu_{1,1,1}$-azido bridges. In the Ni_4 complex containing methoxo group, the triple mixed μ-phenoxo/$\mu_{1,1,1}$-methoxo/*syn-syn* acetate bridge and the double di-$\mu_{1,1,1}$-methoxo bridge propagate weak F interactions between the Ni(II) ions, whereas the unusual μ-phenoxo/$\mu_{1,1,1}$-methoxo bridge mediates weak AF interactions. It should be noted that the substitution of $\mu_{1,1,1}$-methoxo bridges by $\mu_{1,1,1}$-azido bridges provokes that all the magnetic pathways promote ferromagnetic interactions, which are stronger than those found for the compound containing $\mu_{1,1,1}$-methoxo bridges. The sign and nature of the experimental *J* values found for these Ni_4 species were supported by DFT calculations.

Chapter 2

6) Four di-μ-phenoxo/carboxylate bridged dinuclear Ni(II) complexes of formulas $[Ni_2(\mu\text{-}L^1)(\mu\text{-}OAc)(H_2O)_2]NO_3$ (**7**), $[Ni_2(\mu\text{-}L^1)(\mu\text{-}OBz)(H_2O)(MeOH)]NO_3\cdot 3MeOH$ (**8**), $[Ni_2(\mu\text{-}L^1)(\mu\text{-}9\text{-}An)(H_2O)(MeOH)]NO_3$ (**9**) and $[Ni_2(\mu\text{-}L^1)(\mu\text{-}OAc)(H_2O)(N_3)]\cdot CH_3OH$ (**10**) were synthesized using the ligand H_2L^1.

7) The coordination of the *syn-syn* carboxylate group promotes the following changes in the Ni-$(\mu\text{-}O)_2$-Ni bridging fragment: (i) the structure is folded with large hinge angles in the range 32-35°, (ii) the Ni-O-Ni bridging angle (θ) is considerably reduced, and (iii) the τ angle increases to reach values in the 34-42° range.

8) All these changes favour the decrease of the AF contribution to such an extent that weak AF or F couplings should be expected if, as a first approximation, the magnetic pathway through the *syn–syn* carboxylate group is not taken into account. In good agreement with this hypothesis, complexes **7**-**10** exhibit ferromagnetic coupling between the Ni(II) ions.

9) A comparative analysis of the magneto-structural data for **7**-**10** and other di-μ-phenoxo/carboxylate bridged dinuclear nickel(II) complexes allows one to conclude that, in addition to θ, the β and τ angles play an important role in determining the magnetic coupling in this kind of compounds. When the magnetic exchange pathway through the *syn-syn* carboxylate group is also considered for the magnetic coupling of complexes **7**-**10**, the phenomenon of the countercomplementarity between diphenoxo and carboxylate bridging ligands immediately emerges. DFT calculations

unequivocally support the existence of countercomplementarity effects in **7**-**10**, which are essential for the ferromagnetic coupling observed in **7**-**10**.

Chapter 3

10) The compartmental ligand H_2L also allows the preparation of dinuclear Zn(II)Ln(III) complexes, in which the Zn(II) ion occupies the internal N_2O_2 site and the oxophilic Ln(III) ion occupies the external O_4 site. The fifth position of the Zn(II) coordination sphere is occupied by a bridging acetate ion, leading to di-μ-phenoxo/*syn-syn* acetate triple bridged species with the general formula [Zn(μ-L)(μ-OAc)Ln$(NO_3)_2$]·CH_3CN {Ln(III) = Pr (**11**), Nd (**12**), Sm (**13**), Eu (**14**), Gd (**15**), Tb (**16**), Dy (**17**), Ho (**18**), Er (**19**), Tm (**20**) and Yb (**21**)}.

11) Variable temperature susceptibility and field dependent measurements were carried out in all the complexes. As expected, the magnetic properties of these complexes are strongly influenced by the spin-orbit coupling and ligand field effects (excluding Gd(III) based complex **15**), which lead to magnetic anisotropy.

12) Dynamic *ac* magnetic susceptibility measurements as a function of both frequency and temperature showed that only **17** exhibits frequency dependence at zero applied magnetic field. However, when the *ac* measurements were performed in the presence of a small external field of 1000 Oe, complexes **12**, **17**, **19** and **21** showed typical SIM behaviour, with effective thermal energy barriers in the 14.12 - 41.55 K range when considering only the Orbach process.

13) Complex **12** is only the third Nd(III) complex exhibiting SIM behaviour, which shows an effective energy barrier of 14.12 K. The magnetic data suggests that the quantum pathway of the relaxation is not fully suppressed even with the application of an external field of 1000 Oe and the simultaneous fit of Orbach and QTM processes leads to a small increase of U_{eff} (17.10 K instead of 14.12 K).

14) The deviation of experimental relaxation times from linearity in the case of complex **17** suggests the presence of competing Raman and Orbach processes. The obtained effective energy barrier when considering both effects (89.9 K) is more than the double obtained only for the Orbach process (41.55 K).

15) The Er(III) complex **19** displays two distinct relaxation processes, as shown by two distinct frequency-dependent peaks when measured at 10000 Hz. However, the first relaxation process is hardly appreciable and as a consequence, only the second

process has been characterized. The fit of the high temperature data to the Arrhenius equation afforded an effective energy barrier of 21.0 K.

16) The Yb(III) complex **21** shows different relaxation modes that include Orbach, QTM and Raman, as deducted from the deviation of the linearity of the experimental relaxation times. When considering only the Orbach process, a U_{eff} of 18.9 K is obtained, whereas the simultaneous fit of Orbach and QTM leads to a small increase, obtaining a value of 23.65 K.

17) The photophysical properties of these complexes were also studied, showing the ability of the deprotonated ligand L^{2-} to sensitize Sm(III), Eu(III) and Tb(III)-based luminescence in the visible region. Emission decay measurements allowed the estimation of the lifetimes at most intense line of the main transitions at different temperatures for these complexes.

18) The ZnNd and ZnYb derivatives exhibit characteristic luminescence in the NIR region and therefore, both complexes can be considered as dual magneto-luminescent materials combining NIR emission and field-induced SIM behaviour.

Chapter 4

19) The Zn(II) diamagnetic ions of dinuclear complexes of Chapter 3 were substituted for Cu(II), Ni(II) and Co(II) ions, leading to a family of di-μ-phenoxo/*syn-syn* acetate triply bridged dinuclear M(II)Ln(III) complexes with the following general formulas: $[Cu(\mu\text{-}L)(\mu\text{-}OAc)Ln(NO_3)_2]\cdot CH_3CN\cdot H_2O$ {Ln(III) = Gd (**22**), Tb (**23**), Dy (**24**), Er (**25**)), $[Ni(CH_3CN)(\mu\text{-}L)(\mu\text{-}OAc)Ln(NO_3)_2]\cdot CH_3CN$ (Ln(III) = Nd (**26**), Gd (**27**), Tb (**28**), Dy (**29**), Er (**30**), Y(**31**)) and $[Co(CH_3CN)(\mu\text{-}L)(\mu\text{-}OAc)Ln(NO_3)_2]\cdot CH_3CN$ (Ln(III) = Gd (**32**), Tb (**33**), Dy(**34**), Er (**35**), Y(**36**)}.

20) Magnetic exchange interactions between M(II) and Gd(III) metal ions are ferromagnetic in nature and the experimentally obtained weak coupling constants have been supported by DFT calculations for complexes **22** and **27**. The weak coupling constants have been attributed to the fact that all the complexes present folded structures and to the presence of acetate bridges.

21) Dynamic *ac* magnetic susceptibility measurements as a function of the temperature showed that only complexes **29**, **30**, **34** and **36** exhibit frequency dependency of the out-ofphase signals, without any clear maxima in the temperature range technically available except for complex **36**.

22) The CoY complex **36** shows field-induced SIM behaviour with a low effective energy barrier of 15.68 K when considering only an Orbach relaxation process. However, the high value of τ_0, together with the low-temperature curvature of the relaxation times, strongly suggests that the QTM remains operative even with an applied filed of 1000 Oe. After considering the QTM effects, the effective energy barrier increases slightly to 18.56 K. However, the obtained energy barrier is still much lower than the expected value, which indicates that the relaxation takes place through a Raman mechanism.

23) These results, together with the results obtained in Chapter 3, show that the replacement of diamagnetic ions by anisotropic paramagnetic ions usually decreases the U_{eff} in 3d/4f systems.

Chapter 5

24) Nine Mn(II)Gd(III) dinuclear and tetranuclear complexes have been prepared using the compartmental ligands H_2L and H_2L^1, which present the following formulas: [Mn(μ-L)(μ-OAc)Ln$(NO_3)_2$]·CH_3CN·H_2O {Ln(III) = Gd (**37**), Dy (**38**)}, [Mn(CH_3OH)(μ-L_1)Dy$(NO_3)_3$] (**39**), [Mn(μ-L_1)(μ-OAc)Ln$(NO_3)_2$] {Ln(III) = Gd (**40**), Dy (**41**)}, [Mn(μ-L_1)(μ-9-An)Ln$(NO_3)_2$]·$2CH_3CN$ {Ln(III) = Gd (**42**), Dy (**43**)}, {(μ_3-CO_3)$_2$[Mn(μ-L^1)Gd$(NO_3)]_2$}·$2CH_3CN$ (**44**) and {(μ_3-CO_3)$_2$[Mn(μ-L^1)Dy$(NO_3)]_2$}·$2CH_3OH$ (**45**).

25) The magnetic exchange interactions between Mn(II) and Gd(III) ions are AF in the dinuclear complexes **37** and **42** and weak F in complex **40**. The tetranucler complex **44** shows weak F and AF interactions, being the overall interactions AF in nature. The obtained experimental coupling constant values are supported by DFT calculations. The Dy(III) based compound **38** shows AF interactions between Mn(II) and Dy(III) ions, whereas weak F interactions are observed for **41** and **43**.

26) The *alternating current* magnetic properties of **38**, **41** and **43** are also measured, but they only show a very modest frequency dependency of the out-of-phase susceptibility signal.

27) The magneto-thermal properties of **42** have been studied, obtaining a maximum value of $-\Delta S_m$ = 21.51 $J \cdot kg^{-1} \cdot K^{-1}$ at T = 3 K and applied field change of ΔB = 5 T. The results show that the MCE is due to the magnitude rather than to the nature of the magnetic coupling.

28) Experimental magneto-structural correlations are carried out from these and other complexes found in bibliography. The highest ferromagnetic coupling constants are observed in di-μ-phenoxo bridged complexes, which is due to the planarity of the Mn-(μ-O)$_2$-Gd bridging fragment and high Mn-O-Gd angles. The incorporation of a third bridge leads to more folded structures, which reduces the magnetic coupling constant.

29) DFT calculations carried out in a di-μ-phenoxo doubly bridged model compound show that for planar bridging fragments, the crossover point in Mn-O-Gd angle is located at 105°, being the interactions F above this angle and AF below it. The influence of the Mn-(μ-O)$_2$-Gd hinge angle was also studied by fixing the Mn-O-Gd angle to 105° and changing the hinge angle, concluding that J_{MnGd} increases when increasing β until around 20° and decreases from that point on. These calculations also show that the most important factor governing the nature and sign of the magnetic exchange coupling in MnGd dinuclear complexes containing di-μ-phenoxo-bridging fragments is the Mn-O-Gd angle (θ).

Chapter 6

30) Eight Zn(II)Dy(III)Zn(II) trinuclear complexes were prepared using the compartmental ligand H_2L, which show the following formulas: [ZnCl(μ-L)Dy(μ-L)ClZn][ZnCl$_3$(CH$_3$OH)]·3CH$_3$OH (**46**), [ZnCl(μ-L)Dy(μ-L)ClZn]NO$_3$·CH$_3$OH (**48**), [ZnBr(μ-L)Dy(μ-L)BrZn][ZnBr$_3$(CH$_3$OH)]·CH$_3$OH·2H$_2$O (**49**), [ZnBr(μ-L)Dy(μ-L)BrZn]NO$_3$·3CH$_3$OH (**50**), [ZnI(μ-L)Dy(μ-L)IZn]I·CH$_3$OH·3H$_2$O (**51**), [ZnI(μ-L)Dy(μ-L)IZn]NO$_3$·3CH$_3$OH (**52**), [ZnN$_3$(μ-L)Dy(μ-L)N$_3$Zn]NO$_3$·CH$_3$OH·H$_2$O (**53**) and [ZnCl(μ-L)Dy(μ-L)ClZn]PF$_6$ (**54**).

31) An Er(III) based trinuclear complex was also synthesized for comparative purposes, [ZnCl(μ-L)Er(μ-L)ClZn][ZnCl$_3$(CH$_3$OH)]·3CH$_3$OH (**47**), which is isostructural to complex **46**.

32) In all these complexes, the Dy(III) ions exhibit a DyO$_8$ coordination environment with slightly distorted axial D_{4d} symmetry. In the DyO$_8$ coordination sphere, two pairs of large negatively charged phenoxo groups with short Dy-O distances are arranged at opposite sides of the Dy(III) ion, whereas the remaining positions are occupied by neutral aldehyde-oxygen donor atoms.

33) The phenoxo oxygen donor atoms exert a strong crystal field and force the oblate electron density to be perpendicular to them in order to minimize electrostatic

repulsions. This electrostatic charge distributions stabilize the strongly axial M_J = ±15/2 ground Kramer's doublet, with the anisotropic axis pointing to the donor atoms with the greatest electron density and shorter Dy-O distances.

34) Complexes **46** and **48**-**53** show typical SIM behaviour with high thermal energy barriers for the reversal of the magnetization in zero field, which are in the 144-170 K range.

35) *Ab initio* calculations in complex **46** support the easy-axis anisotropy of the ground Kramer's doublet, the direction of the anisotropy axis and the thermally activated mechanism for the slow relaxation of the magnetization.

36) The Er(III) complex does not present significant SIM behaviour as expected for the prolate electron-density distribution of the Er(III) ion.

37) The replacement of the counteranion in **46** for PF_6^- provokes a change towards a more symmetric structure where there exists a C_2 axis on the Dy(III) ion. The presence of the C_2 axis imposes collinearity of the anisotropic axes of the two lowest KDs, so that the thermal activated relaxation is suppressed *via* the first excited KD and takes place *via* the second excited state, giving rise to a dramatic increase in the effective energy barrier (268 K).

Chapter 7

38) The Dy(III) containing complex $\{K_5[Dy(H_2L)(\alpha\text{-}SiW_{11}O_{39})]\}_6 \cdot 46H_2O$ (**55**) was prepared, where the Dy(III) atoms are coordinated to neutral H_2L ligands and $[SiW_{11}O_{39}]^{8-}$ anionic silicotungstates.

39) This compound does not show significant SIM behaviour, as concluded from the slight frequency dependency of the out-of-phase susceptibility signal. The observed behaviour could be due to (i) the fact that the $[Dy(H_2L)(\alpha\text{-}SiW_{11}O_{39})]^{5-}$ units are held in groups of 6 by coordinated potassium atoms and water molecules, what prevents the units to behave as independent entities which favours QTM, (ii) the distortion of the DyO_8 coordination polyhedron from the ideal geometry, which provokes the mixing of the ground state with excited states of lower M_j value, thus increasing the QTM and (iii) the fact that there are not clear shortest Dy-O distances in the DyO_8 coordination polyhedron as to create an axial ligand field for the oblate electron density of the Dy(III) ion.

Chapter 8

40) Several Co(II) compounds and 9-anthracenecarboxylate bridged dinuclear Zn(II)Ln(III) complexes have also been prepared. The magnetic properties of these compounds are still being measured and the grafting of SIMs into polyacrylic surfaces will be studied in the future.

41) Additional work on other trinuclear Zn(II)Dy(III)Zn(II) SIMs and lanthanide based MOFs have also been carried out during this Ph.D. thesis.

APPENDICES

I. GRYSTALLOGRAPHIC DATA, BOND DISTANCES AND ANGLES

Chapter 1

Table A.1.- Crystallographic data for complexes **1**-**6**.

Complex	**1**	**2**	**3**	**4**	**5**	**6**
Formula	$C_{20}H_{26}N_4O_{12}Br_2Ni$	$C_{32}H_{38}N_3O_9Br_2Ni_2$	$C_{23}H_{23}N_3O_6SBr_2Ni_2$	$C_{50}H_{61}N_{11}O_{17}Br_2Ni_3$	$C_{48}H_{72}N_4O_{22}Br_4Ni_4$	$C_{45}H_{54}N_{10}O_{15}Br_4Ni_4$
M_r	732.98	886.90	746.74	1583.87	1611.58	1529.46
Crystal system	Monoclinic	Monoclinic	Monoclinic	Monoclinic	Triclinic	Triclinic
Space group (no.)	*P21/c* (14)	*C2/c* (15)	*I2/a* (15)	*P21/c* (14)	*P-1* (2)	*P-1* (2)
a (Å)	12.3321(6)	20.9791(14)	21.9768(3)	21.6387(9)	11.7285(10)	13.3880(4)
b (Å)	9.5827(4)	14.469(2)	9.7423(10)	10.6943(12)	12.3966(13)	14.4846(5)
c (Å)	21.5074(9)	26.9753(19)	24.826(4)	27.2254(7)	12.6195(15)	14.9568(5)
α (°)	90.00	90.00	90.00	90.00	89.018(9)	106.726(3)
β (°)	94.157(4)	118.361(9)	95.237(2)	111.474(2)	70.217(9)	95.185(3)
γ (°)	90.00	90.00	90.00	90.00	64.859(9)	93.111(3)
V (Å^3)	2534.95(19)	7205.3(13)	5293.2(10)	5862.9(7)	1545.6(3)	2756.53(16)
Z	4	8	8	4	1	2
D_c (g cm^{-3})	1.921	1.635	1.874	1.794	1.731	1.843
μ(MoKα) (mm^{-1}) [a]	3.990	3.318	6.426	3.759	5.046	4.318
T (K)	100(2)	100(2)	100(2)	100(2)	100(2)	100(2)
Observed reflections	5889 (4775)	6345 (5721)	5329 (4677)	10308 (7841)	6058 (4762)	9673 (7112)
R_{int}	0.0438	0.0247	0.0357	0.0414	0.0267	0.0323
Parameters	378	466	337	748	329	694
GOF	1.109	1.107	1.031	1.038	1.094	1.058
R_1 [b,c]	0.0560 (0.0400)	0.0349 (0.0299)	0.0538 (0.0467)	0.0608 (0.0399)	0.0556 (0.0447)	0.0744 (0.0496)
wR_2 [c,d]	0.0909 (0.0843)	0.0687 (0.0666)	0.1071 (0.1030)	0.0934 (0.0862)	0.1298 (0.1239)	0.1302 (0.1192)
Largest difference in peak and hole (e Å^{-3})	1.220 and -0.638	0.920 and -0.544	2.544 and -1.891	1.175 and -0.760	1.744 and -1.010	1.037 and -0.894

[a] μ (CuKα) (mm^{-1}) in **3** and **5**. [b] $R_1 = \Sigma||F_o| - |F_c||/\Sigma|F_o|$. [c] Values in parentheses for reflections with $I > 2\sigma(I)$. [d] $wR_2 = \{\Sigma[w(F_o^2 - F_c^2)^2] / \Sigma[w(F_o^2)^2]\}^{½}$

Table A.2.- Selected bond lengths (Å) and angles (°) for complexes **1**-**6**.

Complex	**1**	**2**	**3**	**4**	**5**	**6**
Ni(1)-O(1A)	2.039(2)					
Ni(1)-O(2A)	1.965(2)	2.125(2)	2.018(3)	2.059(3)	2.066(3)	2.040(4)
Ni(1)-O(3A)	1.981(2)	2.060(2)	1.982(3)	2.020(3)	2.109(3)	2.112(4)
Ni(1)-O(4A)	2.041(2)					
Ni(1)-O(1C)	2.123(2)					
Ni(1)-O(1W)	2.074(3)					
Ni(1)-O(1B)		2.040(2)	1.943(3)		2.065(3)	2.057(4)
Ni(1)-O(2B)		2.011(3)				
Ni(1)-O(1P)				2.137(3)		
Ni(1)-O(1M)					2.058(3)	
Ni(1)-N(1A)		2.130(2)	2.047(4)	2.066(3)	2.114(3)	2.098(5)
Ni(1)-N(2A)		2.135(2)	2.066(3)	2.096(3)	2.126(3)	2.104(5)
Ni(1)-N(1P)				2.077(4)		
Ni(1)-N(1C)						2.113(5)
Ni(2)-O(1A)		2.058(3)	2.041(3)	2.007(3)	2.065(3)	2.047(4)
Ni(2)-O(2A)		2.032(2)	2.019(3)	1.983(3)	2.021(3)	2.017(4)
Ni(2)-O(3A)		2.058(2)	2.014(3)			
Ni(2)-O(3A)*					2.094(3)	2 075(4)
Ni(2)-O(4A)			2.052(3)			
Ni(2)-O(1B)				2.008(3)		
Ni(2)-O(2B)			2.079(3)	1.985(3)	2.043(3)	2.008(4)
Ni(2)-O(1C)		1.980(2)				
Ni(2)-O(2C)		2.016(2)				
Ni(2)-O(1W)		2.091(2)				
Ni(2)-O(1M)					2.065(3)	
Ni(2)-O(1M)*					2.024(3)	
Ni(2)-O(1P)				2.119(3)		
Ni(2)-O(2P)				2.129(3)		
Ni(2)-N(1C)			2.015(4)			2.129(4)
Ni(2)-N(1C)*						2.081(4)
Ni(3)-O(2B)				2.071(3)		
Ni(3)-O(3B)				2.034(3)		
Ni(3)-O(2D)						2.065(4)
Ni(3)-O(3D)						2.133(4)
Ni(3)-O(1E)						2.063(4)
Ni(3)-O(2P)				2.127(3)		
Ni(3)-O(1W)				2.113(3)		
Ni(3)-N(1B)				2.065(3)		
Ni(3)-N(2B)				2.107(3)		
Ni(3)-N(1D)						2.103(5)
Ni(3)-N(2D)						2.115(5)
Ni(3)-N(1F)						2.111(5)
Ni(4)-O(1D)						2.044(4)

Table A.2.- Continuation.

Complex	1	2	3	4	5	6
Ni(4)-O(2D)						2.016(4)
Ni(4)-O(3D)*						2.072(4)
Ni(4)-O(2E)						1.995(4)
Ni(4)-N(1F)						2.156(5)
Ni(4)-N(1F)*						2.082(5)
Ni(1)···Ni(2)		3.203(1)	2.954(1)	3.118(1)	3.009(1)	3.026(1)
Ni(1)···Ni(2)*					3.212(1)	3.273(1)
Ni(1)···Ni(1)*					5.417(1)	5.456(1)
Ni(2)···Ni(2)*					3.067(1)	3.159(1)
Ni(2)···Ni(3)				3.136(1)		
Ni(3)···Ni(4)						3.030(1)
Ni(3)···Ni(4)*						3.266(1)
Ni(3)···Ni(3)*						5.435(1)
Ni(4)···Ni(4)*						3.186(1)
Ni(1)-O(2A)-Ni(2)		100.79(7)	94.1(1)	101.0(1)	94.8(1)	96.5(2)
Ni(1)-O(3A)-Ni(2)		102.16(8)	95.4(1)			
Ni(1)-O(3A)-Ni(2)*					99.7(1)	102.9(2)
Ni(1)-O(1P)-Ni(2)				94.2(1)		
Ni(2)-O(2B)-Ni(3)				101.3(1)		
Ni(2)-O(2P)-Ni(3)				95.0(1)		
Ni(1)-O(1M)-Ni(2)					93.8(1)	
Ni(1)-O(1M)-Ni(2)*					103.8(1)	
Ni(2)-O(1M)-Ni(2)*					97.2(1)	
Ni(1)-N(1C)-Ni(2)						91.1(2)
Ni(1)-N(1C)-Ni(2)*						102.7(2)
Ni(2)-N(1C)-Ni(2)*						97.3(2)
Ni(3)-O(2D)-Ni(4)						95.9(2)
Ni(3)-O(3D)-Ni(4)						101.9(2)
Ni(3)-N(1F)-Ni(4)						90.4(2)
Ni(3)-N(1F)-Ni(4)*						102.3(2)
Ni(4)-N(1F)-Ni(4)*						97.5(2)

Chapter 2

Table A.3.- Crystallographic data for complexes **7**-**10**.

Complex	**7**	**8**	**9**	**10**
Formula	$C_{27}H_{44}N_4O_{11}Ni_2$	$C_{36}H_{60}N_4O_{14}Ni_2$	$C_{41}H_{52}N_4O_{11}Ni_2$	$C_{28}H_{46}N_6O_8Ni_2$
M_r	718.08	890.30	894.29	712.13
Crystal system	Monoclinic	Monoclinic	Triclinic	Triclinic
Space group (no.)	*P21/c* (14)	*P21/c* (14)	*P-1* (2)	*P-1* (2)
a (Å)	12.782(5)	12.2650(5)	13.564(2)	8.26256)
b (Å)	13.864(5)	26.7600(11)	16.014(3)	9.9065(8)
c (Å)	20.835(5)	12.3190(5)	19.338(3)	20.2078(16)
α (°)	90.00	90.00	79.755(3)	80.7740(10)
β (°)	123.340(15)	109.6020(10)	71.845(2)	88.7840(10)
γ (°)	90.00	90.00	81.492(3)	76.4930(10)
V (Å^3)	3084.5(18)	3808.9(3)	3908.5(11)	1587.3(2)
Z	4	4	4	2
D_c (g cm^{-3})	1.546	1.553	1.520	1.490
μ(MoKα) (mm^{-1}) [a]	1.286	1.063	1.032	1.243
*T (*K)	100(2)	100(2)	100(2)	100(2)
Observed reflections	6993 (5871)	7874 (6169)	16791 (13145)	5576 (4888)
R_{int}	0.0411	0.0416	0.0326	0.0289
Parameters	421	448	1076	415
GOF	1.046	1.333	1.141	1.052
R_1[a,b]	0.0459 (0.0368)	0.0747 (0.0628)	0.0799 (0.0673)	0.0391 (0.0335)
wR_2[b,c]	0.0938 (0.0886)	0.1901 (0.1823)	0.1869 (0.1746)	0.0844 (0.0806)
Largest difference in peak and hole (e Å^{-3})	0.960 and -0.311	2.168 and -1.766	4.660 and -1.037	0.602 and -0.313

[a] $R_1 = \Sigma||F_o| - |F_c||/\Sigma|F_o|$.

[b] Values in parentheses for reflections with $I > 2\sigma(I)$.

[c] $wR_2 = \{\Sigma[w(F_o^2 - F_c^2)^2] / \Sigma[w(F_o^2)^2]\}^{½}$

Table A.4.- Selected bond lengths (Å) and angles (°) for complexes **7**-**10**.

Complex	**7**	**8**	**9**	**10**
Ni(1)-O(1A)	2.059(2)	2.087(3)	2.049(2)	2.075(2)
Ni(1)-O(3A)	2.107(2)	2.096(3)	2.092(2)	2.100(2)
Ni(1)-O(1B)	2.042(2)	2.035(3)		2.042(2)
Ni(1)-O(2E)			2.062(2)	
Ni(1)-N(1A)	2.187(2)	2.165(3)	2.173(3)	2.173(2)
Ni(1)-N(2A)	2.109(2)	2.130(3)	2.110(3)	2.123(2)
Ni(1)-N(3A)	2.151(2)	2.170(3)	2.162(3)	2.144(2)
Ni(2)-O(1A)	1.996(2)	2.012(3)	1.997(2)	2.010(2)
Ni(2)-O(2A)	2.157(2)	2.185(3)	2.194(2)	2.224(2)
Ni(2)-O(3A)	2.007(2)	2.034(2)	2.028(2)	2.028(2)
Ni(2)-O(2B)	2.049(2)	2.014(3)		2.039(2)
Ni(2)-O(1W)	2.072(2)	2.072(3)	2.101(2)	2.080(2)
Ni(2)-O(2W)	2.027(2)			
Ni(2)-O(1M)		2.028(3)	2.063(2)	
Ni(2)-O(1E)			2.011(2)	
Ni(2)-N(1C)			2.032(2)	
Ni(3)-O(1B)			2.087(2)	
Ni(3)-O(3B)			2.077(2)	
Ni(3)-O(1D)			2.067(2)	
Ni(3)-N(1B)			2.232(3)	
Ni(3)-N(2B)			2.171(3)	
Ni(3)-N(3B)			2.177(3)	
Ni(4)-O(1B)			2.012(2)	
Ni(4)-O(2B)			2.150(2)	
Ni(4)-O(3B)			2.014(2)	
Ni(4)-O(2D)			2.039(2)	
Ni(4)-O(2M)			2.031(2)	
Ni(4)-O(2W)			2.057(2)	
Ni(1)···Ni(2)	3.013(1)	3.051(1)	3.035(1)	3.048(1)
Ni(3)···Ni(4)			3.040(1)	
Ni(1)-O(1A)-Ni(2)	95.96(7)	96.2(1)	97.18(9)	96.46(7)
Ni(1)-O(3A)-Ni(2)	94.15(7)	95.2(1)	94.88(9)	95.15(7)
Ni(3)-O(1B)-Ni(4)			95.74(9)	
Ni(3)-O(3B)-Ni(4)			95.97(9)	

Chapter 3

Table A.5.- Crystallographic data for complexes **11**, **12**, **14**-**17** and **19**-**21**.

Complex	**11**	**12**	**14**	**15**
Formula	$C_{24}H_{26}N_5O_{12}Br_2ZnPr$	$C_{24}H_{26}N_5O_{12}Br_2ZnNd$	$C_{24}H_{26}N_5O_{12}Br_2ZnEu$	$C_{24}H_{26}N_5O_{12}Br_2ZnGd$
M_r	942.60	945.93	953.65	958.94
Crystal system	Monoclinic	Monoclinic	Monoclinic	Monoclinic
Space group (no.)	*P21/n* (14)	*P21/n* (14)	*P21/n* (14)	*P21/n* (14)
a (Å)	13.45653(19)	13.4135(2)	13.5257(2)	13.4496(5)
b (Å)	14.75424(18)	14.7713(2)	14.9372(2)	14.7776(5)
c (Å)	16.2850(3)	16.1930(2)	15.8049(2)	16.0073(6)
α (°)	90	90	90	90
β (°)	91.4469(14)	91.2300(10)	90.109(2)	91.051(3)
γ (°)	90	90	90	90
V (Å^3)	3232.21(8)	3207.66(8)	3193.15(8)	3181.0(2)
Z	4	4	4	4
D_c (g cm^{-3})	1.937	1.959	1.984	2.002
μ(MoKα) (mm^{-1})[a]	4.770	4.906	18.361	5.400
T (K)	100(2)	100(2)	100(2)	100(2)
Observed reflections	6350 (5141)	5633 (4984)	6406 (6158)	5574 (4651)
R_{int}	0.0306	0.0293	0.0308	0.0392
Parameters	410	410	409	410
GOF	1.013	1.126	1.036	1.076
R_1[b,c]	0.0484 (0.0343)	0.0301 (0.0248)	0.0302 (0.0288)	0.0492 (0.0375)
wR_2[c,d]	0.0697 (0.0642)	0.0680 (0.0654)	0.0818 (0.0805)	0.0989 (0.0930)
Largest difference in peak and hole (e Å^{-3})	1.180 and -0.724	2.035 and -0.478	2.441 and -0.874	2.148 and -1.013

[a] μ(CuKα) (mm^{-1}) in **14**. [b] $R_1 = \Sigma||F_o| - |F_c||/\Sigma|F_o|$. [c] Values in parentheses for reflections with $I > 2\sigma(I)$.

[d] $wR_2 = \{\Sigma[w(F_o^2 - F_c^2)^2] / \Sigma[w(F_o^2)^2]\}^{½}$.

Table A.5.- Continuation.

Complex	**16**	**17**	**19**	**20**	**21**
Formula	$C_{24}H_{26}N_5O_{12}Br_2ZnTb$	$C_{24}H_{26}N_5O_{12}Br_2ZnDy$	$C_{24}H_{26}N_5O_{12}Br_2ZnEr$	$C_{24}H_{26}N_5O_{12}Br_2ZnTm$	$C_{24}H_{26}N_5O_{12}Br_2ZnYb$
M_r	960.61	964.19	968.95	970.62	974.73
Crystal system	Monoclinic	Monoclinic	Monoclinic	Monoclinic	Monoclinic
Space group (no.)	*P21/n* (14)	*P21/n* (14)	*P21/n* (14)	*P21/n* (14)	*P21/n* (14)
a (Å)	13.5017(6)	13.5589(12)	13.5236(2)	13.5836(6)	13.5447(10)
b (Å)	14.7618(4)	14.8592(11)	14.7278(17)	14.8415(5)	14.8034(12)
c (Å)	15.9579(6)	15.8350(12)	15.9106(2)	15.6820(6)	15.7092(11)
α (°)	90	90	90	90	90
β (°)	91.315(4)	90.618(3)	91.294(2)	90.237(3)	90.5320(10)
γ (°)	90	90	90	90	90
V (Å^3)	3179.7(2)	3190.2(4)	3168.2(4)	3161.5(2)	3149.7(4)
Z	4	4	4	4	4
D_c (g cm^{-3})	2.007	2.008	2.031	2.039	2.056
μ(MoKα) (mm^{-1})[a]	5.540	5.647	5.977	6.141	9.852
T (K)	100(2)	100(2)	100(2)	100(2)	100(2)
Observed reflections	6584 (5277)	5617 (4883)	5571 (4995)	6540 (5821)	6446 (6158)
R_{int}	0.0462	0.0426	0.0277	0.0328	0.0236
Parameters	410	410	410	410	410
GOF	1.064	1.080	1.065	1.038	1.088
R_1[b,c]	0.0529 (0.0368)	0.0363 (0.0289)	0.0295 (0.0242)	0.0288 (0.0237)	0.0261 (0.0246)
wR_2[c,d]	0.0875 (0.0807)	0.0786 (0.0750)	0.0611 (0.0583)	0.0505 (0.0489)	0.0636 (0.0627)
Largest difference in peak and hole (e Å^{-3})	1.903 and -0.888	2.851 and -0.398	1.834 and -0.563	0.921 and -0.811	0.848 and -1.138

[a] μ(CuKα) (mm^{-1}) in **21**. [b] $R_1 = \Sigma||F_o| - |F_c||/\Sigma|F_o|$. [c] Values in parentheses for reflections with $I > 2\sigma(I)$. [d] $wR_2 = \{\Sigma[w(F_o^2 - F_c^2)^2] / \Sigma[w(F_o^2)^2]\}^{½}$

Table A.6.- Selected bond lengths (Å) and angles (°) for complexes **11, 12, 14-17** and **19**-**21**.

Complex	**11**	**12**	**14**	**15**	**16**
Ln(1)···Zn(1)	3.437(1)	3.426(1)	3.406(1)	3.399(1)	3.383(1)
Ln(1)-O(1A)	2.432(3)	2.421(2)	2.384(2)	2.364(4)	2.355(3)
Ln(1)-O(2A)	2.471(3)	2.447(2)	2.401(2)	2.401(4)	2.384(3)
Ln(1)-O(3A)	2.424(3)	2.407(2)	2.374(2)	2.367(4)	2.354(3)
Ln(1)-O(4A)	2.454(3)	2.443(2)	2.400(3)	2.380(4)	2.373(4)
Ln(1)-O(2P)bridge	2.393(3)	2.382(2)	2.337(2)	2.318(4)	2.312(4)
Ln(1)-O(1C)nitrate	2.573(3)	2.551(2)	2.486(2)	2.509(4)	2.472(4)
Ln(1)-O(2C)nitrate	2.545(3)	2.536(3)	2.532(2)	2.472(4)	2.492(4)
Ln(1)-O(1D)nitrate	2.557(3)	2.553(2)	2.518(2)	2.480(4)	2.462(4)
Ln(1)-O(2D)nitrate	2.572(3)	2.534(2)	2.494(3)	2.523(4)	2.518(4)
Zn(1)-N(1A)	2.133(3)	2.132(3)	2.131(3)	2.127(4)	2.130(4)
Zn(1)-N(2A)	2.099(3)	2.096(3)	2.105(3)	2.090(5)	2.103(4)
Zn(1)-O(2A)	2.081(3)	2.083(2)	2.077(2)	2.069(4)	2.072(3)
Zn(1)-O(3A)	2.149(3)	2.146(2)	2.130(2)	2.127(4)	2.127(3)
Zn(1)-O(1P)bridge	1.953(3)	1.955(2)	1.967(2)	1.951(4)	1.952(4)
Ln(1)-O(2A)-Zn(1)	97.70(10)	97.94(8)	98.77(9)	98.72(14)	98.55(13)
Ln(1)-O(3A)-Zn(1)	97.26(11)	97.46(9)	98.12(9)	98.16(15)	97.92(13)
O(2A)-Ln(1)-O(3A)	70.09(9)	70.26(7)	70.18(8)	69.90(12)	70.54(11)
O(2A)-Ln(1)-O(2P)bridge	78.55(10)	78.48(8)	78.76(9)	79.14(13)	79.38(12)
O(3A)-Ln(1)-O(2P)bridge	78.87(10)	78.90(8)	79.50(8)	79.90(13)	80.10(13)
O(2A)-Zn(1)-O(3A)	83.26(11)	82.67(8)	81.45(9)	81.22(14)	81.30(13)
O(2A)-Zn(1)-O(1P)bridge	105.74(12)	105.76(9)	104.73(10)	104.99(16)	104.75(14)
O(3A)-Zn(1)-O(1P)bridge	98.62(12)	98.46(9)	98.79(10)	98.58(15)	98.63(15)

Table A.6.- Continuation.

Complex	**17**	**19**	**20**	**21**
Ln(1)···Zn(1)	3.388(1)	3.371(1)	3.371(1)	3.360(1)
Ln(1)-O(1A)	2.345(3)	2.330(3)	2.314(2)	2.303(2)
Ln(1)-O(2A)	2.380(3)	2.361(2)	2.338(2)	2.336(2)
Ln(1)-O(3A)	2.348(3)	2.325(3)	2.316(2)	2.307(2)
Ln(1)-O(4A)	2.369(3)	2.343(3)	2.327(2)	2.320(2)
Ln(1)-O(2P)bridge	2.285(3)	2.275(3)	2.261(2)	2.241(2)
Ln(1)-O(1C)nitrate	2.484(3)	2.462(3)	2.463(2)	2.459(2)
Ln(1)-O(2C)nitrate	2.450(4)	2.432(3)	2.417(2)	2.409(2)
Ln(1)-O(1D)nitrate	2.511(3)	2.485(3)	2.411(2)	2.406(2)
Ln(1)-O(2D)nitrate	2.449(3)	2.427(3)	2.513(2)	2.501(2)
Zn(1)-N(1A)	2.131(4)	2.133(3)	2.128(2)	2.127(2)
Zn(1)-N(2A)	2.106(4)	2.101(3)	2.108(3)	2.109(2)
Zn(1)-O(2A)	2.076(3)	2.071(3)	2.078(2)	2.075(2)
Zn(1)-O(3A)	2.118(3)	2.114(3)	2.114(2)	2.108(2)
Zn(1)-O(1P)bridge	1.960(3)	1.960(3)	1.966(2)	1.961(2)
Ln(1)-O(2A)-Zn(1)	98.78(12)	98.85(10)	99.33(7)	99.05(8)
Ln(1)-O(3A)-Zn(1)	98.54(12)	98.71(10)	98.97(8)	98.98(8)
O(2A)-Ln(1)-O(3A)	70.24(10)	70.31(9)	70.41(7)	80.78(7)
O(2A)-Ln(1)-O(2P)bridge	79.25(11)	79.71(9)	79.93(7)	80.21(7)
O(3A)-Ln(1)-O(2P)bridge	80.08(11)	80.47(9)	80.62(8)	80.78(7)
O(2A)-Zn(1)-O(3A)	80.84(12)	80.29(10)	79.61(8)	79.81(8)
O(2A)-Zn(1)-O(1P)bridge	104.09(13)	104.28(11)	103.43(8)	103.32(8)
O(3A)-Zn(1)-O(1P)bridge	98.53(13)	98.62(11)	98.68(8)	98.25(8)

Chapter 4

Table A.7.- Crystallographic data for complexes **22**-**25**.

Complex	**22**	**23**	**24**	**25**
Formula	$C_{24}H_{28}N_5O_{13}Br_2CuGd$	$C_{24}H_{28}N_5O_{13}Br_2CuTb$	$C_{24}H_{28}N_5O_{13}Br_2CuDy$	$C_{24}H_{28}N_5O_{13}Br_2CuEr$
M_r	975.11	976.78	980.36	985.12
Crystal system	Monoclinic	Monoclinic	Monoclinic	Monoclinic
Space group (no.)	P21/c (14)	*P21/c* (14)	*P21/c* (14)	*P21/c* (14)
a (Å)	13.5609(2)	13.54770(10)	13.56040(10)	13.5532O(10)
b (Å)	14.9879(2)	14.93020(10)	14.90410(10)	14.87700(10)
c (Å)	20.5278(4)	20.5854(2)	20.6481(2)	20.6285(2)
α (°)	90.00	90.00	90.00	90.00
β (°)	130.7740(10)	130.9250(10)	131.0410(10)	131.0700(10)
γ (°)	90.00	90.00	90.00	90.00
V (Å^3)	3159.62(9)	3146.03(4)	3147.51(4)	3135.76(4)
Z	4	4	4	4
D_c (g cm^{-3})	2.046	2.058	2.065	2.082
μ(CuKα) (mm^{-1})[a]	5.354	15.354	16.999	9.282
T (K)	100(2)	100(2)	100(2)	100(2)
Observed reflections	6368(5853)	6320 (6124)	6323(5908)	6294(5881)
R_{int}	0.0181	0.0287	0.0401	0.0302
Parameters	429	429	428	428
GOF	1.047	1.055	1.041	1.048
R_1[b,c]	0.0201(0.0170)	0.0215 (0.0206)	0.0327(0.0297)	0.0252(0.0229)
wR_2[c,d]	0.0385(0.0375)	0.0494 (0.0490)	0.0779(0.0752)	0.0567(0.0554)
Largest difference in peak and hole (e Å^{-3})	0.487 and -0.364	0.410 and -0.597	1.436 and -0.886	0.909 and -0.743

[a] μ(MoKα) (mm^{-1}) in **22**. [b] $R_1 = \Sigma||F_o| - |F_c||/\Sigma|F_o|$. [c] Values in parentheses for reflections with $I > 2\sigma(I)$.

[d] $wR_2 = \{\Sigma[w(F_o^2 - F_c^2)^2] / \Sigma[w(F_o^2)^2]\}^{½}$.

Table A.8.- Crystallographic data for complexes **26-31**.

Complex	**26**	**27**	**28**	**29**	**30**	**31**
Formula	$C_{26}H_{29}N_6O_{12}Br_2NiNd$	$C_{26}H_{29}N_6O_{12}Br_2NiGd$	$C_{26}H_{29}N_6O_{12}Br_2NiTb$	$C_{26}H_{29}N_6O_{12}Br_2NiDy$	$C_{26}H_{29}N_6O_{12}Br_2NiEr$	$C_{26}H_{29}N_6O_{12}Br_2NiY$
M_r	980.32	993.33	995.00	998.58	1003.34	924.99
Crystal system	triclinic	triclinic	triclinic	triclinic	triclinic	triclinic
Space group (no.)	P-1 (2)	P-1 (2)	P-1 (2)	P-1 (2)	P-1 (2)	P-1 (2)
a (Å)	10.217(3)	10.1426(4)	10.2484(13)	10.1327(3)	10.1226(5)	10.1465(5)
b (Å)	13.043(5)	12.9916(5)	13.084(2)	12.9880(6)	12.9640(6)	12.9861(5)
c (Å)	14.137(5)	14.0258(6)	14.137(2)	13.9878(3)	13.9826(4)	13.9911(8)
α (°)	76.953(10)	77.173(4)	76.894(4)	77.099(3)	76.958(4)	76.955(4)
β (°)	70.394(10)	69.930(4)	70.371(4)	69.968(2)	69.879(4)	69.933(5)
γ (°)	68.948(10)	68.995(4)	68.686(4)	68.965(4)	68.983(5)	68.811(4)
V (Å^3)	1644.4(10)	1610.20(11)	1651.4(4)	1603.63(10)	1597.33(13)	1603.61(14)
Z	2	2	2	2	2	2
D_c (g cm^{-3})	1.980	2.049	2.001	2.068	2.086	1.916
μ(MoKα) (mm^{-1})[a]	4.633	5.179	5.183	5.462	9.028	4.951
T (K)	100(2)	100(2)	100(2)	100(2)	100(2)	100(2)
Observed reflections	5709(4411)	5666(5220)	5682(4437)	5650(5280)	6231(5469)	5651(5031)
R_{int}	0.1119	0.0267	0.0715	0.0152	0.0380	0.0220
Parameters	438	438	438	438	438	438
*G*OF	1.028	1.062	1.046	1.042	1.065	1.027
R_1[b,c]	0.0848(0.0644)	0.0345(0.0308)	0.0635(0.0422)	0.0205(0.0182)	0.0499(0.0428)	0.0319(0.0264)
wR_2[c,d]	0.1721(0.1579)	0.0770(0.0742)	0.0962(0.0882)	0.0408(0.0400)	0.1236(0.1186)	0.0586(0.0564)
Largest difference in peak and hole (e Å^{-3})	2.709 and -1.549	1.791 and -1.565	1.574 and -0.839	0.732 and -0.621	2.071 and -1.249	0.562 and -0.369

[a] μ(CuKα) (mm^{-1}) in **30**. [b] $R_1 = \Sigma||F_o| - |F_c||/\Sigma|F_o|$. [c] Values in parentheses for reflections with $I > 2\sigma(I)$. [d] $wR_2 = \{\Sigma[w(F_o^2 - F_c^2)^2] / \Sigma[w(F_o^2)^2]\}^{½}$.

Table A.9.- Crystallographic data for complexes **32**-**36**.

Complex	**32**	**33**	**34**	**35**	**36**
Formula	$C_{26}H_{29}N_6O_{12}Br_2CoGd$	$C_{26}H_{29}N_6O_{12}Br_2CoTb$	$C_{26}H_{29}N_6O_{12}Br_2CoDy$	$C_{26}H_{29}N_6O_{12}Br_2CoEr$	$C_{26}H_{29}N_6O_{12}Br_2CoY$
M_r	993.55	995.22	998.80	1003.56	925.21
Crystal system	triclinic	triclinic	triclinic	triclinic	triclinic
Space group (no.)	P-1 (2)	P-1 (2)	P-1 (2)	P-1 (2)	P-1 (2)
a (Å)	10.191(5)	10.1820(4)	10.1815(6)	10.1576(4)	10.189(3)
b (Å)	13.024(5)	13.0186(6)	12.9982(6)	12.9970(6)	12.996(3)
c (Å)	14.101(5)	14.0454(6)	14.0503(7)	14.0319(7)	14.056(4)
α (°)	76.932(5)	76.909(4)	76.876(4)	76.836(4)	76.808(3)
β (°)	69.771(5)	69.758(3)	69.709(5)	69.859(4)	69.730(3)
γ (°)	69.146(5)	69.177(4)	69.050(5)	69.147(4)	69.011(3)
V (Å^3)	1629.7(12)	1621.29(11)	1617.42(14)	1613.55(13)	1618.5(7)
Z	2	2	2	2	2
D_c (g cm^{-3})	2.025	2.039	2.051	2.066	1.898
μ(MoKα) (mm^{-1})[a]	5.048	5.210	5.346	12.239	4.836
T (K)	100(2)	100(2)	100(2)	100(2)	100(2)
Observed reflections	8444(7775)	6633(6162)	6537(5819)	6043(5720)	7300(5837)
R_{int}	0.0254	0.0172	0.0277	0.0367	0.0408
Parameters	438	438	438	438	438
GOF	1.168	1.042	1.034	1.056	1.045
R_1[b,c]	0.0240 (0.0208)	0.0246(0.0216)	0.0329(0.0272)	0.0332(0.0313)	0.0510 (0.0366)
wR_2[c,d]	0.0497 (0.0480)	0.0461(0.0449)	0.0521(0.0493)	0.0826(0.0812)	0.0745(0.0692)
Largest difference in peak and hole (e Å^{-3})	0.790 and -0.956	0.563 and -0.652	0.900 and -0.877	0.917 and -1.026	0.720 and -0.454

[a] μ(CuKα) (mm^{-1}) in **35**. [b] $R_1 = \Sigma||F_o| - |F_c||/\Sigma|F_o|$. [c] Values in parentheses for reflections with $I > 2\sigma(I)$. [d] $wR_2 = \{\Sigma[w(F_o^2 - F_c^2)^2] / \Sigma[w(F_o^2)^2]\}^{½}$.

Table A.10.- Selected bond lengths (Å) and angles (°) for complexes **22**-**25**.

Complex	**22**	**23**	**24**	**25**
Ln(1)-Cu(1)	3.383(1)	3.370(1)	3.364(1)	3.353(1)
Ln(1)-O(1A)	2.374(2)	2.357(2)	2.350(2)	2.326(2)
Ln(1)-O(2A)	2.367(2)	2.354(2)	2.349(2)	2.326(2)
Ln(1)-O(3A)	2.404(2)	2.390(2)	2.378(2)	2.358(2)
Ln(1)-O(4A)	2.389(2)	2.371(2)	2.360(2)	2.337(2)
Ln(1)-O(2P)bridge	2.290(2)	2.280(2)	2.260(2)	2.254(2)
Ln(1)-O(1C)nitrate	2.479(2)	2.459(2)	2.450(3)	2.472(2)
Ln(1)-O(2C)nitrate	2.523(2)	2.506(2)	2.493(2)	2.426(3)
Ln(1)-O(1D)nitrate	2.486(2)	2.469(2)	2.454(2)	2.429(2)
Ln(1)-O(2D)nitrate	2.534(2)	2.533(2)	2.517(3)	2.494(2)
Cu(1)-N(1A)	2.024(2)	2.023(2)	2.022(3)	2.019(2)
Cu(1)-N(2A)	2.017(2)	2.018(2)	2.024(3)	2.019(2)
Cu(1)-O(2A)	2.057(2)	2.052(2)	2.049(2)	2.044(2)
Cu(1)-O(3A)	2.010(2)	2.007(2)	2.006(2)	1.999(2)
Cu(1)-O(1P)bridge	2.126(2)	2.134(2)	2.140(3)	2.146(2)
Ln(1)-O(2A)-Cu(1)	99.51(6)	99.56(6)	99.57(9)	100.01(7)
Ln(1)-O(3A)-Cu(1)	99.68(6)	99.70(6)	99.92(9)	100.29(7)
O(2A)-Ln(1)-O(3A)	69.80(5)	70.02(5)	70.13(8)	70.03(6)
O(2A)-Ln(1)-O(2P)bridge	80.33(5)	80.58(6)	80.62(9)	80.92(6)
O(3A)-Ln(1)-O(2P)bridge	80.74(5)	80.99(6)	81.01(9)	81.32(6)
O(2A)-Cu(1)-O(3A)	84.32(6)	84.19(6)	84.10(9)	83.32(7)
O(2A)-Cu(1)-O(1P)bridge	96.50(6)	96.11(6)	95.76(10)	95.72(7)
O(3A)-Cu(1)-O(1P)bridge	93.42(6)	93.15(7)	92.73(10)	92.78(7)

Table A.11.- Selected bond lengths (Å) and angles (°) for complexes **26**-**31**.

Complex	**26**	**27**	**28**	**29**	**30**	**31**
Ln(1)-Ni(1)	3.437(2)	3.418(1)	3.414(1)	3.399(1)	3.385(1)	3.393(1)
Ln(1)-O(1A)	2.428(6)	2.393(3)	2.381(4)	2.365(2)	2.341(4)	2.352(2)
Ln(1)-O(2A)	2.387(5)	2.341(3)	2.341(4)	2.321(2)	2.299(4)	2.304(2)
Ln(1)-O(3A)	2.428(6)	2.379(3)	2.356(4)	2.352(2)	2.327(4)	2.339(2)
Ln(1)-O(4A)	2.468(7)	2.422(3)	2.407(5)	2.400(2)	2.377(4)	2.390(2)
Ln(1)-O(2P)bridge	2.369(7)	2.320(3)	2.285(4)	2.284(2)	2.282(4)	2.275(2)
Ln(1)-O(1C)nitrate	2.524(6)	2.481(3)	2.470(4)	2.451(2)	2.428(4)	2.436(2)
Ln(1)-O(2C)nitrate	2.527(6)	2.505(3)	2.507(5)	2.490(2)	2.471(4)	2.478(2)
Ln(1)-O(1D)nitrate	2.527(6)	2.493(3)	2.471(4)	2.464(2)	2.429(4)	2.444(2)
Ln(1)-O(2D)nitrate	2.537(7)	2.511(3)	2.511(4)	2.492(2)	2.473(4)	2.477(2)
Ni(1)-N(1A)	2.087(6)	2.105(3)	2.103(4)	2.102(2)	2.108(4)	2.100(2)
Ni(1)-N(2A)	2.094(8)	2.103(3)	2.101(5)	2.102(2)	2.101(5)	2.104(2)
Ni(1)-O(2A)	2.056(6)	2.063(3)	2.053(4)	2.061(2)	2.054(4)	2.058(2)
Ni(1)-O(3A)	2.134(5)	2.127(3)	2.136(4)	2.126(2)	2.124(4)	2.130(2)
Ni(1)-O(1P)bridge	2.051(6)	2.067(3)	2.069(4)	2.060(2)	2.066(4)	2.060(2)
Ni(1)-N(1F)	2.084(8)	2.070(4)	2.084(6)	2.068(2)	2.060(5)	2.068(2)
Ln(1)-O(2A)-Ni(1)	101.1(2)	101.65(10)	101.81(14)	101.57(7)	101.94(15)	101.99(7)
Ln(1)-O(3A)-Ni(1)	97.6(2)	98.51(10)	98.81(15)	98.63(7)	98.94(14)	98.71(7)
O(2A)-Ln(1)-O(3A)	70.09(18)	70.27(9)	70.39(13)	70.69(6)	70.79(13)	70.76(6)
O(2A)-Ln(1)-O(2P)bridge	76.75(19)	76.91(10)	77.34(14)	77.05(6)	77.08(14)	76.88(7)
O(3A)-Ln(1)-O(2P)bridge	84.5(2)	85.05(10)	84.72(16)	85.19(6)	85.75(14)	85.37(7)
O(2A)-Ni(1)-O(3A)	82.6(2)	80.83(10)	80.48(15)	80.42(7)	79.77(15)	79.87(7)
O(2A)-Ni(1)-O(1P)bridge	100.9(2)	101.37(11)	101.15(16)	101.46(7)	101.15(16)	101.33(8)
O(3A)-Ni(1)-O(1P)bridge	86.0(2)	85.63(11)	85.57(15)	85.50(7)	85.44(16)	85.53(7)

Table A.12.- Selected bond lengths (Å) and angles (°) for complexes **32**-**36**.

Complex	**32**	**33**	**34**	**35**	**36**
Ln(1)-Co(1)	3.431(2)	3.420(1)	3.414(1)	3.395(1)	3.408(1)
Ln(1)-O(1A)	2.403(2)	2.404(2)	2.373(2)	2.353(2)	2.359(2)
Ln(1)-O(2A)	2.357(2)	2.352(2)	2.373(2)	2.306(2)	2.321(2)
Ln(1)-O(3A)	2.366(2)	2.341(2)	2.338(2)	2.316(2)	2.329(2)
Ln(1)-O(4A)	2.420(2)	2.390(2)	2.391(2)	2.375(2)	2.380(2)
Ln(1)-O(2P)bridge	2.328(2)	2.308(2)	2.287(2)	2.275(2)	2.279(2)
Ln(1)-O(1C)nitrate	2.495(2)	2.468(2)	2.447(2)	2.421(2)	2.451(2)
Ln(1)-O(2C)nitrate	2.515(2)	2.491(2)	2.481(2)	2.457(2)	2.486(2)
Ln(1)-O(1D)nitrate	2.481(2)	2.481(2)	2.463(2)	2.433(2)	2.437(2)
Ln(1)-O(2D)nitrate	2.501(2)	2.506(2)	2.494(2)	2.479(3)	2.475(2)
Co(1)-N(1A)	2.174(2)	2.152(2)	2.166(3)	2.173(3)	2.167(3)
Co(1)-N(2A)	2.152(2)	2.164(2)	2.155(3)	2.150(3)	2.154(3)
Co(1)-O(2A)	2.055(2)	2.203(2)	2.055(2)	2.050(2)	2.049(2)
Co(1)-O(3A)	2.202(2)	2.056(2)	2.198(2)	2.194(2)	2.200(2)
Co(1)-O(1P)bridge	2.064(2)	2.058(2)	2.064(2)	2.061(2)	2.061(2)
Co(1)-N(1F)	2.114(2)	2.113(2)	2.114(3)	2.115(3)	2.113(3)
Ln(1)-O(2A)-Co(1)	101.87(6)	97.27(7)	102.05(9)	102.24(9)	102.29(9)
Ln(1)-O(3A)-Co(1)	97.29(6)	101.94(7)	97.59(8)	97.64(9)	97.55(8)
O(2A)-Ln(1)-O(3A)	70.85(6)	71.07(6)	70.98(7)	71.24(8)	71.11(8)
O(2A)-Ln(1)-O(2P)bridge	77.50(6)	84.11(6)	77.64(8)	77.70(8)	77.61(8)
O(3A)-Ln(1)-O(2P)bridge	84.07(6)	77.59(6)	84.29(8)	84.79(9)	84.39(8)
O(2A)-Co(1)-O(3A)	79.94(6)	79.58(7)	79.11(8)	78.66(9)	78.95(8)
O(2A)-Co(1)-O(1P)bridge	104.81(6)	104.91(7)	104.89(9)	104.69(10)	104.76(9)
O(3A)-Co(1)-O(1P)bridge	85.32(6)	85.40(7)	85.38(8)	85.32(9)	85.28(9)

Chapter 5

Table A.13.- Crystallographic data for complexes **37**-**45**.

Complex	**37**	**38**	**39**	**40**	**41**
Formula	$C_{24}H_{28}N_5O_{13}Br_2MnGd$	$C_{24}H_{28}N_5O_{13}Br_2MnDy$	$C_{26}H_{41}N_6O_{14}MnDy$	$C_{27}H_{40}N_5O_{12}MnGd$	$C_{27}H_{40}N_5O_{12}MnDy$
M_r	966.52	971.77	879.09	838.83	844.08
Crystal system	*P21/n* (14)	*P21/n* (14)	*P21/n* (14)	*P21/n* (14)	*P21/n* (14)
Space group (no.)	*Monoclinic*	*Monoclinic*	*Monoclinic*	*Monoclinic*	*Monoclinic*
a (Å)	13.5996(4)	13.5722(2)	12.778(5)	11.3864(7)	11.3871(2)
b (Å)	15.0087(4)	14.9625(2)	16.871(5)	14.6689(7)	14.6552(2)
c (Å)	15.7090(5)	15.7042(2)	15.519(5)	20.13390(10)	20.2125(3)
α (°)	90	90	90	90	90
β (°)	90.7330(10)	90.4762(13)	92.736(5)	101.147(2)	101.4791(14)
γ (°)	90	90	90	90	90
V (Å^3)	3206.14(16)	3189.01(8)	3342(2)	3299.4(3)	3305.59(8)
Z	4	4	4	4	4
D_c (g cm^{-3})	2.002	2.024	1.747	1.689	1.696
μ(MoKα) (mm^{-1})	5.007	5.297	2.671	2.442	2.692
T (K)	100(2)	100(2)	100(2)	100(2)	100(2)
Observed reflections	7727 (6641)	6600 (5979)	5872 (4936)	8426 (6100)	8360 (7071)
R_{int}	0.0477	0.0362	0.0414	0.0515	0.0360
Parameters	422	422	445	421	421
GOF	1.057	1.061	1.035	1.037	1.078
R_1[a,b]	0.0329 (0.0246)	0.0288 (0.0244)	0.0443 (0.0343)	0.0860 (0.0532)	0.0341 (0.0262)
wR_2[c]	0.0620 (0.0587)	0.0548 (0.0570)	0.0779 (0.0732)	0.1174 (0.1056)	0.0640 (0.0619)
Largest difference in peak and hole (e Å^{-3})	1.081 and -1.609	0.893 and -0.922	1.262 and -0.672	4.542 and -1.615	1.652 and -1.103

[a] $R_1 = \Sigma||F_o| - |F_c||/\Sigma|F_o|$. [b] Values in parentheses for reflections with $I > 2\sigma(I)$. [c] $wR_2 = \{\Sigma[w(F_o^2 - F_c^2)^2] / \Sigma[w(F_o^2)^2]\}^{½}$

Table A.13.- Continuation.

Complex	**42**	**43**	**44**	**45**
Formula	$C_{44}H_{52}N_7O_{12}MnGd$	$C_{44}H_{52}N_7O_{12}MnDy$	$C_{60}H_{86}N_{12}O_{20}Mn_2Gd_2$	$C_{56}H_{90}N_8O_{24}Mn_2Dy_2$
M_r	1083.12	1088.37	1719.79	1694.24
Crystal system	*P21/n* (14)	*P21/n* (14)	*P-1* (2)	*P-1* (2)
Space group (no.)	*Monoclinic*	*Monoclinic*	*Triclinic*	*Triclinic*
a (Å)	13.470(5)	13.461(5)	11.410(5)	10.702(5)
b (Å)	23.619(5)	23.617(5)	12.358(5)	12.462(5)
c (Å)	14.908(5)	14.884(5)	14.275(5)	14.270(5)
α (°)	90	90	109.974(5)	111.315(5)
β (°)	102.773(5)	102.675(5)	106.588(5)	104.241(5)
γ (°)	90	90	100.798(5)	98.203(5)
V (Å^3)	4626(3)	4616(3)	1720(1)	1661(1)
Z	4	4	1	1
D_c (g cm^{-3})	1.555	1.566	1.660	1.694
μ(MoKα) (mm^{-1})	1.763	1.948	2.341	2.678
T (K)	100(2)	100(2)	100(2)	100(2)
Observed reflections	8122 (7558)	8111 (7795)	6038 (5238)	5813 (4633)
R_{int}	0.0246	0.0233	0.0535	0.0651
Parameters	595	595	442	426
*G*OF	1.038	1.052	1.031	0.998
R_1[a,b]	0.0262 (0.0241)	0.0212 (0.0203)	0.0470 (0.0370)	0.0645 (0.0457)
wR_2[c]	0.0600 (0.0585)	0.0511 (0.0505)	0.0796 (0.0751)	0.1052 (0.0975)
Largest difference in peak and hole (e Å^{-3})	0.940 and -0.474	0.993 and -0.341	1.243 and -0.560	1.873 and -0.884

[a] $R_1 = \sum||F_o| - |F_c||/\sum|F_o|$. [b] Values in parentheses for reflections with $I > 2\sigma(I)$. [c] $wR_2 = \{\sum[w(F_o^2 - F_c^2)^2] / \sum [w(F_o^2)^2]\}^{1/2}$

Table A.14.- Selected bond lengths (Å) and angles (°) for complexes **37** and **38**.

Complex	**37**	**38**
Ln(1)-Mn(1)	3.414(1)	3.400(1)
Ln(1)-O(1A)	2.384(2)	2.354(2)
Ln(1)-O(2A)	2.394(2)	2.373(2)
Ln(1)-O(3A)	2.389(2)	2.364(2)
Ln(1)-O(4A)	2.392(2)	2.367(2)
Ln(1)-O(2P)bridge	2.329(2)	2.295(2)
Ln(1)-O(1C)nitrate	2.525(2)	2.517(2)
Ln(1)-O(2C)nitrate	2.470(2)	2.442(2)
Ln(1)-O(1D)nitrate	2.505(2)	2.480(2)
Ln(1)-O(2D)nitrate	2.478(2)	2.447(2)
Mn(1)-N(1A)	2.224(2)	2.230(2)
Mn(1)-N(2A)	2.227(2)	2.220(2)
Mn(1)-O(2A)	2.138(2)	2.140(2)
Mn(1)-O(3A)	2.148(2)	2.144(2)
Mn(1)-O(1P)bridge	2.060(2)	2.053(2)
Ln(1)-O(2A)-Mn(1)	97.58(7)	97.64(8)
Ln(1)-O(3A)-Mn(1)	97.48(7)	97.80(8)
O(2A)-Ln(1)-O(3A)	71.09(6)	71.29(7)
O(2A)-Ln(1)-O(2P)bridge	78.88(7)	79.58(8)
O(3A)-Ln(1)-O(2P)bridge	79.87(7)	80.54(8)
O(2A)-Mn(1)-O(3A)	80.89(7)	80.25(8)
O(2A)-Mn(1)-O(1P)bridge	104.54(7)	103.86(9)
O(3A)-Mn(1)-O(1P)bridge	101.57(8)	101.13(9)

Table A.15.- Selected bond lengths (Å) and angles (°) for complexes **39**-**45**.

Complex	**39**	**40**	**41**	**42**
Ln(1)-Mn(1)	3.661(1)	3.474(1)	3.460(1)	3.485(1)
Ln(1)-O(2A)	2.556(3)	2.691(4)	2.718(2)	2.480(2)
Ln(1)-O(5A)	2.312(3)	2.264(4)	2.236(2)	2.320(2)
Ln(1)-O(25A)	2.291(3)	2.342(4)	2.322(2)	2.258(2)
Ln(1)-O(27A)	2.611(3)	2.434(4)	2.420(2)	2.606(2)
Ln(1)-O(1C)nitrate	2.464(3)	2.475(4)	2.444(2)	2.465(2)
Ln(1)-O(2C)nitrate	2.468(3)	2.485(4)	2.458(2)	2.519(2)
Ln(1)-O(1D)nitrate	2.472(3)	2.497(4)	2.481(2)	2.475(2)
Ln(1)-O(2D)nitrate	2.487(3)	2.480(4)	2.450(2)	2.507(2)
Ln(1)-O(1E)nitrate	2.517(3)			
Ln(1)-O(2E)nitrate	2.517(3)			
Ln(1)-O(2P)bridge		2.343(4)	2.318(2)	2.366(2)
Mn(1)-N(12A)	2.377(3)	2.334(4)	2.331(2)	2.273(2)
Mn(1)-N(16A)	2.295(4)	2.305(5)	2.304(2)	2.333(2)
Mn(1)-N(20A)	2.365(4)	2.316(4)	2.320(2)	2.353(2)
Mn(1)-O(5A)	2.146(3)	2.128(3)	2.139(2)	2.206(2)
Mn(1)-O(25A)	2.152(3)	2.213(4)	2.204(2)	2.110(2)
Mn(1)-O(1M)	2.217(3)			
Mn(1)-O(1P)bridge		2.108(4)	2.112(2)	2.156(2)
Ln(1)-O(5A)-Mn(1)	110.36(12)	104.52(15)	104.47(6)	100.70(6)
Ln(1)-O(25A)-Mn(1)	110.93(12)	99.36(13)	99.65(6)	105.80(7)
O(5A)-Ln(1)-O(25A)	66.51(10)	72.43(12)	72.72(5)	71.77(6)
O(5A)-Ln(1)-O(2P)bridge		80.13(13)	80.87(6)	77.99(5)
O(25A)-Ln(1)-O(2P)bridge		78.90(13)	79.38(6)	79.45(6)
O(5A)-Mn(1)-O(25A)	71.95(10)	77.64(14)	76.98(6)	76.86(6)
O(5A)-Mn(1)-O(1P)bridge		95.64(15)	95.13(6)	91.84(6)
O(25A)-Mn(1)-O(1P)bridge		91.69(14)	91.50(6)	93.42(6)

Table A.15.- Continuation.

Complex	**43**	**44**	**45**
Ln(1)-Mn(1)	3.466(1)	3.531(2)	3.498(2)
Ln(1)-Ln(1)		4.025(1)	4.063(1)
Ln(1)-O(2A)	2.460(2)	2.470(3)	2.437(4)
Ln(1)-O(5A)	2.290(2)	2.364(3)	2.331(4)
Ln(1)-O(25A)	2.230(2)	2.316(3)	2.266(4)
Ln(1)-O(27A)	2.601(2)	2.560(3)	2.567(4)
Ln(1)-O(1C)nitrate	2.433(2)	2.513(3)	2.485(5)
Ln(1)-O(2C)nitrate	2.497(2)	2.568(3)	2.528(4)
Ln(1)-O(1D)nitrate	2.440(2)		
Ln(1)-O(2D)nitrate	2.483(2)		
Ln(1)-O(2P)bridge	2.344(2)	2.372(3)	2.382(4)
Ln(1)-O(2P)bridge		2.401(3)	2.420(4)
Ln(1)-O(3P)bridge		2.423(3)	2.375(4)
Mn(1)-N(12A)	2.271(2)	2.354(4)	2.333(5)
Mn(1)-N(16A)	2.332(2)	2.369(4)	2.342(5)
Mn(1)-N(20A)	2.348(2)	2.349(4)	2.362(5)
Mn(1)-O(5A)	2.205(2)	2.212(3)	2.199(4)
Mn(1)-O(25A)	2.115(2)	2.165(3)	2.184(4)
Mn(1)-O(1P)bridge	2.156(2)	2.126(3)	2.117(4)
Ln(1)-O(5A)-Mn(1)	100.89(5)	100.94(11)	101.06(15)
Ln(1)-O(25A)-Mn(1)	105.77(6)	103.94(11)	103.61(16)
Ln(1)-O(2P)-Ln(1)		115.00(11)	115.59(17)
O(5A)-Ln(1)-O(25A)	72.27(5)	73.17(10)	74.51(14)
O(5A)-Ln(1)-O(2P)bridge	78.58(5)	75.37(10)	74.92(14)
O(5A)-Ln(1)-O(2P)bridge		137.05(10)	137.70(15)
O(25A)-Ln(1)-O(2P)bridge	79.70(5)	74.21(10)	74.31(14)
O(25A)-Ln(1)-O(2P)bridge		109.28(10)	103.80(14)
O(5A)-Mn(1)-O(25A)	76.20(5)	79.17(11)	78.87(15)
O(5A)-Mn(1)-O(1P)bridge	91.70(6)	93.99(11)	93.82(16)
O(25A)-Mn(1)-O(1P)bridge	93.13(6)	90.72(12)	89.31(16)

Chapter 6

Table A.16.- Crystallographic data for complexes **46**-**54**.

Complex	**46**	**47**	**48**	**49**
Formula	$C_{44}H_{56}N_4O_{12}Cl_5Br_4Zn_3Dy$	$C_{44}H_{56}N_4O_{12}Cl_5Br_4Zn_3Er$	$C_{41}H_{44}N_5O_{12}Cl_2Br_4Zn_2Dy$	$C_{42}H_{52}N_4O_{12}Br_9Zn_3Dy$
M_r	1688.43	1693.3	1482.59	1882.67
Crystal system	Orthorhombic	Orthorhombic	Triclinic	Monoclinic
Space group (no.)	*Pna21* (33)	*Pna21* (33)	*P-1* (2)	*P21/n* (14)
a (Å)	14.343(5)	14.3668(2)	11.820(2)	14.6756(11)
b (Å)	30.712(5)	30.6628(3)	12.875(2)	13.0146(9)
c (Å)	12.895(5)	12.89490(10)	15.948(3)	30.607(2)
α (°)	90	90	98.179(3)	90
β (°)	90	90	94.615(3)	93.627(2)
γ (°)	90	90	91.774(3)	90
V (Å^3)	5682(3)	5680.54(11)	2392.2(7)	5834.1(7)
Z	4	4	2	4
D_c (g cm^{-3})	1.972	1.977	2.058	2.143
μ(MoKα) (mm^{-1})	5.659	10.020	6.058	8.705
T (K)	100(2)	100(2)	100(2)	100(2)
Observed reflections	9510 (8910)	9943 (9830)	10772 (9031)	14924 (12409)
R_{int}	0.0363	0.0218	0.0442	0.0664
Parameters	668	659	610	647
GOF	1.048	1.063	1.009	1.065
R_1[a,b]	0.0410 (0.0369)	0.0502 (0.0497)	0.0444 (0.0352)	0.0698 (0.0551)
wR_2[c]	0.0841 (0.0822)	0.1360 (0.1356)	0.0832 (0.0785)	0.1357 (0.1254)
Largest difference in peak and hole (e Å^{-3})	1.606 and -1.060	2.447 and -2.646	1.599 and -0.735	3.740 and -3.322

[a] $R_1 = \Sigma||F_o| - |F_c||/\Sigma|F_o|$. [b]Values in parentheses for reflections with $I > 2\sigma(I)$. [c] $wR_2 = \{\Sigma[w(F_o^2 - F_c^2)^2] / \Sigma[w(F_o^2)^2]\}^{½}$

Table A.16.- Continuation

Complex	**50**	**51**	**52**	**53**	**54**
Formula	$C_{43}H_{52}N_5O_{14}Br_6Zn_2Dy$	$C_{41}H_{44}N_4O_{12}Br_4I_3Zn_2Dy$	$C_{43}H_{52}N_5O_{14}Br_4I_2Zn_2Dy$	$C_{41}H_{46}N_{11}O_{13}Br_4Zn_2Dy$	$C_{40}H_{40}N_4O_8Cl_2Br_4F_6PZn_2Dy$
M_r	1635.59	1778.38	1729.57	1513.77	1533.51
Crystal system	Monoclinic	Monoclinic	Monoclinic	Triclinic	Monoclinic
Space group (no.)	*P21/c* (14)	*P21/c* (14)	*P21/c* (14)	*P-1* (2)	*C2/c* (15)
a (Å)	14.6274(3)	14.9193(3)	14.7655(3)	13.6069(7)	17.1014(2)
b (Å)	27.3664(5)	25.4989(3)	27.0577(4)	13.8358(9)	18.2552(3)
c (Å)	14.7306(4)	15.6761(3)	15.1740(3)	15.9283(7)	15.9346(2)
α (°)	90	90	90	99.998(5)	90
β (°)	115.170(3)	116.881(2)	115.552(2)	108.143(5)	97.4595(12)
γ (°)	90	90	90	106.028(5)	90
V (Å^3)	5336.8(2)	5319.21(18)	5469.39(19)	2625.9(3)	4932.51(11)
Z	4	4	4	2	4
D_c (g cm^{-3})	2.036	2.221	2.100	1.851	2.065
μ(MoKα) (mm^{-1})	6.836	7.090	6.338	5.421	5.921
T (K)	100(2)	100(2)	100(2)	100(2)	100(2)
Observed reflections	11840 (8854)	12209 (10629)	12541 (10581)	11643 (7756)	4336 (3679)
R_{int}	0.0564	0.0325	0.0331	0.0610	0.0393
Parameters	650	609	627	590	310
GOF	1.026	1.053	1.051	0.951	1.048
R_1[a,b]	0.0811 (0.0533)	0.0545 (0.0460)	0.0558 (0.0441)	0.0959 (0.0587)	0.0412 (0.0307)
wR_2[c]	0.1235 (0.1085)	0.1225 (0.1177)	0.1083 (0.1022)	0.1254 (0.1114)	0.0653 (0.0613)
Largest difference in peak and hole (e Å^{-3})	2.139 and -2.347	2.041 and -4.678	5.120 and -1.786	1.858 and -1.692	0.891 and -0.540

[a] $R_1 = \Sigma||F_o| - |F_c||/\Sigma|F_o|$. [b] Values in parentheses for reflections with $I > 2\sigma(I)$. [c] $wR_2 = \{\Sigma[w(F_o^2 - F_c^2)^2] / \Sigma[w(F_o^2)^2]\}^{½}$

Table A.17.- Selected bond lengths (Å) and angles (°) for complexes **46**-**54**.

Complex	**46**	**47**	**48**	**49**	**50**
Ln(1)-Zn(1)	3.573(1)	3.572(1)	3.553(1)	3.573(1)	3.569(1)
Ln(1)-Zn(2)	3.588(1)	3.562(1)	3.534(1)	3.572(1)	3.562(1)
Ln(1)-O(1A)	2.397(4)	2.366(6)	2.385(3)	2.393(4)	2.385(4)
Ln(1)-O(2A)	2.323(5)	2.327(5)	2.290(3)	2.335(4)	2.321(5)
Ln(1)-O(3A)	2.253(5)	2.231(5)	2.321(3)	2.235(4)	2.239(4)
Ln(1)-O(4A)	2.443(5)	2.409(6)	2.392(3)	2.448(4)	2.393(5)
Ln(1)-O(1B)	2.387(4)	2.383(6)	2.388(3)	2.405(4)	2.408(5)
Ln(1)-O(2B)	2.349(5)	2.303(5)	2.303(3)	2.330(4)	2.277(5)
Ln(1)-O(3B)	2.244(5)	2.248(5)	2.317(3)	2.251(4)	2.316(5)
Ln(1)-O(4B)	2.439(5)	2.418(6)	2.374(3)	2.426(4)	2.401(4)
Zn(1)-N(1A)	2.178(6)	2.159(6)	2.123(3)	2.173(5)	2.151(6)
Zn(1)-N(2A)	2.104(6)	2.108(7)	2.145(3)	2.102(5)	2.145(6)
Zn(1)-O(2A)	2.041(5)	2.071(5)	2.137(3)	2.055(4)	2.081(4)
Zn(1)-O(3A)	2.146(5)	2.166(5)	2.066(3)	2.148(4)	2.078(5)
Zn(1)-X(1A)	2.216(2)	2.232(2)	2.214(1)	2.356(1)	2.360(1)
Zn(2)-N(1B)	2.168(6)	2.181(6)	2.138(4)	2.163(5)	2.098(5)
Zn(2)-N(2B)	2.099(6)	2.108(7)	2.153(4)	2.122(5)	2.186(6)
Zn(2)-O(2B)	2.056(5)	2.039(5)	2.087(3)	2.057(4)	2.166(5)
Zn(2)-O(3B)	2.168(5)	2.144(5)	2.101(3)	2.142(4)	2.047(5)
Zn(2)-X(1B)	2.223(2)	2.223(2)	2.218(1)	2.355(1)	2.372(1)
Zn(3)-X(1C)	2.247(3)	2.252(3)		2.378(2)	
Zn(3)-X(2C)	2.262(3)	2.257(3)		2.385(2)	
Zn(3)-X(3C)	2.227(3)	2.234(4)		2.350(2)	
Zn(3)-O(4M)	2.02(1)	2.02(1)		2.009(8)	
Ln(1)-O(2A)-Zn(1)	110.4(3)	108.5(2)	106.73(11)	108.82(17)	108.23(19)
Ln(1)-O(3A)-Zn(1)	108.5(3)	108.6(2)	108.08(11)	109.20(17)	111.5(2)
Ln(1)-O(2B)-Zn(2)	108.9(3)	110.1(2)	107.16(11)	108.87(17)	106.59(19)
Ln(1)-O(3B)-Zn(2)	108.4(3)	108.4(2)	106.18(11)	108.79(17)	109.3(2)
O(2A)-Zn(1)-O(3A)	74.2(2)	74.1(2)	75.96(10)	74.23(15)	73.79(18)
O(2B)-Zn(2)-O(3B)	74.3(2)	73.9(2)	76.47(10)	74.30(15)	75.46(18)
O(2A)-Ln(1)-O(3A)	66.9(2)	68.1(2)	68.26(9)	67.41(14)	66.36(16)
O(2B)-Ln(1)-O(3B)	67.7(2)	67.2(2)	68.28(9)	67.22(14)	68.32(16)
Zn(1)-Ln(1)-Zn(2)	141.47(3)	142.11(3)	105.94(2)	143.743(17)	146.77(2)

Table A.17.- Continuation.

Complex	**51**	**52**	**53**	**54**
Ln(1)-Zn(1)	3.568(1)	3.571(1)	3.568(1)	3.550(1)
Ln(1)-Zn(2)	3.546(1)	3.564(1)	3.591(1)	
Ln(1)-O(1A)	2.378(5)	2.389(5)	2.364(5)	2.393(3)
Ln(1)-O(2A)	2.329(5)	2.243(4)	2.350(5)	2.340(3)
Ln(1)-O(3A)	2.246(5)	2.333(4)	2.263(4)	2.275(3)
Ln(1)-O(4A)	2.414(5)	2.390(4)	2.454(5)	2.386(3)
Ln(1)-O(1B)	2.387(5)	2.403(4)	2.397(5)	
Ln(1)-O(2B)	2.322(5)	2.310(4)	2.340(4)	
Ln(1)-O(3B)	2.264(5)	2.279(4)	2.261(5)	
Ln(1)-O(4B)	2.416(5)	2.405(5)	2.412(5)	
Zn(1)-N(1A)	2.169(6)	2.141(5)	2.133(6)	2.153(3)
Zn(1)-N(2A)	2.124(6)	2.158(5)	2.111(6)	2.106(3)
Zn(1)-O(2A)	2.098(5)	2.101(4)	2.044(5)	2.066(3)
Zn(1)-O(3A)	2.100(5)	2.078(4)	2.125(5)	2.138(3)
Zn(1)-X(1A)	2.556(1)	2.5421(8)	1.992(6)	2.217(1)
Zn(2)-N(1B)	2.182(6)	2.188(5)	2.154(6)	
Zn(2)-N(2B)	2.115(6)	2.105(5)	2.114(6)	
Zn(2)-O(2B)	2.058(5)	2.043(4)	2.058(4)	
Zn(2)-O(3B)	2.156(5)	2.171(4)	2.147(5)	
Zn(2)-X(1B)	2.570(1)	2.559(1)	1.971(7)	
Ln(1)-O(2A)-Zn(1)	107.29(19)	110.55(17)	108.4(2)	107.2(1)
Ln(1)-O(3A)-Zn(1)	110.3(2)	107.97(17)	108.8(2)	107.1(1)
Ln(1)-O(2B)-Zn(2)	107.99(19)	109.73(18)	109.3(2)	
Ln(1)-O(3B)-Zn(2)	106.68(19)	106.38(17)	109.1(2)	
O(2A)-Zn(1)-O(3A)	74.62(18)	74.29(15)	75.56(18)	75.9(1)
O(2B)-Zn(2)-O(3B)	75.69(18)	75.23(16)	74.25(18)	
O(2A)-Ln(1)-O(3A)	67.55(17)	66.91(14)	67.24(16)	68.1(1)
O(2B)-Ln(1)-O(3B)	68.66(16)	68.24(14)	66.97(17)	
Zn(1)-Ln(1)-Zn(2)	146.95(2)	146.249(18)	141.56(2)	109.48(1)

Chapter 7

Table A.18.- Crystallographic data for complex **55**.

Complex	**55**
Formula	$Si_3W_{33}C_{60}H_{112}N_6O_{152}Br_6K_{15}Dy_3$
M_r	11054.2
Crystal system	Triclinic
Space group (no.)	*P-1 (2)*
a (Å)	21.7341(3)
b (Å)	24.6274(4)
c (Å)	28.2424(4)
α (°)	113.5829(15)
β (°)	95.4519(13)
γ (°)	104.0082(14)
V (Å^3)	13125.7(3)
Z	2
D_c (g cm^{-3})	2.781
μ(CuKα) (mm^{-1}) [a]	34.425
*T (*K)	100(2)
Observed reflections	33806 (44642)
R_{int}	0.0536
Parameters	1341
GOF	1.036
R_1[a,b]	0.0899 (0.0645)
wR_2[b,c]	0.1902 (0.1675)
Largest difference in peak and hole (e Å^{-3})	4.523 and -5.194

[a] $R_1 = \Sigma||F_o| - |F_c||/\Sigma|F_o|$.
[b] Values in parentheses for reflections with $I > 2\sigma(I)$.
[c] $wR_2 = \{\Sigma[w(F_o^2 - F_c^2)^2] / \Sigma[w(F_o^2)^2]\}^{½}$

Table A.19.- Selected bond lengths (Å) for complexes **55**.

Complex 55	**Dy1**	**Dy2**	**Dy3**
Dy-O(1)ligand	2.375(12)	2.372(13)	2.376(13)
Dy-O(2)ligand	2.321(12)	2.311(12)	2.318(12)
Dy-O(3)ligand	2.290(12)	2.283(13)	2.279(12)
Dy-O(4)ligand	2.464(14)	2.473(13)	2.467(14)
Dy-O(1)POM	2.311(12)	2.306(13)	2.341(13)
Dy-O(2)POM	2.366(13)	2.344(12)	2.369(13)
Dy-O(3)POM	2.326(14)	2.397(11)	2.307(12)
Dy-O(4)POM	2.318(12)	2.362(11)	2.305(12)

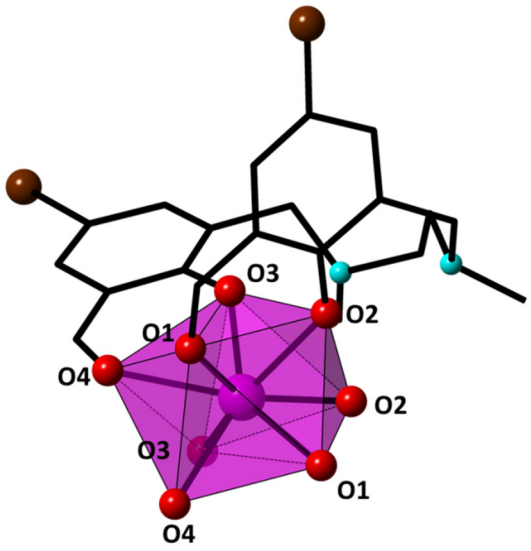

Figure A.1.- Labelling scheme used for complex **55**

II. SHAPE MEASUREMENTS RESULTS

Figures of the closest ideal geometries are collected in Figure A.2 at the end of this section.

Chapter 1

Table A.20.- Shape measures for Ni(II) coordination environments in compounds **1-6**.

Complex	HP-6	PPY-6	OC-6	TPR-6	JPPY-6
1	32.426	29.006	0.136	15.772	32.314
2 (Ni1)	32.244	24.932	0.986	11.338	28.364
2 (Ni2)	32.060	26.187	0.590	13.362	29.818
3 (Ni2)	32.827	25.672	0.651	12.669	29.403
4 (Ni1)	30.446	25.711	0.667	13.103	29.182
4 (Ni2)	32.613	27.424	0.336	14.424	31.285
4 (Ni3)	30.097	25.067	0.876	13.108	28.586
5 (Ni1)	29.448	23.769	1.194	12.525	27.301
5 (Ni2)	28.464	23.536	1.018	12.144	26.623
6 (Ni1)	30.062	23.878	1.198	12.507	27.382
6 (Ni2)	30.054	24.735	0.761	12.934	27.857
6 (Ni3)	30.141	24.444	1.029	13.161	28.008
6 (Ni4)	29.628	23.410	0.987	11.816	26.567

*HP-6: hexagon (D_{6h}); PPY-6: pentagonal pyramid (C_{5v}); OC-6: octahedron (O_h); TPR-6: trigonal prism (D_{3h}); JPPY-6: johnson pentagonal pyramid J2 (C_{5v}).

Table A.21.- Shape measures for NiN_2O_3 coordination environment in compound **3**.

Complex	PP-5	vOC-5	TBPY-5	SPY-5	JTBPY-5
3 (Ni1)	31.239	0.932	5.371	0.526	7.364

*PP-5: pentagon (D_{5h}); vOC-5: vacant octahedron (C_{4v}); TBPY-5: trigonal bipyramid (D_{3h}); SPY-5: square pyramid (C_{4v}); JTBPY-5: Johnson trigonal bipyramid (D_{3h}).

Chapter 2

Table A.22.- Shape measures for Ni(II) coordination environments in compounds **7-10**.

Complex	HP-6	PPY-6	OC-6	TPR-6	JPPY-6
7 (Ni1)	32.812	22.749	1.642	9.339	26.412
7 (Ni2)	33.305	23.833	1.274	12.207	27.820
8 (Ni1)	32.151	22.701	1.306	10.826	26.108
8 (Ni2)	33.926	23.953	1.499	11.653	27.808
9 (Ni1A)	30.417	18.726	2.832	8.108	22.143
9 (Ni2A)	33.926	23.953	1.499	11.653	27.808
9 (Ni1B)	33.136	22.598	1.697	9.422	26.304
9 (Ni2B)	32.511	22.848	1.706	11.458	26.729
10 (Ni1)	33.028	22.335	1.623	9.538	25.931
10 (Ni2)	32.829	24.008	1.423	12.599	28.056

*HP-6: hexagon (D_{6h}); PPY-6: pentagonal pyramid (C_{5v}); OC-6: octahedron (O_h); TPR-6: trigonal prism (D_{3h}); JPPY-6: johnson pentagonal pyramid J2 (C_{5v}).

Chapter 3

Table A.23.- Shape measures for Zn(II) coordination environments in compounds **11-21**.

Complex	PP-5	vOC-5	TBPY-5	SPY-5	JTBPY-5
11	32.271	1.845	3.420	0.463	5.599
12	32.260	1.928	3.395	0.481	5.617
14	31.726	2.130	3.387	0.528	5.748
15	31.847	2.056	3.440	0.522	5.710
16	31.629	2.100	3.350	0.557	5.659
17	31.524	2.212	3.333	0.597	5.722
19	31.425	2.237	3.326	0.618	5.694
20	31.071	2.361	3.350	0.671	5.803
21	31.210	2.349	3.320	0.687	5.771

*PP-5: pentagon (D_{5h}); vOC-5: vacant octahedron (C_{4v}); TBPY-5: trigonal bipyramid (D_{3h}); SPY-5: square pyramid (C_{4v}); JTBPY-5: Johnson trigonal bipyramid (D_{3h}).

Table A.24.- Shape measures for LnO_9 coordination environments in compounds **11-21**.

Complex	JCSAPR-9	CSAPR-9	JTCTPR-9	TCTPR-9	MFF-9
11	2.243	1.412	3.483	2.035	1.567
12	2.197	1.365	3.440	1.971	1.538
14	2.092	1.319	3.127	1.793	1.531
15	1.942	1.206	3.169	1.856	1.454
16	1.874	1.156	3.141	1.827	1.421
17	1.893	1.180	3.041	1.772	1.452
19	1.747	1.045	3.065	1.780	1.341
20	1.748	1.124	2.859	1.721	1.422
21	1.703	1.094	2.829	1.708	1.407

*JCSAPR-9: capped square antiprism (C_{4v}); CSAPR-9: spherical capped square antiprism (C_{4v}); JTCTPR-9: tricapped trigonal prism (D_{3h}); TCTPR-9: (D_{3h}); spherical tricapped trigonal prism: MFF-9: muffin (C_s).

Chapter 4

Table A.25.- Shape measures for Cu(II) coordination environments in compounds **22-25**.

Complex	PP-5	vOC-5	TBPY-5	SPY-5	JTBPY-5
22	31.231	1.648	3.476	0.694	6.363
23	31.106	1.631	3.503	0.723	6.382
24	31.115	1.659	3.517	0.755	6.423
25	30.958	1.742	3.482	0.783	6.428

*PP-5: pentagon (D_{5h}); vOC-5: vacant octahedron (C_{4v}); TBPY-5: trigonal bipyramid (D_{3h}); SPY-5: square pyramid (C_{4v}); JTBPY-5: Johnson trigonal bipyramid (D_{3h}).

Table A.26.- Shape measures for LnO_9 coordination environments in compounds **22-25**.

Complex	JCSAPR-9	CSAPR-9	JTCTPR-9	TCTPR-9	MFF-9
22	2.214	1.460	2.967	1.850	1.615
23	2.113	1.398	2.933	1.835	1.584
24	2.045	1.340	2.922	1.824	1.535
25	1.948	1.262	2.839	1.780	1.482

*JCSAPR-9: capped square antiprism (C_{4v}); CSAPR-9: spherical capped square antiprism (C_{4v}); JTCTPR-9: tricapped trigonal prism (D_{3h}); TCTPR-9: (D_{3h}); spherical tricapped trigonal prism: MFF-9: muffin (C_s).

*Shape measures relative to other reference polyhedron are significantly larger.

Table A.27.- Shape measures for Ni(II) coordination environments in compounds **26-31**.

Complex	OC-6	TPR-6	% Octahedron	% Deviation path
26	0.927	10.884	77.1	2.7
27	0.962	10.929	76.7	3.2
28	1.011	10.804	76.1	3.4
29	1.004	10.798	76.2	3.3
30	1.027	10.761	75.9	3.4
31	1.034	10.750	75.8	3.4

*OC-6: octahedron (O_h); TPR-6: trigonal prism (D_{3h}).

Table A.28.- Shape measures for LnO_9 coordination environments in compounds **26-31**.

Complex	JCSAPR-9	CSAPR-9	JTCTPR-9	TCTPR-9	MFF-9
26	2.940	1.607	3.898	2.690	1.582
27	2.761	1.428	3.525	2.402	1.428
28	2.742	1.449	3.438	2.373	1.513
29	2.699	1.385	3.312	2.252	1.436
30	2.708	1.379	3.244	2.155	1.445
31	2.693	1.366	3.246	2.181	1.430

*JCSAPR-9: capped square antiprism (C_{4v}); CSAPR-9: spherical capped square antiprism (C_{4v}); JTCTPR-9: tricapped trigonal prism (D_{3h}); TCTPR-9: (D_{3h}); spherical tricapped trigonal prism: MFF-9: muffin (C_s).

*Shape measures relative to other reference polyhedron are significantly larger.

Table A.29.- Shape measures for Co(II) coordination environments in compounds **32-36**.

Complex	OC-6	TPR-6	% Octahedron	% Deviation path
32	1.318	10.061	72.7	3.9
33	1.351	9.990	72.4	3.9
34	1.384	9.974	72.0	4.2
35	1.400	9.972	71.9	4.4
36	1.318	9.954	71.9	4.3

*OC-6: octahedron (O_h); TPR-6: trigonal prism (D_{3h}).

Table A.30.- Shape measures for LnO_9 coordination environments in compounds **32-36**.

Complex	JCSAPR-9	CSAPR-9	JTCTPR-9	TCTPR-9	MFF-9
32	2.787	1.479	3.549	2.488	1.503
33	2.785	1.474	3.470	2.449	1.509
34	2.741	1.445	3.364	2.362	1.496
35	2.729	1.421	3.248	2.233	1.494
36	2.712	1.419	3.282	2.282	1.497

*JCSAPR-9: capped square antiprism (C_{4v}); CSAPR-9: spherical capped square antiprism (C_{4v}); JTCTPR-9: tricapped trigonal prism (D_{3h}); TCTPR-9: (D_{3h}); spherical tricapped trigonal prism: MFF-9: muffin (C_s).

*Shape measures relative to other reference polyhedron are significantly larger.

Chapter 5

Table A.31.- Shape measures for Mn(II) coordination environments in compounds **37** and **38**.

Complex	PP-5	vOC-5	TBPY-5	SPY-5	JTBPY-5
37	31.459	3.179	3.590	0.729	6.531
38	31.293	3.272	3.618	0.807	6.522

*PP-5: pentagon (D_{5h}); vOC-5: vacant octahedron (C_{4v}); TBPY-5: trigonal bipyramid (D_{3h}); SPY-5: square pyramid (C_{4v}); JTBPY-5: Johnson trigonal bipyramid (D_{3h}).

Table A.32.- Shape measures for Mn(II) coordination environments in compounds **39**-**45**.

Complex	HP-6	PPY-6	OC-6	TPR-6	JPPY-6
39	30.092	13.284	6.578	5.542	16.842
40	28.826	17.506	3.335	8.020	20.782
41	28.775	17.442	3.356	8.120	20.720
42	28.985	19.112	2.590	9.692	22.615
43	29.043	19.082	2.630	9.700	22.581
44	27.128	17.233	3.186	9.951	20.458
45	27.371	16.489	3.457	9.475	19.476

*HP-6: hexagon (D_{6h}); PPY-6: pentagonal pyramid (C_{5v}); OC-6: octahedron (O_h); TPR-6: trigonal prism (D_{3h}); JPPY-6: Johnson pentagonal pyramid J2 (C_{5v}).

Table A.33.- Shape measures for LnO_9 coordination environments in compounds **37, 38** and **40-45**.

Complex	JCSAPR-9	CSAPR-9	JTCTPR-9	TCTPR-9	MFF-9
37	1.942	1.242	2.983	1.739	1.500
38	2.086	1.324	3.059	1.752	1.552
40	3.903	2.681	4.224	3.015	2.524
41	3.767	2.537	3.983	2.881	2.376
42	3.062	2.107	4.949	2.987	1.774
43	2.879	1.951	4.750	2.863	1.669
44	3.636	2.966	5.058	3.924	2.812
45	3.926	3.061	4.790	3.686	2.230

*JCSAPR-9: capped square antiprism (C_{4v}); CSAPR-9: spherical capped square antiprism (C_{4v}); JTCTPR-9: tricapped trigonal prism (D_{3h}); TCTPR-9: (D_{3h}); spherical tricapped trigonal prism: MFF-9: muffin (C_s).

*Shape measures relative to other reference polyhedron are significantly larger.

Table A.34.- Shape measures for LnO_{10} coordination environment in compound **39**.

Complex	JBCSAPR-10	JSPC-10	SDD-10	TD-10	HD-10
39	4.105	2.693	4.184	3.439	5.773

*JBCSAPR-10: bicapped square antiprism J17 (D_{4d}); JSPC-10: sphenocorona J87 (C_{2v}); SDD-10: staggered dodecahedron (D_2); TD-10: (C_{2v}); tetradecahedron: HD-10: hexadecahedron (D_{4h}).

*Shape measures relative to other reference polyhedron are significantly larger.

Chapter 6

Table A.35.- Shape measures for Zn(II) coordination environments in complexes **46**-**54**.

Complex	PP-5	vOC-5	TBPY-5	SPY-5	JTBPY-5
46-Zn1	33.250	4.011	3.885	0.893	6.914
46-Zn2	32.705	3.970	3.665	0.955	6.619
47-Zn1	33.133	4.045	3.960	0.913	6.965
47-Zn2	32.596	3.999	3.650	0.945	6.738
48-Zn1	32.663	3.344	4.331	0.572	7.493
48-Zn2	32.571	3.700	4.595	0.687	8.146
49-Zn1	33.426	4.677	3.833	1.223	7.206
49-Zn2	33.651	4.559	4.166	1.118	7.675
50-Zn1	32.887	4.792	4.126	1.242	8.049
50-Zn2	33.765	4.569	4.677	1.017	8.041
51-Zn1	33.807	5.574	4.321	1.714	8.478
51-Zn2	33.941	5.627	4.732	1.662	8.603
52-Zn1	34.333	5.532	4.383	1.650	8.560
52-Zn2	34.123	5.478	5.135	1.504	8.914
53-Zn1	31.976	2.884	3.369	0.696	5.913
53-Zn2	31.454	2.979	3.609	0.730	6.058
54	32.506	3.519	4.070	0.678	7.170

*PP-5: pentagon (D_{5h}); vOC-5: vacant octahedron (C_{4v}); TBPY-5: trigonal bipyramid (D_{3h}); SPY-5: square pyramid (C_{4v}); JTBPY-5: Johnson trigonal bipyramid (D_{3h}).

Table A.36.- Shape measures for Dy(III) coordination environments in complexes **46**-**54**.

Complex	SAPR-8	TDD-8	JBTPR-8	BTPR-8	JSD-8
46	0.927	2.173	3.321	2.862	5.750
47	0.934	2.044	3.408	2.759	5.863
48	0.504	2.590	3.078	2.405	5.492
49	0.804	2.329	3.435	2.982	5.837
50	0.544	2.367	2.974	2.454	5.296
51	0.458	2.227	2.892	2.454	5.317
52	0.510	2.377	2.957	2.450	5.384
53	1.060	2.160	3.574	3.142	5.868
54	0.547	2.870	3.365	2.716	5.868

* SAPR-8: square antiprism (D_{4d}); TDD-8: triangular dodecahedron (D_{2d}); JBTPR-8: Biaugmented trigonal prism J50 (C_{2v}); BTPR-8: biaugmented trigonal prism (C_{2v}); JSD-8: Snub diphenoid J84 (D_{2d}).

*Shape measures relative to other reference polyhedron are significantly larger.

Chapter 7

Table A.37.- Shape measures for Dy(III) coordination environments in complex **55**.

Complex 55	SAPR-8	TDD-8	JBTPR-8	BTPR-8	JSD-8
Dy1	0.938	1.501	1.469	0.813	3.624
Dy2	1.052	1.778	1.433	0.745	3.866
Dy3	0.985	1.497	1.460	0.826	3.711

* SAPR-8: square antiprism (D_{4d}); TDD-8: triangular dodecahedron (D_{2d}); JBTPR-8: Biaugmented trigonal prism J50 (C_{2v}); BTPR-8: biaugmented trigonal prism (C_{2v}); JSD-8: Snub diphenoid J84 (D_{2d}).

*Shape measures relative to other reference polyhedron are significantly larger.

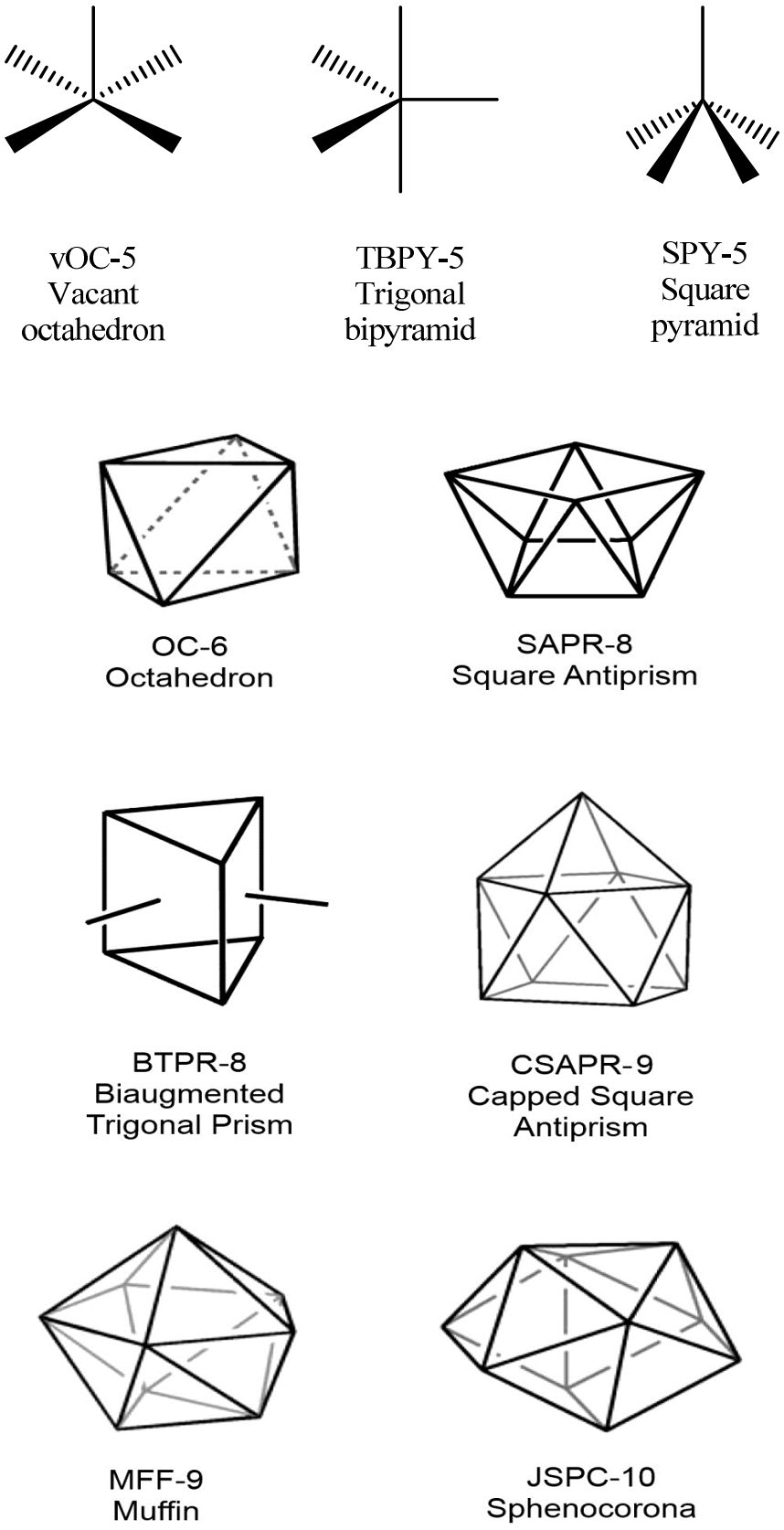

Figure A.2.- Ideal SHAPE geometries employed in CShM calculations

III. POWDER X-RAY DIFFRACTOGRAMS

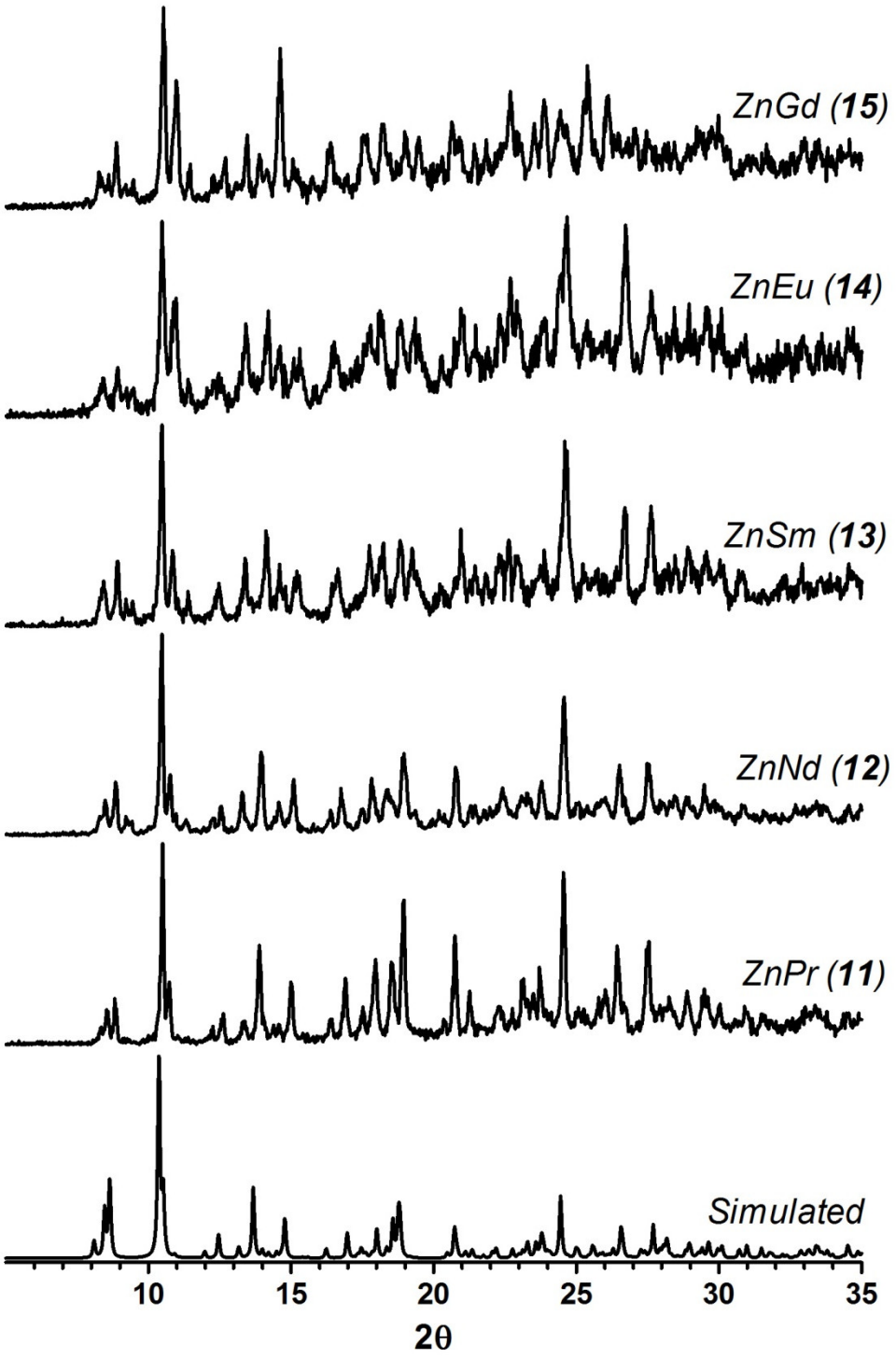

Figure A.3.- Experimental XRPD for complexes **11**-1**5** together with a simulated pattern from single-crystal X-ray diffractions

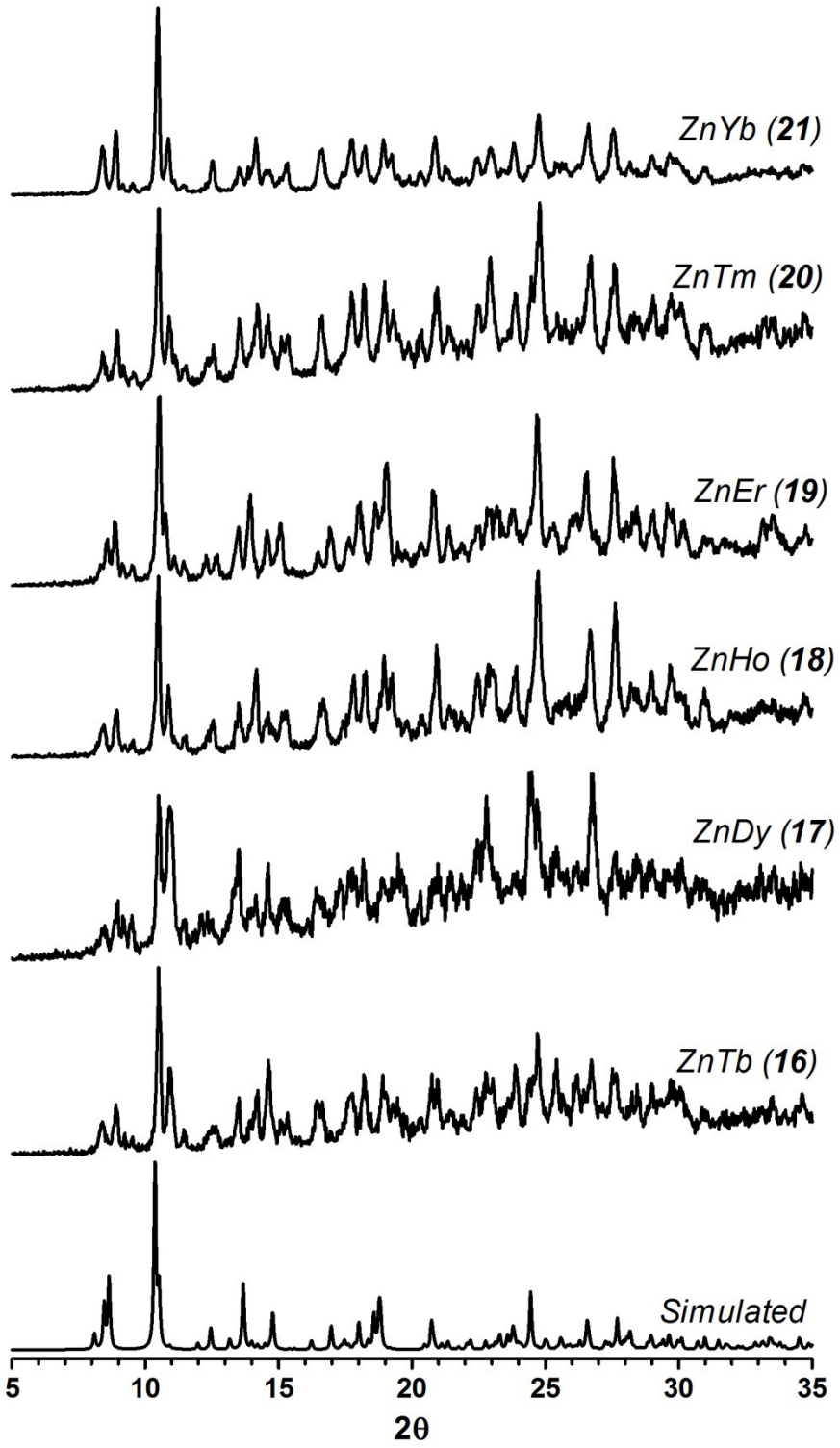

Figure A.4.- Experimental XRPD for complexes **16**-**21** together with a simulated pattern from single-crystal X-ray diffractions.

IV. INSTRUMENTAL METHODS

All the experimental conditions applied for the characterization methods are described in this section. Thermal analyses and diffuse reflectance measurements were performed at Applied Chemistry Department (UPV/EHU Gipuzkoa), whereas the powder and single-crystal X-ray diffraction studies and magnetic susceptibility measurements were carried out at General Research Services (SGIker) of UPV/EHU and University of Granada. Luminescence measurements were performed by Dr. Beñat Artetxe at Applied Physics II Department (UPV/EHU, Bizkaia). The thermogravimetric analysis on compound **56** was carried out at Materials Physics Centre (CFM) in Donostia.

V.1. Elemental analyses.

The C, H and N content of all the compounds was determined in a Leco CHNS-932 microanalyzer.

V.2. Single crystal X-ray diffraction.

Single crystals of suitable dimensions were used for data collection. The diffraction intensities were collected on four different diffractometers:

- Oxford Diffraction Xcalibur diffractometer, equipped with graphite-monochromated Mo Kα radiation (λ = 0.71069 Å).
- Agilent Technologies Super-Nova diffractometer, equipped with monochromated Mo Kα radiation (λ = 0.71069 Å) and Eos CCD detector.
- Agilent Technologies Super-Nova diffractometer, equipped with monochromated Cu Kα radiation (λ = 1.54180–4 Å) and Atlas CCD detector.
- Bruker SMART APEX CCD diffractometer, equipped with graphite-monochromated Mo Kα (λ = 0.71073 Å) radiation.

In the first three cases, data frames were processed (unit cell determinations, intensity data integrations, routine corrections for Lorentz and polarization effects and analytical absorption corrections) using the CrysAlis Pro software package,[1] whereas the “Bruker Saint Plus” program was used for reducing data collected in Bruker SMART APEX CCD diffractometer. The structures were solved by direct methods and refined by full-matrix least-squares with SHELXL-97[2], as included in OLEX[3] or the WinGX[4] software package.

Final R(F), wR(F^2) and goodness of fit agreement factors, details of the data collection and analysis can be found in Section II. Selected bond lengths and angles are also given in Section II.

V.3. Powder X-ray diffraction.

The XRPD patterns were collected on a Phillips X'PERT powder diffractometer with Cu Kα radiation (λ = 1.5418 Å) over the range 5 < 2θ < 50° with a step size of 0.02° and an acquisition time of 2.5 s per step at 25 °C.

V.4. Magnetic measurements.

Variable-temperature magnetic susceptibility and magnetization measurements were carried out with a Quantum Design SQUID MPMS-7T device, Quantum Design SQUID MPMS XL-5 device and PPMS (Physical Property Measurement System) - Quantum Design Model 6000 magnetometer. Diamagnetic corrections were estimated from the Pascal's constants. For complex **46** *dc* magnetic measurements were also carried out using a homemade high-sensitivity micro Hall-effect magnetometer at temperatures down to 0.4 K achieved by a Quantum Design PPMS device. *Alternating-current* (*ac*) susceptibility measurements were performed on the PPMS magnetometer.

V.5. Diffuse reflectance measurements.

UV-vis spectra were measured on a UV-2600 Shimadzu spectrophotometer.

V.6. Photoluminescence measurements.

Photoluminescence (PL) emission spectra and lifetime measurements were carried out for powdered samples from 10 K to room temperature using a close cycle helium cryostat contained in an Edinburgh Instruments FLS920 spectrometer. For the measurements an IK3552R-G HeCd continuous laser (325 nm), a EKSPLA NT 342B tunable OPO laser and a Müller-Elektronik- Optik SVX1450 Xe lamp were used as excitation sources. The lifetime measurements were performed by using a μF1 pulsed microsecond flashlamp as excitation source. Photographs were taken in a micro-photoluminescence system included in an Olympus optical microscope (Colour View III camera) illuminated with a Hg lamp.

V.7. Thermogravimetric analisis.

Thermogravimetric thermal analysis (TGA) of **55** was carried out from room temperature to 600 °C at a rate of 10 °C/min on a TGA Q500 V20.8 Build 34 thermobalance with a 60 mL/min flow of nitrogen.

V. CASIMIR-DU PRÈ AND DEBYE EQUATIONS

In order to relate the measured susceptibility to the relaxation process in a magnetic system, Casimir and Du Pré in 1938 firstly proposed the thermodynamic model for spin-lattice relaxation.[5] Here, if the magnetic system experiences a single-relaxation process characterized by a single-relaxation time, $\tau = \omega^{-1} = 1/(2\pi\nu)$, the Argand diagram ($\chi$" *vs.* χ' diagram) would show a semicircle with a center on the *x*-axis (Figure A.5, left) and the expression for the complex *ac* susceptibility can be derived in a mathematically analogous relations to dielectrics from Debye (Debye model):

$$\chi_{ac}(\omega) = \chi_S + \frac{\chi_T - \chi_S}{1 + i\omega\tau} \qquad (\textit{Equation A.1})$$

where χ_T and χ_S are the isothermal and the adiabatic susceptibility, respectively. If the frequency ω of the *ac* field is low, $\omega\tau \ll 1$, the measured susceptibility is the isothermal susceptibility χ_T in the limit of the lowest field frequencies. On the other hand, if the oscillations of the *ac* field are fast compared to the time constant τ, $\omega\tau \gg 1$, the magnetic system remains isolated from its surroundings, and then the adiabatic susceptibility χ_S, lower than χ_T, is revealed.[6] The real (χ') and imaginary (χ") components can be split into:

$$\chi'(\omega) = \chi_S + \frac{\chi_T - \chi_S}{1 + (\omega\tau)^2} \qquad (\textit{Equation A.2})$$

$$\chi''(\omega) = (\chi_T - \chi_S)\frac{\omega\tau}{1 + (\omega\tau)^2} \qquad (\textit{Equation A.3})$$

The frequency ω peak, at which the absorption reaches its maximum, $\chi_{max} = 1/2(\chi_T - \chi_S)$, determines the relaxation time, $\tau = \omega^{-1} = 1/(2\pi\nu)$. However, for most magnetic samples, the relaxation process is not characterized by a single τ but rather by a distribution of relaxation times. The Argand plot is thus flatten (Figure A.5, right), and the $\chi_{ac}(\omega)$ can be modified in the Cole–Cole expression:[7]

$$\chi_{ac}(\omega) = \chi_S + \frac{\chi_T - \chi_S}{1+(i\omega\tau)^{1-\alpha}} \qquad (\textit{Equation A.4})$$

where *α* is introduced to describe the distribution of relaxation times in a magnetic system, and its value changes between 0 and 1. The wider is the distribution in relaxation times, the larger is the value of *α*. The real (χ') and imaginary (χ") components can be split into:

$$\chi'(\omega) = \chi_S + (\chi_T - \chi_S)\frac{1+(\omega\tau)^{1-\alpha}\sin(\frac{\pi}{2}\alpha)}{1+2(\omega\tau)^{1-\alpha}\sin\left(\frac{\pi}{2}\alpha\right)+(\omega\tau)^{2-2\alpha}} \qquad (\textit{Equation A.5})$$

$$\chi''(\omega) = (\chi_T - \chi_S)\frac{(\omega\tau)^{1-\alpha}\cos(\frac{\pi}{2}\alpha)}{1+2(\omega\tau)^{1-\alpha}\sin\left(\frac{\pi}{2}\alpha\right)+(\omega\tau)^{2-2\alpha}} \qquad (\textit{Equation A.6})$$

Therefore, the real (χ') and imaginary (χ") components for a given *ac* magnetic data can be fitted easily to the Equations A. 5 and A.6, respectively.

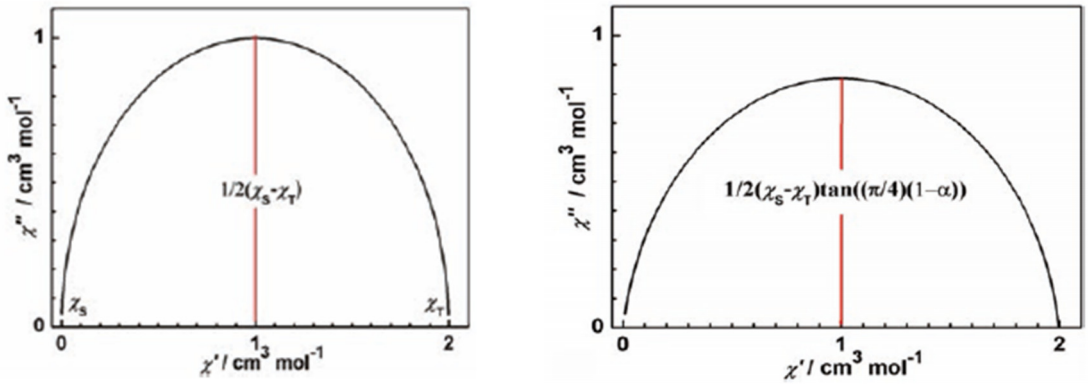

Figure A.5.- The so-called Argan diagram with a single-relaxation process characterized by a single-relaxation time (left) and with a distribution of relaxation times characterized by α parameter (right).

VI. COMPUTATIONAL DETAILS

The theoretical calculations on complexes **2**-**10** were carried out by Dr. Antonio J. Mota at the University of Granada at the density functional theory (DFT) level using the hybrid B3LYP exchange-correlation functional,[8] as implemented in the Gaussian 09 program.[9] A quadratic convergence method was employed in the self-consistent-field process.[10] The triple-ζ quality basis set proposed by Ahlrichs and co-workers has been used for all atoms.[11] Calculations were performed on complexes built from experimental geometries as well as on model complexes. The electronic

configurations used as starting points were created using Jaguar 7.9 software.[12] The approach used to determine the exchange coupling constants for polynuclear complexes has been described in detail elsewhere.[13]

DFT calculations on **22**, **27** and **40** were performed by Dr. Eider San Sebastián at The Basque Country University following the same procedure but using CREMBEL pseudopotential[14] for core electrons of metal atoms instead of the triple-ζ quality basis.

DFT calculations on **37**, **42** and **44** were performed by Dr. A. J. Mota using the SIESTA (Spanish Initiative for Electronic Simulations with Thousands of Atoms) code[15] together with the PBE functional.[16] In complex **37**, bromine atoms were substituted by chlorine atoms.

For complexes **46** and **54**, theoretical calculations were performed by Dr. D. Aravena and Dr. E. Ruiz at the University of Barcelona. Low-energy spectra and g factors of the eight lowest Kramer's doublets were obtained by means of CASSCF+RASSI calculations, as implemented in the MOLCAS 7.8 software package.[17] The method is divided in two steps: 1) CASSCF(9,7) calculations for three different multiplicities (sextet, quartet and doublet), 2) The effect of spin–orbit coupling on the basis of the converged wavefunctions obtained in the previous step is included by the restricted active space state interaction (RASSI) method. Spin Hamiltonian parameters (such as g factors) can be calculated from the wavefunctions resulting from the state interaction step employing the SINGLE ANISO program. We included 21, 128 and 98 roots for the sextet, quartet and doublet CASSCF calculations, while the employed basis set has the following contractions: Dy[9s8p6d4f3g2h]; Br [4s3p2d1f]; Zn [4s3p2d1f]; Cl [4s3p1d]; O [4s3p2d1f]; N [4s3p2d1f]; C [3s2p]; H [2s]. The structure of the model was extracted from the corresponding X-ray structure without any ligand truncation. Electrostatic potential maps were obtained by DFT calculations (functional: B3LYP, basis: TZVP, program: Gaussian09),[9] employing the geometry for the ligand environment of the previous CASSCF + RASSI calculations and removing the DyIII ion.

VII. BIBLIOGRAPHY

[1] *CrysAlisPro Software System*, Agilent Technologies UK Ltd, Oxford, UK, **2012**.

[2] G. M. Sheldrick, *Acta Crystallogr., Sect. A: Fundam. Crystallogr*., **2008**, *64*, 112.

[3] O. V. Dolomanov, L. J. Bourhis, R. J. Gildea, J. A. K. Howard, H. Puschmann, *J. Appl. Crystallogr.,* **2009**, *42*, 339.

[4] L. J. Farrugia, *J. Appl. Crystallogr*., **1999**, *32*, 837.

[5] H. B. G. Casimir, F. K. du Pré, *Physica*, **1938**, *5*, 507.

[6] **a)** D. Gatteschi, R. Sessoli, J. Villain, *Molecular Nanomagnets*, Oxford University Press, Oxford, UK, **2006**; **b)** Y.-N. Guo, G.-F. Xu, Y. Guo Y, J. Tang, *Dalton Trans*., **2011**, *40*, 9953.

[7] K. S. Cole, H. R. Cole, *J. Chem. Phys*, **1941**, *9*, 341.

[8] **a)** A. D. Becke, *Phys. Rev. A*, **1988**, *38*, 3098; **b)** C. T. Lee, W. T. Yang, R. G. Parr, *Phys. Rev. B*, **1988**, *37*, 785; **c)** A. D. Becke, *J. Chem. Phys*., **1993**, *98*, 5648.

[9] M. J. Frisch, G. W. Trucks, H. B. Schlegel, G. E. Scuseria, M. A. Robb, J. R. Cheeseman, J. A. Montgomery Jr., T. Vreven, K. N. Kudin, J. C. Burant, J. M. Millam, S. S. Iyengar, J. Tomasi, V. Barone, B. Mennucci, M. Cossi, G. Scalmani, N. Rega, G. A. Petersson, H. Nakatsuji, M. Hada, M. Ehara, K. Toyota, R. Fukuda, J. Hasegawa, M. Ishida, T. Nakajima, Y. Honda, O. Kitao, H. Nakai, M. Klene, X. Li, J. E. Knox, H. P. Hratchian, J. B. Cross, C. Adamo, J. Jaramillo, R. Gomperts, R. E. Stratmann, O. Yazyev, A. J. Austin, R. Cammi, C. Pomelli, J. W. Ochterski, P. Y. Ayala, K. Morokuma, G. A. Voth, P. Salvador, J. J. Dannenberg, V. G. Zakrzewski, S. Dapprich, A. D. Daniels, M. C. Strain, O. Farkas, D. K. Malick, A. D. Rabuck, R. Raghavachari, J. B. Foresman, J. V. Ortiz, Q. Cui, A. G. Baboul, S. Clifford, J. Cioslowski, B. B. Stefanov, G. Liu, A. Liashenko, P. Piskorz, I. Komaromi, R. L. Martin, D. J. Fox, T. Keith, M. A. Al-Laham, C. Y. Peng, A. Nanayakkara, M. Challacombe, P. M. W. Gill, B. Johnson, W. Chen, M. W. Wong, C. Gonzalez, J. A. Pople, GAUSSIAN 03 (Revision C.0), Gaussian, Inc., Wallingford, CT, **2004**.

[10] G. B. Bacskay, *Chem. Phys*., **1981**, *61*, 385.

[11] A. Schäfer, C. Huber, R. Ahlrichs, *J. Chem. Phys*., **1994**, *100*, 5829.

[12] Jaguar 7.6, Schrödinger, Inc., Portland, OR, **2009**.

[13] **a)** E. Ruiz, J. Cano, S. Alvarez, P. Alemany, *J. Comput. Chem*., **1999**, *20*, 1391; **b)** E. Ruiz, S. Alvarez, A. Rodríguez-Fortea, P. Alemany, Y. Puoillon, C. Massobrio, in *Magnetism: Molecules to Materials*, ed. J. S. Miller and M. Drillon, Wiley-VCH, Weinheim, **2001**, vol. II, p. 5572; **c)** E. Ruiz, A. Rodríguez-Fortea, J. Cano, S. Alvarez, P. Alemany, *J. Comput. Chem*., **2003**, *24*, 982; **d)** E. Ruiz, S. Alvarez, J. Cano, V. Polo, *J. Chem. Phys*., **2005**, 123, 164110.

[14] **a)** M. M. Hurley, L. Fernandez Pacios, P. A. Christiansen, R. B. Ross, W. C. Ermler, *J. Chem. Phys.*, **1986**, *84*, 6840; **b)** R. B. Ross, W. C. Ermler, S. Das, To be published.

[15] J. M. Soler, E. Artacho, J. D. Gale, A. Garcia, J. Junquera, P. Ordejon, D. J. Sanchez-Portal, *Phys.: Condens. Matter*, **2002**, *14*, 2745.

[16] J. P. Perdew, K. Burke, M. Ernzerhof, *Phys. Rev. Lett*., **1996**, *77*, 3865.

[17] F. Aquilante, L. De Vico, N. Ferré, G. Ghigo, P.-Å. Malmqvist, P. Neogrády, T. B. Pedersen, M. Pitoňák, M. Reiher, B. O. Roos, L. Serrano-Andrés, M. Urban, V. Veryazov and R. J. Lindh, *Comput. Chem.,* **2010**, *31*, 224.